

University of Ioannina
School of Sciences
Department of Physics



Detailed assessment of the global dimming and brightening of the Earth under all-sky and clear sky conditions using modern tools and long-term climate data

PhD Thesis

Michael Stamatis

Ioannina, 2025

We acknowledge support of this work by the project “Dioni: Computing Infrastructure for Big-Data Processing and Analysis.” (MIS No. 5047222), which is implemented under the Action “Reinforcement of the Research and Innovation Infrastructure”, funded by the Operational Programme “Competitiveness, Entrepreneurship and Innovation” (NSRF 2014–2020) and co-financed by Greece and the European Union (European Regional Development Fund).



Πανεπιστήμιο Ιωαννίνων
Σχολή Θετικών Επιστημών
Τμήμα Φυσικής



Λεπτομερής εκτίμηση του φαινομένου πλανητικής σκίασης και λάμπρυνσης της Γης υπό συνθήκες ανέφελου και νεφοσκεπούς ουρανού με χρήση σύγχρονων εργαλείων και μακροχρόνιων κλιματικών δεδομένων

Διδακτορική Διατριβή

Μιχαήλ Σταμάτης

Ιωάννινα, 2025

Η εργασία αυτή υλοποιήθηκε στο πλαίσιο της Πράξης «Διώνη: Υπολογιστική Υποδομή Επεξεργασίας και Ανάλυσης Μεγάλου Όγκου Δεδομένων» (MIS No. 5047222) που εντάσσεται στη Δράση «Ενίσχυση των Υποδομών Έρευνας και Καινοτομίας» και χρηματοδοτείται από το Επιχειρησιακό Πρόγραμμα «Ανταγωνιστικότητα, Επιχειρηματικότητα και Καινοτομία» στο πλαίσιο του ΕΣΠΑ 2014-2020, με τη συγχρηματοδότηση της Ελλάδας και της Ευρωπαϊκής Ένωσης (Ευρωπαϊκό Ταμείο Περιφερειακής Ανάπτυξης).



Three-member Advisory Committee:

Nikolaos Hatzianastassiou (Supervisor)
Professor, Department of Physics, University of Ioannina

Martin Wild (Advisor)
Professor, Department of Environmental Systems Science, ETH Zürich

Christos Matsoukas (Advisor)
Associate Professor, Department of Environment, University of the Aegean

Seven-member Examination Committee:

Nikolaos Hatzianastassiou (Supervisor)
Professor, Department of Physics, University of Ioannina

Martin Wild (Advisor)
Professor, Department of Environmental Systems Science, ETH Zürich

Christos Matsoukas (Advisor)
Associate Professor, Department of Environment, University of the Aegean

Andreas Kazantzidis
Professor, Department of Physics, University of Patras

Christos Lolis
Associate Professor, Department of Physics, University of Ioannina

Nikolaos Bakas
Assistant Professor, Department of Physics, University of Ioannina

Angeliki Fotiadi
Assistant Professor, Department of Physics, University of Ioannina

To my family

Acknowledgements

I would like to express my heartfelt gratitude to my supervisor, Prof. Nikolaos Hatzianastassiou. His unwavering support, insightful guidance, and steady encouragement have made an immense difference throughout every stage of my PhD journey. I am truly grateful for his patience, his trust in my abilities, and his readiness to offer help whenever I faced challenges—no matter how big or small. His deep knowledge, constructive feedback, and genuine care for both my academic growth and personal well-being have been a source of inspiration. It has been a privilege to work under his supervision, and I sincerely thank him for being a constant source of strength and motivation during this transformative period of my life.

I am also sincerely grateful to the members of my advisory committee, Prof. Martin Wild and Prof. Christos Matskoukas, for their insightful advice, guidance, and feedback. Additionally, I extend my heartfelt thanks to the examination committee members, Prof. Andreas Kazantzidis, Prof. Christos Lolis, Prof. Nikolaos Bakas and Prof. Aggeliki Fotiadi for their valuable support.

I would also like to thank Dr. Marios-Bruno Korras-Carraca and Dr. Maria Gavrouzou for their support and for making my time in the lab an enjoyable and enriching experience. To my dear friends, thank you for your patience and encouragement during these demanding academic years.

A very special and profound thank you goes to my lovely Ksenia. Her unwavering support, kindness, and encouragement have been a pillar of strength throughout this journey. Her belief in me, even in the most challenging moments, has been truly invaluable.

Last but certainly not least, I am deeply grateful to my parents and my family for their unconditional love and support. Their faith in me and their encouragement at every step have been the foundation of this achievement.

Περίληψη

Η ηλιακή ακτινοβολία μικρού μήκους κύματος αποτελεί την κύρια εξωτερική πηγή ενέργειας της Γης, καθώς και την πρωταρχική και κυρίαρχη πηγή ενέργειας για το κλιματικό της σύστημα. Για το λόγο αυτό, οι διακυμάνσεις στην εισερχόμενη ηλιακή ακτινοβολία στην κορυφή της ατμόσφαιρας και στην επιφάνεια της Γης, μπορούν να έχουν σημαντικές επιπτώσεις στο κλίμα της Γης και στην ποιότητα ζωής στον πλανήτη μας. Πριν φτάσει στην επιφάνεια της Γης, η ηλιακή ακτινοβολία διασχίζει ολόκληρη την ατμόσφαιρα, αλληλεπιδρώντας με τα συστατικά της, όπως τα νέφη, τα αερολύματα και τα αέρια. Η ποσότητα της ηλιακής ενέργειας που φτάνει στο έδαφος αποτελεί μόνο ένα μέρος της ακτινοβολίας που εισέρχεται στην ατμόσφαιρα, καθώς πολλά ατμοσφαιρικά στοιχεία απορροφούν ή/και σκεδάζουν την ακτινοβολία σε συγκεκριμένες περιοχές μήκους κύματος. Κατά μέσον όρο, 340 Wm^{-2} εισέρχονται στην ατμόσφαιρα της Γης σε παγκόσμια κλίμακα και μέση ετήσια βάση, ωστόσο μόνο περίπου 185 Wm^{-2} φτάνουν στην επιφάνεια της Γης (Wild et al., 2013). Ωστόσο, οι τιμές αυτές, που αντιπροσωπεύουν παγκόσμιους και ετήσιους μέσους όρους, μεταβάλλονται σημαντικά ανάλογα με τη γεωγραφική θέση, την εποχή και το έτος και, φυσικά, το ημερήσιο κύκλο.

Οι πολυδεκαετείς διακυμάνσεις της ηλιακής ακτινοβολίας που φθάνει στην επιφάνεια της Γης (SSR) έχουν σημαντικές επιπτώσεις σε πολλές σημαντικές περιβαλλοντικές διεργασίες, καθώς και σε πολυάριθμες πρακτικές εφαρμογές, όπως η παραγωγή ηλιακής ενέργειας, η γεωργική παραγωγή και η ανθρώπινη υγεία, δεδομένου ότι η διαθεσιμότητα του ηλιακού φωτός είναι απαραίτητη για κάθε οικοσύστημα και την ύπαρξη της ζωής εν γένει. Παρά ταύτα, τα αίτια αυτών των διακυμάνσεων εξακολουθούν να αποτελούν αντικείμενο συζήτησης και να στερούνται σαφών αποδείξεων. Στην πραγματικότητα, η SSR μεταβάλλεται σημαντικά κατά τη διάρκεια δεκαετιών, σύμφωνα τόσο με μια σειρά μελετών που εξετάζουν καταγραφές της SSR σε ευρέως διάσπαρτες τοποθεσίες παρατήρησης (π.χ. Wang et al., 2012; Wild 2009, 2016, και αναφορές σε αυτές) όσο και με μελέτες μοντελοποίησης με παγκόσμια κάλυψη με χρήση σύγχρονων δορυφορικών προϊόντων (π.χ. Pinker et al., 2005; Hatzianastassiou et al., 2012). Οι πρώτες ενδείξεις μείωσης της SSR από τη δεκαετία του 1950 καταγράφηκαν στα τέλη της δεκαετίας του 1980 και στις αρχές της δεκαετίας του 1990 σε πολυάριθμες τοποθεσίες (Ohmura and Lang, 1989; Stanhill and Moreshet, 1992). Το φαινόμενο αυτό απέκτησε στη συνέχεια ευρεία αναγνώριση και αναφέρθηκε ως "παγκόσμια σκίαση" ή global dimming (Stanhill and Cohen, 2001). Στις αρχές της δεκαετίας του 2000 συνειδητοποιήθηκε ότι η μείωση της SSR είχε σταματήσει και είχε, στην πραγματικότητα, αντιστραφεί σε πολλές από τις τοποθεσίες παρατήρησης από τη δεκαετία του 1980 - ένα φαινόμενο γνωστό ως "παγκόσμια λάμπρυνση" ή global brightening (Wild et al., 2005), δηλαδή η SSR άρχισε να αυξάνεται. Το φαινόμενο λοιπόν της αύξησης και μείωσης της SSR ονομάστηκε παγκόσμια σκίαση και λάμπρυνση ή global dimming and brightening (GDB). Στη συνέχεια, στην πρώτη δεκαετία του 21ου αιώνα παρατηρήθηκε μια εξομάλυνση της λάμπρυνσης ή ακόμη και μια ασθενής σκίαση, η οποία συνοδεύτηκε από μια λάμπρυνση κατά τη διάρκεια της δεκαετίας του 2010 (Wild, 2016, Hatzianastassiou et al., 2020; Stamatis et al., 2022, 2023). Σύμφωνα με διάφορες μελέτες (π.χ. Hatzianastassiou et al., 2005; Pfeifroth et al., 2018; Pinker et al., 2005, Posselt et al., 2014; Sanchez-Lorenzo et al., 2017), τα προϊόντα που προέρχονται από δορυφόρους έχουν επίσης δείξει τάσεις SSR από τα μέσα της δεκαετίας του '80. Οι μεταβολές της φωτεινότητας από τον Ήλιο δεν μπορούν να εξηγήσουν

τις δεκαετείς μεταβολές της SSR, καθώς αυτές είναι τουλάχιστον μια τάξη μεγέθους μικρότερες (Willson and Mordvinov 2003) και φαίνεται ότι είναι ασυσχέτιστες (Aparicio et al., 2020). Συνεπώς, οι μεταβολές στη διαφάνεια της ατμόσφαιρας, οι οποίες εξαρτώνται από τα νέφη, τα αερολύματα και τα αέρια, πρέπει να είναι η αιτία των παρατηρούμενων μεταβολών της SSR (Kim and Ramanathan 2008; Kvalevag and Myhre 2007). Πράγματι, τα αερολύματα και τα νέφη αναφέρθηκαν ως οι κύριοι παράγοντες του φαινομένου, συμβάλλοντας στο GDB σε διαφορετικό βαθμό ανάλογα με την περιοχή και τη δεκαετία (Hatzianastassiou et al., 2020; Wild 2016). Παρόλο που οι διακυμάνσεις της νεφοκάλυψης επηρεάζουν αποτελεσματικά το GDB σε από έτος-σε-έτος βάση, δεν είναι πάντα σαφές πώς αυτές οι διακυμάνσεις σχετίζονται με τις πιο μακροπρόθεσμες (δεκαετείς) τάσεις μεταβολής της SSR που έχουν παρατηρηθεί (π.χ. Qian et al. 2006; Norris and Wild 2007). Έχουν επίσης αναφερθεί σκίαση και λάμπρυνση σε καθαρές ατμόσφαιρες, στις οποίες απουσιάζουν τα νέφη, σε διάφορα μέρη, γεγονός που υποδηλώνει ότι τα ατμοσφαιρικά αερολύματα παίζουν σημαντικό ρόλο (π.χ. Wild et al. 2005, 2021; Alpert et al., 2005; Norris and Wild 2007; Sanchez-Lorenzo et al. 2009; Ohvril et al. 2009; Zerefos et al. 2009; Correa et al., 2024a,b,c; Ruckstuhl and Norris 2009; Allen et al. 2013; Turnock et al. 2015; Norris et al. 2016; Freychet et al. 2019; Cherian and Quaas 2020; Nabat et al. 2014). Τα αερολύματα, τα οποία δρουν ως πυρήνες συμπύκνωσης νεφών (CCN) ή πυρήνες πάγου (IN), μπορούν να αυξήσουν την ανακλαστικότητα και τη διάρκεια ζωής των νεφών (πρώτη και δεύτερη έμμεση επίδραση) και μέσω αυτών και την ηλιακή ακτινοβολία. Εκτός αυτού, τα αερολύματα μπορούν να εξασθενήσουν άμεσα την ηλιακή ακτινοβολία σκεδάζοντας και απορροφώντας την (άμεση επίδραση) (Ramanathan et al. 2001; Lohmann and Feichter 2005). Τις τελευταίες δεκαετίες, η ανθρωπογενής ατμοσφαιρική ρύπανση έχει μεταβάλει σημαντικά τις ποσότητες των ατμοσφαιρικών αερολυμάτων (Stern 2006; Ruckstuhl et al. 2008; Streets et al. 2006, 2009; Wang et al. 2012). Σύμφωνα με τους Streets et al. (2009), οι εκπομπές αερολυμάτων και του οπτικού τους βάθους (Aerosol Optical Depth ή AOD) είναι συνεπείς με τις παρατηρούμενες τάσεις σκίασης/λάμπρυνσης σε ορισμένες περιοχές της Γης, υποδεικνύοντας ότι η ανθρωπογενής ατμοσφαιρική ρύπανση μπορεί να είναι ένας σημαντικός παράγοντας για την εξήγηση των διακυμάνσεων της SSR. Ωστόσο, πολλές άλλες έρευνες (Liepert, 1997; Wild et al. 2005; Liley, 2009; Kumari and Goswami, 2010; Augustine and Dutton, 2013; Allen et al. 2013; Mateos et al., 2014; Wild 2016; Norris et al. 2016; Sanchez-Lorenzo et al. 2017; Pfeifroth et al., 2018; Correa et al., 2024a,b,c) έδειξαν επίσης ότι οι αλλαγές στα χαρακτηριστικά των νεφών αποτελούν σημαντικές αιτίες σκίασης ή/και λάμπρυνσης. Οι μεταβολές στη νεφοκάλυψη που προκαλούνται από την εσωτερική δεκαετή μεταβλητότητα της ατμόσφαιρας και του ωκεανού, μπορεί επίσης να έπαιξαν ρόλο στις μεταβολές της SSR (Romanou et al., 2007; Folini et al., 2017; Augustine, J. A., & Capotondi, A., 2022; Chtirkova et al., 2022, 2023, 2024). Το σύνολο της βιβλιογραφίας που συζητήθηκε παραπάνω καταδεικνύει μια συνεχιζόμενη επιστημονική συζήτηση σχετικά με τα αίτια του GDB.

Παρά τις σημαντικές προόδους, εξακολουθεί να υπάρχει έλλειψη πλήρους βεβαιότητας, ιδίως όσον αφορά στη συμβολή των ατμοσφαιρικών συστατικών στο υπό μελέτη φαινόμενο. Έτσι, η παρούσα μελέτη είναι κρίσιμη για την αντιμετώπιση αυτών των κενών, παρέχοντας μια ολοκληρωμένη ανάλυση που καλύπτει τόσο τις επιφάνειες της ξηράς όσο και των ωκεανών, καλύπτοντας μια εκτεταμένη περίοδο μελέτης που ξεπερνά πολλές προηγούμενες μελέτες. Επιπλέον, χρησιμοποιούνται ατμοσφαιρικά δεδομένα τελευταίας τεχνολογίας, προσφέροντας υψηλότερο επίπεδο ακρίβειας και ανάλυσης από τα προηγούμενα διαθέσιμα σύνολα δεδομένων. Προσδιορίζοντας τα αίτια του GDB με μεγαλύτερη ακρίβεια, ιδίως μέσω της χρήσης μοντέλου διάδοσης ακτινοβολίας (RTM), βελτιώνεται όχι μόνο η

κατανόηση των παρελθουσών και σημερινών μεταβολών της SSR, αλλά και ενισχύεται η δυνατότητα πρόβλεψης μελλοντικών φάσεων του GDB γνωρίζοντας τις αναμενόμενες αλλαγές σε συγκεκριμένες ατμοσφαιρικές παραμέτρους.

Πέραν του φαινομένου και των αιτιών του, υπάρχουν ενδείξεις για κάποιες επιπτώσεις του στο κλίμα, όπως ενδείξεις ότι ο υδρολογικός κύκλος έχει αποδυναμωθεί λόγω της σκίασης (Liepert and Romanou, 2005). Η ζωή των φυτών μπορεί επίσης να επηρεαστεί σημαντικά από τη σκίαση και τη λάμπρυνση, ιδίως σε περιοχές μεγάλων γεωγραφικών πλατών όπου η φωτοσύνθεση και, κατά συνέπεια, ο ρυθμός ανάπτυξης περιορίζονται τόσο από τη θερμοκρασία του αέρα όσο και από τη διαθεσιμότητα του φωτός. Από την άλλη πλευρά, υπάρχουν ενδείξεις ότι το GDB μπορεί να επηρεάσει τους ρυθμούς υπερθέρμανσης του πλανήτη. Πιο συγκεκριμένα, έχει προταθεί (Wild et al. 2007) ότι η ηλιακή σκίαση από τα μέσα του 20ου αιώνα μέχρι τη δεκαετία του 1980 έκρυψε την εξελισσόμενη θέρμανση λόγω του ανθρωπογενούς φαινομένου του θερμοκηπίου, η οποία έγινε πλήρως εμφανής σε παγκόσμια κλίμακα μόνο κατά τη διάρκεια της λάμπρυνσης που ακολούθησε τη δεκαετία του 1980 κι έπειτα. Από την άλλη πλευρά, τα τελευταία χρόνια, η ύπαρξη του μειωμένου ρυθμού υπερθέρμανσης του πλανήτη κατά τη δεκαετία του 2000, η οποία συνέπεσε χρονικά με την εξασθένιση της λάμπρυνσης, έχει συγκεντρώσει την επιστημονική προσοχή (England et al. 2015; Trenberth and Fasullo, 2013). Η συζήτηση και οι διαφωνίες για αυτή την επιβράδυνση υπογραμμίζει την πολυπλοκότητα του κλιματικού συστήματος Γης-ατμόσφαιρας και την ανάγκη λεπτομερούς ανάλυσης για τη διάκριση των βραχυπρόθεσμων διακυμάνσεων από τη συνολική τάση θέρμανσης που οφείλεται στο ανθρωπογενές φαινόμενο του θερμοκηπίου.

Συνεπώς, η μελέτη του GDB είναι ζωτικής σημασίας, διότι επηρεάζει την αλλαγή του κλίματος διαμορφώνοντας το ενεργειακό ισοζύγιο της Γης. Η κατανόηση των αιτιών του GDB είναι επίσης σημαντική, καθώς ο προσδιορισμός του κατά πόσον το GDB οφείλεται σε ανθρώπινες δραστηριότητες (π.χ. ρυθμός εκπομπής αερολυμάτων) ή σε φυσικούς παράγοντες (π.χ. ηφαιστειακές εκρήξεις, El Niño–Southern Oscillation (ENSO), μεταβλητότητα των νεφών) βοηθά στον προσδιορισμό της έκτασης της ανθρώπινης επίδρασης στο κλίμα και την κλιματική αλλαγή. Επίσης, οι γνώσεις σχετικά με το GDB και τα αίτιά του είναι απαραίτητες για την ακριβή μοντελοποίηση του κλίματος, τη μείωση των αβεβαιοτήτων της τρέχουσας επιστημονικής γνώσης, την πρόβλεψη των επιπτώσεων, τη βελτιστοποίηση των συστημάτων ηλιακής ενέργειας και τη διαχείριση των οικοσυστημάτων. Βοηθά, επίσης, τους υπεύθυνους χάραξης πολιτικής στην ανάπτυξη αποτελεσματικών μέτρων προσαρμογής και μετριασμού του κλίματος για την αντιμετώπιση των παγκόσμιων περιβαλλοντικών προκλήσεων.

Άρα, το βασικό ερώτημα της παρούσας διατριβής είναι: Πόσο, πού και πότε οι τάσεις μεταβολής των ατμοσφαιρικών παραμέτρων και ειδικά των νεφών και των αερολυμάτων επηρέασαν τις τάσεις της SSR κατά την περίοδο μελέτης 1984-2018. Στόχος είναι η βελτίωση της κατανόησης των παραμέτρων και του βαθμού στον οποίο αυτές συμβάλλουν στη σκίαση και λάμπρυνση της Γης, και η διερεύνηση των συσχετίσεων μεταξύ του GDB και των ρυθμών θέρμανσης του πλανήτη, δηλαδή ανοιχτών επιστημονικών ζητημάτων για τα οποία χρειάζεται περεταίρω διερεύνηση και μείωση της αβεβαιότητας.

Για το σκοπό αυτό, χρησιμοποιήθηκε ένα λεπτομερές φασματικό μοντέλο διάδοσης ακτινοβολίας (FORTH-RTM: Foundation for Research and Technology – Hellas Radiative Transfer Model), το οποίο περιγράφεται και αξιολογείται διεξοδικά από τους Hatzianastassiou et al. (2020), Stamatis et al. (2023) και άλλους (μέσα στις αναφορές αυτών των εργασιών) και διακρίνει την ατμόσφαιρα σε ανέφελα και νεφοσκεπή (χαμηλού, μεσαίου και υψηλού επιπέδου/υψομέτρου νέφη) κλάσματα. Επιλύει ένα σύνολο μονοχρωματικών εξισώσεων διάδοσης ακτινοβολίας χρησιμοποιώντας την τροποποιημένη μέθοδο Delta Eddington και λαμβάνει υπόψη τη σκέδαση και απορρόφηση νεφών και αερολυμάτων, τη σκέδαση Rayleigh, τη μοριακή απορρόφηση στο υπεριώδες, στο ορατό και στο εγγύς υπέρυθρο φάσμα της ηλιακής ακτινοβολίας και την ανακλαστικότητα της επιφάνειας. Το μοντέλο τρέχει σε μηνιαία βάση με ανάλυση γεωγραφικού πλάτους × μήκους 0.5° × 0.625° και υπολογίζει την SSR (σε Wm^{-2}) στις αντίστοιχες χρονικές και χωρικές αναλύσεις. Τα εν χρήσει λεπτομερή δεδομένα εισόδου νεφών μόνο κατά τη διάρκεια του φωτισμένου τμήματος της ημέρας είναι η νεφοκάλυψη (Cloud Amount ή CA) για χαμηλού (CA1), μεσαίου (CA2) και υψηλού επιπέδου νέφη (CA3), το οπτικό βάθος νεφών (Cloud Optical Thickness ή COT) για χαμηλού (COT1), μεσαίου (COT2) και υψηλού (COT3) επιπέδου νέφη και η πίεση στην κορυφή του νέφους για νέφη υγρής και στερεής φάσης). Τα δεδομένα αυτά προήλθαν από τη βάση δεδομένων CLARISC η οποία δημιουργήθηκε στα πλαίσια αυτού του διδακτορικού και είναι ουσιαστικά η συνέργεια δύο δορυφορικών προϊόντων, του CLARA-A2 (CM-SAF Cloud, Albedo And Surface Radiation από το σύνολο δεδομένων AVHRR data–second edition) και του ISCCP-H (International Satellite Cloud Climatology Project-H series) . Αυτό έγινε για να απαλειφθούν οι διεθνώς καταγεγραμμένες ασυνέπειες στις τάσεις μεταβολής των νεφών από το ISCCP-H, οι οποίες οφείλονται στις ασυνέπειες στις γεωμετρίες παρατήρησης των δορυφόρων τους. Το οπτικό βάθος αερολυμάτων (AOD), η ανακλαστικότητα μεμονωμένης σκέδασης (Single Scattering Albedo ή SSA), ο παράγοντας ασυμμετρίας (Asymmetry parameter ή AP), η συγκέντρωση του όζοντος, η επιφανειακή albedo και η ειδική υγρασία υπολογίστηκαν από δεδομένα που ελήφθησαν από το Modern-Era Retrospective analysis for Research and Applications, Version 2 (MERRA-2) Reanalysis, όπως περιγράφεται από τους Gelaro et al. (2017) και Korras-Corraca et al. (2021).

Αρχικά, τα προετοιμασμένα δεδομένα εισόδου CLARISC και MERRA-2 εισήχθησαν στο FORTH-RTM, το οποίο έτρεξε και υπολόγισε τις ροές SSR. Αυτή η έκδοση του μοντέλου καλείται FMC (FORTH-MERRA-CLARISC) και είναι η έκδοση που χρησιμοποιήθηκε τελικά στην παρούσα διατριβή. Οι υπολογισμένες μηνιαίες ροές SSR επικυρώθηκαν έναντι μετρήσεων από τα επίγεια παγκόσμια δίκτυα σταθμών αναφοράς GEBA και BSRN. Σε αυτήν τη διαδικασία εφαρμόστηκαν συγκεκριμένα κριτήρια διαθεσιμότητας δεδομένων για την παροχή του βέλτιστου επιπέδου αξιοπιστίας για τα ευρήματα και τα συμπεράσματα που παράγονται. Βάσει αυτών, οι ροές SSR κάθε έτους έπρεπε να περιλαμβάνουν τουλάχιστον 10 μήνες με δεδομένα, προκειμένου να εξασφαλισθεί επαρκής εποχική εκπροσώπηση, η οποία θα υποβάθμιζε την ποιότητα της σύγκρισης. Επιπλέον, η υψομετρική διαφορά μεταξύ του σταθμού και του αντίστοιχου κελιού του MERRA-2 μέσα στο οποίο βρίσκεται ο σταθμός απαιτήθηκε να είναι μικρότερη από 500 μέτρα. Από τους αρχικούς 1545 σταθμούς GEBA και 73 BSRN, αντίστοιχα, 1091 σταθμοί GEBA και 64 BSRN έγιναν διαθέσιμοι ως αποτέλεσμα της χρήσης αυτών των κριτηρίων. Στη συνέχεια, οι μηνιαίες ροές SSR από το RTM και τους σταθμούς χρησιμοποιήθηκαν για τον υπολογισμό των στατιστικών δεικτών αξιολόγησης, του συντελεστή συσχέτισης Pearson's R, της απόλυτης και σχετικής απόκλισης (BIAS) και της απόλυτης και σχετικής ρίζας μέσου τετραγώνου του σφάλματος

(RMSE). Κάθε κυψελίδα του μοντέλου η οποία περιελάβανε σταθμό αξιολογήθηκε με αυτόν τον τρόπο. Επίσης, η ίδια αξιολόγηση, δηλαδή η ανάλυση συσχέτισης, επαναλήφθηκε με εκτίμηση και χρήση μέσων μηνιαίων απεποχοποιημένων ανωμαλιών SSR, με σκοπό την αφαίρεση του ισχυρού ετήσιου κύκλου της ηλιακής ακτινοβολίας. Επιπλέον, υπολογίστηκε η μη παραμετρική και πιο αξιόπιστη κλίση του Theil-Sen (Theil 1992, Sen 1968) η οποία εφαρμόστηκε στις χρονοσειρές ανωμαλιών της SSR και τελικά οι τάσεις μεταβολής της SSR του FORTH-RTM, δηλαδή το GDB, υπολογίστηκαν και συγκρίθηκαν με τις αντίστοιχες υπολογιζόμενες από τις επίγειες μετρήσεις των Σταθμών GEBA και BSRN. Σε αυτό το βήμα της εργασίας χρησιμοποιήθηκαν μόνο χρονοσειρές με κάλυψη δεδομένων μεγαλύτερη από το 70% της προσαρμοσμένης στο RTM προσωρινής διαθεσιμότητας ολόκληρης της χρονικής περιόδου κάθε δικτύου (1984-2018 για το GEBA και 1992-2018 για το BSRN), ενώ η στατιστική σημαντικότητα των τάσεων μεταβολής εκτιμήθηκε με το τεστ Mann-Kendall (Mann 1945; Kendall 1975).

Εκτός από τη διαδικασία αξιολόγησης, διερευνήθηκαν οι τάσεις μεταβολής των παραμέτρων εισόδου του μοντέλου για όλη τη χρονική περίοδο μελέτης 1984-2018 όπως και για τις 4 τελευταίες δεκαετίες παγκοσμίως, σε ημισφαιρική κλίμακα καθώς επίσης και πάνω από 18 συγκεκριμένες επιλεγμένες περιοχές ξηράς του πλανήτη. Αυτές οι περιοχές επιλέχθηκαν για να αντιπροσωπεύουν όλες τις ηπείρους. Η διερεύνηση των μεταβολών των παραμέτρων εισόδου του FORTH-RTM έγινε για τον ποιοτικό προσδιορισμό των αιτίων του GDB, καθώς η αυξητική/φθίνουσα τάση μεταβολής αυτών των δεδομένων εισόδου (που καθορίζουν τη διαφάνεια της ατμόσφαιρας) οδηγεί σε μείωση/αύξηση της SSR, προκαλώντας έτσι σκίαση/λάμπρυνση. Ωστόσο, προκειμένου να εντοπιστούν και να προσδιοριστούν με μεγαλύτερη ακρίβεια τα αίτια του GDB, συγκεκριμένα η συνεισφορά των τάσεων μεταβολής στα νέφη, στα αερολύματα, στους υδρατμούς και στο όζον, στο εκτιμώμενο GDB κατά τη διάρκεια της 35ετίας 1984 - 2018, εφαρμόστηκε μια άλλη μέθοδος. Σύμφωνα με αυτή, η συνεισφορά στο GDB (σε Wm^{-2}) κάθε φυσικής ατμοσφαιρικής παραμέτρου εισόδου P υπολογίζεται μέσω δύο τρεξιμάτων του RTM. Στο πρώτο τρέξιμο, η παράμετρος P διατηρήθηκε σταθερή στις αρχικές συνθήκες της, δηλαδή εκείνες του πρώτου έτους της περιόδου μελέτης, δηλαδή το 1984, ενώ όλες οι υπόλοιπες παράμετροι μεταβλήθηκαν κανονικά. Στο δεύτερο τρέξιμο όλες οι παράμετροι εισόδου ήταν ενεργοποιημένες και μεταβαλλόταν κανονικά (κύρια εκτέλεση RTM). Στη συνέχεια, οι αλλαγές της SSR (GDB) εκτιμήθηκαν με βάση τις δύο εκτελέσεις RTM. Από τη διαφορά μεταξύ του GDB της κύριας εκτέλεσης RTM, με όλες τις παραμέτρους ενεργοποιημένες, και του GDB από εκτελέσεις με σταθερές παραμέτρους P, υπολογίστηκε η συμβολή της παραμέτρου P στο συνολικό GDB. Όταν η συνεισφορά μιας παραμέτρου ήταν θετική, σημαίνει ότι οι τάσεις μεταβολής της παραμέτρου P οδήγησαν σε αύξηση της SSR και είτε συνέβαλαν ή προκάλεσαν εν μέρει την εκτιμώμενη λάμπρυνση, είτε εξουδετέρωσαν την εκτιμώμενη σκίαση. Από την άλλη πλευρά, εάν η συνεισφορά μιας παραμέτρου ήταν αρνητική, αυτό σημαίνει ότι οι τάσεις μεταβολής της παραμέτρου P οδήγησαν σε μείωση της SSR και είτε συνέβαλαν ή προκάλεσαν εν μέρει την εκτιμώμενη σκίαση, είτε εξουδετέρωσαν την εκτιμώμενη λάμπρυνση.

Για τη διερεύνηση των αιτίων των διακυμάνσεων των μηνιαίων ανωμαλιών SSR από το 1984 έως το 2018, χρησιμοποιήθηκαν τρεις συμπληρωματικές αναλυτικές μέθοδοι: η συσχέτιση Pearson, η παλινδρόμηση Ridge και η Random Forest παλινδρόμηση. Κάθε μέθοδος επιλέχθηκε για τη μοναδική ικανότητά της να αντιμετωπίζει διαφορετικές πτυχές των δεδομένων και να προσφέρει πληροφορίες για τις πολύπλοκες σχέσεις μεταξύ των διακυμάνσεων της SSR και των παραμέτρων που την μεταβάλουν (οδηγοί). Η

συσχέτιση Pearson χρησιμοποιήθηκε για τον εντοπισμό αρχικών, απλών γραμμικών συσχετίσεων μεταξύ της SSR και των οδηγών της, όπως τα νέφη, τα αερολύματα, οι υδρατμοί και το όζον. Η παλινδρόμηση Ridge χρησιμοποιήθηκε στη συνέχεια για να βελτιωθεί το επίπεδο κατανόησης αντιμετωπίζοντας τους περιορισμούς των γραμμικών μοντέλων όταν κάποιες ανεξάρτητες μεταβλητές συσχετίζονται έντονα μεταξύ τους (πολυσυγγραμμικότητα). Τέλος, η μέθοδος μηχανικής εκμάθησης, Random Forest παλινδρόμηση, χρησιμοποιήθηκε για να καταγράψει τις μη γραμμικές, πολύπλοκες αλληλεπιδράσεις μεταξύ της SSR και των οδηγών της που δε μπορούν να αντιμετωπιστούν επαρκώς με τη συσχέτιση Pearson ή την παλινδρόμηση Ridge. Με το συνδυασμό αυτών των τριών μεθόδων, επιτεύχθηκε μια όσο το δυνατό πιο ολοκληρωμένη κατανόηση των παραγόντων που επηρεάζουν τις από μήνα-σε-μήνα μεταβολές της SSR.

Επιπρόσθετα, έγινε η προσπάθεια ανίχνευσης πιθανής σχέσης του GDB και των ρυθμών θέρμανσης της Γης. Για το σκοπό αυτό, υπολογίστηκαν αρχικά οι συντελεστές συσχέτισης Pearson (R), μαζί με τη στατιστική τους σημαντικότητα σε επίπεδο εμπιστοσύνης 95%, ποσοτικοποιώντας τη συσχέτιση μεταξύ των μηνιαίων χρονοσειρών των απεποχικοποιημένων ανωμαλιών SSR και θερμοκρασίας στα 2 μέτρα από την επιφάνεια της Γης (μέση-Tmean, μέγιστη ημερήσια - Tmax, ελάχιστη ημερήσια - Tmin, ενδοημερήσιο θερμοκρασιακό εύρος - DTR). Αυτοί οι συντελεστές υπολογίστηκαν για κάθε κελί πλέγματος για ολόκληρη τη χρονική περίοδο 1984-2018. Στη συνέχεια, παρήχθησαν οι χρονοσειρές των μέσων ετήσιων ανωμαλιών της SSR και των θερμοκρασιών, που υπολογίστηκαν σε σχέση με ολόκληρη την περίοδο μελέτης. Στη συνέχεια, το χαμηλοπερατό φίλτρο Savitzky–Golay (SG, Schafer, 2011), εφαρμόστηκε στις ετήσιες μέσες χρονοσειρές με μέγεθος παραθύρου 10 ετών, προκειμένου να αποκαλυφθούν πιθανές μακροπρόθεσμες σχέσεις μεταξύ της SSR και των επιφανειακών θερμοκρασιών σε παγκόσμια, ημισφαιρική, χερσαία και ωκεάνια κλίμακα καθώς και κατά τη θερμή (Απρίλιος-Σεπτέμβριος) και ψυχρή (Οκτώβριος-Μάρτιος) περίοδο του έτους. Επίσης, εφαρμόστηκε η μη παραμετρική και αξιόπιστη κλίση Theil-Sen και το τεστ Mann-Kendall για τον προσδιορισμό των ετήσιων μεταβολών της SSR και των θερμοκρασιών και της στατιστικής σημαντικότητας τους στο επίπεδο εμπιστοσύνης 95%. Επιπλέον, για τις προαναφερθείσες επιλεγμένες 18 περιοχές ξηράς του πλανήτη, που καλύπτουν σχεδόν όλες τις ηπείρους, υπολογίστηκαν και συγκρίθηκαν μεταξύ τους οι δεκαετιακές μεταβολές της SSR και των θερμοκρασιών για 3 διαφορετικές χρονικές περιόδους (1984-1999, 2000-2009, 2010-2018).

Προχωρώντας στην συζήτηση των αποτελεσμάτων της παρούσας διατριβής, στο πρώτο μέρος, το FORTH-RTM υπολόγισε την SSR και υπολογίστηκε το αντίστοιχο GDB. Οι μέσες μηνιαίες τιμές της SSR, παγκοσμίως για την περίοδο 1984-2018, κυμαίνονται μεταξύ 0 και 301 Wm^{-2} και η μέση ετήσια πλανητική τιμή είναι 183.99 Wm^{-2}. Σε τοπικό επίπεδο, οι υψηλότερες τιμές παρατηρούνται στις ανέφελες περιοχές του Ατλαντικού και Ειρηνικού Ωκεανού (περιοχές μόνιμων αντικυκλώνων), στον Κόλπο του Μεξικού, στην Κεντρική Αμερική, τη Νότια Αφρική, τον Ινδικό Ωκεανό και βόρεια της Αυστραλίας. Αντίθετα, οι χαμηλότερες τιμές εμφανίζονται στην Κίνα, τη Μογγολία, το βορειοανατολικό και βορειοδυτικό Ειρηνικό Ωκεανό, καθώς και στις περιφερειακές περιοχές των ζωνών καταιγίδων του βόρειου και του νότιου ημισφαιρίου. Επίσης, χαμηλές τιμές εμφανίζονται στις νεφοσκεπής θαλάσσιες περιοχές στα ανοιχτά των δυτικών ακτών των ηπείρων, στη Βόρεια και Νότια Αμερική και στη νότια Αφρική.

Οι μέσες πλανητικές ανωμαλίες της SSR του FORTH-RTM κυμαίνονται εμφανίζοντας μεγάλη μεταβλητότητα από −14 έως 4 Wm^{-2} πριν από το 2000, ενώ μετά το 2000 οι ανωμαλίες SSR έχουν πολύ μικρές διακυμάνσεις σε ένα εύρος 5 Wm^{-2}. Το εφαρμοζόμενο χαμηλοπερατό φίλτρο Savitzky-Golay με παράθυρο 120 μηνών (10 έτη) στη χρονοσειρά των 35 ετών υποδεικνύει ότι μεταξύ 1984 και 1989 εμφανίστηκε μια σχετικά σταθερή εξέλιξη της SSR με μια τάση για αδύναμη σκίαση, ενώ λάμπρυνση παρατηρήθηκε τη δεκαετία του 1990 και μέχρι τις αρχές της δεκαετίας του 2000. Ακολούθως, έλαβε χώρα μία μείωση της λάμπρυνσης με σταθεροποίηση των διακυμάνσεων ή και μία πολύ ασθενής σκίαση την πρώτη δεκαετία του 21ου αιώνα, ακολουθούμενη από λάμπρυνση την τελευταία δεκαετία, δηλαδή τη δεκαετία του 2010, εκτός από τους ωκεανούς που παρουσιάζουν ασθενή σκίαση τη δεκαετία του 2010. Αυτό έχει ως αποτέλεσμα μια συνολική θετική τάση μεταβολής της SSR (λάμπρυνση) κατά τη διάρκεια ολόκληρης της περιόδου μελέτης 1984–2018, τόσο παγκοσμίως (0.69 $Wm^{-2}decade^{-1}$) όσο και στα δύο ημισφαίρια (1.31 και 0.10 $Wm^{-2}δεκαετία^{-1}$ για NH και SH, αντίστοιχα). Οι ηπειρωτικές εκτάσεις του πλανήτη παρουσίασαν μια ισχυρή και στατιστικά σημαντική λάμπρυνση ίση με 2.73 $Wm^{-2}decade^{-1}$, που συνέβη τόσο στο Βόρειο Ημισφαίριο (North Hemisphere ή NH) όσο και στο Νότιο Ημισφαίριο (South Hemisphere ή SH), ενώ οι ωκεανοί εμφάνισαν μια ασθενή σκίαση ίση με -0.10 $Wm^{-2}decade^{-1}$ που σημειώθηκε ως επί το πλείστον στους ωκεανούς του νοτίου ημισφαιρίου (-0.58 $Wm^{-2}decade^{-1}$). Οι ισχυρές μειώσεις της SSR που προκλήθηκαν από τη μεγάλη ηφαιστειακή έκρηξη του Pinatubo (1991), καθώς και από τις ισχυρές φάσεις El-Nino (1997, 2002, 2009 ή 2016), αναπαρήχθησαν από το FORTH-RTM. Αντίθετα, τα χρόνια που επηρεάστηκαν από την ανάκαμψη από την έκρηξη του Pinatubo, καθώς και από τις φάσεις La-Nina (1989, 1999 ή 2006), χαρακτηρίστηκαν από θετικές ανωμαλίες της SSR.

Σε τοπικό επίπεδο, κυψελίδων, το μοντέλο υποδεικνύει μια μακροχρόνια μέση παγκόσμια λάμπρυνση (αύξηση της SSR) από το 1984 έως το 2018, ίση με 0.88 $Wm^{-2}decade^{-1}$. Αυτή η λάμπρυνση έλαβε χώρα στο 63% του συνόλου των πλεγματικών σημείων του πλανήτη. Τόσο οι χερσαίες όσο και οι ωκεάνιες περιοχές του πλανήτη υπέστησαν λάμπρυνση, ωστόσο η αύξηση της SSR πάνω από την ξηρά ήταν ισχυρότερη από εκείνη των ωκεανών (2.57 $Wm^{-2}decade^{-1}$ έναντι 0.19 $Wm^{-2}decade^{-1}$). Επίσης, σε αντιστοιχία, σημειώθηκε ισχυρότερη αύξηση της SSR πάνω από το βόρειο ημισφαίριο (NH), ίση με 1.4 $Wm^{-2}decade^{-1}$, έναντι της ασθενούς αύξησης της SSR κατά 0.39 $Wm^{-2}decade^{-1}$ πάνω από το νότιο ημισφαίριο (SH). Όμως, αυτές οι ευρείες γεωγραφικά μεσοποιημένες τιμές του GDB κρύβουν διαφοροποιημένα, όσον αφορά το πρόσημο και το μέγεθος, μοτίβα. Έτσι, είναι αξιοσημείωτη οι έντονη λάμπρυνση πάνω από την Ευρώπη, την Αμερική, το υψίπεδο του Θιβέτ, την Ινδονησία, την Ανταρκτική, την Αυστραλία και ορισμένες ωκεάνιες περιοχές, ενώ η σκίαση κυριαρχεί πάνω από τμήματα της Κίνας και της Ινδίας, την Αραβική Χερσόνησο, τη Σαχάρα, την Αρκτική, τον Νότιο Ωκεανό και τις θαλάσσιες περιοχές με μόνιμα χαμηλά νέφη. Τα αποτελέσματα αυτά είναι διαφορετικά από τα ευρήματα της προηγούμενης μελέτης (Stamatis et al., 2023) με ίδιο RTM και για την ίδια χρονική περίοδο μελέτης 1984-2018, αλλά με μόνη διαφορά τη χρήση δεδομένων εισόδου στο μοντέλο για νέφη εξ' ολοκλήρου από το ISCCP-H. Αυτή η έκδοση του μοντέλου (αποκαλούμενη FMI) η οποία δεν χρησιμοποιήθηκε περαιτέρω για τη διερεύνηση των αιτίων του GDB στα πλαίσια αυτού του διδακτορικού, υπέδειξε μια παγκόσμια σκίαση κατά την ίδια περίοδο μελέτης (1984 – 2018), και η διαφοροποίηση των αποτελεσμάτων τώρα οφείλεται σε πιο ρεαλιστικές πληροφορίες εισόδου στο μοντέλο για τα νέφη (CLARISC αντί ISCCP-H).

Στο δεύτερο μέρος της μελέτης, εξετάστηκε η αξιοπιστία των αποτελεσμάτων του FORTH-RTM για τις ροές SSR και το GDB. Τα αποτελέσματα του FORTH RTM είναι αξιόπιστα, όπως αποδεικνύεται από την αξιολόγησή τους με δεδομένα από παγκόσμια δίκτυα σταθμών αναφοράς. Οι ροές SSR του μοντέλου και οι ανωμαλίες τους συσχετίζονται πολύ καλά με τους επίγειους σταθμούς GEBA και BSRN (R ίσο με 0.97 χρησιμοποιώντας τις ροές SSR ή 0.75 χρησιμοποιώντας τις ανωμαλίες για το GEBA και 0.94 χρησιμοποιώντας τις ροές SSR ή 0.71 χρησιμοποιώντας τις ανωμαλίες για το BSRN). Σε επίπεδο σταθμών, οι υπολογισμένες τιμές R κυμαίνονται από -0.21 έως 0.98, αλλά η πλειονότητά τους (70%) είναι υψηλότερες από 0.7, με τις χαμηλότερες τιμές να εμφανίζονται σε μικρά γεωγραφικά πλάτη, πιθανώς λόγω αβεβαιοτήτων στα δεδομένα εισόδου των νεφών και των αερολυμάτων. Σε γενικές γραμμές, υπάρχει μια σχετικά μικρή υπερεκτίμηση του FORTH-RTM SSR σε σύγκριση με το GEBA και μια μικρή υποεκτίμηση σε σύγκριση με τις μετρήσεις του BSRN. Η μέση απόκλιση είναι ίση με 4.46 Wm^{-2} και -2.49 Wm^{-2}, ή 2.7% και -1.3%, αντίστοιχα. Το FORTH-RTM υπερεκτιμά ισχυρότερα την SSR στα χαμηλά γεωγραφικά πλάτη, πιθανώς λόγω της υποεκτίμησης της νεφοκάλυψης και των δεδομένων οπτικού βάθους αερολυμάτων σε αυτές τις περιοχές. Η γενική υπερεκτίμηση υποδηλώνει ότι η ατμόσφαιρα του FORTH-RTM είναι πιο διαφανής από ό,τι θα έπρεπε. Η μέση τιμή RMSE είναι ίση με 20.93 Wm^{-2} (που αντιστοιχεί σε 12.8%) για τη σύγκριση του FORTH-RTM με τους GEBA σταθμούς, ενώ η αντίστοιχη τιμή για τους σταθμούς BSRN είναι ίση με 29.02 Wm^{-2} ή 15.4%, υποδεικνύοντας μια μάλλον μικρή απόκλιση της μοντελοποιημένης από τη μετρούμενη SSR. Οι μεγαλύτερες τιμές RMSE παρατηρούνται στις περιοχές μικρού και μεγάλου γεωγραφικού πλάτους. Η σύγκριση της χρονοσειράς των κινητών μέσων όρων 12 μηνών μεταξύ των ανωμαλιών SSR του FORTH-RTM και των αντίστοιχων θέσεων GEBA/BSRN δείχνει ότι οι ανωμαλίες SSR του μοντέλου είναι μεγαλύτερες από τις ανωμαλίες SSR του σταθμού, αρνητικές στην αρχή της περιόδου μελέτης και θετικές μετά το 2010, γεγονός που μπορεί να επηρεάσει το υπολογιζόμενο GDB. Πράγματι, οι τάσεις μεταβολής του FORTH-RTM SSR παρουσιάζουν ισχυρότερη λάμπρυνση από τις τάσεις των σταθμών. Το εκτιμώμενο από το μοντέλο GDB συμφωνεί ικανοποιητικά ως προς το πρόσημο με εκείνο των σταθμών, συγκεκριμένα για το 80% των σταθμών GEBA και το 65% των σταθμών BSRN, ενώ η συμφωνία είναι ακόμη καλύτερη για τις στατιστικά σημαντικές τάσεις (συμφωνία για το 90% των σταθμών GEBA και το 88% των σταθμών BSRN). Παρόμοια αξιολόγηση διεξήχθη επίσης ξεχωριστά για τις 4 δεκαετίες της περιόδου μελέτης και η συμφωνία ήταν και πάλι πολύ καλή συμφωνία σε ποσοστά (από 62% έως 73%). Για την Ευρώπη, την Ινδία και την Ιαπωνία, υπάρχει ισχυρή συμφωνία μεταξύ του FORTH-RTM και των σταθμών όσον αφορά στα πρόσημα GDB, γεγονός που δημιουργεί εμπιστοσύνη στην ποιοτική εκτίμηση του GDB σε αυτές τις περιοχές του πλανήτη. Από την άλλη πλευρά, το FORTH-RTM παρουσιάζει πιο περιορισμένη συμφωνία με τους σταθμούς όσον αφορά στο μέγεθος των αλλαγών της SSR (του GDB). Πιο συγκεκριμένα, υπερεκτιμά την λάμπρυνση στις περισσότερες περιοχές. Αυτό θα μπορούσε να οφείλεται σε ανεπαρκή δεδομένα εισόδου του μοντέλου, αλλά και σε προβλήματα με τις μετρήσεις των σταθμών.

Επιπλέον, πραγματοποιήθηκε η αξιολόγηση των τάσεων μεταβολής των ροών της ηλιακής ακτινοβολίας τόσο στην επιφάνεια της Γης όσο και στην κορυφή της ατμόσφαιρας (TOA) σε πλανητική κλίμακα χρησιμοποιώντας δεδομένα από την πλέον αξιόπιστη βάση δεδομένων CERES (Clouds and the Earth's Radiant Energy System) για την περίοδο 2001–2018. Είναι σημαντικό να σημειωθεί ότι το CERES μετρά απευθείας την εξερχόμενη στην κορυφή της ατμόσφαιρας ηλιακή ακτινοβολία (OSR), ενώ οι ροές SSR προκύπτουν χρησιμοποιώντας έναν εξειδικευμένο αλγόριθμο ανάκτησης, συνιστώντας μια εξαιρετικά

αξιόπιστη βάση δεδομένων τόσο για την OSR όσο και για την SSR (Kato et al., 2018). Μια σύγκριση των τάσεων SSR μεταξύ του FORTH-RTM και του CERES δείχνει συμφωνία στο 75% των κυψελίδων παγκοσμίως. Και τα δύο σύνολα δεδομένων δείχνουν λάμπρυνση στην Ευρώπη, τη Νότια Αφρική, τη Βραζιλία, πολλές περιοχές του τροπικού Ειρηνικού Ωκεανού και τον Ειρηνικό Ωκεανό στα δυτικά των ΗΠΑ. Συμφωνούν επίσης ως προς τις φθίνουσες τάσεις της SSR στην Ινδία, τη Μέση Ανατολή, τη Σαχάρα, την Κεντρική Αφρική, την Αρκτική και σε τμήματα των τροπικών ωκεανών. Ωστόσο, διαφωνίες παρατηρούνται στην Αυστραλία, σε μέρη της Ασίας και στη Νότια Αμερική. Η μέση πλανητική σκίαση για το FORTH-RTM είναι -0.061 $Wm^{-2}decade^{-1}$, διαφέροντας σε πρόσημο από τη μέση πλανητική λάμπρυνση 0.029 $Wm^{-2}decade^{-1}$ του CERES, με τη διαφορά να αποδίδεται κυρίως σε ισχυρότερες αρνητικές τάσεις μεταβολής της SSR του μοντέλου. Παρομοίως, αναλύθηκαν οι τάσεις μεταβολής στην κορυφή της ατμόσφαιρας. Και τα δύο σύνολα δεδομένων παρουσιάζουν συνολική μέση πλανητική μείωση της OSR, με τιμές -0.225 $Wm^{-2}decade^{-1}$ για το μοντέλο και -0.650 $Wm^{-2}decade^{-1}$ για το CERES. Η μικρότερη μείωση του μοντέλου οφείλεται κυρίως στις ισχυρότερες αυξητικές τάσεις σε ορισμένες περιοχές, ιδιαίτερα σε θαλάσσιες περιοχές με επίμονη χαμηλή νέφωση, όπως δυτικά της Νότιας Αμερικής και της Νότιας Αφρικής. Συνολικά, υπάρχει συμφωνία στις τάσεις μεταβολής της OSR βρίσκεται στο 73% του παγκόσμιου αριθμού κυψελίδων. Τόσο το μοντέλο όσο και το CERES καταγράφουν τη μείωση της OSR στην Ευρώπη, τη Νότια Αφρική, την Αμερική, τον Αρκτικό κύκλο, το Νότιο Ωκεανό, σε τμήματα του τροπικού Ειρηνικού Ωκεανού και σε μεγάλες εκτάσεις της Ασίας. Συμφωνία παρατηρείται επίσης ως προς τις αυξανόμενες τάσεις OSR σε συγκεκριμένες ωκεάνιες περιοχές, τη θάλασσα νότια της Νότιας Αμερικής, τον Περσικό Κόλπο και την Ινδονησία. Ασυμφωνίες εντοπίζονται σε τμήματα της Ινδίας, της Μέσης Ανατολής, της Ασίας και σε ορισμένες ωκεάνιες περιοχές. Συνολικά, το ποσοστό των κελιών όπου το μοντέλο συμφωνεί με το CERES τόσο στην επιφάνεια όσο και στην κορυφή της ατμόσφαιρας είναι 62%, υποδηλώνοντας μια ικανοποιητική απόδοση στην αποτύπωση των προσήμων των τάσεων μεταβολής της ηλιακής ακτινοβολίας μικρών μηκών κυμάτων κατά την περίοδο 2001-2018.

Επίσης, οι αξιολογήσεις των αποτελεσμάτων του μοντέλου έναντι των μετρήσεων πραγματοποιήθηκαν και συγκρίθηκαν μεταξύ τους για διάφορα σύνολα δεδομένων SSR και GDB κατά τη διάρκεια των ετών 1984-2018 και 2001-2018. Τα σύνολα δεδομένων που χρησιμοποιήθηκαν ήταν τα εξής: FMI, FMC, CERES, CLARA, ERA5, MERRA-2, JRA55 (Japanese 55-year Reanalysis), GFDL_CM2p1 (Geophysical Fluid Dynamics Laboratory Climate Model 2.1), NCEP-R1, NCEP-R2 (National Centers for Environmental Prediction Reanalysis 1 & 2), ISCCP_HXG, και W5E5 (WATCH Forcing Data applied to ERA5 with ERA5 bias correction). Τα αποτελέσματα αυτής της πολλαπλής σύγκρισης επιβεβαίωσαν ότι το FMC είναι ένα μοντέλο με τις καλύτερες επιδόσεις στην ποιοτική συμφωνία για το GDB (καλύτερη συμφωνία από τις προηγούμενες εκδόσεις του μοντέλου αυτού) σε σύγκριση με τις μετρήσεις, ενισχύοντας περαιτέρω την αξιοπιστία του. Επιπλέον, τα αποτελέσματα του FMC συγκαταλέγονται μεταξύ των συνόλων δεδομένων με τις καλύτερες επιδόσεις για την SSR, ενισχύοντας την εμπιστοσύνη στην ικανότητά του να αναπαράγει τις μακροπρόθεσμες τάσεις μεταβολής της SRR και τις φάσεις του GDB σε παγκόσμια κλίμακα.

Πιο συγκεκριμένα, χρησιμοποιώντας απεποχοποιημένες ανωμαλίες SSR, η υψηλότερη συσχέτιση με τους σταθμούς αναφοράς παρατηρήθηκε για το ERA5, με συντελεστές συσχέτισης 0.76 για τους σταθμούς GEBA και 0.72 για τους σταθμούς BSRN. Το FMC ακολούθησε πολύ κοντά, με τιμές 0.75 και 0.71, αντίστοιχα, ενώ το FMI κατέλαβε την τρίτη θέση με 0.74 και 0.71. Εναντίον των σταθμών GEBA, το FMC

παρουσίασε την υψηλότερη συμφωνία με 80%, ακολουθούμενο από τα ERA5 και W5E5 με 78%, με το FMI να κατατάσσεται τέταρτο με συμφωνία 66%. Έναντι των σταθμών BSRN, το FMC βρέθηκε και πάλι να είναι το καλύτερο με συμφωνία 65%, ενώ το FMI κατέλαβε την πέμπτη θέση με 52%. Σε ότι αφορά στις στατιστικά σημαντικές τάσεις μεταβολής, το ERA5 παρουσίασε την καλύτερη συμφωνία με 94%, ακολουθούμενο από το FMC με 90%, με το FMI να κατατάσσεται τέταρτο με 80%. Έναντι των BSRN, που όμως είναι μόνο 4 σταθμοί με στατιστικά σημαντικές τάσεις, το GFDL_CM2p1 πέτυχε συμφωνία 100%, ενώ το FMC κατέλαβε τη δεύτερη θέση με 88% και το FMI κατέλαβε την έκτη θέση με 50%. Επιπλέον, η ποιοτική συμφωνία του FMC με τα άλλα δύο καλύτερα σύνολα δεδομένων μετά το FMC σε περίπου 60% των κυψελίδων του πλανήτη ενισχύει την εμπιστοσύνη στην αξιοπιστία του, ιδιαίτερα σε περιοχές ιδιαίτερου ενδιαφέροντος όπως η Ευρώπη, η Νότια Αμερική, η βόρεια Ινδία, οι ωκεάνιες περιοχές δυτικά των ηπείρων με χαμηλή νέφωση και ο Νότιος Ωκεανός.

Στο τρίτο μέρος της μελέτης, διερευνήθηκαν τα αίτια του GDB με βάση τις τάσεις μεταβολής των παραμέτρων εισόδου στο FORTH-RTM. Κατά τη διάρκεια των τεσσάρων δεκαετιών, η SSR παρουσίασε διακριτές τάσεις μεταβολής. Στη δεκαετία του 1980 σημειώθηκε μια ασθενής σκίαση στο NH (-0.69 %decade^{-1}) και μια ασθενής λάμπρυνση στο SH (0.53 %decade^{-1}) αποδίδοντας μηδενική τάση παγκοσμίως, η οποία ακολουθήθηκε από μια σημαντική λάμπρυνση στη δεκαετία του 1990 (+2.43 %decade^{-1}) λόγω των μεγάλων μειώσεων του οπτικού βάθους του αερολύματος (AOD) και του οπτικού πάχους των νεφών (COT). Τη δεκαετία του 2000 σημειώθηκε ασθενέστερη παγκόσμια λάμπρυνση (+0.74 %decade^{-1}), καθώς οι αυξήσεις των αερολυμάτων και των CA1 και CA3 αντισταθμίστηκαν εν μέρει από τις μειώσεις του COT και της CA2. Τέλος, στη δεκαετία του 2010 σημειώθηκε άλλη μια περίοδος λάμπρυνσης (+0.83 %decade^{-1}), η οποία οφείλεται σε μειώσεις τόσο των νεφών όσο και των αερολυμάτων, ιδίως πάνω από την ξηρά. Καθ' όλη τη χρονική περίοδο (1984-2018), παρατηρήθηκε μεγάλη μείωση του COT3 και του CA2 σε ολόκληρο τον πλανήτη, γεγονός το οποίο είναι σύμφωνο με τη γενική – καθ’ όλη τη διάρκεια της περιόδου μελέτης – αύξηση της SSR (λάμπρυνση). Αντίθετα, υπήρξαν μεγάλες αυξήσεις στο COT2 και COT1, καθώς και στην CA1 πάνω από το Νότιο Ημισφαίριο και τους ωκεανούς, που πάντως δεν υπερίσχυσαν σε βαθμό που να επιφέρουν σκίαση. Στη γενική λάμπρυνση έπαιξε ρόλο και το AOD που μειώθηκε εκτός από τις χερσαίες περιοχές του Νοτίου Ημισφαιρίου. Σύμφωνα λοιπόν με την παρούσα μελέτη, οι κυριότεροι παράγοντες που οδήγησαν στην λάμπρυνση ήταν οι αλλαγές (μειώσεις) στο CA2 και στο COT3, ενώ η συμβολή των αλλαγών (μειώσεων) του AOD είναι αξιοσημείωτη πάνω από συγκεκριμένες χερσαίες περιοχές με έντονη ανθρωπογενή ρύπανση, όπως η Ευρώπη, η Ινδία και η Ανατολική Κίνα. Η συμβολή άλλων οπτικών ιδιοτήτων του αερολύματος, δηλαδή των SSA, AP, καθώς και των υδρατμών και του όζοντος, ήταν ασήμαντη.

Κατά τη διάρκεια της δεκαετίας του 1980 (1984-1989), το AOD γενικά μειώθηκε, ενώ το COT3 αυξήθηκε γενικά και το CA3 επίσης αυξήθηκε παντού εκτός από την ξηρά του SH. Η ύπαρξη θετικών και αρνητικών τάσεων των οδηγών του GDB είχε ως αποτέλεσμα είτε μια ασθενή σκίαση, όπως στο NH και πάνω από τη ξηρά, είτε μια ασθενή λάμπρυνση, όπως στο SH. Σε επίπεδο επιλεγμένων περιοχών ξηράς του πλανήτη, οι μεταβολές του AOD είχαν τη μεγαλύτερη συμβολή στο GDB κατά τη διάρκεια αυτής της δεκαετίας είτε παγκοσμίως είτε πάνω από 11/18 χερσαίες περιοχές, ακολουθούμενες από τις μεταβολές της CA3.

Κατά τη διάρκεια της δεκαετίας του 1990, οι μεγάλες μειώσεις στο AOD, το COT και εν μέρει στην CA εξηγούν τη γενική αύξηση της SSR κατά τη δεκαετία αυτή. Πιο συγκεκριμένα, οι μεταβολές του AOD διαπιστώθηκε ότι ήταν ο ισχυρότερος παράγοντας που συνέβαλε στο GDB κατά τη διάρκεια αυτής της δεκαετίας γενικά, καθώς και σε 11/18 περιοχές ξηράς, ακολουθούμενες από τις μεταβολές της CA3. Αξίζει να σημειωθεί ότι οι υδρατμοί, παρά τον γενικά αδύναμο ρόλο τους στο GDB, παρουσίασαν κάποια σημαντική συμβολή τη δεκαετία αυτή πάνω από την Αυστραλία και το Μεξικό.

Κατά τη διάρκεια της δεκαετίας του 2000, το AOD και η CA1 και CA3 αυξήθηκαν, ενώ το COT2 και η CA2 μειώθηκαν σε μεγάλο βαθμό. Ο συνδυασμός αυτών των τάσεων μεταβολής οδήγησε σε μια συνολική ασθενή λάμπρυνση. Ειδικότερα, οι μεταβολές του COT3, ακολουθούμενες από εκείνες του AOD, είχαν την ισχυρότερη συμβολή στο GDB κατά τη δεκαετία του 2000 είτε σε παγκόσμιο επίπεδο είτε σε 7/18 χερσαίες περιοχές. Εκτός αυτού, οι μεταβολές της SSA είχαν σημαντική συμβολή στο GDB πάνω από την Ανατολική Κίνα.

Στη δεκαετία του 2010, σημειώθηκαν μεγάλες μειώσεις τόσο στα νέφη όσο και στα αερολύματα, οι οποίες ήταν εντονότερες πάνω από περιοχές ξηράς. Αντίθετα, υπήρξε αύξηση του COT1 και της CA2 και CA3 πάνω από τους ωκεανούς. Το τελικό αποτέλεσμα ήταν μια γενική λάμπρυνση, εκτός από τους ωκεανούς του SH, όπου επικράτησε σκίαση. Οι μεταβολές τόσο του AOD όσο και των νεφών συνέβαλαν σημαντικά στο GDB, με τις μεταβολές του AOD να έχουν την ισχυρότερη συμβολή σε 8/18 χερσαίες περιοχές και να ακολουθούνται από την μεταβολή στην CA3. Επιπλέον, οι υδρατμοί συνέβαλαν σημαντικά πάνω από το Μεξικό.

Συνολικά, η εργασία αυτή επιβεβαίωσε τη μεταβλητότητα της SSR σε δεκαετείς κλίμακες, αποκαλύπτοντας ότι η SSR υπέστη αξιοσημείωτες αλλαγές κατά τις τελευταίες 4 δεκαετίες, από τα μέσα της δεκαετίας του 1980. Αποδείχθηκε επίσης η πολύπλοκη φύση του φαινομένου, το οποίο αλλάζει μέγεθος, αλλά ακόμη και πρόσημο, μεταξύ γειτονικών περιοχών του κόσμου. Η πολυπλοκότητα ενισχύεται περαιτέρω, δεδομένου ότι τα αίτια του GDB (τάσεις μεταβολής της SSR) ποικίλλουν από δεκαετία σε δεκαετία ή από περιοχή σε περιοχή πάνω στη Γη. Διαπιστώθηκε ότι οι κινητήριοι παράγοντες του φαινομένου είναι τόσο φυσικοί όσο και ανθρωπογενείς, γεγονός που περιπλέκει ακόμη περισσότερο την κατάσταση. Είναι σημαντικό ότι βρέθηκε πως οι μεταβολές των φορτίων αερολυμάτων (AOD) ήταν ο κύριος παράγοντας του GDB πάνω από περιοχές με σημαντική ανθρωπογενή δραστηριότητα, δηλαδή την Ευρώπη, την Ανατολική Κίνα και την Ινδία. Ωστόσο, ο ρόλος του AOD ήταν σημαντικός και σε παγκόσμιο επίπεδο κατά τις δεκαετίες του 1980 και 1990. Τα αποτελέσματα αυτά αναδεικνύουν τον κλιματικό ρόλο των μειωμένων ανθρωπογενών εκπομπών σωματιδίων, τα οποία μπορούν να μετριάσουν το ρόλο τους στην εξισορρόπηση της αύξησης της θερμοκρασίας του θερμοκηπίου. Από την άλλη πλευρά, οι μεταβολές των νεφών, ιδίως η μεταβολή του COT3 και της CA2, αποτελούν τους κύριους παράγοντες του GDB σε παγκόσμιο και ημισφαιρικό επίπεδο καθ' όλη τη διάρκεια της κλιματικής περιόδου, αλλά και κατά τη δεκαετία του 2000. Τέτοιες αλλαγές στις ιδιότητες των νεφών μπορεί να είναι αποτέλεσμα τόσο φυσικών όσο και ανθρωπογενών διεργασιών, κάτι που μένει να διερευνηθεί.

Η παρούσα μελέτη αναδεικνύει το σημαντικό ρόλο του φαινομένου GDB για το κλίμα της Γης, καθώς έχει τη δυνατότητα να προκαλέσει μια παγκόσμια ψύξη/θέρμανση λόγω ακτινοβολίας, που έχει τη

δυνατότητα είτε να αποδυναμώσει είτε να ενισχύσει την αύξηση της θερμοκρασίας που προκαλείται από τα αέρια του φαινομένου του θερμοκηπίου. Ωστόσο, παρόλο που το GDB του FORTH-RTM βρίσκεται σε αρκετά καλή συμφωνία με το GDB των σταθμών, μπορεί να βελτιωθεί περαιτέρω και να αυξήσει την αξιοπιστία του μέσω σημαντικών βελτιώσεων στα δορυφορικά δεδομένα εισόδου του μοντέλου και στα δεδομένα της επανανάλυσης. Μια τέτοια βελτίωση μπορεί να μειώσει περαιτέρω τις αβεβαιότητες σχετικά με τα αίτια του εκτιμώμενου GDB.

Ακόμη, από τα αποτελέσματα της στατιστικής ανάλυσης, η συσχέτιση Pearson προσδιορίζει άμεσες γραμμικές σχέσεις, αποκαλύπτοντας την ισχύ και την κατεύθυνση δράσης μεμονωμένων οδηγών της SSR, όπως η συνολική ισχυρότερη αρνητική συσχέτιση μεταξύ SSR και CA3 και COT2. Η παλινδρόμηση Ridge βελτιώνει αυτά τα ευρήματα μετριάζοντας την πολυσυγγραμμικότητα, προσφέροντας μια πιο ακριβή ποσοτικοποίηση της συνεισφοράς κάθε παράγοντα – υπογραμμίζοντας, για παράδειγμα, τον κυρίαρχο αντίκτυπο των CA3 και COT2. Εν τω μεταξύ, η Random Forest παλινδρόμηση καταγράφει πολύπλοκες μη γραμμικές αλληλεπιδράσεις, κατατάσσοντας την CA3 ως τον παράγοντα με τη μεγαλύτερη επιρροή, ακολουθούμενο από το COT2 και το COT3, ενισχύοντας την καθοριστική επίδραση των ιδιοτήτων των νεφών στη μηνιαία μεταβλητότητα της SSR. Η στατιστική ανάλυση επιβεβαιώνει επίσης ότι τα φορτία των αερολυμάτων (AOD) διαδραματίζουν δευτερεύοντα, αλλά σημαντικό ρόλο, ιδιαίτερα σε συγκεκριμένες χερσαίες περιοχές με έντονη εξαγωγή ερημικής σκόνης όπως η Σαχάρα και η Μέση Ανατολή, ενώ και οι άλλες παράμετροι συμβάλλουν στη διακύμανση SSR, όμως σε πολύ μικρότερο βαθμό. Συνδυάζοντας τα αποτελέσματα και των τριών στατιστικών μεθόδων, η CA3 ξεχωρίζει ως ο παράγοντας που επηρεάζει περισσότερο τις διακυμάνσεις SSR από μήνα σε μήνα, ακολουθούμενο από το COT2. Το COT3 και η CA2 συμβάλλουν επίσης σημαντικά, αν και σε μικρότερο βαθμό, με τις επιπτώσεις τους να κατατάσσονται ακριβώς μετά από αυτές των CA3 και COT2. Αξίζει να σημειωθεί ότι κατά την περίοδο 1984–2018, ο ισχυρότερος καθοδηγητικός παράγοντας του GDB ήταν το COT3, ακολουθούμενο από την CA2, όπως συζητήθηκε προηγουμένως με βάση την ανάλυση των συνεισφορών. Αυτή η εκτίμηση, μαζί με τα ευρήματα της ανάλυσης παλινδρόμησης, υπογραμμίζει τον κυρίαρχο ρόλο των μεσαίων και υψηλών νεφών στην πρόκληση αλλαγών της SSR κατά την περίοδο μελέτης 1984-2018, τουλάχιστον σε παγκόσμια και ημισφαιρική κλίμακα.

Στο τέταρτο μέρος της μελέτης, εξετάστηκε ο ρόλος της σκίασης και λάμπρυνσης σε σχέση με την πρόσφατη υπερθέρμανση του πλανήτη. Σύμφωνα με την ανάλυση αυτή, οι εκτιμώμενες φάσεις του GDB συμφωνούν με τις δεκαετείς μεταβολές της μέσης ημερήσιας θερμοκρασίας (Tmean), της ημερήσιας μέγιστης θερμοκρασίας (Tmax), της ημερήσιας ελάχιστης θερμοκρασίας (Tmin), καθώς και του ημερήσιου θερμοκρασιακού εύρους (Diurnal Temperature Range ή DTR) σε ορισμένες περιοχές του πλανήτη με σημαντική ανθρωπογενή ρύπανση, όπως η Ευρώπη και η Ανατολική Ασία, καθώς και σε παγκόσμια κλίμακα. Οι διαδεκαετείς φάσεις του GDB φαίνεται να τροποποιούν και να διαφοροποιούν τους ρυθμούς θέρμανσης που προκαλούνται κυρίως από την μονοτονικά αυξανόμενη συγκέντρωση των αερίων του θερμοκηπίου. Πιο συγκεκριμένα, από τα μέσα της δεκαετίας του 1980, όταν παρατηρήθηκε η λάμπρυνση, η απόκριση της παγκόσμιας μέσης θερμοκρασίας της ξηράς, η οποία αρχικά καθοδηγήθηκε από το εξελισσόμενο ανθρωπογενές φαινόμενο του θερμοκηπίου, ήταν μια ταχεία αύξηση της θερμοκρασίας. Αυτή η αύξηση επιβραδύνθηκε ή και σταμάτησε κατά τη δεκαετία του 2000, όταν σημειώθηκε μια σταθερή τάση της SSR στη ξηρά του NH ή και μια ασθενής σκίαση σε περιοχές

ξηράς με ιδιαίτερο ενδιαφέρον όπως η Ευρώπη, η Ινδία και η Ανατολική Ασία, η οποία εν μέρει συγκάλυψε την ανθρωπογενή αύξηση της θερμοκρασίας. Στη συνέχεια, κατά τη μετάβαση από την σκίαση σε μια νέα περίοδο λάμπρυνσης στη δεκαετία του 2010, η θέρμανση από το φαινόμενο του θερμοκηπίου δεν συγκαλύφθηκε πλέον και οι ρυθμοί θέρμανσης αυξήθηκαν και πάλι.

Αυτή η σχέση μεταξύ GDB και της θερμοκρασίας της γήινης επιφάνειας κατά την 35ετή περίοδο μελέτης 1984-2018 είναι σύμφωνη με τα συμπεράσματα που εξήγαγαν οι Wild et al. (2007) για τις δεκαετίες 1950-2000. Πιο συγκεκριμένα, για την περίοδο 1950-2000 είχε βρεθεί ότι η σκίαση των δεκαετών από το 1950 έως το 1980 συγκάλυψε την ανθρωπογενή αύξηση της θερμοκρασίας με αποτέλεσμα να παρατηρηθεί επιβράδυνση της παγκόσμιας θέρμανσης. Ενώ, κατά τη χρονική διάρκεια 1980-2000 η λάμπρυνση επέτρεψε να εκδηλωθεί πλήρως η η ανθρωπογενής επίδραση στους ρυθμούς θέρμανσης. Επιπλέον, διαπιστώθηκε ότι η διαχρονική μεταβολή της SSR παίζει επίσης ρόλο στις ετήσιες μεταβολές της θερμοκρασίας της επιφάνειας της Γης, αν και αυτές οι θερμοκρασιακές μεταβολές καθορίζονται από άλλους παράγοντες, όπως η ανθρωπογενής αύξηση της θερμοκρασίας λόγω των αυξημένων εκπομπών των αερίων του θερμοκηπίου, οι ηφαιστειακές εκρήξεις και το ENSO (Gou et al., 2022; Santer, 2014; Solomon, 2011; Watanabe et al., 2014). Το GDB βρέθηκε ότι συσχετίζεται πιο έντονα και καθοδηγεί σε μεγάλο βαθμό την Tmax, ενώ δευτερευόντως τη μέση θερμοκρασία της επιφάνειας και το ημερήσιο θερμοκρασιακό εύρος (DTR). Αυτά τα συμπεράσματα ισχύουν περισσότερο στις χερσαίες περιοχές του πλανήτη παρά στις ωκεάνιες, ενώ παρατηρούνται σε σημαντικό βαθμό σε παγκόσμια κλίμακα. Επιπλέον, σε περιοχές όπου σημειώθηκε έντονη λάμπρυνση, η Tmax αυξήθηκε περισσότερο από την Tmin (η οποία αυξήθηκε κυρίως λόγω της θέρμανσης του θερμοκηπίου), οδηγώντας σε αύξηση της DTR. Αυτό επιβεβαιώνει ότι το GDB παίζει σημαντικό ρόλο στις μεταβολές της Tmax και της DTR. Ωστόσο, τα μεγέθη των λαμπρύνσεων πριν και μετά την σκίαση της δεκαετίας του 2000 δε συνδέονται άμεσα με τα αντίστοιχα μεγέθη επιφανειακής θέρμανσης, επιβεβαιώνοντας την πολυπλοκότητα της άμεσης σύνδεσης μεταξύ του GDB και των μεταβολών της επιφανειακής θερμοκρασίας, καθώς και τη σημασία του ανθρωπογενούς φαινομένου του θερμοκηπίου ως κύριου παράγοντα για τη συνεχιζόμενη υπερθέρμανση του πλανήτη.

Abstract

In the present PhD study, the Global Dimming and Brightening (GDB), its causes and possible links with global warming rates were investigated for the 35-year period 1984-2018. To this aim, detailed radiative transfer calculations were performed by the FORTH-RTM (Foundation for Research and Technology-Hellas Radiative Transfer Model) on a monthly basis and 0.5° x 0.625° spatial resolution using modern and improved satellite (CLARISC: CLARA-A2.1 and ISCCP-H synergy for a new cloud database) and reanalysis (MERRA-2) datasets for clouds and aerosols as well as surface and atmospheric properties, respectively. This analysis was also performed on decadal time periods of the entire study period, since GDB is a decadal scale phenomenon. It has been also done worldwide, hemispherically, over ocean and land, and over specific land areas, enabling a complete understanding of the spatial and temporal features of GDB on a climatological basis all over the world.

First, the FORTH RTM with CLARISC cloud data (or FMC) ran to provide the surface solar radiation (SSR) and the corresponding SSR trends (GDB) were computed. The model indicates a global mean brightening (increasing SSR) from 1984 to 2018, equal to 0.88 $Wm^{-2}decade^{-1}$. This brightening is observed in 63% of the global grid points. Both land and ocean regions of the world underwent brightening; yet the land SSR increase is stronger than the oceans' one (2.57 $Wm^{-2}decade^{-1}$ vs 0.19 $Wm^{-2}decade^{-1}$). Also, in line with this, a stronger brightening occurred over the North Hemisphere (NH), equal to 1.4 $Wm^{-2}decade^{-1}$, versus a weak brightening of 0.39 $Wm^{-2}decade^{-1}$ over the South Hemisphere (SH). All the above SSR changes are statistically significant at the 95% confidence level. Yet, the spatially averaged GDB conceals diversified, in terms of sign and magnitude, patterns. Thus, strong tendencies toward brightening are noteworthy over Europe, the Americas, the Tibetan Tableau, Indonesia, Antarctica, Australia and some oceanic regions, whereas the dimming dominates over parts of China and India, the Arabian Peninsula, the Sahara, the Arctic, the Southern Ocean and the marine stratocumulus areas. These results revise the findings of our previous FORTH-RTM version using ISCCP-H cloud data (FMI) which suggested a global dimming over the same period, and this revision is due to more realistic cloud information (CLARISC instead of ISCCP-H cloud dataset).

In a next step, the reliability of the estimated FORTH-RTM SSR fluxes and GDB was investigated. The model results are reliable, as proven from their successful evaluation against data from global reference station networks. The model SSR fluxes and their anomalies correlate very well with GEBA and BSRN ground-based stations (correlation coefficient R equal to 0.97 using SSR fluxes or 0.75 using flux anomalies and 0.94 using SSR fluxes or 0.71 using flux anomalies, respectively), having small biases (less than 3%) and satisfactory RMSE (less than 15%). The model estimated GDB nicely agrees in terms of sign with the stations, namely for 80% of GEBA and 65% of BSRN stations, while the agreement is even better for statistically significant trends agreement (for 90% of GEBA and 88% of BSRN). A similar evaluation was also conducted separately for the 4 decades of the study period and the agreement was again very good (ranging from 62% to 73%). Also, similar evaluations against ground truth and inter-comparisons were also performed for several other SSR and GDB datasets during the periods 1984-2018 and 2001-2018. The

results of this inter-comparison approved that FORTH-RTM is a top-performing dataset in qualitative agreement for GDB when compared to observational measurements, further reinforcing its reliability. Additionally, FORTH-RTM ranks among the best-performing datasets for SSR, enhancing confidence in its ability to study long-term GDB trends on a global scale.

Subsequently, the causes of GDB were investigated based on the trends of the SSR and the input parameters to the FORTH-RTM which influence SSR. Over the four decades, surface solar radiation (SSR) exhibited distinct trends. In the 1980s, a weak dimming (-0.69 %decade^{-1}) occurred over NH and a weak brightening over SH (0.53 %decade^{-1}), followed by a significant brightening in the 1990s (+2.43 %decade^{-1}) due to large reductions in aerosol optical depth (AOD) and cloud optical thickness (COT). The 2000s saw a weaker global brightening (+0.74 %decade^{-1}) as increases in aerosols and low/high cloud amounts were partially offset by reductions in COT and mid-level cloud amount. Finally, the 2010s experienced another period of brightening (+0.83 %decade^{-1}), driven by reductions in both clouds and aerosols, particularly over land. In the following step of the investigation of the GDB causes, the contribution of the GDB drivers to the overall GDB were computed. Over the entire time period (e.g. 1984-2018), there have been large declines in high-level COT and mid-level CA across the planet in line with the general (global) increase in SSR. On the contrary, there were large increases in the COT of middle and low clouds as well as of low-level cloud amount over the SH and the oceans. The AOD decreased except over land areas of the SH. According to our analysis, the major drivers of the overall GDB (brightening) have been changes (decreases) in mid-level CA and high-level COT, while the contribution of the AOD changes (decreases) was remarkable over specific land areas with intense anthropogenic pollution, such as Europe, India and East China. The contribution of other aerosol optical properties, i.e. SSA, AP, as well as of water vapor and ozone was insignificant. During the 1980s (1984-1989), AOD generally decreased, whereas COT3 increased above in general and high-level CA increased also everywhere except over land of the SH. The existence of positive and negative trends of the GDB drivers resulted either in a weak dimming, as in the NH and over land, or in a weak brightening, as in the SH. AOD changes had the largest contribution to GDB during this decade either globally or over 11 out of 18 land selected areas of the globe, being followed by changes in high-level CA. Throughout the 1990s, large reductions in AOD, COT, and partially in CA, explain the general observed increase in SSR during this decade. More specifically, AOD changes are found to have been the strongest contributor to GDB during this decade in general, as well as over 11/18 land areas, followed by changes in high-level CA. Notably, water vapor, in spite of its generally weak role for GDB, showed some significant contribution over Australia and Mexico in this decade. Across the 2000s, AOD, and cloud amount of low- and high-level clouds increased, while COT and mid-level CA largely decreased. The coincidence of these trends led to an overall weak brightening. Especially, the changes of high-level COT, followed by those of AOD, had the strongest contribution to GDB in the 2000s either globally or over 7/18 land areas. Besides, SSA changes had significant contribution to GDB over East China in the 2000s. In the 2010s, there were large reductions in both clouds and aerosols, being stronger over land areas. On the contrary, there was an increase in COT of low clouds, and cloud amount of mid- and high-level clouds over the oceans. The general reduction in GDB drivers led to a general brightening, except over the oceans of SH where dimming prevailed. Changes in both AOD and clouds contributed strongly to GDB, with AOD being the most common contributor (over 8/18 land areas) followed by high-level CA. Moreover, in this decade water vapor significantly contributed over Mexico. The noticeable contribution of water vapor in

the 1990s and 2010s against its insignificant role during the entire 35-year study period shows that one must be careful assessing the strength of the contribution of a physical parameter to climatic phenomena, like GDB, in terms of the chosen time period, since counterbalancing effects may exist during shorter periods.

In final part of this PhD, the role of solar dimming and brightening in relation to the recent global warming was examined. According to our findings, the estimated GDB phases are in line with the decadal variations of T_{mean} as well as T_{max}, T_{min}, and DTR over certain land areas of the globe with significant anthropogenic pollution, such as Europe and East Asia, as well as over global land. The interdecadal phases of GDB seem to complementarily modify and differentiate the rates of warming primarily caused by the monotonically increasing concentration of greenhouse gases. More specifically, since the mid-1980s, when solar brightening took place, the global land mean temperature response, originally driven by the evolving anthropogenic greenhouse effect, was a rapid warming, which was decelerated or even stopped in the 2000s when solar dimming occurred over areas with intense anthropogenic pollution such as Europe, India and East Asia and partly masked the anthropogenic greenhouse global warming. Then, during the transition from dimming to a renewed brightening in the 2010s, the greenhouse warming was no longer masked and the warming rates increased again. This relationship between GDB, namely the rates of change of SSR, and the Earth's surface temperature during the 35-year period 1984-2018 is in line with the conclusions drawn by other researchers for the decades from 1950-2000. Moreover, it is found that the inter-annual SSR variation also plays a role in the year-to-year changes of the Earth's surface temperature, although of course these are also driven by other factors, e.g. anthropogenic greenhouse gases warming, volcanic eruptions or ENSO. The GDB was found to largely drive and to be more strongly related to T_{max} and secondarily to the mean surface-air temperature and the daily temperature range. The derived conclusions are more valid over the global land than ocean areas and apply to a considerable degree on the global scale. Also, in many regions where strong brightening occurred, T_{max} increased more than T_{min} (which increased primarily due to greenhouse warming), leading to an increase of DTR, confirming that GDB plays an important role in the T_{max} and DTR changes. However, the rates of brightening before and after the 2000s' dimming are not associated with proportional surface warming rates, confirming the complexity of the links between SSR and surface temperature changes as well as the importance of the anthropogenic greenhouse effect as main factor of the ongoing global warming.

List of papers

The results of the present PhD study have been published in the following international ISI journals with peer review:

Paper I
Stamatis, M.; Hatzianastassiou, N.; Korras-Carraca, M.B.; Matsoukas, C.; Wild, M.; Vardavas, I. Interdecadal Changes of the MERRA-2 Incoming Surface Solar Radiation (SSR) and Evaluation against GEBA & BSRN Stations. Appl. Sci. **2022**, 12, 10176. https://doi.org/10.3390/app121910176

Paper II
Stamatis, M.; Hatzianastassiou, N.; Korras-Carraca, M.-B.; Matsoukas, C.; Wild, M.; Vardavas, I. An Assessment of Global Dimming and Brightening during 1984–2018 Using the FORTH Radiative Transfer Model and ISCCP Satellite and MERRA-2 Reanalysis Data. Atmosphere **2023**, 14, 1258. https://doi.org/10.3390/atmos14081258

Paper III
Stamatis, M.; Hatzianastassiou, N.; Korras-Carraca, M.-B.; Matsoukas, C.; Wild, M.; Vardavas, I. How strong are the links between global warming and surface solar radiation changes? Climatic Change 177, 156 (**2024**). https://doi.org/10.1007/s10584-024-03810-6

Paper IV
Stamatis, M.; Hatzianastassiou, N.; Korras-Carraca, M.-B.; Matsoukas, C.; Wild, M.; Vardavas, I. Which are the main drivers of Global Dimming and Brightening? Atmospheric Research, Volume 322, **2025**, 108140, ISSN 0169-8095. https://doi.org/10.1016/j.atmosres.2025.108140

Also, the following publications in peer reviewed International Conference Proceedings were made based on the results of this PhD:

1. **Stamatis**, M.; Hatzianastassiou, N.; Korras-Carraca, M.-B.; Matsoukas, C.; Wild, M.; Vardavas, I. On the Contribution of Aerosols and Clouds to Global Dimming and Brightening Using a Radiative Transfer Model, ISCCP-H Cloud and MERRA-2 Aerosol Optical Properties. Environ. Sci. Proc. **2023**, 26, 34. Proceedings of 16th International Conference on Meteorology, Climatology and Atmospheric Physics—COMECAP 2023. https://doi.org/10.3390/environsciproc2023026034
2. **Stamatis**, M.; Ioannou, P.; Korras-Carraca, M.-B.; Hatzianastassiou, N. The Global and Diffuse Solar Radiation Trends Using GEBA & BSRN Ground Based Measurements during 1984–2018. Environ. Sci. Proc. **2023**, 26, 141. Proceedings of 16th International Conference on Meteorology, Climatology and Atmospheric Physics—COMECAP 2023. https://doi.org/10.3390/environsciproc2023026141

Furthermore, the following presentations in International Conference were made based on the results of this PhD:

1. Stamatis, M., Hatzianastassiou, N., Korras Carraca, M. B., Matsoukas, C., Wild, M., and Vardavas, I.: Comparative analysis of the incoming surface and outgoing top of atmosphere solar radiation

based on MERRA-2 & CERES data, EGU General Assembly 2021, online, 19–30 Apr 2021, EGU21-13200, https://doi.org/10.5194/egusphere-egu21-13200, 2021.

2. Stamatis, M., Hatzianastassiou, N., Korras Carraca, M. B., Matsoukas, C., Wild, M., and Vardavas, I.: Detailed analysis of the Global Dimming & Brightening from 1980 to 2020 based on MERRA-2 reanalysis data, EGU General Assembly 2022, Vienna, Austria, 23–27 May 2022, EGU22-586, https://doi.org/10.5194/egusphere-egu22-586, 2022.
3. Stamatis, M., Hatzianastassiou, N., Korras Carraca, M. B., Matsoukas, C., Wild, M., and Vardavas, I.: The Global Dimming and Brightening Based on MERRA-2 Reanalysis data and its Evaluation Against GEBA & BSRN Ground-Based Networks. International Radiation Symposium (IRS) 2022, Thessaloniki, Greece, 4-8 July 2022
4. Stamatis, M., Hatzianastassiou, N., Korras Carraca, M. B., Matsoukas, C., Wild, M., and Vardavas, I.: A detailed assessment of the contribution of aerosols to Global Dimming and Brightening using a radiative transfer model and MERRA-2 aerosol optical properties. 11th International Aerosol Conference (IAC) 2022, Athens, Greece, 4-9 September 2022
5. Stamatis, M., Hatzianastassiou, N., Korras Carraca, M. B., Matsoukas, C., Wild, M., and Vardavas, I.: The Global Dimming & Brightening based on FORTH radiative transfer model during 1984-2018 and its evaluation against GEBA & BSRN ground-based networks, EGU General Assembly 2023, Vienna, Austria, 24–28 Apr 2023, EGU23-13064, https://doi.org/10.5194/egusphere-egu23-13064, 2023.
6. Stamatis, M., Hatzianastassiou, N., Korras Carraca, M. B., Matsoukas, C., Wild, M., and Vardavas, I.: A comprehensive study on the causes of Global Dimming and Brightening using a radiative transfer model and satellite and reanalysis input data, EGU General Assembly 2024, Vienna, Austria, 14–19 Apr 2024, EGU24-17894, https://doi.org/10.5194/egusphere-egu24-17894, 2024.

Table of Contents

Chapter 1: Introduction and Theory **32**

1.1 Motivation 32

1.2 Research Questions and Innovation 33

1.3 Thesis Structure 35

1.4 Radiative Transfer in the Atmosphere 35

1.4.1 Energy balance of the Earth-atmosphere system 35

1.4.2 Interaction of solar radiation with the atmosphere and the Earth's surface 36

1.4.2.1 Solar radiation scattering and asymmetry parameter 36

1.4.2.1.1 Rayleigh scattering 37

1.4.2.1.2 Mie Scattering 37

1.4.2.1.3 Asymmetry parameter 38

1.4.2.2 Absorption of solar radiation 39

1.4.2.3 Radiation interaction with the Earth's surface 39

1.4.2.4 Basic concepts and radiation transfer equation 40

1.5 The atmospheric components and the solar radiation 42

1.5.1 The clean, dry atmosphere 42

1.5.2 Water vapor 42

1.5.3 Aerosols 43

1.5.4 Clouds 43

1.5.5 Interactions between clouds, aerosols, water vapor, and SW radiation 45

1.5.6 Large scale circulation patterns 45

1.6 The literature review 45

1.6.1 Observations: Global dimming and brightening 46

1.6.2 Solar irradiance's effects on dimming and brightening 46

1.6.3 Radiatively active gases' effects on dimming and brightening 46

1.6.4 Aerosol and cloud effects on dimming and brightening 47

1.6.5 Global dimming and brightening in satellite retrievals and RTMs 48

1.6.6 Global dimming and brightening in Reanalysis 49

1.6.7 Global dimming and brightening in CMIPs 50

Chapter 2: Data and Methodology **51**
2.1 Data and used Model 51
2.1.1 The Radiative Transfer Model 51
2.1.2 Sensitivity tests of monthly means 53
2.1.3 Input data to RTM 54
2.1.3.1 ISCCP-H 55
2.1.3.2 CLARISC: CLARA-A2 and ISCCP-H synergy 55
2.1.3.2.1 Description of the CLARISC 55
2.1.3.2.2 Cloud Climatology and Trends of CLARISC and comparison with ISCCP-H and CERES 58
2.1.3.3 MERRA-2 59
2.1.4 Evaluation data 59
2.1.4.1 GEBA and BSRN 59
2.1.4.2 CERES-EBAF 4.2 61
2.1.5 Complementary data 61
2.1.5.1 ERA5 61
2.1.5.2 MERRA-2 62
2.1.5.3 JRA-55 62
2.1.5.4 NCEP R1 63
2.1.5.5 NCEP R2 63
2.1.5.6 W5E5 63
2.1.5.7 ISCCP HXG 63
2.1.5.8 GFDL_CM2P1 64
2.1.5.9 CERES EBAF 4.2 SSR Retrievals 64
2.1.5.10 CLARA-A2 64
2.2 Methods 65
2.2.1 SSR and GDB drivers fluctuations 66
2.2.2 Evaluation methods 66
2.2.3 Contributions to GDB analysis 67
2.2.4 Correlation and Regression Analysis 68
2.2.5 The links between GDB and global warming 69

Chapter 3: The RTM SSR and GDB **71**

3.1 Introduction 71
3.2 Annual and seasonal global distribution of SSR and GDB drivers 71
3.2.1 Annual and seasonal global distribution of SSR 71
3.2.2 Annual and seasonal global distribution of GDB drivers 72
3.2.3 Latitudinal variations and annual cycle of SSR 74
3.2.4 SSR timeseries 77
3.2.5 Timeseries comparison between SSR and GDB drivers 78
3.3 The Global Dimming and Brightening 79
3.3.1 The GDB during 1984-2018 79
3.3.2 The GDB during 1984-1984 81
3.3.3 The GDB during 1990-1999 83
3.3.4 The GDB during 2000-2009 86
3.3.5 The GDB during 2010-2018 86
3.4 The FMI-based Global Dimming and Brightening 89

Chapter 4: FORTH-RTM SSR and GDB evaluations and intercomparisons 96
4.1 Introduction 96
4.2 FMI evaluation 96
4.2.1 Evaluation of FMI SSR 96
4.2.1.1 All Stations 97
4.2.1.2 At Station Level 98
4.2.2 Evaluation of FMI GDB 102
4.3 FMC evaluation 111
4.3.1 Evaluation of FMC SSR 111
4.3.1.1 All Stations 112
4.3.1.2 At Station Level 114
4.3.2 Evaluation of FMC GDB 117
4.3.3 Evaluation of FMC's SSR and OSR trends 125
4.4 SSR and GDB Intercomparisons 127
4.4.1 Intercomparison for 1984-2018 128
4.4.2 Intercomparison for 2001-2018 135

Chapter 5: The causes of GDB **144**
5.1 Introduction 144
5.2 Changes of the GDB drivers 145
5.3 Contributions of GDB drivers 152
5.3.1 Contributions at global scale 152
5.3.2 Contributions on a regional scale 156
5.4 Correlation & Regression Analysis 160
5.4.1 Pearson correlation coefficients 160
5.4.2 Ridge regression analysis 165
5.4.3 Random Forest Regression 167
5.4.4 Assessment of different correlation and regression analyses 170

Chapter 6: The links between GDB and global warming **173**
6.1 Introduction 173
6.2 Correlation between SSR and surface temperature 174
6.3 The long-term changes of SSR and temperature over land and oceans and their relationship 175
6.4 The relationship between the changes of SSR and surface temperature over various land areas 179
6.5 Limitations of this study 184

Chapter 7: Summary and Conclusions **185**
7.1 Summary and main findings 185
7.2 Future Plans 189
7.3 EarthSense: Interactive exploration of this PhD 190

Bibliography **192**
Appendix A **210**
Appendix B **245**
Appendix C **253**
Appendix D **261**
Appendix E **271**
Appendix F **276**

List of Acronyms

AOD	Aerosol Optical Depth
AP	Asymmetry Parameter
BIAS	mean value of FORTH-RTM minus mean value of stations
BIAS (%)	100×BIAS/mean value of stations
BSRN	Baseline Surface Radiation Network
CA	Cloud Amount
CA1	Cloud Amount for low-level clouds
CA2	Cloud Amount for middle-level clouds
CA3	Cloud Amount for high-level clouds
CERES	Clouds and Earth's Radiant Energy Systems
CLARA	The CM SAF Cloud, Albedo And Surface Radiation dataset from AVHRR data
CLARISC	CLARA-A2.1 and ISCCP-H synergy for a new cloud database
COT	Cloud Optical Thickness
COT1	Cloud Optical Thickness for low-level clouds
COT2	Cloud Optical Thickness for middle-level clouds
COT3	Cloud Optical Thickness for high-level clouds
DJF	December-January-February season
DM	Directly model-computed monthly SSR
DTR	Diurnal Temperature Range
ERA5	European Centre for Medium-Range Weather Forecasts (ECMWF) v5
FMC	FORTH-RTM with MERRA-2 and CLARISC
FMI	FORTH-RTM with MERRA-2 and ISCCP
FORTH-RTM	Foundation for Research and Technology-Hellas - Radiative Transfer Model
GDB	Global Dimming and Brightening
GEBA	Global Energy Balance Archive
ISCCP	International Satellite Cloud Climatology Project
JJA	June-July-August season
MAM	March-April-May season
MERRA-2	Modern-Era Retrospective Analysis for Research and Applications v.2
NH	Northern Hemisphere
OSR	Outgoing Solar Radiation

R	Pearson’s correlation coefficient
RF	Random Forest regression
RMSE	Root Mean Squared Error
RRMSE	Relative Root Mean Squared Error
RTM3H	Averaged SSR from 3-hourly model computations
SG	Savitzky-Golay low-pass filter
SH	Southern Hemisphere
SON	September-October-November season
SSA	Single Scattering Albedo
SSR	Surface Solar Radiation
SW	Shortwave
TOA	Top of the Atmosphere
Δ(OSR)	Changes of OSR
Δ(SSR)	change of SSR (equivalent to GDB)

Chapter 1: Introduction and Theory

1.1 Motivation

Shortwave (SW) radiation from the Sun is the Earth's external energy source, as well as the primary input and dominating source of energy for the climate system. As a result, changes in the SW radiation at the top of the atmosphere (TOA) and its transmission through the atmosphere may have a significant impact on the quality of life on Earth. Before reaching the Earth's surface, solar radiation travels through the whole atmosphere, where it interacts with a variety of gases and particles. The amount of solar energy that reaches the ground is a portion of the radiation that reaches the top of the atmosphere because many atmospheric elements absorb and/or scatter radiation within specific wavelength ranges. On average, 340 Wm^{-2} enter the terrestrial atmosphere worldwide, but only around 185 Wm^{-2} remain after reaching the surface (Wild et al. 2013). These are worldwide averaged values, though, and they change significantly between locations, seasons, and, of course, the diurnal cycle. Moreover, significant variations in the incoming solar radiation at the surface have been noted worldwide since the mid-1900s (Wild 2016). A broad decline in surface solar radiation (SSR) of roughly 4 Wm^{-2} on average was recorded for the years 1950–1980; this is now commonly known as "global dimming" (Wild 2012). Since the 1980s, SSR has slightly increased, a phenomenon appropriately referred to as "brightening," depending on the region (Wild et al. 2005). However, the dimming period has persisted in some areas (Wild 2012). According to certain data, variations in the concentration of aerosols in the atmosphere were mostly responsible for the trends in SSR that were seen over the dimming period; that is, SSR declined as aerosol concentrations increased (Wild 2012 and references therein). According to other data (both satellite and ground-truth measurements), regional SSR trends have been significantly influenced by changes in cloud cover that are not related to the presence of aerosols (e.g. Norris and Wild 2009; Pfeifroth et al. 2018; Long et al. 2009). Regarding the proportional contributions of clouds, aerosols, and other mechanisms to the causes of the SSR changes, there is no agreement (Wild 2016).

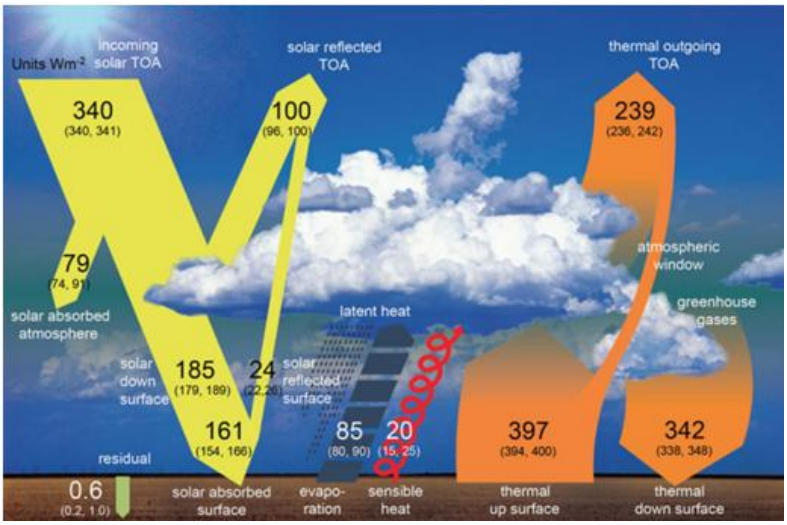


Figure 1.1. The energy balance of the Earth-atmosphere system. The numbers given correspond to the best and most recent (early 21st century) estimate of the various physical quantities, and the range of values they can take (in parentheses). The magnitudes are given in Wm^{-2}. (Source: Wild et al., 2013)

The different elements that interact with radiation throughout the Earth-atmosphere system include aerosols, clouds, water vapor, and ozone. The first two elements—clouds and aerosols—are very significant. The Earth's best defense against sunshine is its cloud cover. Clouds reflect around 23% of the solar radiation that reaches the Earth's atmosphere and absorb a further 3% (Trenberth et al., 2009). Variations in cloud cover are significant locally. More cloud cover and lower SSR are linked to cyclones and convective activity; however, for clouds to explain long-term SSR trends, corresponding long-term trends in cloud cover must also be present. Climate change has led to regional observations of such cloud cover patterns, although the extent and sign of these trends vary by region (Norris et al. 2016). Another element of the atmosphere that can significantly impact the radiative transmissivity of the atmosphere is aerosols (Wild 2016). Both natural and man-made emissions cause aerosols to enter the atmosphere. Although the dates vary by location (Streets et al., 2006), there has been a significant change in the worldwide emissions of aerosols and aerosol precursors during the dimming and brightening eras (Wild 2012).

Additionally, there are signs that the hydrological cycle has been weakened by dimming (Liepert and Romanou, 2005). Plant life can also be significantly impacted by dimming and brightening, particularly in high latitude regions where photosynthesis and, consequently, growth rate are constrained by both air temperature and light availability. For instance, a global dimming of the Arctic region has been associated with apparent differences between temperature records and tree-ring densities (Stine and Huybers, 2014). According to some theories, the northern hemisphere's phase of less warming ("hiatus") between the 1950s and 1980s was caused by a decrease in SW irradiation, which somewhat offset global warming (Murphy et al., 2009; Magnus et al., 2011). Furthermore, there is evidence that GDB can affect the global warming rates. More specifically, it has been proposed (Wild et al. 2007) that the solar dimming from the mid of the 20th century until the 1980s has concealed the evolving greenhouse warming, which has only become fully apparent on a global scale during the brightening that followed the 1980s. On the other hand, in recent years, the concept of a "hiatus" in global warming has gathered scientific attention, referring to a perceived slowdown in the rate of surface temperature increase observed from the late 20th century to the first decade of the 21st century (England et al. 2015; Trenberth and Fasullo 2013). The hiatus debate underscores the complexity of the Earth-atmosphere climate system and the need for detailed analysis to discern short-term variations from the overarching warming trend due to the anthropogenic greenhouse effect.

Thus, studying the GDB is crucial because it influences climate change by modulating the Earth's energy balance. Understanding the causes of the GDB is also important since identifying whether GDB is driven by human activities (e.g., aerosol emissions) or natural factors (e.g., volcanic eruptions, cloud variability) helps in determining the extent of human impact on climate and climate change. Also, the knowledge on GDB and GDB causes is essential for accurate climate modeling, reducing the uncertainties in the current scientific knowledge, predicting impacts on food security, optimizing solar energy systems, and managing ecosystems. It also guides policymakers in developing effective climate adaptation and mitigation measures to address global environmental challenges.

1.2 Research Questions and Innovation

The key question addressed in this thesis is: How did cloud and aerosol changes and trends influence SSR trends from 1984 to 2018? The goal is to improve knowledge of the factors that contribute to solar dimming and brightening, the links between the GDB and the global warming rates as well as the agreement between observed and simulated SSR. Many studies have been conducted on dimming and brightening, so it is important to make explicit what this thesis offers that hasn't been fully covered in earlier publications. The following research questions are addressed in this thesis:

- Which are the main GDB drivers during the period 1984-2018 and its decadal sub-periods?
- Where, when and how strong was the contribution of each GDB driver to the phenomenon?
- Did the GDB affect the global warming rates during the recent decades?
- How well do FORTH-RTM and other simulations reproduce SSR and SSR trends?

The following tasks have been performed to answer the above questions:

1. Utilization of the FORTH-RTM and calculations of SSR on a monthly basis, globally.
2. Computations of the trends in SSR and in the model (FORTH-RTM) input parameters.
3. Evaluation of the FORTH-RTM SSR and GDB against to observations.
4. Intercomparison between several SSR and GDB datasets.
5. Several FORTH-RTM runs with constant (“frozen”) input parameters to compute the contributions of the changes of each input parameter to the GDB.
6. Analysis of the contributions of GDB drivers to the estimated GDB.
7. Investigation of the links between FORTH-RTM GDB and global warming rates.

Furthermore, this study extends and introduces several innovations compared to previous works which used the same FORTH-RTM to study changes of SSR (Hatzianastassiou et al., 2005; 2012; 2020):

1. The higher spatial resolution of model SSR and GDB, computed here on a 0.5° × 0.625° latitude-longitude grid over the entire globe, i.e. in a more appropriate resolution for regional studies.
2. The quite long study period of 1984–2018.
3. The use of state-of-the-art RTM input datasets.
4. The columnar closure study, where the long-term changes in FORTH-RTM reflected/outgoing solar radiation fluxes at TOA are compared to corresponding fluxes from CERES-EBAF, which serve as a reference. This comparison further strengthens the robustness of the conclusions and enhances the reliability of the computed GDB (at surface).
5. The intercomparison of the FORTH-RTM-derived SSR and GDB with other datasets for the periods 1984–2018 and 2001–2018. This comparison was crucial for assessing the model’s performance across different independent datasets.
6. The calculation of the contributions of the GDB drivers to GDB over a larger time period than previously (e.g. Hatzianastassiou et al., 2020) and its sub-decadal time periods as well as on annual and seasonal basis.
7. The use of machine learning techniques to further investigate the relationship of the SSR variations with the GDB drivers.

8. The detailed investigation of the relationship between FORTH-RTM GDB and global warming rates.

1.3 Thesis Structure

The layout of the thesis is as follows: The first chapter includes the motivation, the research questions and the innovation of this PhD whereas it summarizes the theoretical basis on which this thesis is founded along with an updated review of the scientific literature on global dimming and brightening. The second chapter introduces the FORTH-RTM, and the datasets used and describes the methodology of the analysis conducted. The third chapter presents the global distributions and the timeseries of the average SSR and the GDB drivers as well as the global distributions of the GDB during the entire and decadal time periods. The fourth chapter contains the evaluation results of the FORTH-RTM SSR and GDB as well as the inter-comparison across several datasets. The fifth chapter contains the investigation of the main GDB drivers with the contributions analysis and machine learning techniques. Then, the sixth chapter includes the examination of the links between global warming rates and GDB while the final chapter summarizes the main findings of this PhD and suggests further research related to the present work.

1.4 Radiative Transfer in the Atmosphere

1.4.1 Energy balance of the Earth-atmosphere system

Earth, the third planet from the Sun, receives its primary source of energy from the Sun's electromagnetic radiation. As a main sequence star, the Sun generates this energy through thermonuclear fusion, converting hydrogen into helium. From the surface of the Sun, a power $P = 3.92 \times 10^{23}$ KW is emitted into space, which corresponds to the power emitted by a spherical black body with a temperature of 5777 K and a radius of 7.0×10^{8} m (Liou, K. N., 2002). At the average Earth-Sun distance ($R_0 = 1.5 \times 10^{11}$ m), the solar radiation flux I_0 is given by the equation:

$$I_0 = \frac{P}{4\pi R_0^2} \qquad \text{(Eq. 1.1)}$$

and according to the most recent estimates (Wild et al., 2013), it is equal to 1361 Wm^{-2}. This value of the radiative flux is called the solar constant (I_0) and corresponds to an average solar power per unit surface area, at the top of the atmosphere averaged over a year, of 340 Wm^{-2}. Of this amount, 30% is reflected to space by clouds, the atmosphere (gases, aerosols) and the Earth's surface. This amount is called the planetary reflectivity. Clouds and the atmosphere also absorb an amount of 23%, so the amount of energy absorbed by the Earth's surface corresponds to less than half (~47%) of the energy at the top of the atmosphere (Wild et al., 2013). The absorption of solar radiation by the Earth and its atmosphere leads to its heating. This results in the emission of radiation at longer wavelengths (infrared spectrum), and the flux of infrared radiation can be calculated using the Stefan-Boltzmann law:

$$E^* = \varepsilon\sigma T^4 \qquad \text{(Eq. 1.2)}$$

where ε is the emissivity and σ is the Stefan-Boltzmann constant ($\sigma=5.67\times10^{-8}$ $Wm^{-2}K^{-4}$). Infrared (terrestrial) radiation is strongly absorbed by clouds, water vapor and atmospheric gases such as carbon dioxide (CO_2), ozone (O_3) and methane (CH_4) (greenhouse gases). The Earth's radiation escaping into space causes cooling of the Earth-atmosphere system and compensates for the heating from short-wavelength, solar radiation. An overview of the climate system, as described above, using recent data (Wild et al., 2013) is provided in Figure 1.1. The energy balance can be disturbed, and climate changes can be induced by an increase in greenhouse gases, which ultimately leads to a reduction in the amount of infrared radiation escaping to space, or by an increase/decrease in planetary reflectivity, which has the direct effect of reducing/increasing the amount of solar radiation absorbed by the Earth-atmosphere system. Finally, climate changes can also be influenced by variations in the solar constant, which is linked to fluctuations in solar activity or to changes in the Earth orbital characteristics. The interactions between solar radiation—both shortwave and infrared—and the diverse components of the Earth-atmosphere system are highly complex, involving multiple atmospheric and surface processes.

1.4.2 Interaction of solar radiation with the atmosphere and the Earth's surface

After entering the Earth's atmosphere, solar radiation interacts with the molecules of atmospheric gases, clouds and aerosols. Two of the most important interaction mechanisms are scattering and absorption. The most important parameters regarding these two phenomena are:

- the wavelength, λ, of the incident radiation,
- the size of the scattering particles (atmospheric gas molecules, cloud droplets or aerosols), especially with respect to the incident wavelength, usually expressed in terms of the dimensionless size parameter α, based on the equation

$$\alpha = 2\pi r/\lambda = \pi D_p/\lambda \,, \qquad \text{(Eq. 1.3)}$$

  where r and D_p are the radius and diameter of the particle, respectively, and
- the complex refractive index N of the scattering particle,

$$N = n + ik, \qquad \text{(Eq. 1.4)}$$

  where *n* and *k* are the real and imaginary parts of the refractive index (*N*), both functions of the wavelength and related to the scattering and absorption of solar radiation by the particle, respectively.

1.4.2.1 Solar radiation scattering and asymmetry parameter

Light scattering plays a prominent role in the radiation transfer in the atmosphere as it changes the direction of photons (Vardavas and Taylor, 2011). Scattering can be divided into backward scattering and forward scattering. Two main types of scattering are observed in the atmosphere and will be discussed in more detail below: Rayleigh scattering and Mie scattering. Both are considered elastic as the

energy of the scattered photons remains constant, with no significant thermal energy transfer to the atmosphere (Vardavas and Taylor, 2011). Therefore, the incident and scattered radiation have the same frequency. At this point it is useful to introduce the concept of the phase function, which expresses the angular distribution of the scattered energy as a function of the scattering angle ϑ and is defined for molecules, clouds and aerosols (Korras-Carraca et al., 2015).

1.4.2.1.1 Rayleigh scattering

When a photon of wavelength λ interacts with a relatively small particle with a size parameter α<<1, or a radius of no more than 1/10 of λ (e.g. atmospheric molecules), the scattering is called Rayleigh scattering. The intensity of the scattered radiation is a function of the wavelength λ, the refractive index and the angle between the scattered and incident radiation. For the case of non-polarized light, the intensity of the scattered electromagnetic radiation (I), at an angle θ and at a distance R from the center of scattering, is calculated as follows:

$$I = \frac{I_0}{R^2}\frac{1+cos^2\theta}{2}\left(\frac{2\pi}{\lambda}\right)^4\left(\frac{n^2-1}{n^2+2}\right)^2\left(\frac{d}{2}\right)^6, \quad \text{(Eq. 1.5)}$$

where *d* is the diameter of the scattering particle, *n* is the real part of the refractive index and *λ* is the wavelength. Rayleigh scattering shows a strong dependence on wavelength (it is stronger for shorter *λ*) which accounts for the blue color of the sky.
In Rayleigh scattering, the radiation is scattered in all directions, exhibiting symmetry both along its path and perpendicular to it. For the case of non-polarized light, the phase function P can be expressed as follows:

$$P(\theta,\varphi) = \frac{3}{4}cos^2\theta, \quad \text{(Eq. 1.6)}$$

i.e. it is independent of the azimuth ϕ. A typical example of Rayleigh scattering in which the wavelength dependence and the aforementioned symmetries are distinguished is given in Figure 1.2.

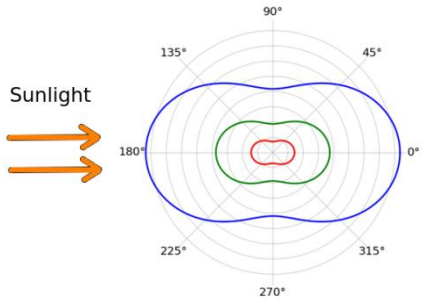


Figure 1.2. Polar diagram of the intensity of the scattered monochromatic radiation of 450 nm (cyan), 550 nm (green) and 700 nm (red) from particles of radius r = 0.010 μm.

1.4.2.1.2 Mie Scattering

For particles of approximately the same size as the wavelength of the radiation (a~1), such as cloud and aerosol particles, Mie scattering occurs. During Mie scattering, scattering of all wavelengths

occurs and the intensity of the scattered radiation is a function of the particle size and λ, the refractive index, the size of the scattering particles and the angle between the directions of scattered and incident radiation. In contrast to Rayleigh scattering, symmetry is observed only in the direction of propagation of the radiation. A typical example of Mie scattering and its dependence on the size of the scattering particles is given in Figure 1.3.

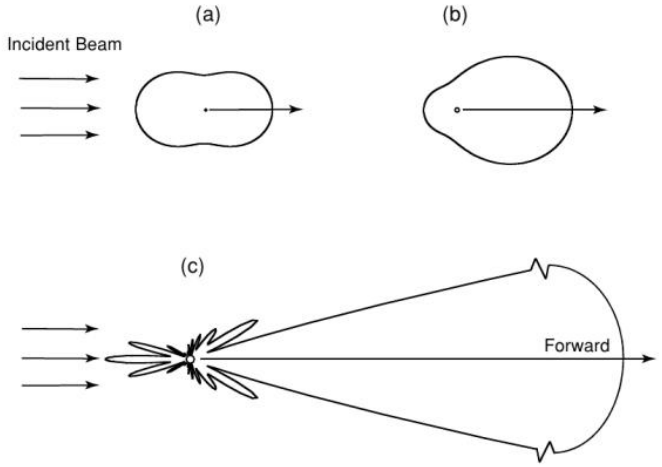


Figure 1.3. Polar diagram of the intensity of scattered 500 nm monochromatic radiation from spherical particles with radius (a) 10^{-4} μm, (b) 0.1 μm and (c) 1 μm. The forward part of the distribution of scattered radiation from the 1 μm radius particle is drawn under scale in order to make it possible to show it, as in reality the forward scattering is much stronger. (Source: Liou, 2002)

1.4.2.1.3 Asymmetry parameter

The asymmetry parameter or factor is defined by:

$$g = \frac{\widetilde{\omega}_1}{3} = \frac{1}{2}\int_{-1}^{1} P(cos\Theta)cos\Theta dcos\Theta \qquad \text{(Eq. 1.7)}$$

where *P* is the phase function. The phase function can be expressed using Legendre polynomials $P_l(cos\theta)$, with expansion coefficients $\widetilde{\omega}_l$ (Liou, 2002) for l=1 ($\widetilde{\omega}_1$ in Eq. 1.7). The asymmetry factor is the first term of the phase function and is an important parameter in terms of radiation transfer. For isotropic scattering, or less restrictively for symmetry between forward scattering and backscattering (the case of Rayleigh molecular scattering), g = 0. The asymmetry parameter increases as the maximum of the scattered radiation distribution becomes sharper. For Lorenz-Mie type particles (aerosols, cloud droplets), the asymmetry parameter takes positive values indicating the predominance of forward scattering of radiation which becomes stronger as the particle size increases, as can be seen in the example in Figure 1.3. The asymmetry parameter may take negative values in the case where the maximum of the phase function is observed behind the particle (at angles of 90-180°). Therefore, negative values of g indicate backscattering of radiation. In conclusion, the asymmetry parameter is a simple expression of the phase function (as it is the first term in its Legendre expansion), hence the importance of its use in radiation transfer models. It is also used extensively to describe the size of aerosols as well as in climate models or general atmospheric circulation models.

1.4.2.2 Absorption of solar radiation

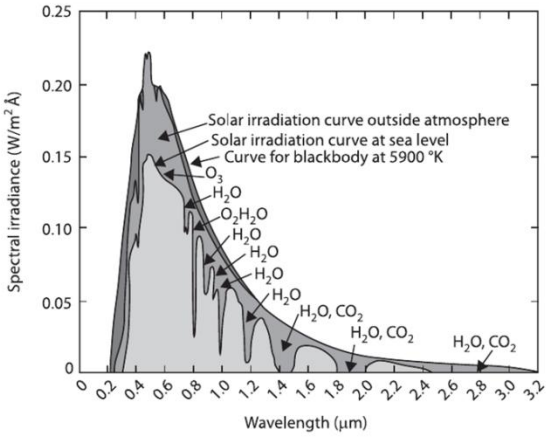


Figure 1.4. Low-resolution image of the solar radiation spectrum at the top of the atmosphere and at the sea surface level. The spectral regions in which the various atmospheric gases absorb are distinguished. (Source: Vardavas and Taylor, 2011)

The interaction of a photon with a particle that results in the conversion of the photon's energy into thermal energy is called absorption (Vardavas and Taylor, 2011) and is mainly related to the transitions between the allowed quantized energy levels of the molecules (electronic, oscillatory and rotational). The main absorbers of solar (short-wavelength) radiation are atmospheric gases - mainly water vapor (H_2O), ozone (O_3), oxygen (O_2) and carbon dioxide (CO_2) - and aerosols. Of the 20% of incoming solar radiation at the top of the atmosphere that is absorbed within the atmosphere (see Section 1.2), about 18% is absorbed by the above-mentioned atmospheric gases and aerosols, while the remaining 2% is absorbed by clouds. The effect of the absorption of radiation from various atmospheric gases on the solar spectrum at the lower limit of the atmosphere is given in Figure 1.4. As can be seen, the most important absorber of solar radiation is ozone (O_3), which strongly absorbs UV radiation. Significant absorption is also observed at wavelengths longer than 0.7 μm, mainly by water vapor and to a lesser extent by CO_2. Absorption of radiation is particularly important in terms of the energy balance and the global climate, as it leads to the warming of the atmosphere.

1.4.2.3 Radiation interaction with the Earth's surface

Part of the incident solar radiation on the Earth's surface is absorbed by the Earth's surface, while the rest is reflected. The ratio of reflected to incident radiation is called the surface albedo. Albedo can take values between 0 (total absorption) and 1 (total scattering of radiation by the ground). Different surfaces have quite different values of albedo. For example, the albedo of oceans and forests is quite low. On the other hand, desert areas or land covered by snow and ice are characterized by high values of albedo. Furthermore, the albedo is dependent on the wavelength of the incident radiation and, especially for water surfaces, it is also dependent on the angle of incidence.

1.4.2.4 Basic concepts and radiation transfer equation

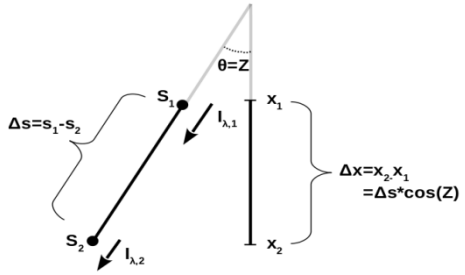


Figure 1.5. Schematic representation of radiation transfer in a medium, between 2 points s_1 and s_2, at an angle θ=Z with the vertical.

When a radiation beam propagates within a medium (e.g. atmosphere), it is attenuated by scattering and absorption of radiation by the medium. The relative attenuation of a beam of monochromatic radiation wavelength λ and intensity I_λ travelling over an elementary interval ds is given by Beer's law:

$$\frac{dI_\lambda}{I_\lambda} = -k_\lambda \rho ds, \qquad \text{(Eq. 1.8)}$$

where k_λ is the mass extinction cross section of the medium (in units of area to mass) and ρ is its density. The mass extinction cross section is equal to the sum of the corresponding mass scattering cross section and mass absorption cross section.

The attenuation of a beam of radiation travelling between s_1 and s_2 (Figure 1.5) is calculated by integrating equation 1.8 between s_1 and s_2:

$$\frac{I_{\lambda,1}}{I_{\lambda,2}} = exp\left(-\int_{s_1}^{s_2} k_\lambda \rho ds\right) = exp\left(-\int_{s_1}^{s_2} \beta_{ext}\, ds\right), \qquad \text{(Eq. 1.9)}$$

where $I_{\lambda,1}$ and $I_{\lambda,2}$ are, respectively, the monochromatic intensity of the radiation at points s_1 and s_2. The product $k_\lambda\rho$ is called the extinction coefficient, $\beta_{ext}(\lambda)$, of the medium and has length units^{-1}. The ratio $I_{\lambda,1}$ to $I_{\lambda,2}$ is called the monochromatic transmissivity (T_λ). In the case of a non-scattering medium:

$$A_\lambda = 1 - T_\lambda, \qquad \text{(Eq. 1.10)}$$

where A_λ is the monochromatic absorptivity of the medium and expresses the fraction of the radiation absorbed by it. If scattering of radiation from the medium takes place, a fraction of the incoming radiation will be backscattered. The fraction of the backscattered (reflected) radiation from the medium is called the monochromatic reflectivity (R_λ). From the principle of conservation of energy it follows that for a scattering and absorbing medium it will hold:

$$T_\lambda + A_\lambda + R_\lambda = 1 \qquad \text{(Eq. 1.11)}$$

The integral within the exponential is called the optical attenuation thickness (τ_{ext}) of the medium between points s_1 and s_2:

$$\tau_{ext} = \int_{s_1}^{s_2} k_\lambda \rho ds = \int_{s_1}^{s_2} \beta_{ext}\, ds \qquad \text{(Eq. 1.12)}$$

If we consider the case of solar radiation transfer within a layer of the Earth's atmosphere, with the direction of propagation forming an angle θ with the vertical, where θ=Z (zenith angle), ds=dx/cosZ (Figure 1.5) and equation 1.9 can be written as follows:

$$\frac{I_{\lambda,1}}{I_{\lambda,2}} = exp\left(-\int_{x_1}^{x_2} \beta_{ext}\, dx/cosZ\right), \qquad \text{(Eq. 1.13)}$$

where x_1 and x_2 are the heights at which points s_1 and s_2 are located (with $x_1>x_2$).
The $\int_{x_1}^{x_2} \beta_{ext}\, dx$ integral is often referred to as vertical optical thickness or optical depth (Liou, 2002).
Therefore, the optical depth of an atmospheric layer is the same as its optical thickness in the case where radiation propagates vertically.
Corresponding to the attenuation coefficient, the scattering coefficients $\beta_{scat}(\lambda)$ and absorption coefficients $\beta_{abs}(\lambda)$ are defined:

$$\beta_{ext}(\lambda) = \beta_{scat}(\lambda) + \beta_{abs}(\lambda) \qquad \text{(Eq. 1.14)}$$

Correspondingly, we can define the optical depths of scattering (τ_{scat}) and absorption (τ_{abs}) of an atmospheric layer.

The ratio of the scattering coefficient to the extinction coefficient (or equivalently, the optical scattering thickness to the optical extinction thickness) is called the single scattering albedo (ω). The single scattering albedo takes values from 0 (exclusively absorbing layer) to 1 (exclusively scattering atmospheric layer). Both the optical depth and the single scattering albedo are extremely important parameters with regard to the radiation-atmosphere (clouds, atmospheric gases and aerosols) interaction. For this reason, their use is essential in radiation transfer models.

In addition to the extinction of the radiation beam as it propagates through the medium, due to scattering and absorption by the medium, the intensity of the beam may be increased by radiation emission from the medium and multiple scattering in the direction of beam propagation. In simple terms, photons from emission or scattering are added to the beam. The increase in the intensity of the monochromatic beam dI_λ which travels over an elementary interval ds is calculated as follows:

$$dI_\lambda = j_\lambda \rho ds, \qquad \text{(Eq. 1.15)}$$

where j_λ is the source function coefficient, which has a similar physical meaning to the mass extinction cross section (Liou, 2002). Therefore, by combining equations 1.8 and 1.15, it follows that for a radiation

beam travelling over an elementary interval ds, the variation of its intensity dI_λ due to scattering, absorption, emission and the contribution from multiple scattering is given by the following relation:

$$dI_\lambda = -k_\lambda \rho I_\lambda ds + j_\lambda \rho ds. \quad \text{(Eq. 1.16)}$$

Dividing both members by $k_\lambda \rho ds$ gives:

$$\frac{dI_\lambda}{k_\lambda \rho ds} = -I_\lambda + S_\lambda, \quad \text{(Eq. 1.17)}$$

where $S_\lambda = j_\lambda / \kappa_\lambda$ is the source function. The source function has the same units as the monochromatic intensity of radiation and in the case of a non-scattering medium in local thermodynamic equilibrium is equal to Planck's function (B_λ). Equation 1.17 is independent of the reference system and is the general form of the radiation transfer equation (Liou, 2002).

1.5 The atmospheric components and the solar radiation

1.5.1 The clean, dry atmosphere

Molecular nitrogen (78% N_2), oxygen (21% O_2), and trace amounts of argon (1% Ar) essentially make up clean, dry air. In the context of global dimming and brightening, the concentration of these elements can be regarded as constant and only varies on geological time scales. Trace gases are other molecules (not water vapor) that exist in lower amounts. Their distribution is determined by their lifetimes in the atmosphere. Some trace gases, like carbon dioxide, methane, and ozone, change over time and/or space. According to Rayleigh scattering theory, all air molecules scatter radiation throughout the shortwave spectrum, with the strongest scattering occurring at shorter wavelengths. Since the concentration of the primary molecular components of the atmosphere remains constant over long time scales, Rayleigh scattering within the atmosphere can be regarded as stable despite variations in air pressure and density. Only certain wavelength bands, which differ based on the absorbing molecules, are used to absorb SW radiation (Figure 1.4). For instance, the majority of transmitted UV light is absorbed by ozone (O_3). There are absorption bands in the near infrared spectrum of carbon dioxide (CO_2), whose concentration is continuously rising as a result of human activity, but the biggest absorption takes place in the longwave spectrum. Although the radiative balance in some parts of the spectrum has been affected by the different atmospheric concentrations of these absorbing gases, the overall SW irradiance has been barely affected (Barker, 2007; Cutchis, 1974).

1.5.2 Water vapor

With several absorption bands in the near-infrared and infrared regions of the sun spectrum, water vapor is a powerful absorber of SW radiation (Figure 1.4). Depending on the location and time of day, the amount of water vapor in the atmosphere can vary greatly, ranging from 0% to 5% of the atmospheric concentration by volume (Wallace and Hobbs, 2006). Water vapor has the greatest capacity

to alter the overall SW irradiance among the gaseous components of the atmosphere. According to sensitivity studies using radiative transfer models, significant variations in water vapor concentrations would be necessary to account for the 20th-century SW trends that have been observed (Wild, 2009). Globally, the observed dimming and brightening cannot be explained by changes in humidity alone (Wild, 1997). However, through both direct absorption of SW radiation and its impact on the cloud field, rising atmospheric water vapor concentrations might have had a significant role in local or regional dimming (Yang et al., 2012). Water vapor concentrations could rise to the point where they significantly reduce SW irradiation in a future warming environment (Haywood et al., 2011).

1.5.3 Aerosols

Dry or liquid particles suspended in the atmosphere are called aerosols. Aerosols vary widely in size, shape, and material composition, with comparable radii ranging from 10^{-3} to 10^{2} μm (Iqbal, 1983, Chapter 5). Depending on their optical characteristics, aerosols can either scatter or absorb SW radiation, which directly affects SW irradiance. SW radiation is better dispersed by smaller particles than by bigger ones. Aerosols can be formed in the atmosphere from gases (primary and secondary) or directly injected into the atmosphere. The secondary aerosols are more optically efficient because they are typically smaller (<1 μm). Sulfur, nitrogen, and organic and carbonaceous materials can all combine to generate gas-to-particle aerosols. Anthropogenic sources account for the great majority of sulfate and nitrate gas-to-particle aerosols in the northern hemisphere (Wallace and Hobbs, 2006, Table 5.3). Examples of naturally occurring aerosols include dust, pollen, salt from ocean spray, and soot from forest fires. On decadal to multidecadal time scales, it is not possible to assume that all natural aerosol sources are stable. For instance, the occurrence of Sahara dust outbreaks and forest fires can fluctuate significantly over time (Miller et al., 2012; Goudie, 2009). Anthropogenic climate change can influence the frequency of these occurrences, blurring the line between natural and anthropogenic aerosol changes. Road dust, soil dust from agricultural tillage, burning biomass, emissions from combustion engines, and other industrial processes are the primary sources of anthropogenic aerosols, while they can originate from a range of human activities. Both anthropogenic (industrial processes, combustion engines) and natural (volcanic eruptions) sources produce sulfuric acid particles (Wallace and Hobbs, 2006). Stratospheric sulfur aerosols reflect SW radiation and thus effectively reduce the total SW irradiance. Volcanic eruptions provide a chance to study the influence of sulfur emissions on SW radiation and the climate system. During recent events, such as the eruption of El Chicón (Mexico) in April-May 1986 and Mount Pinatubo (Philippines) in June 1991, notable reductions of SW irradiance were detected across the globe (Alados-Arboledas et al., 1997). In recent decades, the emissions have been reduced as a result of stricter regulations on industrial air pollution. The emissions of sulfur oxides (SOx) in Europe have decreased from approximately 25.8×10^{9} kg in 1990 to 4×10^{9} kg in 2012 (EEA Technical report, 2014).

1.5.4 Clouds

SW radiation is absorbed and scattered by clouds. Clouds have a greater impact on the fluctuations of SW attenuation than any other atmospheric process on short time intervals, ranging from hourly to interannual. The optical characteristics, ice or water phase, cloud dispersion, cloud optical

thickness, and cloud height all affect a cloud's albedo (reflectance) and the direction in which SW irradiation is reflected (Kokhanovsky, 2004). When the humid air becomes supersaturated with water or ice, clouds are created (Wallace and Hobbs, 2006, Chapter 6). When an air parcel rises to higher altitudes, it becomes supersaturated, allowing the air to expand and cool adiabatically. Conversely, sinking air (subsidence) warms adiabatically through compression, which may cause any existing clouds to dissipate. When supersaturation occurs, cloud droplets form upon small particles that are referred to as cloud seeds or cloud condensation nuclei (CCN) (Hudson, 1993). If no CCN are available, very high super-saturation can occur without cloud droplets forming (Katz and Ostermier, 1967). Since CCN are generally present in the atmosphere, super saturation levels above 1–2 % are rarely found in ◦the atmosphere (Wallace and Hobbs, 2006, Chapter 6). Clouds above the 0 C altitude level may contain both super-cooled droplets and ice particles. Ice particles form upon the surface of ice nuclei (IN), particles with a molecular structure similar to the hexagonal structure of ice. In the atmosphere, formation of ice particles without IN occurs only at high altitudes where the temperature is very low (< −35◦ C). In a pristine environment with few aerosols in the atmosphere, cloud droplets tend to be fewer and larger than when there are aerosols available to act as CCN. Assuming all else is the same, an increase of the CCN amount increases the reflectivity of the clouds because the smaller droplets are more reflective. A higher concentration of CCN also prevents cloud droplets from combining, which prevents precipitation and lengthens the clouds' lifespan (Koren and Feingold, 2011). Cumuliform and stratiform clouds are the two main varieties. When heated air in an unstable atmosphere rises, cumuliform clouds are created. When an entire layer is pushed upward, frequently in tandem with a weather front, stratiform clouds are created. Clouds are limited to the troposphere, the lowest layer of the atmosphere that makes up over 80% of the atmospheric mass, with the exception of uncommon kinds of ice clouds (Wallace and Hobbs, 2006, Chapter 1). At higher elevations, ice and mixed phase clouds are more common since the troposphere's temperature drops with altitude. Compared to clouds at mid- and high-altitudes, low-level clouds often have a greater optical thickness. An illustration of the different cloud types and their relative heights can be found in Figure 1.7. Multiple scattering within or between clouds increases the path length of the SW radiation and therefore increases SW absorption by cloud droplets as well as other absorbing constituents in the atmosphere (Kokhanovsky, 2004).

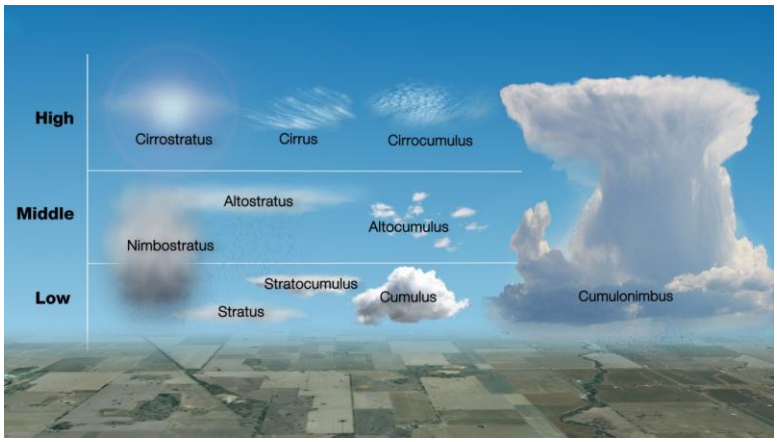


Figure 1.7. The variety of cloud types and their general heights. Image via Australian Bureau of Meteorology [https://media.bom.gov.au/social/upload/images/cloud%20types.jpg].

1.5.5 Interactions between clouds, aerosols, water vapor, and SW radiation

The aforementioned atmospheric forces are not entirely autonomous. By serving as cloud condensation nuclei, aerosol particles can indirectly affect SW radiation by altering the albedo (reflectivity) and lifetime of clouds. The semi-direct aerosol effect is a process by which absorbing aerosols can stabilize the atmosphere in highly polluted areas by heating the atmosphere, which inhibits the development of clouds. Aerosols are influenced by the atmospheric conditions. The direction of the wind affects how aerosols are transported from the emission source. Aerosol deposition is influenced by precipitation and air turbulence, which changes the overall quantity and size distribution of the particles. The size and, consequently, the optical characteristics of hygroscopic aerosols are influenced by atmospheric humidity. Cloud formation and atmospheric circulation can also be impacted by variations in SW irradiation. Changes in SW irradiance may also have an impact on ocean salinity through evaporation, which may in turn affect sea surface temperatures and the flow of heat between the atmosphere and the ocean (Durack et al., 2012; Pierce et al., 2012). Through the distribution of clouds, humidity, and wind, all of this could provide feedback to the SW irradiance.

1.5.6 Large scale circulation patterns

Meteorological structures with horizontal scales of around 1000 km are referred to as large scale or synoptic weather patterns. Low and high-pressure systems are the most prevalent synoptic weather patterns in mid- and high latitudes. The winds in the Earth's atmosphere move in cyclonic (counterclockwise on the northern hemisphere) and anticyclonic (counterclockwise on the northern hemisphere) patterns around the low-pressure centers and the iso-bars (lines of constant pressure), respectively. Planetary waves, sometimes referred to as Rossby waves, guide the eastward migration of the low- and high-pressure systems at mid-latitudes. The Earth's rotation modifies the general atmospheric circulation, which is fueled by differential heating. For a comprehensive overview of atmospheric dynamics and synoptic meteorology, refer to Wallace and Hobbs (2006) (chapters 7 and 8). The distribution of clouds and humidity is the main way that the large-scale circulation affects the local SW irradiance at a place. Precipitation and clouds are linked to cyclonic weather patterns. The rising air cools adiabatically, causing clouds to develop. A large portion of cyclone-related weather is typically centered along frontal zones, which indicate abrupt changes in wind and temperature. When two masses of air collide, the warmer, less dense air rises above the colder air to produce a frontal zone. Because of subsidence, cloud-free conditions are linked to anti-cyclonic weather patterns. Through the effects of precipitation and wind direction on aerosol deposition and transportation, the circulation patterns may also have an impact on SW irradiance. Furthermore, human-induced climate change may have an impact on atmospheric circulation (Bengtsson et al., 2006; Wu et al., 2010). Therefore, the natural SW irradiance variability may not be completely separated from anthropogenic influence, even if the atmospheric circulation-driven SW irradiance variability is successfully separated from the SW variability caused by other sources.

1.6 The literature review

A substantial amount of study literature has previously been produced on dimming and brightening. An overview of the body of research on these topics is given in this chapter.

1.6.1 Observations: Global dimming and brightening

In wide regions of the earth, measurements of incoming solar radiation (SSR) showed significant fluctuations during the second half of the 20th century. Globally, sun photometers and ground-based radiometers recorded significant drops in SSR from the 1950s to the 1980s (Wild 2009). Ohmura and Lang (1989) first reported the finding of decreasing SSR trends in an abstract for the 1988 International Radiation Symposium that centered on Europe. The term "global dimming" was soon created to describe the decline in SSR after the 1950s, following a lot of research on declining trends in other parts of the world during the 1990s (e.g. Russak 1990; Stanhill and Moreshet 1994; Stanhill and Kalma 1995; Abakumova et al. 1996). It should be mentioned that the term "global" in global dimming was originally a contraction of the technical term "global radiation dimming" where "global radiation" refers to the total of direct and diffuse radiation, rather than the global scale at which the SSR reduction was occurring (Wild 2009). However, since it is not usually stated clearly, it is unclear if "global dimming" is used in all texts to refer to this technical word or the worldwide scale of dimming (Wild 2020). Since dimming was discovered, global and regional studies have been published. As stated in Chapter 1, the total dimming between the 1950s and 1980s was estimated to be a drop in SSR of roughly 4 Wm^{-2}. Since the 1980s, the SSR trend has reversed in several regions of the world, specifically Europe, North America, and some parts of Asia, and this reversal tendency has been called "brightening" (Wild et al., 2005; Wild 2012). However, in some locations, such as India, the dimming period lasted longer (Soni et al., 2016).

1.6.2 Solar irradiance's effects on dimming and brightening

According to Willson and Mordvinov (2003) and Hoyt and Schatten (1993), fluctuations in the Sun's luminance are at least an order of magnitude smaller than the changes detected from surface observations of SSR. Extraterrestrial influences can thus be neglected in the interpretation of the observed variations in SSR. This implies that only the transmissivity components of the atmosphere could be the primary contributors to dimming, and because these components can be influenced by a variety of circumstances, the explanation could be rather convoluted. Furthermore, satellite-based measurements of shortwave irradiance show that solar output changes are at least an order of magnitude smaller than reported SW irradiance trends on Earth's surface (Lean, 2010; Fröhlich, 2011). It is plausible to believe that the reasons of dimming and brightening are found in the atmosphere.

1.6.3 Radiatively active gases' effects on dimming and brightening

Several atmospheric gases are radiatively active in the solar radiation spectrum, most notably water vapor and ozone (O3). This means that alterations in the presence of such gases have the potential to influence SSR. However, according to Stanhill and Cohen (2001), Wild (2016), and references therein, variations in levels of these gases were not significant enough during the relevant period to generate the

dimming and brightening trends. Therefore, this thesis also examines the potential influence of trends in radiatively active gases.

1.6.4 Aerosol and cloud effects on dimming and brightening

The previous two sections concluded that changes in the Sun's luminosity and variations in the atmospheric load of radiatively active gases were not the cause of global dimming and brightening. Aerosols and clouds are the only remaining probable causes. Because of aerosol-cloud interactions (ACI), cloud and aerosol effects on SSR are inextricably linked and impossible to investigate separately. A great variety of observational studies have been carried out to investigate cloud and aerosol contributions to SSR changes. From early on, it was thought that the main cause of the wide-reaching dimming trend was extinction from increasing amounts of aerosols in the atmosphere: Stanhill and Cohen 2001, who introduced the term "global dimming", reviewed the literature on dimming that had been published in the decade beforehand, and concluded that the most likely cause of the worldwide dimming was the increase in aerosol emissions, especially due to the aerosol's enhancement of cloud optical depth through ACI. For Europe and China, Norris and Wild 2007 and Norris and Wild 2009 found that SSR trends were identical under all-sky and clear-sky conditions, implying that cloud variations could not be the cause of the SSR trends. However, Norris and Wild 2009 found that cloud cover fluctuations significantly influenced Japanese SSR patterns between 1971 and 2002. Stanhill et al. (2014) discovered that changes in cloud cover, rather than aerosol load, were likely the primary source of dimming and brightening at the five sites evaluated. Parding (2014) found that in Bergen, Norway, the first dimming trend until 1990 was caused by cloud trends, and the succeeding brightening trend was caused by a drop in aerosol optical depth. However, Pfeifroth et al. (2018) examined satellite data over Europe and determined that the majority of the European brightening was caused by cloud changes, while not ruling out indirect impacts of aerosols as potentially causal to the relevant cloud changes. Liley (2009) found that in New Zealand, SSR patterns corresponded to fluctuations in cloudiness. In the United States, Long et al. (2009), Augustine and Dutton (2013), and Augustine (2020) indicate that brightening between 1996 and the late 2000s was not predominantly caused by aerosol changes. The latter two studies argue that the brightening trend is primarily attributable to changes in cloud cover. Nonetheless, many publications continue to support the assumption that the overall trends are primarily attributable to aerosol changes. Streets et al., (2006) examined global, interannual fluctuations in SSR from 1980 to 2000 and discovered that SSR matched the trend in SO2 and black carbon emissions. They determined that changes in the aerosol burden caused by changing anthropogenic emission patterns are likely to contribute to worldwide trends in surface solar radiation levels. Mishchenko et al. (2007) analyzed worldwide AOD from a satellite-measured dataset between 1991 and 2005 and discovered that global AOD dropped over this period, coinciding with a global increase in SSR, implying that the trend in AOD contributed to the SSR trend. One other analysis emphasizes the importance of atmospheric absorption changes for dimming and brightening patterns, implying contributions from absorbing aerosols, particularly black carbon (Schwarz et al. 2020). Other research arguing that aerosol extinction is essential to dimming and brightening patterns include Zerefos et al. (2009) and Sanchez-Lorenzo et al. (2009). In summary, many research studies appear to corroborate the general conclusion that aerosol effects are responsible for long-term trends in SSR since the mid-20th century. However, the significance of cloud changes is still highlighted in certain studies, particularly those

with a regional focus. Thus, the issue is far from resolved. According to the present literature, the reasons of global dimming and brightening are likely to be complicated.

1.6.5. Global dimming and brightening in satellite retrievals and RTMs

Due to the large-scale GDB phenomenon, accurate inferences cannot be formed from surface measurements alone. The knowledge of the phenomenon from ground-based measurements should be supplemented by satellite observations/models and reanalysis datasets, which offer large and complete spatial, as well as temporal, coverage. However, since such datasets more or less involve theory, they have limited consistency in terms of trends and must be evaluated against ground-based measurements to ensure their reliability. Other reasons for such an evaluation are the detection of errors in cloud and aerosol input data to the models and inhomogeneities in the assimilated data records in reanalysis, which may cause possible uncertainties in the estimated fluxes (Zhang et al., 2016; Jia et al., 2013; Kambezidis et al., 2017; Zhang et al., 2018; Feng et al., 2019; Deneke et al., 2008). Several studies using model simulations and/or satellite data (Hatzianastassiou et al., 2020; Hatzianastassiou et al., 2005; Haywood et al., 2011; Ruckstuhl et al., 2009; Hatzianastassiou et al., 2012; Pinker et al., 2005; Hinkelman et al., 2009; Zhang et al., 2015; Wang et al., 2022) found that the dimming and brightening during the 1980s and 1990s, respectively, were global rather than local, whereas they also reported divergent trends in SSR even over neighboring regions. More specifically, the investigation by (Hatzianastassiou et al., 2005) based on the International Satellite Cloud Climatology Project-D2 series (ISCCP-D2) identified substantial increasing trends in SSR, i.e., brightening, between 1984 and 2000, yielding an average increase of 2.4 $Wm^{-2}decade^{-1}$. Additionally, using satellite retrievals from ISCCP-D1, Pinker et al. (2005) computed a global brightening of 1.6 $Wm^{-2}decade^{-1}$ between 1983 and 2001, which was associated with decreasing cloud cover fraction. According to the analysis performed by Hinkelman et al. (2009) using data from the Global Energy and Water Exchanges Project- Surface Radiation Budget version 2.8 (GEWEX-SRB V2.8), there was a dimming of −2.51 $Wm^{-2}decade^{-1}$ between 1983 and 1991, a brightening of 3.17 $Wm^{-2}decade^{-1}$ from 1991 to 1999, a subsequent dimming of −5.26 $Wm^{-2}decade^{-1}$ during 1999–2004, and an overall brightening of 0.25 $Wm^{-2}decade^{-1}$ during 1983–2004. Moreover, Haywood et al. (2011) calculated a global dimming of −2.0 Wm^{-2} from 1920 to 2000, which is in line with simulations from 10 models used in the Fourth Assessment Report (IPCC-AR4) of the United Nations Intergovernmental Panel on Climate Change (UNIPCC), which reported a dimming that is ranging in different models from −1 to −4 Wm^{-2} globally during the entire 20th century (Romanou et al., 2007). Moreover, they (Haywood et al., 2011) noticed a dimming trend from 1968 to 1977, followed by a brightening trend in the 1980s and 1990s.

There were few attempts to extend GDB beyond 2000 and even fewer beyond 2010 using satellite-derived SSR, showing a tendency for dimming in the years following 2000. A study by Hatzianastassiou et al. (2012) using a radiation transfer model with input from ISCCP-D2 satellite data for the years 2001–2006 revealed a just slight (0.17 Wm^{-2}) brightening in the Northern Hemisphere and a dimming (−2.88 Wm^{-2}) in the Southern Hemisphere, where dimming was primarily seen over the oceans and a slight brightening over land. The same authors (Hatzianastassiou et al., 2020), using the same radiative transfer model with input cloud data from ISCCP-D2, aerosol data from MODIS (Moderate Resolution Imaging Spectroradiometer) C006, and meteorological data from NCEP/NCAR (National Centers for Environmental Predictions and National Center for Atmospheric Research), during 2000–2009,

computed an overall dimming, weaker in the Northern than in the Southern Hemisphere (−2.2 and −3.1 Wm^{-2}, respectively). According to that study, both land and ocean areas in either hemisphere showed dimming, but the one in Southern Hemisphere's land was more prominent. Furthermore, using retrieved Clouds and the Earth's Radiant Energy System (CERES) satellite SSR data for the years 2001 to 2012, (Zhang et al., 2015) found a brightening equal to 0.03 $Wm^{-2}decade^{-1}$. The same authors using GEWEX-SRB V3.0 and ISCCP-FD SSR data for the Globe, computed a significant dimming between 1984 and 1991, followed by a brightening from 1992 to 2000 and a return to significant dimming over 2001–2007. Also, they noticed a disagreement between ground-based records and satellite-derived products over China, suggesting that the differences between satellite estimates and surface measurements might have been related to aerosols, clouds, and their interactions as represented in the satellite algorithm, but also to questionable pyranometer's accuracy and measurement methods. Besides, Alexandri et al. (2017) using the CM-SAF SARAH (Satellite Application Facility on Climate Monitoring Solar surfAce RAdiation Heliosat) satellite-based product found that during 1983-2013 a brightening (0.2 ± 0.05 Wm^{-2}year−1) occurred in the southeastern Mediterranean, being similar over land and sea. Another study by Pfeifroth et al. (2018) using SARAH-2 and CLARA-A2 (CM SAF cLoud, Albedo and surface RAdiation dataset from AVHRR) computed an overall brightening in Europe since the 1980s, equal to 2.4 $Wm^{-2}decade^{-1}$ at 53 European GEBA stations and 1.9 $Wm^{-2}decade^{-1}$ at the corresponding SARAH-2 grid cells, with substantial decadal and spatial variability, during the period 1983–2015. Moreover, the study of Sanchez-Lorenzo et al. (2017) using satellite-derived data over Europe (1983–2010) showed a widespread increase of SSR in a major part of Europe, especially in spring. Also, they reported a significant difference between the trends of ground-based and satellite observations, which is not explained by calibration issues of the satellite product alone. Additionally, Dong et al. (2023) using satellite-derived products (ISCCP-FH) and reanalyses (ERA5 and NCEP-NCAR reanalysis II) show consistent increases in SSR and decreases in cloud cover over North America and Europe from the 1980s to 2010s.

1.6.6 Global dimming and brightening in Reanalysis

On the other hand, along with the satellite-derived products, reanalysis SSR datasets, which incorporate both observations and models, have also the benefit of offering complete spatial coverage and extensive temporal coverage, and as a result, they are frequently employed in atmospheric sciences and studies of climate change (Zhang et al., 2016). The interdecadal variation of various reanalysis SSR was computed and evaluated against ground-based stations over specific world regions, such as in China using Modern-Era Retrospective analysis for Research and Applications, version 2 (MERRA-2) by Feng et al. (2019), in Europe using 20CRv2c, 20CRv3, ERA20C, and CERA20C by Wohland et al. (2020) or globally with MERRA-2 by Stamatis et al. (2022). It should be noted, however, that reanalysis products generally tend to overestimate the SSR (Zhang et al., 2016; Zhang et al., 2020) and further improvements are necessary for better representation of SSR trends (Stamatis et al., 2022; Wohland et al., 2020), since they have difficulties reproducing the SSR trends. The study by Wang et al., (2022) evaluated the SSR of MERRA-2 reanalysis against ground-based (GEBA and CMA) stations. For regions with good SSR evaluation metrics, they also investigated the SSR long-term trends from 1980 to 2019 and estimated and examined the corresponding trends of clouds and aerosols. They found that during 1980–2019, there has been a widespread decline of SSR (dimming) in North America, Northeast Asia and Oceania, equal to −0.32, −0.00

and −1.14 $Wm^{-2}decade^{-1}$, respectively, and an increase of 0.63 $Wm^{-2}decade^{-1}$ over Europe. Apart from this study, Stamatis et al., 2022 found that according to MERRA-2, strong and statistically significant brightening over Europe, Central Africa, Mongolia, Mexico, Brazil, Argentina and some parts of the tropical oceans while statistically significant dimming occurs over the western Tropical Warm Pool, India, Southern East China, Amazonia, stratocumulus covered areas and some parts of oceans.

1.6.7 Global dimming and brightening in CMIPs

The CMIP (Coupled Model Intercomparison Project) is a common framework for ESM (Earth System Models) experiments that compares ESM simulations and investigates the spread in outcomes using identical input variables and simulation protocols (Meehl et al. 2000). These experiments enable the assessment and comparison of different ESMs, as well as the estimation of uncertainty in future projections. Historical CMIP experiments are useful for studying global dimming and brightening. These experiments aim to replicate the Earth's climate between 1850 and the present day. The most recent phase of the CMIP is CMIP6. Dwyer et al. (2010) investigated 13 CMIP3 models' capacity to reproduce dimming and brightening. Their findings revealed that climate models consistently underestimated aerosol effects on SSR in China and Japan, since the simulations significantly underestimated dimming and brightening trends in these two countries. Wild and Schmucki (2010), evaluated the ability of 23 CMIP3/IPCC-AR4 models to reproduce these decadal variations. The results were analyzed in five different climatic regions where strong decadal variations in surface solar radiation (SSR) have been observed. Only about half of the models are capable of reproducing the observed decadal variations in a qualitative way, and all models show much smaller amplitudes in these variations than seen in the observations. Largely differing tendencies between the models are not only found under all-sky conditions, but also in cloud-free conditions and in the representation of cloud effects. Allen et al., (2013) analyzed 42 CMIP5 models' simulations of historical SSR in Europe, China, India, and Japan. Similarly, their investigation found that none of the included models could replicate the magnitude of dimming in China, India, or Japan. Storelvmo et al. (2018) analyzed historical simulations from 33 CMIP5 models and found that they showed little to no dimming in Asia and the Americas, with only weak brightening in Europe. Their study suggested that if aerosol emissions were the primary driver of observed dimming trends, Earth System Models (ESMs) responded too weakly to those emissions. More recently, Moseid et al. (2020) examined how well eight CMIP6 models reproduced dimming and brightening trends. Their findings indicated that while the models captured SSR trends accurately in Europe, they failed to do so in China. The study proposed that since the ESMs correctly translated emissions into radiative effects in Europe, the discrepancies in China might stem from inaccuracies in the region’s emission inventory.

Chapter 2: Data and Methodology

2.1 Data and used Model

In this section, the satellite, reanalysis and ground-truth data that were used in the PhD work are described along with the used RTM. Specifically, in sub- section 2.1.1 the utilized FORTH-RTM is described. Next, in sub-section 2.1.2, the sensitivity analysis conducted to determine whether the model should use 3-hourly or monthly mean data, is presented. The input data to the RTM is described in detail in sub-section 2.1.3 while the ground-truth and satellite observational data which was used to evaluations is presented in sub-section 2.1.4. Details about the additional data that were used in the PhD work (i.e. temperature data and SSR data from several datasets) are presented in sub-section 2.1.5.

2.1.1 The Radiative Transfer Model

The utilized FORTH spectral radiative transfer model, which is described in detail in the works by Hatzianastassiou et al. (2004, 2005, 2007), was developed from a radiative-convective model (Vardavas and Carver, 1984). The atmosphere is seperated into clear and cloudy (for low-, mid-, and high-level clouds) fractions. The RTM solves, for an absorbing/multiple-scattering atmosphere, the radiative transfer equations for 118 separate wavelengths for the ultraviolet-visible part of the solar spectrum (wavelengths between 0.2 and 1.0 μm), and for ten bands for the near-infrared part (between 1.0 and 10.0 μm), using the modified Delta-Eddington method of Joseph et al. (1976) that relies on the Henyey–Greenstein phase function, which is an extension of the Eddington method outlined in Shettle and Weinman (1970) and Hatzianastassiou et al. (2007). Rayleigh scattering, molecular absorption in the ultraviolet, visible and near-infrared, aerosol and cloud scattering and absorption, and surface reflection are all considered. In the wavelengths of the ultraviolet and visible spectral region (UV-VIS), absorption by ozone (Chappuis and Hartley-Huggins bands), oxygen (Hertzberg continuum), and Rayleigh scattering by air are taken into account. Near-IR absorption includes absorption from water vapor, carbon dioxide and methane. More specifically, when applying the delta-Eddington method the physical parameters of optical thickness (τ), asymmetry parameter (g), and single-scattering albedo (ω), are replaced using the following transformations:

$$\tau' = (1 - \omega f)\tau \qquad \text{(eq. 2.1)}$$

$$\omega' = \frac{(1-f)\omega}{(1-\omega f)} \qquad \text{(eq. 2.2)}$$

$$g' = \frac{g}{1+g} \qquad \text{(eq. 2.3)}$$

where $f = g^2$

The atmosphere is separated into distinct layers, in each of which the total optical thickness is calculated as follows:

$$\tau = \tau_{aers} + \tau_{aera} + \tau_{ma} + \tau_R + \tau_{cs} + \tau_{ca} \quad \text{(eq. 2.4)}$$

Where τ_{aers}, τ_{aera} are, respectively, the scattering and absorption optical thicknesses of aerosols, τ_{ma} is the optical thickness of molecular absorption, τ_R the optical thickness of Rayleigh scattering, while τ_{cs} and τ_{ca} are the scattering and absorption optical thicknesses, respectively, of clouds. The single-scatter albedo for each layer is given by the following relation:

$$\omega = \omega_{aer} + \omega_R + \omega_c \quad \text{(eq. 2.5)}$$

where $\omega_{aer} = \tau_{aers}/\tau\,, \omega_R = \tau_R/\tau, \omega_c = \tau_{cs}/\tau$ (eq. 2.6)

Finally, the asymmetry factor of each layer of the model is calculated from the relation:

$$g = \frac{g_{aer}\omega_{aer} + g_R\omega_R + g_c\omega_c}{\omega} \quad \text{(eq. 2.7)}$$

in which g_{aer} is the aerosol asymmetry parameter, g_c is the asymmetry parameter of clouds, and g_R is the Rayleigh scattering asymmetry parameter (equal to 0, due to isotropic scattering of solar radiation from atmospheric gases). The temporal resolution of the current version of FORTH-RTM utilized here is monthly and the spatial resolution is 0.5° × 0.625° latitude x longitude. The cloud properties required by the model, namely cloud amount, cloud optical depth, and cloud-top pressure separately for liquid and ice phases, are taken from the CLARISC and ISCCP-H dataset for the model versions of FMC and FMI, respectively. The aerosol optical depth, single scattering albedo, asymmetry parameter, specific humidity, ozone concentration, and surface albedo were computed from data taken from the MERRA-2 Reanalysis. All the original input data were converted to monthly means, and regridded to the 0.5° × 0.625° latitude-longitude spatial resolution, to be used in the RTM. The incoming solar irradiance at the TOA is computed between 0.2–10.0 μm, based on the spectral profile of (Gueymard, 2004), using a solar constant S = 1367 Wm^{-2} (Willson, 1997), which is corrected for the Earth's elliptical orbit (Figure 2.1).

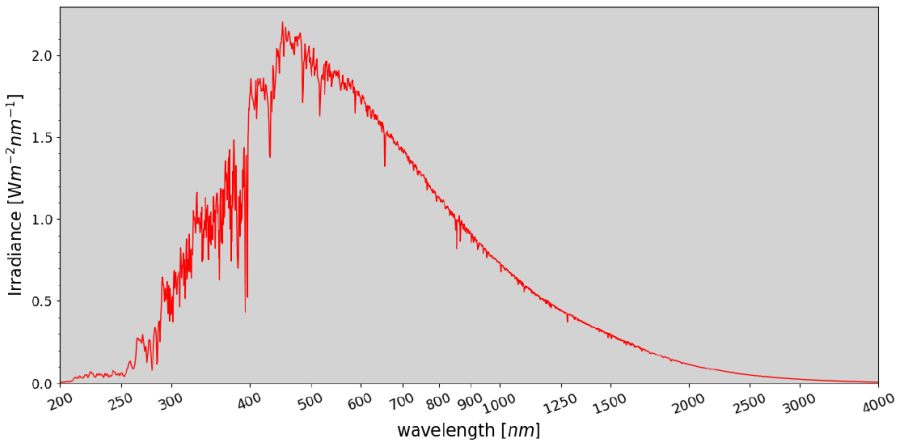


Figure 2.1. Incoming solar radiation at the Top of Atmosphere (in $Wm^{-2}nm$) based on synthetic Gueymard spectrum (source: Korras-Carraca (2022)).

The mixing ratio of CH_4 is set equal to 9×10^{-4} gcm^{-2} (or 1.7 parts per million by volume (ppmv)), CO_2 equal to 0.58 gcm^{-2} (or 371 ppmv, the value of 2001), and N_2O equal to 4.5×10^{-4} gcm^{-2} (or 0.3 ppmv). The output of the model consists of the upwelling and downwelling solar fluxes at the surface of the Earth, at 50 levels within the atmosphere, and at the top of the atmosphere (Figure 2.2). Solar fluxes are computed separately for the spectral regions of the ultraviolet-visible, near-infrared, and the entire spectrum (0.2–10 μm). In the current study, the downwelling at the Earth's surface, shortwave solar radiation flux for the entire spectrum was used for the evaluation and GDB assessment.

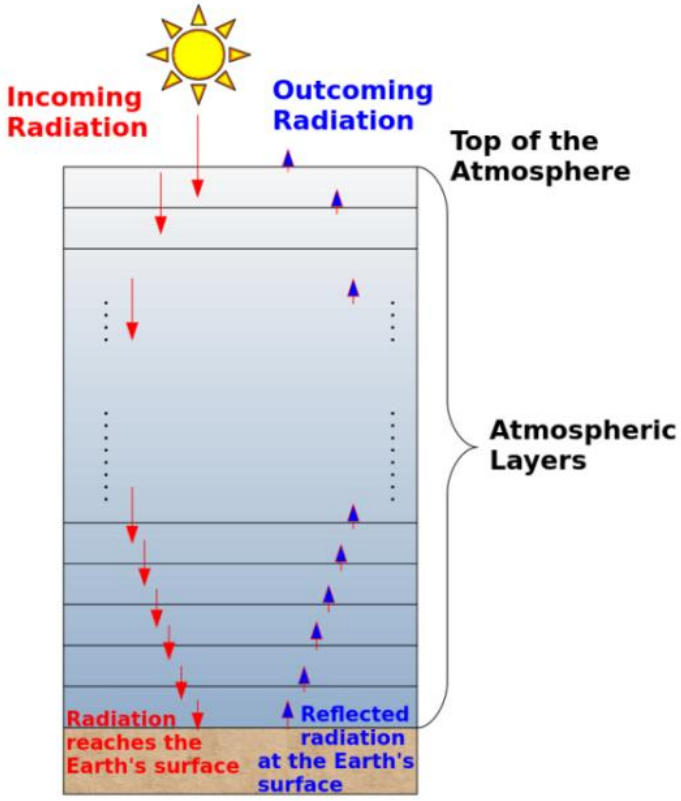


Figure 2.2. Schematic illustration of the downwelling and upwelling radiation fluxes in the atmosphere, as they are simulated by the FORTH RTM.

Various versions of the above described radiation transfer model have been used in studies concerning the calculation of radiation fluxes, as well as the effect of aerosols and clouds on solar radiation and the energy balance, both at a local (e.g. Mediterranean, Greece) scale (Matsoukas et al., 2005, Fotiadi et al., 2006, Matsoukas et al, 2010, Benas et al., 2011, Matsoukas et al., 2011, Papadimas et al. 2012, Pyrina et al., 2015), as well as on a planetary scale (Hatzianastassiou et al., 2004a,b, 2005, 2007a,b). The model results have been successfully evaluated through extensive comparisons with ground-based and satellite-based radiation measurements (Hatzianastassiou et al, 2004c, 2005, 2005, 2012, 2020), as well as through comparisons with other models (Randles et al., 2013).

2.1.2 Sensitivity tests of monthly means

In climate studies, the accuracy and resolution of solar radiation estimates may play an important role in understanding surface energy fluxes and their impacts on climate variability. This section focuses on evaluating the sensitivity of solar radiation computations by the RTM by comparing solar fluxes computed at two different temporal resolutions, namely the monthly mean solar radiation fluxes directly estimated by the model and the average monthly solar radiation derived from the originally computed 3-hourly fluxes estimated by the model. By contrasting these two approaches, it is aimed to assess the reliability and potential discrepancies that may arise when using coarser temporal resolutions in radiative transfer models. The results of this sensitivity test will provide insights into the level of detail required for accurate climate modeling and whether finer temporal resolution leads to significant differences in solar radiation estimations. The applied approach involved running the model on both a monthly and a three-hourly basis for two indicative months, summer and winter, namely July 2018 and January 2018, to determine whether the average monthly value derived from three-hourly data (RTM3H) differs significantly from the directly calculated monthly value (DM). According to this sensitivity, for July 2018, the average SSR for RTM3H was 179.6 Wm^{-2} (Figure AA8a), while for DM, it was 168.8 Wm^{-2} (Figure AA8b), resulting in a percentage difference of 7.3% (Figure AA8c), indicating that RTM3H SSR values were higher than those of DM. The fluxes were also compared with the SSR from CERES, revealing a percentage difference of -3.7% (Figure AA9a) for RTM3H and -10% (Figure AA9b) for DM. Comparison with ground-based measurements (Figure AA10) showed similar correlation coefficients (~0.96), slopes (~0.9) for the best linear fit, and RMSE values. However, the BIAS difference was more pronounced, with RTM3H at 1.5% and DM at -4.5%. A similar analysis was conducted for January 2018. The average SSR for RTM3H was 192.3 Wm^{-2} (Figure AA11a), while for DM, it was 180.3 Wm^{-2} (Figure AA11b), yielding a percentage difference of 7.9% (Figure AA11c), again showing that RTM3H SSR values were higher than those of DM. When compared with CERES, the RTM3H fluxes exhibited a percentage difference of -5.3% (Figure AA12a), whereas DM showed a -12% difference (Figure AA12b). The comparison with ground measurements (Figure AA13) revealed similar correlation coefficients (~0.98) and slopes (~0.9) for the best linear fit. However, the difference in BIAS/RMSE was more evident, with RTM3H at -3.6%/14% and DM at -10.5%/19%. The substantial data volume and computational demand of the three-hourly simulations were also considered. The results indicated that the monthly-from-three-hourly (RTM3H) SSR fluxes exhibited just slightly better performance compared to ground-based SSR measurements, than the directly calculated monthly (DM) SSR fluxes. Finally, the marginal performance improvement of the three-hourly model, combined with its high computational and storage requirements, led to the decision to proceed with the analysis using directly calculated monthly SSR fluxes.

2.1.3 Input data to RTM

The radiation transfer model, which is used for the needs of this thesis, requires input data for the physical quantities/parameters that interact with solar radiation. The cloud properties required by the model, namely cloud amount (CA), cloud optical thickness (COT), and cloud-top pressure (CTP) separately for liquid and ice phases, for low-, mid- ad high-level clouds, are taken from the CLARISC and ISCCP-H dataset. The aerosol optical depth (AOD), single scattering albedo (SSA), asymmetry parameter (AP), specific humidity, ozone concentration, and surface albedo were computed from 3-hourly data taken from the MERRA-2 Reanalysis. All the original input data were converted to monthly means, and regridded to

the 0.5° × 0.625° latitude-longitude spatial resolution applying the first-order conservative remapping method (Jones et al., 1999) from the Climate Data Operators (CDO) with the "remapcon" command, to be used in the RTM. It should be stressed that for the purposes of this thesis the model was suitably modified to make use for the first time of cloud data from the new cloud database, namely, CLARISC (previous model versions were using mainly the ISCCP dataset) which has been created during this PhD and a more detailed description is given below. All the input to RTM parameters which contribute to atmospheric transmissivity (i.e. CA, COT, AOD, SSA, AP, water vapor and ozone) will henceforth be referred to as the GDB drivers. The primary contributions of these drivers will be computed in Chapter 5.

2.1.3.1 ISCCP-H

The ISSCP-H climate data record contains the full (level 2) and basic (level 3) products for monitoring the distribution and variation of cloud and surface properties, which are derived from both geostationary and polar-orbiting satellite imaging radiometers with one visible (VIS ≈ 0.65 ± 0.05–0.20 μm) and one infrared (IR ≈ 10.5 ± 0.5–0.75 μm) "window" channels. The Basic H-series data that are used in this study currently span the period from July 1983 to December 2018 with plans for regular updates (Young et al., 2018). They have global coverage with spatial resolution of 1°×1° degree, equal angle grid. The improvements of the ISCCP H-series, compared to its predecessors C- and D-series are several and include quality control measures, modified ancillary inputs, higher spatial resolution input and output products, and calibration refinements (Young et al., 2018). The cloud types include 3 low-, 3 middle-, and 3 high-level cloud types, each one in liquid and ice phases, thus the overall number of ISCCP-H cloud types is 18. Here, the basic, monthly ISCCP H Gridded Monthly (HGM) data are used and more specifically the properties with names "cldamt_types", "tau_types" and "pc_types" corresponding to the mean cloud amount, mean cloud-top pressure and mean cloud optical depth for 18 cloud types. The mean monthly data were computed by averaging each 3-hourly time step for a month and then by averaging the eight (8) 3-hourly mean values in the month. All ISSCP-H data products are available in [https://www.ncei.noaa.gov/access/metadata/landing-page/bin/iso?id=gov.noaa.ncdc:C00956 (accessed on 2 August 2023)].

2.1.3.2 CLARISC: CLARA-A2 and ISCCP-H synergy

2.1.3.2.1 Description of the CLARISC

Improved and state-of-the-art databases for cloud and aerosol properties, such as EUMETSAT's CLARA-A2.1, NASA's ISCCP-H and MERRA-2, were used as input data to the RTM. The same model was utilized during the framework of this PhD, in the work by Stamatis et al. (2023), but using as input only data from ISCCP-H (for clouds) and MERRA-2 (for aerosols and other meteorological data). However, as described in detail in that work, artificial patterns were detected in the changes of SSR, i.e. GDB, originating from corresponding artificial patterns in the ISSCP-H cloud satellite data, which are associated with changes in satellite viewing geometries. Thus, in order to rectify these artificial patterns, it was decided to prepare a new cloud input dataset to the model, free from these artifacts. To this aim, a new cloud database was created containing the model required low-, medium- and high-level cloud amount

and optical thickness for liquid and ice phase clouds, similar to those provided by the ISCCP-H. To achieve this the CLARA-A2.1 satellite database was chosen, because its data do not suffer from changing satellite viewing geometries or artificial patterns due to the applied methodology for cloud screening. This methodology produced enhancements by utilizing high-quality cloud data also from CALIPSO-CALIOP. Additionally, the original AVHRRGAC Level 1b dataset was significantly improved through rigorous quality control measures, including the removal of orbit overlaps (Karlsson and Hakansson 2018). CLARA-A2.1 is built using historical data from the Advanced Very High Resolution Radiometer (AVHRR), which was used aboard NOAA satellites in polar orbit, and the Metop polar orbiters, run by EUMETSAT since 2006. Five spectral channels—two visible and three infrared—with an initial horizontal field-of-view (FOV) size of 1.1 km are measured by AVHRR. The first edition of the data record, that was released in 2012 (Karlsson et al., 2013), is enhanced and expanded upon by CLARA-A2.1, which now spans a 40-year period (1982–2022). Cloud mask/cloud amount, cloud top temperature/pressure/height, cloud thermodynamic phase, cloud optical thickness (for liquid and ice clouds separately), particle effective radius, and cloud water path are among the cloud products provided by CLARA-A2.1. These cloud products can be found as daily and monthly averages in a latitude-longitude grid of 0.25° by 0.25", as well as daily global products (Level 2b) that have been resampled on a grid of 0.05° by 0.05°. The monthly products are averages of all the daily means. In the present study the following parameters from CLARA-A2.1 database were utilized: (a) the day-time Fractional Cloud Cover (CFC) or cloud amount (CA) in % for the total atmospheric column, (b) the day and night-time CFC in % for the total atmospheric column and for low-, middle- and high level clouds, which used to produce initially the day-time CA for low-, middle- and high level CA (Eq. 2.8), (c) the Cloud Optical Thickness (COT) for liquid and for solid phase clouds and (d) the Cloud Top Pressure (CTP) in hPa. However, CLARA-A2.1 only provides the total daytime cloud amount and optical depth in the entire atmospheric column and not low-, middle- and high-level cloud amounts which are used as input data in our RTM. Thus, the CLARA-A2.1 cloud amount and cloud optical thickness had to be apportioned to low-, middle- and high-level clouds, all separately in both liquid and solid phases. The new cloud input data were produced using the original CLARA-A2.1 data combined with information from ISCCP-H, specifically the ratios of the ISCCP-H cloud amounts of a specific level *i* (low, middle, high) and phase *j* (liquid, ice) over the ISCCP-H total cloud amount. The new cloud amounts were estimated using Eqs. 2.8 and 2.9. The cloud optical thickness (COT) wasn't computed directly by the ISCCP-H COT ratios, but first the cloud transmissivity (tr) was calculated as shown in Eqs. 2.10 – 2.14 (Vardavas and Taylor, 2011) with the help of the corresponding ISCCP-H transmissivity ratios and then the computed transmissivity for low-, middle-, high-level clouds for liquid and ice phase converted to the corresponding COT (Eq. 2.15). Note here that *g* is the cloud scattering asymmetry factor, μ is the cosine of zenith angle and the *k* is the ratio of absorbing cloud optical depth to scattering cloud optical depth.

$$CA_i^{daytime} = \frac{CA_i^{CLARA,\ day+nighttime}}{CA_{total}^{CLARA,\ day+nighttime}} \times CA_{total}^{CLARA,\ daytime} \quad \text{(Eq. 2.8)}$$

$$CA_{i,j}^{CLARISC,\ daytime} = \frac{CA_{i,j}^{ISCCP,\ daytime}}{CA_{i,liq+ice}^{ISCCP,\ daytime}} \times CA_{i}^{CLARA,\ daytime} \quad \text{(Eq. 2.9)}$$

$$tr = \frac{4 \times u}{(u+1)^2 \times e^{v} - (u-1)^2 \times e^{-v}} \quad \text{(Eq. 2.10)}$$

$$u = \sqrt{\frac{1 - w \times g}{1 - w}} \quad \text{(Eq. 2.11)}$$

$$v = \sqrt{(1 - w) \times (1 - w \times g)} \times \left(\frac{COT + COT \times k}{\mu}\right) \quad \text{(Eq. 2.12)}$$

$$w = \frac{1}{1+k} \quad \text{(Eq. 2.13)}$$

$$tr_{i,j}^{CLARISC,\ daytime} = \frac{tr_{i,j}^{ISCCP,\ daytime}}{tr_{total,j}^{ISCCP,\ daytime}} \times tr_{total,j}^{CLARA,\ daytime} \quad \text{(Eq. 2.14)}$$

$$COT_{i,j}^{CLARISC} = \frac{2 \times (1 - tr_{i,j}^{CLARISC,\ daytime}) \times \mu}{(1-g) \times (tr_{i,j}^{CLARISC,\ daytime} + k)} \quad \text{(Eq. 2.15)}$$

Due to the synergy between CLARA and ISCCP, the CLARISC cloud types include one low-, one middle-, and one high-level cloud types, each one in liquid and ice phases, thus the overall number of CLARISC cloud types is 6. According to the new cloud database, produced based on the synergy of CLARA-A2.1 and ISCCP-H and named as CLARISC, the cloud changes, though being partially similar over land to the corresponding ones based on ISCCP-H, do not show artificial patterns (Figure AD1). For example, as it is shown in Figure AD1ia-d, the artificial pattern over the Atlantic Ocean is linked to the actual coverage from the geostationary satellite METEOSAT (Karlsson and Devasthale 2018), while the pattern over the Indian Ocean is linked to the region where geostationary data were unavailable until 1997 and AVHRR polar-orbiting satellite data were used instead (Evan et al., 2007). The removal of ISCCP-H artificial

patterns in the CLARISC cloud amount changes resulted (as it will be shown in the next section) in a similar absence in the associated model computed SSR changes.

2.1.3.2.2 Cloud Climatology and Trends of CLARISC and comparison with ISCCP-H and CERES

Clouds play a fundamental role in the Earth's radiation budget, influencing both incoming solar radiation and outgoing longwave radiation. Accurate representation of cloud properties, such as cloud amount and cloud optical thickness, is crucial for understanding climate variability and improving radiative transfer modeling. In this section, the climatologies and trends of cloud properties derived from three global satellite-based datasets: CLARISC, ISCCP-H and CERES-EBAF 4.2 are analyzed and intercompared. By evaluating differences between these datasets, this study aims to assess their consistency, highlight potential improvements in cloud representation, and examine long-term trends in cloud cover and optical properties. As explained in the previous section, the new cloud database (CLARISC) was created to eliminate inconsistencies in cloud trends over certain regions caused by issues with the optical geometry of satellites. Indeed, CLARISC is not reproducing the inconsistencies found in ISCCP, because its primary cloud data source is now CLARA, which does not exhibit these inconsistencies. Figure AA1 and AA2 presents the global distributions of the mean annual values for cloud cover and cloud optical thickness, respectively, for low-, mid-, high-level, and total clouds. Figure AA3 and AA4 illustrates the corresponding CA and COT changes, respectively, for the period 1984-2018. Figure AA5 displays the global time series of absolute values and anomalies for total CA and COT from CLARISC, ISCCP, and the CERES, which has provided measurements since 2001. Note that the CERES total cloud amount is daytime and nighttime product, while for CLARISC and ISCCP-H is daytime only. It is worth noting that, in terms of average annual values, the two databases are similar in terms of CA, but this is not the case for cloud optical thickness, which appears significantly greater in ISCCP. This contrasts also in the timeseries (Figures AA5) with the notably lower values reported by CERES and CLARISC after 2001. The overestimation of COT in ISCCP appears to be a crucial factor contributing to the significantly lower SSR values in model versions that relied solely on ISCCP data. Regarding the trends during 1984-2018, both databases exhibit agreement in some regions and discrepancies in others throughout the study period.

Furthermore, an extensive comparison of the two databases was conducted to assess whether, beyond addressing inconsistencies, the new database also provides improved reliability in trend analysis. To this end, data from CERES, including total cloud cover and total cloud optical thickness, were used as reference points. Global trends for total CA (Figure AA6) and total COT (Figure AA7) were calculated for two distinct periods: 2001-2009 and 2010-2018 for the three datasets. By comparing the signs of their trends (Table AA3) at each grid cell between CLARISC, ISCCP, and CERES, it was found that for cloud cover, the two databases perform similarly. Specifically, for the period 2001-2009, CLARISC agrees with CERES at 68% overall and 98% for statistically significant trends, while ISCCP shows 67% overall agreement and 95% for statistically significant trends. The agreement between CLARISC and ISCCP is 67% overall and 98% for statistically significant trends. For the period 2010-2018, CLARISC shows 67% agreement overall (99% for statistically significant trends), while ISCCP exhibits 70% agreement overall (98% for statistically significant trends). Their agreement (between CLARISC and ISCCP-H) stands at 61% overall and 86% for statistically significant trends. In contrast, when comparing optical cloud thickness, CLARISC demonstrates better performance than ISCCP. For the period 2001-2009, the agreement between CLARISC and CERES is 56%

overall, increasing to 80% for statistically significant trends. ISCCP, however, shows lower agreement at 47% overall and 59% for statistically significant trends. Similarly, for 2010-2018, CLARISC agrees with CERES at 63% overall (84% for statistically significant trends), while ISCCP shows only 51% overall agreement (64% for statistically significant trends). The agreement between CLARISC and ISCCP is 48% overall (62% for statistically significant trends) for 2001-2009 and 55% overall (72% for statistically significant trends) for 2010-2018. From the analysis and comparison of these databases, it is evident that CLARISC not only eliminates the inconsistencies present in ISCCP but also offers improved reliability, particularly in trends related to cloud cover and COT, at least for the period 2001-2018. This further reinforces the reliability of CLARISC, along with its associated SSR model and GDB.

2.1.3.3 MERRA-2

The MERRA-2 is a state-of-the-art reanalysis produced by the NASA Global Modeling and Assimilation Office (GMAO) in 2017 (Randles et al., 2017). Its advances in assimilation techniques make it the updated version of MERRA, while for the first time, it assimilates space-based observations of aerosols that interact with physical processes in the climate system on a multidecadal scale. MERRA-2 provides aerosol optical depth (AOD) data in a 3-hourly temporal resolution and 0.5° × 0.625° spatial resolution, assimilating (a) ocean-only reflectances from the Advanced Very High-Resolution Radiometer (AVHRR) instruments (1979–2002), (b) reflectances from the Moderate Resolution Imaging Spectroradiometer (MODIS) instruments on Terra (2000-present) and Aqua (2002-present), (c) AOD from the Multi-Angle Imaging SpectroRadiometer (MISR) over the bright desert regions (2000–2014) and (d) AOD observations from the AErosolROboticNETwork (AERONET) surface station network (1999–2014) (Korras-Carraca et al., 2021). The MERRA-2 provides vertically resolved (in 72 layers) 3-hourly instantaneous aerosol mixing ratios from which the mean monthly aerosol optical depth, single scattering albedo, and asymmetry parameter are computed (only for the lower 50 layers since in higher altitudes, i.e., 30–34 km, the aerosol loadings are insignificant, as described by (Korras-Carraca et al., 2021) due to the requirements of FORTH-RTM). Note that the monthly mean AOD, SSA, and g were calculated by averaging the 3-hourly optical properties only during the daytime. The initial MERRA-2 data are freely available in [http://disc.sci.gsfc.nasa.gov/mdisc/ (accessed on 2 August 2023)]. In addition to aerosol optical properties, the vertical atmospheric profile of pressure, specific humidity (in the same layers as those for aerosols), surface albedo data (in the visible and near-infrared) as well as columnar ozone (O_3) concentration data were also obtained from MERRA-2. Note that apart from these input data used for the FORTH-RTM runs, MERRA-2 also provides SSR fluxes computed at an hourly time step. These data, which have been evaluated on a monthly basis by (Stamatis et al., 2022) against GEBA and BSRN for 1980–2019, are computed with the same meteorological and aerosol data which was used in the FORTH-RTM in the present study, but with a different radiation transfer scheme and cloud input data.

2.1.4 Evaluation data

2.1.4.1 GEBA and BSRN

The GEBA network is maintained at the Institute for Climate and Atmospheric Sciences of the ETH (Zürich, Switzerland) and contains data from worldwide distributed ground-based measurements. It gives mean monthly values of 15 energy flux components, including surface albedo, longwave downward and upward radiation, and global, diffuse, and direct shortwave radiation, measured from 2500 globally distributed sites, with over 600,000 monthly values. Numerous stations offer measurements going back to the 1950s, and some even as far back as the 1930s. Their accuracy has been evaluated by (Gilgen et al., 1998) to be 5% of monthly means and 2% of annual means in terms of relative random measurement error. For the current study period 1984–2018, 1545 stations provided SSR monthly data, which were measured using pyranometers (Michalsky et al., 1999; Wild et al., 2013). After registering at [https://geba.ethz.ch/ (accessed on 2 August 2023)], users can use the GEBA data for free.

The World Climate Research Programme's Radiation Panel project, the BSRN, is sponsored by GEWEX (WCRP). Since January 1992, it has been supplying high-quality radiation measurements with a high temporal resolution (one to three minutes) from 73 sites spread throughout different climate zones of the Earth. These measurements are sent to the Alfred Wegener Institute's (AWI) BSRN Archive in Bremerhaven, Germany. SSR measurements from 73 BSRN sites for the years 1992 to 2018 are used in this study. Aside from the global shortwave flux (measured with pyranometers), the BSRN stations also measure the direct shortwave flux (measured with a pyrheliometer) and the diffuse shortwave flux (measured with a shaded pyranometer). The BSRN solar and thermal radiation data quality is described in detail in (Driemel et al., 2018). Under ideal observation conditions, an accuracy of up to 5 Wm^{-2} has been estimated using single pyranometers in conjunction with the component sum approach at BSRN locations (Michalsky et al., 1999). This precision satisfies the BSRN standards. The daily data, which are derived from the instantaneous (minute level) data, are utilized to create the mean monthly BSRN data used for the evaluation of FORTH-RTM SSR and GDB. The BSRN data are available for free download at [https://bsrn.awi.de/data/ (accessed on 2 August 2023)] via PANGEA or ftp. Figure 2.3 depicts the geographical distribution of the initially accessible GEBA and BSRN stations. These networks, especially GEBA, cover practically the entire globe (continental areas) with varying degrees of density (GEBA is denser than BSRN), while there is a dense GEBA network of stations in Europe and East Asia.

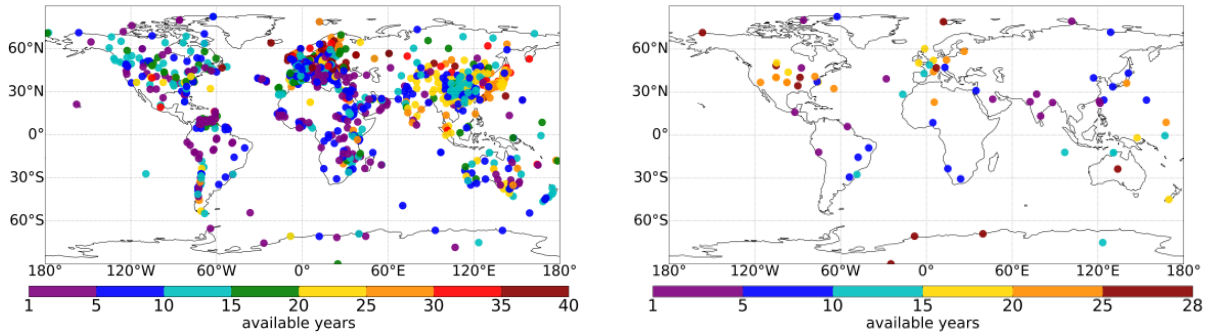


Figure 2.3. Global distribution of: (a) Global Energy Balance Archive (GEBA) 1545 stations and (b) Baseline Surface Radiation Network (BSRN) 73 stations, initially accessible (last visit on 24th July 2024) for the evaluation of the FORTH-RTM surface solar radiation (SSR) data. The availability of each station's monthly data in years is indicated in the colorbars. The coordinates and elevation of the stations are given in Appendices AA1 and AA2.

2.1.4.2 CERES-EBAF 4.2

The Clouds and the Earth's Radiant Energy System—Energy Balanced and Filled (CERES-EBAF) 4.2 product contains 1° × 1° gridded global monthly mean shortwave, longwave, and net fluxes that are observed at the Top of Atmosphere and computed at the Earth's surface, under clear and all-sky conditions. CERES instruments fly on the Terra, Aqua, Suomi National Polar-Orbiting Partnership (SNPP), and NOAA-20 satellites (Figure 2.4). They measure filtered radiances in the shortwave between 0.3 and 5 µm, in total between 0.3 and 200 µm, and in window spectral regions between 8 and 12 µm (Loeb et al., 2018). The unfiltered shortwave, longwave, and window radiances are transformed from the filtered following the (Loeb et al., 2001) scheme and are then converted to instantaneous TOA radiative fluxes using empirical angular distribution models (Su et al., 2015). Then, the instantaneous TOA fluxes are spatially averaged on a 1° equal-area grid, interpolated between measured values at 1 h intervals for each hour in coordinated universal time (UTC) of every month, and then averaged across all the hour boxes in that month (Doelling et al., 2013). In order to detect decadal variations in the Earth's Radiation Budget from the surface to the top of the atmosphere as well as the accompanying cloud and aerosol properties, CERES-EBAF data cover the period from March 2000 to the present. Here, we utilize the "toa_sw_all_mon" EBAF Edition 4.2 level 3b Top-of-Atmosphere monthly mean shortwave flux for the period January 2001–December 2018, with the aim to examine the degree of the agreement in the sign of the slopes of shortwave reflected radiation at the TOA between FORTH-RTM and CERES over locations where the FORTH-RTM GDB qualitatively agree with the ground-based observations. Moreover, the total day and nighttime cloud amount and daytime total optical thickness were analyzed to evaluate the CLARISC and ISCCP-H total cloud amount and cloud optical thickness. The remapping method used to regrid from 1° × 1° to 0.5° × 0.625° spatial resolution is the same as described in 2.1.2 for the ISCCP-H data and the dataset can be assessed from https://Ceres.Larc.Nasa.Gov/Data/ (accessed on 30 June 2023).

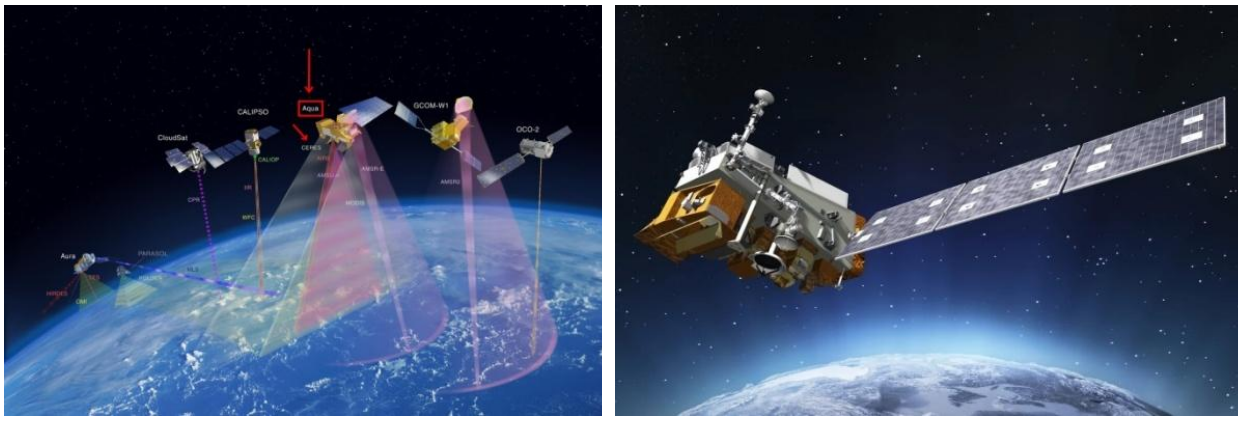


Figure 2.4. NASA's satellites (a) Aqua [https://aqua.nasa.gov/] and (b) NOAA-20 [https://oceancolor.gsfc.nasa.gov/about/missions/noaa20/]

2.1.5 Complementary data

2.1.5.1 ERA5

ERA5 (Hersbach et al. 2020) is the fifth generation of atmospheric reanalysis data produced by the European Centre for Medium-Range Weather Forecasts (ECMWF). It provides climate data from 1940 to the present. Although ERA5, MERRA-2, and CLARA extend to the present, this study is limited to the temporal coverage of ISCCP-H, which spans from 1984 to 2018. ERA5 offers hourly estimates of various atmospheric and land surface parameters, as well as ocean wave data, with a horizontal resolution of 0.25° × 0.25° (latitude × longitude). The ERA5 temperature data used in this study (Hersbach et al. 2020) were regridded to match the 0.5° × 0.625° resolution of the FORTH-RTM SSR fluxes. The 2m temperature refers to the air temperature measured at 2 meters above the surface of land, sea, or inland waters. It is derived by interpolating between the lowest model level and the Earth's surface while considering atmospheric conditions. The temperature is measured in kelvin (K) and can be converted to degrees Celsius (°C) by subtracting 273.15. The minimum/maximum 2m temperature represents the lowest/highest recorded air temperature at 2 meters above the surface within a given forecast period. Both values are derived using the same interpolation method. The diurnal temperature range (DTR) is calculated as the difference between the maximum and minimum 2m temperatures. All temperature values in this study are provided on a daily basis and then averaged into monthly means. Besides, ERA5 provides monthly SSR (MSDWSWRF measured in Wm^{-2}) which represents the total solar radiation reaching a horizontal surface at the Earth's surface, including both direct and diffuse components. The dataset is widely used for climate research, policymaking, and operational applications. ERA5 data can be accessed freely via the Copernicus Climate Data Store (CDS) platform [https://cds.climate.copernicus.eu/datasets/reanalysis-era5-single-levels-monthly-means?tab=download (last access on 02/04/2025)], with updates provided daily and consolidated after two months for quality assurance.

2.1.5.2 MERRA-2

As already said, MERRA-2 is a global atmospheric reanalysis produced by the NASA Global Modeling and Assimilation Office (GMAO) in 2017 (Randles et al., 2017). It provides data beginning in 1980, with continuous updates, having high spatial (0.5° latitude × 0.625° longitude and 72 hybrid sigma-pressure layers from the surface to 0.01 hPa) and temporal (hourly) resolution, that is freely available at [http://disc.sci.gsfc.nasa.gov/mdisc/]. MERRA-2 is the first long-term satellite-era global reanalysis to assimilate space-based observations of aerosols, representing their interactions with other physical parameters in the climate system. More specifically, the MERRA-2 SSR fluxes are utilized in the present study, computed by the shortwave radiation parameterization described by (Chou et al., 1999). The total SSR flux at each pressure level and at the Earth's surface is the weighted (by the fraction of extraterrestrial solar flux contained in the above-mentioned bands) sum of these fluxes. For the aim of this study monthly MERRA-2 SSR fluxes, called "SWGDN", are utilized.

2.1.5.3 JRA-55

The JRA-55 (https://jra.kishou.go.jp/JRA-55/index_en.html (last access on 02/04/2025)) is a next-generation reanalysis dataset provided by the Japan Meteorological Agency, building upon the JRA-25. It is the first extensive reanalysis dataset to implement the 4D-Var assimilation method since the ECMWF

45-year reanalysis. Covering global atmospheric data since 1958, JRA-55 offers a spatial resolution of 1.25°. The dataset provides predictions at a temporal resolution of 3 hours, while observational data is available at 6-hour intervals. It incorporates both conventional and remote sensing data. For this study, the downward shortwave radiation flux ("dswrf") was used with a monthly temporal resolution. Further details on JRA-55 can be found in its official user manual.

2.1.5.4 NCEP R1

The NCEP/NCAR Reanalysis 1 (NCEP R1) (Schneider et al., 2013) is a global atmospheric reanalysis produced by the National Centers for Environmental Prediction (NCEP) and the National Center for Atmospheric Research (NCAR). Spanning the period from 1948 to the present, the dataset provides global atmospheric fields at a spatial resolution of approximately 2.5° × 2.5° (latitude × longitude). It uses a T62 spectral model and a variational assimilation system to combine observational data from a wide range of sources. The NCEP R1 dataset includes surface solar radiation estimates ("dswrf") and has been widely used in studies of climate variability and model validation. The dataset can freely be downloaded here [https://psl.noaa.gov/data/gridded/data.ncep.reanalysis.html (last access on 02/04/2025)].

2.1.5.5 NCEP R2

The NCEP/DOE R2 dataset (Kanamitsu et al. 2002) is an improved version of R1, addressing some of its limitations. It spans from January 1979 to March 2025 with a spatial resolution of approximately 1.875° x 2.5°. Temporal resolution includes daily and monthly averages and can be found here [https://psl.noaa.gov/data/gridded/data.ncep.reanalysis2.html (last access on 02/04/2025)].

2.1.5.6 W5E5

The W5E5 dataset (Lange 2019) was developed to support bias adjustment of climate input data for impact assessments in ISIMIP3b. It provides global coverage at a 0.5° horizontal resolution with daily data spanning from 1979 to 2016. W5E5 merges WFDE5 data over land with ERA5 data over the ocean, ensuring consistency across different surfaces. One of the key variables in W5E5 is Surface Downwelling Shortwave Radiation (rsds), which represents the solar radiation reaching the Earth's surface. Over land, W5E5 SSR is derived from daily mean WFDE5 values, while over the ocean, it is aggregated from hourly ERA5 data. This dataset is essential for climate impact studies, as it provides a harmonized source of SSR data for analyzing solar energy availability and surface radiation balance. It is free to download it here [https://dataservices.gfz-potsdam.de/pik/showshort.php?id=escidoc:4855898 (last access on 02/04/2025)]

2.1.5.7 ISCCP HXG

The ISCCP-HXG SSR dataset is a high-resolution global product with a spatial resolution of approximately 10 km and a 3-hour temporal resolution, covering the period from July 1983 to December 2018. It was developed using an improved physical parameterization approach described by Tang et al.

(2017). Tang et al. (2019) replaced the earlier aerosol parameterization with the model from Tang et al. (2016), which accounts for both aerosol absorption and scattering. The updated algorithm is fully physics-based, computationally efficient, and accurately represents the interactions between clouds, aerosols, and atmospheric gases. It was applied globally using ISCCP-HXG cloud data, MODIS aerosol and albedo products, and ERA5 reanalysis inputs, including water vapor, ozone, and surface pressure. The "monthly_global_radiation" was used in this study and can be downloaded from here [https://data.casearth.cn/dataset/5feae827819aec33049b7ceb (last access on 02/04/2025)].

2.1.5.8 GFDL_CM2P1

The GFDL CM2P1 (historical r1i1p1, https://catalogue.ceda.ac.uk/uuid/3614113edb264a6081bccc15abac1241/ (last access on 02/04/2025)) is a coupled climate model simulation produced by the Geophysical Fluid Dynamics Laboratory (GFDL) in the United States. The model, based on the CM2 family of models, includes a fully coupled ocean-atmosphere-land system, offering simulations of climate variables such as surface solar radiation over long periods. The GFDL CM2P1 model simulation is particularly known for its use in assessing long-term climate projections and energy fluxes under different greenhouse gas emission scenarios. It provides useful insights into monthly surface solar radiation (rsds) and other climate variables, especially in the context of future climate scenarios.

2.1.5.9 CERES EBAF 4.2 SSR Retrievals

The monthly mean satellite derived SSR retrievals with a spatial resolution of 1° × 1° from the CERES EBAF product (Ed 4.2), which has been reported to be more accurate than other gridded SSR products (Zhang et al., 2016; Ma et al., 2015; Rahimikhoob et al., 2013), are used in this study. The CERES EBAF retrieves shortwave fluxes based on TOA radiance observations from the passive Terra, Aqua, and Suomi-National Polar-Orbiting Partnership satellites (Lenaerts et al., 2017). Furthermore, the CERES EBAF retrieval algorithm adjusts surface irradiances with radiative kernels. The surface irradiance adjustment procedure consists of bias correction and a Lagrange multiplier (Kato et al., 2018). The bias correction procedure corrects the bias in temperature and specific humidity between 200 and 500 h Pa using observations from the atmospheric infrared sounder (AIRS) on the MODIS-Aqua satellite. The bias in the cloud fraction (CF) is adjusted using data from the Cloud-Aerosol Lidar and Infrared Pathfinder Satellite Observations (CALIPSO) and CloudSat. The Lagrange multiplier technique corrects faults in surface, cloud, and atmospheric properties. In high-latitude areas, cloud features are retrieved from Terra and Aqua reflectance data using one of two retrieval algorithms based on the presence of snow and ice (Lenaerts et al., 2017, Minnis et al., 2011). Surface irradiances (sfc_sw_down_all_mon) are limited using the CERES-derived TOA irradiance (Kato et al., 2013), which reduces inaccuracy and increases consistency. This dataset can be downloaded from here [https://asdc.larc.nasa.gov/project/CERES/CERES_EBAF_Edition4.2 (last access on 02/04/2025)]

2.1.5.10 CLARA-A2

The CLARA-A2 dataset, derived from the Advanced Very High Resolution Radiometer (AVHRR) sensors onboard NOAA and METOP polar-orbiting satellites, provides global data on cloud fraction, cloud properties, surface radiation, and surface albedo from 1982 to 2015, with a spatial resolution of 0.25° × 0.25° (Karlsson et al., 2017a,b). Surface incoming shortwave radiation (SSR) from CLARA-A2 is available as daily and monthly averages (Table 1), and this study validated the monthly SSR means for the period 1993–2015. The measurement periods and satellite orbits covered by CLARA-A2 are detailed in Figure 1 of Karlsson et al. 2017a. Since only one satellite was operational between 1982 and 1991, this period was excluded to minimize the impact of missing data on validation results (Pfeifroth et al., 2018). SSR retrieval in CLARA-A2 follows a look-up-table method, linking top-of-atmosphere reflected fluxes to surface fluxes under cloudy conditions. For clear-sky situations, the mesoscale atmospheric global irradiance code (MAGIC, http://gnu-magic.sourceforge.net/) algorithm is used to estimate surface irradiance (SIS). The SIS can be freely downloaded here [https://navigator.eumetsat.int/product/EO:EUM:DAT:0338 (last access on 02/04/2025)]. Additionally, auxiliary datasets such as a surface albedo map, monthly-averaged integrated water vapor, and an aerosol climatology are incorporated into the retrieval process. More details on the methodology can be found in Mueller et al. 2009 and Karlsson et al. 2013.

2.2 Methods

This section outlines the methodology employed at each stage of data analysis. It begins with an analysis of the FORTH-RTM SSR dataset (sub-section 2.2.1), covering its global distribution on an annual and seasonal scale, as well as the computation of absolute values and deseasonalized anomalies. The evaluation process against ground-based observations follows (sub-section 2.2.2), including the statistical metrics used. This is followed by the approach for identifying the causes of GDB using the Contributions Analysis (sub-section 2.2.3) and the machine learning techniques used to assess the correlation between the monthly variability of SSR and GDB drivers (sub-section 2.2.4). Finally, the process for examining the relationship between GDB and global warming is presented (sub-section 2.2.5). An overview of the steps of this Thesis can be found in Figure 2.5.

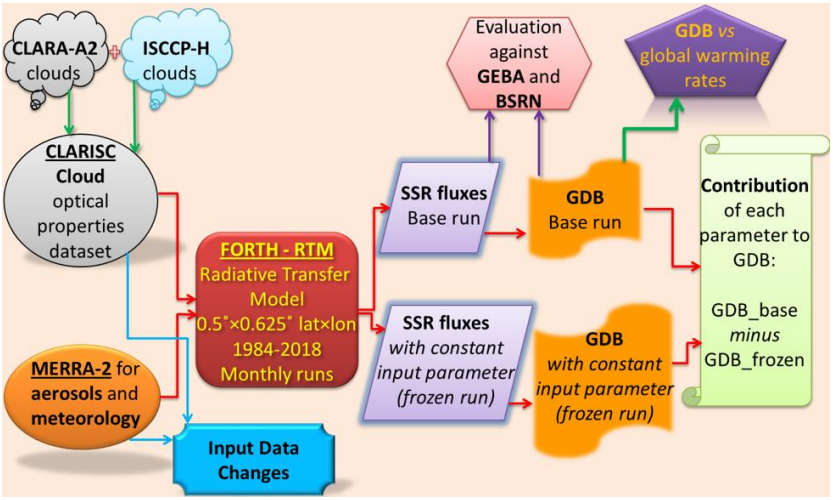


Figure 2.5. The flowchart diagram with the methodology applied in the current study.

2.2.1 SSR and GDB drivers' fluctuations

The FORTH-RTM SSR dataset was analyzed globally on both an annual and seasonal scale, alongside the GDB drivers, for the entire period from 1984 to 2018. Additionally, SSR time series and trends were computed using both absolute values and deseasonalized anomalies (where the anomalies were obtained by subtracting the corresponding long-term monthly mean from each monthly value), after being spatially averaged with latitude-based weighting. To identify long-term variations, the low-pass Savitzky–Golay (SG) filter (Schafer, 2011) was applied to the monthly mean time series using a 120-month (10-year) window at global, hemispherical, land, and ocean scales. In parallel, linear trends of Theil-Sens slope were calculated for the monthly time series, including their upper and lower limits at a 95% confidence level, with statistical significance assessed using the Mann-Kendall test. The same analysis was conducted for the deseasonalized anomalies of GDB drivers on a global scale, and Pearson's correlation coefficient (R) was computed between the monthly anomalies and their SG-filtered counterparts to identify potential relationships between SSR and GDB drivers.

2.2.2 Evaluation methods

The FORTH-RTM GDB was evaluated against GEBA and BSRN measurements using monthly mean SSR deseasonalized anomalies (created by subtracting the relevant long term averaged value, which is different for each station, from each monthly SSR value) and fluxes. Since the use of deseasonalized anomalies reduces the seasonal component of temporal variability forced by the Earth's orbital parameters, anomalies were preferred in the computation and evaluation of both the correlation coefficients and the trends of time series. Moreover, the absolute monthly SSR fluxes were used to compute/evaluate the other statistical metrics of FORTH-RTM SSR, including the absolute and relative percent bias and root mean squared error (RMSE). In order to assure the highest level of robustness for the resulting findings and conclusions, specific data availability criteria have been employed in the study. So, to avoid years with poor seasonal representation, which would worsen the comparison quality, each year's fluxes were required to contain more than 10 monthly measurements. The Pearson's correlation coefficient (R), Root Mean Squared Error (RMSE) and % relative RMSE (RRMSE), bias, and relative bias were used to measure the degree of agreement/disagreement between the FORTH-RTM model and reference stations' SSR. Their respective equations are:

$$R = \frac{\sum_{i=1}^{n}(M_i - M)(G_i - G)}{\sqrt{\sum_{i=1}^{n}(\mathrm{M}_i - M)^2}\sqrt{\sum_{i=1}^{n}(G_i - G)^2}} \qquad \text{(Eq 2.16)}$$

$$RMSE = \sqrt{\frac{1}{n}\sum_{i=1}^{n}(M_i - G_i)^2} \qquad \text{(Eq 2.17)}$$

$$RRMSE = \frac{\sqrt{\frac{1}{n}\sum_{i=1}^{n}(M_i - G_i)^2}}{G}100\% \qquad \text{(Eq 2.18)}$$

$$BIAS = M - G \quad \text{(Eq 2.19)}$$

$$BIAS(\%) = \frac{M-G}{G} 100\% \quad \text{(Eq 2.20)}$$

where n is the number of monthly data, Mi and Gi are the FORTH-RTM model and ground-based stations' respective monthly values (for the −i month), and M and G are their respective means. The RMSE (Eq. 2.17) measures the typical magnitude of the error, i.e., the typical difference between the FORTH-RTM and ground station values, whereas the R (Eq. 2.16) value measures how strongly the two variables correlate. The RMSE gives a relatively high weight to large errors because they are squared before being averaged; as a result, it is most helpful when large errors are particularly undesirable. The normalized relative percent RMSE is also computed in Eq. 2.18. The bias (Eq. 2.19) quantifies the difference between the mean values of FORTH-RTM and observations. However, the relative percent bias (Eq. 2.20) is also used since it more accurately captures the difference, except for very small values. Linear regression is applied to the series of monthly deseasonalized SSR anomalies in order to assess the GDB, namely the change of SSR (Δ(SSR)) of both RTM and the measurements. The slope values were computed either for each station or the corresponding FORTH-RTM pixels, which include the stations. For the slope computation, we used a criterion for sufficient data availability, according to which, each time series should have an availability of more than 70% of the overall number of monthly values of the total period of each network. An additional criterion has been considered in evaluating the final version of the RTM (FMC), along with assessments of various datasets for more representative results: the altitude difference between the station and the model's pixel should not exceed 500 meters. The Theil–Sen slope estimator (Theil 1992; Sen 1968), which is the median of all plausible linear slopes, was used to calculate the slope values because it is a more reliable nonparametric method. The computed slopes, which measure the changes per month, were multiplied by the temporal duration (in number of months) for each time series to produce the SSR changes Δ(SSR). The non-parametric Mann–Kendall Test (Kendall 1975; Mann 1945), which is used to determine whether a time series has a monotonic upward or downward trend or not, was used to calculate the statistical significance of the slopes at a 95% confidence level. The slopes for each station were then compared with the slopes of the FORTH-RTM pixels that include the stations, to determine if they agree in terms of their signs of slope. For a given pixel, the qualitative agreement of the SSR changes (or GDB) between the FORTH-RTM and the GEBA/BSRN stations is indicated by the same signs of slopes of the FORTH-RTM and stations' time series of SSR anomalies, whereas the opposite signs suggest a disagreement. This assessment is valuable because it measures how closely the FORTH-RTM GDB agrees, in signs, with the reference ground-based stations, quantifying the FORTH-RTM GDB confidence.

2.2.3 Contributions to GDB analysis

Apart from the evaluation process, the changes of the model input parameters were investigated for the entire time period of 1984-2018 as well as for the 4 last decades worldwide, on a hemispherical scale and also over 18 specific land areas displayed in Figure AD2. These areas (study sub-regions, Figure

AD2) of the globe were chosen to represent all continents. The criteria for selecting these areas were that they define specific continental entities, while having relatively cohesive GDB patterns (deduced from the performed analysis of GDB). The investigation of changes of input parameters is done to qualitatively determine the GDB drivers, since increase/decrease in input data (which determine the transparency of the atmosphere) lead to decrease/increase of SSR, thus causing dimming/brightening. Nevertheless, in order to identify and determine more accurately, and quantitatively, the GDB drivers, namely the contribution of changes in clouds (cloud amount-CA and cloud optical thickness-COT of low, middle, high-level clouds), aerosol optical properties (AOD, SSA and AP), water vapor and ozone to GDB during the 35-year period 1984-2018, another method was applied. According to this method, the contribution to GDB (in Wm^{-2}) of each physical input parameter P is estimated through two RTM runs in which, first, the P parameter is kept 'frozen' at its initial conditions, that is those in the first year of the study period, i.e. 1984, and second all the input parameters were activated (main RTM run). Next, the changes of SSR (GDBs) have been estimated based on the two RTM runs. Then, from the difference between the GDB of the main RTM run, with all parameters being activated, and the GDB from runs with 'frozen' P parameters, the contribution of the P parameter to the overall GDB was estimated (Eq. 2.21). When the contribution of a parameter is positive (reddish colors on the maps), it means that the changes of the P parameter resulted in an increase of SSR, and the interdecadal changes of this parameter contributed to, or partially caused, the estimated brightening or counteracted the estimated dimming. On the other hand, if the contribution of one parameter is negative (bluish colors on the maps below), it means that the changes of P parameter resulted in a decrease of SSR and the interdecadal changes of this parameter contributed to, or partially caused, the estimated dimming or counteracted the estimated brightening.

$$Contribution\ of\ P\ to\ GDB = GDB_{baserun} - GDB_{frozenrun} \qquad \text{(Eq. 2.21)}$$

For a more detailed investigation, the contributions to GDB were estimated not only for the entire 35-year study period 1984-2018, but also for the 4 decades (e.g., 1984-1989, 1990-1999, 2000-2009, 2010-2018) separately. Also, the contributions to GDB were spatially averaged over the Globe, NH, SH, land, ocean and over the aforementioned 18 specific land areas of the Earth. This enabled us to identify the main causes of GDB not only on planetary/hemispherical, but also on a regional scale, which is important since different areas of the Globe are affected by specific natural and anthropogenic processes and variability.

2.2.4 Correlation and Regression Analysis

To investigate the drivers of monthly SSR anomalies from 1984 to 2018, three complementary analytical methods were employed: Pearson correlation, Ridge Regression, and Random Forest Regression. Each method was chosen for its unique ability to address different aspects of the data and offer insights into the complex relationships between variations in SSR and its drivers. Pearson correlation (Benesty et al., 2009) is a straightforward, widely used statistical technique to measure the strength and direction of linear relationships between two variables. Here, the Pearson correlation was used to identify initial, simple linear associations between SSR and the GDB drivers, such as clouds, aerosols, water vapor,

and ozone. The major advantage of Pearson correlation lies in its simplicity and ease of interpretation, providing a quick overview of potential relationships. However, Pearson correlation has limitations: it only captures linear dependencies and cannot account for non-linear interactions between variables. Moreover, it is sensitive to multicollinearity, meaning that if two predictors are highly correlated, it may lead to misleading interpretations of their individual effects. Despite these limitations, Pearson correlation was an essential first step in revealing broad patterns and guiding subsequent analysis. Ridge Regression was employed next to refine our understanding by addressing the limitations of linear models under multicollinearity. Ridge regression (Hoerl et al., 1970), an extension of ordinary least squares regression, introduces an L2 regularization term that penalizes large coefficients, helping to prevent overfitting and stabilize the model when predictors are highly correlated. Ridge regression is particularly useful when dealing with multicollinearity, as it allows for a more reliable estimation of the coefficients for each driver, even when predictors are not completely independent. The advantage of Ridge Regression is that it provides clear, interpretable coefficients while reducing the risk of overfitting, making it ideal for modeling relationships where multicollinearity may distort results. However, its major drawback is that it still assumes linearity in the relationships between the predictors and the target variable (SSR). Furthermore, Ridge Regression requires careful tuning of the regularization parameter, which can impact the model's performance if not optimized properly. Despite these limitations, Ridge Regression was crucial in refining our understanding of the linear relationships while controlling for multicollinearity. Finally, Random Forest Regression (Breiman 2001) was used to capture the non-linear, complex interactions between SSR and its drivers that cannot be adequately addressed by Pearson correlation or Ridge Regression. Random Forest is an ensemble machine learning technique that builds multiple decision trees using different subsets of the data and averages their predictions to improve accuracy and reduce overfitting. The strength of Random Forest lies in its ability to model non-linear relationships and interactions without requiring prior assumptions about the form of these relationships. It also provides useful insights into the relative importance of each predictor in explaining SSR variations. However, the main disadvantage of Random Forest is that it is computationally intensive, especially for large datasets, and lacks transparency in terms of interpretability, as the individual decision trees are not easily explainable. Despite these drawbacks, Random Forest was invaluable in identifying complex interactions and interactions between predictors that the other methods could not capture. By combining these three methods, a comprehensive understanding of the factors influencing SSR anomalies is gained. Pearson correlation allowed to identify simple linear relationships, Ridge Regression helped refine these relationships under multicollinearity, and Random Forest helped to capture non-linear interactions. This multi-method approach provided a more robust, nuanced view of the drivers behind SSR variability and their regional and temporal variations.

2.2.5 The links between GDB with global warming

First, the Pearson correlation coefficients (r), along with their statistical significance at 95% confidence level, quantifying the correlation between the monthly timeseries of the deseasonalized SSR and temperature (T_{mean}, T_{max}, T_{min}, DTR) anomalies, were computed for each grid cell on a global scale for the entire time period (1984-2018). The deseasonalized monthly anomalies refer to the entire study period (1984-2018) and were calculated by subtracting the average value of all corresponding months within the entire time period from the current monthly value. Then, the timeseries of the annual mean

anomalies of SSR and temperatures, computed with respect to the entire study period, were produced. Next, the low-pass Savitzky–Golay (SG, Schafer, 2011) filter, was applied to the annual mean timeseries with a window size of 10 years, in order to reveal possible long-term relations between SSR and surface temperatures on global, hemispherical, land and ocean scale as well as during the boreal cold (November to April) and warm (May to October) periods of the year. Note that the SG filter relies on polynomial-based local least-squares fitting of the data and is a widely used technique for noisy data derivative computations and data smoothing. Also, the non-parametric robust Sens's slope and the Mann-Kendall test are applied to determine the annual changes and their significance at the 95% confidence level. The annual change is given in $Wm^{-2}decade^{-1}$ or $^{o}Cdecade^{-1}$. Along with the value of change, also the uncertainty of this change was calculated using the lower and upper bound of the confidence interval of the slope which we multiplied by the length of the time period to provide inside brackets next to the value of change the lower and upper limits of the change (i.e. change [low change, high change]). In a further step, the per decade changes of monthly deseasonalized SSR and temperature anomalies were computed at each grid cell utilizing the Sen's slope, while the Mann-Kendall test was applied to estimate their significance at the 95% and 70% confidence level. This analysis has been performed for 3 time-periods and 18 land regions. The 18 land regions (study sub-regions, Figure AE1) of the globe were selected, covering almost all continents. The selection of these areas was made based on the criterion that they define specific continental entities and also have roughly coherent patterns of GDB. Over these sub-regions the decadal changes of either SSR and temperatures were calculated for 3 different time periods that are characterized, according to the station measurements-based literature (Stamatis et al. 2023; Wild 2009), by brightening (1984-1999), weak brightening (2000-2009) and brightening (2010-2018). Then, the calculated changes were spatially averaged for each sub-region and sub-period. Moreover, we calculated the standard deviation of these spatial averages along with the percentage number of grid-cells having statistically significant trends at the 95% and 70% confidence level. This regional analysis aims to examine to what extent the warming of the planet is accelerating during solar brightening or decelerating during solar dimming on a specific regional basis, over a certain region. This is an important information, given the regional patterns in both GDB (Hatzianastassiou et al. 2020; Norris and Wild 2009; Ohmura 2009; Stamatis et al. 2023; Wild 2012) and planetary warming (Cheshmehzangi 2020; Hansen et al. 2006; IPCC 2021,2022; Semenov et al. 2010). To effectively test the hypothesis that brightening allows surface warming due to anthropogenic greenhouse effect to fully occur, or better reinforces it, while dimming slows down the rate of warming, we examined to what extent this relationship between GDB and surface temperature (T_{mean}) is observed over the selected 18 world areas where and when we have brightening and dimming. Thus, for each of the 18 regions and each of the three time periods, namely for 54 cases, we searched for the cases in which the solar brightening coexists with surface warming, as well as the dimming coexists with weak warming. Besides, to increase the reliability of our results, we used a threshold to identify in which cases there were strong positive trends both in SSR and temperature and also in which cases there were dimming or weak brightening along with weak warming. Thus, if the % per decade SSR/temperature change is larger in absolute terms than that of the global land average change during 1984-2018 (i.e., 1.4% and 0.1% per decade for SSR and temperature, respectively), then the change is considered as strong and it is noticed with bold, otherwise it is considered as no strong.

Chapter 3: The RTM SSR and GDB

3.1 Introduction

The SSR represents the amount of solar energy reaching the Earth's surface, which is fundamental to driving the planet's energy balance, climate systems, and ecological processes. SSR varies widely due to atmospheric effects such as absorption, scattering, and reflection by aerosols, clouds, and gases. Understanding the spatial and temporal patterns of SSR along with the climatic parameters that affect SSR is crucial for evaluating its role in climate dynamics, ecosystem productivity, and renewable energy applications. Furthermore, the SSR has undergone significant variations over the past decades due to changes in atmospheric composition, cloud cover, and aerosol concentrations. These variations, commonly described as global dimming and brightening (GDB), have important implications for climate, ecosystems, and renewable energy applications. Understanding the spatial and temporal patterns of GDB is essential for assessing its potential drivers and impacts on global energy balance. In this chapter, in Section 3.2, the global distribution of SSR and the GDB drivers from 1984 to 2018 on annual and seasonal basis using the FMC-RTM is analyzed. Latitudinal SSR variations and timeseries of SSR and the GDB drivers were also investigated to qualitatively estimate the strongest contributions of the GDB drivers to SSR fluctuations. By leveraging deseasonalized SSR anomalies, the magnitude, significance, and spatial distribution of long-term SSR trends for the entire time-period and for its 4 decadal sub-periods is quantified in Section 3.3. The analysis is conducted globally, with a focus on distinguishing regional differences, land-ocean contrasts, and seasonal variability. Also, a short analysis of the SSR fluctuations and trends based on the initial FORTH-RTM version (i.e. FMI) is presented in the last section (3.4).

3.2 Annual and seasonal global distribution of SSR and GDB drivers

3.2.1 Annual and seasonal global distribution of SSR

The highest values of solar radiation entering the Earth's surface appear in the subtropical regions where there is reduced cloud cover, as will be seen in the results that follow. The incoming solar flux at TOA largely determines the latitudinal gradient of the 35-year average SSR, whereas cloud and surface characteristics largely influence the patterns of longitudinal variation. Figure 3.1a shows the average annual planetary distribution of the SSR, as calculated by the model, for the period 1984-2018. The values range between 0 and 301 Wm^{-2} and the mean annual planetary value is 183.99 Wm^{-2}, while the highest values are found in the Atlantic and Pacific Oceans (areas of permanent anticyclones), in the Gulf of Mexico, in Central America, South Africa, the Indian Ocean and north of Australia. On the contrary, the lowest values appear in China, Mongolia, the northeastern and northwestern Pacific Oceans, as well as in the peripheral areas of the storm zones of the northern and southern hemispheres. Also, low values appear on the western coasts of the continents, North and South America and southern Africa.

Large SSR fluxes, which are equivalent to around 350–380 Wm^{-2} over Antarctica in DJF and 200–250 Wm^{-2} over the Arctic in JJA, are thus present in polar regions (Figure 3.1) throughout local summer. In DJF and JJA, the SSR gradually declines from the summer to the winter pole, reaching zero values poleward of mid-to-high latitudes. The grey areas in Figure 3.1 correspond to missing CLARISC model input

data, but they do not affect our results since they coincide with polar night conditions. During the polar night, there is no solar radiation for the satellite to observe. This means that the satellite cannot measure the reflected solar radiation, making it impossible to retrieve cloud properties that depend on this measurement. The latitudinal gradient of SSR becomes less pronounced during spring and autumn (Figure 3.1). In general, SSR reaches its highest values over subsidence regions characterized by anticyclonic conditions and minimal cloud cover, including oceanic areas in the low latitudes of the summer hemisphere and the polar regions of the same hemisphere. Conversely, lower SSR values are observed in areas with substantial cloud cover, such as the mid-latitudes of the summer hemisphere. Thus, SSR values as low as 140 Wm^{-2} are found over the storm track zone of southern hemisphere (50◦–70◦S) in DJF, whereas values down to about 100 Wm^{-2} are computed in SON. Corresponding features, with SSR values equal to 100–140 Wm^{-2} in MAM and JJA, exist over northern Pacific Ocean's areas with large cloud amounts (equal to about 0.9). Overall, SSR exhibits a strong inverse relationship with cloud amount. Notably, off the western coasts of South America and South Africa during JJA, SSR values are lower than those in adjacent regions at the same latitude, which can be attributed to high cloud cover (around 0.8). Similarly, in southeastern Asia during JJA, SSR remains relatively low (approximately 180 Wm^{-2}) due to the presence of extensive cloud cover (≈0.8) linked to monsoonal activity. Beyond oceanic regions, several continental areas experience high SSR values, including the United States, Southern Europe, North Africa, and the Middle East in MAM and JJA, as well as South America, South Africa, and Australia in DJF and SON.

3.2.2 Annual and seasonal global distribution of GDB drivers

SSR is influenced not only by incoming solar flux at the TOA but also by atmospheric components such as clouds, water vapor, and aerosols. The patterns of mean SSR can be understood by analyzing the annual average values of these influencing factors, as shown in Figure 3.2. CA1 is most pronounced in marine areas like the Southern Ocean and Arctic Ocean, as well as along the marine stratocumulus areas, with a global average of 0.20. CA2 reaches its highest values in polar regions, particularly at the South Pole, and in certain subtropical areas such as Peru and Southeast Asia, averaging 0.18 worldwide. In contrast, CA3 is more dominant in tropical regions, with a mean value of 0.24. The sum of the three cloud amount categories results in the total cloud amount shown in Figure 3.2l, which has a global average of 0.62. Total cloud cover is highest over the Southern Ocean, the North Pacific and Atlantic Oceans, and across mid-latitude and tropical regions. COT at all levels peaks in polar regions, as well as in certain mid-latitude areas and southeastern China, with mean values of 5.10, 5.60, and 4.60 for COT1, COT2, and COT3, respectively. AOD is highest over the Sahara, Arabian Peninsula, India, and Southeast Asia, with a global average of 0.14. The global average SSA is 0.96, with higher values over the oceans than land. The lowest SSA values, below 0.92, are found in South Africa, India, and Southeast Asia, indicating the presence of absorbing aerosols. AP has a global average of 0.77, also higher over oceans than land. Water vapor concentrations peak in tropical and subtropical regions, averaging 0.13 globally. Meanwhile, ozone has a global mean of 0.29 DU, with higher concentrations over mid-latitude and northern polar regions, as well as the Southern Ocean, while reaching its lowest values over Antarctica.

Similarly, the global distribution of the averages of each input parameter for the 4 seasons of the year calculated and are shown in Figures AB1, AB2, AB3 and AB4. More specifically, over the oceans, as well as in regions west of the continents and at mid-latitudes, CA1 shows significantly higher values in all

seasons, reaching 0.84 in SON. On a planetary scale, the maximum occurs in JJA at 0.21, while the minimum is in MAM at 0.19. During northern hemisphere winter, the highest CA1 values are observed over land areas such as Europe and eastern Asia. CA2 exhibits higher values primarily at high latitudes, reaching 0.91 in MAM, with the highest values occurring at the South Pole. In DJF and MAM, extensive

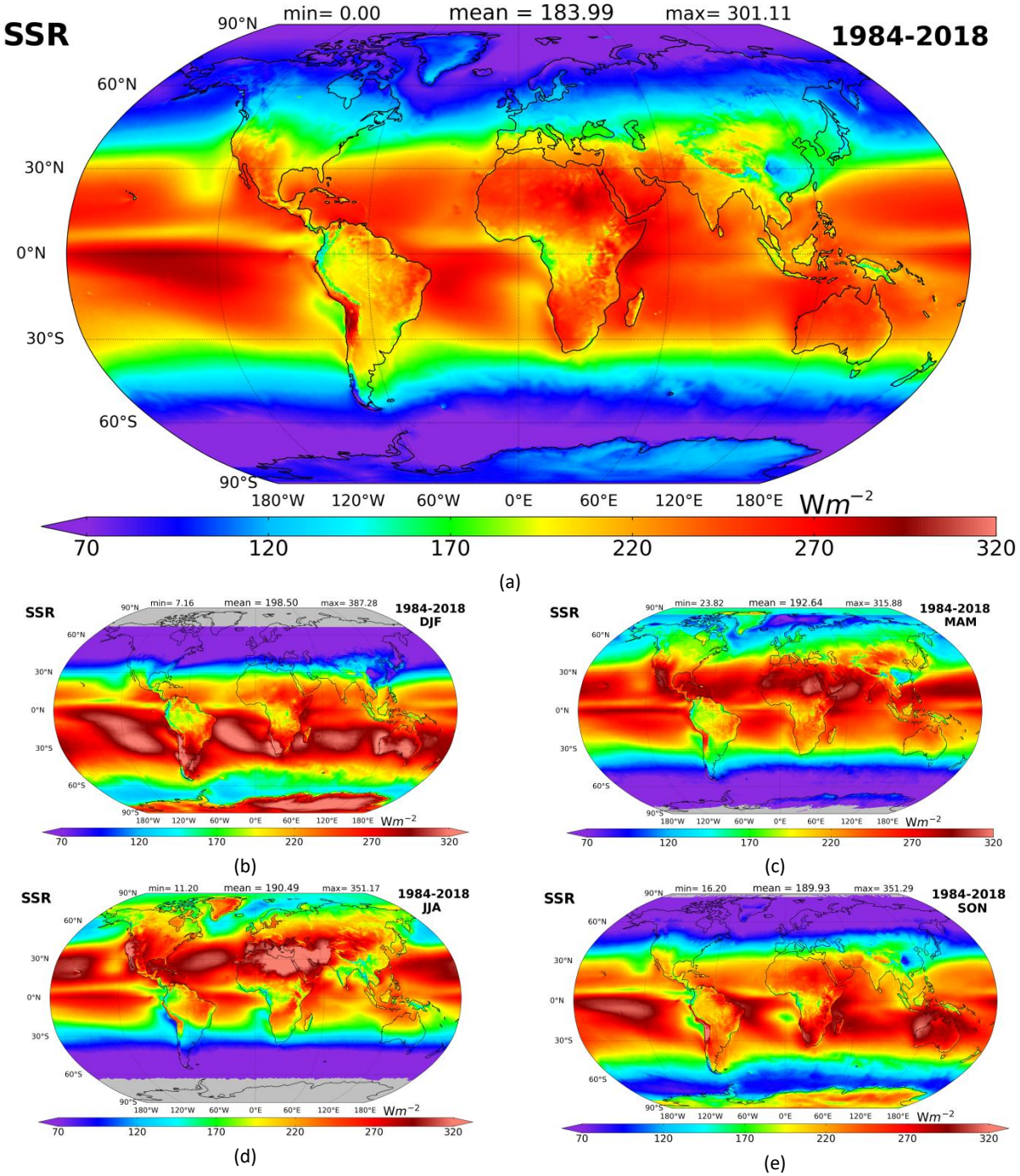


Figure 3.1. Global distribution of average SSR on annual (a) and seasonal (DJF-b, MAM-c, JJA-d, SON-e) basis for the 1984-2018 time period.

and elevated values are also found over land areas in the northern hemisphere. The planetary mean is highest in DJF at 0.18, while the lowest occurs in JJA at 0.15. For CA3, the pattern differs, as these clouds remain relatively constant across all seasons. The highest values are concentrated over tropical and subtropical regions, while significantly lower amounts are observed in regions west of the continents. The planetary averages show little variation, with MAM having the highest value of 0.25 and SON the lowest at 0.24. Total cloud cover generally reaches its highest values in mid and high latitudes throughout the year, with a maximum planetary mean of 0.62 in SON and a minimum of 0.61 in JJA. Regarding COT1, high values are mainly found in the polar regions, reaching 36.4 in DJF. Over land in the northern hemisphere during DJF, values remain high, reaching up to 18. In global mean terms, the highest values occur in SON at 4.99, driven by elevated values over South Pole, while the lowest values appear in JJA at 4.41. COT2 displays the highest values predominantly in the polar regions, with the greatest mean value occurring in SON (5.43) and the lowest in JJA (4.41). Similarly, COT3 follows a comparable pattern, with maximum values in SON (4.56) and minimum values in JJA (4.00). Continuing with the optical properties of aerosols, AOD exhibits seasonal variation, with the highest planetary mean in JJA (0.15) and the lowest in DJF (0.12). High AOD values are concentrated in desert regions of the tropics and subtropics, as well as in South-East Asia and India, where localized pollutant emissions occur. In MAM, the highest values are observed over the Mediterranean, Europe, India, South-East Asia, and the eastern USA. Meanwhile, AOD peaks over the Sahara and the Arabian Peninsula in JJA. SSA shows no significant seasonal variation, maintaining a mean value of 0.97 in DJF and MAM, while the lowest mean value occurs in SON at 0.96. Generally, SSA values are higher over oceans than over land. However, during DJF, values over India, eastern China, and central Africa—as well as in DJF and SON over southern Africa—are notably lower. The aerosol AP exhibits no strong seasonal variations, with a maximum value of 0.77 in DJF and a minimum of 0.76 in SON. Higher values are generally observed over oceans, while lower values appear over land, with the lowest recorded value in South Africa at 0.63. The water vapor maintains consistently high values in the tropics and subtropics throughout the year, without significant seasonal variation. On a global mean scale, the highest value is recorded in JJA (0.14), while the lowest is found in DJF (0.12). The lowest values occur over India and Southeast Asia, while water vapor displays the highest values over land in the northern hemisphere summer. Finally, ozone shows distinct seasonal variability at mid and high latitudes. In the northern hemisphere, maximum values occur in winter and spring, reaching up to 0.42 DU on global average scale. In the southern hemisphere, peak values occur in JJA and SON, reaching up to 0.376 DU, with the Antarctic ozone hole forming in SON (southern hemisphere spring).

3.2.3 Latitudinal variations and annual cycle of SSR

Latitude zonal averages of monthly mean SSR over the 35-year period (Figure 3.3) reveal fluxes ranging from zero to 360 Wm^{-2}. Peak values occur over subtropical and polar regions in both hemispheres during summer, reaching approximately 310 Wm^{-2} and 360 Wm^{-2}, respectively. The higher maximum at the South Pole compared to the North Pole is attributed to the slightly shorter Earth-Sun distance, reduced cloud cover, and a drier atmosphere. In the tropics, seasonal variations in SSR remain minimal due to weak fluctuations in solar declination and cloudiness throughout the year. The seasonal variation of SSR intensifies toward the poles, reaching up to 360 Wm^{-2}. In JJA, high SSR values extend from the equator to the North Pole, while in DJF, the southern hemisphere experiences relatively lower SSR fluxes, around 150

Wm^{-2} between 50°S and 70°S, due to extensive cloud cover along the storm-track zone. In both hemispheres, SSR peaks in subtropical regions (10°–35° latitude) rather than in the tropics, apart from the poles. This occurs because total cloud cover is at a minimum (~0.5) in these subtropical areas, whereas along the equator, the ITCZ sustains higher cloud cover values of approximately 0.6–0.7, as indicated by

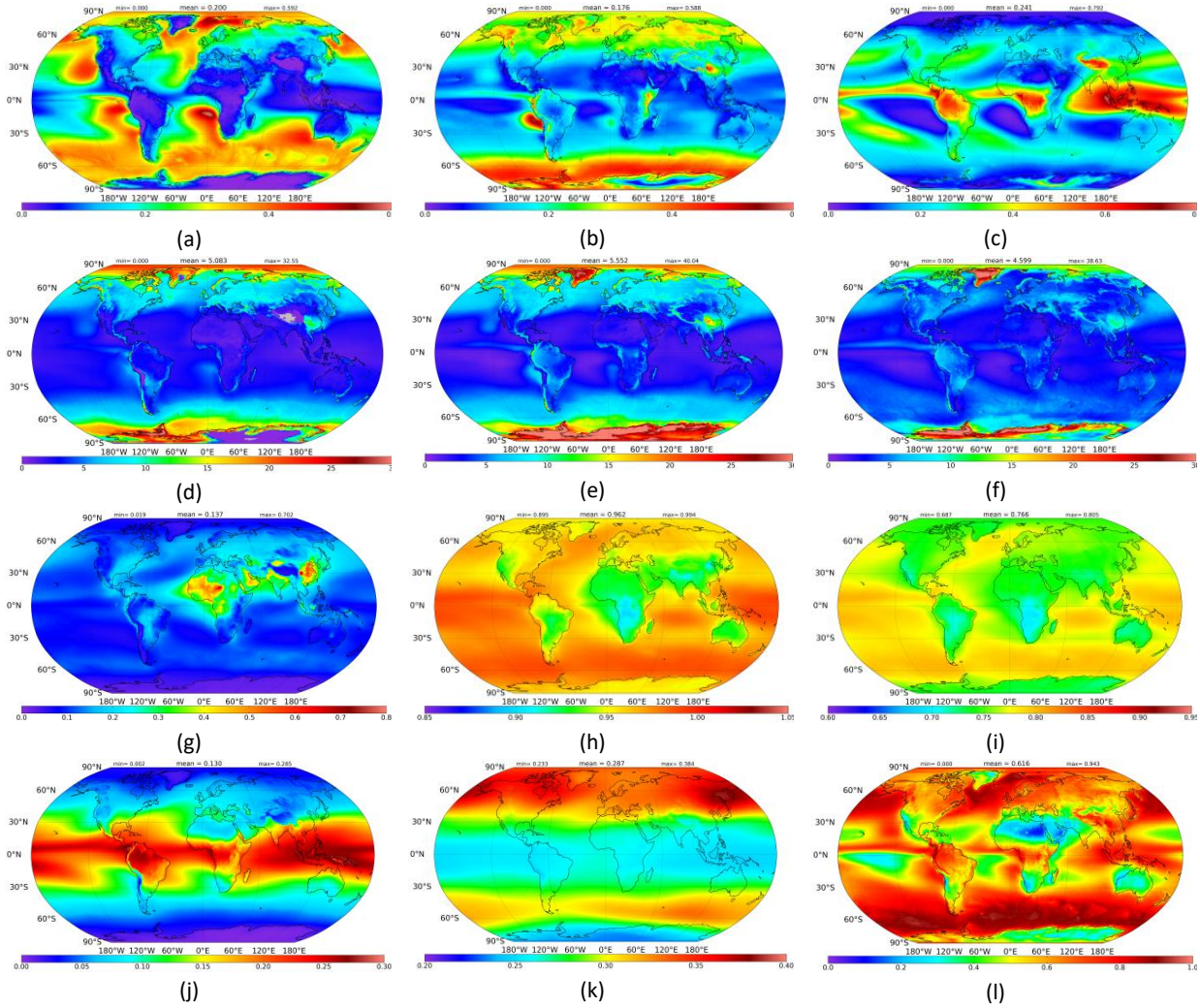
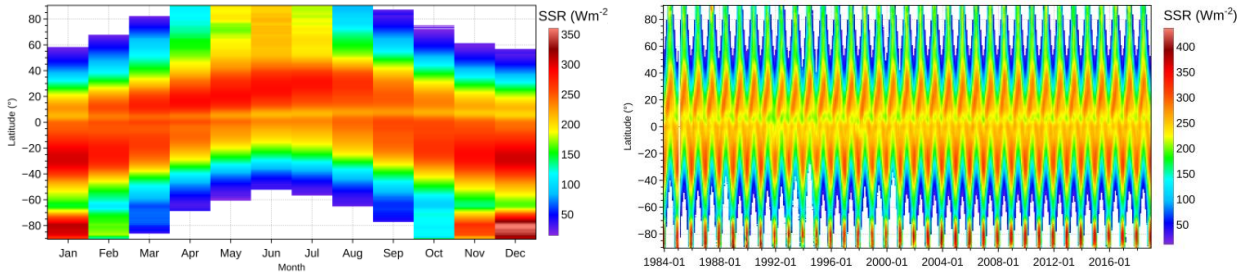


Figure 3.2. Global distribution of annual average of CA1 (a), CA2 (b), CA3 (c), COT1 (d), COT2 (e), COT3 (f), AOD (g), SSA (h), AP (i), water vapor (j), ozone (k) and total cloud amount (l) for the 1984-2018 time period.

CLARISC data. In the tropics, (20◦ S–20◦ N), maximum SSR values occur during spring and autumn, and not in summer as in sub-tropical, mid-latitude and polar areas. This behaviour, which has been also reported by Darnell et al. (1992), Hatzianastassiou and Vardavas (1999) and Hatzianastassiou et al. (2005), is attributed to maximum values in the incoming solar radiation at TOA during these seasons over the tropics, as well as to relevant features in the annual cycle of cloudiness and total precipitable water. The time series of global zonally averaged monthly mean SSR fluxes over the entire 420-month period 1984–2018 indicate that the patterns shown in Figure 3.3a are repeated over the 35-year period (Figure 3.3b). As a result, peak SSR values of approximately 260–280 Wm^{-2} are observed over subtropical regions (10°–40° N and S) during their respective summers. Similarly, high SSR values occur in polar regions during

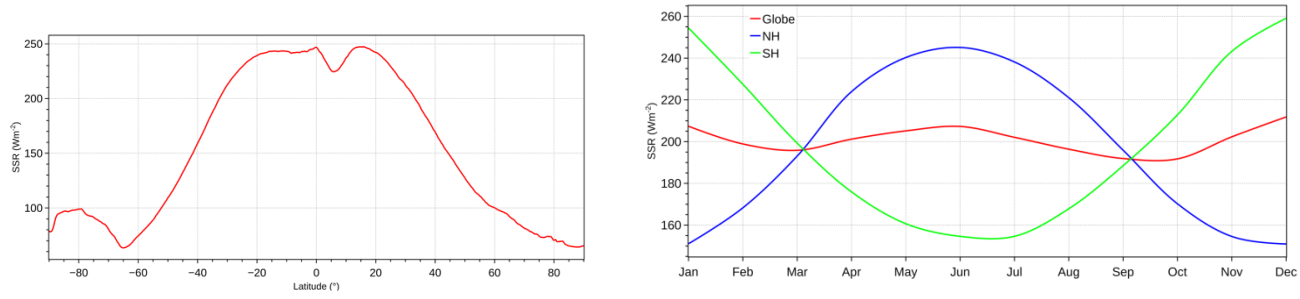
summer, with slightly higher values at the South Pole compared to the North Pole. Local SSR minima, around 200 Wm^{-2}, appear in equatorial regions due to ITCZ cloud cover, as well as in mid-to-high latitudes (around 60° N and S) of both hemispheres, where extensive stratiform cloud cover over the oceans reduces SSR. The summer SSR maximum in the Southern Hemisphere reaches about 240 Wm^{-2}, slightly exceeding the 230 Wm^{-2} observed in the Northern Hemisphere.



(a) (b)

Figure 3.3. Seasonal and latitudinal variation of 35-year (1984- 2018) averages of monthly mean SSR (a) along with time-series of 10-degree latitude-zonal averages of monthly mean SSR (b). Monthly mean quantities over a 0.5◦×0.625◦ geographical grid are used.

The latitudinal distribution of mean annual SSR flux shows peak values of approximately 250 Wm^{-2} in subtropical regions, while it declines sharply to around 100 Wm^{-2} toward the poles (Figure 3.4a). A local minimum, around 225 Wm^{-2}, is observed near the equator due to cloud cover linked to the ITCZ. There is also a local maximum of 230 Wm^{-2} in SSR around 15°N, in agreement with previous studies (Liou, 1992; Hatzianastassiou and Vardavas, 1999 and Hatzianastassiou et al., 2005) while Darnell et al. (1992) reported a similar local maximum, but shifted poleward by 10°latitude. Note that in the South Hemisphere, there are local minimum and maximum SSR values around 60°S and at the south pole, respectively, while in the North Hemisphere there is a continuous equator-to 60°N decrease in SSR while then to 90°N SSR show a small increase. The local SSR minimum around 60°S is attributed to the persistent and extensive cloud cover over the oceanic region of the Southern Hemisphere, highlighting the crucial influence of clouds—alongside solar declination—in shaping SSR fluxes. The mean hemispherical SSR fluxes exhibit opposite seasonal patterns, fluctuating between 150 and 260 Wm^{-2}. Consequently, the global mean SSR flux remains within the range of 190 to 210 Wm^{-2} throughout the year (Figure 3.4b).



(a) (b)

Figure 3.4. Latitudinal variation (a) and seasonal variation of hemispherical and global averages (b) of FORTH-RTM SSR averaged over the period January 1984 through December 2018.

3.2.4 SSR timeseries

The SSR averages over land and oceans (Figure 3.5) balance each other to produce a monthly mean global average SSR with a small seasonal variability (≈20 Wm^{-2}), with primary and secondary maxima and minima. The seasonal variability over global land (≈60 Wm^{-2}) is much larger than the variability over global oceans (≈30 Wm^{-2}). Over NH, the differences in seasonal variability over land and oceans are much smaller with a larger minimum for the lands whereas over the SH, land shows always larger maxima than the oceans. The applied Savitzky-Golay low pass filter with 120 months window shows rather a steady flat fluctuation of SSR fluxes with a general not statistically significant brightening over the NH equal to 0.70 $Wm^{-2}decade^{-1}$ and a not statistically significant dimming over SH equal to -0.75 $Wm^{-2}decade^{-1}$, which results in weak not statistically significant dimming for the globe equal to -0.04 $Wm^{-2}decade^{-1}$. However, using deseasonalized SSR anomalies instead of absolute SSR fluxes helps remove the strong seasonal cycle, making it easier to see real long-term trends. This avoids seasonal biases, reduces noise, and gives a clearer picture of how solar radiation is actually changing over time. The time series of the calculated average deseasonalized SSR anomalies for the Globe, the northern hemisphere (NH), and the southern hemisphere (SH), for the total globe, land and oceans, over the 35-year period from January 1984 to December 2018 is shown in Figure 3.5ii, providing an easy assessment of the interdecadal patterns of global and hemispherical GDB. The FORTH-RTM global mean SSR anomalies vary up to 18 Wm^{-2} (from −14 to 4 Wm^{-2}) before 2000 whereas after 2000 SSR anomalies have quite small variations up to 5 Wm^{-2}, while the northern/southern hemispherical SSR anomalies range from −11/−18 to 6/8 Wm^{-2}, respectively. The applied Savitzky-Golay low pass filter to the 35-year time series indicates that between 1984 and 1989 a general decreasing SSR tendency occurred, which reversed to a brightening in the 1990s and till early 2000s. Subsequently, a level-off of brightening (steady fluctuations or very weak dimming) took place in the first decade of the 21st century, followed by a brightening in the last decade, i.e., in the 2010s except for the oceans which show a weak dimming. This results in an overall positive trend (brightening) during the entire 1984–2018 period, either globally (0.69 $Wm^{-2}decade^{-1}$) or in both hemispheres (1.31 and 0.10 $Wm^{-2}decade^{-1}$ for NH and SH). The global land experienced a strong and statistically significant brightening equal to 2.73 $Wm^{-2}decade^{-1}$ which is coming both from NH and SH, while the global oceans exhibited a weak dimming equal to -0.10 $Wm^{-2}decade^{-1}$ which is mostly arising from the SH ocean dimming (-0.58 $Wm^{-2}decade^{-1}$). Most existing measurements-based and modeling studies agree with the increase in SSR suggested by FORTH-RTM during the years from 1990 to 2000 (Hatzianastassiou et al., 2005; Stanhill and Cohen 2001; Liepert 2022; Wild et al., 2005), while the trend stabilization for the years 2000 to 2009 is also consistent with other studies (Hatzianastassiou et al., 2020; Hatzianastassiou et al., 2012; Hinkelman et al., 2009). Strong SSR decreases brought on by the large volcanic eruption of Pinatubo (1991), as well as by strong El-Nino phases (1997, 2002, 2009, or 2016), are reproduced by FORTH-RTM. Years that were affected by the recovery from Pinatubo, as well as the La-Nina phases (1989, 1999, or 2006), are distinguished by positive anomalies. These results demonstrate that the FORTH-RTM satisfactorily reproduces natural processes that affect Earth's radiation budget and climate, such as volcanic eruptions and the ENSO (El Nino Southern Oscillation). Note, that a similar analysis to that shown in Figure 3.5ii was performed by (Stamatis et al., 2022) using the MERRA-2 SSR, which did not reveal the brightening phases in the 1990s or in the 2010s, although both MERRA-2 SSR and

FORTH-RTM SSR were computed with the same aerosol information. This underlines how the different cloud data (CLARISC vs. MERRA-2 calculated clouds) impact the estimated GDB.

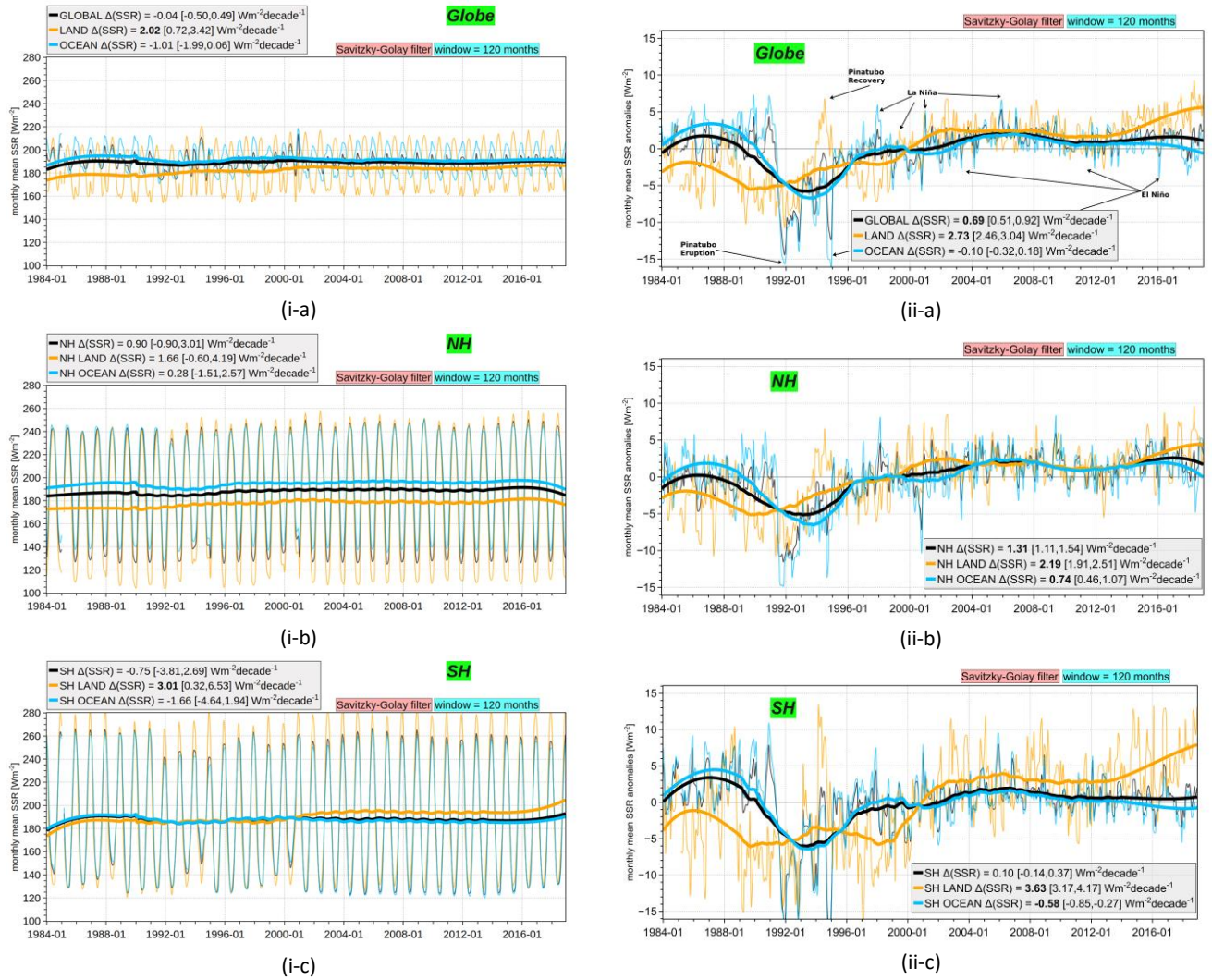


Figure 3.5. Time series of FORTH-RTM average global (black line) and land/ocean (orange/blue) monthly mean SSR fluxes (i) along with deseasonalized SSR anomalies (ii) for the Globe (a), for NH (b) and for SH (c) during the period January 1984–December 2018. The low pass filtered data of Savitzky-Golay filter with 10 years window along with associated Δ(SSR) in $Wm^{-2}decade^{-1}$ and the confidence slope intervals in 95% CL are also shown. The statistically significant trends in 95% CL are shown in bold.

3.2.5 Timeseries comparison between SSR and GDB drivers

In order to simply examine the relationship of the interdecadal variability of SSR and the GDB drivers, the monthly deseasonalized anomalies of SSR and 12 fundamental model input variables that influence SSR fluctuations (Figure 3.6) were averaged and then the low pass Savitzky-Golay filter applied to them. A distinct solar dimming phase is observed during the period from 1984 to the early 1990s. This dimming occurs alongside an increasing trend in all input variables, except for the AP and ozone, which remain exceptions to this overall pattern with decreasing trends. During the 1990s, SSR begins to exhibit an increasing trend. This rise in SSR does not align with the increasing trends of CA1, water vapor, ozone,

and AP. Conversely, cloud amounts at mid and high levels (CA2 and CA3), COT, AOD, and SSA show a decreasing trend during this decade, thereby contributing to the overall increase in SSR. In the 2000s, the trend shifts again, with SSR showing a general decrease. During the time-period 2000-2018, a stabilization of the SSR trend exists which is in line with similar stabilization in CA2, CA3, AOD and SSA. During the 2000s, a very weak dimming estimated which is in line with the increasing trends of CA1 and total cloud amount. Moving into the 2010s, SSR resumes a very weak increasing trend. This increase is consistent with a slight decline in total cloud amount and a more pronounced decrease in COT, particularly in comparison to the changes in CA. Aerosol optical properties, on the other hand, do not display a clear trend, while both water vapor and ozone continue to increase. Globally, the strongest anti-correlation between SSR and the GDB drivers is observed for total cloud amount, with a correlation coefficient of -0.74. This is followed by AOD and SSA, which has an R value of -0.71, and then by COT3 and CA2, with R values of -0.69 and -0.68, respectively. COT2 and COT1 shows a weaker negative correlation, with R = -0.51 and -0.48 whereas AP is the only variable exhibiting a strong positive correlation with SSR, having an R value of 0.76. Using the low pass filtered data, globally, the strongest anti-correlation between SSR and the GDB drivers is observed for total cloud amount, with a correlation coefficient of -0.84. This is followed by COT3 and SSA, which have an R value of -0.83, and then by CA2 and AOD, with R values of -0.81 and -0.72, respectively. All the other parameters show insignificant correlation except for AP which shows significant correlation of 0.84. These findings underscore that the GDB is influenced by different factors across various time periods. At a global scale, COT3 and CA2 overall clearly dominates the SSR variations (except for the Pinatubo signal at the beginning of the 1990s), both in terms of inter-annual variations (e.g., strong peak in 1994 explained by cloud optical thickness low peak) as well as the longer term variations (low-pass filtered data of SSR and cloud amount and cloud optical thickness fit very well), and even in the overall trend. Thus, for each decade, a qualitative assessment of the causes behind SSR changes have been made based on the estimated variations in input parameters. However, determining the precise contribution of each driver to the GDB, as well as understanding how these contributions vary by region and decade, requires further detailed investigation. This will be examined in more depth in the Chapter 5.

3.3 The Global Dimming and Brightening

3.3.1 The GDB during 1984-2018

In the second step of this analysis, the RTM deseasonalized SSR anomalies were used to determine the GDB on a global scale and over the 35-year climatological period 1984-2018 (Figure 3.7). The global distribution of GDB shown in Figure 3.7 informs about the presence, the magnitude, and the significance of the SSR trends. Note that the global distribution of the data availability from which the trends derived is shown in Figure AB5 where between 60°N and 60°S there is almost full coverage but in polar regions the data availability is decreasing either for the missing input data or the lack of solar radiation at specific seasons with polar nights. Both the solar dimming (decreasing SSR, bluish colors) and brightening (increasing SSR, yellowish and reddish colors) are statistically significant, at 95% confidence level, to a substantial extent (in 47% of the total number of pixels). The computed spatially averaged GDB for the period 01/1984-12/2018 is equal to 0.88 $Wm^{-2}decade^{-1}$ for the Globe, 1.4 $Wm^{-2}decade^{-1}$ for the NH and

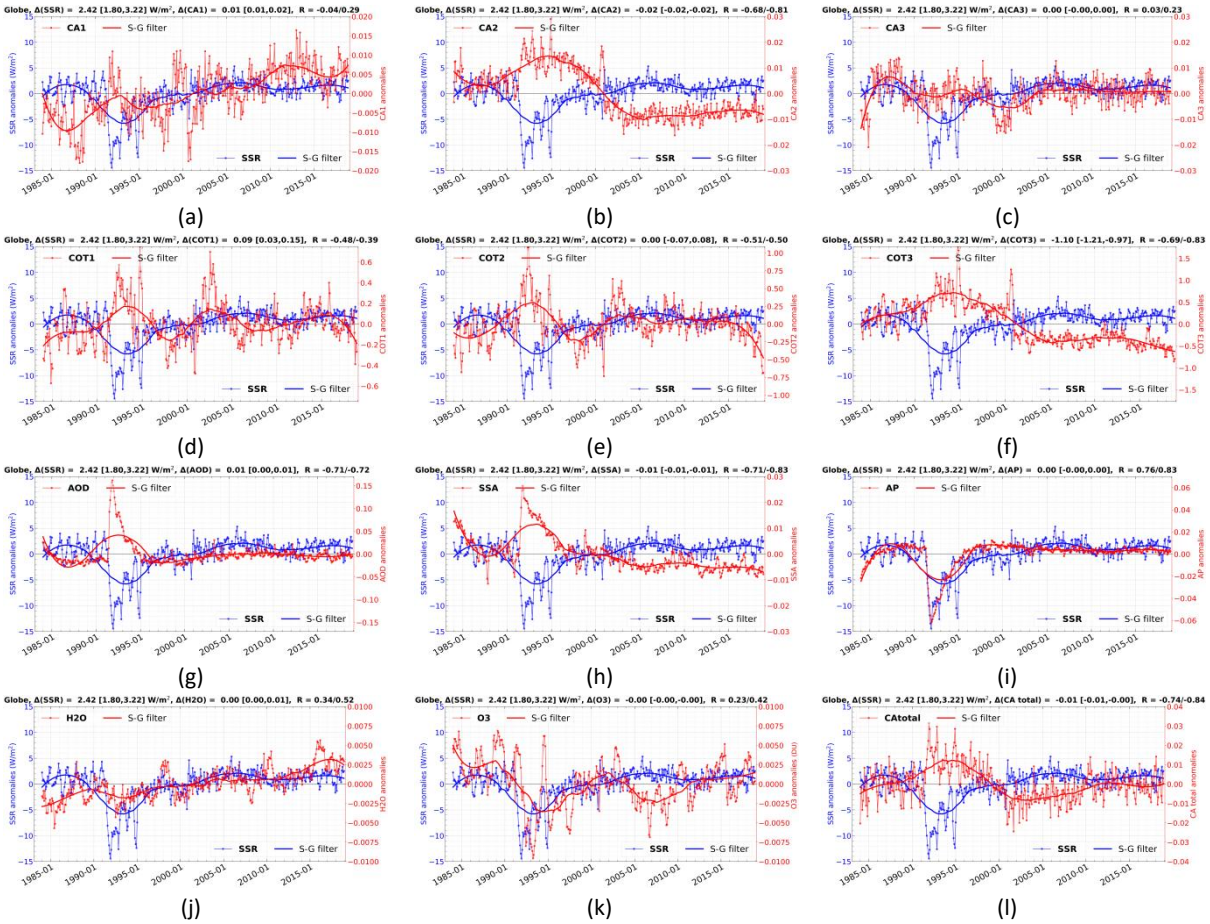


Figure 3.6. Time series of monthly global mean deseasonalized SSR (in blue) and model input data (in red) which are relevant for GDB: CA1 (a), CA2 (b), CA3 (c), COT1 (d), COT2 (e), COT3 (f), AOD (g), SSA (h), AP (i), water vapor (j), ozone (k) and total cloud amount (l) over the period 1984–2018. The low pass filtered data of Savitzky-Golay filter with 10 years window along with the associated changes and the confidence slope intervals in 95% CL are also shown. The statistically significant trends in 95% CL are shown in bold. The Pearson's R values are also shown computed with the monthly anomalies and with the low pass filtered data.

0.39 $Wm^{-2}decade^{-1}$ for SH, indicating that a brightening has taken place over the globe since the early 1980s, which was stronger in the NH than SH. Stronger brightening is observed over land than oceans (2.57 $Wm^{-2}decade^{-1}$ vs 0.19 $Wm^{-2}decade^{-1}$, respectively, on average) during the 35-year study period. Note that all the aforementioned trends are statistically significant in 95% confidence level. Overall, in 63% of the grid cells brightening has taken place opposed to 37% of cells with dimming, resulting in the overall global brightening. Our findings indicate that over a large portion of cells (in 54% of the grid cells with brightening and 34% of cells with dimming), as indicated by the black dots in Figure 3.7, the trends are statistically significant (at the 95% confidence level). Strong and statistically significant brightening tendencies are noteworthy over Europe, Americas, Tibetan Plateau, Indonesia, Antarctica, Australia and some oceanic regions, whereas the dimming dominates over parts of China and India, Arabian Peninsula, Sahara, Arctic, Southern Ocean and marine stratocumulus areas of the southern subtropical anticyclones. However, not statistically significant SSR tendencies are observed in other regions, such as Siberia, Southern Ocean, Western Sahara and central Arabian Peninsula. Positive tendencies make up 73% of cells

with statistically significant tendencies, while negative tendencies make up 27%. Therefore, when areas with statistically significant GDB are considered, brightening seems to be dominating again, strengthening the conclusion that the Earth's surface has experienced a solar brightening during the last four decades. It should be noted that the GDB regime from 1984 to 2018 (Figure 3.7) is somewhat similar to the one in the work by Stamatis et al., 2023, which was derived using the same RTM and input data, except for using ISCCP-H cloud data instead of CLARA-A2.1 – ISCCP-H synergy data (CLARISC, see Section 2) used here. The GDB data produced for a similar time period (1984–2018) in this study reproduce patterns partially similar to those in Stamatis et al. (2023) over many regions, such as Europe, Mexico, Southern South America, Antarctica, the Sahara, India, East China, and the South Ocean. However, there are notable differences in the sign of the GDB trend over Australia, South Africa, and Western Canada. Unlike the previous study, which observed a negative overall trend, brightening appears to dominate in the present study. This shift in the sign of the trend is a significant update and can largely be attributed to the newly derived and improved cloud dataset (CLARISC). As demonstrated in the validation, this dataset plays a crucial role in enhancing the accuracy of global SSR trend estimations. Seasonal change of GDB features on a regional level is revealed by additional information about the FORTH-RTM GDB derived on a seasonal basis (Figure 3.7b,c,d,e). For instance, the annual brightening seen over Europe (Figure 3.7a) is driven by substantial brightening in boreal spring, namely the months of March, April, May, in boreal summer (June, July, August) and in boreal autumn (September, October, November) while dimming is observed therein during winter (December, January, February). Moreover, the annual dimming over Siberia arises mainly from dimming in boreal spring months, while the dimming over India is stronger in boreal winter and over Sahara and Arabian Peninsula in boreal summer. A stronger dimming is seen in the months of June through November over East China and December through March over SE Asia, causing the respective annual mean dimming patterns. A systematic dimming is seen throughout the year across the marine stratocumulus areas, being stronger in boreal winter and spring months. Additionally, the annual brightening over Australia (Figure 3.7a) results from a brightening that occurs all the months of the year. Finally, in all seasons the global average GDB indicates a brightening being the largest in boreal autumn equal to 1.30 $Wm^{-2}decade^{-1}$.

3.3.2 The GDB during 1984-1989

Since the GDB exhibits decadal variability with possible alternating phases of increase and decrease, it is analyzed on a decadal scale to capture these decadal patterns.

Figure 3.8 depicts the global distribution of GDB from 1984 to 1989, providing insight into the prevalence, size, and statistical significance of SSR trends. Both solar dimming (decreased SSR, represented by bluish colors) and solar brightening (increased SSR, represented by yellowish and reddish colors) are statistically significant at the 95% confidence level across 13% of the total number of pixels. The computed spatially averaged GDB is 0.45 $Wm^{-2}decade^{-1}$ for the globe, -0.5 $Wm^{-2}decade^{-1}$ for the NH, and 1.35 $Wm^{-2}decade^{-1}$ for the SH, indicating a weak global brightening trend since the early 1980s. Over land, dimming is observed at -2.17 $Wm^{-2}decade^{-1}$, whereas over oceans, brightening reaches 1.5 $Wm^{-2}decade^{-1}$. Overall, 49% of the grid cells exhibit brightening, while 51% show dimming, resulting in an overall weak net brightening trend. Strong and statistically significant brightening trends are particularly evident over northern Europe, the Americas, southern India, the Philippines, Antarctica, and some oceanic regions.

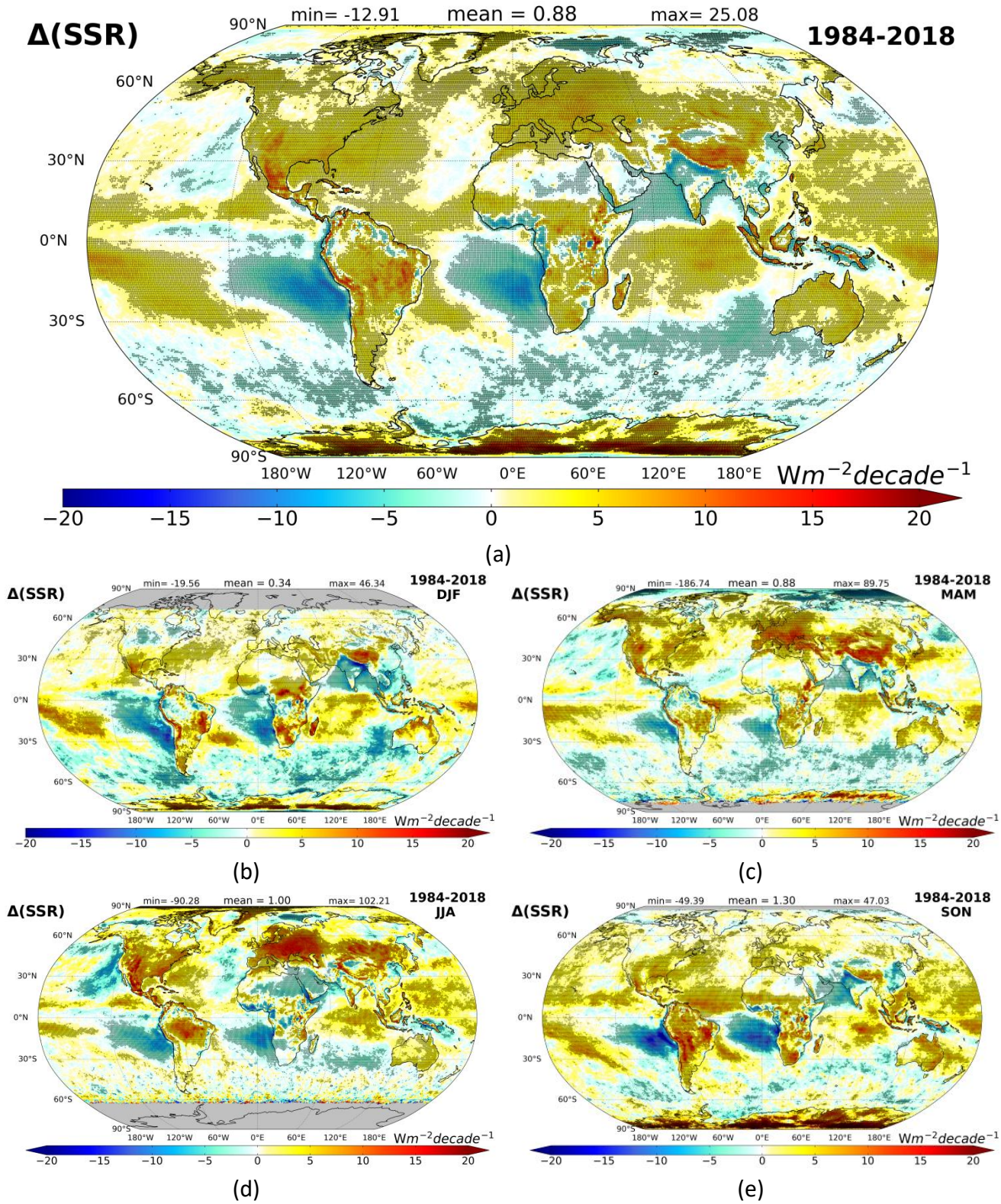


Figure 3.7. Global distribution of changes of FORTH-RTM GDB, namely changes of deseasonalized SSR anomalies, over the 35-year period 01/1984–12/2018 for annual basis (a), DJF (b), MAM (c), JJA (d) and SON (d). Areas shaded with reddish/bluish colors are those with positive/negative trends (brightening/dimming). Areas (pixels) with statistically significant trends are indicated by black dots.

In contrast, dimming is dominant over parts of China and Siberia, the Arabian Peninsula, the Sahara, the Arctic, Brazil, and sections of the Southern Ocean. Among statistically significant trends, positive tendencies account for 43% of affected grid cells, while negative tendencies make up 57%. Seasonal variations in GDB trends at the regional level are further highlighted by the FORTH-RTM GDB dataset, derived on a seasonal basis (Figure 3.8b,c,d,e). For instance, the annual brightening observed over northern Europe (Figure 3.8a) is primarily driven by substantial increases in SSR during boreal spring and autumn (September, October, and November). Conversely, the annual dimming over Siberia is mainly attributed to reductions in SSR during boreal summer. The brightening over southern India is more pronounced in boreal winter, while dimming over the Sahara and the Arabian Peninsula is strongest in boreal summer. A systematic dimming trend is observed throughout the year across Brazil, with the most significant reductions occurring in boreal winter. Additionally, the annual brightening over North America results from strong positive trends during boreal autumn and spring. Finally, on a global scale, seasonal variations in GDB reveal the strongest brightening trend in boreal spring, with an increase of 1.25 $Wm^{-2}decade^{-1}$, whereas boreal autumn shows a weak dimming trend of -0.01 $Wm^{-2}decade^{-1}$.

3.3.3 The GDB during 1990-1999

The global pattern of GDB from 1990 to 1999, illustrated in Figure 3.9, offers valuable insights into the extent, intensity, and statistical significance of SSR trends. Both solar dimming (a decline in SSR, shown in bluish colors) and solar brightening (an increase in SSR, represented by yellowish and reddish hues) are observed with statistical significance at the 95% confidence level across a considerable portion of the world, encompassing 20% of all analyzed pixels. The computed spatially averaged GDB is 4.73 $Wm^{-2}decade^{-1}$ for the globe, 6.43 $Wm^{-2}decade^{-1}$ for the NH, and 3.08 $Wm^{-2}decade^{-1}$ for the SH, indicating a global brightening trend during the 1990s. Over land, brightening is observed at 5.00 $Wm^{-2}decade^{-1}$, while over oceans, it reaches 4.62 $Wm^{-2}decade^{-1}$. Overall, 70% of the grid cells exhibit brightening, compared to 30% showing dimming, resulting in a net global brightening. Strong and statistically significant brightening trends are particularly evident over Eastern Europe, the Americas, southern India, East Asia, the Arctic, and the majority of tropical and subtropical oceanic regions. In contrast, dimming is more pronounced over parts of the Sahara, the Arctic, Indonesia, Australia, Antarctica, and sections of the Southern Ocean. Among statistically significant trends, positive tendencies account for 89% of affected grid cells, while negative tendencies make up 11%. Seasonal variations in GDB trends at the regional level are further highlighted by the FORTH-RTM GDB dataset, derived on a seasonal basis (Figure 3.9b,c,d,e). For instance, the annual brightening observed over Eastern Europe is driven primarily by substantial increases in SSR during boreal spring and summer. Conversely, the annual dimming over Indonesia is mainly attributed to reductions in SSR during boreal winter, autumn, and spring. Brightening over southern India is more pronounced in boreal summer, whereas dimming over Australia is strongest in boreal summer. A systematic brightening is evident throughout the year across Mexico, with the most significant increases occurring in boreal winter. Additionally, the annual brightening over subtropical oceans results from strong positive trends observed in all seasons, particularly in boreal autumn. Finally, on a global scale, seasonal variations in GDB reveal the strongest brightening trend in boreal autumn, with an increase of 7.15 $Wm^{-2}decade^{-1}$.

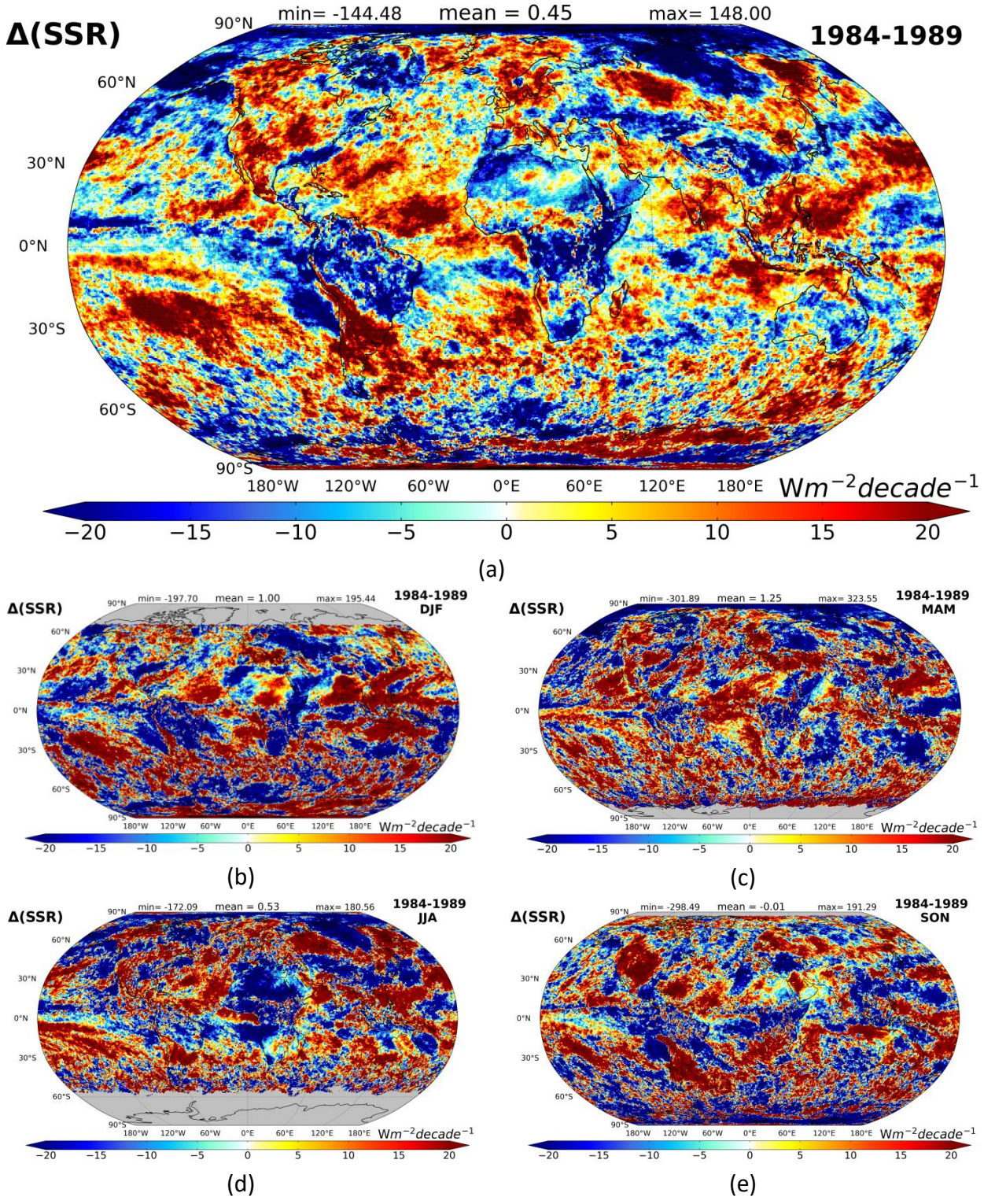


Figure 3.8. Global distribution of changes of FORTH-RTM GDB, namely changes of deseasonalized SSR anomalies, over the 6-year period 01/1984–12/1989 for annual basis (a), DJF (b), MAM (c), JJA (d) and SON (d). Areas shaded with reddish/bluish colors are those with positive/negative trends (brightening/dimming). Areas (pixels) with statistically significant trends are indicated by black dots.

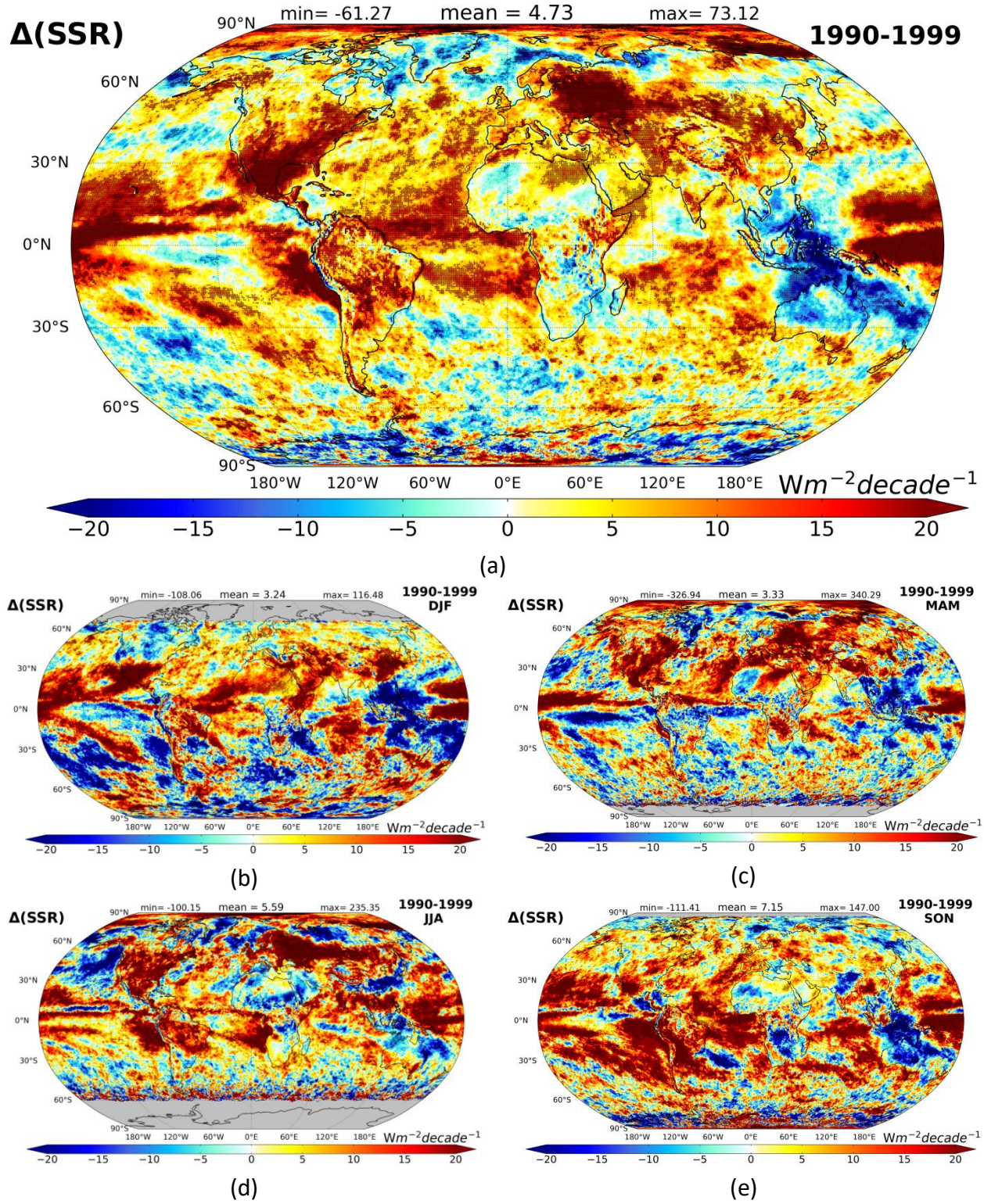


Figure 3.9. Global distribution of changes of FORTH-RTM GDB, namely changes of deseasonalized SSR anomalies, over the 10-year period 01/1990–12/1999 for annual basis (a), DJF (b), MAM (c), JJA (d) and SON (d). Areas shaded with reddish/bluish colors are those with positive/negative trends (brightening/dimming). Areas (pixels) with statistically significant trends are indicated by black dots.

3.3.4 The GDB during 2000-2010

The global distribution of GDB during 2000–2009, as shown in Figure 3.10, provides insights into the presence, magnitude, and statistical significance of SSR trends. Both solar dimming (decreasing SSR, represented by bluish colors) and solar brightening (increasing SSR, depicted in yellowish and reddish colors) are statistically significant at the 95% confidence level across a portion of the globe (15% of the total number of pixels). The computed spatially averaged GDB is 1.83 $Wm^{-2}decade^{-1}$ for the globe, 2.4 $Wm^{-2}decade^{-1}$ for the NH, and 1.29 $Wm^{-2}decade^{-1}$ for the SH, indicating a global brightening trend during the 2000s. Over land, brightening is observed at 1.03 $Wm^{-2}decade^{-1}$, while over oceans, brightening is stronger, reaching 2.16 $Wm^{-2}decade^{-1}$. Overall, 59% of the grid cells exhibit brightening, compared to 41% showing dimming, leading to an overall global brightening. Strong and statistically significant brightening trends are particularly evident over the Indian Ocean, Argentina, South Africa, Australia, Antarctica, and several tropical and subtropical oceanic regions, whereas dimming is more pronounced over parts of the Sahara, the Arabian Peninsula, India, the eastern Arctic, and portions of the Southern Ocean. Europe and North America do not exhibit significant trends, with dimming and brightening occurring in neighboring areas. Among statistically significant trends, positive tendencies account for 67% of affected grid cells, while negative tendencies make up 33%. Seasonal variations in GDB trends at the regional level are further highlighted by the FORTH-RTM GDB dataset, derived on a seasonal basis (Figure 3.10b,c,d,e). For instance, the annual brightening observed over the Indian Ocean (Figure 3.10) is driven by substantial increases in SSR across all seasons, with the strongest brightening occurring in boreal autumn. Conversely, the annual dimming over India and the Arabian Peninsula is mainly attributed to reductions in SSR during boreal winter and summer, respectively. Brightening over Argentina is more pronounced in boreal spring and autumn, whereas dimming over the eastern Arctic is stronger in boreal spring and summer. Additionally, the annual brightening over Australia is primarily driven by strong brightening trends occurring in boreal winter. Finally, on a global scale, seasonal variations in GDB reveal the strongest brightening trend in boreal summer, with an increase of 2.29 $Wm^{-2}decade^{-1}$.

3.3.5 The GDB during 2010-2018

Figure 3.11 illustrates the global distribution of GDB from 2010 to 2018, revealing key patterns in the magnitude and statistical significance of SSR trends. Both solar dimming (a decrease in SSR, shown in bluish colors) and solar brightening (an increase in SSR, represented by yellowish and reddish colors) are statistically significant at the 95% confidence level, covering 18% of the total number of pixels worldwide. The computed spatially averaged GDB is 1.32 $Wm^{-2}decade^{-1}$ for the globe, 2.42 $Wm^{-2}decade^{-1}$ for the NH, and 0.19 $Wm^{-2}decade^{-1}$ for the SH, indicating a global brightening trend during the 2010s. Over land, brightening is observed at 5.51 $Wm^{-2}decade^{-1}$, whereas over oceans, a dimming trend of -0.37 $Wm^{-2}decade^{-1}$ is detected. Overall, 56% of the grid cells exhibit brightening, compared to 44% showing dimming, leading to a net global brightening. Strong and statistically significant brightening trends are particularly evident over Europe, Australia, the Tibetan Plateau, East Asia, Indonesia, South Africa, Antarctica, and certain oceanic regions, while dimming dominates over parts of the western Arctic and large portions of the oceans. Seasonal variations in GDB trends at the regional level are further highlighted

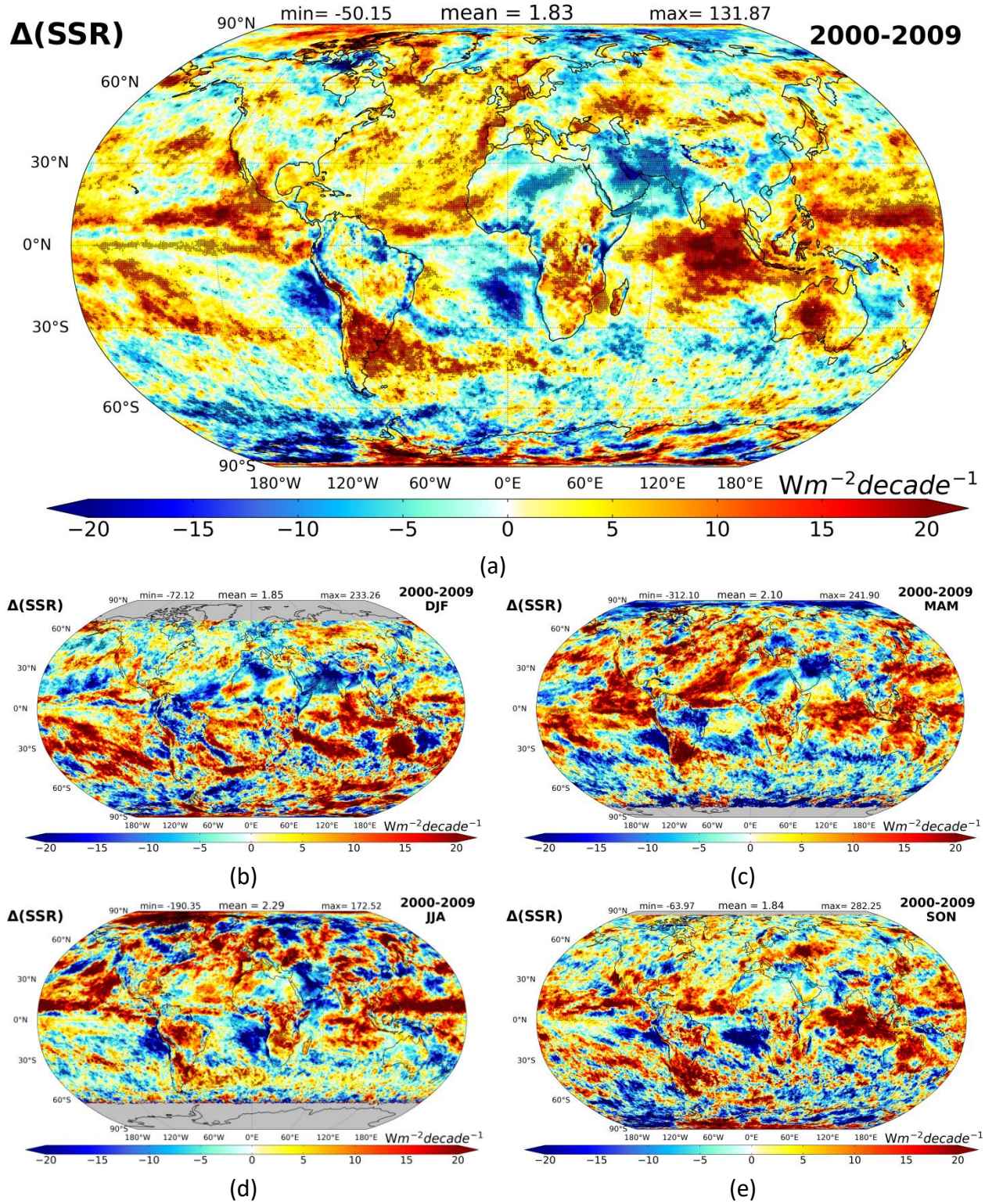


Figure 3.10. Global distribution of changes of FORTH-RTM GDB, namely changes of deseasonalized SSR anomalies, over the 10-year period 01/2000 – 12/2009 for annual basis (a), DJF (b), MAM (c), JJA (d) and SON (d). Areas shaded with reddish/bluish colors are those with positive/negative trends (brightening/dimming). Areas (pixels) with statistically significant trends are indicated by black dots.

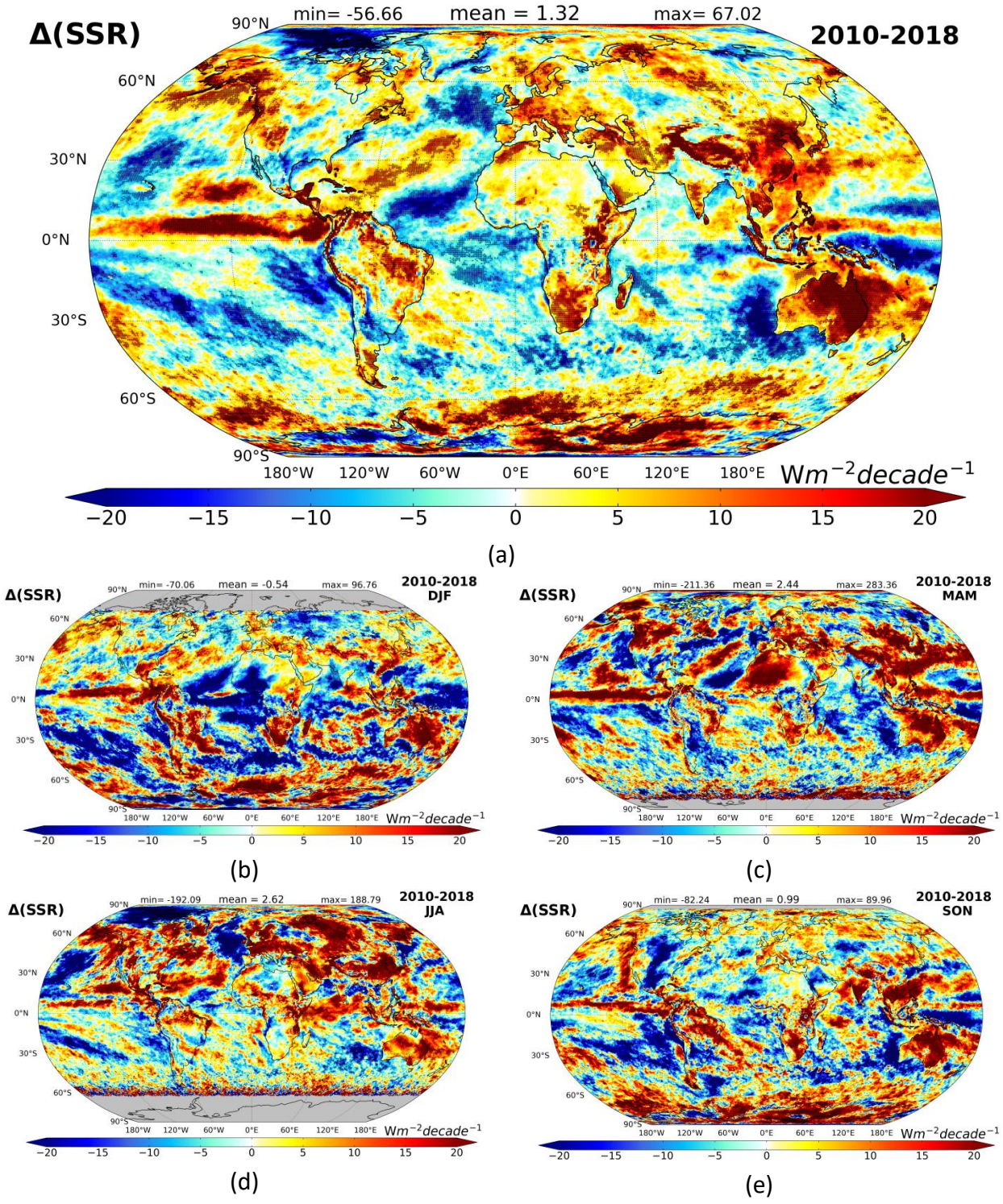


Figure 3.11. Global distribution of changes of FORTH-RTM GDB, namely changes of deseasonalized SSR anomalies, over the 9-year period 01/2010–12/2018 for annual basis (a), DJF (b), MAM (c), JJA (d) and SON (d). Areas shaded with reddish/bluish colors are those with positive/negative trends (brightening/dimming). Areas (pixels) with statistically significant trends are indicated by black dots.

by the FORTH-RTM GDB dataset, derived on a seasonal basis (Figure 3.11b,c,d,e). For instance, the annual brightening observed over Europe is primarily driven by substantial increases in SSR during boreal spring and summer. Conversely, the annual dimming over the tropical Atlantic Ocean is mainly attributed to reductions in SSR during boreal winter and spring, while dimming over the western Arctic is most pronounced in boreal summer. Similarly, the mid-latitude Atlantic Ocean experiences stronger dimming during boreal summer. A systematic brightening trend persists throughout the year across East Asia, with the most intense increases occurring in boreal spring and summer. Additionally, the annual brightening over Australia is the result of a consistent increase in SSR across all months of the year. Finally, on a global scale, seasonal variations in GDB reveal the strongest brightening trend in boreal summer, with an increase of 2.62 $Wm^{-2}decade^{-1}$, while boreal winter is the only season showing a net dimming trend, computed at -0.54 $Wm^{-2}decade^{-1}$.

The analysis of GDB from 1984 to 2018 reveals that global brightening has been the prevailing trend, with stronger increases in SSR over land than over oceans and more pronounced brightening in the Northern Hemisphere. The results indicate that 63% of the analyzed grid cells experienced brightening, while 37% showed dimming, leading to an overall net increase in SSR over the last four decades. This trend is particularly evident in regions such as Europe, the Americas, the Tibetan Plateau, and parts of the Southern Hemisphere, including Australia and Antarctica. Conversely, persistent dimming has been detected over areas such as parts of China, India, the Arabian Peninsula, the Arctic, and the marine stratocumulus regions of the subtropical oceans. The study also highlights the strong seasonal dependence of GDB trends. For instance, brightening in Europe is most pronounced in spring and summer, while regions like East China and Southeast Asia experience substantial dimming during specific months of the year. Such seasonal fluctuations underscore the complex interplay between cloud cover, aerosol loading, and large-scale atmospheric circulation patterns that modulate SSR trends at different timescales. A key finding of this analysis is the impact of dataset improvements on SSR trend estimations. Compared to previous studies, the use of the CLARISC dataset has led to notable differences in trend magnitudes and even trend reversals in some regions, such as Australia and parts of South Africa. This underscores the importance of high-quality, updated input data when assessing long-term radiative flux changes. Overall, these results reinforce the conclusion that the Earth's surface has experienced a net increase in solar radiation over the past four decades, with strong regional and seasonal variations. Given the implications of SSR trends for climate modeling, agriculture, and renewable energy development, continued efforts to refine observational datasets and improve radiative transfer modeling are essential for accurately capturing future changes in Earth's energy balance. The causes of the estimated GDB will be in detail analyzed in the Chapter 5 where a sensitivity analysis was performed along with the analysis of the trends of SSR and the GDB drivers annually and on seasonal basis.

3.4 The FMI-based Global Dimming and Brightening

Given the better performance of FMC than FMI for SSR and GDB, the FMC-RTM is used for the main analysis of this PhD. However, a brief overview of the SSR and GDB derived from FMI is also provided

here for comparison and completeness. The global distribution of the FMI-RTM GDB, or Δ(SSR), during the 35-year period from 1984 to 2018, is shown in Figure 3.12. The calculated Δ(SSR) values came from applying linear regression to the time series of deseasonalized monthly FORTH-RTM SSR anomalies for each pixel and computing the Sen's slope. The same figure also contains information about the statistically significant GDB (dotted pixels). Over southern and eastern Europe, the Middle East, Central African Republic, western North Africa, Mexico and the southern USA, several areas of the Tropical and sub-tropical oceans, as well as Brazil and Argentina, strong and statistically significant brightening (up to 100.49 Wm^{-2} or 2.87 $Wm^{-2}year^{-1}$) is observed, according to FORTH-RTM. On the other hand, strong and statistically significant dimming, as large as –46.2 Wm^{-2} or -1.32 $Wm^{-2}year^{-1}$, is observed across the western Tropical Pacific, India, Mainland Southeast Asia, East China, Indonesia, Guinea Gulf and offshore SW Africa, western Australia, Siberia, northern South America and several remote oceanic regions, including the Southern and Arctic Ocean. Over many regions including large parts of North America, central Europe, Russia, eastern Australia, and the Eastern Sahara, no statistically significant trends were computed. In nearby regions over extended world areas including Africa, North and South America, Australia, the eastern Tropical Pacific, and the Eastern Mediterranean, SSR trends are opposite. Dimming is found in 53.7% of pixels, against 46.3% showing brightening, leading to an overall global dimming equivalent to 2.2 Wm^{-2}. In 50% of pixels globally, the SSR changes are statistically significant, according to our findings. In those cells with statistically significant GDB, solar dimming dominates even more, occurring in 63% of them. While brightening somewhat predominates over land (brightening/dimming occurring in 54.7%/45.3% of pixels), a dimming is observed over oceans (brightening/dimming in 42.1%/57.9% of pixels) explaining the overall global dimming.

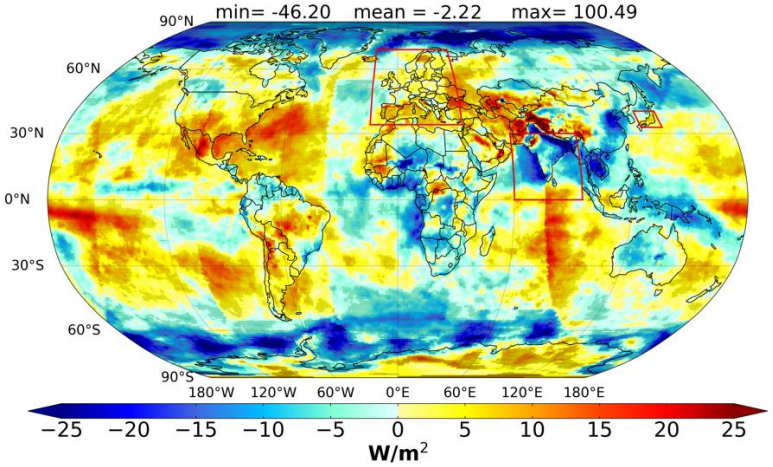


Figure 3.12. Global distribution of changes of FORTH-RTM GDB, namely changes of deseasonalized SSR anomalies, over the 35-year period 01/1984 – 12/2018. Areas shaded with reddish/bluish colors are those with positive/negative trends (brightening/dimming). Areas (pixels) with statistically significant trends are indicated by black dots. World land areas (Europe, India and Japan) enclosed by red rectangles are characterized by homogeneous SSR trends (reference is made to them in Figure 3.14).

Seasonal change of GDB features on a regional level is revealed by additional information about the FORTH-RTM GDB derived on a seasonal basis (Figure AB6). For instance, the annual brightening seen over Europe (Figure 3.12) is driven by substantial brightening in boreal spring, namely the months of March, April, May, and in boreal summer (June, July, August) while dimming is observed therein during autumn (September, October, November) and winter (December, January, February). Besides, the annual dimming over Siberia arises mainly from dimming in boreal summer months, while the dimming over

Australia is stronger in boreal winter and over Northern S. America in boreal spring. A stronger dimming is seen in the months of June through November over East China and December through March over SE Asia, causing the respective annual mean dimming patterns. A systematic dimming is seen throughout the year across the Southern Ocean, being stronger in boreal winter and spring months, the Pacific Tropical Warm Pool, and India, culminating in an annual dimming over these regions. Additionally, the annual dimming over the Sahara (Figure 3.12) results from a dimming that occurs mainly during boreal summer and secondarily boreal autumn. The identified SSR changes are attributed to the changes in the model input data that are relevant for SSR, namely cloud cover, cloud optical thickness, aerosol optical depth and water vapor. The global distribution of these changes during the study period (1984-2018) are shown in Figure AB7. According to them, it seems that the decreasing SSR trends over India, Guinea Gulf, Indonesia, N. South America and East Asia, are caused by the statistically significant increasing trends of AOD, cloud optical thickness and water vapor (cloud cover showing either decreasing or weak increasing trends over these regions). On the other hand, the brightening over Europe arises from the decreasing AOD and cloud cover whereas cloud optical thickness and water vapor show increasing trends. Moreover, the solar dimming observed over Australia is found to arise from increasing trends of water vapor and cloud cover. These findings indicate that the main causes of GDB are different from a world region to another, which underlines the complexity of the phenomenon. It is noticeable that some similar patterns of brightening (over Europe, Mexico, Central Africa and parts of tropical oceanic regions) and dimming (over India, Australia, Northern South America, Guinea Gulf and Indonesia) were revealed by the work of (Stamatis et al., 2022) during almost the same time period of 1980-2019 and using the MERRA-2 SSR product. It should be mentioned that the artificial patterns of GDB that can been observed in Figure 3.12 are introduced by the artifacts on ISCCP-H cloud data, which are linked with changes in satellite viewing geometries (Campbell 2004; Evan et al., 2007; Norris 2000; Norris and Evan 2005). More specifically, there are relevant patterns centered in the Atlantic, Indian, Western Pacific and Eastern Pacific Oceans which correspond to the geostationary "footprints" that describe the area observed by each satellite. At the edge of these footprints the satellite zenith angle is much higher, corresponding to a longer path length through the atmosphere that light must travel before it is detected by the sensor. For instance, the pattern over the Indian Ocean is connected to the area where geostationary data was not available until 1997, and AVHRR polar orbiting satellite data was used instead (Evan et al., 2007), while the pattern in the Atlantic Ocean is linked to the actual coverage from the geostationary satellite METEOSAT (Karlsson et al., 2018). However, these artificial patterns occur mostly over ocean areas, and thus could not be validated against ground truth measurements. Yet, on the contrary, they are absent over land areas, thus providing confidence about the reliability of the FORTH-RTM GDB at least in qualitative terms, as demonstrated by the evaluation performed in the previous section.

The time series of the calculated average deseasonalized SSR anomalies for the Globe, the northern hemisphere (NH), and the southern hemisphere (SH) over the 35-year period from January 1984 to December 2018 is shown in Figure 3.13, providing an easy assessment of the interdecadal patterns of global and hemispherical GDB. The FORTH-RTM global mean SSR anomalies vary up to 16.86 Wm^{-2} (from -7.33 to 9.53 Wm^{-2}), while the northern/southern hemispherical SSR anomalies range from -10.23/-9.36 to 7.49/16.46 Wm^{-2}, respectively. The applied 4th-order polynomial fit to the global 35-year time series indicates that between 1984 and 1989 a decreasing SSR tendency occurred over the Globe, which reversed to a brightening in the 1990s and till 2000. Subsequently, a dimming took place in the first decade

of 21st century, followed by a brightening in the last decade, i.e., in the 2010s. This results in an overall negative trend (dimming) during the entire 1984–2018 period, either globally or in both hemispheres. Note that globally, according to the Figure AB8, which shows the interannual and interdecadal variability of mean annual SSR fluxes and 4 basic model input data, the solar dimming during 1984-1989 is primarily due to increasing cloud optical thickness, while the brightening in the 1990s is attributed to decreasing cloud optical thickness, cloud cover and AOD. Also, it is found that the global dimming during 2000-2009 is caused mainly by the increasing cloud optical thickness and AOD, while the brightening in the 2010sisattributedto cloud cover, optical thickness and AOD. These results highlight that the GDB is not only driven by different factors over different world areas, but that even for a given area the factors can be different from a decade to another, thus further perplexing the phenomenon. Remarkably, at least globally, cloud optical thickness overall clearly dominates the SSR variations (except for the Pinatubo signal at the beginning of the 1990s), both in terms of inter annual variations (e.g. strong peak in 1994 explained by cloud optical depth low peak) as well as the longer term variations (polynomials of SSR and cloud optical thickness fit very well), and even in the overall trend. Between 1984 and 1995, the SH (red line in Figure 3.13) experienced stronger positive anomalies than the NH (green line), whereas afterwards the SH experienced larger positive anomalies than the NH until 2018 (the opposite inter-hemispherical predominance exists for the negative SSR anomalies). Strong SSR decreases brought on by the large volcanic eruption of Pinatubo (1991), as well as by strong El-Nino phases (1997, 2002, 2009 or 2016), are reproduced by FORTH-RTM. Years that were affected by the recovery from Pinatubo as well as La-Nina phases (1989, 1999, or 2006) are distinguished by positive anomalies. These results demonstrate that the FORTH-RTM satisfactorily reproduces natural processes that affect Earth's radiation budget and climate, such as volcanic eruptions and the ENSO (El Nino Southern Oscillation). Note, that a similar analysis to that shown in Figure 3.13 was done by (Stamatis et al., 2022) using the MERRA-2 SSR, which did not reveal the brightening phases neither in the 1990s nor in the 2010s, although both MERRA-2 SSR and FORTH-RTM SSR are computed with the same aerosol information. This underlines how the different cloud data (ISCCP-H observations vs MERRA-2 calculated clouds) impact the estimated GDB.

The FORTH-RTM has the advantage of covering a quite long 35-year (climatological) time period that includes the strong anthropogenic global warming (starting from the ‘80s). There have been theories and studies on how GDB interacts with the current rapid global warming, either accelerating or counteracting it (Philipona et al., 2009; Wild et al., 2007; Wild 2009; Ramanathan et al., 2007; Ruckstuhl et al., 2008), most of which are based on surface station data of SSR. Hence, the FORTH-RTM based determination of GDB at vast geographical (global) and temporal (35-year) scales allows for a better assessment and comprehension of the contribution of GDB to the global warming, in connection to the dominant role of anthropogenic greenhouse gases. To do this, the four sub-periods which were previously defined were selected as characterized by different phases of GDB. The results computed on a worldwide and hemispherical scale, as well as separately for land and ocean areas, are shown in Table 3.1. According

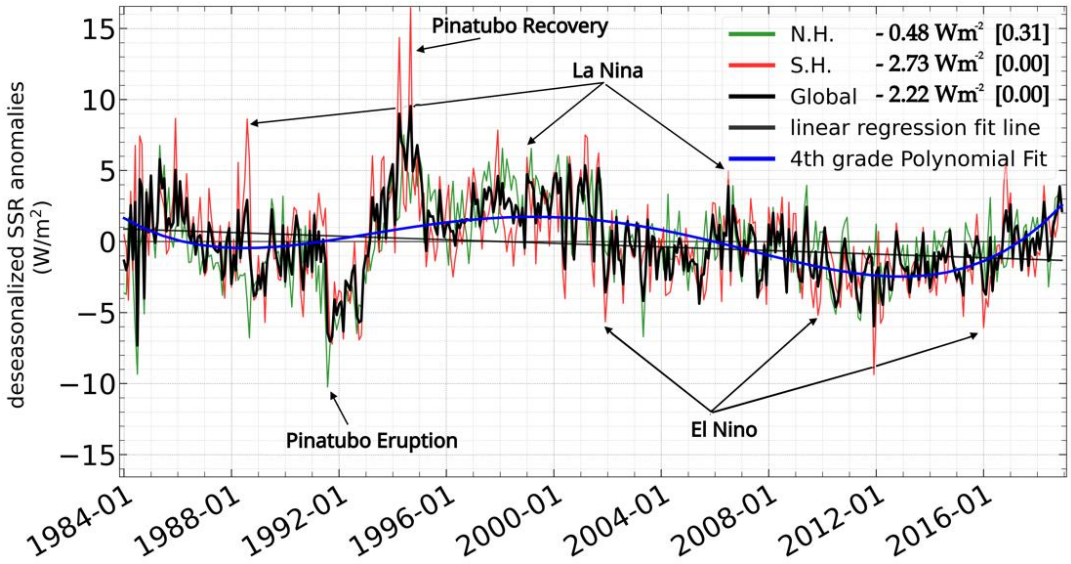


Figure 3.13. Timeseries of FORTH-RTM average global (black line) and hemispherical (NH and SH, green and red lines) monthly mean deseasonalized SSR anomalies for the period January 1984–December 2018. Linear regression fit line, along with associated Δ(SSR), the p-value inside the brackets and the 4th-order polynomial fit applied to the global time series of FORTH-RTM SSR are also shown.

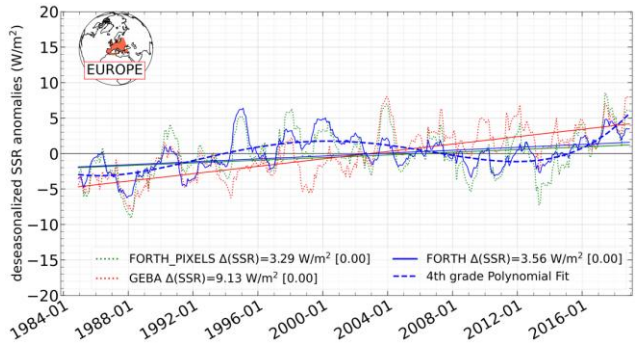
to the FORTH-RTM, the overall Δ(SSR) during the period 1984–2018 is equal to -2.22 Wm^{-2} or -0.063 $Wm^{-2}year^{-1}$ on a global scale (dimming), with dimming being detected in both hemispheres (-0.48 and -2.73 Wm^{-2} or 0.014 $Wm^{-2}year^{-1}$ and -0.078 $Wm^{-2}year^{-1}$, being stronger over SH. Note that the aforementioned Δ(SSR) changes are all statistically significant at 95% confidence level (CL). Oceans show a stronger dimming (-2.56 Wm^{-2} or -0.073 $Wm^{-2}year^{-1}$,statistically significant at 95% CL) than land (-1.04 Wm^{-2} or 0.03 $Wm^{-2}year^{-1}$, not statistically significant), which is consistent with the stronger global warming (+0.32 °C $decade^{-1}$ and +0.14 °C $decade^{-1}$, (NOAA National Centers for Environmental Information, Climate at a Glance: Global Mapping. Available online: https://www.ncei.noaa.gov/access/monitoring/climate-at-a-glance/global/mapping (accessed on 2 August 2023))) recorded over land than oceans. The two hemispherical land and oceanic regions, and thus the two hemispheres and the globe, have the same sign of GDB for each time sub-period. Specifically, over the globe, the two hemispheres, and the NH and SH land and ocean areas, solar dimming occurred between 1984 and 1989, followed by a stronger brightening between 1990 and 1999, which is consistent with the accelerated greenhouse global warming after 1980 (Masson-Delmotte et al., 2021; Gulev et al., 2021). Then, during the first decade of 21st century, a decreasing SSR trend (dimming) took place over the globe, the two hemispheres, and the land and ocean areas of both NH and SH, which is in line with the hiatus of the global warming during this decade (Gulev et al., 2021; Easterling et al., 2009; Foster et al., 2011). Then the tendency shifted into an increasing SSR trend (brightening) between 2010 and 2018, which is compatible with the recent acceleration of global warming (Gulev et al., 2021, Morice et al., 2021).

Table 3.1. Changes of FORTH-RTM deseasonalized SSR anomalies (Δ(SSR)), i.e., GDB, computed at global and hemispherical scales, as well as for land and ocean areas. Results are given for the entire 35-year period (1984–2018) as well as for four separate sub-periods. Red and blue vectors indicate solar brightening and dimming, respectively, while numbers in bold indicate trends that are statistically significant at 95% CL.

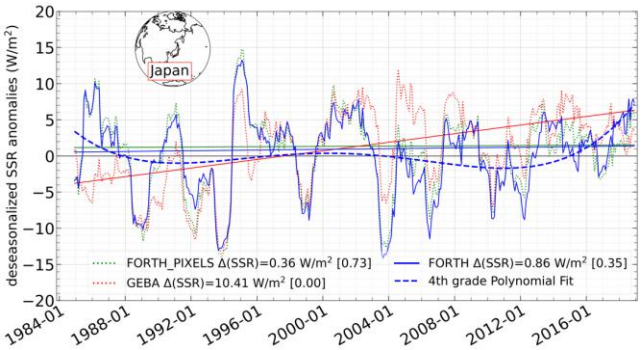
FORTH	1984-2018	1984-1989	1990-1999	2000-2009	2010-2018
GLOBAL	-2.22 ↘	-3.53 ↘	5.52 ↗	-2.57 ↘	3.26 ↗
N.H.	-0.48 ↘	-2.84 ↘	7.58 ↗	-2.71 ↘	3.43 ↗
S.H.	-2.73 ↘	-3.60 ↘	3.59 ↗	-2.46 ↘	2.70 ↗
LAND	-1.04 ↘	-3.56 ↘	5.47 ↗	-3.47 ↘	2.56 ↗
LAND N.H.	-0.41 ↘	-2.87 ↘	6.70 ↗	-3.48 ↘	1.51 ↗
LAND S.H.	-1.37 ↘	-2.11 ↘	2.76 ↗	-1.64 ↘	3.74 ↗
OCEAN	-2.56 ↘	-3.43 ↘	5.38 ↗	-2.56 ↘	3.41 ↗
OCEAN N.H.	-0.46 ↘	-2.11 ↘	8.07 ↗	-2.45 ↘	4.17 ↗
OCEAN S.H.	-2.83 ↘	-3.80 ↘	4.12 ↗	-2.60 ↘	2.42 ↗

Given that GDB is a regional phenomenon (Figure 3.12), a regional study was carried out to identify decadal scale GDB features. To achieve this, three distinct regions of the globe were chosen, (Europe's, Japan's and India's land areas, shown within the rectangles in Figure 3.12), each of which has adequate station coverage and displays homogeneous GDB patterns (Figure 3.12). For each selected area, three time series of deseasonalized SSR anomalies (for the period January 1984–December 2018) were created, one for the region's GEBA stations (122 sites in Europe, 18 in Japan, and 7 in India) that meet the slope estimation criterion as stated in Section 2.2, a second time series for the corresponding FORTH-RTM pixels including the GEBA stations and a third for all of the FORTH-RTM pixels within the geographical limits of the region. The time series are provided in Figure 3.14 together with their applied linear regression, while the polynomial 4-th order fit applied to the third (all model pixels) time series is also plotted. This analysis enables us to assess the ability of the FORTH-RTM GDB to reproduce the GDB measured at the sites of GEBA stations within each region. In general, it is revealed that FORTH-RTM satisfactorily represents the month-to-month and year-to-year variability of SSR (correlation coefficients equal to 0.61, 0.70, and 0.59, respectively, for Europe, Japan, and India). For India we compute a strong dimming for the GEBA measurements (−32.15 Wm^{-2}) against a smaller dimming for the corresponding model pixels (−9.58 Wm^{-2}) and for the total land of India (dimming equal to −6.72 Wm^{-2}). This much stronger dimming for GEBA is associated with the much larger/lower GEBA than model positive/negative anomalies before/after 1994/2010. In contrast, over Japan a brightening equal to 10.41 Wm^{-2} occurred according to GEBA station measurements, stronger than a marginal brightening of 0.36 for the FORTH-RTM pixels and 0.86 for the total land of Japan. Regarding the European land areas, a brightening during the entire time period is computed, which is stronger for GEBA stations (9.13 Wm^{-2}) than the corresponding FORTH-RTM land pixels (3.29 Wm^{-2}) and all Europe's land pixels (3.56 Wm^{-2}). Over Europe, the brightening in the 1990s is followed by a dimming in the 2000s and then by a brightening again after 2010. It should be noted that the dimming of 2000s and the consequent brightening is also found over Japan and Indian subcontinent. Our findings demonstrate the FORTH-RTM's capacity to qualitatively represent the GDB (dimming or brightening) observed at GEBA stations over the continental regions of Europe, Japan, and India. The obtained results of Figure 3.14 show that, in line with other studies (Wild 2009 and references therein), there was a brightening over Europe (land) from 1984 to 2000. According to our results, this brightening reversed to a weak dimming after 2000, that is relatively similar to the

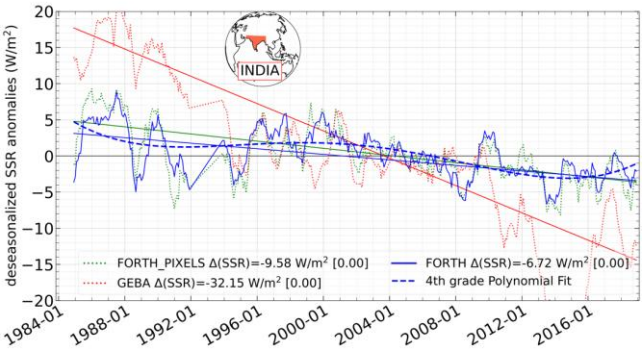
tendency of SSR stabilization since the early 21st century suggested by (Sanchez-Lorenzo et al., 2015). Agreement is also found with the limited available literature for India, according to which (Padma Kumari et al., 2010) a dimming was observed over India during 1981-2004, based on 12 ground-based stations while the study by (Soni et al., 2016) also based on 12 ground based Indian stations, estimated a level-off of the dimming in the late 2000s over most stations. On the other hand, according to (Tanaka et al., 2016), who used 14 ground-based meteorological Japanese stations, there has been a dimming during the 1980s which reversed to brightening phase in the 1990s in line with our results.



(a)



(b)



(c)

Figure 3.14. Timeseries (01/1984 - 12/2018) of deseasonalized SSR anomalies for three selected world areas with homogeneous trends (see red rectangles in Figure 3.12), namely, Europe (i), Japan (ii) and India (iii). For every area, results are given based on GEBA stations (red dotted lines), the corresponding FORTH-RTM pixels (including the stations, green dotted lines) and all the FORTH-RTM pixels of the areas (blue lines). Moreover, the linearly fitted lines to each time series are also displayed with similar colors, while blue dashed line displaying the 4th-order polynomial fit applied to the time series of FORTH-RTM SSR for the entire world areas are also shown. The SSR changes along with their p-values inside the brackets are also shown.

Chapter 4. FORTH-RTM SSR and GDB evaluations and inter-comparisons

4.1 Introduction

This study extends previous research by taking a significant step forward in improving our understanding of the ongoing GDB and its climatic role. Here, for the first time, the GDB was assessed on a global scale over a long climatological period (1984–2018), including recent years that have not yet been covered in the literature. The analysis is conducted using the FORTH-RTM as described in Section 2.2, which has been employed in previous studies (Hatzianastassiou et al., 2005, 2012, 2020). To ensure the reliability of the GDB estimates over the 35-year period, a detailed evaluation of the RTM-derived monthly SSR and its long-term changes (or GDB) through comparisons with ground-based observations from the reference GEBA and BSRN networks was performed. Deseasonalized anomalies are used for evaluation at multiple spatial scales, ranging from local (station level) to global/hemispheric, and for different temporal ranges, from the full 35-year period to selected sub-periods. It is important to note that two versions of the FORTH-RTM SSR dataset are analyzed in this study. It should be noted that 2 versions of the FORTH-RTM were evaluated in this PhD and are presented in this chapter. The initial FORTH-RTM version, i.e. FMI, utilized state-of-the-art cloud (ISCCP-H) and aerosol (MERRA-2) input data and its evaluation is presented in Section 4.2. However, even though there is reasonable agreement of the FMI results with ground-truth measurements, inconsistencies in cloud amount and cloud optical thickness trends affected the computed SSR trends, raising concerns about their reliability and the further usage of this dataset to investigate the causes of GDB and the links with global warming. To mitigate these inconsistencies, a new cloud database was developed by integrating ISCCP-H and CLARA-A2 products, as described in Section 2.1.3.2. This approach eliminated artificial patterns in cloud and SSR trends, leading to the creation of an improved RTM version, FMC, which incorporated clouds from the new CLARISC database. The evaluation results of FMC are presented in Section 4.3. After demonstrating the superior performance of FMC compared to FMI and other several independent datasets as it is described in Section 4.4, the FMC version was used for the remainder of this PhD study.

4.2 FMI evaluation

4.2.1 Evaluation of FMI SSR

Foremost, a thorough evaluation of FORTH-RTM SSR is done in this section, which is a requirement for the FORTH-RTM GDB evaluation. The evaluation is conducted either for all stations (Section 4.2.1.1) or on an individual station level (Section 4.2.1.2). The long-term (1984-2018) average of the FORTH-RTM SSR is shown in Figure 4.1, along with the corresponding long-term average SSR of GEBA and BSRN stations. The results reveal a generally nice agreement between the model and the ground truth SSR data.

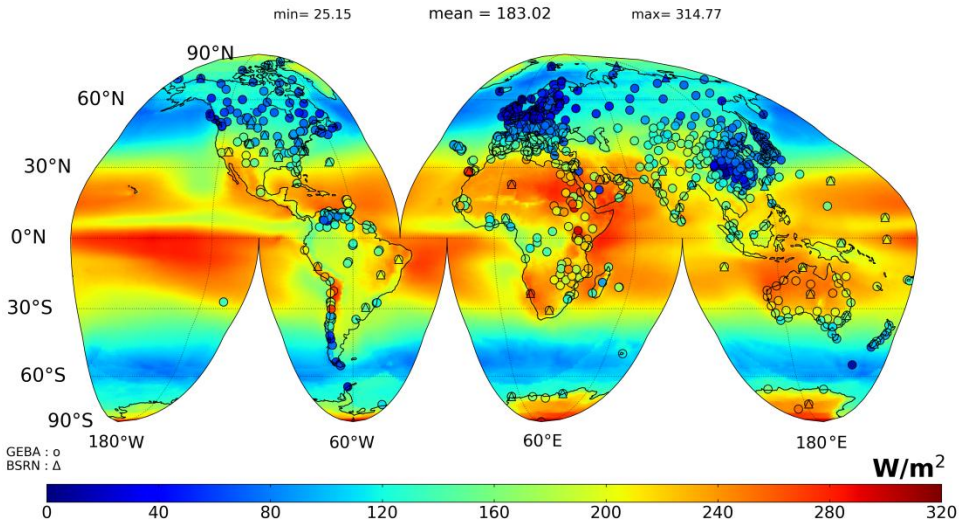


Figure 4.1. Global distribution of the long-term (1984-2018) average FORTH-RTM SSR. The average SSR of the GEBA and BSRN stations, which are used to validate the RTM, is also shown.

4.2.1.1. All Stations

The statistics of the overall comparison of FORTH-RTM SSR fluxes and anomalies against 1193 GEBA and 66 BSRN measurement-based fluxes and anomalies are given in Table 4.1, while Figure 4.2 provides the corresponding scatterplot comparisons. It seems that FORTH-RTM SSR anomalies are satisfactorily correlated with GEBA and BSRN station anomalies yielding R values equal to 0.72 and 0.80, respectively (for the non-deseasonalized SSR fluxes the R values are much higher, as expected, equal to 0.96 for both GEBA and BSRN). Overall, the FORTH-RTM slightly underestimates SSR with respect to GEBA and BSRN, having negative mean biases equal to –4.71 and –14.29 Wm^{-2}, respectively, corresponding to relative biases equal to –2.9% and –7.7%. The general underestimation of FORTH-RTM SSR against GEBA/BSRN may suggest that FORTH-RTM's atmosphere is less transparent, which is consistent with other studies using the same model (Hatzianastassiou et al., 2005, 2012, 2020). This could be the result of the overestimation of ISCCP cloud cover over the regions between 40° and 60° (where the majority of GEBA and BSRN stations occur) in both hemispheres as reported by (Boudala et al., 2021). They evaluated the ISCCP-H cloud cover against satellite data Cloud-Aerosol Lidar and Infrared Pathfinder Satellite Observation Cloud Product (CALIPSO-GOCCP) for 2000-2017 and their findings for Europe are in line (in terms of ISCCP overestimation) with those by (Tzallas et al., 2019) who validated ISCCP-H cloud cover over Europe against 22 meteorological ground-based stations from the European Climate Assessment & Dataset (ECA&D) for the period 1984-2012. Moreover, it seems that the aerosol input data do not contribute to the overall underestimation of FORTH-RTM SSR, since the MERRA-2 aerosols optical depth is in generally good agreement with observations as revealed by (Che et al., 2019) who evaluated the MERRA-2 AOD against 468 AERONET stations globally for 1993-2016 and against 37 CARSNET (China Aerosol Remote Sensing Network) stations over China for 2002-2014. It should be noted that it has been reported in the literature (Wang et al., 2018) that the Chinese stations from GEBA, which count a significant number (103 stations), may not be as representative due to strong urbanization effects, so this can affect the comparison. In these stations, the FORTH-RTM overestimates the SSR by 2.66 Wm^{-2}. Thus, excluding them from the comparison led to a stronger SSR overall underestimation equal to -5.45 Wm^{-2}

(larger than the original by 15.7%). The estimated RMSE, which is equal to 21.02 Wm^{-2} for GEBA and 27.68 Wm^{-2} for BSRN (corresponding to 13.1% and 14.9% of the station networks' mean values), shows that FORTH-RTM deviates slightly more from the BSRN and less from GEBA measurements. The slope values of the scatterplot comparison are 0.94 and 0.92, respectively for GEBA and BSRN, while the corresponding values for SSR anomalies are equal to 0.68 and 0.82. It should be noted that in an assessment (Hatzianastassiou et al., 2005) of FORTH-RTM SSR, with shorter period 1984-2000, lower spatial resolution (2.5^ox2.5^o) and different input datasets (clouds from ISCCP-D2, aerosols from Global Aerosol Data Set, and meteorology from NCEP/NCAR global reanalysis data), the R values were equal to 0.99 for 700 GEBA and 22 BSRN stations, while the bias/RMSE values were equal to -6.49/23.44 Wm^{-2} for GEBA and –14/30.56 Wm^{-2} for BSRN), indicating again, similarly to the present work, that the model has larger underestimation and RMSE values against BSRN than GEBA stations. Moreover, the work by (Hatzianastassiou et al., 2012) and (Hatzianastassiou et al., 2020) used the FORTH-RTM for the period 2001-2006 and 2001-2009, respectively, with the same input data as (Hatzianastassiou et al., 2005) except for the aerosol data, which were taken from Moderate Resolution Imaging Spectroradiometer (MODIS)-Terra C005 and C006, respectively. The estimated SSR fluxes were validated against GEBA and BSRN stations and revealed similar performance to the work of (Hatzianastassiou et al., 2005) and the present study.

In addition to the FORTH-RTM SSR evaluation on an annual scale, this has also been done on a seasonal basis because this may help to more easily identify possible sources of errors. It should be noted that not only the absolute, but also the relative biases were computed, because of the significant seasonal change of SSR fluxes. Table 4.1 shows that R using SSR anomalies and relative percent bias do not show significant seasonal changes, which are as large as 0.07 and 5.9%, respectively (the variability of relative bias is much smaller for GEBA, equal to 2.4%). Contrarily, BIAS and RMSE exhibit a discernible seasonal variation, up to 5.74 and 8.48 Wm^{-2}, respectively, with maximum values in NH (North Hemisphere) summer due to the highest absolute amounts of SSR, except over the BSRN sites where the highest BIAS occurs in NH winter. The relative RMSE also shows seasonal variations (up to 6.8/11.4% for GEBA/BSRN, respectively). Given the six-month shift in extreme seasons between the two hemispheres, the seasonal variation of the three main statistical metrics, namely R, RMSE (in absolute and percentage terms), and bias (in absolute and percentage terms), were also calculated separately for the two hemispheres and is shown in Figure 4.3. Except for R, which was calculated using deseasonalized SSR anomalies, the results of this figure were derived using SSR fluxes (the corresponding R using absolute SSR fluxes is given in Figure AC2). Figure 4.3 shows that in general, the model correlates better with BSRN than GEBA, but it deviates more for BSRN than GEBA station measurements. Moreover, the statistical metrics do not exhibit a significant seasonal variation except for the absolute and relative values of BIAS and RMSE in the SH (South Hemisphere) for BSRN stations.

4.2.1.2. At Station Level

In order to examine if regional patterns exist in the metrics of the evaluation, it is necessary to study and compare the fluxes on an individual station basis as part of the evaluation of the FORTH-RTM SSR. The spatial distribution of the correlation coefficient (R) between the FORTH-RTM and GEBA/BSRN

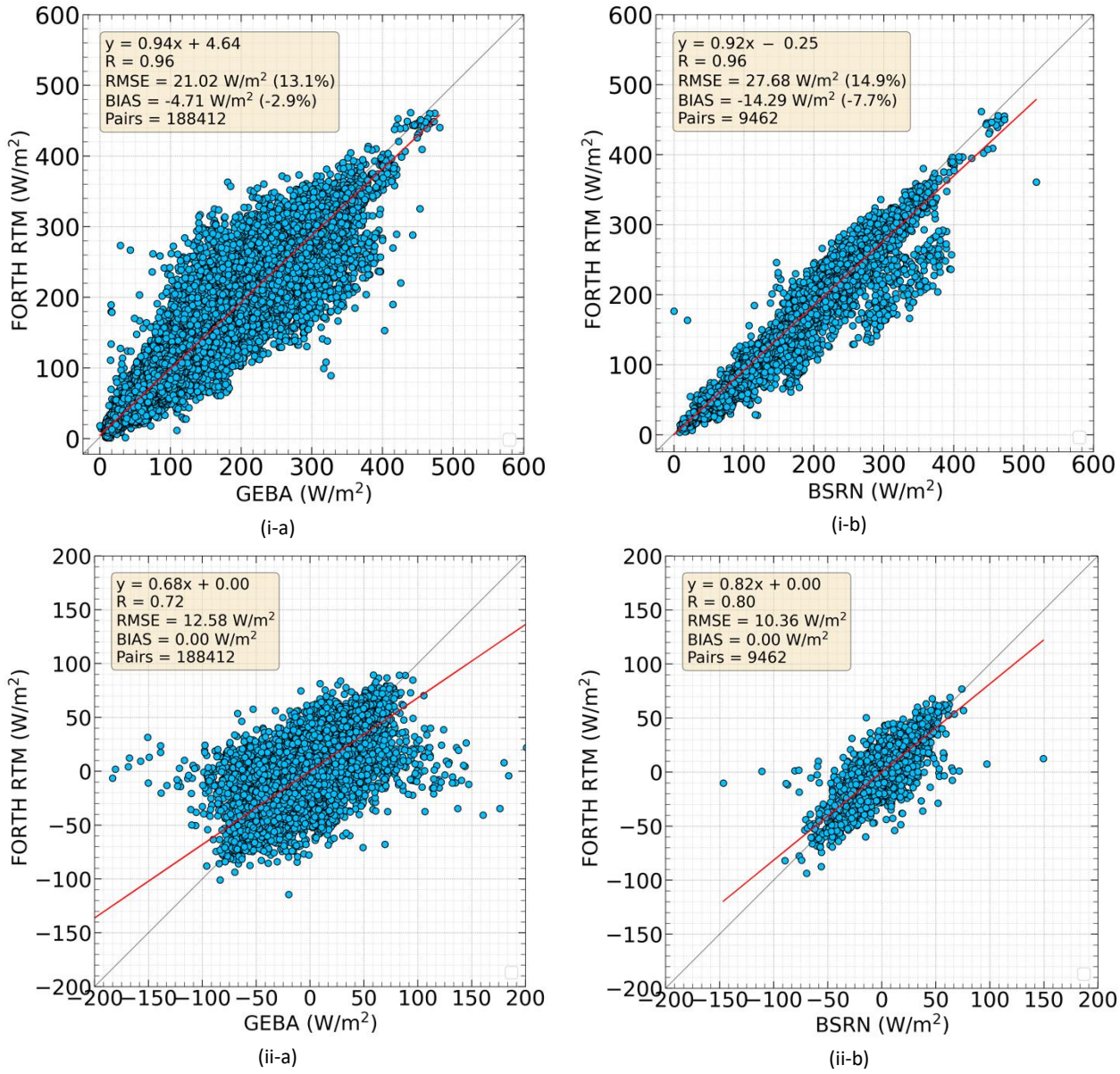


Figure 4.2. Scatterplot comparison between FORTH-RTM and GEBA (i-a), and BSRN (i-b) SSR fluxes, and between FORTH-RTM and GEBA (ii-a) and BSRN (ii-b) deseasonalized SSR anomalies. The applied linear regression fit, and the associated main statistical metrics, namely the equation of the applied linear fitting, the correlation coefficient (R), the root-mean squared error (RMSE), the bias and the total number of matched data pairs, are also shown.

stations SSR anomalies is shown in Figure 4.4, along with the distribution of the RMSE, RRMSE, bias, and relative bias computed using SSR fluxes. For the GEBA stations, R ranges from –0.27 to 0.98, while for the BSRN stations, it ranges from 0 to 0.96. For 70% of GEBA/BSRN station data the computed R values are greater than 0.62/0.67 (Figure AC3). Satisfactory R values (orange and reddish colors) can be seen throughout Europe, East Asia, North America, and Australia. On the other hand, the tropical and subtropical world areas, such as Africa, South America, India, and Indonesia, tend to have worse R values

Table 4.1. Comparison between FORTH-RTM and GEBA/BSRN SSR on an annual and seasonal basis (December-January-February, March-April-May, June-July-August and September-October-November), along with the computed main statistical parameters (number of matched data pairs, N, slope value of applied linear regression fit, absolute and percent relative biases of FORTH-RTM relative to the mean GEBA/BSRN values, root mean squared error, RMSE, percent relative RMSE (RRMSE) with respect to the mean GEBA/BSRN values, correlation coefficient, R, the mean GEBA and BSRN values and the number of available stations, id, whose SSR measurements are used in the comparison). In addition, the R and slope values computed using deseasonalized SSR anomalies are given in parentheses. The percent relative bias and RMSE values are also given in parentheses.

FORTH-GEBA	ANNUAL	DJF	MAM	JJA	SON
R	0.96 (0.72)	0.97 (0.67)	0.92 (0.74)	0.90 (0.73)	0.97 (0.71)
BIAS	-4.71 (-2.9%)	-1.52 (-1.5%)	-7.26 (-3.9%)	-7.26 (-3.3%)	-2.63 (-2.0%)
RMSE	21.02 (13.1%)	18.17 (17.9%)	22.86 (12.1%)	24.35 (11.1%)	17.77 (13.5%)
slope	0.94 (0.68)	0.96 (0.63)	0.9 (0.68)	0.89 (0.7)	0.97 (0.68)
intercept	4.64	2.1	11.34	17.43	1.3
mean_FORTH	156.24	99.92	181.07	212.57	128.95
mean_stations	160.94	101.44	188.33	219.83	131.57
N	188412	45658	47813	47539	47402
stations	1193	1177	1190	1177	1191

FORTH-BSRN	ANNUAL	DJF	MAM	JJA	SON
R	0.96 (0.80)	0.96 (0.77)	0.95 (0.81)	0.94 (0.81)	0.95 (0.82)
BIAS	-14.29 (-7.7%)	-16.65 (-11.1%)	-17.15 (-8.6%)	-12.12 (-5.2%)	-11.29 (-7.0%)
RMSE	27.68 (14.9%)	32.76 (21.8%)	26.47 (13.2%)	24.28 (10.4%)	26.72 (16.6%)
slope	0.92 (0.82)	0.87 (0.82)	0.97 (0.83)	0.9 (0.79)	0.93 (0.84)
intercept	-0.25	3.03	-11.03	11.36	0.42
mean_FORTH	171.93	133.27	183.04	220.71	149.89
mean_stations	186.22	149.92	200.2	232.82	161.19
N	9462	2275	2429	2342	2416
stations	66	59	65	63	65

(green colors and R smaller than 0.6). The same regional patterns, but with clearly higher values, appear for R computed using non-deseasonalized SSR fluxes (Figure AC4). It can be assumed that the low correlation of FORTH-RTM SSR in these regions may be caused by uncertainties in cloud cover and optical properties, as also suggested by other studies (Zhang et al., 2015, 2016, 2020), given that clouds are one of the primary factors driving the SSR (Hatzianastassiou et al., 2005). Indeed, clouds are linked to the highest level of uncertainty in climate modeling (Baker et al., 2008; Stensrud 2007), whereas the accuracy of ISCCP-H cloud cover is low over tropical and polar latitudes, as shown by (Boudala et al., 2021) who evaluated the ISCCP–H cloud cover against the CALIPSO-GOCCP (GOCCP) during 2000-2017. Apart from clouds, however, aerosols can also contribute to the poor correlation in the tropics. An indication for this could be the low R values that can be observed in regions with little cloud cover, such as the Middle East and Egypt, which have high aerosol loads (Korras-Carraca et al., 2021; Gavrouzou et al., 2021). Polar locations also exhibit weak correlation, where the disparities may be brought on by issues with ISCCP clouds (Kotarba et al., 2015) as well as snow and ice cover (Hinkelman 2019; Cullather et al., 2012). In

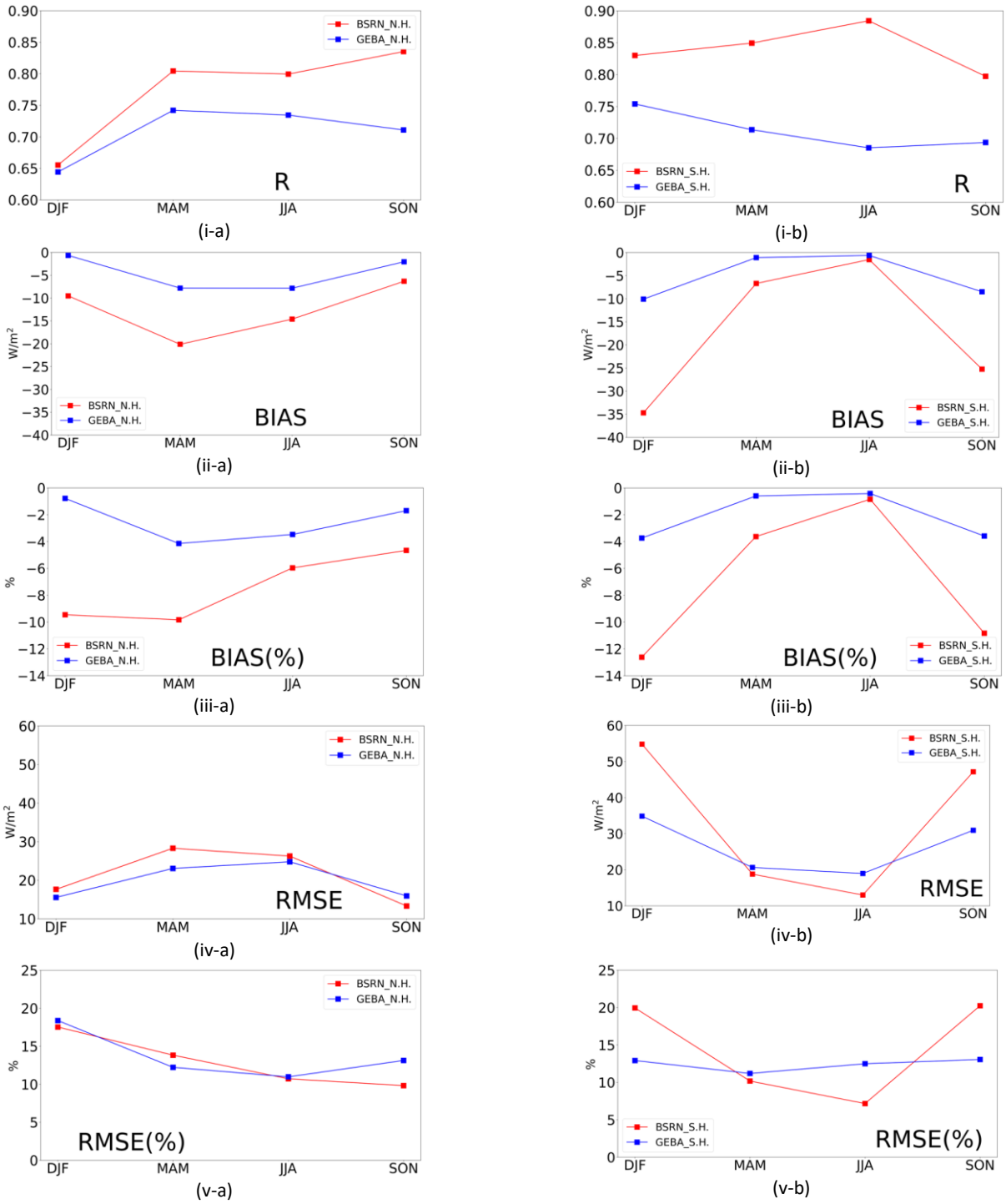


Figure 4.3. Seasonal variation of hemispherical averages of correlation coefficient R (i), bias in Wm^{-2} (ii), percent relative bias in % (iii), root mean squared error (RMSE in Wm^{-2}) (iv) and percent relative RMSE in % (v) between the FORTH-RTM and GEBA (blue) and BSRN (red) stations. Results, computed using SSR fluxes (except for R that is computed using deseasonalized SSR anomalies), are given for the North Hemisphere (a-left column) and South Hemisphere (b-right column).

addition, southern China has lower R values than northern China (Figures 4.4 and AC4). Strong air pollution, as well as uncertainty in clouds, aerosols, and their interaction, might all be responsible for this pattern, as documented in previous research (Zhang et al., 2016).

The difficulty of FORTH-RTM to accurately represent SSR in tropical and sub-tropical regions is confirmed by the large RMSE values observed in such areas than higher latitudes (Figure 4.4). Indeed, the range of RMSE values is 6.6-125 Wm^{-2} and 8.4-125 Wm^{-2}, respectively in the tropics and sub-tropics, while outside of them the corresponding ranges are 5.7-83.6 Wm^{-2}. Similar regional patterns may also be observed for the relative RMSE, with high values being most prevalent across Southern China, polar regions, and some tropical and subtropical regions. In general, the FORTH-RTM underestimates SSR with respect to GEBA, overestimating it (yellow and red colors in Figure 4.4) over several tropical and subtropical areas, according to the results for the absolute and relative bias. This overestimation over low latitudes can be attributed to the underestimation of ISCCP-H cloud amount (Boudala et al., 2021) and MERRA-2 aerosol loadings (Shi et al., 2019). Overall, the model underestimates SSR fluxes in 832 stations, while overestimating it in 361 stations, yielding an underestimation of –4.71 Wm^{-2} for SSR fluxes on average. On the other hand, there is also an overall model underestimation of SSR fluxes by –14.29 Wm^{-2} when compared to the far fewer (66) BSRN sites (12 out of 66 overestimate). Absolute and relative percent bias range from –86.12 to 122.57 Wm^{-2} and from –41 to 92.7%, respectively. Yet, absolute and relative % bias values for 70% of the GEBA stations are less than 0.22 Wm^{-2}/0.1%, respectively (Figure AC3). At the BSRN sites, the relative % and absolute bias values range from –41.4 to 20.1% and –80.98 to 34.53 Wm^{-2}, respectively, and 70% of the stations have relative and absolute bias less than –2.8%/-6.16 Wm^{-2}, respectively. It should be noted that in the low latitudes, where the FORTH-RTM tends to overestimate the SSR fluxes, there are many more GEBA than BSRN stations, which can explain the weaker underestimation against GEBA than BSRN. Also, there are many sites that have a high mean bias over China, which is greater in its southern part, due to its incorrect assessment of cloud fraction and aerosol loadings (Zhang et al. 2015, 2020; Wang et al., 2018; Xia et al., 2006; Ma et al., 2015).

4.2.2 Evaluation of FMI GDB

After the detailed assessment of the FORTH-RTM SSR fluxes, which revealed a quite good performance, the FORTH-RTM SSR inter-decadal (1984–2018) changes (or GDB) are examined here. It should be emphasized that FORTH-RTM GDB has not yet undergone this examination over such a large time period (35 years), spatial distribution (0.5°x0.625°) and use of state-of-art input data (ISCCP-H and MERRA-2). First, the GDB is evaluated either for the entire sample (all stations) or on a single station basis (Section 4.2.2.1). Thereafter, Section 4.2.2.2 assesses and discusses the gridded FORTH-RTM GDB on a global and regional mean basis. The GDB from the reference data of GEBA and BSRN stations was used to compare and evaluate the gridded FORTH-RTM GDB. By applying linear regression to the time series of monthly mean deseasonalized SSR anomalies, and then computing the slope values, the two sets of GDB, i.e., from the FORTH-RTM and the stations, were calculated. In order to ensure a high level of confidence for the results, this analysis was conducted for 222 (out of 1193) GEBA and 22 (out of 66) BSRN stations that satisfied the data availability criterion stated in Section 2.2 (more than 70% of the overall number of monthly values of the total period of each network. It should be mentioned here that the time period

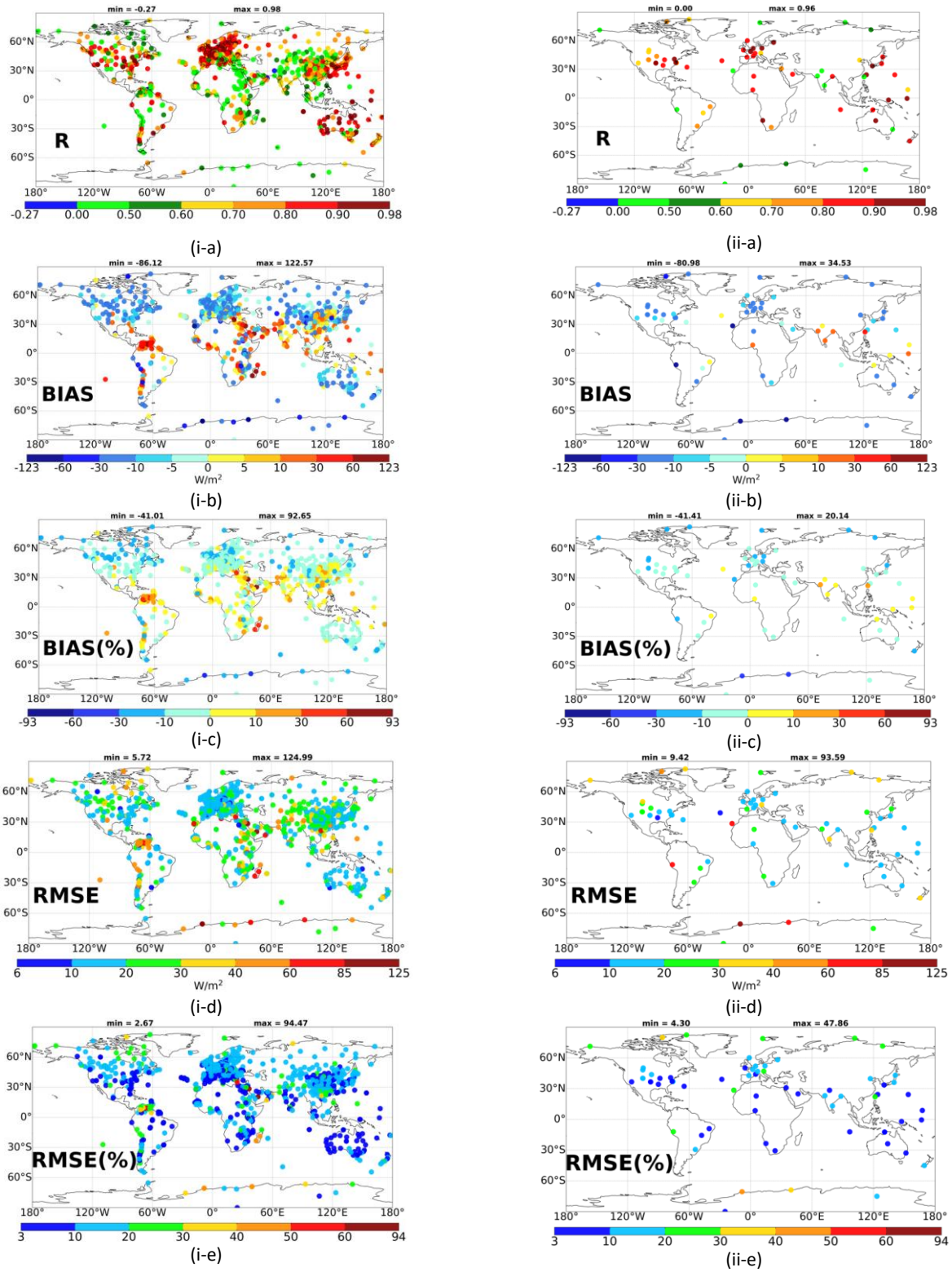


Figure 4.4. Global distribution of correlation coefficient (a), bias (b) and relative percent bias (c) root mean squared error (d), relative root mean squared error (e), computed for the comparison between FORTH-RTM and each GEBA (i, left column) and BSRN (ii, right column) station SSR fluxes, except for R that is computed using deseasonalized SSR anomalies.

varies from station to station, ranging from 25 to 35 years for GEBA stations, and 19 to 27 years for BSRN stations, depending on the original temporal coverage of each station's measurements and the applicable availability criterion (as shown in Figure AC1). Each FORTH-RTM's time period was finally adjusted to the time period of the station's available data, i.e. 1984-2018.

All Stations

The comparison of the trends of SSR anomalies (in Wm^{-2}) from the FORTH-RTM and GEBA/BSRN stations is shown in Figure 4.5 using a scatterplot. The correlation is poor, with average R values of 0.25 for GEBA and 0.32 for BSRN. Also, the slope values are low (0.11 for GEBA and 0.36 for BSRN) indicating that the model significantly underestimates the magnitude of GDB compared to stations. This is also demonstrated by the calculated biases (FORTH-RTM GDB—stations GDB), which are equivalent to –4.39/-4.59 Wm^{-2} for GEBA/BSRN. Likewise, the poor fit is revealed by the estimated RMSE values, which are equal to 11.95/7.67 Wm^{-2} for GEBA/BSRN. All these metrics prove that it is difficult for a model to reproduce the magnitude of the station GDB values. However, this is not unexpected, since there are essential differences between the two sets of compared GDB, i.e., the modeled and measured ones, the most important one being that the model GDB refers to areas of 0.5˚×0.625˚ latitude x longitude, opposite to station GDB that pertain to specific sites.

Contrary to the magnitude of GDB, it is expected that it is more feasible for a model to reproduce the sign of GDB. This performance is easily assessed by the distribution of the Figure 4.5 scatterplot points to the four quartiles, with those lying in the first and third quartiles indicating similarity of signs. There are 141 (115 in the first and 26 in the third quartiles) such data pairs for FORTH-RTM-GEBA (corresponding to 63.5% of the total number of points for the FORTH-RTM-GEBA scatterplot) and 12 (9 and 3 pairs) for FORTH-RTM-BSRN (corresponding to 54.5% of the total number of points for the FORTH-BSRN scatterplot), revealing that the FORTH-RTM reproduces partially satisfactorily the sign of stations GDB. Moreover, as to the performance of FORTH-RTM GDB, it was also assessed with respect to the altitude of stations, taking into account that the corresponding FORTH-RTM 0.5˚×0.625˚ grid cells' mean altitude might not match the altitude of high-level stations. Most of the GEBA stations have altitude differences with their corresponding cells between 0-500 m. For such stations, as it concerns GEBA the agreement in sign of the slopes is 66%, while for BSRN is 54.5% (note that all BSRN stations have altitude differences lower than 500 m). For the much fewer (6) GEBA stations that have altitude differences between 500-1000 m there is agreement in 2 out of 6 stations and for those with differences larger than 1000 m there is agreement only in 1 out of 4 stations. These findings indicate that the performance of the model decreases in the case of stations with high altitude, but this does not significantly affect the overall model performance since the number of those stations is small.

Another aspect of the GDB comparison, apart from the overall scatterplot shown in Figure 4.5, is the overall performance of the RTM GDB, namely how the modeled GDB compares to that of stations on the average, as well as how the temporally varying averaged SSR anomalies match those of stations. In this aspect, the computed 12-month moving averages of SSR anomalies of all stations and the corresponding

FORTH-RTM pixels over the total period for each network, i.e., 1984-2018 for GEBA and 1992-2018 for BSRN, are shown in Figure 4.6. Along with the 12-month moving averages, the number of stations that

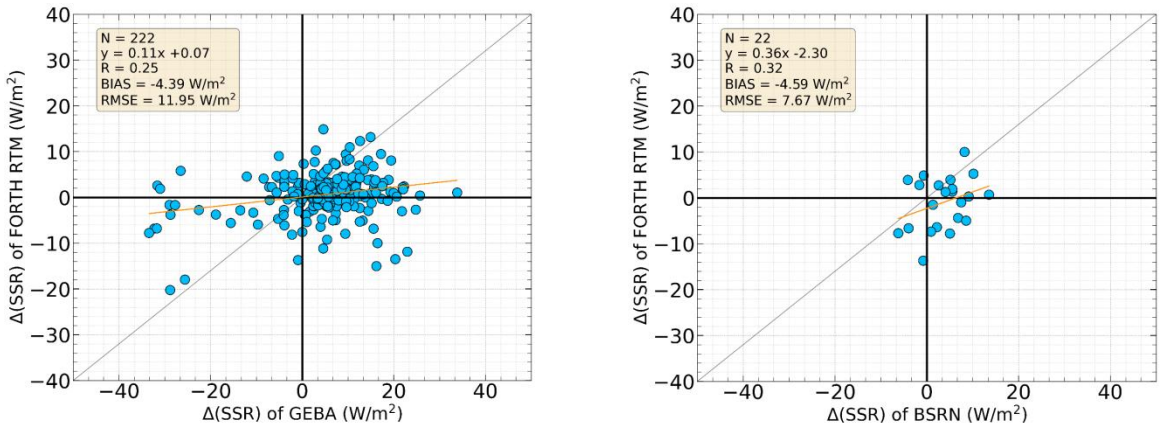


Figure 4.5. Scatterplot comparison between FORTH-RTM and GEBA (a), and FORTH-RTM and BSRN (b) Δ(SSR) or GDB (in Wm^{-2}). The linear regression fit, and the associated statistical metrics, namely the equation of the applied linear fitting, the correlation coefficient (R), the root-mean squared error (RMSE), the bias (FORTH-RTM minus stations) and the total number of matched data pairs, are also shown.

were accessible in each month/year is also shown. Since FORTH-RTM consistently shows larger/smaller positive SSR anomalies than GEBA before/after the year 2000, this results in low slope values and small average biases (FORTH-RTM—stations) equal to -0.072 and 0.064 Wm^{-2} against GEBA and BSRN stations, respectively. In association with the smaller slope values, weaker GDB is estimated by the RTM than for stations. Specifically, using the non-parametric Mann Kendall test, GEBA stations (Figure 4.6a) suggest a statistically significant brightening, or positive Δ(SSR), equal to 5.82 Wm^{-2} as opposed to a lesser not statistically significant, brightening computed using FORTH-RTM (Δ(SSR) = 0.26 Wm^{-2}). Comparable conclusions are reached from a similar analysis of FORTH-RTM and BSRN (Figure 4.6b). Indeed, a statistically significant brightening (Δ(SSR) = 5.31 Wm^{-2}) is computed compared to a small, but not statistically significant, brightening of FORTH-RTM equal to 0.17 Wm^{-2}. It is interesting to note that both GEBA and BSRN suggest a comparable brightening and that FORTH-RTM is, at least, able to reproduce the same sign of Δ(SSR) against both station networks. Here, it is also examined to what extent the number of stations, which changes with time, affects the differences between the 12-month moving average time series of stations and FORTH-RTM SSR. With respect to the GEBA stations, their number decreases after 2008, but this does not seem to have an effect on the differences. On the other hand, regarding the much fewer BSRN stations, the few available stations till 1999 produce larger differences on the time series than after 1999 when the stations availability increased.

At Station Level

Figure 4.7 shows the GDB for the GEBA/BSRN stations (the time period varies for each station) and the FORTH-RTM pixels that contain these stations. These findings make it possible to evaluate the GDB produced from the model and stations and to compare them in terms of the sign and magnitude of either GDBs. In addition to the calculated trends, the results of the non-parametric Mann-Kendall test, which

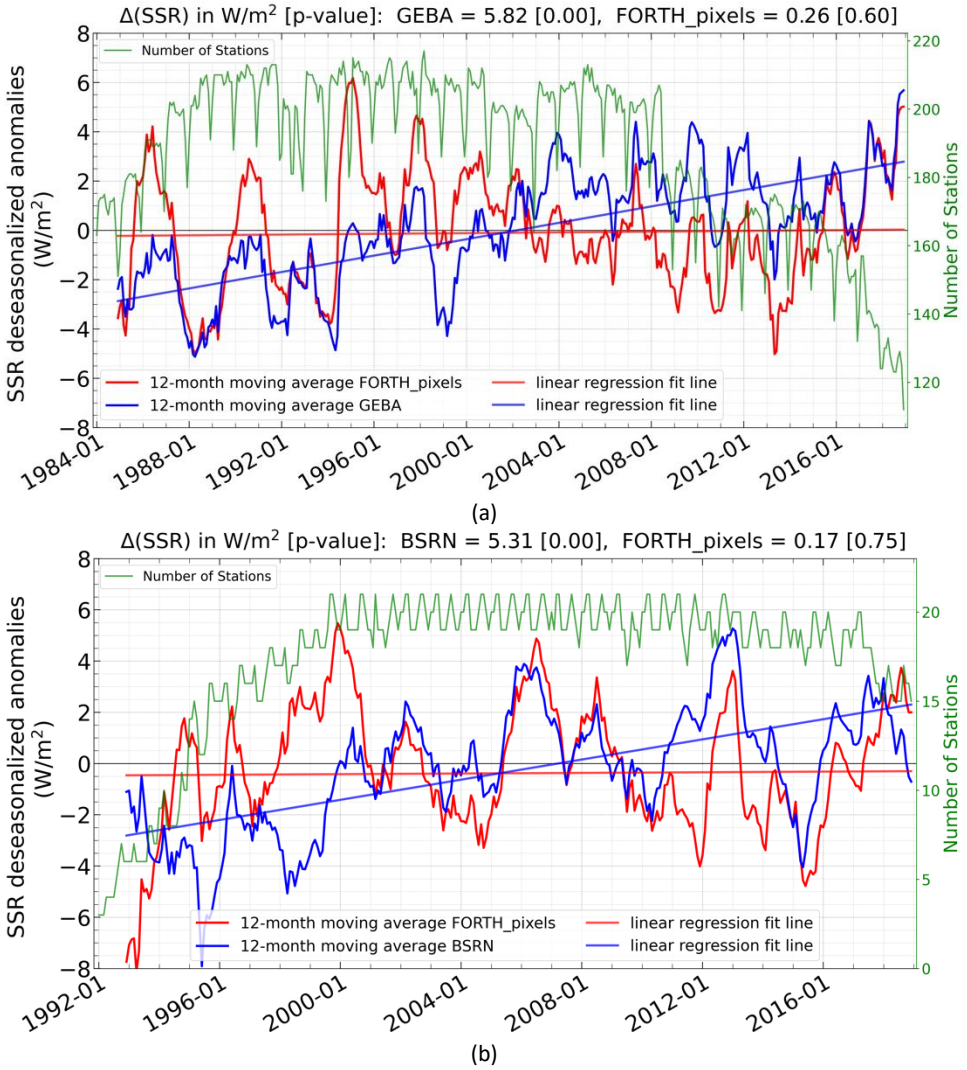


Figure 4.6. Time series of 12-month moving averages of SSR anomalies for GEBA stations (a, blue curve) and BSRN stations (b, blue curve) along with those for the corresponding FORTH-RTM pixels (red curves). The number of available stations for each month is also shown in green color. The computed Δ(SSR) and the associated p-values for the two sets of time series (1984-2018 for GEBA and 1992-2018 for BSRN) are given at the top of each figure.

has been applied to estimate their statistical significance at the 95% level, are also shown in Figure 4.7. Mostly positive and statistically significant trends over Europe and East Asia are revealed by the stations', especially GEBA, GDB, in contrast to mainly negative and statistically significant trends over India. The positive and negative trends for GEBA stations range from 0 to 33.81 Wm^{-2} and from -0.38 to –33.44 Wm^{-2} whereas the respective ranges for BSRN stations are 0.92-13.55 and -(0.7-6.24) Wm^{-2}. It should be noticed that irrespective of their sign, statistically significant trends are identified for 161 out of 222 (or 72.5%) GEBA and 11 out of the 22 (50%) BSRN stations. The 222 GEBA stations that have been used show an average brightening of 5.00 Wm^{-2}, compared to 3.58 Wm^{-2} (brightening as well) for the 22 BSRN stations.

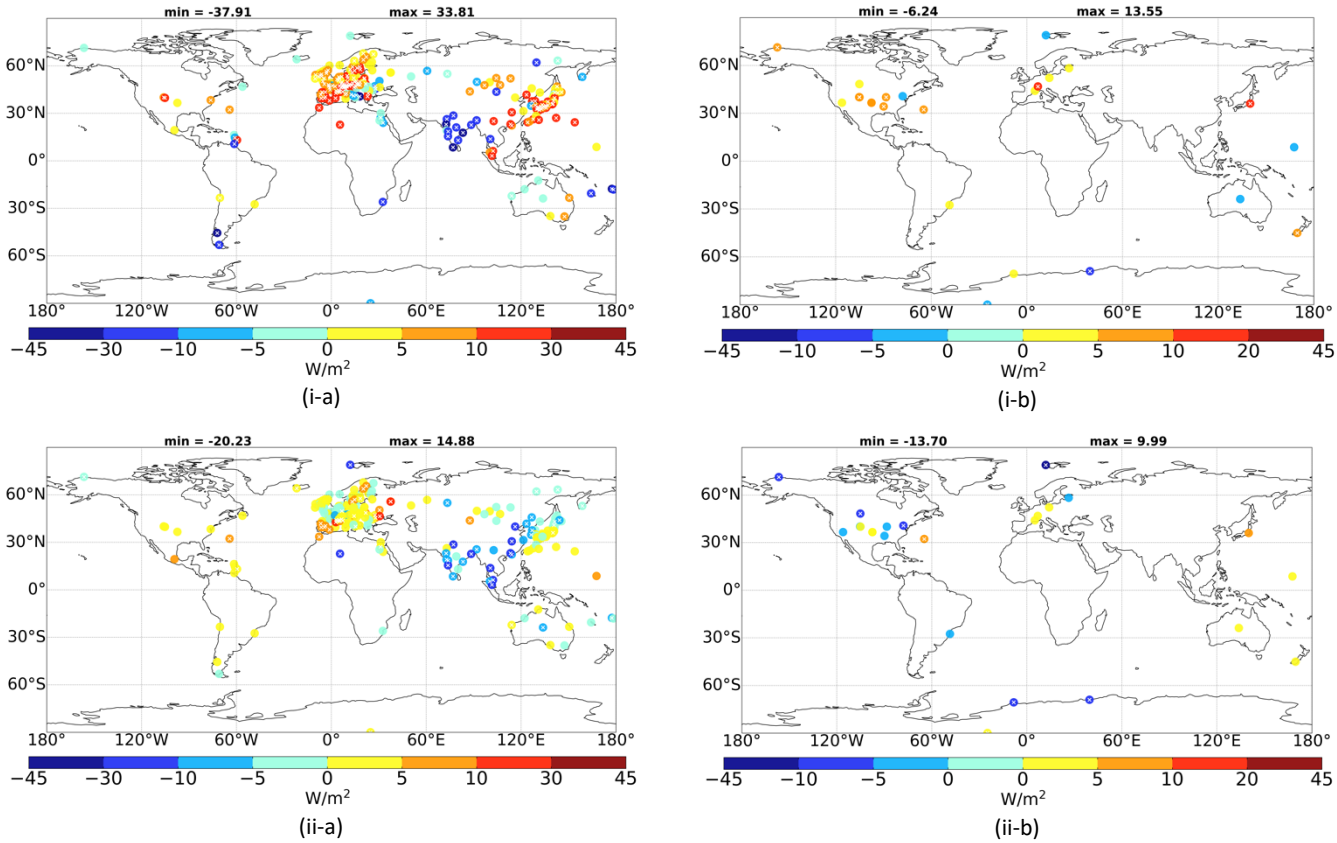


Figure 4.7. Computed GDB (or Δ(SSR), in Wm^{-2}) for GEBA (i-a) and BSRN (i-b) stations and for the corresponding pixels of FORTH-RTM containing the GEBA (ii-a) and BSRN (ii-b) stations. Negative values, shown in blue and green colors, indicate dimming, and positive values, in yellow, orange and red colors, indicate brightening. The embedded white x symbols indicate trends which are statistically significant (at the 95% confidence level, assessed by applying the non-parametric Mann Kendall test). The trends are estimated over the periods covered by each station (shown in Figure AC1).

While the corresponding ranges of GDB for the FORTH-RTM pixels that include the BSRN stations are 0.30-9.99 and -(0.99-13.7) Wm^{-2}, the obtained trends of GDB for FORTH-RTM pixels including the GEBA stations show larger positive trends, ranging from 0.06 to 14.88 Wm^{-2}, and negative trends from 0.01 to 20.23 Wm^{-2}. The positive and negative ranges of GEBA GDB are both larger than the corresponding FORTH-RTM ranges, whereas the positive/negative ranges of BSRN GDB are larger/much smaller than the FORTH-RTM corresponding pixels. Based on the results of Figures 4.7ii-a and 4.7ii-b, the average GDB of the FORTH-RTM pixels including the GEBA sites is a brightening of 0.61 Wm^{-2}, which is smaller than the 5.00 Wm^{-2} equivalent brightening of GEBA sites, while the average GDB of the FORTH-RTM pixels including the BSRN sites is a dimming of –1.01 Wm^{-2}, opposite to the brightening of 3.58 Wm^{-2} for the BSRN stations. Irrespective of their sign, statistically significant trends are identified for 56 out of 222 FORTH-RTM pixels including GEBA stations (i.e., for 25.2%) and for 8 out of the 22 (36.6%) pixels containing BSRN stations. Besides, the same findings, namely agreement/disagreement in sign of GDB between the FORTH-RTM and GEBA/BSRN stations, are found if only pixels with either model and stations statistically significant GDBs are used. The mean GDB for GEBA/BSRN sites is 6.41 and 5.79 Wm^{-2}, whereas the average FORTH-RTM GDB for GEBA/BSRN sites is 0.32 and –4.45 Wm^{-2}. Moreover, strong and statistically significant dimming over India and strong brightening over Europe are both shown by FORTH-RTM pixels and GEBA stations,

but with GEBA stations showing a stronger brightening than FORTH-RTM. On the other hand, there are other regions such as Korea and China where there is disagreement, with the RTM showing a dimming against the brightening indicated by the stations. This disagreement also occurred in the comparison of MERRA-2 and GEBA GDB made by (Stamatis et al., 2022), suggesting that this disagreement could be attributed to possible problems in the common input aerosol data (from MERRA-2). According to our analysis, this dimming in our model primarily arises from increasing MERRA-2 aerosols loadings. This increase, which continues during the period 2001-2016 as also revealed by (Che et al., 2019) in mainland East Asia, is in strong disagreement with the MODIS/Terra and MISR observations. However, on the other hand, there are issues in GEBA stations associated with the strong urbanization effects (Wang et al., 2018) which can also explain the disagreement in SSR changes between FORTH-RTM and GEBA stations in Korea and China.

The agreement or disagreement between the signs of GDB estimated (using SSR anomalies) by either the FORTH model or the GEBA/BSRN stations is clearly shown in Figure 4.8. The signs of FORTH-RTM and GEBA GDBs show a satisfactory percentage of overall agreement (63.5%), whereas the percentage for the much fewer BSRN stations is lower (54.5%). Furthermore, it is found that for cases (pixels) with statistically significant trends, the percentage of agreement is higher for GEBA, equaling 76.7% and lower, equal to 50%, for BSRN stations (which are however only 4). The obtained results from the analysis utilizing GEBA stations, which offer a fair amount of geographical coverage throughout continents like Europe, India, or Australia, allow to infer confident conclusions about a fairly systematic agreement over these world regions. Thus, it is found that most stations (66.4%) in Europe exhibit qualitative agreement (same sign of GDB). Additionally, there is a complete agreement over India, extraordinarily for all GEBA stations. Also, almost all stations over Australia (80%) and most stations in Japan (73.1%) show an agreement as well. In North America, a mixed pattern exists with agreement/disagreement in 5/5 (i.e., 50/50%) BSRN stations. It's interesting to note that while in the current analysis, using the values of the 22 chosen BSRN stations, agreement in the sign of GDB is found at 54.5% of stations, when the total number of BSRN stations (66) is used, without applying the availability criterion in the computation of SSR trends, agreement is found at more stations, i.e., 66.7% of stations. On the other hand, for the entire group of GEBA stations (1193), an agreement of 66% is found, just slightly higher than 63.5% for the selected 222 stations. The results of the present study are comparable to those obtained with similar versions of the same model (FORTH-RTM), but using somewhat different input datasets and referring to much shorter time periods, i.e. 2001-2009 in (Hatzianastassiou et al., 2020) and 2001-2006 in (Hatzianastassiou et al., 2012) and numbers of GEBA/BSRN stations (105/20 in (Hatzianastassiou et al., 2020) and 91/14 in (Hatzianastassiou et al., 2012)), suggesting that the FORTH-RTM GDB has a good qualitative agreement with GEBA stations (for more than 60%) and a poorer, but still reasonable, agreement against the much smaller sample of BSRN stations, which is greatly affected by the number of available stations and it is larger than 54.5%. In a recent study, (Stamatis et al., 2022) estimated the MERRA-2 GDB and the degree of its agreement with GEBA and BSRN stations almost for the same time period (1980-2019) with the present study. They reported that the MERRA-2 GDB agrees for 63.4% GEBA and 50% BSRN stations, indicating that the degrees of FORTH-RTM and MERRA-2 GDB agreement with the GEBA/BSRN reference stations are comparable, suggesting possible issues in the common input data from MERRA-2.

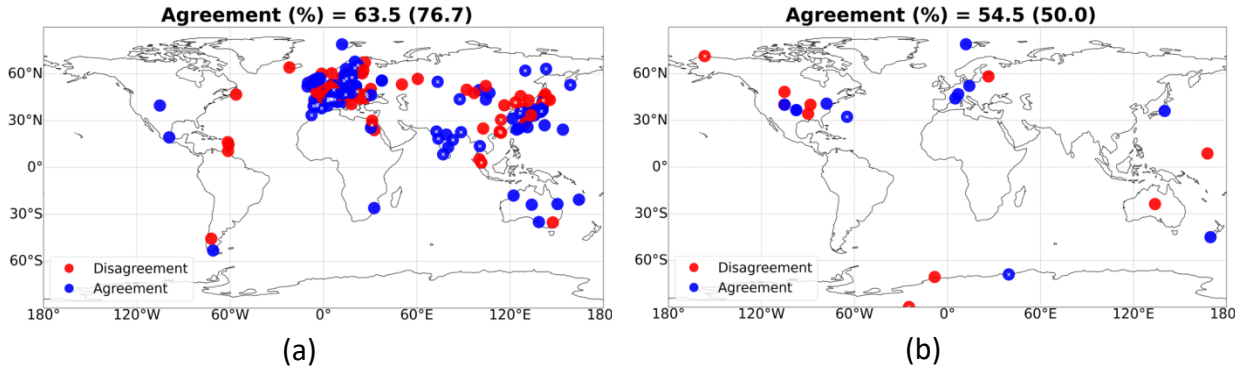


Figure 4.8. Agreement (blue dots) and disagreement (red dots) between trends of FORTH-RTM and GEBA (a) and BSRN (b) station deseasonalized SSR anomalies. The embedded white "x" symbols indicate the statistically significant trends for both FORTH-RTM and stations. The numbers at the top of the plots provide the percentage of stations for which there is agreement/disagreement (first number) in the sign of GDB, while the corresponding numbers in parentheses refer to statistically significant trends.

SSR strongly depends on solar radiation absorbed and reflected in the overlying atmosphere at every location. Thus, an additional analysis was conducted to examine if the FORTH-RTM fluxes successfully represent the closure of the solar radiation budget with the aim of more fully assessing the robustness of the modelled GDB. To achieve this, specific GEBA/BSRN stations that offer GDB agreement with the model were initially chosen. Then, the computed trends of the FORTH-RTM Outgoing Solar Radiation (OSR) at TOA for these stations were compared to the matching OSR from CERES-EBAF satellite data for the time period 01/2001–12/2018 to investigate if they agree or disagree in terms of sign of Δ(OSR). For those sites where both the modelled Δ(SSR) and Δ(OSR) qualitatively agree with the corresponding reference surface and satellite measurements, the Earth's SW radiation budget is successfully closed qualitatively. It should be noted that in this case the available number of stations is 256 for GEBA and 32 for BSRN based on the criterion according to which each station should have availability of more than 70% of the number of months for the entire time-period (2001-2018). It should be noted that during this period the MERRA-2 products assimilated modern satellite data, leading to more homogenous time series (Korras-Carraca et al., 2021) for the FORTH-RTM aerosol input data. In this case, with shorter time period than previously (1984-2018), the level of agreement between the sign of slopes of stations and FORTH-RTM pixels slightly improved for GEBA and hardly decreased for BSRN. Figure 4.9 compares the signs of the computed FORTH-RTM Δ(SSR) and Δ(OSR) with the equivalent GEBA/BSRN Δ(SSR) and CERES-EBAF Δ(OSR) signs. At the surface, 67.6% of GEBA (173 out of 256) stations and 53.1% of BSRN (17 out of 32) stations agree with FORTH-RTM in terms of Δ(SSR) sign (blue dots in Figures 4.9i-a and 4.9i-b, respectively). Then, just for those stations (providing agreement at surface), the signs of Δ(OSR) from FORTH-RTM and CERES were compared. Out of the 173 GEBA sites, there was qualitative agreement at TOA for 145 stations, i.e., in 83.8% of them. Accordingly, agreement was observed for 88.2% of the 17 BSRN locations, which is almost equal to the percentage for GEBA. Overall, 145/15 (56.6/46.9 %) of GEBA/BSRN stations provided agreement in sign of both Δ(SSR) and Δ(OSR). The obtained results of this part of the analysis, focusing on the comparison between the changing solar fluxes at the Earth's surface and TOA as estimated with the FORTH-RTM against reference surface and TOA fluxes, prove that FORTH-RTM partially satisfactorily reproduces the changing SW radiation budget and especially GDB.

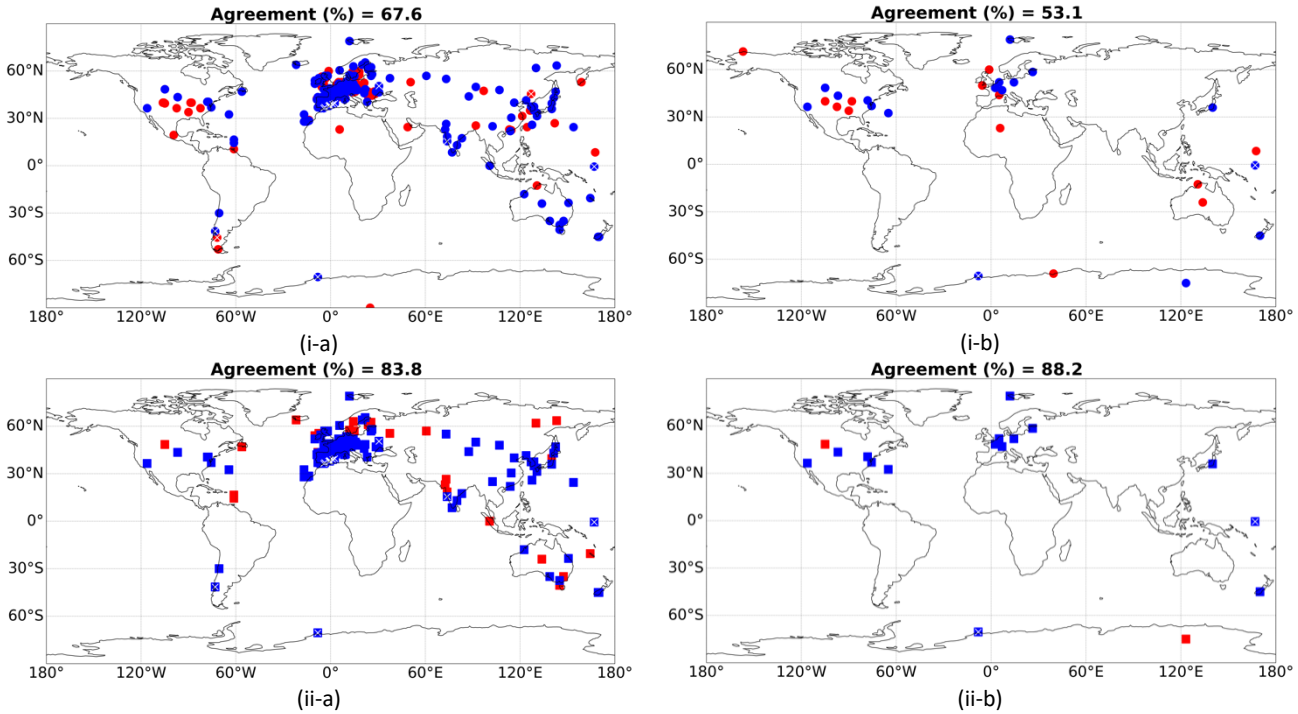


Figure 4.9. Agreement (blue dots) and disagreement (red dots) between trends of FORTH-RTM and station deseasonalized SSR anomalies (Δ(SSR)), for GEBA (i-a) and BSRN (ii-a) stations for the period 01/2001–01/2018. The stations showing agreement at the surface against GEBA stations (Figure 4.9i-a) and BSRN stations (Figure 4.9ii-a), also having agreement of Δ(OSR) with CERES at TOA, during the same period, are shown in Figures 4.9i-b and 4.9ii-b, respectively, with blue rectangles, while those having disagreement at TOA with red rectangles. Also, the embedded white "x" symbols indicate the statistically significant trends for both FORTH-RTM and stations. At the top of each figure the percentage number of stations (i) and CERES pixels (ii) that agree in sign of slopes with the FORTH-RTM pixels is shown.

Since GDB experiences variations on a decadal scale, as described in Section 1, the agreement/disagreement between the FORTH-RTM and stations' GDB has also been evaluated across certain sub-periods. According to the literature (Wild 2016; Wild et al., 2009) based on station measurements, the chosen sub-periods and the accompanying GDB patterns are 1984–1989 (dimming), 1990–1999 (brightening), 2000–2009 (reduced brightening), and 2010–2018 (brightening & dimming). For each sub-period, time series of deseasonalized FORTH-RTM and station SSR anomalies were produced, a linear regression was applied to them, and the Sen's slope computed. The results are shown at a station level in Figure AC5, whereas Tables 4.2 and 4.3 for GEBA and BSRN, respectively, emphasize the agreement or disagreement between the sign of the computed average GDB from all stations and the corresponding FORTH-RTM pixels. According to Table 4.2, 66.1% of GEBA stations during the 1980s had qualitative agreement with the FORTH-RTM in terms of the GDB sign, compared to 60% during the 1990-1999, 51.2% during the 2000 to 2009 period, and 73.2% for 2010-2018. The higher level of agreement during the first, second and fourth periods is in line with (or results in) the identical sign of overall (averaged) GDBs from the model and GEBA stations, consisting of dimming in 1984-1989 and brightening in 1990-1999 and 2010-2018. Regarding the comparison against BSRN stations (Table 4.3), agreement is found for 63.6% of stations from 1992 to 1999, 50% from 2000 to 2009, and 65.9% from 2010 to 2018. Again, during the first (1990s) and third (2010s) periods, the higher percent number of stations with agreement, results in same sign of GDB (brightening in both periods) as estimated from the model and

BSRN stations. It is also noticeable that during the 1980s, 1990s and 2010s, the FORTH-RTM qualitatively reproduces the GDB indicated by both reference GEBA and BSRN station networks, exhibiting a good performance. Only in the 2000s there is opposite sign of modeled GDB than the one suggested by stations, namely a modeled dimming against station-based brightening. With respect to the magnitude of model GDB, it doesn't necessarily follow the interdecadal changes suggested by the GEBA and BSRN stations (for example the GEBA brightening in 2010s is about 1.3 times stronger than that in the 1990s, while the corresponding modeled is 1.9 times, whereas the corresponding 2010s/1990s GDB ratios for BSRN stations are 0.07 for BSRN and 1.4 for FORTH-RTM), but this is of secondary importance compared to the similarity/dissimilarity of the estimated GDB itself.

Table 4.2. Agreement between the GDB (Δ(SSR)) of FORTH-RTM and GEBA stations over four different time periods. The percent number of GEBA stations for which same sign of GDB is found with the corresponding model pixels is given, along with the average Δ(SSR) and the number of stations/pixels with brightening and dimming (shown in parentheses) for both GEBA and FORTH. Red and blue vectors indicate Brightening and Dimming, respectively.

GEBA periods	Agreement (%)	GEBA Δ(SSR) (Wm^{-2})	GEBA (BRI,DIM)	FORTH_pixel Δ(SSR) (Wm^{-2})	FORTH_pixel (BRI,DIM)
1984-1989	66.1	-2.51 ↘	(251, 318)	-1.03 ↘	(261, 308)
1990-1999	60	1.40 ↗	(260, 215)	2.75 ↗	(341, 134)
2000-2009	51.2	2.99 ↗	(228, 104)	-1.70 ↘	(114, 218)
2010-2018	73.2	1.88 ↗	(221, 118)	5.18 ↗	(287, 52)

Table 4.3. As in Table 4.2, but for BSRN stations.

BSRN periods	Agreement (%)	BSRN Δ(SSR) (Wm^{-2})	BSRN (BRI,DIM)	FORTH_pixel Δ(SSR) (Wm^{-2})	FORTH_pixel (BRI,DIM)
1992-1999	63.6	2.05 ↗	(7,4)	2.14 ↗	(5,6)
2000-2009	50	0.5 ↗	(18,14)	-0.68 ↘	(14,18)
2010-2018	65.9	0.14 ↗	(20,21)	3.06 ↗	(30,11)

4.3 FMC evaluation

4.3.1 Evaluation of FMC SSR

The assessment of the improved version of the FORTH-RTM (FMC) SSR is carried out in this section, which is a requirement for the FMC GDB evaluation. In this study and below in the inter-comparisons (Section 4.3), for more accurate results, all stations have altitude differences with their corresponding model's grid-cells between 0–500 m. The evaluation is conducted either for all stations (Section 4.3.1.1) or on an individual station level (Section 4.3.1.2). The long-term (1984–2018) average of the FORTH-RTM SSR is shown in Figure 4.13, along with the corresponding long-term average SSR of GEBA and BSRN stations. The results show a generally good agreement between the model and the observed ground truth SSR data.

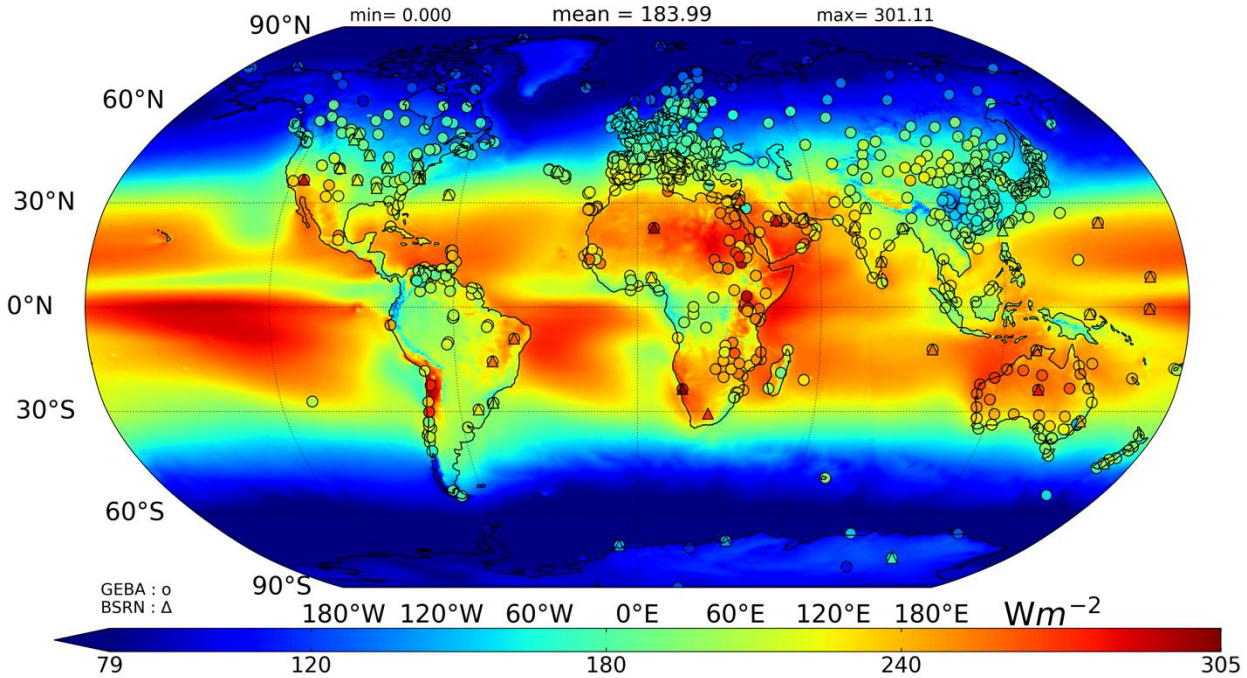


Figure 4.13. Global distribution of the long-term (1984–2018) average FORTH-RTM SSR. The average SSR of the GEBA and BSRN stations, which are used to validate the RTM, is also shown.

4.3.1.1. All Stations

The statistics of the overall comparison of FORTH-RTM SSR fluxes and anomalies against 1091 GEBA and 64 BSRN measurement-based fluxes and anomalies are given in Table 4.4, while Figure 4.14 provides the corresponding scatterplot comparisons. It seems that FORTH-RTM SSR anomalies are satisfactorily correlated with GEBA and BSRN station anomalies yielding R values equal to 0.75 and 0.71, respectively (for the non-deseasonalized SSR fluxes the R values are much higher, as expected, equal to 0.97 and 0.94 for both GEBA and BSRN). Overall, the FORTH-RTM slightly overestimates SSR with respect to GEBA and slightly underestimates SSR with respect to BSRN, having mean biases equal to 4.46 and –2.49 Wm^{-2}, respectively, corresponding to relative biases equal to 2.7% and –1.3%. The general overestimation of FORTH-RTM SSR against the denser GEBA network may suggest that FORTH-RTM's atmosphere is more transparent than it should be which differs from the conclusion for the FMI versions which generally underestimates SSR and has less transparent atmosphere. Since the only difference between these 2 model versions is the cloud input datasets (ISSCP-H vs CLARISC), the more transparent atmosphere of FMC versions is due to the underestimation of the CLARISC clouds. This underestimation of the CLARISC cloud cover globally is reported by Karlsson et al., 2023a,b and it was found by the intercomparison between CERES, ISCCP-H and CLARISC total cloud cover as shown in Figures AA1, AA2 and AA5. However, the bias of FMC is generally smaller than the bias of the FMI. Moreover, it seems that the aerosol input data do not contribute to the overall overestimation of FORTH-RTM SSR, since the MERRA-2 aerosol's optical depth is in generally good agreement with observations as revealed by (Che et al., 2019) who evaluated the MERRA-2 AOD against 468 AERONET stations globally for 1993–2016 and against 37 CARSNET (China Aerosol Remote Sensing Network) stations over China for 2002–2014. It should be noted that it has been reported in the literature (Wang et al., 2018) that the Chinese stations from

GEBA, which count a significant number (85 stations), may not be as representative due to strong urbanization effects, so this can affect the comparison. In these stations, the FORTH-RTM overestimates the SSR by 10.26 Wm^{-2}. Thus, excluding them from the comparison led to a weaker SSR overall overestimation equal to 3.91 Wm^{-2} (smaller than the original by 12.3%). The estimated RMSE, which is equal to 20.93 Wm^{-2} for GEBA and 29.02 Wm^{-2} for BSRN (corresponding to 12.8% and 15.4% of the station networks' mean values), shows that FORTH-RTM deviates slightly more from the BSRN and less from GEBA measurements. The slope values of the scatterplot comparison are 0.99 and 0.93, respectively, for GEBA and BSRN, while the corresponding values for SSR anomalies are equal to 0.78 and 0.64. It should be noted that in an assessment (Hatzianastassiou et al., 2005) of FORTH-RTM SSR, with a shorter period (1984–2000), lower spatial resolution ($2.5^{\circ} \times 2.5^{\circ}$) and different input datasets (clouds from ISCCP-D2, aerosols from Global Aerosol Data Set, and meteorology from NCEP/NCAR global reanalysis data), the R values were equal to 0.99 for 700 GEBA and 22 BSRN stations, while the bias/RMSE values were equal to −6.49/23.44 Wm^{-2} for GEBA and –14/30.56 Wm^{-2} for BSRN), indicating again, similarly to the present work, that the model has larger RMSE values against BSRN than GEBA stations and SSR underestimation over BSRN but our study differentiates from the previous study in terms of the overestimation over GEBA network which wasn't estimated previously due to the different cloud input. Moreover, the work by (Hatzianastassiou et al., 2012) and (Hatzianastassiou et al., 2020) used the FORTH-RTM for the period 2001–2006 and 2001–2009, respectively, with the same input data as (Hatzianastassiou et al., 2005) except for the aerosol data, which were taken from Moderate Resolution Imaging Spectroradiometer (MODIS)-Terra C005 and C006, respectively. The estimated SSR fluxes were validated against GEBA and BSRN stations and revealed better performance to the work of (Hatzianastassiou et al., 2005) and this of Section 4.2 where FMI used. Thus, the current version of the FORTH-RTM has significant improvement and a difference from the other similar previous studies which is the small in magnitude overestimation of the SSR over the dense GEBA network which is not in line with the previous works (larger in magnitude underestimation), indicating that the utilization of CLARA-ISCCP synergy (CLARISC) lead to this difference.

In addition to the FORTH-RTM SSR evaluation on an annual scale, this has also been carried out on a seasonal basis because this may help to easily identify possible sources of errors. It should be noted that not only the absolute but also the relative biases were computed, because of the significant seasonal change of SSR fluxes. Table 4.4 shows that globally, RMSE for GEBA does not show significant seasonal changes, which are as large as 2 Wm^{-2}. Contrarily, R (both using SSR fluxes and anomalies), BIAS, relative BIAS and relative RMSE exhibit a discernible seasonal variation, up to 0.11, 8, 5% and 17%, respectively. Given the six-month shift in extreme seasons between the two hemispheres, the seasonal variation of the three main statistical metrics, namely R, RMSE (in absolute and percentage terms), and bias (in absolute and percentage terms) were also calculated separately for the two hemispheres and is shown in Figure 4.15. Except for R, which was calculated using deseasonalized SSR anomalies, the results of this figure were derived using SSR fluxes (the corresponding R using absolute SSR fluxes is given in Figure AC7). Figure 4.15 shows that in general, the model correlates better with BSRN than GEBA in SH whereas in NH the model correlates better with GEBA than BSRN. Besides, it deviates more for GEBA than BSRN station measurements in both hemispheres. Also, the RMSE values do not show significant differences for both networks. Moreover, for NH, the statistical metrics do not exhibit a significant seasonal variation except

Table 4.4. Comparison between FORTH-RTM and GEBA/BSRN SSR on an annual and seasonal basis (December–January–February, March–April–May, June–July–August, and September–October– November), along with the computed main statistical parameters (number of matched data pairs, N, slope value of applied linear regression fit, absolute and percent relative biases of FORTH-RTM relative to the mean GEBA/BSRN values, root mean squared error, RMSE, percent relative RMSE (RRMSE) with respect to the mean GEBA/BSRN values, correlation coefficient, R, the mean GEBA and BSRN values and the number of available stations, id, whose SSR measurements are used in the comparison). In addition, the R and slope values computed using deseasonalized SSR anomalies are given in parentheses. The percent relative bias and RMSE values are also given in parentheses.

FORTH-GEBA	**ANNUAL**	**DJF**	**MAM**	**JJA**	**SON**
R	0.97 (0.75)	0.97 (0.67)	0.93 (0.78)	0.91 (0.76)	0.96 (0.70)
BIAS	4.46 (2.73%)	3.34 (3.17%)	2.82 (1.5%)	5.43 (2.46%)	6.19 (4.67%)
RMSE	20.93 (12.82%)	19.91 (18.92%)	21.54 (11.48%)	22.85 (10.38%)	19.05 (14.38%)
slope	0.99 (0.78)	0.98 (0.71)	0.98 (0.81)	0.96 (0.80)	0.99 (0.74)
intercept	6.11	5	7.16	14.8	5.85
mean_FORTH	167.73	108.55	190.50	225.56	138.69
mean_stations	163.26	105.22	187.68	220.14	132.49
N	169,204	38,636	44,025	43,706	42,837
stations	1091	1070	1089	1079	1091
FORTH-BSRN	**ANNUAL**	**DJF**	**MAM**	**JJA**	**SON**
R	0.94 (0.71)	0.92 (0.66)	0.93 (0.72)	0.94 (0.72)	0.93 (0.68)
BIAS	-2.49 (-1.32%)	-9.72 (-6.28%)	-1.7 (-0.83%)	2.64 (1.14%)	-1.52 (-0.93%)
RMSE	29.02 (15.37%)	38.87 (25.1%)	24.03 (11.81%)	19.98 (8.62%)	30.22 (18.47%)
slope	0.93 (0.64)	0.83 (0.67)	0.98 (0.61)	0.92 (0.67)	0.91 (0.64)
intercept	11.65	16.37	2.61	20.18	12.58
mean_FORTH	186.27	145.14	201.80	234.38	162.12
mean_stations	188.76	154.86	203.50	231.74	163.64
N	9556	2293	2439	2394	2430
stations	64	58	63	60	64

for the R which is the lowest in the winter and larger in the spring-summer season. On the other hand, over SH, significant variation shows the absolute and relative values of BIAS and RMSE for BSRN stations.

4.3.1.2 At Station Level

In order to examine if regional patterns exist in the metrics of the evaluation, it is necessary to study and compare the fluxes on an individual station basis as part of the evaluation of the FORTH-RTM SSR. The spatial distribution of the correlation coefficient (R) between the FORTH-RTM and GEBA/BSRN stations SSR anomalies is shown in Figure 4.16, along with the distribution of the RMSE, RRMSE, bias, and relative bias computed using SSR fluxes. For the GEBA stations, R ranges from –0.21 to 0.98, while for the BSRN stations, it ranges from 0.26 to 0.96. For 70% of GEBA/BSRN station data, the computed R values are greater than 0.68/0.72 (Figure AC8). Satisfactory R values (orange and reddish colors) can be seen throughout Europe, East Asia, North America, and Australia. On the other hand, the tropical and subtropical world areas, such as Africa, South America, India, and Indonesia, tend to have worse R values (orange-green colors and R smaller than 0.6). The same regional patterns, but with clearly higher values, appear for R computed using non-deseasonalized SSR fluxes (Figure AC9). It can be assumed that the low correlation of FORTH-RTM SSR in these regions may be caused by uncertainties in cloud cover and optical

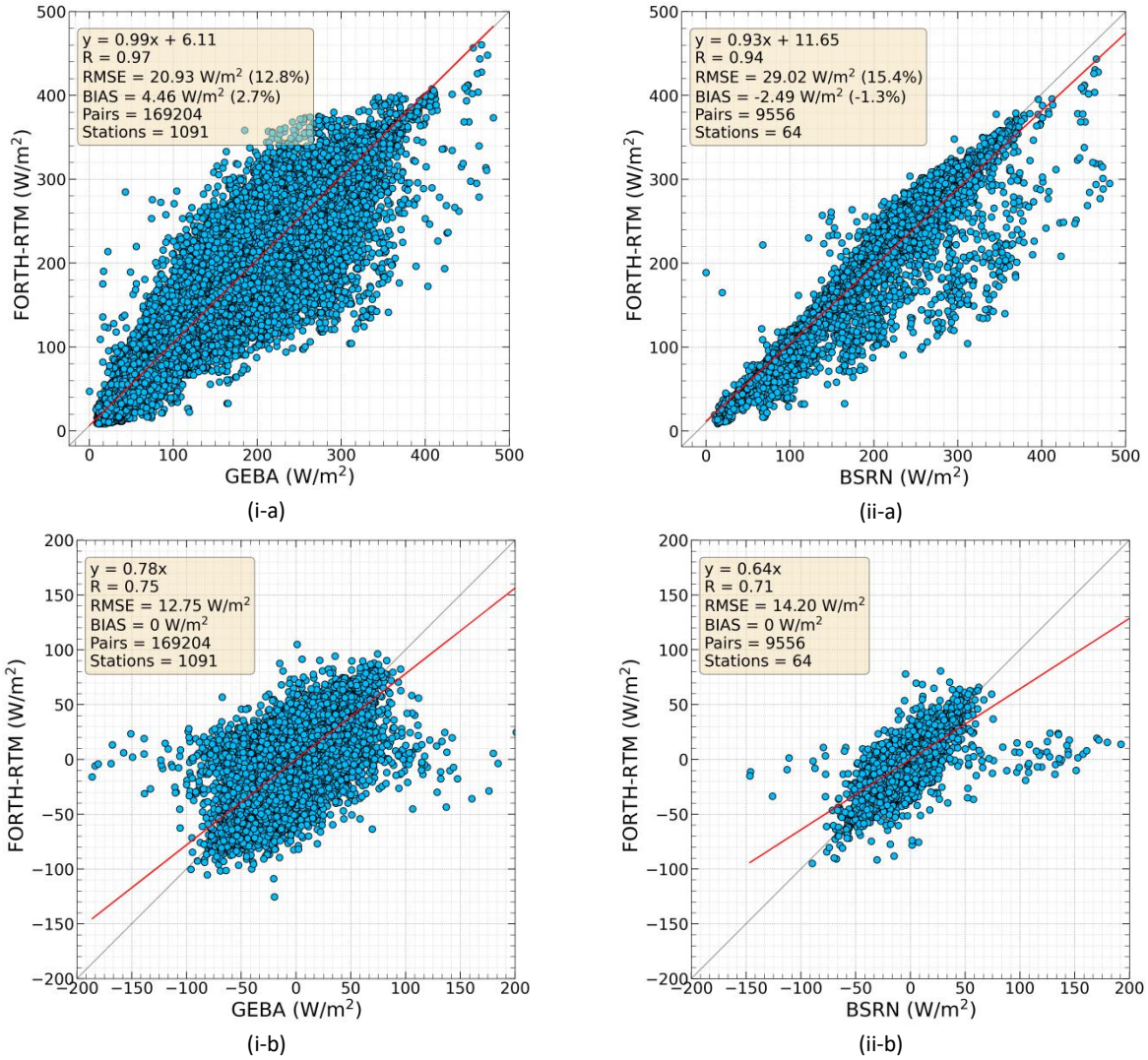


Figure 4.14. Scatterplot comparison between FORTH-RTM and GEBA (i-a), and BSRN (ii-a) SSR fluxes, and between FORTH-RTM and GEBA (i-b) and BSRN (ii-b) deseasonalized SSR anomalies. The applied linear regression fit (red line), and the associated main statistical metrics, namely the equation of the applied linear fitting, the correlation coefficient (R), the root-mean-squared error (RMSE), the bias, and the total number of matched data pairs, are also shown.

properties, as also suggested by other studies (Zhang et al., 2015, 2016, 2020), given that clouds are one of the primary factors driving the SSR (Hatzianastassiou et al., 2005). Indeed, clouds are linked to the highest level of uncertainty in climate modeling (Baker et al., 2008; Stensrud 2007), whereas the accuracy of ISCCP-H and CLARA cloud cover is low over tropical and polar latitudes, as shown by (Boudala et al., 2021) who evaluated the ISCCP–H cloud cover against the CALIPSO-GOCCP (GOCCP) during 2000–2017 and by Liu et al., 2023 who evaluated the CLARA cloud amount against ground observation data by the International Comprehensive Ocean-Atmosphere Data Set (ICOADS) and the Climatic Research Unit gridded Time Series (CRU TS) during 2000–2020. Apart from clouds, however, aerosols can also contribute to the poor correlation in the tropics. An indication of this could be the low R values that can be observed in regions with little cloud cover, such as the Middle East and Egypt,

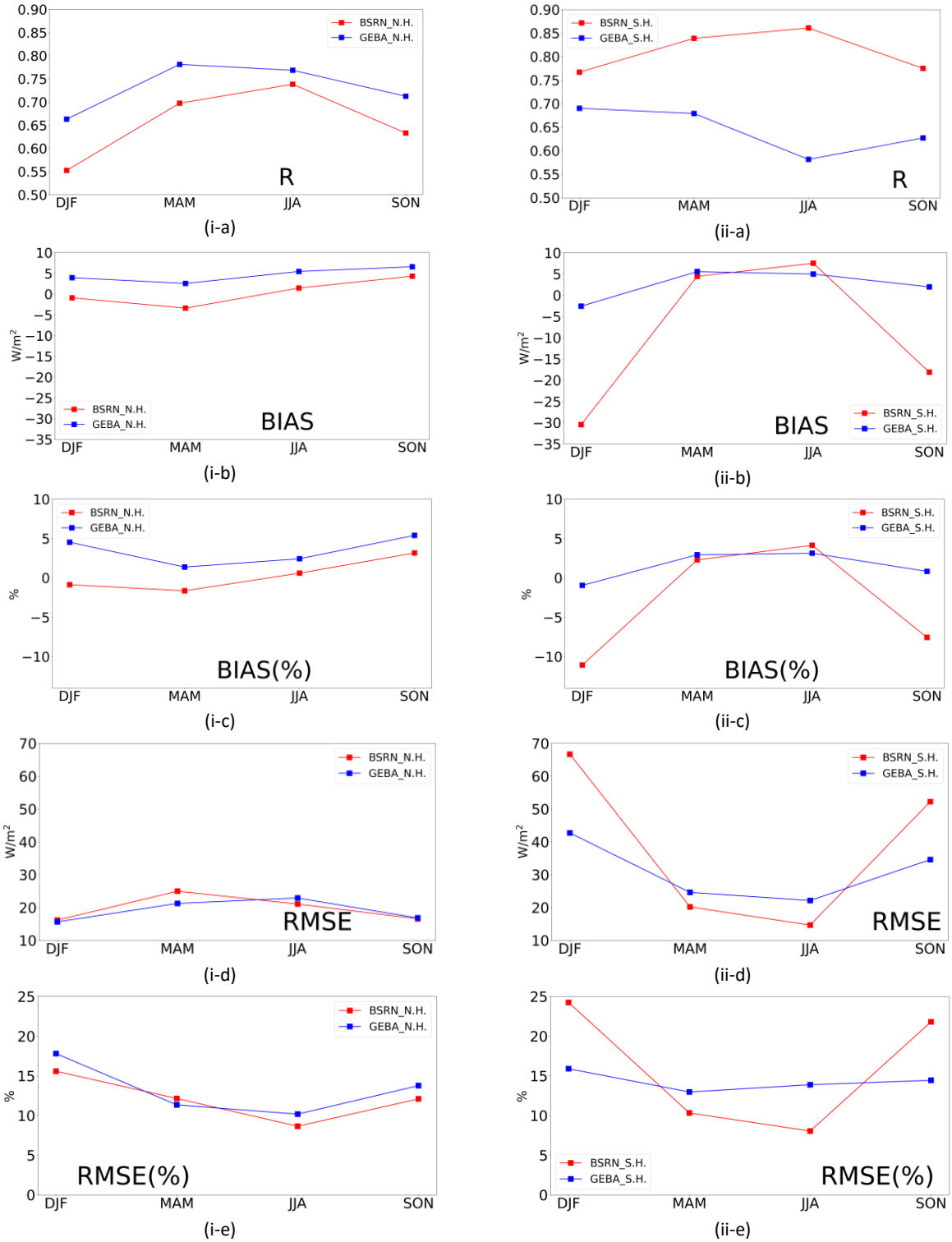


Figure 4.15. Seasonal variation of hemispherical averages of correlation coefficient R (a), bias in Wm^{-2} (b), percent relative bias in % (c), root mean squared error (RMSE in Wm^{-2}) (d), and percent relative RMSE in % (e) between the FORTH-RTM and GEBA (blue) and BSRN (red) stations. Results, computed using SSR fluxes (except for R, which is computed using deseasonalized SSR anomalies), are given for the North Hemisphere (i-left column) and South Hemisphere (ii-right column).

which have high aerosol loads (Korras-Carraca et al., 2021; Gavrouzou et al., 2021). Polar locations also exhibit weak correlation, where the disparities may be brought on by issues with ISCCP and CLARA clouds (Kotarba et al., 2015; Liu et al., 2023) as well as snow and ice cover (Hinkelman et al., 2019; Cullather et al., 2012). In addition, southern China has lower R values than northern China (Figure 4.16 and Figure AC9). Strong air pollution, as well as uncertainty in clouds, aerosols, and their interaction, might all be responsible for this pattern, as documented in previous research (Zhang et al., 2016). The difficulty of FORTH-RTM to accurately represent SSR in tropical and sub-tropical regions is confirmed by the large RMSE values observed in such areas as well as over polar latitudes (Figure 4.16). Indeed, the average RMSE is 30.5 Wm^{-2} and 19 Wm^{-2}, over GEBA and BSRN, respectively, in the tropics and sub-tropics, while outside of them the corresponding ranges are 16.9 and 25 Wm^{-2}. Similar regional patterns may also be observed for the relative RMSE, with high values being most prevalent across Southern China, polar regions, and some tropical and subtropical regions. In general, the FORTH-RTM overestimates SSR with respect to GEBA, underestimating it (bluish colors in Figure 4.16) over middle and high latitudes while strongly overestimates (orange-red colors) over several tropical and subtropical areas, according to the results for the absolute and relative bias. This overestimation over middle-low latitudes can be attributed to the underestimation of CLARA cloud amount (Karlsson et al., 2018, 2023) and MERRA-2 aerosol loadings (Shi et al., 2019). Overall, the model overestimates SSR fluxes in 763 stations, while underestimating it in 328 stations, yielding an overestimation of 4.46 Wm^{-2} for SSR fluxes on average. On the other hand, there is an overall weak model underestimation of SSR fluxes by –2.49 Wm^{-2} when compared to the far fewer (64) BSRN sites (34 out of 64 overestimate but the overestimation is weaker than the underestimation in the 25 out of 64 stations). Absolute and relative percent bias range from –115.3 to 88.1 Wm^{-2} and from –46.4 to 99%, respectively. Yet, absolute and relative % bias values for 70% of the GEBA stations are less than -0.38 Wm^{-2}/-0.22%, respectively (Figure AC8). At the BSRN sites, the relative % and absolute bias values range from –46.9 to 13% and –136.6 to 26.4 Wm^{-2}, respectively, and 70% of the stations have relative and absolute bias less than –1.4%/–3 Wm^{-2} , respectively. It should be noted that in the low latitudes, where the FORTH-RTM tends to stronger overestimate the SSR fluxes, there are many more GEBA than BSRN stations, which can explain the stronger overestimation against GEBA than BSRN. Moreover, there are many sites that have a high mean bias over China, which is greater in its southern part, due to its incorrect assessment of cloud fraction and aerosol loadings (Zhang et al. 2015, 2020; Wang et al., 2018; Xia et al., 2006; Ma et al., 2015).

4.3.2 Evaluation of FMC GDB

After the detailed assessment of the FORTH-RTM SSR fluxes, which revealed quite a good performance, the FORTH-RTM SSR inter-decadal (1984–2018) changes (or GDB) are examined here. It should be emphasized that FORTH-RTM GDB has not yet undergone this examination over such a large time period (35 years), spatial distribution (0.5◦ × 0.625◦), and use of state-of-art input data (ISCCP-H, CLARA and MERRA-2). First, the GDB is evaluated either for the entire sample (all stations) or on a single-station basis (Section 4.3.2.1). Thereafter, Section 4.3.2.2 assesses and discusses the FORTH-RTM's SSR and OSR trends agreement.

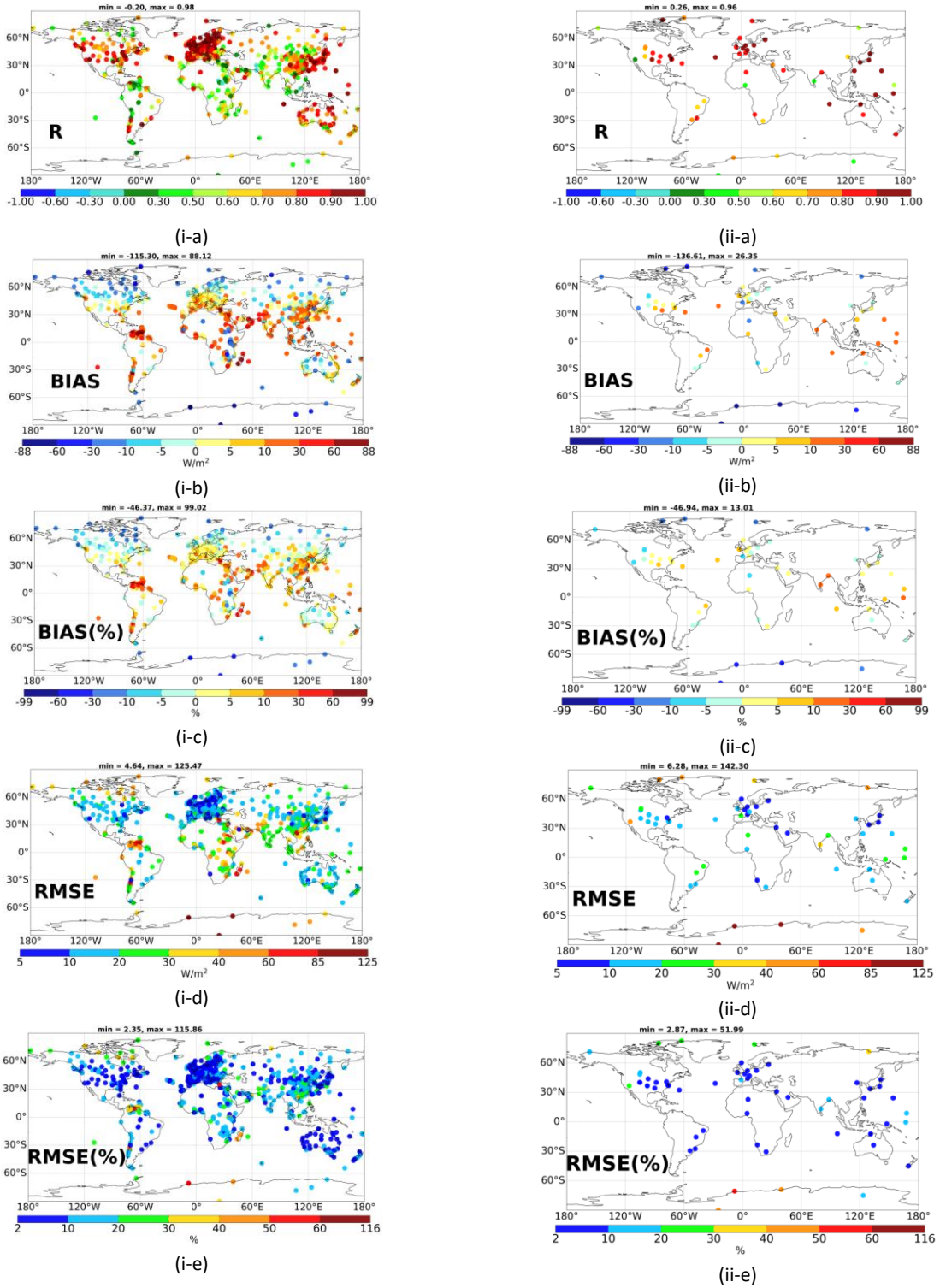


Figure 4.16. Global distribution of correlation coefficient (a), bias (b) and relative percent bias (c) root mean squared error (d), relative root mean squared error (e), computed for the comparison between FORTH-RTM and each GEBA (i, left column) and BSRN (ii, right column) station SSR fluxes, except for R that is computed using deseasonalized SSR anomalies.

The GDB from the reference data of GEBA and BSRN stations was used to compare and evaluate the gridded FORTH-RTM GDB. By applying linear regression to the time series of monthly mean deseasonalized SSR anomalies, and then computing the slope values, the two sets of GDB, i.e., from the FORTH-RTM and the stations, were calculated. In order to ensure a high level of confidence for the results, this analysis was conducted for 211 (out of 1091) GEBA and 23 (out of 64) BSRN stations that satisfied the data availability criterion stated in Section 2.2 (more than 70% of the overall number of monthly values of the total period of each network. It should be mentioned here that the time period varies from station to station, ranging from 25 to 35 years for GEBA stations, and 19 to 27 years for BSRN stations, depending on the original temporal coverage of each station's measurements and the applicable availability criterion (as shown in Figure AC6). Each station's time period was finally adjusted to the time period of the FORTH-RTM available data, i.e., 1984–2018.

All Stations

The comparison of the trends of SSR anomalies (in Wm^{-2}) from the FORTH-RTM and GEBA/BSRN stations is shown in Figure 4.17 using a scatterplot. The correlation is poor, with average R values of 0.35 for GEBA and 0.31 for BSRN while the slope values are low (0.24 for GEBA and 0.33 for BSRN). The calculated biases (FORTH-RTM GDB—stations GDB) are equivalent to 3.92/1.44 Wm^{-2} for GEBA/BSRN indicating that the model overestimates the magnitude of GDB compared to stations. Likewise, the poor fit is revealed by the estimated RMSE values, which are equal to 12.24/6.75 Wm^{-2} for GEBA/BSRN. All these metrics prove that it is difficult for a model to reproduce the magnitude of the station GDB values. However, this is not extraordinary, since there are essential differences between the two sets of compared GDB, i.e., the modeled and measured ones, the most important one being that the model GDB refers to areas of 0.5◦ × 0.625◦ latitude x longitude, opposite to station GDB that pertain to specific sites.

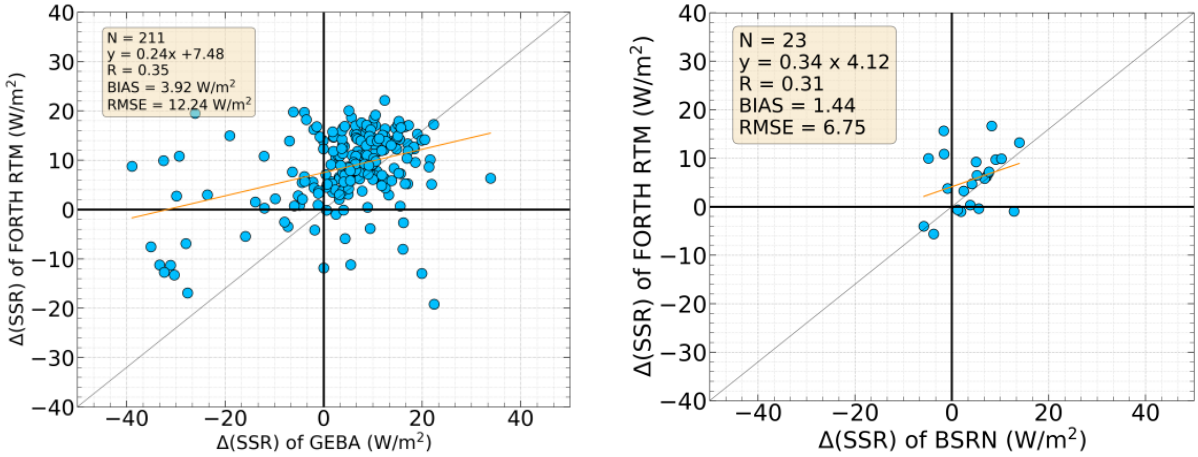


Figure 4.17. Scatterplot comparison between FORTH-RTM and GEBA (a), and FORTH-RTM and BSRN (b) Δ(SSR) or GDB (in Wm^{-2}). The linear regression fit, and the associated statistical metrics, namely the equation of the applied linear fitting, the correlation coefficient (R), the root-mean-squared error (RMSE), the bias (FORTH-RTM minus stations), and the total number of matched data pairs, are also shown.

Contrary to the magnitude of GDB, it is expected that it is more feasible for a model to reproduce the sign of GDB. This performance is easily assessed by the distribution of the Figure 4.17 scatterplot points to the four quartiles, with those lying in the first and third quartiles indicating the similarity of signs. There are 168 (156 in the first and 12 in the third quartiles) such data pairs for FORTH-RTM-GEBA (corresponding to 80% of the total number of points for the FORTH-RTM-GEBA scatterplot) and 15 (13 and 2 pairs) for FORTH-RTM-BSRN (corresponding to 63% of the total number of points for the FORTH-RTM-BSRN scatterplot), revealing that the FORTH-RTM reproduces partially satisfactorily the sign of stations GDB. Another aspect of the GDB comparison, apart from the overall scatterplot shown in Figure 4.17, is the overall performance of the RTM GDB, namely how the modeled GDB compares to that of stations on the average, as well as how the temporally varying averaged SSR anomalies match those of stations. In this aspect, the computed 12-month moving averages of SSR anomalies of all stations and the corresponding FORTH-RTM pixels over the total period for each network, i.e., 1984–2018 for GEBA and 1992–2018 for BSRN, are shown in Figure 4.18. Along with the 12-month moving averages, the number of stations that were accessible in each month/year is also shown. Since FORTH-RTM consistently shows smaller/larger SSR anomalies than GEBA before/after the year 2000, this results in low slope values and small average biases (FORTH-RTM—stations) equal to 0.16 and 0.070 Wm^{-2} against GEBA and BSRN stations, respectively. In association with the smaller slope values, weaker GDB is estimated by the stations than for RTM. Specifically, using the non-parametric Mann–Kendall test, FORTH-RTM (Figure 4.18a) suggest a statistically significant brightening, or positive Δ(SSR), equal to 10.26 Wm^{-2} as opposed to a lesser statistically significant, brightening computed by GEBA stations (Δ(SSR) = 5.27 Wm^{-2}). Comparable conclusions are reached from a similar analysis of FORTH-RTM and BSRN (Figure 4.18b). Indeed, a RTM statistically significant brightening (Δ(SSR) = 11.01 Wm^{-2}) is computed compared to a smaller, but statistically significant, brightening of BSRN stations equal to 5.83 Wm^{-2} . It is interesting to note that both GEBA and BSRN suggest a comparable brightening and that FORTH-RTM is, at least, able to reproduce the same sign of Δ(SSR) against both station networks. Here, it is also examined to what extent the number of stations, which changes with time, affects the differences between the 12-month moving average time series of stations and FORTH-RTM SSR. With respect to the GEBA stations, their number decreases after 2008, but this does not seem to have an effect on the differences. On the other hand, regarding the much fewer BSRN stations, the few available stations till 1999 produce larger differences on the time series than after 1999 when the stations availability increased.

At Station Level

Figure 4.19 shows the GDB for the GEBA/BSRN stations (the time period varies for each station) and the FORTH-RTM pixels that contain these stations. These findings make it possible to evaluate the GDB produced from the model and stations and to compare them in terms of the sign and magnitude of GDBs. In addition to the calculated trends, the results of the non-parametric Mann–Kendall test, which has been applied to estimate their statistical significance at the 95% level, are also shown in Figure 4.19. Mostly positive and statistically significant trends over Europe and East Asia are revealed by the stations, especially GEBA and GDB, in contrast to mainly negative and statistically significant trends over India. The positive and negative trends for GEBA stations range from 0 to 36.28 Wm^{-2} and from −0.2 to –54.68 Wm^{-2} whereas the respective ranges for BSRN stations are 0.92–16.64 and −(0.9–15.31) Wm^{-2}. It should be

noticed that irrespective of their sign, statistically significant trends are identified for 154 out of 211 (or 73%) GEBA and 12 out of the 24 (50%) BSRN stations. The 211 GEBA stations that have been used show an average brightening of 5.41 Wm^{-2}, compared to 4.33 Wm^{-2} (brightening as well) for the 24 BSRN stations.

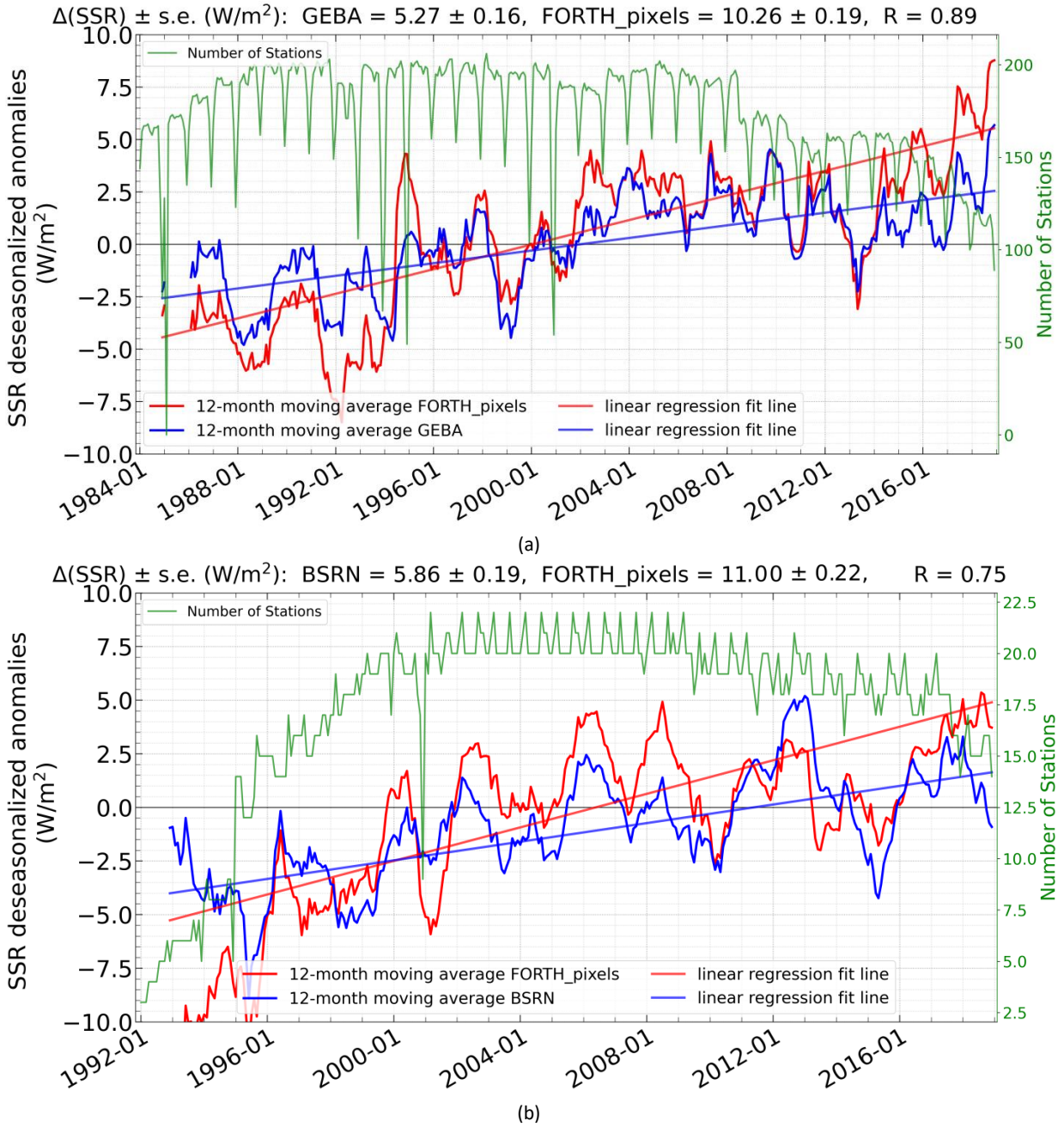


Figure 4.18. Time series of 12-month moving averages of SSR anomalies for GEBA stations ((a), blue curve) and BSRN stations ((b), blue curve) along with those for the corresponding FORTH-RTM pixels (red curves). The number of available stations for each month is also shown in green color. The computed Δ(SSR), the associated errors and the correlation coefficients for the two sets of time series (1984–2018 for GEBA and 1992–2018 for BSRN) are given at the top of each figure.

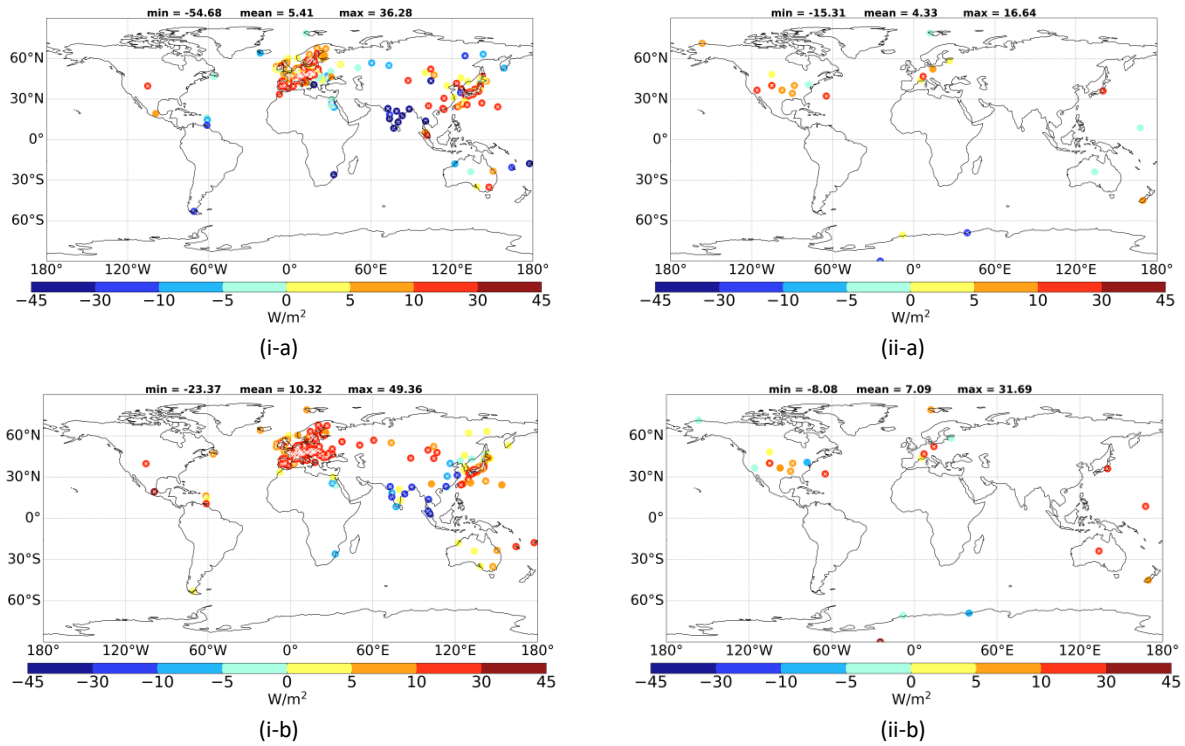
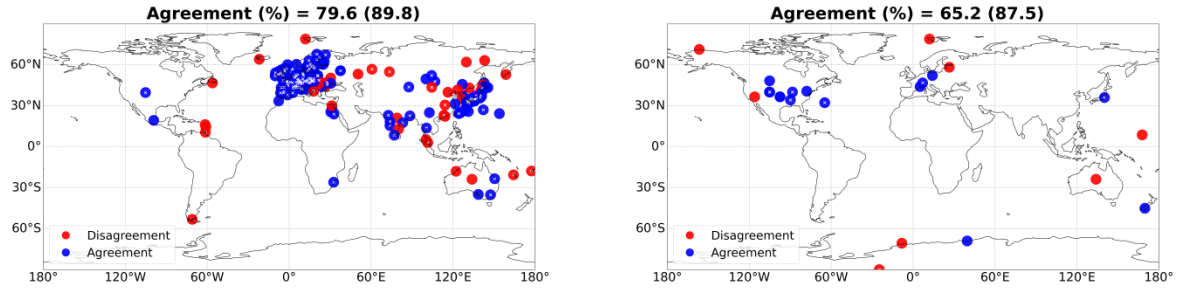


Figure 4.19. Computed GDB (or Δ(SSR), in Wm^{-2}) for GEBA (i-a) and BSRN (ii-a) stations and for the corresponding pixels of FORTH-RTM containing the GEBA (i-b) and BSRN (ii-b) stations. Negative values, shown in blue and green colors, indicate dimming, and positive values, in yellow, orange, and red colors, indicate brightening. The embedded white × symbols indicate trends that are statistically significant (at the 95% confidence level, assessed by applying the non-parametric Mann–Kendall test). The trends are estimated over the periods covered by each station (shown in Figure AC6).

While the corresponding ranges of GDB for the FORTH-RTM pixels that include the BSRN stations are 0.21–31.69 and −(0.8–8.08) Wm^{-2}, the obtained trends of GDB for FORTH-RTM pixels including the GEBA stations show larger positive trends, ranging from 0.2 to 49.36 Wm^{-2}, and negative trends from 0.11 to 21.37 Wm^{-2}. Based on the results of Figure 4.19 (i-b, ii-b), the average GDB of the FORTH-RTM pixels including the GEBA sites is a brightening of 10.32 Wm^{-2} , which is stronger than the 5.41 Wm^{-2} equivalent brightening of GEBA sites, while the average GDB of the FORTH-RTM pixels including the BSRN sites is a brightening of 7.09 Wm^{-2} , similar to the brightening of 4.33 Wm^{-2} for the BSRN stations. Irrespective of their sign, statistically significant trends are identified for 167 out of 211 FORTH-RTM pixels including GEBA stations (i.e., for 79%) and for 12 out of the 24 (50%) pixels containing BSRN stations. Moreover, the same findings, namely agreement/disagreement in the sign of GDB between the FORTH-RTM and GEBA/BSRN stations, are found if only pixels with either model or stations with statistically significant GDBs are used. The mean GDB for GEBA/BSRN sites is 6.63 and 6.61 Wm^{-2}, whereas the average FORTH-RTM GDB for GEBA/BSRN sites is 11.94 and 13.2 Wm^{-2} . Moreover, strong and statistically significant dimming over India and strong brightening over Europe are both shown by FORTH-RTM pixels and GEBA stations but with GEBA stations showing a weaker brightening than FORTH-RTM. On the other hand, there are other regions such as Korea and China where there is disagreement, with the RTM showing a dimming against the brightening indicated by the stations. This disagreement also occurred in the comparison of MERRA-2 and GEBA GDB made by (Stamatis et al., 2022), suggesting that this disagreement could be attributed

to possible problems (data assimilation issues, insufficient emissions) in the common input aerosol data (from MERRA-2). According to our analysis, this dimming in our model primarily arises from increasing MERRA-2 aerosol loadings. This increase, which continues during the period 2001–2016 as also revealed by (Che et al., 2019) in mainland East Asia, is in strong disagreement with the MODIS/Terra and MISR observations. However, on the other hand, there are issues in GEBA stations associated with the strong urbanization effects (Wang et al., 2018) which can also explain the disagreement in SSR changes between FORTH-RTM and GEBA stations in Korea and China. The agreement or disagreement between the signs of GDB estimated (using SSR anomalies) by either the FORTH model or the GEBA/BSRN stations is clearly shown in Figure 4.20. The signs of FORTH-RTM and GEBA GDBs show a satisfactory percentage of the overall agreement (80%), whereas the percentage for the much fewer BSRN stations is lower (65%). Furthermore, it is found that for cases (pixels) with statistically significant trends, the percentage of agreement is higher for GEBA, equaling 90%, and lower, equal to 88%, for BSRN stations (which are however only 8). The obtained results from the analysis utilizing GEBA stations, which offer a fair amount of geographical coverage throughout continents like Europe, India, or Australia, allow the inference of confident conclusions about a fairly systematic agreement over these world regions. Thus, it is found that most stations (91%) in Europe exhibit qualitative agreement (same sign for GDB). Additionally, there is a nice agreement equal to 75% over India. Moreover, 60% of the stations in Australia and most stations in Japan (86%) show an agreement as well. In North America, a good agreement exists over 80% of the BSRN stations. It is interesting to note that while in the current analysis, using the values of the 24 chosen BSRN stations, agreement in the sign of GDB is found at 65% of stations, when the total number of BSRN stations (66) is used, without applying the availability criterion in the computation of SSR trends, agreement is found at more stations, i.e., 70% of stations. On the other hand, for the entire group of GEBA stations (1091), an agreement of 70% is found, just slightly lower than 80% for the selected 211 stations.



(a) (b)

Figure 4.20. Agreement (blue dots) and disagreement (red dots) between the sign of trends of FORTH-RTM and GEBA (a) and BSRN (b) station deseasonalized SSR anomalies. The embedded white "x" symbols indicate the statistically significant trends for both FORTH-RTM and stations. The numbers at the top of the plots provide the percentage of stations for which there is agreement/disagreement (first number) in the sign of GDB, while the corresponding numbers in parentheses refer to statistically significant trends.

Since GDB experiences variations on a decadal scale, as described in Section 1, the agreement/disagreement between the FORTH-RTM and stations' GDB has also been evaluated across certain sub-periods. According to the literature (Wild 2016; Wild et al., 2009) based on station measurements, the chosen sub-periods and the accompanying GDB patterns are 1984–1989 (dimming), 1990–1999 (brightening), 2000–2009 (reduced brightening), and 2010–2018 (brightening). For each sub-

period, time series of deseasonalized FORTH-RTM and station SSR anomalies were produced, a linear regression was applied to them, and Sen's slope was computed. The results are shown at a station level in Figure AC10, whereas Tables 4.5 and 4.6 for GEBA and BSRN, respectively, emphasize the agreement or disagreement between the sign of the computed average GDB from all stations and the corresponding FORTH-RTM pixels. According to Table 4.5, 71% of GEBA stations during the 1980s had a qualitative agreement with the FORTH-RTM in terms of the GDB sign, compared to 62% during 1990–1999, 67% during the 2000 to 2009 period, and 73% for 2010–2018. Regarding the comparison against BSRN stations (Table 4.6), agreement is found for 64% of stations from 1992 to 1999, 72% from 2000 to 2009, and 70% from 2010 to 2018. It is also noticeable that during all the decades, the FORTH-RTM qualitatively reproduces the GDB indicated by both reference GEBA and BSRN station networks, exhibiting good performance. With respect to the magnitude of model GDB, it not necessarily follows the interdecadal changes suggested by the GEBA and BSRN stations (for example the GEBA brightening in the 2010s is about 2.8 times stronger than that in the 1990s, while the corresponding modeled one is 1 time, whereas the corresponding 2010s/1990s GDB ratios for BSRN stations are 7 for BSRN and 0.4 for FORTH-RTM), but this is of secondary importance compared to the similarity/dissimilarity of the estimated GDB itself.

Table 4.5. Agreement between the GDB (Δ(SSR)) of FORTH-RTM and GEBA stations over four different time periods. The percent number of GEBA stations for which the same sign of GDB is found with the corresponding model pixels is given, along with the average Δ(SSR) and the number of stations/pixels with brightening and dimming (shown in parentheses) for both GEBA and FORTH. Red and blue vectors indicate Brightening and Dimming, respectively.

GEBA Periods	Agreement (%)	GEBA Δ(SSR) (Wm^{-2})	GEBA (BRI, DIM)	FORTH_Pixel Δ(SSR) (Wm^{-2})	FORTH_Pixel (BRI, DIM)
1984–1989	71 (89)	-2.66 ↘	(240,278)	-1.14 ↘	(244,274)
1990–1999	62 (60)	0.91 ↗	(234,201)	5.72 ↗	(367,68)
2000–2009	67 (92)	3.44 ↗	(216,94)	2.31 ↗	(209,101)
2010–2018	73 (90)	2.53 ↗	(210,110)	5.97 ↗	(259,61)

Table 4.6. As in Table 4.5, but for BSRN stations

BSRN Periods	Agreement (%)	BSRN Δ(SSR) (Wm^{-2})	BSRN (BRI, DIM)	FORTH_Pixel Δ(SSR) (Wm^{-2})	FORTH_Pixel (BRI, DIM)
1992–1999	64 (100)	2.74 ↗	(7,4)	8.85 ↗	(9,2)
2000–2009	72 (0)	0.48 ↗	(19,13)	2.01 ↗	(22,10)
2010–2018	70 (100)	1.20 ↗	(20,20)	3.48 ↗	(28,12)

The results of the present study are comparable to those obtained with similar versions of the same model (FORTH-RTM), but using somewhat different input datasets and referring to much shorter time periods, i.e., 2001–2009 in (Hatzianastassiou et al., 2020) and 2001–2006 in (Hatzianastassiou et al., 2012) and numbers of GEBA/BSRN stations (105/20 in (Hatzianastassiou et al., 2020) and 91/14 in (Hatzianastassiou et al., 2012)), suggesting that the FORTH-RTM GDB has a good qualitative agreement with GEBA stations (for more than 60%) and a poorer, but still reasonable, agreement against the much smaller sample of BSRN stations, which is greatly affected by the number of available stations and it is larger than 54.5%. It

should be noted that the evaluation metrics of the FORTH-RTM SSR and GDB in this work are better than those in the previous Section in which only ISCCP-H cloud input data were used instead of the ISCCP-CLARA synergy (CLARISC) used, here. The ascertained improvement of the FORTH-RTM SSR and GDB allows us to use these datasets with greater confidence in the present analysis focusing on the contributions and causes of GDB.

4.3.3 Evaluation of FMC's SSR and OSR trends

SSR strongly depends on solar radiation absorbed and reflected in the overlying atmosphere at every location. Thus, an additional analysis was conducted to examine if the FORTH-RTM fluxes successfully represent the closure of the solar radiation budget with the aim of more fully assessing the robustness of the modeled GDB. To achieve this, specific GEBA/BSRN stations that offer GDB agreement with the model were initially chosen. Then, the computed trends of the FORTH-RTM Outgoing Solar Radiation (OSR) at TOA for these stations were compared to the matching OSR from CERES-EBAF satellite data for the time period 01/2001–12/2018 to investigate if they agree or disagree in terms of the sign of Δ(OSR). For those sites where both the modeled Δ(SSR) and Δ(OSR) qualitatively agree with the corresponding reference surface and satellite measurements, the Earth's SW radiation budget is successfully closed. It should be noted that in this case, the available number of stations is 211 for GEBA and 23 for BSRN based on the criterion according to which each station should have availability of more than 70% of the number of months for the entire time period (2001–2018). It should be noted that, during this period, the MERRA-2 products assimilated modern satellite data, leading to a more homogenous time series (Korras-Carraca et al., 2021) for the FORTH-RTM aerosol input data. In this case, with a shorter time period than previously (1984–2018), the level of agreement between the sign of slopes of stations and FORTH-RTM pixels didn't change neither for GEBA nor BSRN. Figure 4.21 compares the signs of the computed FORTH-RTM Δ(SSR) and Δ(OSR) with the equivalent GEBA/BSRN Δ(SSR) and CERES-EBAF Δ(OSR) signs. At the surface, 79.6% of GEBA (168 out of 211) stations and 65.2% of BSRN (15 out of 23) stations agree with FORTH-RTM in terms of Δ(SSR) sign (blue dots in Figure 4.21 (i-a,ii-a), respectively). Then, just for those stations (providing agreement on the surface), the signs of Δ(OSR) from FORTH-RTM and CERES were compared. Out of the 168 GEBA sites, there was qualitative agreement at TOA for 145 stations, i.e., in 86.3% of them. Accordingly, an agreement was observed for 86.6% of the 15 BSRN locations, which is almost equal to the percentage for GEBA. Overall, 145/13 (68.7/62.5%) of GEBA/BSRN stations provided agreement in the sign of both Δ(SSR) and Δ(OSR). The obtained results of this part of the analysis, focusing on the comparison between the changing solar fluxes at the Earth's surface and TOA as estimated with the FORTH-RTM against reference surface and TOA fluxes, prove that FORTH-RTM quite satisfactorily reproduces the changing SW radiation budget and especially GDB.

The evaluation of flux change trends at both the surface and the top of the atmosphere was conducted globally using data from CERES for the period 2001–2018 as it is shown in Figure 4.22. It is important to note that CERES directly measures the OSR at the TOA, while SSR fluxes are derived using a specialized retrieval algorithm, resulting in a highly reliable database for both OSR and SSR. A comparison of the sign of the SSR trends between the FORTH-RTM and CERES shows agreement in 75% of the pixels worldwide. Both datasets indicate brightening over Europe, South Africa, Brazil, many parts of the tropical

Pacific Ocean, and the ocean west of the USA. They also concur on dimming trends over India, the Middle East,

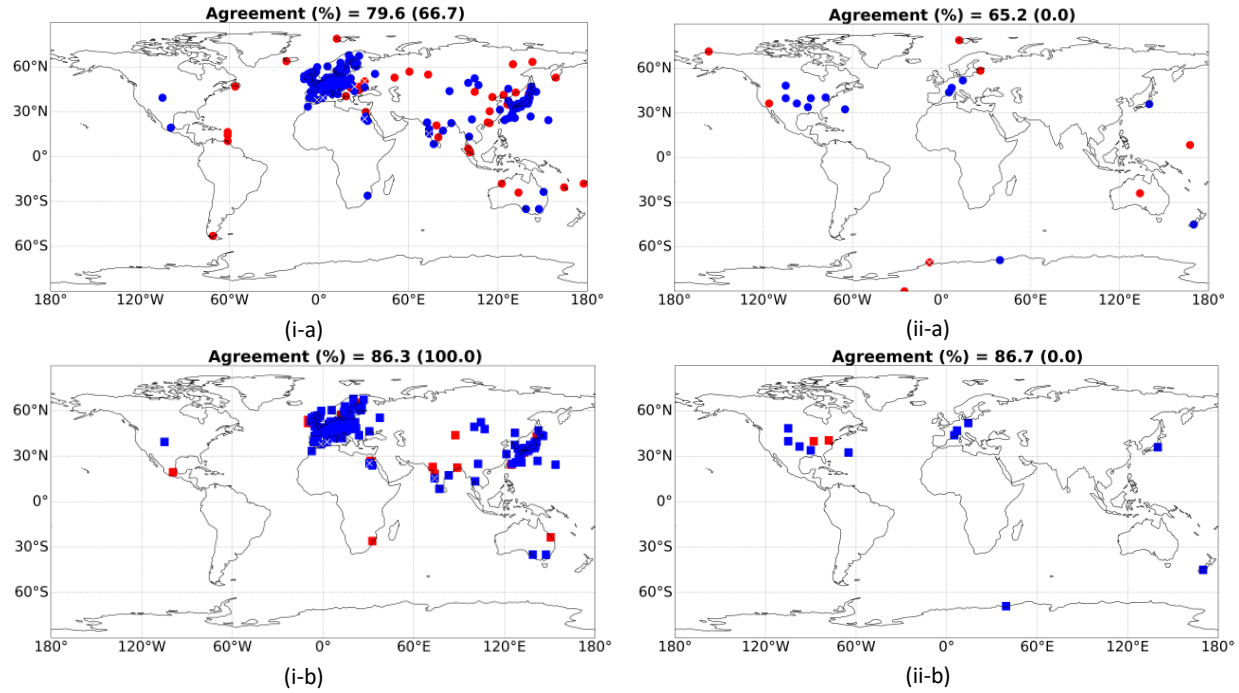


Figure 4.21. Agreement (blue dots) and disagreement (red dots) between trends of FORTH-RTM and station deseasonalized SSR anomalies (Δ(SSR)), for GEBA (i-a) and BSRN (ii-a) stations for the period 01/2001–01/2018. The stations showing agreement at the surface against GEBA stations (i-a) and BSRN stations (ii-a), also having agreement of Δ(OSR) with CERES at TOA, during the same period, are shown in (i-b,ii-b), respectively, with blue rectangles, while those having disagreement at TOA with red rectangles. The embedded white "×" symbols indicate the statistically significant trends for both FORTH-RTM and stations. At the top of each figure, the percentage number of stations (a) and CERES pixels (b) that agree in the sign of slopes with the FORTH-RTM pixels is shown.

the Sahara, Central Africa, the Arctic, and parts of the tropical ocean. However, discrepancies are observed in Australia, parts of Asia, and South America. The global mean flux change for the model is -0.061 $Wm^{-2}decade^{-1}$, compared to 0.029 $Wm^{-2}decade^{-1}$ for CERES, with the difference primarily attributed to stronger negative trends in the model. Similarly, trends at the top of the atmosphere were analyzed. Both datasets exhibit a global mean reduction, with values of -0.225 $Wm^{-2}decade^{-1}$ for the model and -0.65 $Wm^{-2}decade^{-1}$ for CERES. The smaller reduction in the model is mainly due to stronger increasing trends in certain regions, particularly over marine areas with persistent cloud cover, such as west of South America and South Africa. Overall, agreement in OSR trends is found in 73% of the global pixels. Both the model and CERES capture the reduction of OSR over Europe, South Africa, America, the Arctic, the Southern Ocean, parts of the tropical Pacific Ocean, and large regions of Asia. Agreement is also observed in the increasing OSR trends over specific oceanic regions, the sea south of South America, the Persian Gulf, and Indonesia. Some disagreement is found in parts of India, the Middle East, Asia, and certain oceanic areas. Overall, the percentage of pixels where the model agrees with CERES at both the surface and the top of the atmosphere is 62%, indicating a satisfactory performance in capturing the shortwave radiation budget trends during 2001-2018.

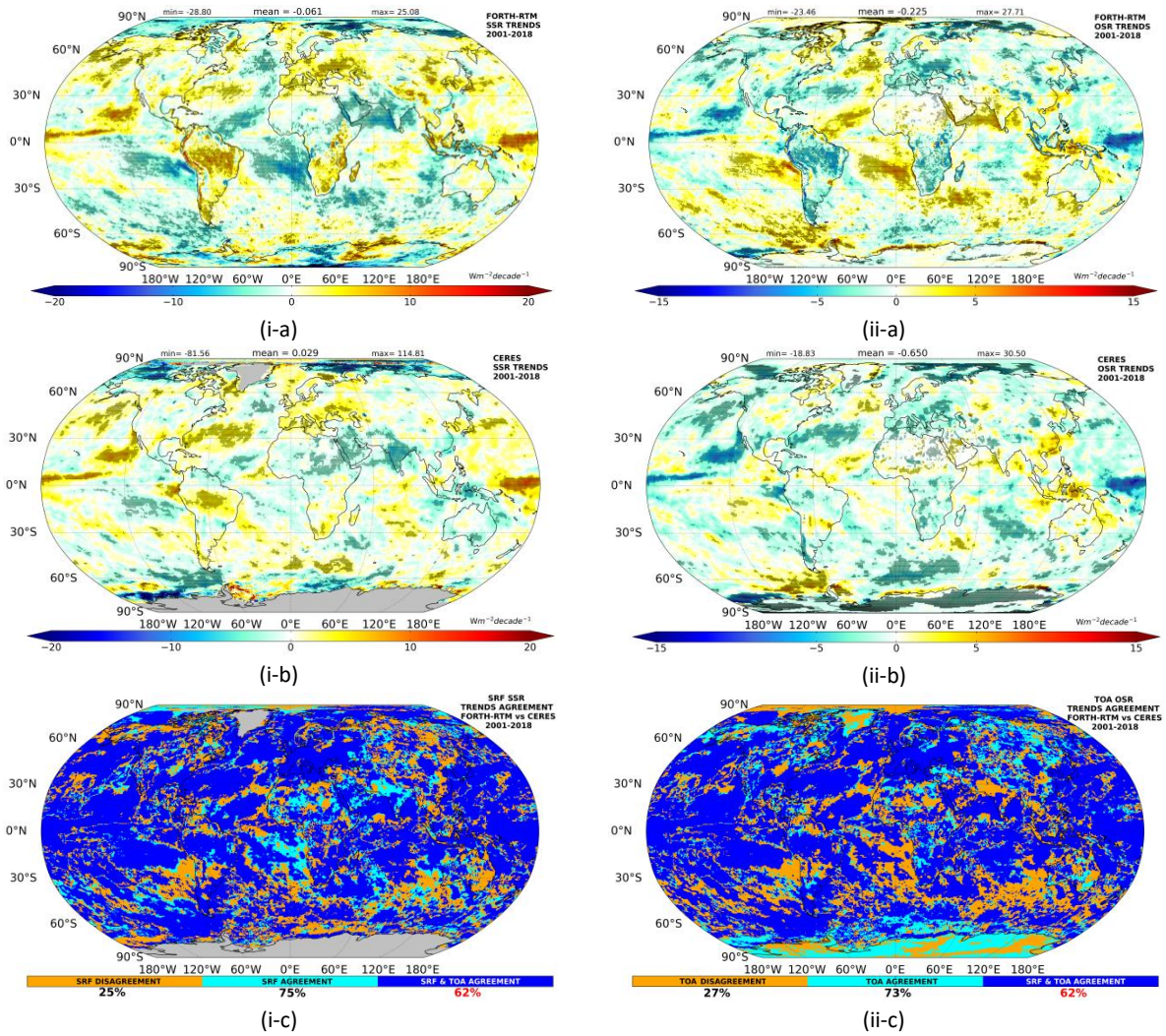


Figure 4.22. Computed SSR (i) and OSR (ii) trends, in $Wm^{-2}decade^{-1}$ for FORTH-RTM (a) and CERES (b). Negative values, shown in blue and green colors, indicate reduction, and positive values, in yellow, orange, and red colors, indicate increase. The embedded black dot symbols indicate trends that are statistically significant (at the 95% confidence level, assessed by applying the non-parametric Mann–Kendall test). The agreement in the sign of the SSR (i-c) and OSR (i-c) trends is indicating with cyan (agreement only at the surface or TOA) and blue colors (agreement both in surface and TOA) while the disagreement is indicating with orange. Along with the colorbar the percentage of the pixels that show the corresponding agreements are shown.

4.4 SSR and GDB Intercomparisons

The evaluation results at Section 4.3 demonstrated a generally nice agreement between the FORTH-RTM and reference measurements for both SSR and GDB. These results were compared with previous evaluations of the same model using different input datasets, revealing that FMC, the latest version of the model, exhibits the best performance so far. Given this, it was deemed appropriate to extend the evaluation to other SSR databases and their corresponding GDB, comparing them to FMC. A comprehensive evaluation was conducted for a total of ten different SSR databases over the entire study period (1984–2018). The performance of FMC was analyzed in relation to other SSR and GDB datasets to determine its relative standing among various simulations. The datasets used in the comparison include

FMI, FMC, ERA5, MERRA-2, JRA55, GFDL_CM2p1, NCEP-R1, NCEP-R2, ISCCP_HXG and W5E5 (Section 2.1.5). To ensure consistency, all databases were adjusted to match the availability of FMC data, allowing for direct comparisons over the same months and geographic regions. The evaluation commenced with a comparison of SSR and GDB against ground-based measurements from GEBA and BSRN, following the methodology outlined in Section 2.2.

4.4.1 Intercomparison for 1984-2018

Using deseasonalized SSR anomalies, the highest correlation with the ground-based stations was observed for ERA5, with correlation coefficients of 0.76 against GEBA and 0.72 against BSRN. FMC followed closely, with values of 0.75 and 0.71, respectively, while FMI ranked third with 0.74 and 0.71. The poorest performance was exhibited by GFDL_CM2p1, which showed negligible correlation. When evaluating absolute SSR fluxes, all datasets demonstrated strong correlations ranging from 0.90 to 0.98, with ERA5 again achieving the highest values. These findings indicate that both FMC and FMI effectively capture the month-to-month variability of SSR, placing them among the best datasets in terms of monthly correlation. Regarding BIAS, GFDL_CM2p1 exhibited the smallest BIAS against GEBA, with a value of 3.07 Wm^{-2}. FMC ranked fourth with a BIAS of 4.46 Wm^{-2}, while FMI recorded a slightly lower BIAS of -4.38 Wm^{-2}. Against BSRN, the lowest BIAS was observed in W5E5, with FMC securing third place at -2.49 Wm^{-2}. Conversely, the largest BIAS was found in NCEP-R1, with values reaching 50.65 Wm^{-2} and 37.76 Wm^{-2} for GEBA and BSRN, respectively. Similar trends were observed for the relative BIAS. Examining the RMSE, ISCCP_HGX exhibited the lowest RMSE against GEBA at 19.66 Wm^{-2}, with FMC ranking fifth at 20.93 Wm^{-2}, though the differences among the top datasets were minimal. Against BSRN, ERA5 had the lowest RMSE at 18.65 Wm^{-2}, while FMC ranked sixth with a value of 29.02 Wm^{-2}. The highest RMSE was recorded for NCEP-R1, with similar patterns observed in the relative RMSE analysis. A critical metric in this study was the agreement in the sign of the GDB trends. Against GEBA, FMC demonstrated the highest agreement at 79.62%, followed by ERA5 and W5E5 at 78.2%, with FMI ranking fourth at 65.88%. Against BSRN, FMC again led with an agreement of 65.22%, while FMI ranked fifth at 52.17%. When analyzing statistically significant trends, ERA5 exhibited the highest agreement at 93.85%, followed by FMC at 89.76%, with FMI ranking fourth at 79.59%. Against BSRN, which however are only 4 stations with statistically significant trends, GFDL_CM2p1 achieved a 100% agreement, while FMC ranked second at 87.5%, and FMI ranked sixth at 50%. Overall, these results highlight that FMC is the top-performing dataset in qualitative agreement for GDB when compared to observational measurements, further reinforcing its reliability. Additionally, FMC ranks among the best-performing datasets for SSR, enhancing confidence in its ability to study long-term GDB trends on a global scale. Tables 4.7a and 4.7b represents this ranking for each evaluation metric in order to distinguish the dataset with the best and the worst performance on SSR and GDB against GEBA an BSRN stations, respectively.

Table 4.8 provides the average SSR values for the entire planet, as well as for land and ocean regions across all datasets. FMC recorded an average SSR of 196.3 Wm^{-2} globally, with values of 198.3 Wm^{-2} over land and 195.5 Wm^{-2} over the ocean. The highest values were observed in NCEP-R1 (221.2 Wm^{-2} globally), while the lowest were recorded in FMI (187.2 Wm^{-2} globally). FMC's global SSR has the smallest

Table 4.7a. The ranked SSR datasets from the best to the worst based on the validation against GEBA stations for the time period 1984-2018.

Ranked Dataset vs GEBA	R-anomalies	R-fluxes	Bias	%-Bias	RMSE	%RMSE	Agreement
1	ERA5	ERA5	GFDL_CM2p1	GFDL_CM2p1	ISCCP_HXG	ISCCP_HXG	**FMC**
2	**FMC**	ISCCP_HXG	ISCCP_HXG	ISCCP_HXG	FMI	FMI	W5E5
3	FMI	W5E5	FMI	FMI	W5E5	W5E5	ERA5
4	ISCCP_HXG	FMI	**FMC**	**FMC**	ERA5	ERA5	FMI
5	W5E5	**FMC**	W5E5	W5E5	**FMC**	**FMC**	GFDL_CM2p1
6	JRA55	JRA55	ERA5	ERA5	JRA55	JRA55	MERRA2
7	MERRA2	MERRA2	JRA55	JRA55	MERRA2	MERRA2	NCEP1
8	NCEP2	NCEP1	MERRA2	MERRA2	GFDL_CM2p1	GFDL_CM2p1	JRA55
9	NCEP1	NCEP2	NCEP2	NCEP2	NCEP2	NCEP2	ISCCP_HXG
10	GFDL_CM2p1	GFDL_CM2p1	NCEP1	NCEP1	NCEP1	NCEP1	NCEP2

Table 4.7b. The ranked SSR datasets from the best to the worst based on the validation against BSRN stations for the time period 1992-2018.

Ranked Dataset vs BSRN	R-anomalies	R-fluxes	Bias	%-Bias	RMSE	%RMSE	Agreement
1	ERA5	ERA5	W5E5	W5E5	ERA5	ERA5	**FMC**
2	FMI	W5E5	GFDL_CM2p1	GFDL_CM2p1	W5E5	W5E5	NCEP2
3	**FMC**	ISCCP_HXG	**FMC**	**FMC**	ISCCP_HXG	ISCCP_HXG	ERA5
4	ISCCP_HXG	JRA55	ERA5	ERA5	JRA55	JRA55	NCEP1
5	W5E5	FMI	ISCCP_HXG	ISCCP_HXG	MERRA2	MERRA2	W5E5
6	JRA55	MERRA2	MERRA2	MERRA2	FMI	FMI	FMI
7	MERRA2	**FMC**	JRA55	JRA55	**FMC**	**FMC**	JRA55
8	NCEP2	NCEP1	FMI	FMI	GFDL_CM2p1	GFDL_CM2p1	MERRA2
9	NCEP1	NCEP2	NCEP2	NCEP2	NCEP2	NCEP2	ISCCP_HXG
10	GFDL_CM2p1	GFDL_CM2p1	NCEP1	NCEP1	NCEP1	NCEP1	GFDL_CM2p1

difference/relative difference with the ISCCP_HXG equal to -0.4 Wm^{-2}/ -0.2%. Over land, FMC has the lowest difference/relative difference against the FMI which is equal to -4.2 Wm^{-2} / -2.1% followed by the W5E5 with difference/relative difference equal to 8.3 Wm^{-2} / 4.2%. On the other hand, over oceans, FMC has the lowest difference/relative difference against the NCEP-R2 which is equal to 1.9 Wm^{-2} / 1%.

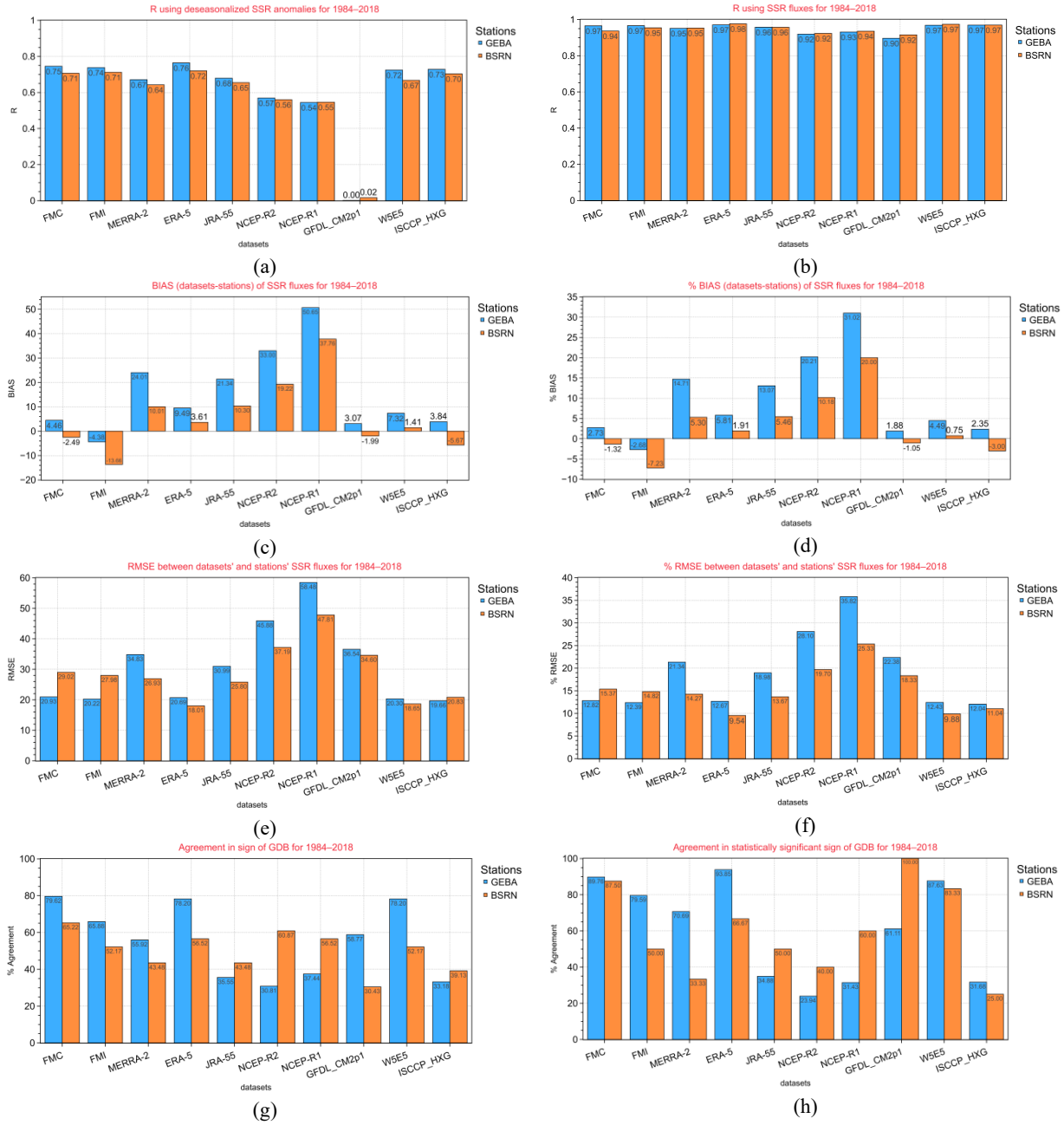


Figure 4.23. The evaluation metrics of the 10 SSR and GDB datasets against ground-truth measurements from GEBA (blue) and BSRN (orange) for the entire time-period 1984-2018. The metrics were: the R using deseasonalized SSR anomalies (a) and SSR fluxes (b), the BIAS (c) and the relative BIAS (d), the RMSE (e) and the relative RMSE (f), along with the agreement in sign of slopes (g) and the agreement for only statistically significant trends at 96% confidence level (h).

Figure 4.24 presents the series of annual mean SSR values (Figure 4.24a) and SSR anomalies (Figure 4.24b) during the time-period of 1984-2018, revealing significant SSR deviations before the year 2000, with relatively smoother fluctuations thereafter (due to assimilation of satellite data). NCEP-R1 exhibited noticeably high SSR fluxes, while FMI displayed the lowest values (as it was also observed in the Table 4.10). These averages are further illustrated through box plots (Figure 4.24c) and the annual cycle (Figure

Table 4.8. Spatially averaged SSR (Wm^{-2}) values among the 10 datasets for the total globe, for land and oceans. Along with the average values, the differences and the relative differences between each dataset and the FMC (dataset - FMC) are shown.

name	globe	land	ocean	dif_globe	dif_land	dif_ocean	dif_globe (%)	dif_land (%)	dif_ocean (%)
FMC	196.3	198.3	195.5	0	0	0	0	0	0
FMI	187.2	194.1	184.5	-9.1	-4.2	-11.1	-4.6	-2.1	-5.7
MERRA2	198.7	215.1	192.1	2.4	16.8	-3.4	1.2	8.5	-1.8
ERA5	201.1	209.1	197.8	4.7	10.8	2.3	2.4	5.4	1.2
JRA55	203.3	217.2	197.7	7	18.9	2.2	3.5	9.5	1.1
NCEP2	202	213.3	197.5	5.7	15	1.9	2.9	7.6	1
NCEP1	221.2	244.9	211.7	24.9	46.6	16.1	12.7	23.5	8.3
GFDL_CM2p1	201.1	208.4	198.1	4.8	10.2	2.6	2.4	5.1	1.3
W5E5	200.3	206.6	197.7	3.9	8.3	2.2	2	4.2	1.1
ISCCP_HXG	196	206.7	191.6	-0.4	8.4	-3.9	-0.2	4.2	-2

4.24d), confirming that all models capture the expected seasonal SSR variations, with peaks during summer months in each hemisphere (June and December) and minima during equinoxes (March and September).

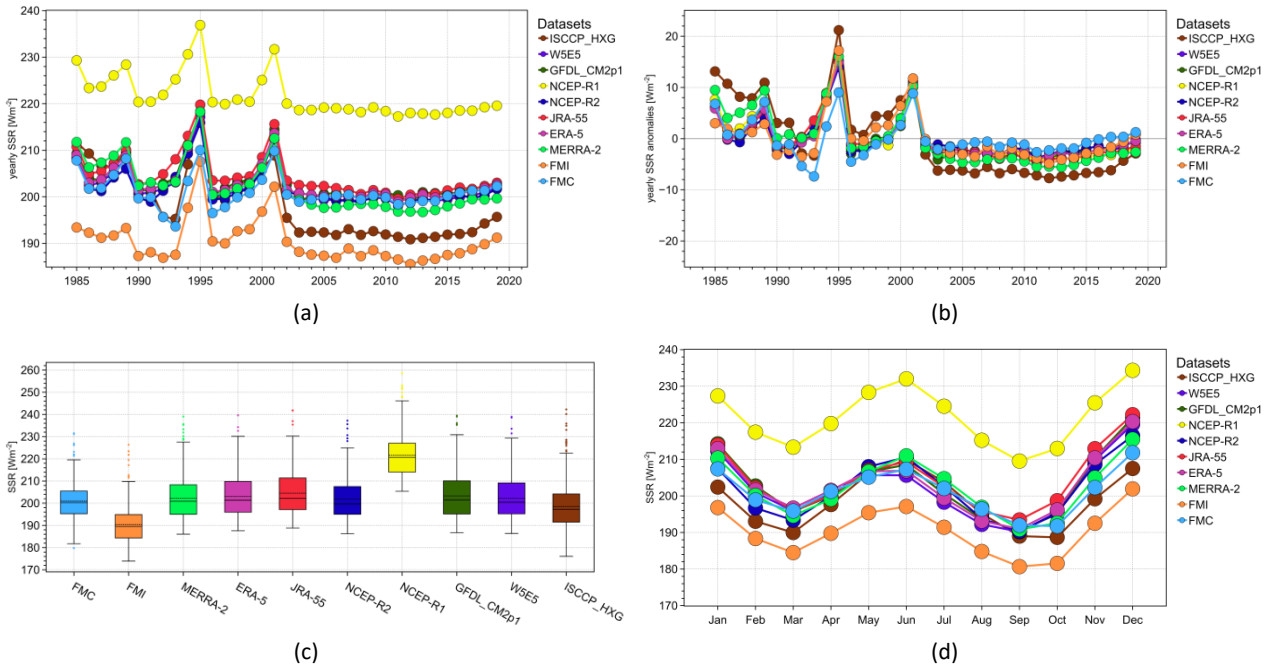


Figure 4.24. This figure illustrates comparisons within the 10 datasets for the time-period 1984-2018 for annual globally averaged SSR (a) and SSR annual anomalies (b) along with the box-plot comparison (c) and the annual cycle of SSR (d).

Further analysis was conducted to compare SSR trend patterns across all simulations, as depicted in Figure 4.25. The results indicate an overall increase in SSR over most land areas, except for localized dimming observed over India, Southeast China, and parts of the Sahara. Dimming is more widespread over ocean regions, particularly in the Southern Ocean and west of continental landmasses where persistent anticyclones prevail. These general patterns are largely reproduced by other datasets. For example, FMI, ISCCP_HGX, JRA55, and MERRA-2 exhibit similar brightening trends over Europe, with partial agreement

from ERA5 and W5E5. However, FMI uniquely suggests significant brightening over Australia, partially supported by ISCCP_HGX. Most models indicate declining SSR over India, with FMC, NCEP-R1, and NCEP-R2 aligning in their depiction of northern India, while GFDL_CM2p1 entirely contradicts this trend. For Southeast Asia, FMC predominantly shows dimming, aligning with FMI, ERA5, MERRA-2, and ISCCP_HGX, whereas W5E5, the NCEP datasets, JRA55, and GFDL_CM2p1 differ. Brightening trends over the Americas in FMC align with JRA55, while in southern Africa, GFDL_CM2p1, JRA55, and ISCCP_HGX support FMC's findings. Dimming west of the continental coasts is corroborated by ERA5, MERRA-2, and GFDL_CM2p1, while the Southern Ocean dimming trend is reinforced by FMI, ERA5, MERRA-2, and GFDL_CM2p1. In the polar regions, most models indicate no strong trends, with FMI partially agreeing in Antarctica but contradicting Arctic brightening trends.

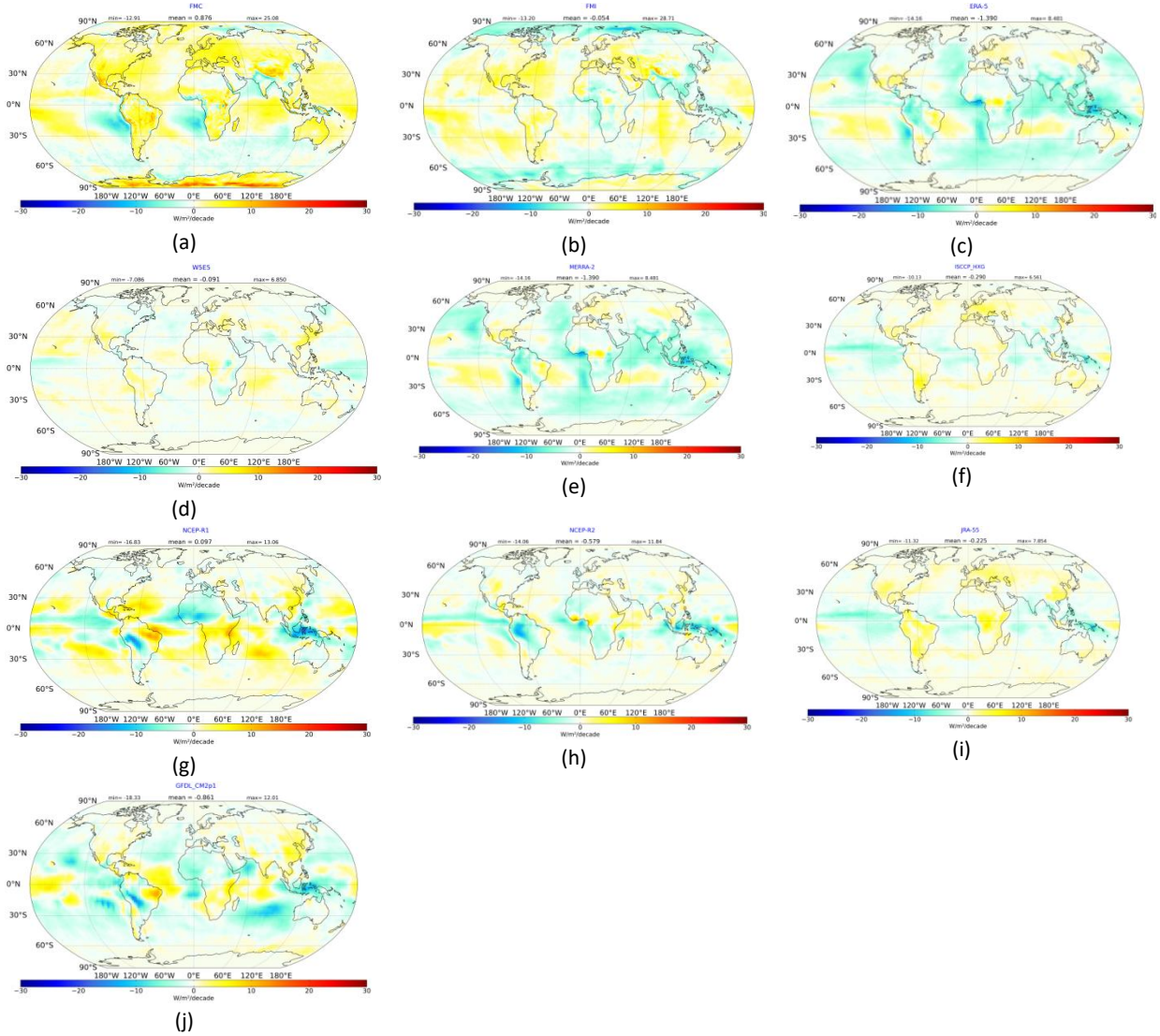


Figure 4.25. Global distribution of GDB ($Wm^{-2}decade^{-1}$) during 1984-2018 among the 10 datasets namely FMC (a), FMI (b), ERA5 (c), W5E5 (d), MERRA-2 (e), ISCCP_HXG (f), NCEP-R1 (g), NCEP-R2 (h), JRA-55 (i), and GFDL_CM2p1 (j). Yellow-red colors indicate increasing SSR trends while blues indicate decreasing SSR trends.

Figure 4.26 highlights areas where FMC's GDB aligns with the two best-performing models, ERA5 and W5E5. The three datasets concur on brightening over Europe, South America, Antarctica, the Arctic, Mexico, central Africa, eastern Australia, and parts of central Asia, along with oceanic regions east of the USA and tropical waters. Similarly, they agree on SSR reductions over the northern Indian Ocean, Southern Ocean, coastal waters west of continents, and the Persian Gulf. When considering the top four models (ERA5, W5E5, MERRA-2, and FMI), agreement is found for brightening over the Mediterranean, northeastern Europe, Mexico, central Africa, South America, Australia, and Antarctica, while dimming is consistently observed in the Southern Ocean, Persian Gulf, and Indian Ocean. Agreement declines when six models are included (adding NCEP-R1 and R2), with only a few common areas remaining for both brightening and dimming trends. Full agreement among all models is rare, with widespread brightening observed in only a few locations, such as parts of Eastern Europe and Central America, while dimming remains largely confined to the Southern Ocean and the Indonesian Gulf.

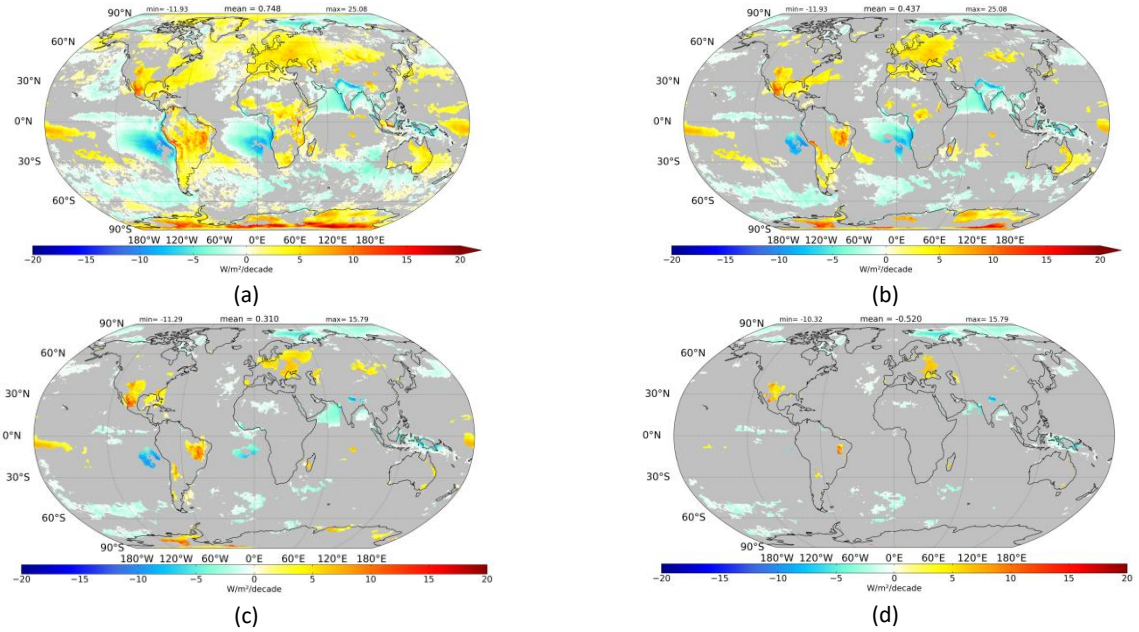


Figure 4.26 Global distribution of the FMC GDB ($Wm^{-2}decade^{-1}$) during 1984-2018 over areas where FMC agrees with the 2 top-performing datasets (a) with the 4 best datasets (b), with the 6 best datasets (c) and with all datasets (d). Yellow-red colors indicate increasing SSR trends while blues indicate decreasing SSR trends.

Also, Figure 4.27 provides an overview of the GDB (spatially averaged GDB) for the entire planet, NH, SH, as well as for land and ocean. FMC recorded an average GDB of 0.88 Wm^{-2}/decade globally, with values of 2.58 Wm^{-2}/decade over land and 0.2 Wm^{-2}/decade over oceans. It should be noted that FMC exhibits positive average GDB values everywhere except the SH ocean, diverging from the global dimming trend observed in most other datasets, a result attributed to its higher or more spatially extend estimates of brightening. Over land, the FMC brightening is in line only with ERA5 and W5E5 while the other datasets show dimming. Above oceans, only NCEP-R2 agrees in the brightening over the global ocean while over the SH ocean where dimming occurred in FMC this is in line with all other datasets except for NCEP-R2. In general, across most regions the majority of datasets shows a dimming, while over land only FMC and ERA5, along with W5E5 show brightening. However, these 3 datasets have shown the best performance

in terms of agreement in the sign of GDB against the land-based stations. Thus, what the majority of the datasets indicates may not necessarily be true, which is why the GDB signs, whether globally or especially over oceans, are questionable and require more effort and caution for their assessment. Furthermore, it is important to recognize that regional variations may not always be fully captured by global or hemispherical averages, underscoring the importance of detailed regional analysis which can be shown in Figure 4.28 where the GDB averaged spatially only over specific 18 land regions of the planet.

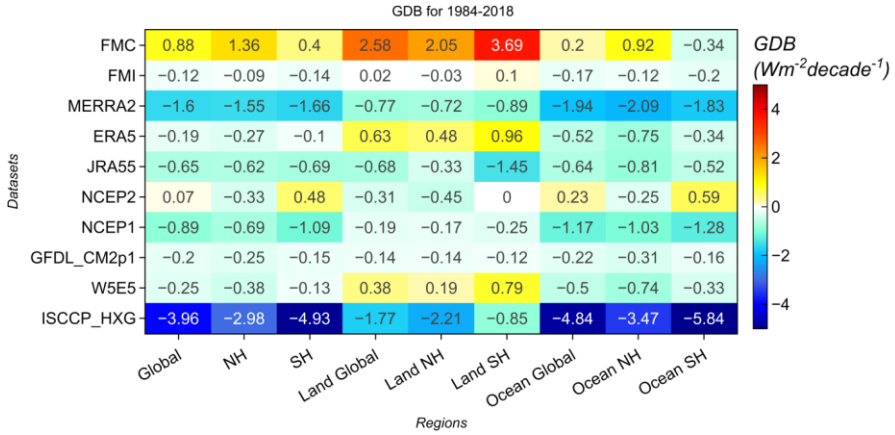


Figure 4.27. The spatially averaged GDB (in $Wm^{-2}decade^{-1}$) of each dataset over the globe, the two hemispheres and the globe's and the two hemispheres' land and ocean areas during the entire study period 1984-2018. Reddish/bluish colors indicate brightening/dimming.

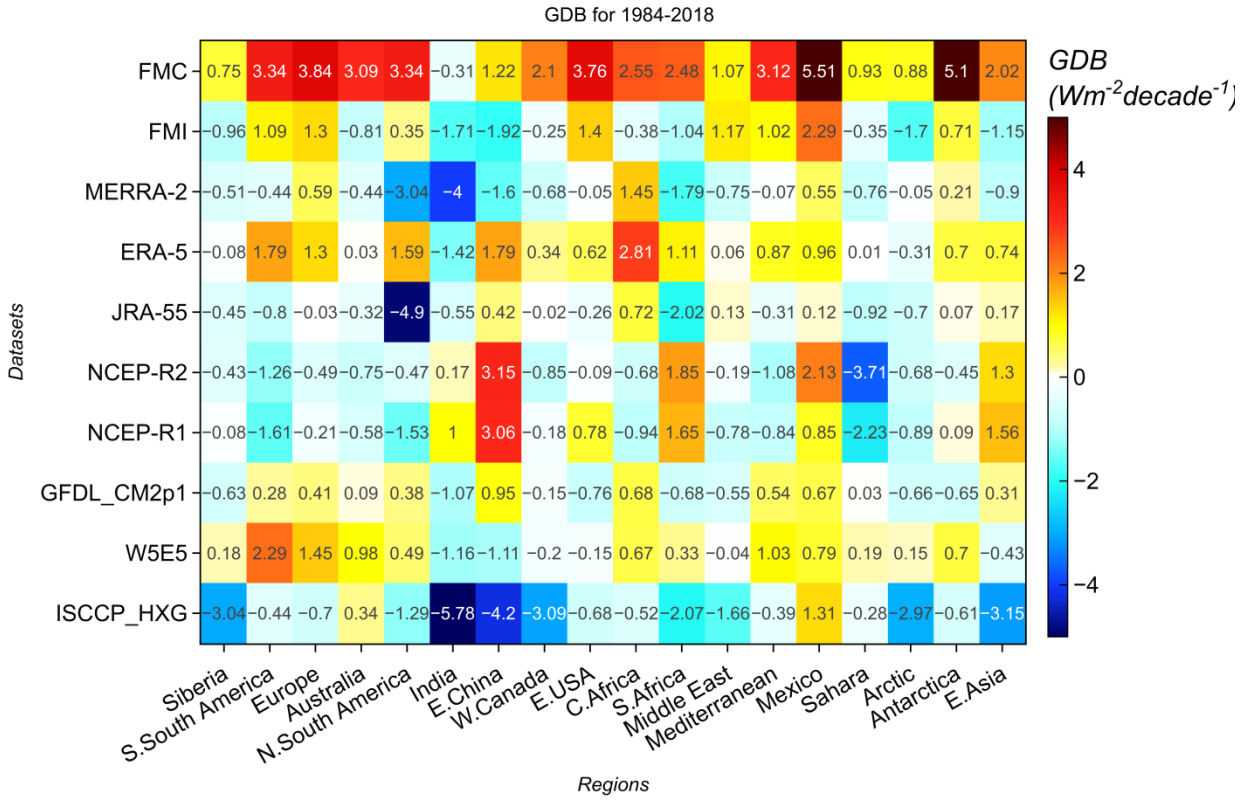


Figure 4.28. The spatially averaged GDB (in $Wm^{-2}decade^{-1}$) over the specific 18 land areas during the entire study period 1984-2018. Reddish/bluish colors indicate brightening/dimming.

Now, exploring the averaged GDB over land regions, much more datasets agree with the FMC brightening (with varying magnitudes) in many regions while a disagreement continues to exist in some other regions for some datasets. For instance, over Europe, FMC, FMI, MERRA-2, ERA5, W5E5 and GFDL_CM2p1 agree in the brightening while over India all the datasets show a dimming except for NCEP-R1 and –R2. Over East China, the FMC suggests a brightening (equal to 1.22 $Wm^{-2}decade^{-1}$) which is in line with ERA5, JRA55, NCEP-R1 and -R2, and GFDL_CM2p1 while disagrees with FMI, MERRA-2, W5E5 and ISCCP_HXG. Note that FMC and FMI disagree in the case of East China (and East Asia) while the only difference between them was the different cloud input but with the same aerosol data, indicating again the crucial impact on the cloud input data (and their trends). Also, the unique case where all datasets agree for the brightening is over Mexico.

This extensive study underscores the substantial variations in GDB trends among different models, even in adjacent regions, emphasizing the necessity of validation against observational data. Furthermore, the strong agreement of FMC with the two best-performing models (ERA5 and W5E5) over approximately 60% of the planet enhances confidence in its reliability, particularly in key regions such as Europe, South America, northern India, the oceanic regions west of continents, and the Southern Ocean.

4.4.2 Intercomparison for 2001-2018

A thorough evaluation was carried out for twelve different SSR databases over the study period (2001–2018). This additional analysis was performed to include in the datasets the exceptional CERES satellite product and to focus on the shorther and more recent time period. FMC's performance was assessed in comparison with other SSR and GDB datasets to determine its relative accuracy among various simulations. The datasets included in the analysis are FMI, FMC, CERES, CLARA, ERA5, MERRA-2, JRA55, GFDL_CM2p1, NCEP-R1, NCEP-R2, ISCCP_HXG, and W5E5. To ensure consistency, all databases were adjusted to align with FMC's data availability, enabling direct comparisons over the same months and geographic regions. The evaluation began with a comparison of SSR and GDB against ground-based measurements from GEBA and BSRN, following the methodology detailed in previous chapters.

As it is shown in Figure 4.29, using deseasonalized SSR anomalies, the highest correlation with the reference stations was observed for CERES, with correlation coefficients of 0.87 for GEBA and 0.75 for BSRN. CLARA followed closely, with values of 0.87 and 0.73, respectively, while FMC ranked fourth with 0.85 and 0.72. FMI is ranked fifth together with ERA5 with R values equal to 0.83 and 0.71 against GEBA and BSRN, respectively. The poorest performance was exhibited by GFDL_CM2p1, which showed negligible correlation. When evaluating absolute SSR fluxes, all datasets demonstrated strong correlations ranging from 0.91 to 0.99, with CERES again achieving the highest values. These findings indicate that both FMC and FMI effectively capture the month-to-month variability of SSR, placing them among the best datasets in terms of monthly correlation. Regarding BIAS, CLARA exhibited the smallest BIAS against GEBA, with a value of 1.3 Wm^{-2}. FMC ranked fifth along with ERA5 with a BIAS of 5.3 Wm^{-2}, while FMI recorded a slightly higher BIAS of -7.4 Wm^{-2}. Against BSRN, the lowest BIAS was observed in FMC equal to -0.3

Wm^{-2}, with CERES to be following with BIAS equal to -0.4 Wm^{-2}, while FMI shows quite larger BIAS of -13.8 Wm^{-2}. Conversely, the largest BIAS was found in NCEP-R1, with values reaching 45.7 Wm^{-2} and 37.3 Wm^{-2} for GEBA and BSRN, respectively. Similar patterns were observed for the relative BIAS. Examining the RMSE, CERES exhibited the lowest RMSE against GEBA at 13.43 Wm^{-2}, with FMC ranking fifth at 16.45 Wm^{-2}, though the differences among the top datasets were minimal. Against BSRN, CERES had the lowest RMSE at 16.65 Wm^{-2}, while FMC ranked fifth with a value of 25.13 Wm^{-2}. The highest RMSE was recorded for NCEP-R1, with similar patterns observed in the relative RMSE analysis. A critical metric in this study was the agreement in the sign of the GDB trends. Against GEBA, CERES demonstrated the highest agreement at 76%, followed, with small difference, by FMC and W5E5 at 74%, with FMI ranking fourth at 70%. Against BSRN, CERES and FMC together led with a top agreement of 68%, while FMI ranked fifth at 52%. When analyzing statistically significant trends, ISCCP_HXG exhibited the highest agreement at 96%, followed by FMI at 95%, with FMC ranking sixth at 79%. Against BSRN, which however are only 4 stations with statistically significant trends, all datasets achieved a 100% agreement except for NCEP-R1, -R1 and GFDL_CM2p1 which have much lower agreement equal to 50%, 50% and 0% respectively. Overall, these results highlight that CERES and FMC are both top-performing datasets in qualitative agreement for GDB when compared to observational measurements during 2001-2018, further reinforcing its reliability. Additionally, FMC ranks among the best-performing datasets for SSR, enhancing confidence in its ability to study long-term GDB trends on a global scale. Along with the Figure 4.29, Tables 4.9a and 4.9b represents this ranking for each evaluation metric in order to distinguish the dataset with the best and the worst performance on SSR and GDB against GEBA an BSRN stations, respectively.

Table 4.9a. The ranked SSR datasets from the best to the worst based on the validation against GEBA stations for the time period 2001-2018.

Ranked Dataset vs GEBA	**R-anomalies**	**R-fluxes**	**Bias**	**%-Bias**	**RMSE**	**%RMSE**	**Agreement**
1	CERES	CERES	CLARA	CLARA	CERES	CERES	CERES
2	CLARA	ISCCP_HXG	GFDL_CM2p1	GFDL_CM2p1	ISCCP_HXG	ISCCP_HXG	W5E5
3	ISCCP_HXG	ERA5	ISCCP_HXG	ISCCP_HXG	CLARA	CLARA	**FMC**
4	**FMC**	**FMC**	CERES	CERES	W5E5	W5E5	ISCCP_HXG
5	ERA5	W5E5	**FMC**	**FMC**	**FMC**	**FMC**	CLARA
6	FMI	CLARA	W5E5	W5E5	ERA5	ERA5	FMI
7	W5E5	FMI	ERA5	ERA5	FMI	FMI	ERA5
8	MERRA2	JRA55	FMI	FMI	JRA55	JRA55	MERRA2
9	JRA55	MERRA2	JRA55	JRA55	MERRA2	MERRA2	GFDL_CM2p1
10	NCEP2	NCEP1	MERRA2	MERRA2	GFDL_CM2p1	GFDL_CM2p1	JRA55
11	NCEP1	NCEP2	NCEP2	NCEP2	NCEP2	NCEP2	NCEP2
12	GFDL_CM2p1	GFDL_CM2p1	NCEP1	NCEP1	NCEP1	NCEP1	NCEP1

Table 4.9b. The ranked SSR datasets from the best to the worst based on the validation against BSRN stations for the time period 2001-2018.

Ranked Dataset vs BSRN	R-anomalies	R-fluxes	Bias	%-Bias	RMSE	%RMSE	Agreement
1	CERES	CERES	**FMC**	**FMC**	CERES	CERES	CERES
2	ISCCP_HXG	ERA5	CERES	CERES	ERA5	ERA5	**FMC**
3	CLARA	W5E5	W5E5	W5E5	W5E5	W5E5	CLARA
4	**FMC**	ISCCP_HXG	GFDL_CM2p1	GFDL_CM2p1	ISCCP_HXG	ISCCP_HXG	W5E5
5	FMI	FMI	ERA5	ERA5	**FMC**	**FMC**	MERRA2
6	ERA5	JRA55	CLARA	CLARA	JRA55	JRA55	ERA5
7	W5E5	MERRA2	ISCCP_HXG	ISCCP_HXG	MERRA2	MERRA2	JRA55
8	JRA55	**FMC**	JRA55	JRA55	CLARA	CLARA	ISCCP_HXG
9	MERRA2	CLARA	MERRA2	MERRA2	FMI	FMI	FMI
10	NCEP2	NCEP1	FMI	FMI	GFDL_CM2p1	GFDL_CM2p1	NCEP2
11	NCEP1	NCEP2	NCEP2	NCEP2	NCEP2	NCEP2	NCEP1
12	GFDL_CM2p1	GFDL_CM2p1	NCEP1	NCEP1	NCEP1	NCEP1	GFDL_CM2p1

Table 4.10 provides the average SSR values for the entire planet, as well as for land and ocean regions across all datasets. FMC recorded an average SSR of 196.1 Wm^{-2} globally, with values of 198.1 Wm^{-2} over land and 195.3 Wm^{-2} over the ocean. The highest values were observed in NCEP-R1 (216.3 Wm^{-2} globally), while the lowest were recorded in FMI (184.2 Wm^{-2} globally). FMC's global SSR has the smallest difference/relative difference with the W5E5 equal to 0.2 Wm^{-2} / 0.1%. Over land, FMC has the lowest difference/relative difference against the ISCCP_HXG which is equal to 0.2 Wm^{-2} / 0.1% followed by the CERES with difference/relative difference equal to 0.5 Wm^{-2} / 0.2%. On the other hand, over oceans, FMC has the lowest difference/relative difference against the W5E5 which is equal to 0 Wm^{-2} / 0%.

Figure 4.30 presents the average annual SSR values (Figure 4.30a) and SSR anomalies (Figure 4.30b) regarding the time-period of 2001-2018, revealing relatively smooth fluctuations with a weak dimming for the 2000s in all datasets and an increasing SSR trend after 2010. NCEP-R1 exhibited noticeably high SSR fluxes, while FMI displayed the lowest values (as it was also observed in the Table 4.10). These averages are further illustrated through box plots (Figure 4.30c) and the annual cycle (Figure 4.30d), confirming that all models capture the expected seasonal SSR variations, with peaks during summer months in each hemisphere (June and December) and minima during equinoxes (March and September).

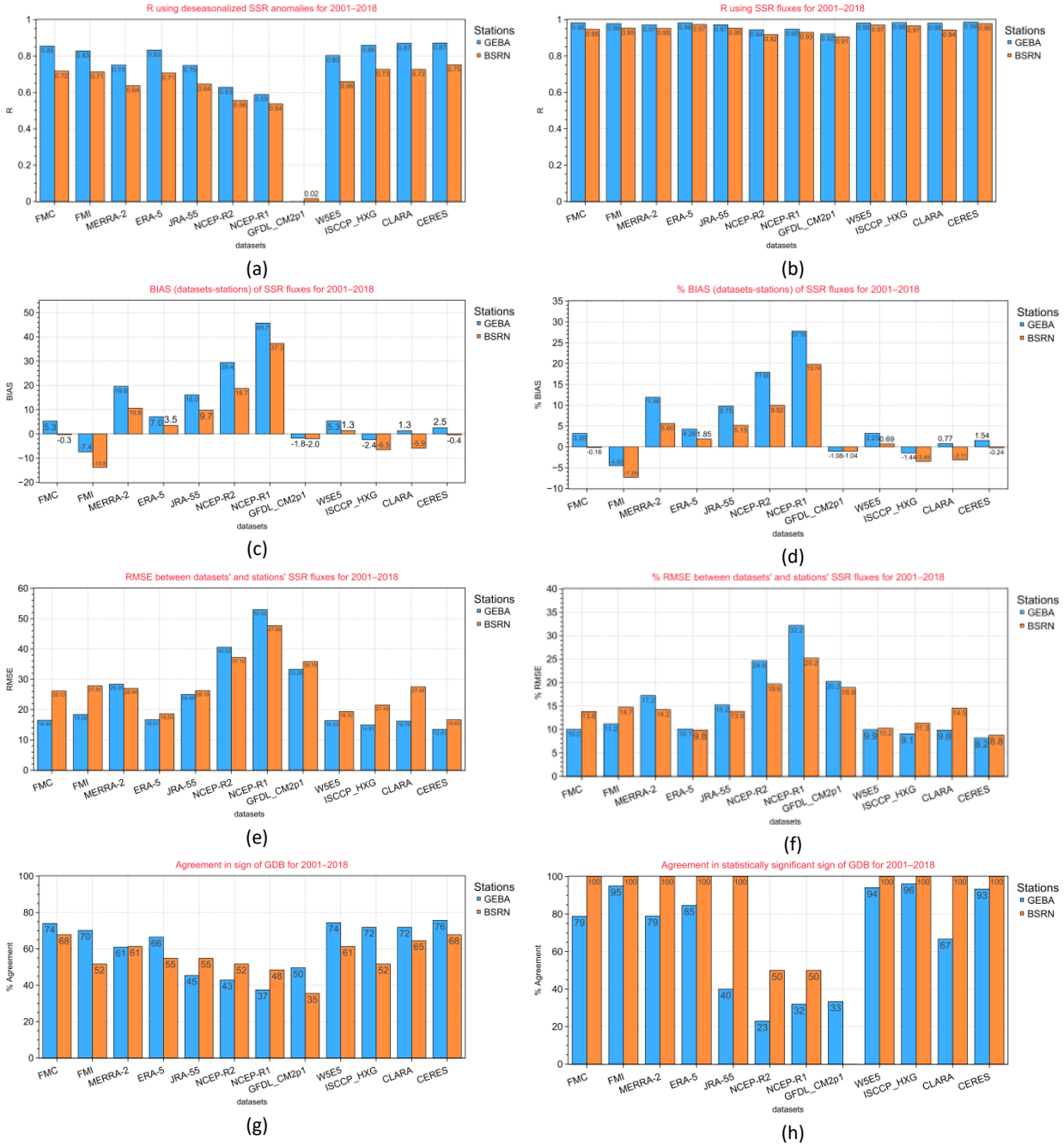


Figure 4.29. The evaluation metrics of the 12 SSR and GDB datasets against ground-truth measurements from GEBA (blue) and BSRN (orange) for the entire time-period 2001-2018. The metrics were: the R using deseasonalized SSR anomalies (a) and SSR fluxes (b), the BIAS (c) and the relative BIAS (d), the RMSE (e) and the relative RMSE (f), along with the agreement in sign of slopes (g) and the agreement for only statistically significant trends at 96% confidence level (h).

Further analysis was conducted to compare SSR trend patterns across all simulations, as depicted in Figure 4.31. The FMC results indicate an overall global small decrease in SSR equal to -0.047 $Wm^{-2}decade^{-1}$ which is coming from the coexistence of both brightening and dimming across the planet. Dimming observed over India, Middle East, Sahara and central Africa, polar regions and over large parts of the oceans. On

Table 4.10. Spatially averaged SSR (Wm^{-2}) values among the 12 datasets for the total globe, for land and oceans. Along with the average values, the differences and the relative differences between each dataset and the FMC (dataset - FMC) are shown.

name	globe	land	ocean	dif_globe	dif_land	dif_ocean	dif_globe (%)	dif_land (%)	dif_ocean (%)
FMC	196.1	198.1	195.3	0	0	0	0	0	0
FMI	184.2	187.9	182.8	-11.9	-10.2	-12.5	-6.1	-5.1	-6.4
MERRA2	194.1	209.5	188.5	-1.9	11.4	-6.8	-1	5.7	-3.5
ERA5	197.1	201.9	195.4	1.1	3.8	0.1	0.5	1.9	0
JRA55	199	209.7	195.1	3	11.6	-0.2	1.5	5.9	-0.1
NCEP2	198.4	206.2	195.6	2.4	8.1	0.3	1.2	4.1	0.2
NCEP1	216.3	237.3	208.5	20.2	39.3	13.2	10.3	19.8	6.8
GFDL_CM2p1	197.6	201.5	196.2	1.6	3.4	0.9	0.8	1.7	0.5
W5E5	196.3	198.9	195.3	0.2	0.9	0	0.1	0.4	0
ISCCP_HXG	189.2	198.2	185.8	-6.9	0.2	-9.5	-3.5	0.1	-4.8
CLARA	193	196	191.9	-3	-2.1	-3.4	-1.6	-1	-1.7
CERES	195.6	198.6	194.5	-0.5	0.5	-0.8	-0.3	0.2	-0.4

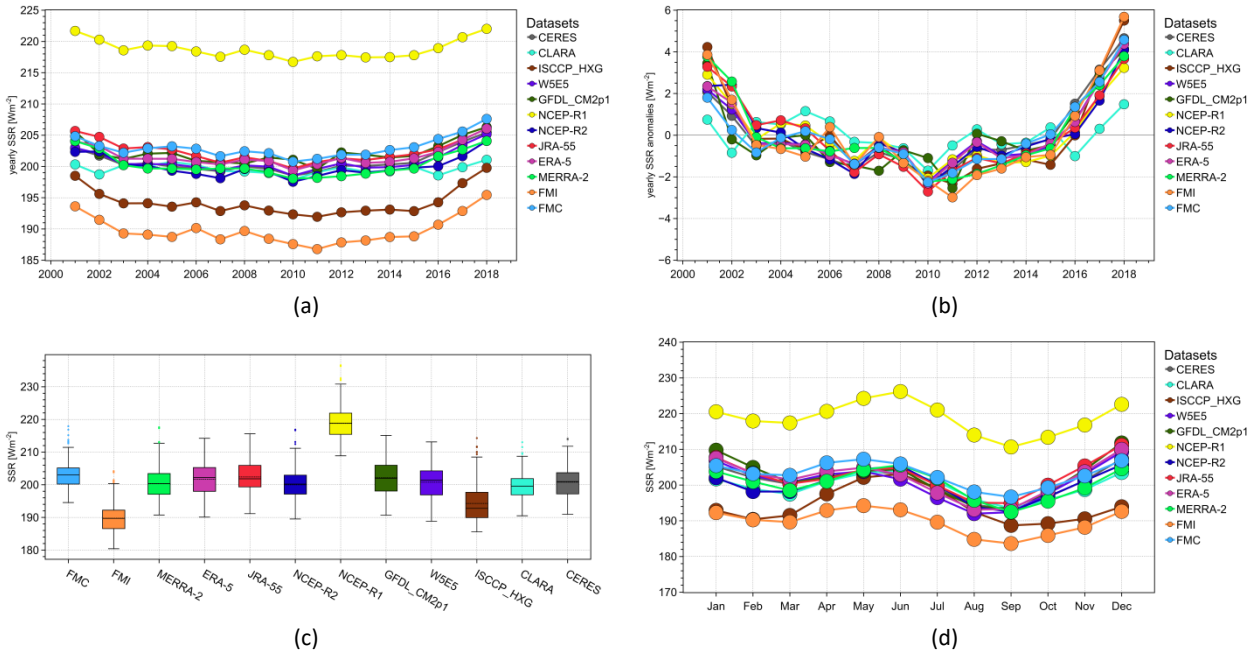


Figure 4.30. This figure illustrates comparisons within the 12 datasets for the time-period 2001-2018 for annual globally averaged SSR (a) and SSR annual anomalies (b) along with the box-plot comparison (c) and the annual cycle of SSR (d).

the other hand, brightening exists over Europe, south Africa, Americas being stronger in South America, Australia, large parts of Asia and of the Pacific Ocean. The global solar dimming is captured by all other datasets except for CERES which a weak brightening shows equal to 0.029 $Wm^{-2}decade^{-1}$. Besides, the regional GDB patterns are not the same across all the datasets and have some significant differences. For example, FMI, CERES, CLARA, W5E5, ERA5 and ISCCP_HGX exhibit similar brightening trends over Europe, with partial agreement from GFDL_CM2p1, while the others a dimming suggest over Europe. Most models indicate declining SSR over India, except for the NCEP-R1 which entirely contradicts this trend while there

is a partial agreement for dimming for MERRA-2, CLARA and GFDL_CM2p1. For Southeast Asia, FMC shows an overall weak brightening, which is not aligning with all other datasets except for GFDL_CM2p1. Over Middle East and Arabian Peninsula a dimming is estimating across all the datasets. The widespread brightening trends over the Americas in FMC align with CERES and CLARA, while in southern Africa, all datasets support FMC's brightening except for the GFDL_CM2p1 and partially for MERRA-2. Dimming west of the continental coasts is corroborated only by CLARA dataset. Note that the main source of FMC's cloud input is CLARA cloud dataset which is also for the CLARA SSR computations. In the polar regions, the most models agree with FMC and indicate an overall general dimming.

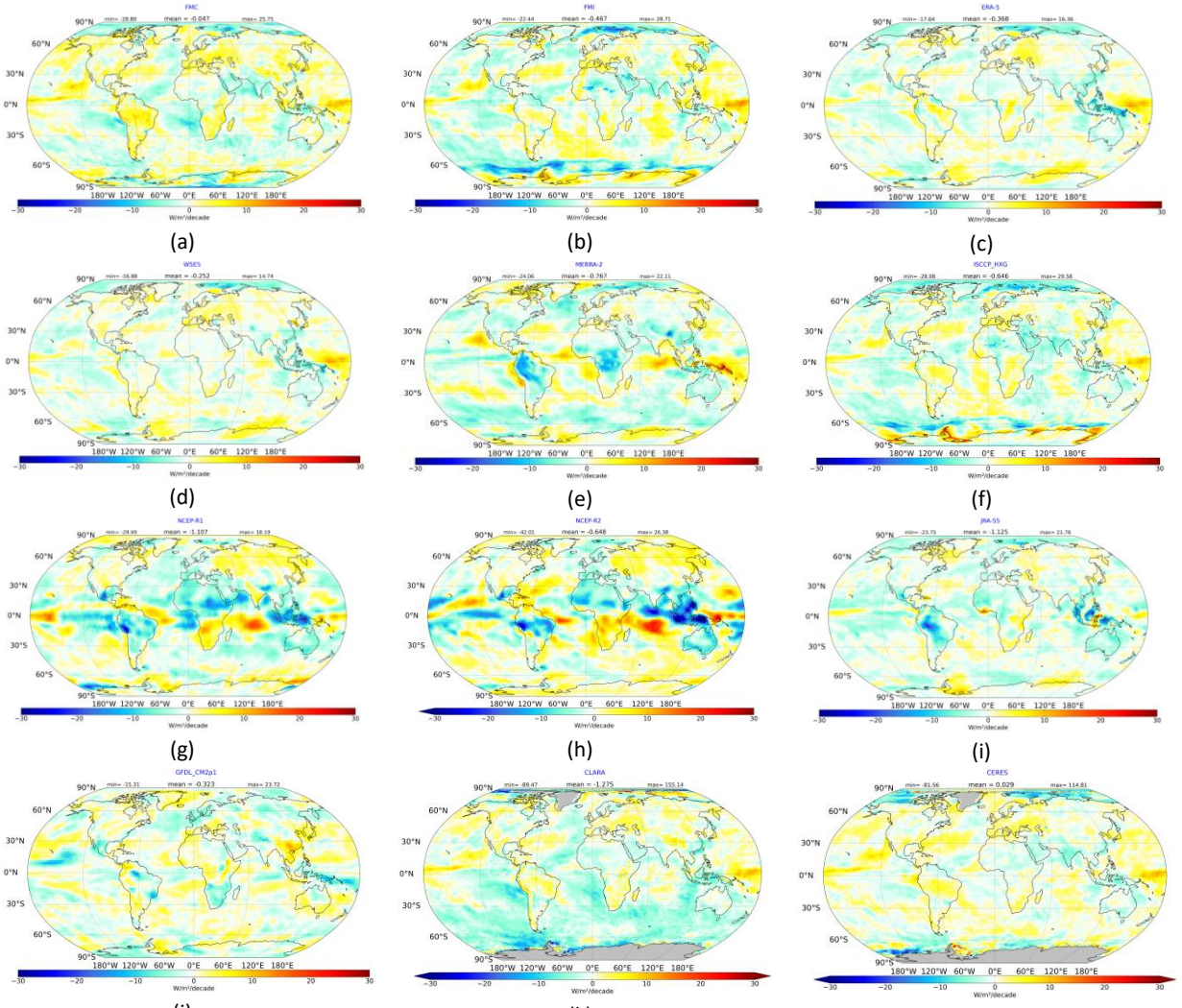


Figure 4.31. Global distribution of GDB ($Wm^{-2}decade^{-1}$) during 2001-2018 among the 12 datasets namely FMC (a), FMI (b), ERA5 (c), W5E5 (d), MERRA-2 (e), ISCCP_HXG (f), NCEP-R1 (g), NCEP-R2 (h), JRA-55 (i), GFDL_CM2p1 (j), CLARA (k), CERES (l). Yellow-red colors indicate increasing SSR trends while blues indicate decreasing SSR trends.

Figure 4.32 highlights areas where FMC's GDB aligns with the two best-performing models, CERES and CLARA. The three datasets concur on brightening over Europe, South America, Mexico, South Africa, parts of central Asia, along with oceanic regions east of the USA, west of Canada and tropical oceans. Similarly,

they agree on SSR reductions over some parts of Southern Ocean, oceans over the west of continents, the Arabian sea, Arabian Peninsula, India, parts of Sahara and over various oceanic parts. When considering the top four models (ERA5, W5E5, CLARA, and CERES), agreement is found for brightening over the Mediterranean, and in general over Europe, parts of central and south America, south Africa, Korea, Japan and over tropical ocean, while dimming is consistently observed in the west Southern Ocean, Arabian sea, India, Arabian Peninsula, parts of Sahara and over various oceanic regions. Agreement declines when six models are included (adding FMI and ISCCP_HXG), with only a few common areas remaining for both brightening and dimming trends. Full agreement among all models is rare, with widespread brightening observed in only a few locations, such as Japan, Korea, parts of Russia and tropical ocean, while dimming remains largely confined to the north Atlantic Ocean and parts of Arabian Peninsula and Arabian sea.

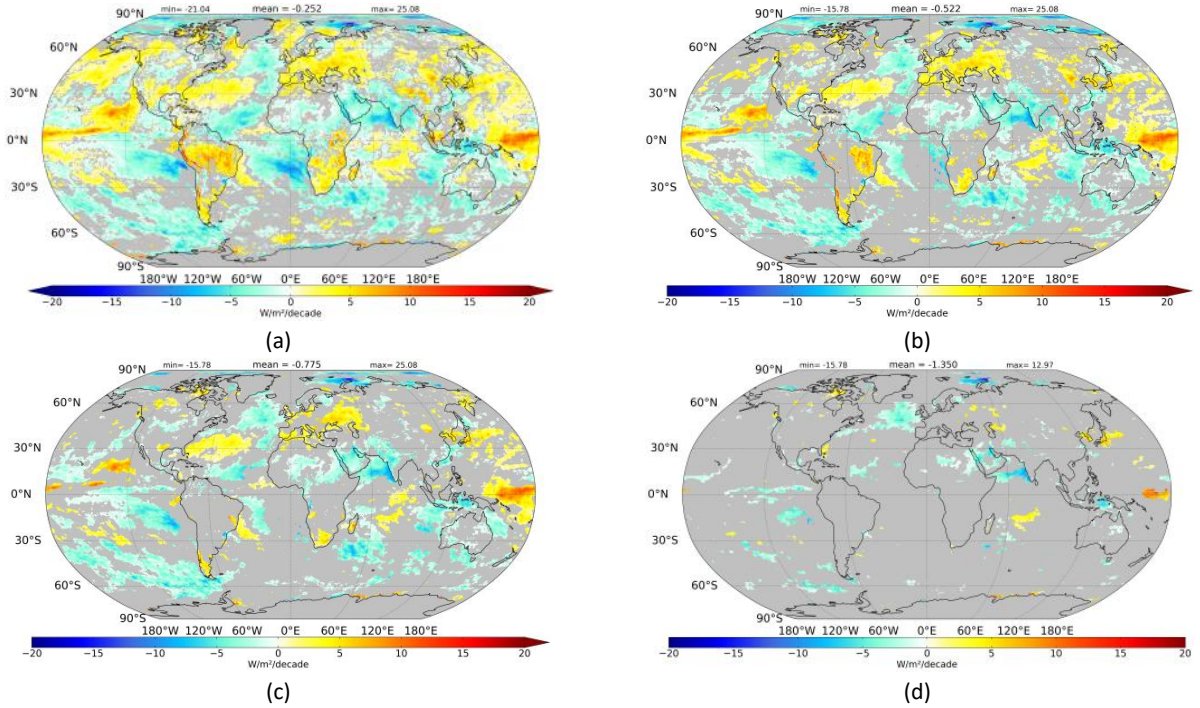


Figure 4.32. Global distribution of the FMC GDB ($Wm^{-2}decade^{-1}$) during 2001-2018 over areas where FMC agrees with the 2 top-performing datasets (a) with the 4 best datasets (b), with the 6 best datasets (c) and with all datasets (d). Yellow-red colors indicate increasing SSR trends while blues indicate decreasing SSR trends.

Also, Figure 4.33 provides an overview of the GDB (spatially averaged GDB) for the entire planet, NH, SH, as well as for land and ocean. FMC recorded an average GDB of -0.05 Wm^{-2}/decade globally, with values of 0.85 Wm^{-2}/decade over land and -0.41 Wm^{-2}/decade over oceans. It should be noted that for the globe, all the datasets show a dimming except for CERES which estimates a very weak brightening equal to 0.03 Wm^{-2}/decade while the FMC exhibits the weakest dimming equal to -0.05 Wm^{-2}/decade. Over land, the FMC brightening is in line only with CLARA while the other datasets show dimming. Over NH land the FMC brightening is in line only with the W5E5 but over SH land FMC's brightening agrees with FMI, ISCC-_HXG, CLARA and CERES. Above oceans, all datasets show a dimming except for the brightening which was estimated by CERES. Note, over the NH oceans only FMC and CERES suggest a brightening in contrast with all other datasets while over SH oceans all datasets show dimming except for NCEP-R2. In general, across

the most regions the majority of datasets shows a dimming, while over land only FMC and CLARA show brightening. Furthermore, it is important to recognize that regional variations may not always be fully captured by global or hemispherical averages, underscoring the importance of detailed regional analysis which can be shown in Figure 4.34 where the GDB averaged spatially only over specific 18 land regions of the planet.

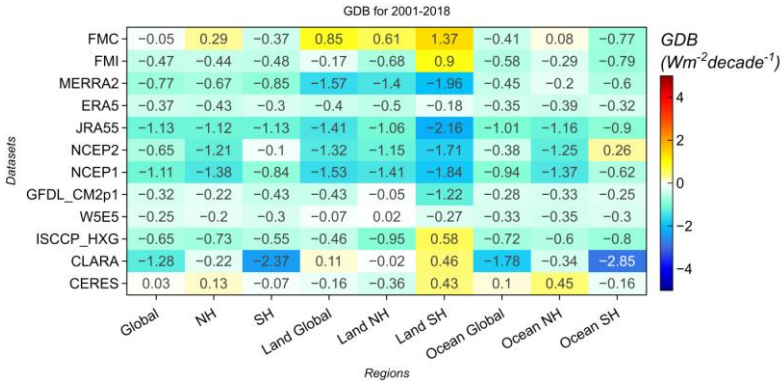


Figure 4.33. The spatially averaged GDB (in $Wm^{-2}decade^{-1}$) of each dataset over the globe, the two hemispheres and the globe's and the two hemispheres' land and ocean areas during the entire study period 2001-2018. Reddish/bluish colors indicate brightening/dimming.

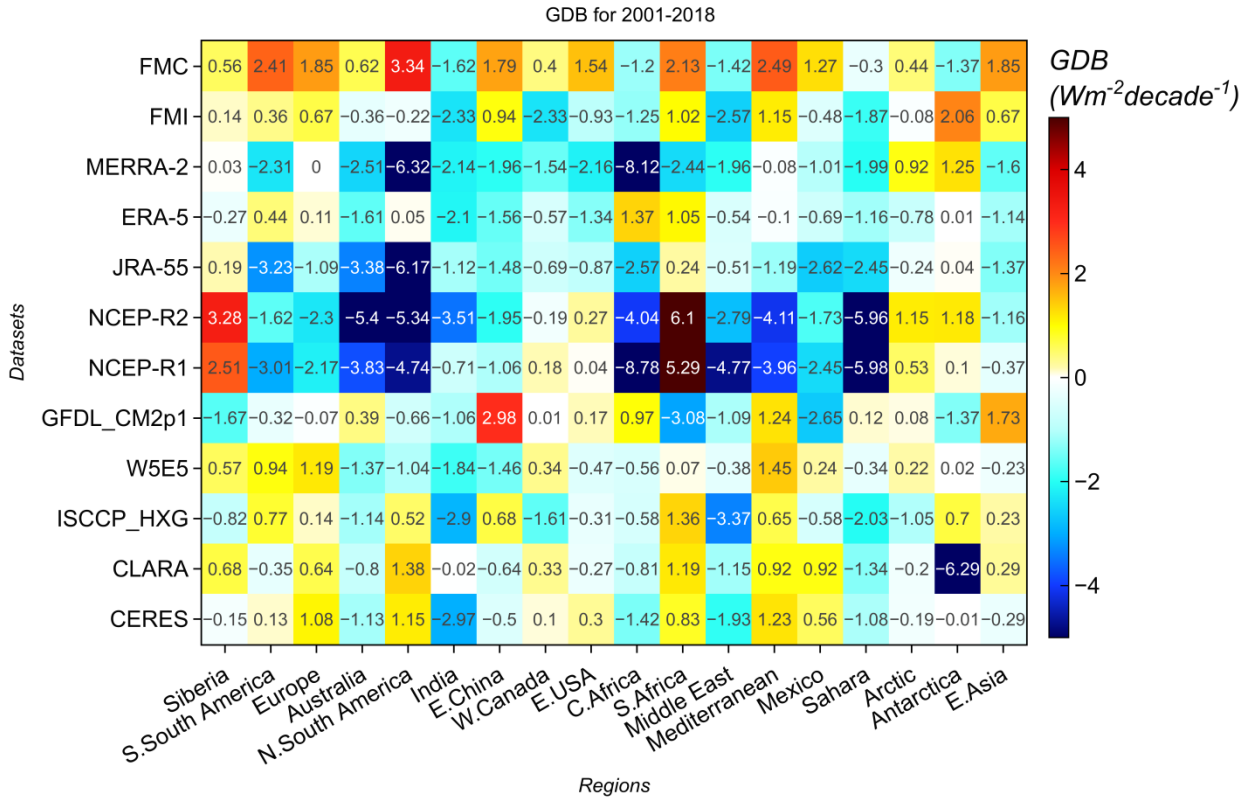


Figure 4.34. The spatially averaged GDB (in $Wm^{-2}decade^{-1}$) over the specific 18 land areas during the entire study period 2001-2018. Reddish/bluish colors indicate brightening/dimming.

Now, exploring the averaged GDB over land regions, much more datasets agree with the FMC brightening (with varying magnitudes) in many regions while a disagreement continues to exist in some other regions

for some datasets. For instance, over Europe, CLARA, CERES, FMC, FMI, ERA5, W5E5 and ISCCP_HXG agree in the brightening while over India and Middle East all the datasets show a dimming. Over East China, the FMC suggests a brightening (equal to 1.79 $Wm^{-2}decade^{-1}$) which is in line only with ISCCP_HXG, GFDL_CM2p1 and FMI. Note that FMC and FMI disagree in the case of East USA and Australia while the only difference between them was the different cloud input but with the same aerosol data, indicating again the crucial impact on the cloud input data (and their trends). Finally, if CERES could be considered as the best reference for GDB since 2001, comparing the best performant GDB datasets, can be concluded that CLARA agrees in the sign of GDB over 14 of 18 regions (77.8%), FMC and W5E5 in 13/18 (72.2%), ERA5 in 12/18 (66.7%) and FMI in 10/18 (55.6%). This indicates again the nice performance of FMC GDB among other datasets during 2001-2018 confirming the reliability of the FMC and the reasonable improvement over the FMI. This comprehensive study highlights the significant differences in GDB trends across various models, even in neighboring regions, reinforcing the importance of validation against observational data. Moreover, FMC's strong alignment with the two top-performing models over nearly 55% of the globe strengthens confidence in its accuracy, especially in crucial areas like Europe, South America, India, the oceanic regions west of continents, and the Southern Ocean.

Chapter 5: The causes of GDB

5.1 Introduction

Multi-decadal variations in SSR, i.e. GDB, have significant implications for many important environmental processes as well as numerous practical applications, such as solar power generation, agricultural production, and human health, since sunlight availability is essential for any ecosystem and the existence of life in general. In spite of this, the causes of these variations are still up for debate and lack clear evidence. Variations in solar illumination cannot account for the decadal changes in SSR, since these are at least an order of magnitude smaller (Willson and Mordvinov 2003) and it seems that they are uncorrelated (Aparicio et al., 2020). Thus, changes in the transparency of the atmosphere, which are related to clouds, aerosols, and radiatively active gases, must be the cause of the observed SSR variations (e.g., Kim and Ramanathan 2008; Kvalevag and Myhre 2007). Indeed, aerosols and clouds were reported to be the main drivers of the phenomenon, contributing to GDB to different degrees depending on the world region (Hatzianastassiou et al., 2020; Wild 2016). Although variations in cloud cover efficiently affect SSR on an inter-annual level, it is not always clear how these variations relate to the longer-term (decadal) SSR patterns that have been observed (e.g., Qian et al. 2006; Norris and Wild 2007). There have also been reports of dimming and brightening in clear atmospheres at different places, suggesting that atmospheric aerosols play a significant role (e.g., Wild et al. 2005, 2021; Alpert et al., 2005; Norris and Wild 2007; Sanchez-Lorenzo et al. 2009; Ohvril et al. 2009; Zerefos et al. 2009; Correa et al., 2024a,b,c; Ruckstuhl and Norris 2009; Allen et al. 2013; Turnocket al. 2015; Norris et al. 2016; Freychet et al. 2019; Cherian and Quaas 2020; Nabat et al. 2014). Aerosols, which act as cloud concentration nuclei (CCN) or ice nuclei (IN), can increase cloud reflectivity and lifetime (first and second indirect effects). Besides, aerosols can directly attenuate solar radiation by scattering and absorbing it (direct effect) (e.g., Ramanathan et al. 2001; Lohmann and Feichter 2005). Over the past few decades, anthropogenic air pollution has significantly altered the amounts of atmospheric aerosol (Stern 2006; Ruckstuhl et al. 2008; Streets et al. 2006, 2009; Wang et al. 2012). According to Streets et al. (2009), AOD emission histories are consistent with the observed dimming/brightening tendencies in some places, indicating that anthropogenic air pollution may be a major factor in explaining SSR fluctuations. However, a number of other research (e.g., Liepert, 1997; Wild et al 2005; Liley, 2009; Kumari and Goswami, 2010; Augustine and Dutton, 2013; Allen et al. 2013; Mateos et al., 2014; Wild 2016; Norris et al. 2016; Sanchez-Lorenzo et al. 2017; Pfeifroth et al., 2018; Correa et al., 2024a,b,c) also indicated that changes in cloud features were significant causes of dimming and/or brightening. Changes in cloudiness brought on by the atmosphere's and the ocean's internal decadal variability, may have also played a role in the SSR changes (Romanou et al., 2007; Folini et al., 2017; Augustine, J. A., & Capotondi, A., 2022; Chtirkova et al., 2022, 2023, 2024). The extensive body of literature discussed above demonstrates a robust and ongoing debate regarding the causes of GDB. Despite significant advancements, there remains a lack of complete certainty, particularly concerning the contributions of atmospheric components. Thus, this PhD study is critical in addressing these gaps by providing a comprehensive analysis that spans both land and ocean surfaces, covering an extended study period that surpasses many earlier studies. Moreover, state-of-the-art atmospheric data was employed, offering a higher level of accuracy and resolution than previously available datasets. By identifying the causes of GDB with greater precision, especially through the use of

radiative transfer models (RTMs), we improve not only our understanding of past and present SSR variations but also enhance the potential to forecast future phases of GDB by knowing the expected changes in specific atmospheric parameters. It should be noted that the GDB drivers which will be analyzed and are the atmospheric input parameters to the RTM are the cloud amount for low-, middle- and high-level clouds (CA1, CA2, CA3), cloud optical thickness for low-, middle- and high-level clouds (COT1, COT2, COT3), aerosol optical depth (AOD), single scattering albedo (SSA), asymmetry parameter (AP), water vapor and ozone. Section 5.2 provides an overview of the changes of the GDB drivers both on annual and seasonal basis giving a qualitative estimation of the major causes of the GDB; Section 5.3 presents, quantifies and discusses the contributions of the GDB drivers, and finally Section 5.4 presents the correlation and regression analysis results for the monthly variations of SSR and GDB drivers.

5.2 Changes of the GDB drivers

In this section the results of the analysis on the changes of parameters that are the main causes of GDB are presented. Clouds and aerosols, which have been reported to be the main drivers of GDB, as well as water vapor and ozone, are included in this analysis. Yet, special emphasis is given to the changes of cloud properties (cloud amount and optical thickness) by category (high, medium and low), and aerosols, which primarily affect GDB under clear skies.

As shown in Figure 5.1a, the low-level cloud amount mainly increased during 1984-2018 and this increase is equal to 1.50 %decade^{-1} at a global scale. This increase is more notable over oceans, especially over the oceans west of continents, where the permanent anticyclones of SH exist and over the Arctic Ocean. On the contrary, a reduction of low CA is observed over almost all the Earth's continents, which is stronger over northern South America, Mexico, southern Africa, across the Sahel and Australia. The middle CA has mainly decreased (Figure 5.1b), by -4.05 %decade^{-1} globally. However, there are few regions with increasing trends, such as over the oceanic areas west of S. America and the Sahara. With respect to the high-level CA (Figure 5.1c) it has largely increased in the middle latitudes, Arctic and over some areas along the equator, while it has widely decreased across almost all the tropical and subtropical regions. The global mean value of the changes of high-level CA is equal to 0.74 %decade^{-1}. In addition, the total cloud amount (Figure AD1a) has largely increased over the permanent anticyclonic areas of SH, over the eastern Arctic, Sahara and central Australia, while it has widely decreased across almost all the land regions, except Siberia and Sahara. The global mean value of the changes of total CA is equal to -0.62 %decade^{-1}. The annual planetary distribution of change of the optical thickness of low clouds (Figure 5.1d) indicates an overall increase (global mean value equal to 0.83 %decade^{-1}). However, there is a contrasting feature, with an increase over oceans and generally over the SH, being strongest over the Southern Ocean, against a decrease over NH lands, especially over the Arctic. A quite similar pattern is found for mid-level COT, which yields a global mean increase equal to 0.26 %decade^{-1}. There are characteristic opposed patterns in the polar regions, with an increase in Antarctica and a decrease in the Arctic. The pattern of changing high-level COT is clearer, indicating a decrease all over the globe, except for Antarctica (Figure 5.1f) yielding a global mean decrease equal to -6.91 %decade^{-1}. It should be mentioned that both natural and man-made factors contribute to cloud changes, and both of them are essential in regulating the Earth's climate system and radiation balance. Climate events including El Niño and La Niña, ocean currents, and atmospheric circulation patterns are examples of natural processes that affect cloud

formation and moisture transport (Teng et al., 2014; Wagner et al., 2005). Cloud cover is redistributed across latitudes by large-scale circulation movements, while warm ocean currents increase evaporation, raising atmospheric humidity and encouraging cloud formation. Local humidity and convection processes are also influenced by land/sea-atmosphere interactions and geographic factors, including vegetation, topography, and surface water availability (Sikma et al., 2018; Sato et al., 2007). Anthropogenic influences significantly modify cloud properties and coverage. Cloud dynamics and precipitation patterns are impacted by greenhouse gas emissions, which change atmospheric temperature gradients (Bony et al., 2004; Sun et al., 2000). Urbanization contributes to the heat island effect, changing local meteorological conditions and cloud formation mechanisms (Rao et al., 2004; Pyrgou et al., 2019). Aerosols, both natural and anthropogenic, serve as CCN or IN, influencing cloud microphysics by increasing droplet number and decreasing droplet size, enhancing cloud albedo (the "Twomey effect": Twomey, 1977;) while potentially suppressing precipitation and extending cloud lifetimes (Wang et al., 2008; Stevens et al., 2009; Myhre et al., 2013; IPCC 2021). In addition, the relationship between CA and COT changes could be complex and can lead to scenarios where CA decreases while COT increases such as over Central Africa (Figure 5.1), while in other areas, e.g. Australia, both parameters decrease. It should be also noted that CA and COT are independent cloud parameters, which are not necessarily dependent on the same factors. Similarly, their changes may or may not be driven by common factors. Among them, apart from aerosol effects and varying cloud microphysical processes, changes of meteorological/climatological parameters like sea surface and atmospheric temperatures, lapse rates, humidity, also as responses to atmospheric warming and climatic changes, or to natural variability, may also be responsible for changes of CA and/or COT (Kishcha et al., 2007; Zhang et al., 2020). For instance, increased aerosol concentrations together with rather stable humidity can provide more CCN, leading to the formation of more numerous, yet smaller, cloud droplets that enhance scattering and increase COT (Twomey, 1977; Bellouin et al., 2020). However, this increase in droplet number can suppress precipitation efficiency, as smaller droplets are less effective at coalescing into larger droplets necessary for precipitation, while increasing the cloud lifetime and possibly CA (Lohmann et al., 2003; Yuan et al., 2011). Also, in the case of the trade wind cumuli clouds, it was found that while the COT increases due to the higher droplet count, further increases in aerosols result in a reduction in CA because the clouds become less effective at producing rain, leading to faster evaporation and dissipation of the cloud mass (Xue et al., 2008). Yet, on the other hand, if the cloud develops vertically (as convective clouds do) this may not be associated with increased CA. Also, the similarity between magnitudes of CA and COT varies with cloud types. For example, one can think of stratiform clouds which have large CA, but small COT, against convective clouds characterized by rather large COT and relatively small CA. Changes in the dominant cloud types may result in fewer optically thin clouds and more optically thicker clouds, which would raise the overall COT even if the total CA would be reduced (Bouniol et al., 2012). The global distribution of the change in aerosol optical depth (AOD) at 550 nm (Figure 5.1g) shows a global mean decrease of -0.90 %decade^{-1}. The largest increases occurred in eastern China, India, South Africa, and northern South America, primarily due to increased anthropogenic sulfate and carbonaceous aerosols from industry, fossil fuel combustion, and biomass burning (Korras-Carraca et al., 2021). In China and India, high sulfate concentrations dominate, with contributions from organic and black carbon, as well as desert dust in India. In northern South America, biomass burning emissions over the Amazonian basin are a key driver of the strong AOD increase there. A smaller increase is observed over the Arabian Sea and Peninsula, associated with desert dust aerosols, while the increase

in the subtropical Atlantic Ocean results from strengthened exported biomass burning and dust aerosols from African forests and deserts. Conversely, the strongest AOD decreases are seen over Europe, Mexico, and central Africa, arising mainly from reduced sulfate and black carbon emissions due to the application of stricter air quality regulations and changing biomass burning patterns (Korras-Carraca et al., 2021). Further declines are observed over the eastern USA, northern Asia, the polar regions, and vast oceanic areas, linked to reduced pollution outflows. On the other hand, sea-salt remains the dominant aerosol over remote ocean regions and its changes interpret the changes of AOD there. Besides, note that our findings reveal regional variations in AOD trends also during 2001-2018, including the dipole pattern over Asia, while SSA trends remain positive (Figure AD3). This pattern has already been noted also by Xiang et al. (2023) who studied AOD trends for the time period since 2003 using MODIS Terra and Aqua and by Ramachandran et al. (2022) who studied AOD trends for the time-period 2000-2018 using CMIP6 model simulations. Our findings agree with their findings with regards to the Asian AOD dipole for the similar time period. The aerosol single scattering albedo at 550 nm (Figure 5.1h) shows a general decrease globally except for a strong increase over East China, India, parts of central Africa, central S. America and eastern Australia, yielding a global mean value equal to -0.44% decade^{-1}.Opposite to SSA, the aerosol asymmetry parameter at 550 nm has slightly increased globally, by 0.20 %decade^{-1}, having increased/decreased over most ocean/land areas of the globe. The biggest increase occurred in Mexico, western South America, eastern Australia and Indonesia, while the largest decrease took place in the Arctic Ocean. The atmospheric water vapor (Figure 5.1j) has increased by 1.3 %decade^{-1} at a global scale, with strongest increases over Europe, South America, India and Australia, and decreases over few tropical and sub-tropical areas and the Southern Ocean. Finally, the ozone concentration (Figure 5.1k) mainly was reduced over middle latitude areas, while it increased over the tropics and the poles, yielding a slight global mean change equal to -0.07 %decade^{-1}. The changes of all the above discussed parameters during the 35-year study period combine and result in the changes in SSR from 1984 to 2018 shown in Figure 5.1l. Overall, the estimated solar brightening over most land areas is associated with the general decreasing trends in cloud amount (except for some mid latitude NH areas for high-level CA) and cloud optical thickness (except for South America, Central Africa and Antarctica)as well as AOD and SSA for the NH. The dimming over India and China could be explained by the remarkably increasing AOD, thus aerosol loadings and associated extinction, in these areas, while the strong dimming over the marine stratocumulus areas (in southern Pacific and Atlantic Oceans) is explained by the increase in low and middle-level cloud amount and cloud optical thickness. The changes in water vapor and ozone do not seem to be in line with the observed GDB, which confirms that clouds and aerosols are the major drivers of the phenomenon.

The (percent) overall (during the 35-year study period) and decadal (in the 1980's, 1990's, 2000's and 2010's) changes of all the examined parameters were also assessed over the entire globe, hemispheres, and global land and oceans (Figure 5.2) on an average basis. This analysis provides an easy assessment of the overall changes of the examined parameters. As shown in Figure 5.2a, over the entire time period (e.g. 1984-2018), there have been large decreases in high-level COT and mid-level CA across the planet implying an increase in SSR. On the contrary, there were large increases in the COT of middle and low clouds as well as the low-level cloud amount, especially in the SH and in particular over the oceans. The AOD decreased except overland in the SH, where it increased, whereas SSA decreased

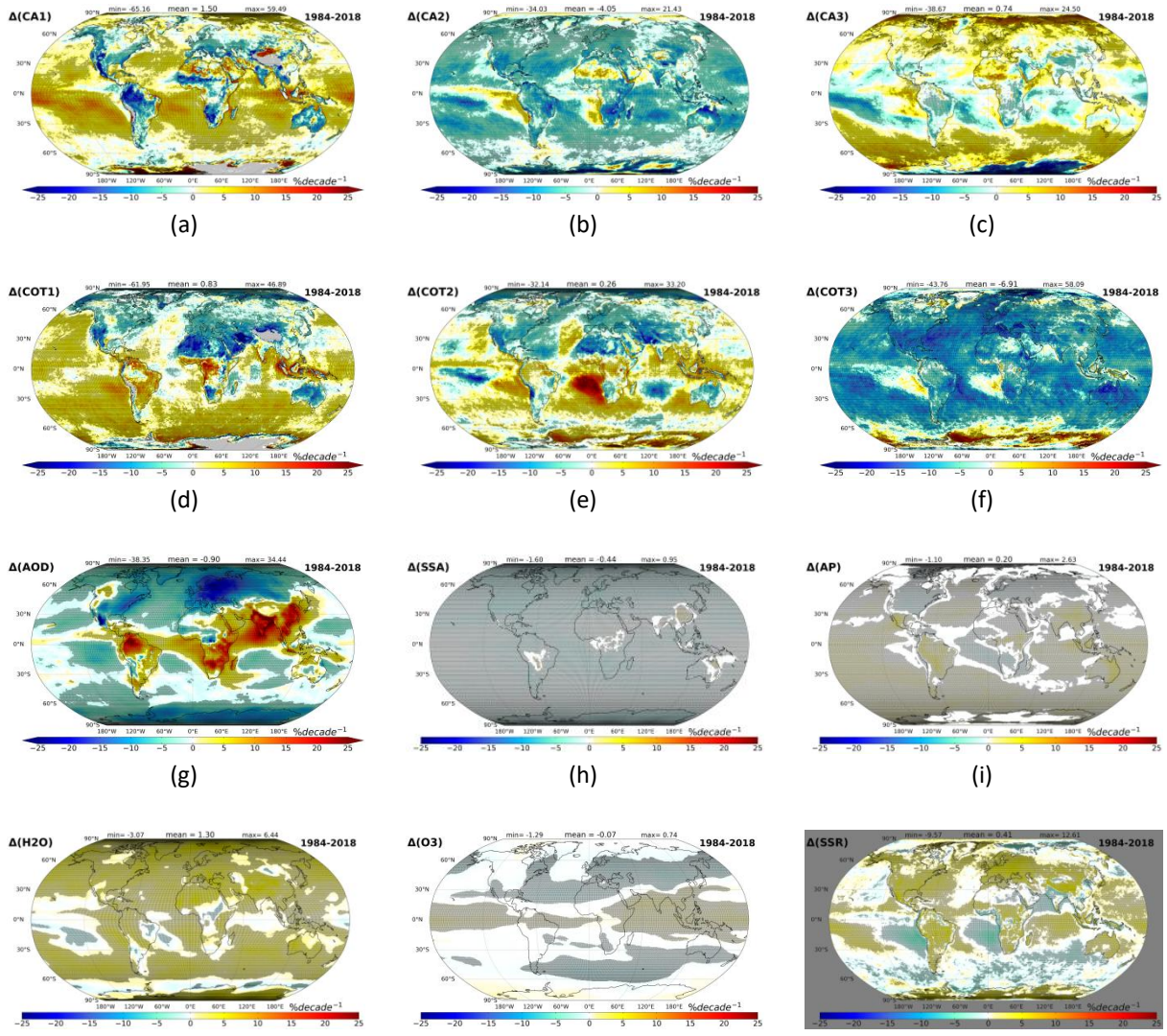


Figure 5.1. Global distribution of %per decade changes in the low cloud amount (CA1, a), middle CA(CA2,b), high CA(CA3, c), low-level cloud optical thickness (COT1, d), mid-level COT (COT2, e), high-level COT(COT3, f), aerosol optical depth (AOD, g),aerosol single scattering albedo (h), aerosol asymmetry parameter (i), water vapor (j), ozone (k) and SSR (l) during 1984-2018. Reddish/bluish colors indicate increasing/decreasing trends while black dots indicate pixels with statistically significant trends.

everywhere. Besides, water vapor and ozone decreased, the aerosols' asymmetry parameter and water vapor increased, whilst ozone slightly decreased. However, as shown in Figures 5.2b,c,d,e, these parameters' trends change from a decade to another over the last 4 decades. During the 1980s (1984-1989, Figure 5.2b), AOD greatly decreased everywhere, while COT increased above land, while the CA of high clouds increased a lot everywhere except overland in the SH. The existence of positive and negative trends of the various GDB drivers results in a weak dimming over the globe (-0.07 %decade^{-1}), arising from counteracting dimming and brightening in the NH and SH as well as over the global land and ocean areas, respectively. These counteracting trends in GDB highlight the complex nature of the phenomenon, which apart from being assessed on a global scale must be examined at least on a hemispherical and continental

basis. During the next decade (1990s) large reductions in AOD and COT took place again, explaining to a large part the remarkable overall increase in SSR (2.43 %decade^{-1}, Figure 5.2c). Then, in the 2000s, AOD and CA of low and high clouds increased, while COT and mid-level CA largely decreased (Figure 5.2d) and the counteracting trends eventually led to a global weak brightening (0.74 %decade^{-1}). Finally, during the 2010s (Figure 5.2e) there were large reductions in both clouds and aerosols, being stronger over land in the SH, whereas there was an increase in the low-level COT and the cloud amount of low and high clouds over the oceans. As a result, a brightening occurred over the globe (0.83 %decade^{-1}), stronger over land (2-3 %decade^{-1})), except only over the oceans of the SH where dimming prevailed. The corresponding trends on seasonal basis can be found in Figures AD4-AD7.

During the DJF of the period 1984-2018, SSR increased by 0.34 %decade^{-1}. This increase is primarily due to the rise in SSR over land, which reached 1.26 %decade^{-1}, while over the oceans, there was a slight dimming of -0.02 %decade^{-1}. The overall global brightening appears to be driven by significant decreases in COT3 and CA2, which were -6.05 %decade^{-1} and -4.11 %decade^{-1}, respectively. For the decade 1984-1989, dimming over land appears to dominate, possibly due to large increases in COT. In contrast, brightening over the oceans may be attributed to substantial decreases in AOD and CA2. Globally, a dimming of -0.4 %decade^{-1} is observed, seemingly driven by significant increases in COT. In the following decade, 1990-1999, brightening occurs globally as both aerosols and clouds generally decrease, except in CA1. The reduction in AOD is notably larger than other drivers, followed by decreases in COT2. This results in a total global brightening of 2.84 %decade^{-1}, which is nearly twice as strong over land compared to the ocean (4.35 %decade^{-1} vs. 2.25 %decade^{-1}). During the decade 2000-2009, dimming is observed in the NH, while brightening occurs in the SH, leading to a global brightening of 0.76 %decade^{-1}. This increase in SSR seems to be driven by significant decreases in COT3, COT1, and CA2, though a sharp increase in AOD acted in the opposite direction. The rise in AOD contributed to dimming in the NH, whereas the brightening in the SH appears to be primarily due to decreases in COT3, COT1, and CA2. Finally, in the decade 2010-2018, a global dimming of -0.11 %decade^{-1} prevails, originating from the SH, attributed to increases in CA and irrigated water. In contrast, the NH experiences a brightening of 0.11 %decade^{-1}, mainly due to decreases in COT. Moving into MAM for the period 1984-2018, SSR shows an overall increase of 0.38 %decade^{-1}, which is particularly strong over land (2.11 %decade^{-1}), while the world's oceans exhibit dimming of -0.3 %decade^{-1}. This period is marked by significant decreases in COT3 and CA2, alongside an increase in AOD. From 1984-1989, SSR increased globally by 1.54 %decade^{-1}, likely due to large decreases in AOD. However, in the NH, dimming of -1.25 %decade^{-1} was recorded, likely resulting from substantial cloud increases, while in the SH, brightening prevailed due to reductions in both clouds and aerosols. During 1990-1999, a general decrease in both AOD and clouds is observed, except for low cloud cover, leading to a global brightening of 2.1 %decade^{-1}. In the 2000s, aerosols increased, while cloud cover exhibited both increases and decreases. This resulted in a modest global brightening of 0.19 %decade^{-1}, with a significantly larger brightening of 2.16 %decade^{-1} in the NH, counterbalanced by dimming of -1.8 %decade^{-1} in the SH. Finally, during 2010-2018, widespread decreases in both clouds and aerosols led to a global brightening of 1.84 %decade^{-1}. During the JJA months of the period 1984-2018, substantial decreases in COT3 and CA2 resulted in a global brightening of 0.6% decade^{-1}, which was more pronounced over land (1.86 %decade^{-1}) compared to the ocean (0.11 %decade^{-1}). Between 1984-1989, total brightening of 0.82% decade^{-1} is attributed to significant decreases in AOD. However, dimming over land (-1.94 %decade^{-1}) appears to

stem from large increases in COT3 and CA3. During 1990-1999, brightening dominates globally, primarily driven by substantial decreases in aerosols and COT. In 2000-2009, SSR increased globally by 0.96 %decade^{-1}, largely due to significant decreases in COT3, COT1, and CA2. However, an increase in AOD offset some of the brightening caused by the decrease in clouds, resulting in a relatively low global brightening value. Finally, in the 2010s, brightening prevails globally, with an overall increase of 1.8% decade^{-1}, primarily driven by reductions in both aerosols and clouds, particularly COT3. Turning to SON, for the entire period 1984-2018, brightening is estimated at 0.95 %decade^{-1}, primarily driven by reductions in COT3 and CA2. From 1984-1989, both increasing and decreasing trends in clouds, along with a decline in AOD, resulted in slight global dimming of -0.03 %decade^{-1}, with brightening in the NH and dimming in the SH. In the 1990s, brightening dominates globally, primarily due to strong decreases in AOD and cloud cover, especially COT2. During 2000-2009, global brightening of 1 %decade^{-1} is recorded, particularly strong over land. This general brightening appears to be driven by reductions in CA2 and COT3 rather than AOD trends, which are increasing overall. Finally, for the period 2010-2018, SSR continues to rise globally by 1.4 %decade^{-1}, mainly due to significant reductions in COT3 and COT2. The global SSR in SON exhibits a continuous increase, except during 1984-1989. In both JJA and MAM, global SSR increases across all decades, while in DJF, it only increases during the period 1990-2009. These variations in SSR appear to be primarily driven by significant changes in AOD, particularly between 1984-1999, as well as fluctuations in COT3 and CA2. The seasonal analysis generally confirms the overall trends observed in the annual analysis. However, beyond these qualitative observations, a more detailed quantitative determination of the drivers in the GDB will follow below (5.3).

Since averaging on a hemispheric scale can hide important regional changes, a similar analysis was made on a smaller spatial scale, namely over specific regions, i.e. the selected 18 land areas and the results are shown in Figure 5.3. Here, in relation to what was described discussing the results of Figure 5.2, the general patterns of changes are similar both in the hemispherical averages (Figure 5.2) and in the regional averages (Figure 5.3). However, the regional analysis is able to distinguish some cases/regions that present an opposite change from the analysis on a hemispherical basis, where the distinguished region exists. For example, while AOD decreased during the period 1984-2018 over the NH land (Figure 5.2a), this was not the case for India and eastern China where AOD significantly increased (Figure 5.3a). Besides, over the Sahara in the 2010s (2010-2018, Figure 5.3e), the large increase in COT and high-level CA is opposite to the more general decrease over land in the NH (Figure 5.2e). It should be noted that generally the trends are sensitive to the time period chosen for the analysis. Examining shorter or longer periods could result in different trends, including opposite slope signs. Additionally, the trends can be influenced by large anomalies at the beginning or end of the time period, which may alter the direction of the trend. This effect is particularly noticeable in regions like India and China, where large AOD peaks from the Pinatubo eruption in the start of the 1990s led to large decrease of AOD in the 1990s. However, the use of radiative transfer calculations ensures coherence between the input and output and their trends, providing consistency and confidence in our sensitivity analysis.

Apart from the comparison of the changes in SSR and the GDB drivers (input parameters to the RTM), it is necessary to estimate the effect of changes of the input parameters on SSR changes. A detailed assessment of the effects of different physical parameters on SSR has been conducted by Hatzianastassiou

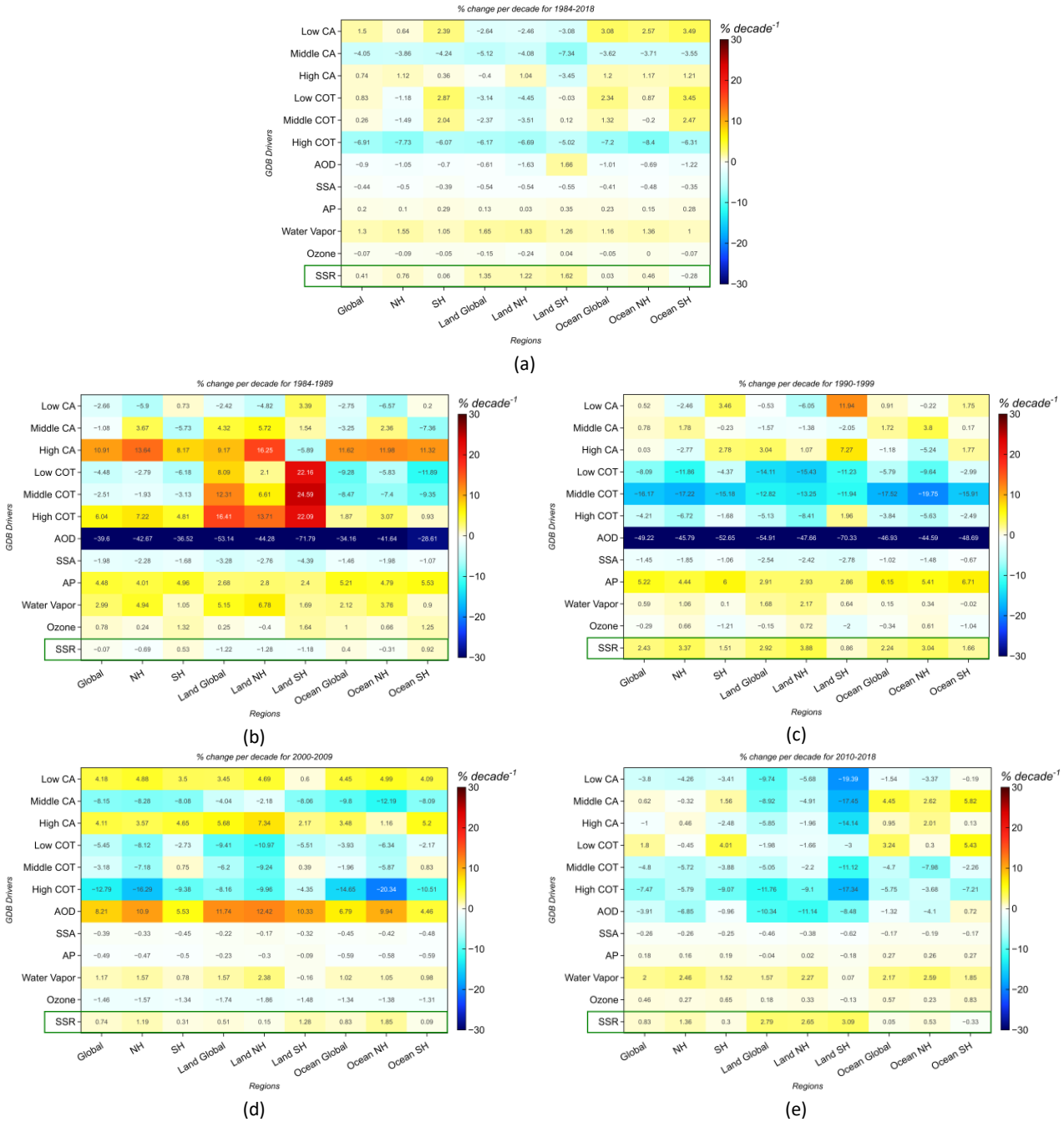


Figure 5.2. The spatially averaged percentage per decade changes of the GDB drivers over the globe, the two hemispheres and the globe's and the two hemispheres' land and ocean areas during the entire study period 1984-2018 (a), as well as during 1984-1989 (b), 1990-1999 (c), 2000-2009 (d) and 2010-2018 (e). Reddish/bluish colors indicate increasing/decreasing trends of the drivers and RTM input parameters along with the SSR in the last row.

et al., 2005, who provided a comprehensive sensitivity analysis of SSR to various parameters on a global scale. They performed a series of sensitivity tests using an older version of the same RTM, where key parameters like cloud cover, cloud optical depth, cloud asymmetry parameter, total precipitable water, and aerosols optical depth were systematically increased by a hypothetical percentage value. The results showed that

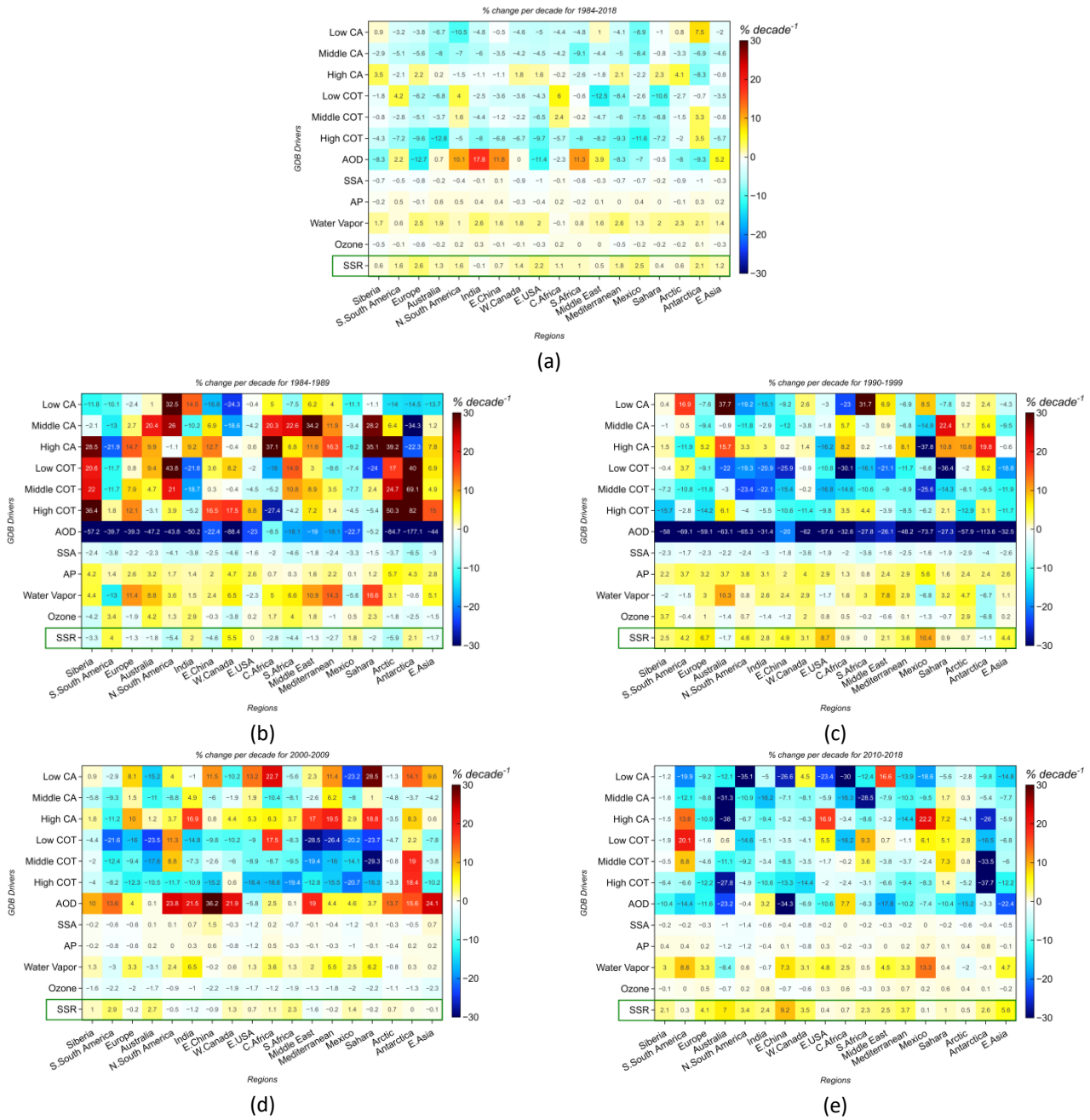


Figure 5.3. The spatially averaged percentage per decade changes of the GDB drivers over the specific 18 land areas during the entire study period 1984-2018 (a), as well as during 1984-1989 (b), 1990-1999 (c), 2000-2009 (d) and 2010-2018 (e). Reddish/bluish colors indicate increasing/decreasing trends of the drivers and RTM input parameters along with the SSR in the last row.

cloud parameters, particularly cloud cover and cloud optical thickness, have the most significant effect on SSR changes. For example, increasing cloud cover by 10% led to a decrease in SSR by up to 3.2 Wm^{-2} globally. The detailed insights from their study provide a bridge to the following section, where we discuss and quantify the contributions of the GDB drivers to GDB.

5.3 Contributions of GDB drivers

The analysis of the previous section, emphasizing the changes of the drivers of GDB, offers a first qualitative estimation of the causes of GDB. Nevertheless, it does not enable a detailed and accurate assessment of the magnitude of the contribution of each parameter/driver to GDB. Such a quantification of the contribution of various GDB drivers, which can only be done with a model, is of primary importance in order to rank and highlight the most important ones. Thus, this part of the study deals with the determination of these contributions to GDB (in Wm^{-2}) using the RTM and the specific methodology described in section 2.3.The contributions were estimated at pixel-level all over the globe for the entire 35-year study period, as well as on a decadal scale, for the 1980s, 1990s, 2000s and 2010s, at global and hemispherical scale and also separately for the global land/ocean areas. Moreover, the same contributions were determined for the specific 18 land areas of the Earth. It should be reminded that positive contribution (reddish colors) indicates that the change of the examined parameter, resulting in an increased SSR, contributed to the estimated overall brightening or counteracted the estimated overall dimming. On the other hand, negative contribution (bluish colors) means that the change of the parameter, resulting in decreased SSR, contributed to the estimated dimming or counteracted the estimated brightening.

5.3.1 Contributions at global scale

The contribution of the changes of low-level CA to GDB (Figure 5.4a) is equal to -1.33 Wm^{-2} on a global mean basis, i.e. low clouds induced a dimming globally from 1984 to 2018. Yet, despite of the overall induced dimming, low clouds caused either dimming or brightening regionally. Thus, their change contributed negatively (caused dimming) over Egypt, Arabian Peninsula, Antarctica, the poles and almost all oceanic regions of the globe, with the largest contributions over the permanent anticyclones of SH and the eastern Arctic Ocean. Conversely to oceans, low-level CA contributes positively to GDB over almost all the land areas of the globe, with the exception of those already mentioned before, with largest values over Europe, Canada and southern Australia, where they caused the strongest increase of SSR. The contribution to GDB of mid-level CA (Figure 5.4b) during 1984-2018 has been positive and equal to 2.74 Wm^{-2} on a mean global basis, thus exceeding (doubling) the corresponding global dimming of low-level CA. This strong positive contribution arises from corresponding positive contributions of mid-level CA almost all over the globe, with the largest contributions observed over the Southern Ocean and Antarctica (reddish colors). On the contrary, mid-level CA contributed negatively to GDB mainly over limited ocean areas, like off the west coasts of South America and South Africa. Next, the contribution to GDB of high-level CA (Figure 5.4c) to GDB is rather mixed (negative and positive) resulting in a slightly negative global mean contribution equal to -0.12 Wm^{-2}. The negative contribution is observed over several areas of the planet both over land and ocean, whereas positive contributions occurred mostly over tropical and subtropical areas. More specifically, negative contributions are found for example in the northern and southern Pacific Ocean, Europe, Canada, northern Asia, Guinea Gulf and Southern Ocean. On the contrary, over the Tibetan Plateau, southern Africa, South America, Mexico, Antarctica and large parts of the tropical oceans high-level CA appears to have contributed negatively to GDB. It should be noted here that the effect of clouds on SSR differs depending on their altitude, the effect of low-level clouds being larger than that of high-level clouds (e.g., Matuszko 2012). Given this, it is quite uncertain to draw conclusions about the contribution of different level cloud amounts to GDB, whilst such an uncertainty is absent based

on the results obtained in this section, where the realistic magnitude of the different cloud amount effect is quantified and thus can be safely summed up to estimate the overall (all-type) cloud amount affect. In this respect, it is found that the overall effect of all clouds' amount is equal to 1.29 Wm^{-2}, i.e. it is equivalent to a global average brightening during the period 1984-2018.In addition to the cloud amount, the contribution of COT was also computed. The contribution of low-level COT to GDB is on a global average basis equal to -0.85 Wm^{-2}. It is found (Figure 5.4d) that the change in low-level COT during 1984-2018 contributed positively over the poles, the Mediterranean, Sahara and Arabian Peninsula. On the contrary, it contributed negatively over most oceans, more over the stratocumulus covered marine areas, Southern Ocean and parts of Eastern Europe. The contribution of mid-level COT (Figure 5.4e) is in general similar to that of low-level COT, but slightly less negative, i.e. more areas with positive contribution exist, yielding a global mean value equal to -0.15 Wm^{-2}. As already stated, the areas with positive contribution of low-level COT, e.g. the global continents, are also characterized by positive contribution of mid-level COT, but they are more extended or having larger values, while it is the same with the areas with negative contribution. Things are totally different as it concerns the contribution of high-level COT, which is mainly positive over most areas of the planet (Figure 5.4f) yielding a global average value of 3.68 Wm^{-2}, while it is stronger over the Indian Ocean and the Tibetan Plateau. On the contrary, COT of high-level clouds contributed negatively, over some limited parts of Antarctica, Indonesia and Guinea Gulf, whereas the contributions are close to zero over several marine stratocumulus areas. Changes of AOD at 550 nm (Figure 5.4g) during 1984-2018 contributed to GDB by 0.46 Wm^{-2} on a mean global basis, resulting in a slight overall brightening driven by dominant brightening across many regions, despite significant dimming in some areas. Indeed, the estimated contribution of AOD has strong negative values over India, East China, East Asia, Southern Africa, Middle East and Northern South America, where the 35-year changes of AOD decreased the SSR. On the other hand, significant positive contribution of AOD, equivalent to increased SSR, is found along central Africa, Europe, Eastern USA, Mexico and Antarctica. The long-term change of another important aerosol optical property, namely of SSA, contributed to GDB negatively almost all over the globe (Figure 5.4h), yielding a global average value being equal to -0.35 Wm^{-2}, which practically counterbalanced the positive contribution of AOD. Exceptions to the overwhelming negative contribution of SSA are the noticeable positive contributions over East China, India, central Africa and central Southern America. Besides, the contribution of changes of AP is very weak all over the globe (Figure 5.4i), with a near zero global mean value (-0.06 Wm^{-2}). Likewise, the contributions of water vapor and ozone to GDB (Figures 5.4j and 5.4k, respectively) are insignificant with mean global values equal to -0.21Wm^{-2} and 0.03 Wm^{-2} and without a noticeable contribution over a specific world region.

Based on the obtained results for the contribution of the various GDB drivers to the phenomenon during the entire study period 1984-2018, it is clear that they produced a lot of counteracting and competing effects both at regional and global scales. All these effects resulted in dimming and brightening of varying magnitudes over the globe, with opposite phenomena in adjacent world areas, but the brightening was dominant yielding a considerable global mean brightening equal to 3.06 Wm^{-2} (9.01 Wm^{-2} for land and 0.67 Wm^{-2} for oceans). Clearly, clouds and aerosols are found to have been the major drivers of GDB during the 35-year study period, with aerosols acting mainly at the local scale and clouds dominating both locally and globally. As for clouds, the cloud optical thickness of high-level clouds (Figure 5.4f) seems to have played a more decisive role in the total GDB compared to the middle- and low-level clouds.

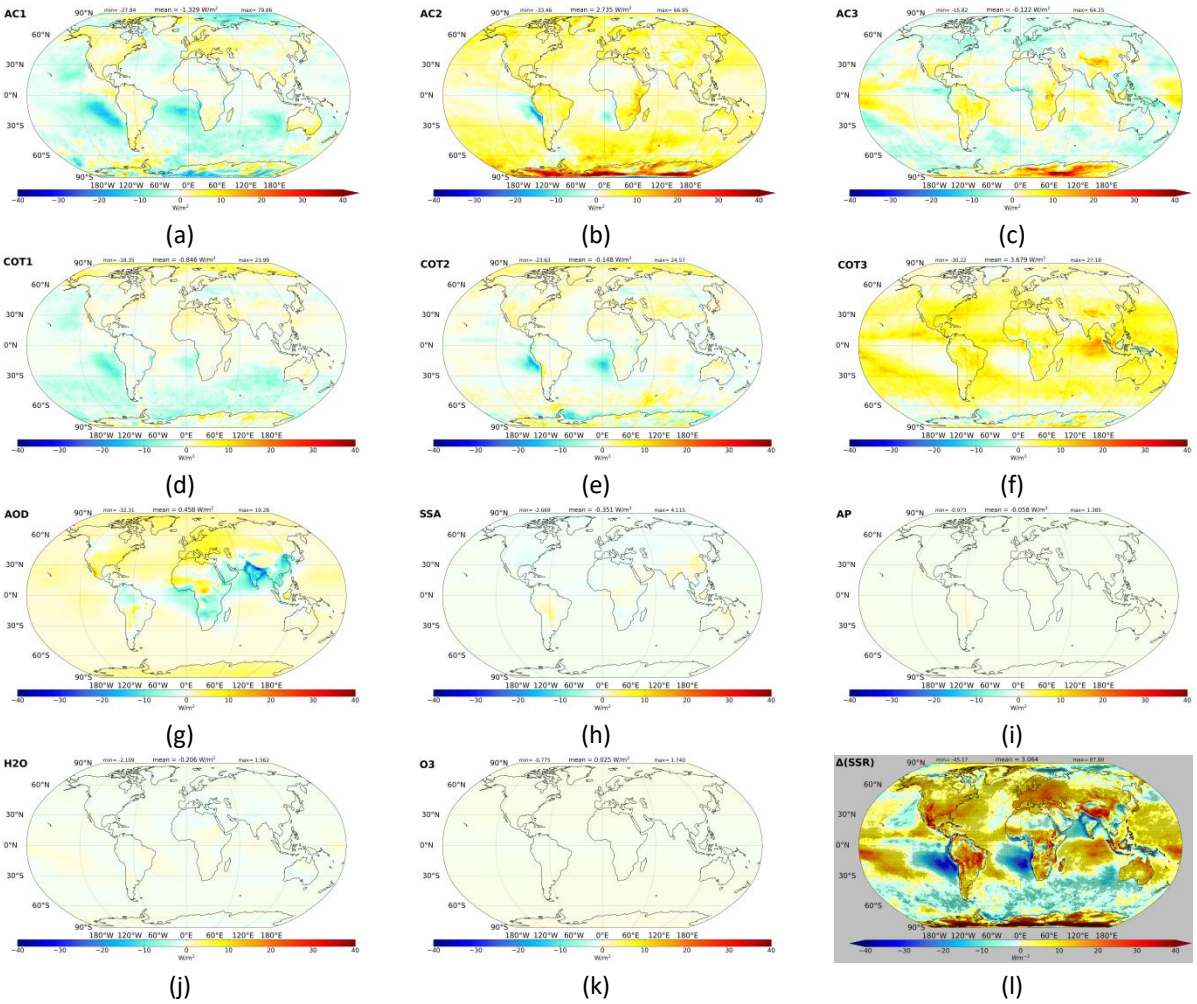


Figure 5.4. Global distribution of the contribution to GDB (in Wm^{-2}) of changes in low-level CA (a), mid-level CA (b), high-level CA (c), low-level COT (d), mid-level COT (e), high-level COT (f), AOD (g), SSA (h), AP (i), water vapor (j) and ozone (k), and the associated GDB (l) during 1984-2018. Reddish/bluish colors indicate contribution/counteraction to the estimated brightening or counteraction/contribution to the estimated dimming.

Actually, the contribution of the changes of COT of high-level clouds was positive practically all over the globe, with a global mean value of 3.68 Wm^{-2}, either contributing to brightening or counteracting the dimming caused by other drivers. Also, cloud amount of all cloud types, low, middle and high ones, seems to provide a significant contribution, with the contribution of mid-level cloud amount (2.73 Wm^{-2}), which is positive almost all over the globe, being greater than of the low- and high-level COTs (-1.33 Wm^{-2} and -0.12 Wm^{-2}, respectively). It should be noted that over areas with strong anthropogenic activities and significant air pollution (such as Europe, India and East China) the major driver of the GDB is the (changing) AOD. Yet, it should be noted that a small global mean contribution of a driver does not exclude the possibility that this driver can play an important or even primary role in a specific area of the globe (since large regional contributions of opposite sign counterbalance and result in a close to zero global mean contribution). Thus, it is important to also assess the contribution of GDB drivers to the phenomenon on a regional scale, which is done in the next section.

5.3.2 Contributions on a regional scale

Given the interdecadal nature of GDB and the changes of its sign during the decades, along with its spatially inhomogeneous patterns, it is necessary to examine the contribution to GDB of its drivers (parameters) not only for the entire time period (as done in the previous section) but also for the 4 sub-periods-decades of the study period, as well as over specific regions of the Earth. Thus, here, using the calculated global distribution of the contributions (Figure 5.4), these were spatially averaged over the entire globe, hemispherically, over land and oceans and over each of the 18 selected world areas, where this was done for both the entire study period 1984-2018 and the four decades contained in this period. Thus, five corresponding heatmaps were produced, shown in Figures 5.5 and 5.6, providing the averaged values of the contribution of each parameter for each region. In these heatmaps, based on the utilized color scales, intense colors (red and blue) indicate a strong contribution, while less intense colors (yellow, white, light blue) show small contribution.

For the entire study period (1984-2018, Figure 5.5a), it is observed that high-level COT along with the mid-level CA have been the major drivers of GDB, both contributing(positively) to the observed brightening in all cases, i.e. the globe, the two hemispheres and the global and hemispherical land and oceans, except for the SH oceans where they counteracted the observed dimming. During the 1980s (1984-1989, Figure 5.5b), the contribution of AOD seems to dominate, contributing to the brightening observed over the oceans and counteracting the dimming over land. Here it is worth noting the large contributions of COT, primarily of mid-level and secondarily of high-level clouds, over the land areas of the SH, which have caused a stronger dimming than the AOD brightening, ultimately resulting in an overall dimming. In the next decade, namely in the 1990s (Figure 5.5c), AOD remains the main GDB driver throughout the planet and hemispheres, both over land and oceans, contributing to the estimated brightening everywhere. The situation changes in the 2000s (Figure 5.5d), when high-level COT emerges as the main GDB driver, followed by the mid-level CA together with AOD, COT and CA causing brightening while AOD caused a dimming. The former two parameters contribute positively, whereas AOD negatively, to the observed overall brightening, more or less everywhere, during this decade. It should be noted that in a previous study, Hatzianastassiou et al. (2020) using a previous version of the same RTM applying the same methodology for the period 2001-2009 and cloud input data from ISCCP-D2 and aerosols from MODIS-Terra C006 also found clouds to be the major driver of GDB and AOD playing a secondary role.

Nevertheless, they found that middle-level CA is the primary GDB driver, opposite to COT having a small contribution to GDB, whereas our findings suggest that high-level COT is the major GDB driver followed by the middle-level CA. This difference might be attributed to the presence of positive contributions of high-level COT that appear homogeneously distributed across the planet except for the poles based on the present data set (CLARISC). In contrast, based on the study of Hatzianastassiou et al. (2020) and the ISCCP-D2 dataset the contribution of high-level COT is not homogeneously distributed (showing both positive and negative contributions) mainly due to the presence of artifacts and this led to small global average values. During the 2010s (Figure 5.5e), clouds and aerosols have quite comparable contributions in terms of both sign and magnitude. More specifically, CA and COT of all cloud types, and AOD mostly have caused brightening, with a few exceptions for CA, primarily of middle-level clouds, which

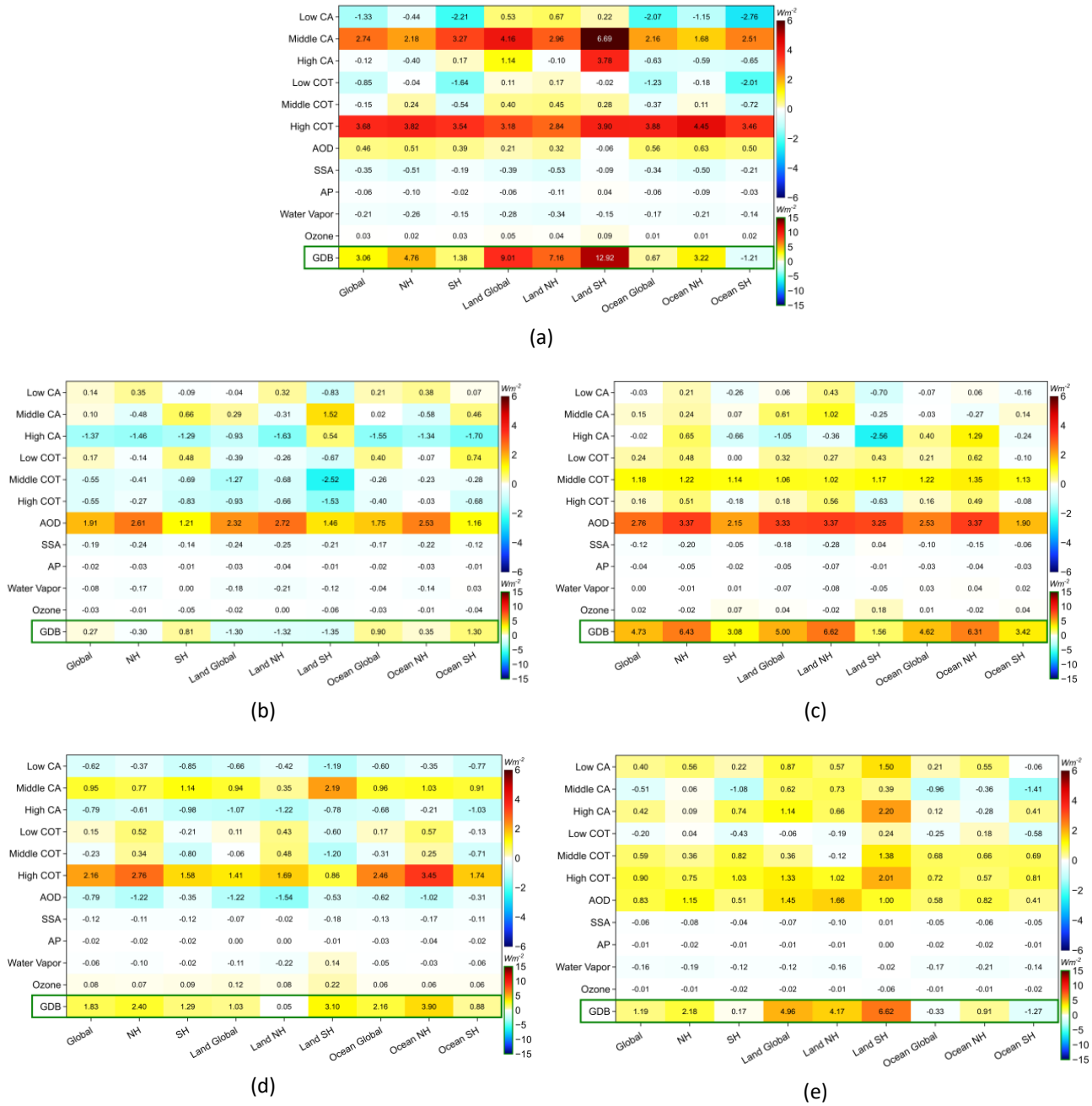


Figure 5.5. The spatially averaged contribution to GDB (in Wm^{-2}) of each GDB driver over the globe, the two hemispheres and the globe's and the two hemispheres' land and ocean areas during the entire study period 1984-2018 (a), as well as during 1984-1989 (b), 1990-1999 (c), 2000-2009 (d) and 2010-2018 (e). Reddish/bluish colors indicate contribution/counteraction to the overall estimated brightening or counteraction/contribution to the overall estimated dimming. The last row includes the corresponding overall GDB in Wm^{-2} with reddish colors indicating brightening and bluish dimming.

occasionally (in some cases, e.g. in SH oceans and the globe), caused dimming. The corresponding trends on seasonal basis can be found in Figures AD8-AD11.

During DJF in the period 1984–2018, the largest contribution to the GDB came primarily from COT3, followed by CA2. In the periods 1984–1989 and 1990–1999, changes in AOD made the strongest

contribution to the GDB. In the 2000s, the main contributor appears to be COT3, followed by AOD and CA2. For the period 2010–2018, the contributions of clouds and AOD are of similar magnitude. In MAM, the overall contribution to the estimated GDB is dominated by COT3 and COT2. During both 1984–1989 and 1990–1999, AOD had the largest impact, followed by CA3. In the period 2000–2009, COT3 contributed most to the GDB, whereas in the 2010s, AOD generally dominated—with a notable exception over southern hemisphere land areas, where CA1 and CA2 had the most significant influence. In JJA during 1984–2018, COT3 and CA2 again played the largest roles in driving the GDB. For the periods 1984–1989 and 1990–1999, AOD was the main contributor. In the 2000s, COT3 emerged as the dominant factor. In the period 2010–2018, contributions from both clouds and aerosols were of similar magnitude. Notably, during this time, AOD made a strong contribution in the NH, while over land, CA2 had the strongest impact on the GDB. Finally, during SON in the period 1984–2018, COT3 and CA2 once again had the most significant influence. In general, AOD dominated in the 1984–1989 and 1990–1999 periods, with a major exception in the southern hemisphere land areas where CA2 was the leading contributor. In the 2000–2009 period, COT3 was the main contributor, followed by CA2 and AOD. In the final period, 2010–2018, COT3 and CA3 appear to have slightly stronger contributions to the GDB than the other parameters. Although minor seasonal variations exist in terms of the leading contributors to the GDB, the overall pattern closely aligns with the results of the annual analysis presented earlier. This consistency between seasonal and annual analyses suggests a degree of stability in the dominant factors influencing the GDB across decades. Specifically, AOD played a decisive role in shaping the GDB during the 1984–1999 period, both seasonally and annually. In the 2000s, COT3 took the lead, with AOD making secondary contributions. Finally, during the 2010–2018 period, both seasonally and annually, the contributions of clouds and aerosols were fairly similar in magnitude.

Beyond the global/hemispherical/continental analysis, we delved into smaller areas over land, namely the specific selected 18 world areas included in the trend analysis. The general picture for the four decades (Figure 5.6) looks similar to some degree with that of Figure 5.5. First of all, it is observed that in all 4 decades, clouds (cloud amount and optical thickness) and aerosols, specifically AOD, were the main GDB drivers, having the largest contribution, much larger (by about one order of magnitude) than the contribution of SSA and water vapor, whereas the contributions of ozone and AP are even smaller. In the 1980s, dimming occurred over 13 of 18 regions, arising mostly from the negative contribution of clouds, due to their general increase over this decade as shown in Figure 5.3 and by Devasthale and Karlsson (2023). On the other hand, AOD has everywhere positively contributed, which means that the AOD changes (decreases) caused brightening, either contributing to the overall brightening or counteracting the overall dimming. The most common strongest contributor (in 11/18 areas) is AOD, whose changes played a decisive role over many regions such as Europe, East Asia, India and eastern USA. During the 1990s, brightening occurred over all regions except for Australia, Antarctica and South Africa. This brightening resulted primarily by the decreasing AOD, except for the eastern US and Mexico, where the strongest contributor there was high-level CA and then AOD, and eastern China and Asia, where the primary contributor was low-level CA and then AOD. As it concerns the dimming and the areas where it took place, cloud amount played a decisive role, especially the CA of high-level clouds over Australia and Antarctica and the CA of low clouds over southern Africa. Again, as in the 1980s, the most frequent strongest contributor to GDB has been AOD since it was the strongest contributor in 11/18 areas during

the 1990s. Our results clearly indicate a reduction in AOD, which is in line with other studies highlighting the AOD changes as main cause of the brightening during this decade (e.g., Norris and Wild 2007; Nabat et al., 2014; Chin et al., 2014). This decrease in aerosol load is in line with the measures taken to reduce the air pollution (Streets et al., 2006; Mishchenko et al. 2007; Nabat et al., 2013).In the next decade, that is in the 2000s, the brightening of the previous decade seems to have leveled off and even reversed into dimming in several areas as other studies also suggested (Wild 2007, Wild 2016). More specifically, the strong 1980s' brightening in Europe (9.73 Wm^{-2}) converted to a slight dimming apparently due to increased low- and high-level CA. On the other hand, the dimming in northern South America is mainly due to high-level CA, in India it is mainly due to AOD and secondarily to high-level CA, in East Asia and China the strongest driver was increasing AOD, in the Sahara the high-level CA and in the Middle East AOD. On the contrary, the brightening in Siberia, Arctic and Antarctica was caused mainly by the changes (decreases) of mid-level CA, while in southern South America it was due to the changes in high-level CA, in Australia, eastern USA, central and southern Africa and Mexico is attributed to the high-level COT and in western Canada to the mid-level COT. In this decade, the most frequent strongest contributor to GDB was COT of high-level clouds, dominating in 7/18 areas. In the next/last decade, that of 2010, a strong brightening prevailed in all areas, roughly similar to the 1990s.Again, as in the previous three decades, this brightening was not due to just one factor, but to different ones depending on the area. For example, the changes of AOD contributed more than those of other drivers to GDB over Siberia, Europe, Eastern China and Asia, the Middle East, the Mediterranean, the Sahara and the Arctic. Low-level CA had the largest contribution over southern South America and the eastern USA, mid-level CA was stronger over western Canada and southern Africa, while high-level CA was the primary contributor over Australia, northern South America, central Africa and India. While the mid-level COT was the strongest contributor over Antarctica, the high-level COT was dominant over Mexico. During this decade, AOD changes was the most common strongest contributor being the primary driver of GDB over 8/11 areas.

In summary, the results clearly demonstrate the great complexity regarding the causes of GDB on a regional and decadal scale basis. It was shown that the primary drivers differ from one region to another and from a decade to another. Yet, some main conclusions can be drawn. Thus, according to our analysis, it appears that overall, for the 4 decades and the 18 world land regions, i.e. for 72 cases, the most frequent strongest contribution to GDB was made by the changing AOD, which dominated in 35 of 72 cases or in 48.6%. AOD was followed by the high-level CA (18/72 or 25% of cases), mid-level CA (9/72 or 12.5%), high-level COT (7/72 or 9.7%), mid-level COT (2/72 or 3.8%) and low-level CA (1/72 or 1.4%). The AOD changes were the main drivers of GDB over areas with intense anthropogenic pollution such as China, Europe and India. Indeed, similar findings were also reported by other studies for China (Yang et al., 2021; Tang et al., 2022; Shi et al., 2020), for Europe (Power, 2003; Wild et al, 2005; Streets et al., 2009; Manara et al., 2016, Wild et al., 2021) and for India (Soni et al., 2012, 2016). On the other hand, over USA, clouds seem to have played a dominant role in the changing phases of GDB and this agrees with the studies by Long et al., 2009, Augustine and Dutton, 2013 and Augustine and Capotondi, 2022. Although SSA, H_2O, O_3 and AP contributed much less than clouds and AOD, the largest contribution (larger than 1 Wm^{-2}) of SSA occurred over eastern China in the 2000s, which was actually greater than the contribution of cloud amount to this region in this decade. This positive contribution of the SSA to GDB means that the scattering contribution to the total extinction (scattering and absorbing) increased (in other words, the scattering aerosols

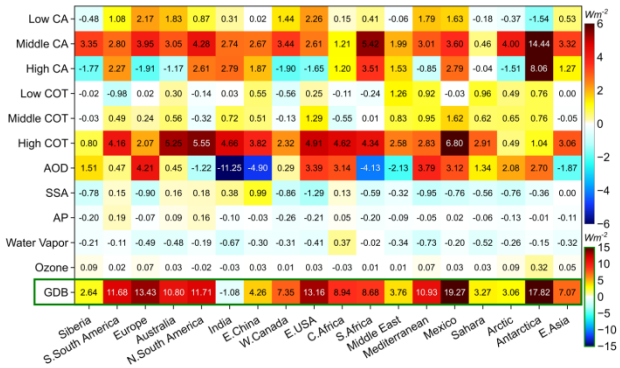
increased), counteracting the estimated dimming over East China in the 2000s. Indeed, the estimated SSA increased over E. China in the 2000s, agreeing with the reported increased scattering AOD in this region and decade (Kang et al., 2019). It should be noted that this increase of SSA added to increased AOD, causing a dimming over East China in the 2000s. Opposite to AOD, but also SSA, the AP had consistently very small contribution in all decades. On the other hand, the contribution of water vapor to GDB was considerable in Mexico in the 1990s, 2000s and 2010s due to large decreasing and increasing trends in water vapor, respectively (Figure 5.6). Indeed, over the wider area of Mexico our results, in agreement to others (Zhao et al., 2023) indicate decreasing water vapor trends during the 1990s, weak increasing trends in the 2000s and increasing trends in the 2010s. Another case with significant contribution (negative) of water vapor is in Australia during the 1990s, when large increasing trends of water vapor are observed according to our MERRA-2 data as well as to the literature (Parracho et al., 2018). As to the ozone, its contribution is generally smaller than of the water vapor. However, its contribution is greatest, greater than that of water vapor, SSA and AP, over Antarctica in the 1990s and 2000s, when it caused significant brightening counteracting the overall observed dimming there. Our estimated reduced ozone absorption over Antarctica in the 1990s and 2000s is in line with decreasing MERRA-2 ozone trends, which are in agreement with the observations (Bian et al., 2012; Steinbrecht et al. 2018) that suggest a strong reduction of ozone in Antarctica inthe1990s along with a weak ozone decrease in the 2000s.

5.4 Correlation & Regression Analysis

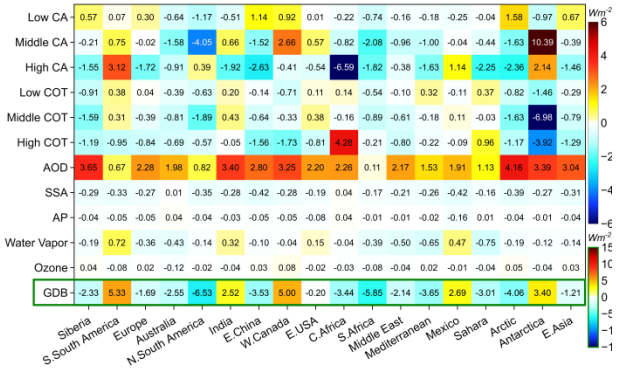
While it is highly interesting to understand multi-decadal changes in SSR, examining month-to-month variations and their driving factors offers crucial insights into the mechanisms shaping long-term trends. By computing correlation coefficients between SSR and individual GDB drivers—such as cloud properties and aerosols—on a monthly basis for each pixel (as, for example, shown in Figure 5.7), short-term relationships can be captured, which collectively influence long-term variability. Our findings reveal a strong association between SSR and low- to mid-level clouds, while other parameters exhibit comparatively weaker but still noteworthy contributions. These monthly correlations underscore the role of seasonal fluctuations, which, when accumulated over time, contribute to broader trends in SSR. Incorporating this finer temporal resolution enhances the robustness of our multi-decadal analysis, offering a more comprehensive understanding of the complex interactions driving SSR variability. The results highlight significant regional disparities, emphasizing the necessity of accounting for both cloud and aerosol properties when assessing their impact on solar radiation. The combined use of Pearson correlation (sub-section 5.4.1), ridge regression (sub-section 5.4.2), and Random Forest feature importance (sub-section 5.4.3) provides a holistic and robust perspective on the factors influencing monthly SSR variations.

5.4.1 Pearson correlation coefficients

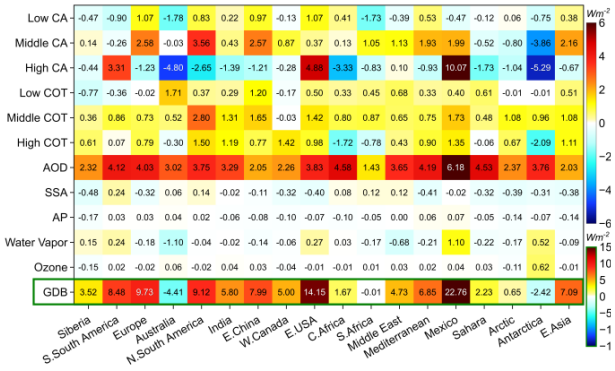
The Pearson correlation coefficients (R) presented in Figures 5.7, 5.8, and 5.9 offer a comprehensive assessment of the relationships between surface solar radiation (SSR) and GDB drivers, including cloud amounts (CA1, CA2, CA3), cloud optical thickness (COT1, COT2, COT3), aerosol optical depth (AOD), single-



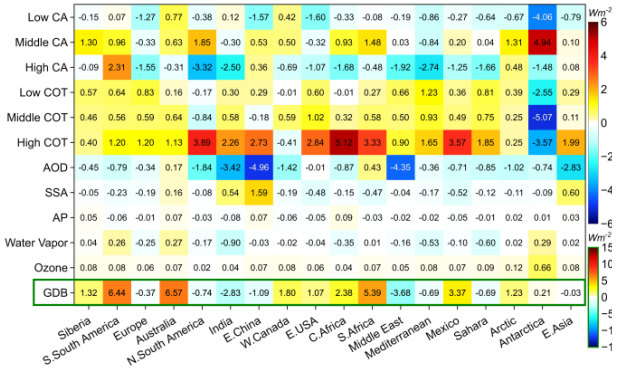
(a)



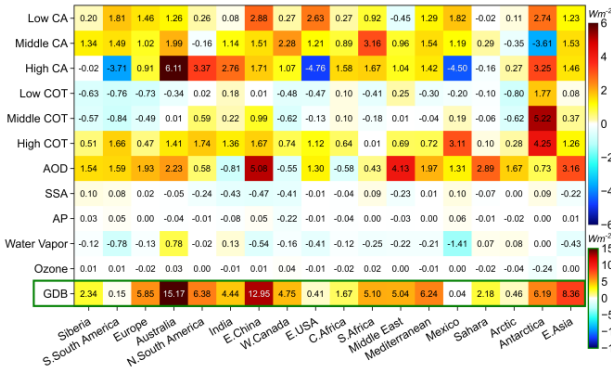
(b)



(c)



(d)



(e)

Figure 5.6. The spatially averaged contribution to GDB (in Wm^{-2}) of each GDB driver over the specific 18 land areas during the entire study period 1984-2018 (a), as well as during 1984-1989 (b), 1990-1999 (c), 2000-2009 (d) and 2010-2018 (e). Reddish/bluish colors indicate contribution/counteraction to the estimated brightening or counteraction/contribution to the estimated dimming. The last row includes the corresponding GDB in Wm^{-2} with reddish/bluish colors indicating brightening/dimming.

scattering albedo (SSA), aerosol properties (AP), water vapor (H_2O), and ozone (O_3). These figures provide a multi-scale analysis, from global to regional perspectives, revealing the complex interplay between these

atmospheric components and SSR. Figure 5.7 illustrates the global correlation maps, highlighting regions of both strong and weak correlations. The spatial distribution of these correlations suggests that cloud properties and aerosols influence SSR differently depending on location. Figure 5.8 further extends this analysis by presenting global, hemispheric, and regional averages, which help to identify larger-scale patterns and trends. Lastly, Figure 5.9 focuses on specific land-regional correlations, particularly over Europe, India, and East China, offering deeper insights into localized variations in SSR responses to changes in cloud and aerosol characteristics. In general, clouds, aerosols, and water vapor exhibit negative correlations with SSR, with varying strengths. However, an exception is observed for low-level clouds (CA1) over some tropical oceanic regions, where a strong positive correlation up to 0.8 is detected. Although this may seem counterintuitive, it can be explained by the fact that these areas typically have very few low-level clouds (Figure 3.2a). When SSR increases, the environmental conditions become more favorable for the occasional formation of these clouds, resulting in a slight increase in their presence alongside higher solar radiation. This behavior contrasts with regions dominated by persistent stratocumulus decks, where extensive cloud cover blocks sunlight, resulting in a negative correlation between cloud amount and SSR. Additionally, low correlation values are found globally for SSA, AP, and ozone, indicating a relatively weaker influence of these parameters on SSR at a broad scale. Specifically, the correlation between CA1 and SSR is -0.12 on a global mean basis, with stronger negative values over NH land, Siberia, the Arctic, and Europe. Middle-level clouds (CA2) demonstrate a stronger anti-correlation with SSR, reaching a global mean value of -0.4, with particularly pronounced negative correlations over land regions, including Antarctica, Europe, and the Middle East. CA3 show their strongest negative correlations over land areas such as Australia, India, Mexico, the Sahara, and the Middle East, with a global mean value of -0.52. The correlation between low-level cloud optical thickness (COT1) and SSR is -0.40 globally, with stronger values over SH oceans and East China. COT2 has an even stronger anti-correlation, with a global mean of -0.57, peaking over oceans, East China, and the eastern United States while COT3 shows significant negative correlations over NH oceans, northern South America, and central Africa, with a global mean value of -0.48. Aerosols also contribute to the reduction of SSR, with AOD showing a global mean correlation of -0.24, with the strongest values over NH land, particularly the Sahara, the Mediterranean, the Middle East, and central Africa. SSA exhibits a weaker anti-correlation with SSR (-0.21), with the strongest effects observed over NH oceans, the eastern United States, and Mexico. AP shows an even weaker relationship with SSR, with a global mean correlation of -0.02, but with higher values over NH land, Europe, and East China. Notably, a small positive correlation (0.20) is observed over oceanic regions. Water vapor displays strong negative correlations with SSR, with a global mean value of -0.34. The strongest correlations are found over SH land regions, including Australia, the Middle East, and the Sahara. Finally, ozone stands out as the only parameter exhibiting a global positive correlation with SSR, with a mean value of 0.07. This positive relationship is prevalent across most regions except for Europe, western Asia, and western North America, where negative correlations are observed. The most pronounced negative values are found over NH land and Europe, whereas the strongest positive correlations appear over SH oceans and central Africa. Overall, these results highlight the intricate and regionally dependent nature of SSR interactions with clouds, aerosols, water vapor and ozone. The findings emphasize the dominant role of cloud properties in modulating SSR, followed by aerosols and water vapor, with ozone playing a more nuanced role depending on geographical location. These insights

are crucial for improving radiative transfer models and understanding the spatial variability of solar radiation reaching the Earth's surface.

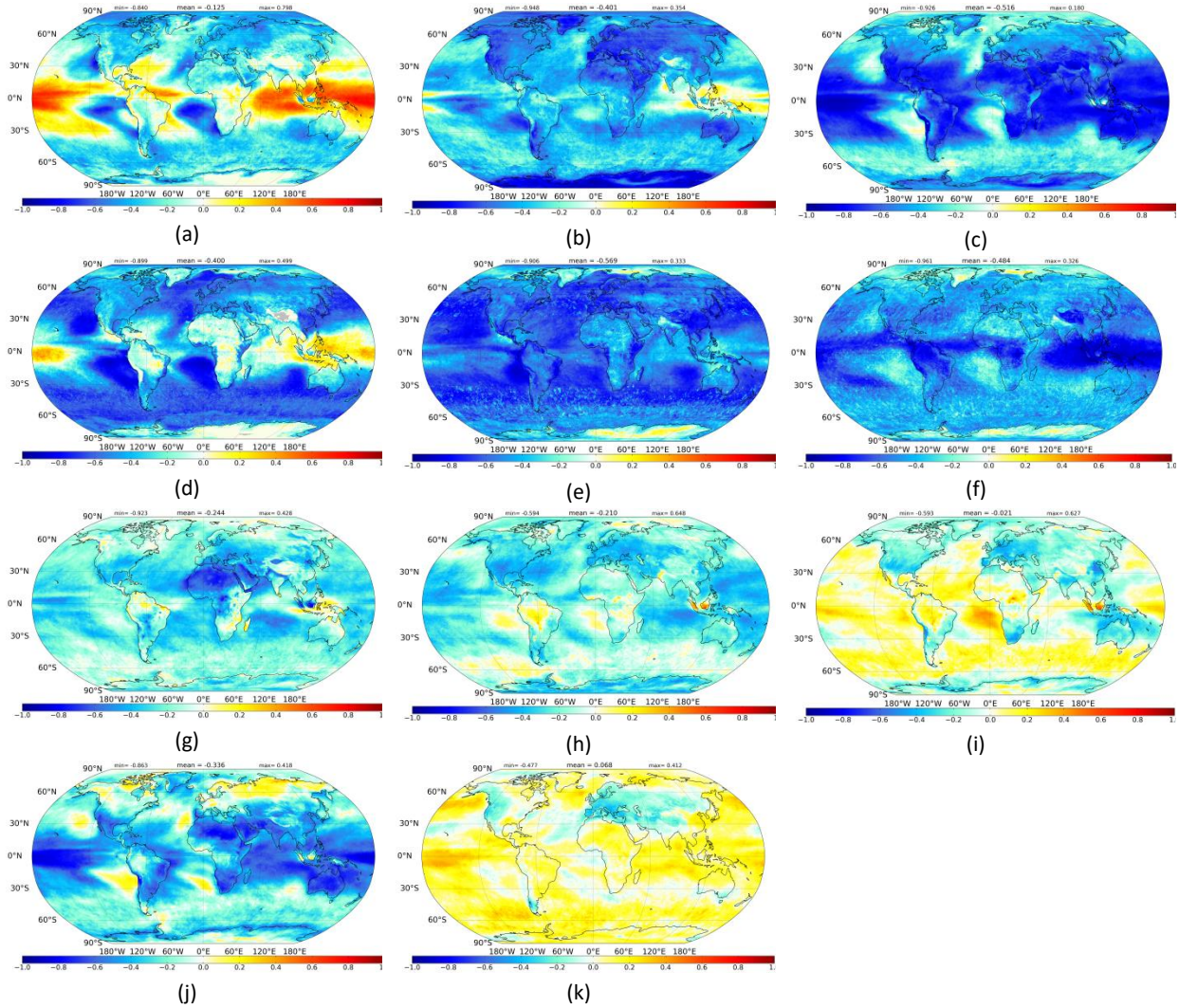


Figure 5.7. Global distribution of Pearson's R between the monthly anomalies of SSR and the low cloud amount (CA1, a), middle CA(CA2,b), high CA(CA3, c), low-level cloud optical thickness (COT1, d), mid-level COT (COT2, e), high-level COT(COT3, f), aerosol optical depth (AOD, g),aerosol single scattering albedo (h), aerosol asymmetry parameter (i), water vapor (j), and ozone (k) during 1984-2018. Reddish/bluish colors indicate positive/negative R values.

As shown in Figure 5.8, the highest average anticorrelation with SSR is shown by COT2 equal to -0.57 both globally and in the NH and SH, which is mainly due to the strong anticorrelation over the oceans, while over land CA3 has the most significant anticorrelation equal to -0.59. It is also interesting to investigate the anticorrelations in different land areas of the planet. For example, over Europe, the Mediterranean, Siberia, Western Canada and the polar regions, CA2 shows a stronger anticorrelation of up to -0.79. In Australia, India, southern South America, Mexico, southern Africa, the Middle East and the Sahara, CA3 shows the highest anticorrelation with SSR. On the other hand, East Asia and China, and the eastern USA

appear to have COT2 with the highest anticorrelation. It should be noted here that AOD has the highest anticorrelation with SSR over the Sahara (equal to -0.58) the Middle East, the Mediterranean and central Africa. The remaining parameters generally have small R values except for water vapor which shows a strong anticorrelation in Australia (-0.65).

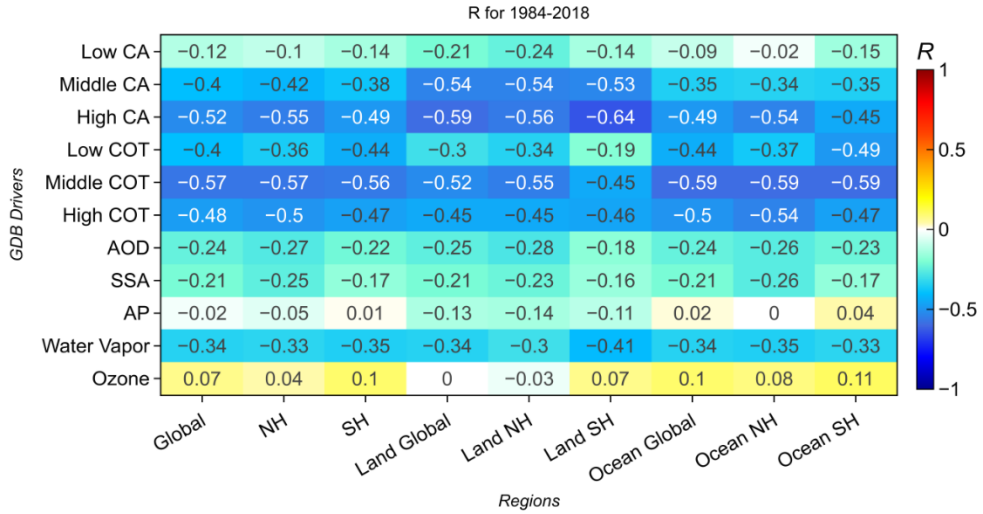


Figure 5.8. The spatially averaged Pearson's R between the monthly anomalies of SSR and the GDB drivers over the globe, the two hemispheres and the globe's and the two hemispheres' land and ocean areas during the entire study period 1984-2018. Reddish/bluish colors indicate positive/negative R values.

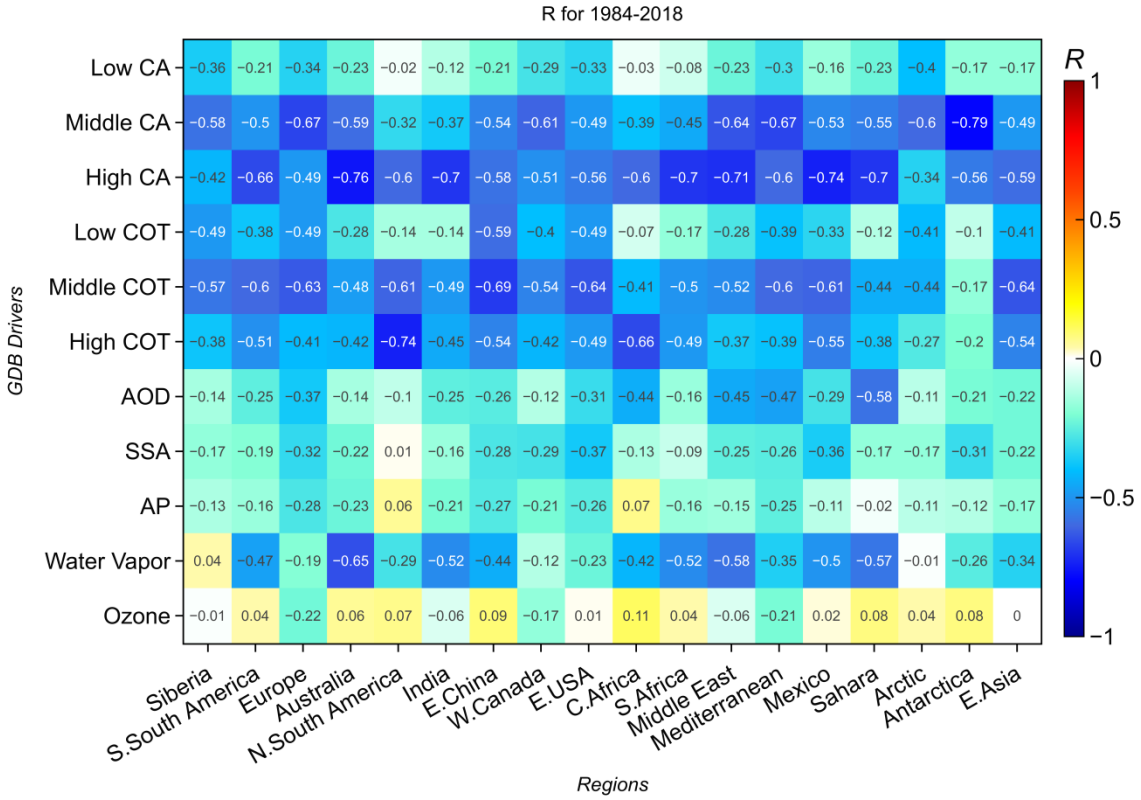


Figure 5.9. The spatially averaged Pearson's R between the monthly anomalies of SSR and the GDB drivers over 18 land regions of the globe during the entire study period 1984-2018. Reddish/bluish colors indicate positive/negative R values.

5.4.2 Ridge regression analysis

The ridge regression coefficients (β) presented in Figures 5.10, 5.11, and 5.12 offer a comprehensive assessment of the relationships between surface solar radiation (SSR) and GDB drivers. Figure 5.10 illustrates the global coefficient maps, highlighting regions of both strong and weak influences. The spatial distribution of these coefficients suggests that cloud properties, aerosols, and atmospheric gases influence SSR differently depending on location. Figure 5.11 further extends this analysis by presenting global, hemispheric, and regional averages, which help to identify larger-scale patterns and trends. Lastly, Figure 5.12 focuses on specific regional coefficients, offering deeper insights into localized variations in SSR responses to changes in cloud and aerosol characteristics. In general, clouds, aerosols, water vapor and ozone exhibit coefficients with SSR, with varying magnitudes. The strongest coefficients computed are between SSR and CA, especially the CA3, while the COT (especially COT3) is following. Also, AOD exhibits the highest coefficients only over specific land regions such as central Africa, South America, Indonesia and eastern Asia. Additionally, low coefficient values are found globally for SSA, AP, and ozone, indicating a relatively weaker influence of these parameters on SSR at a broad scale. Specifically, the coefficient between CA1 and SSR is -4.9 on a global mean basis, with stronger negative values over SH ocean, the Arctic, and East USA. It is noteworthy that, in contrast to the Pearson correlation, the ridge correlation analysis does not yield any positive coefficients for low-level cloud amount (CA1), even in the tropical ocean regions where Pearson's R shows strong positive values (up to 0.8). This difference arises from the distinct sensitivities of the two methods: Pearson's R is purely a measure of linear association and can be strongly influenced by the underlying distribution and outliers in the data. In areas with generally low amounts of low-level cloud, sporadic increases in cloudiness during periods of high solar radiation can artificially inflate the linear correlation, suggesting a positive relationship that may not be physically robust. Ridge correlation, by contrast, is more resilient to such artifacts, as it regularizes the influence of variables and reduces the impact of collinearity and extreme values. As a result, ridge correlation provides a more conservative and physically meaningful estimate of the relationship (Hoerl et al., 1970). The absence of positive ridge correlation coefficients implies that the observed positive Pearson correlations do not represent a true underlying physical link between low-level cloud cover and surface solar radiation, but are rather statistical artifacts driven by the rarity and variability of clouds in these regions. This highlights the importance of using complementary correlation metrics to accurately interpret physical processes in climate data analysis. CA2 demonstrate a comparable to CA1 negative coefficient with SSR, reaching a global mean value of -4.5, with particularly pronounced negative coefficients over SH land regions, including Antarctica, East China and the Arctic. High-level cloud amount (CA3) shows the largest coefficient comparing to CA1 and CA2, being the strongest over SH land areas such as Australia, Mexico and South Africa, with a global mean value of -8. The coefficient between COT1 and SSR is -2 globally, with stronger values over SH oceans, the Arctic and Siberia. COT2 has an even stronger negative coefficient, with a global mean of -3.7, peaking over NH land, Siberia and Europe. COT3 shows significant negative coefficients over SH lands, northern South America, and central Africa, with a global mean value of -3.7. Aerosols also contribute to the reduction of SSR, with AOD showing a global mean coefficient of -1.9, with the strongest values over NH land, particularly the Sahara, India and central Africa. SSA exhibits a much weaker negative coefficient with SSR (-0.01), with the strongest effects observed over NH lands,

India, East China and central Africa. AP shows also a weak relationship with SSR, with a global mean coefficient of -0.01, but with higher values over NH land, Europe, and Antarctica. Water vapor displays a strong negative coefficient with SSR, with a global mean value of -1.2. The strongest coefficients are found over SH oceanic regions, including Australia and Antarctica. Finally, ozone stands out with a mean value of -0.03. This relationship is prevalent across NH land regions, the Arctic and Siberia. In addition, SSR was predicted using Ridge regression, and the model's performance was evaluated by computing the R^2 score between the deseasonalized anomalies of the Ridge-predicted SSR and those from the FORTH-RTM dataset, as illustrated in Figure 5.10l. The results indicate that the Ridge regression model effectively captures the variability of SSR within the latitude band of 60°N to 60°S. However, its performance declines noticeably outside this range—particularly in high-latitude regions which could be attributed to less data availability and less reliable satellite input data over polar regions. The findings emphasize the dominant role of cloud properties in modulating SSR, followed by aerosols and water vapor, with ozone playing a more nuanced role depending on geographical location. It's important to interpret the small positive ridge coefficients with caution in this context. They may reflect localized or coincidental co-variability, rather than a physically meaningful mechanism. Ridge regression minimizes the influence of outliers and multicollinearity, but positive coefficients—especially if they are very small—often indicate residual or indirect links in the data.

As shown in Figure 5.11, according to Ridge regression, CA3 has the greatest effect on SSR worldwide in both the NH and SH, as well as on land and oceans. This is also found in Figure 5.12, where the land areas are examined in detail. In the majority, the effect of CA3 prevails, except for Siberia and Europe, where COT2 prevails. In addition, in western Canada, Antarctica and the Arctic, CA2 prevails, in central Africa, COT3 and in the Sahara, AOD. It is worth noting that AOD has a great effect on SSR not only in the Sahara but also in central Africa and India. Comparing ridge regression coefficients with Pearson's R reveals that, while both methods often highlight similar dominant drivers of SSR at large scales, their results can differ in regions with strong collinearity or limited data variability. Ridge regression is more robust in handling multicollinearity and tends to suppress spurious correlations, making its results generally more reliable in complex atmospheric systems. However, its coefficients can be less intuitive to interpret due to the regularization process. Pearson's R is straightforward and widely used, but it may overestimate associations when variables are interdependent. Using both approaches provides a more balanced and physically meaningful understanding of SSR relationships. In most cases, Pearson's R and ridge coefficients are in agreement, typically showing negative correlations between SSR and the main GDB drivers—highlighting the dominant role of clouds in modulating SSR variability. However, some differences do arise; for example, over India and East China, the coefficients for SSA and AP are small and negative according to Pearson's R, but small and positive with ridge regression. These discrepancies underscore how ridge regression can reveal subtle or masked associations that Pearson's R might overlook, especially in the presence of collinearity among variables. But it should be noted that small coefficients, whether from Pearson's R or ridge regression, typically indicate a weak or negligible association between the physical variables.

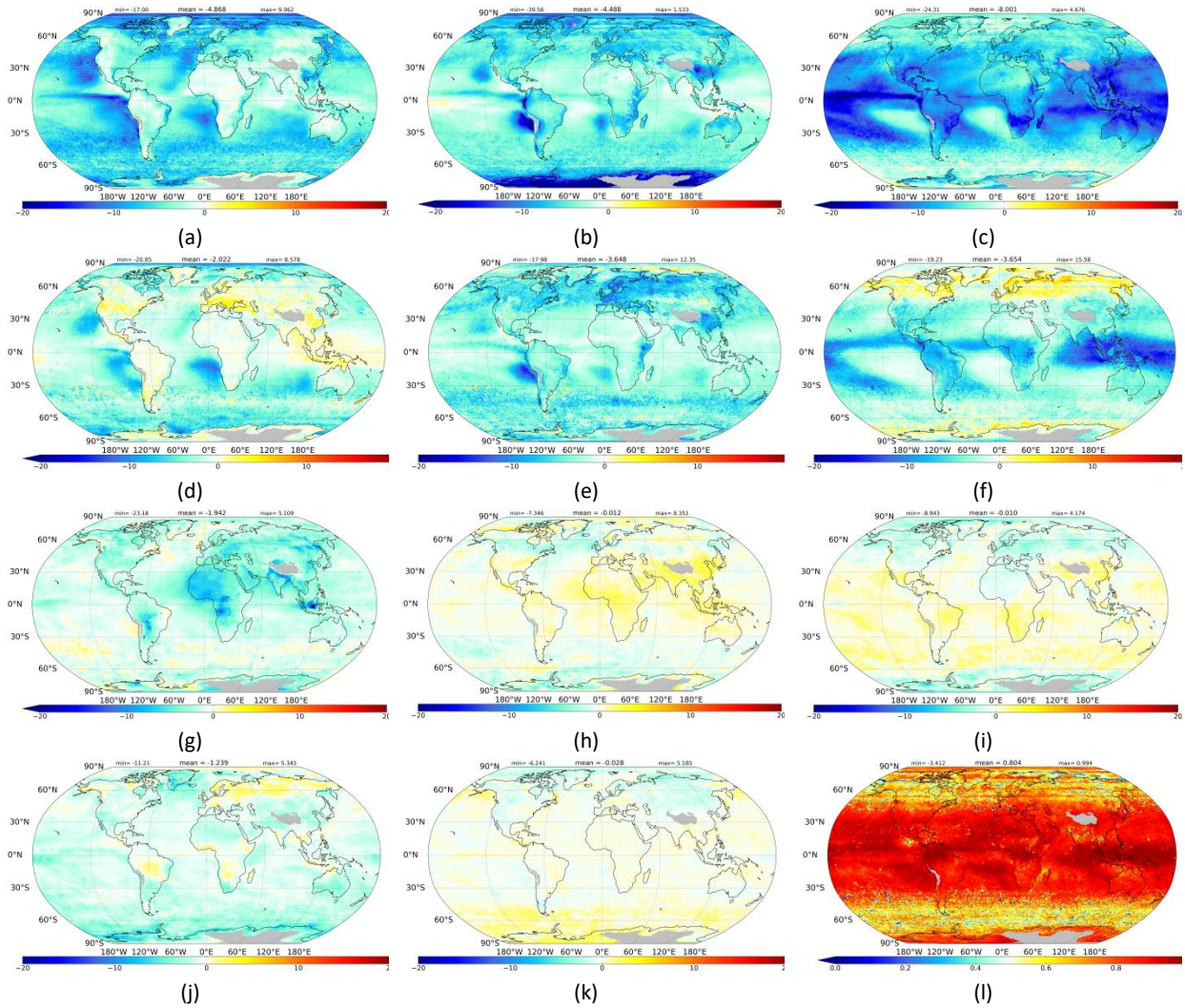


Figure 5.10. Global distribution of Ridge beta coefficients between the monthly anomalies of SSR and the low cloud amount (CA1, a), middle CA (CA2,b), high CA (CA3, c), low-level cloud optical thickness (COT1, d), mid-level COT (COT2, e), high-level COT (COT3, f), aerosol optical depth (AOD, g), aerosol single scattering albedo (h), aerosol asymmetry parameter (i), water vapor (j), and ozone (k) during 1984-2018. Reddish/bluish colors indicate positive/negative coefficients. Also, in the lower right it is shown the R^2 score of the Ridge SSR anomalies predictions in comparison with the FORTH-RTM SSR anomalies.

5.4.3 Random Forest Regression

The feature importance values derived from the Random Forest regression analysis, as depicted in Figures 5.13, 5.14, and 5.15, provide valuable insights into the relative contributions of GDB drivers to SSR. The figures offer a multi-scale assessment, highlighting key drivers of SSR variability at global and regional levels. Figure 5.13 presents global feature importance maps, showcasing areas where specific parameters exert stronger or weaker influences on SSR. It is important to clarify that feature importance values, as derived from Random Forest regression, are not the same as correlation coefficients. While

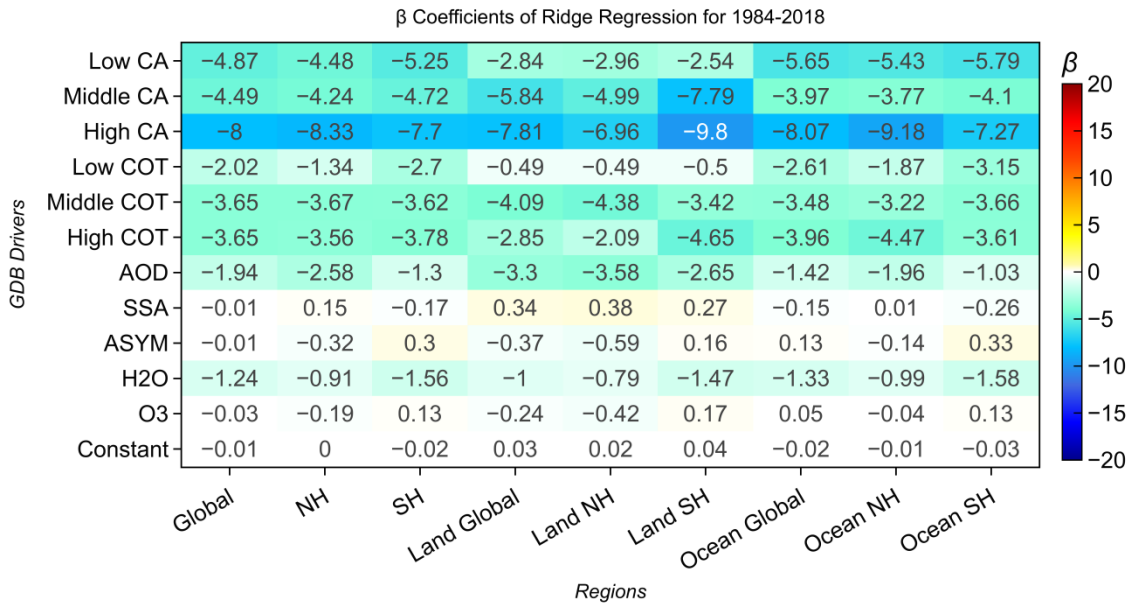


Figure 5.11. The spatially averaged Ridge beta coefficients between the monthly anomalies of SSR and the GDB drivers over the globe, the two hemispheres and the globe's and the two hemispheres' land and ocean areas during the entire study period 1984-2018. Reddish/bluish colors indicate positive/negative coefficients.

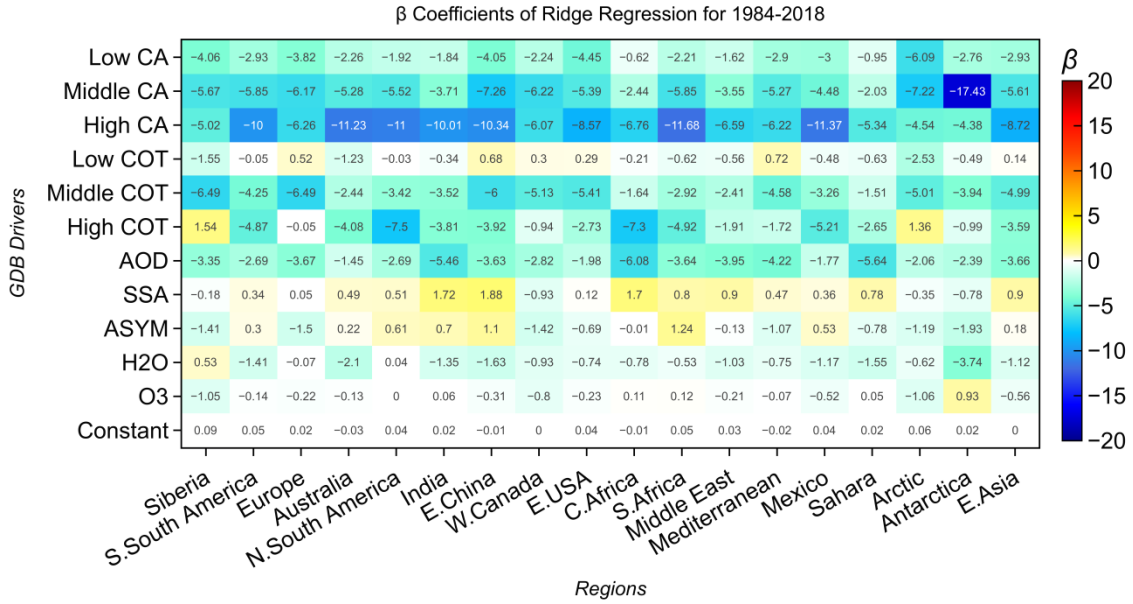


Figure 5.12. The spatially averaged Ridge beta coefficients between the monthly anomalies of SSR and the GDB drivers over 18 land regions of the globe during the entire study period 1984-2018. Reddish/bluish colors indicate positive/negative coefficients.

both metrics provide information about relationships between variables, they measure different things. Correlation coefficients (like Pearson's R or ridge regression coefficients) quantify the strength and direction of a linear association between two variables. In contrast, feature importance reflects how much each predictor (or feature) contributes to the model's predictive power, considering all possible

interactions and non-linear effects. In other words, a variable can have a low linear correlation with SSR but still be highly important for predicting SSR in the Random Forest model if it interacts strongly with other variables or has a non-linear effect. Therefore, feature importance and correlation coefficients are related concepts, but they are not identical and should not be interpreted in the same way. Figure 5.14 complements this understanding by summarizing global, hemispheric, and regional average importance values, revealing broader spatial patterns. Finally, Figure 5.15 zooms into specific regions, providing a more detailed analysis of localized variability in SSR sensitivity to cloud and aerosol properties. In general, COT has the largest importance across all over the world following by the CA3. In contrast, SSA, AP, and ozone generally exhibit lower importance globally, suggesting a more limited impact on SSR variations. Specifically, CA1 shows a low global mean importance value of 0.05, with low importance over all the regions globally, where it plays a weak role in influencing SSR. Middle-level cloud amount (CA2) exhibit a feature importance with a global mean value of 0.09, showing particularly strong contributions over middle and polar latitudes. CA3 has its strongest influences across all the cloud amounts with a global mean importance of 0.21, being stronger over SH land regions such as Australia, and Mexico and tropical and sub-tropical oceans. Furthermore, COT parameters have the strongest importance. Low-level cloud optical thickness (COT1) has a global mean importance of 0.14, with stronger contributions over SH oceans and the Arctic. COT2 is identified as a more critical factor, with a global mean importance of 0.21, showing peak values over oceans, East China, and the eastern United States. COT3 plays a major role in influencing SSR over NH oceans, northern South America, and central Africa, with a global mean importance of 0.19. Among aerosol parameters, AOD exhibits a global mean importance value of 0.04, with stronger contributions over NH land, particularly the Sahara, the Mediterranean, the Middle East, and central Africa. SSA and AP play a less prominent role, with a global mean importance of 0.02 and 0.02, respectively. Water vapor has a global mean importance of 0.03. The strongest contributions occur over land regions, including Australia, the Arabian Peninsula, and the Sahara. Finally, ozone is exhibiting a global mean importance value of 0.01. Besides, SSR was predicted using Random Forest regression, and its performance was evaluated by computing the R^2 score between the deseasonalized anomalies of the RF-predicted SSR and those from the FORTH-RTM dataset, as illustrated in Figure 5.13l. The results indicate that the RF regression effectively captures the variability of SSR within the latitude band of 60°N to 60°S. However, its performance declines noticeably outside this range—particularly in high-latitude regions—likely due to limited data coverage and reduced reliability of satellite-derived inputs in polar regions. Overall, these results underscore the dominant role of cloud properties in driving SSR variations, followed by AOD contributing in a more localized manner.

As shown in Figure 5.14, the greatest importance is found in CA2 and COT2. CA2 contributes more strongly over land, while COT2 in the oceans. More specifically in land areas (Figure 5.15), the greatest importance is found in COT2 in Siberia, Europe, eastern China and Asia, western Canada and the eastern United States, while COT3 has the greatest importance in northern South America, and central Africa. CA3 has the greatest importance in southern South America, Australia, India, southern Africa, the Middle East, Mexico and the Sahara, while CA2 prevails in the Mediterranean, Arctic and Antarctic.

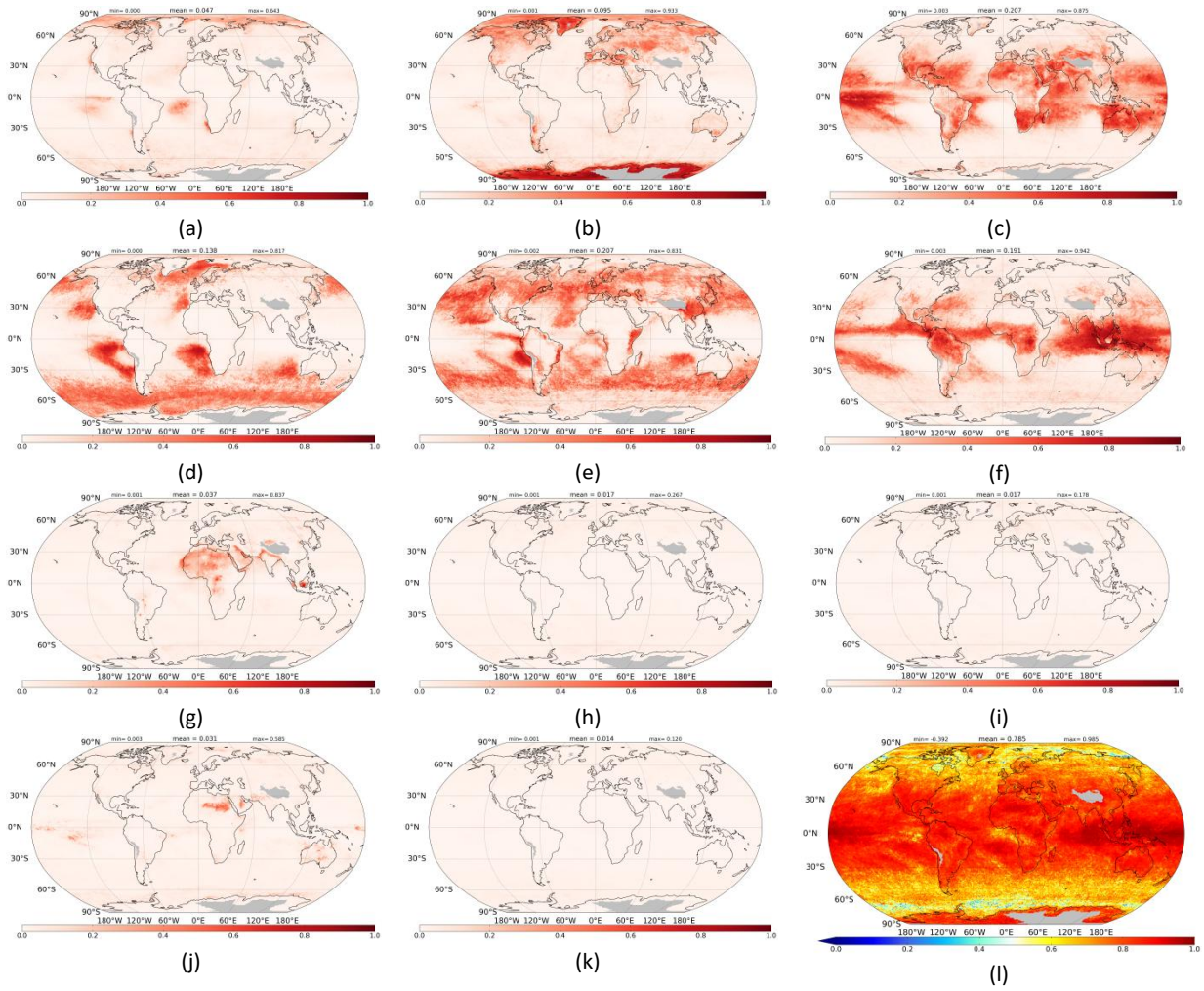


Figure 5.13. Global distribution of the Random Forest Feature Importance between the deseasonalized anomalies of SSR and the CA1 (a), CA2 (b), CA3 (c), COT1 (d), COT2 (e), COT3 (f), AOD (g), SSA (h), AP (i), water vapor (j) and ozone (k) during 1984-2018. The strong red colors indicate large contribution of the under-investigation parameter to the predicted SSR anomalies. Also, in the lower right it is shown the R^2score of the Random Forest SSR anomalies predictions in comparison with the FORTH-RTM SSR anomalies.

5.4.4 Assessment of different correlation and regression analyses

The combined use of Pearson correlation, ridge regression, and Random Forest feature importance provides a holistic and robust perspective on the factors influencing monthly SSR variations. Pearson correlation identifies direct linear relationships, revealing the strength and direction of individual GDB drivers, such as the overall strongest negative correlation between SSR and CA3 and COT2. Ridge regression refines these findings by mitigating multicollinearity, offering a more precise quantification of each factor's unique contribution—highlighting, for instance, the dominant negative impact of CA3 and COT2. Meanwhile, Random Forest captures complex non-linear interactions, ranking CA3 as the most influential factors, followed by COT2 and COT3, reinforcing the dominance of cloud properties in SSR variability. The analysis also confirms that aerosols (AOD) play a secondary yet significant role, particularly

over specific land regions with heavy dust export such as Sahara and Middle East, while the other parameters contribute to SSR variation, though to a much lesser extent.

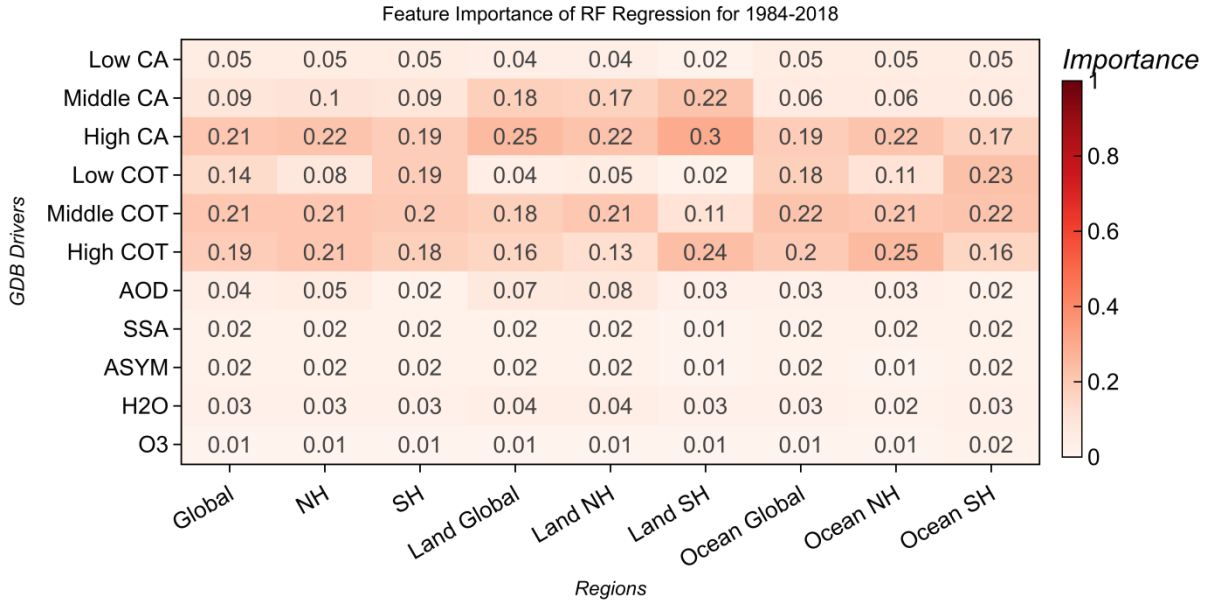


Figure 5.14. The spatially averaged RF importance between the monthly anomalies of SSR and the GDB drivers over the globe, the two hemispheres and the globe's and the two hemispheres' land and ocean areas during the entire study period 1984-2018.

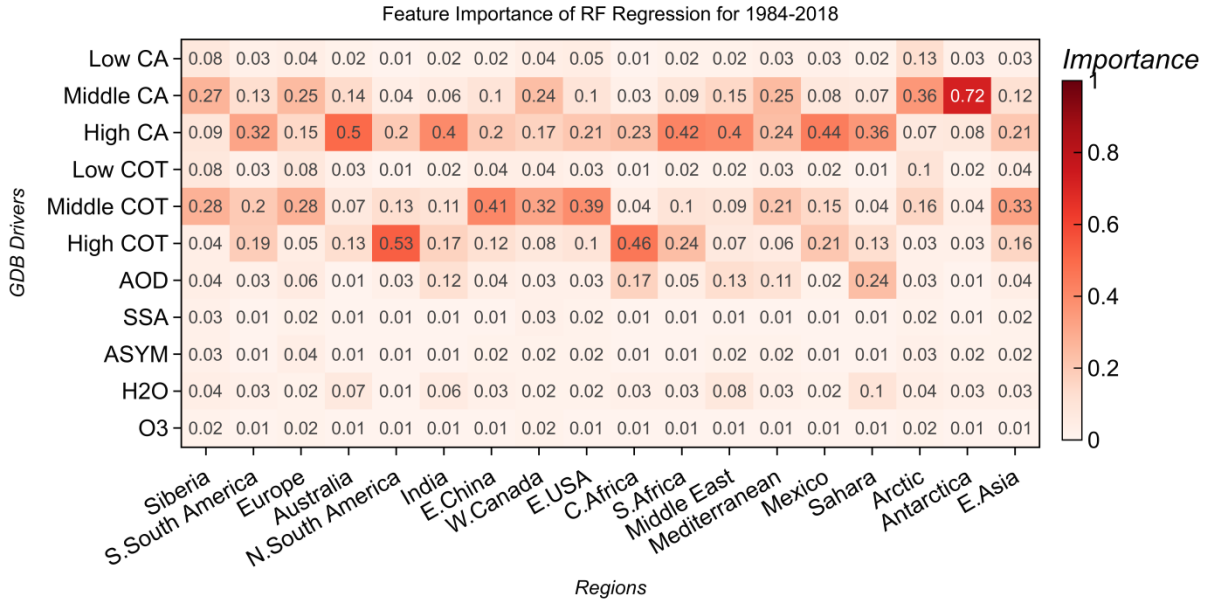


Figure 5.15. The spatially averaged RF importance between the monthly anomalies of SSR and the GDB drivers over 18 land regions of the globe during the entire study period 1984-2018.

Finally, combining the results of all three methods, CA3 stands out as the most influential factor driving month-to-month SSR fluctuations, closely followed by COT2. COT3 and CA2 also contribute

meaningfully, though to a lesser extent, with their impacts ranking just after those of CA3 and COT2. It is worth noting that over the 1984–2018 period, the largest contributor to GDB was COT3, followed by CA2, as discussed in Section 5.3 based on the frozen analysis. This estimation, together with the findings of the regression analysis, underscores the dominant role of mid-level and high-level clouds in driving SSR changes during 1984–2018, at least at global and hemispheric scales.

Chapter 6. The links between GDB and global warming

6.1. Introduction

Temperature and the incoming surface solar radiation at the Earth's surface are two crucial parameters for climate and life on the Earth. They both significantly changed during the past decades, contributing to climate change (IPCC 2021; Wild 2009). The increase in surface temperature over the last decades is mainly attributed to the increase in anthropogenic emissions of greenhouse gases, which trap the emitted thermal energy of the Earth (IPCC 2021). However, the Earth's emitted thermal radiation depends on the main energy source of the Earth, that is the incoming solar radiation, which penetrates the terrestrial atmosphere undergoing scattering and absorption by the atmospheric constituents and reaches the Earth's surface determining the available energy that is absorbed by the planet. It is well known that SSR experiences interdecadal changes with increasing or decreasing phases, a phenomenon known as Global Dimming and Brightening (GDB) (Stanhill and Cohen 2001; Wild et al. 2005; Wild 2009). It has been suggested (Hatzianastassiou et al. 2020; Ruckstuhl et al. 2008; Stamatis et al. 2023; Wild et al. 2021) that GDB is mainly caused by changes in clouds and aerosols, which are the main GDB drivers. Such changes, e.g. in cloud reflectance, scattering aerosols or variations in the solar flux incident at the top of the atmosphere, modify the total amount of solar energy absorbed by the climate system leading to changes in surface temperature (Ramanathan et al. 2001; Wild et al. 2007; Wild 2009). Thus, the SSR fluctuations, namely GDB, have been linked with the recent anthropogenic global warming (Glantz et al. 2022; Ramanathan 2007; Ruckstuhl et al. 2008; Trenberth and Fasullo 2009; Stamatis et al. 2022; Stamatis et al. 2023; Wang and Dickinson 2013; Wild et al. 2007). Specifically, it has been proposed (Wild et al. 2007) that the solar dimming from the mid of the 20th century until the 1980s has concealed the evolving greenhouse warming, which has only become fully apparent on a global scale during the brightening that followed the 1980s. Nevertheless, it has been pointed out that the brightening has not substituted the greenhouse effect as the main cause of global warming (Glantz et al. 2022; Wang and Dickinson 2013; Wild et al. 2007; Wild 2009). Both GDB and global warming are climatic phenomena that have attracted a strong interest of the scientific community since a few decades. Indeed, numerous studies have delved into the nuanced behavior of GDB over the recent decades, revealing stabilizations of brightening or even a dimming during the 2000s (Hatzianastassiou et al. 2020; Sanchez-Lorenzo et al. 2015; Stamatis et al. 2022,2023; Wild 2009) over many areas and a general brightening after 2010 (Dong et al. 2022; Stamatis et al. 2022,2023; Wild et al. 2021; Wohland et al. 2020). On the other hand, in recent years, the concept of a "hiatus" in global warming has gathered scientific attention, referring to a perceived slowdown in the rate of surface temperature increase observed from the late 20th century to the first decade of the 21st century (England et al. 2015; Trenberth and Fasullo 2013). The hiatus debate underscores the complexity of the Earth-atmosphere climate system and the need for detailed analysis to discern short-term variations from the overarching warming trend due to the anthropogenic greenhouse effect. Recent investigations attempting to explain the hiatus have also focused on factors such as natural climate variability (Watanabe et al. 2014), ocean heat uptake (Liu et al. 2016a) slowdown in radiative forcing caused by anthropogenic aerosols or volcanic eruptions (Kaufmann 2011; Santer 2014; Solomon 2011), decreasing surface solar radiation (Kaufmann 2011), and the role of specific atmospheric and oceanic phenomena (Arora et al. 2016). Researchers studying the recent hiatus in global warming often explored

the role of internal variability such as El Niño–Southern Oscillation (ENSO), Pacific Decadal Oscillation (PDO), and Atlantic Multi-decadal Oscillation (AMO), in influencing short-term temperature trends (Arora et al. 2016; Augustine and Capotondi 2022; Chtirkova et al., 2023; Loeb et al., 2018). While anthropogenic greenhouse gas emissions drive the centennial scale warming trend, internal variability and SSR trends (GDB) can lead to periods of slower or accelerated warming over shorter timeframes, e.g. over decadal scales (Gou et al. 2022). An example, concerning the role of GDB, was the hypothesis of (Wild et al. 2007) that GDB can modulate the global warming rates, which was based on analyses of GDB and global warming from 1958 till 2002. After 2010 and following the period of the recent hiatus in the 2000s, the rates of warming continued the accelerating pace (Jenkins et al. 2022). Therefore, it is important to further expand the time period in order to test again the hypothesis under the evolving phases, including the more recent ones, of GDB and global warming. In the present work we attempt to do this by examining the interdecadal changes of SSR and surface temperature from the early 1980s through to 2018, i.e. over 35 years, in order to confirm the hypothesis that the Earth's land surface air temperature fluctuations are impacted by dimming and brightening, which may contribute and partly control the progressing warming of our planet. Section 6.2 investigates the global distribution of the correlation between surface solar radiation (SSR) and surface temperature. Section 6.3 presents long-term changes in SSR and temperature over land and ocean regions, along with their interrelationship. Section 6.4 examines the relationship between changes in SSR and surface temperature across various land areas. Finally, Section 6.5 outlines the limitations of the study.

6.2 Correlation between SSR and surface temperature

In order to examine and quantify the theoretically established dependence of surface temperature on SSR, the deseasonalized anomalies of these two parameters were correlated all over the globe, on a monthly basis, and the 35-year study period (1984-2018). In general, SSR is positively correlated with surface temperature (yellowish and reddish colors), as expected, over most areas of the globe. Figure 6.1a shows that T_{mean} is more strongly correlated with SSR over land areas such as Europe, much of Asia, especially its southern parts, and South America, as well as over western North America and eastern southern Africa, where values reach 0.70. On the other hand, however, a negative correlation appears mainly over the polar regions and the Sahara with the maximum negative value being -0.62. While, theoretically, a positive correlation (i.e., more solar radiation leading to higher temperatures) is generally expected, local and regional factors, such as changing surface albedo or changes in temperature advection through changes in atmospheric circulation, can influence the distribution of heat within a region and introduce complexities. For instance, regions with high and increasing surface reflectivity (albedo), such as areas covered by snow, ice, or deserts, may experience lower temperatures due to the decrease of the surface absorbed solar radiation. The dependence of surface temperature on SSR is expected to be stronger for T_{max}, since the temperature daily maximum values, occurring around noon, are largely determined by the surface incoming solar radiation, especially in cloudless skies (Wild 2009). Indeed, this is confirmed in Figure 6.1b, which shows larger correlation coefficients between SSR and T_{max} than between SSR and T_{mean}. Now, the regions that already had high correlation coefficients with T_{mean} show even higher coefficients with T_{max}, with values reaching 0.78, again being larger over land than over ocean. Yet still a slight negative correlation remains over the polar regions and the Sahara. The R values between

SSR and T_{min} generally remain the lowest in Figure 6.1c, which has to do with the fact that the daily minimum temperature, practically occurring during the night, is determined by the emitted thermal radiation by the Earth's surface and the associated longwave radiative cooling and not by solar radiation (Campbell et al. 1997; Makowski et al. 2008; Wild et al. 2007). The strongest correlation is found between SSR and DTR, but this is valid over land, whereas over the oceans the corresponding R values are either smaller in magnitude when positive or larger in magnitude when negative, i.e. they are worse than R values for the SSR and T_{max} and the SSR and T_{min} pairs. This can be expected, since the sea surface temperature and the temperature near over the sea change much less over the course of a day than over land. Hence, the correlation coefficients between SSR and DTR range between -0.84 and 0.88, reaching larger values for positive correlation over land and negative correlation over ocean. This confirms that DTR is a good proxy of the interannual change of SSR over land, as it is expected, since the subtraction of T_{min} from T_{max}, minimizes the thermal effects in the DTR records (Wild et al. 2007; Wild 2009). The stronger negative correlation between SSR and DTR over oceans should be attributed either to the larger thermal inertia of oceans compared to land as well as to the different meteorological conditions that prevail over them. The larger thermal inertia of oceans means that they respond more slowly to changes in solar radiation, as the heat absorbed during the day is released more gradually over time. Besides, evaporation from the ocean surface absorbs a significant amount of solar energy, leading to cooling. This latent heat flux can act as a buffer, dampening the direct impact of solar radiation on surface temperature over oceans (Hastenrath 1991). There is a noticeable strong anticorrelation between SSR and surface temperatures (T_{mean}, T_{max}, T_{min} and DTR) over the tropical oceans, which is even more evident for DTR (Figure 6.1d). This can be explained by the intricate interplay of factors unique to tropical climates. The combination of high convective cloud activity, which limits solar radiation impact, and the thermal dynamics associated with elevated temperatures and enhanced latent heat release can contribute to an anticorrelation between SSR and temperatures. Furthermore, the influence of phenomena like El Niño and the trade winds introduce additional complexities, altering atmospheric circulation patterns and intensifying the estimated negative correlation between solar radiation and DTR in tropical regions (Hastenrath 1991).

6.3 The long-term changes of SSR and temperature over land and oceans and their relationship

In the next step, we investigated if there is a correlation between the long-term changes of SSR, namely the GDB, and the Earth's surface temperatures, but on a global average scale and annual basis and the results are shown in Figure 6.2. Different temporal changing patterns are observed between the time series of both SSR and temperatures over land and ocean as it is shown in detail in Table AE1. More specifically, over land (Figure 6.2a), in parallel to the brightening (0.58 [-5.74, 5.71] $Wm^{-2}decade^{-1}$) occurring from 1984-1999 there is a corresponding accelerated rate of land warming, with the changes of T_{mean}, T_{max} and T_{min} being equal to 0.37 [0.12, 0.63], 0.37 [0.11, 0.68] and 0.35 [0.11, 0.63] $^{o}Cdecade^{-1}$, respectively. On the contrary, when the brightening over land ceased during 2000-2009 and GDB converted to a slight dimming (-0.02 [-3.56, 2.35] $Wm^{-2}decade^{-1}$), the land warming slowed down, actually at least halved to 0.19 [-0.45, 0.65], 0.26 [-0.38, 0.74] and 0.11 [-0.32, 0.65] $^{o}Cdecade^{-1}$ for T_{mean}, T_{max} and T_{min}, respectively, corresponding to the so-called recent hiatus (Douville et al. 2015; Gou et al. 2022; Xie and Kosaka 2017; Yan et al. 2016; Yang et al. 2023). This behavior is remarkable as similar findings were

observed in the 1950-1980 dimming (Wang and Dickinson 2013; Wild et al. 2007) which preceded the brightening starting in the early 1980s. Following the 2000's slight dimming and recent hiatus, in the absence of dimming during the 2010s, the SSR increased producing a brightening of 7.47 [4.93, 11.18] $Wm^{-2}decade^{-1}$ (note that this high value is associated with the negative 2012 anomaly of -1.65 Wm^{-2} and the large 2017 and 2018 anomalies both 3.44 Wm^{-2} and 5.72 Wm^{-2}, respectively), while the land warming continued its accelerating pace, with the T_{mean} increasing by 0.45 [-0.29, 1.22] $^{o}Cdecade^{-1}$.

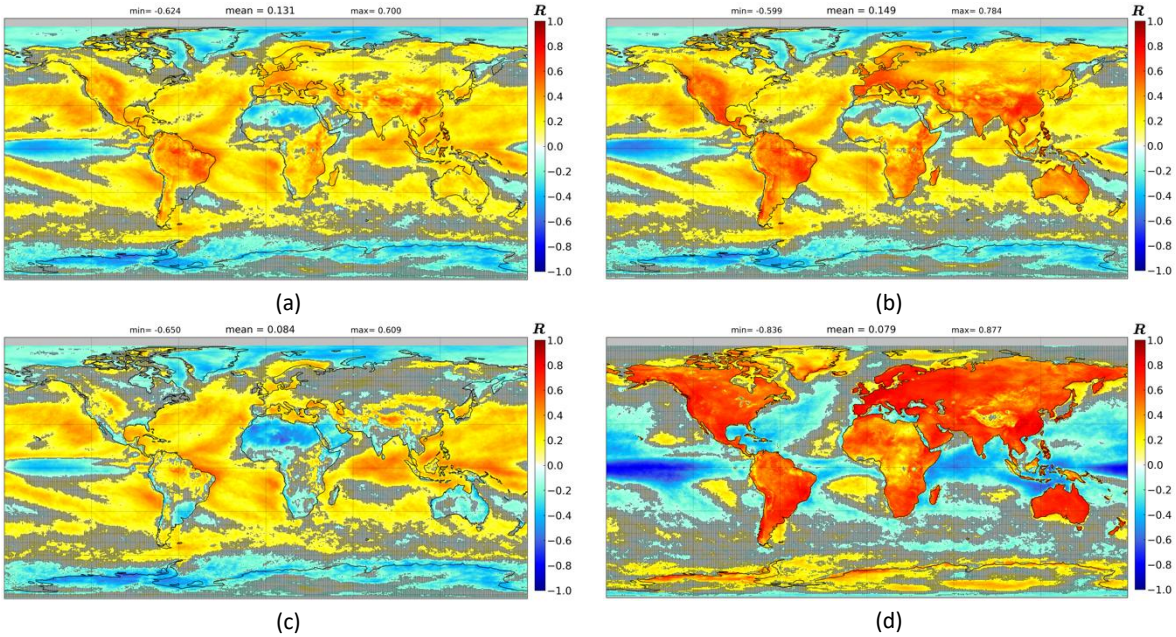


Figure 6.1. The global distribution of correlation coefficients (R) between monthly deseasonalized anomalies of FORTH-RTM SSR and ERA5 temperatures (T_{mean}-a, T_{max}-b, T_{min}-c, DTR-d) during 1984-2018. Positive correlation is depicted in yellow and red whereas negative correlation in blue colors. The statistically no significant R values at the 95% confidence level are denoted with black x symbols.

Thus, our findings reinforce the hypothesis that a solar dimming is accompanied by a decelerated warming of global land areas, while the brightening is associated with an accelerated global warming. It should be noted that in contrast to the clear increase in temperatures (T_{mean}, T_{max}, T_{min}) over the entire 35-year study period, the DTR does not show a noticeable change, but only a small increase equal to 0.06 [0.05, 0.08] $^{o}Cdecade^{-1}$, which is qualitatively consistent with the overall increase of SSR (1.79 [0.58, 3.21] $Wm^{-2}decade^{-1}$) over the entire study period of 1984-2018. Furthermore, the interdecadal changes of DTR, which are clearly smaller than those of the other surface temperature variables, do not seem to be in line with the phases of GDB. On the other hand, the interdecadal changes show a bit different behavior over oceans. The temperature appears to have undergone a much smaller increase compared to over land, 0.54 [0.43, 0.66] versus 1.19 [0.97, 1.39] ^{o}C, respectively for the entire time period 1984-2018, while it appears to be increasing continuously (0.15 [0.12, 0.19] $^{o}Cdecade^{-1}$ for T_{mean}, T_{max}, T_{min} and 0.005 [0.0002, 0.01] $^{o}Cdecade^{-1}$ for DTR) despite the decreasing SSR during the study period. Note that although during the 2000s the dimming is stronger over the oceans than land areas (-0.35 [-7.19, 3.04] versus -0.02 [-3.56, 2.35] $Wm^{-2}decade^{-1}$), the decelerated rate of the warming, in comparison to the rate of the 1990s, is more apparent over the land than the ocean (maybe also related to the higher heat capacity and associated

inertia of the oceans), indicating a stronger link of GDB with the global warming rate over land areas that over oceans.

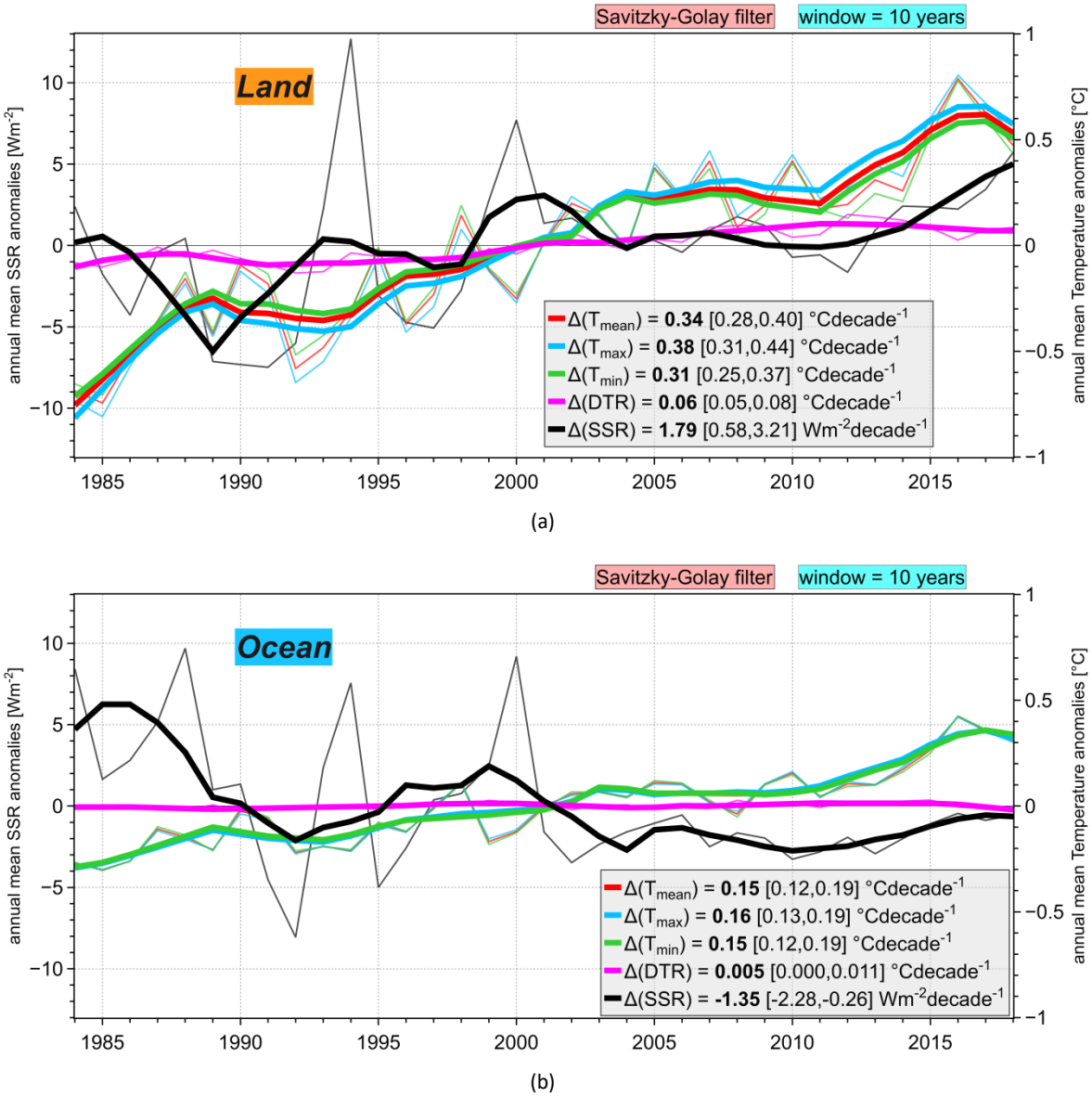


Figure 6.2. Timeseries of annual anomalies of globally averaged SSR (with black) and ERA5 Earth surface temperatures (T_{mean}-red, T_{max}-blue, T_{min}-green, DTR-purple) during 1984-2018. Results are given separately over global land (a) and ocean (b) areas. The thick lines represent the Savitzky-Golay filtered data with the window size of 10 years. Anomalies are computed with respect to the entire study period 1984-2018, while inside the legend the associated per decade linear trends are shown and specifically with bold the statistically significant trends at the 95% confidence level.

The same analysis was performed for the Northern and Southern Hemispheres, both over land and oceans (Figure 6.3). The warming is larger for the NH than SH, being equal to 0.31 [0.26, 0.35] and 0.11 [0.08, 0.15] ^{o}Cdecade^{-1}, respectively. In addition, this warming is stronger over land than oceans in both hemispheres with the largest rate of warming occurring over land in the NH (0.40 [0.32, 0.48] ^{o}Cdecade^{-1}). With respect to the GDB, the NH experienced a brightening equal to 0.60 [0.05, 1.20]

$Wm^{-2}decade^{-1}$ during the study period, which arose mainly from land, while the SH underwent a dimming that mainly occurs over the oceans. Moreover, Figure 6.3 reveals that during the 2000s the warming rate slowed down with respect to the period 1984-99 on the NH, which is not evident on the SH, although the 2000s dimming seems to be stronger on the SH. This is rather expected since during the 2000s dimming over land, the decelerated rate of the warming is more apparent than over the ocean as Figure 6.2 shows, and the NH contains much more land areas than the SH. Also, the stronger dimming in the 2000s over NH land leads to a clearer slowdown of the warming rate than over SH land, which experiences a weak dimming, while oceans show an almost steadily increasing warming despite the GDB phases.

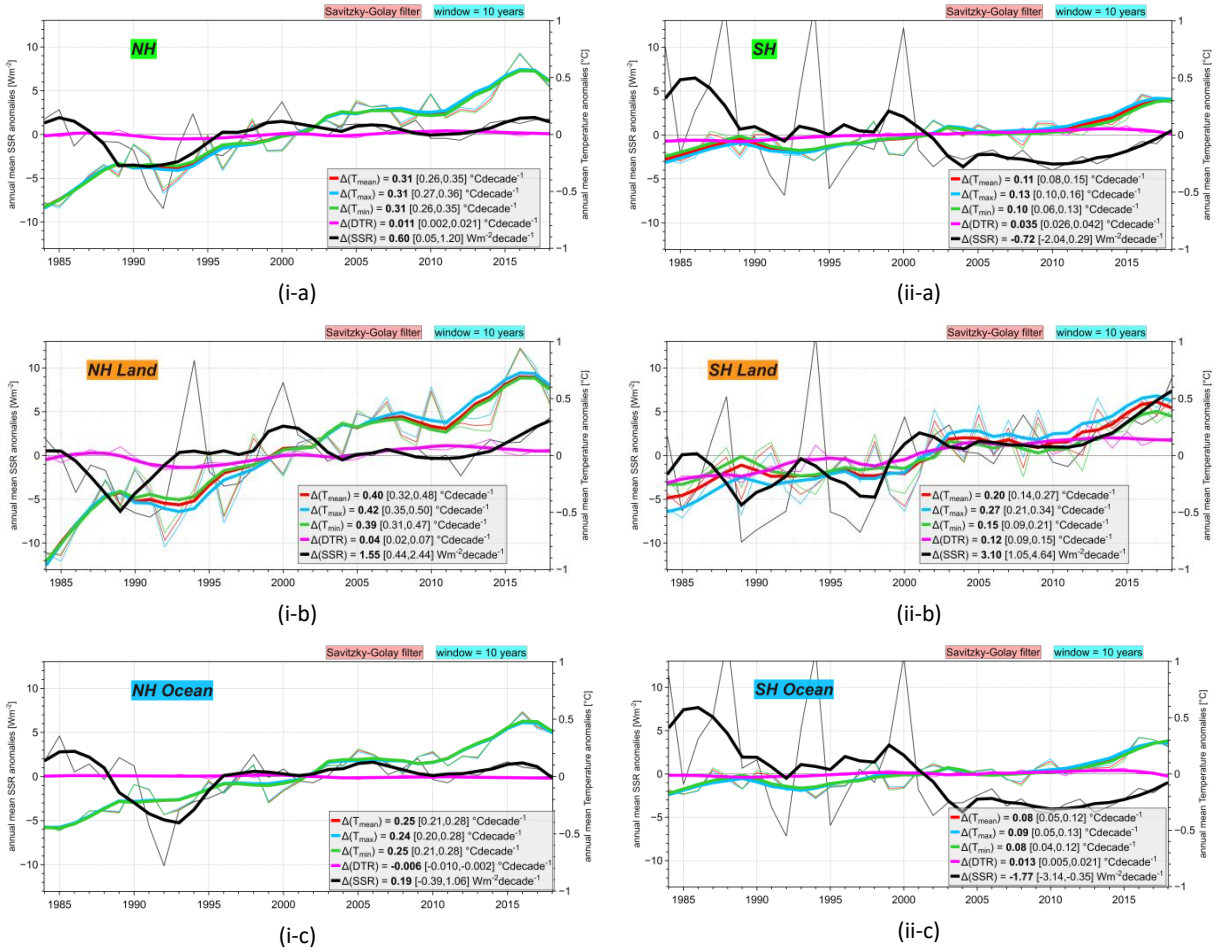


Figure 6.3. Anomalies of spatially averaged timeseries over North Hemisphere (NH-i) and South Hemisphere (SH-ii) for FORTH-RTM SSR (with black) and ERA5 temperatures (T_{mean}-red, T_{max}-blue, T_{min}-green, DTR-purple) over the entire hemisphere (a), over land (b) and over ocean (c). The thick lines represent the Savitzky-Golay filtered data with the window size of 10 years. Note that the reference period for the anomalies is the entire study period 1984-2018, while the linear per decade trends are displayed inside the legend, and the statistically significant trends at 95% confidence level are indicated in bold.

Moreover, the timeseries of the annual SSR and temperature anomalies are also investigated for the Northern Hemisphere separately for the warm (May to October) and the cold (November to April) periods of the year, both over land and ocean (Figure 6.4). Similarly to our previous findings, the rate of global warming seems to slow down during the dimming of 2000s over land over both periods, this being more apparent during the cold (with stronger dimming (-2.30 [-12.17, 1.91] $Wm^{-2}decade^{-1}$)) than the

warm (with weak brightening (0.09 [-3.74, 4.02] $Wm^{-2}decade^{-1}$)) period of the year (respective values equal to 0.32 [-0.19, 0.86] and 0.35 [-0.45, 0.89]$^{o}Cdecade^{-1}$), while over oceans, in both cold and warm periods the surface temperature over oceans are steadily increasing despite the solar dimming occurring (more during the cold than the warm period) in both periods.

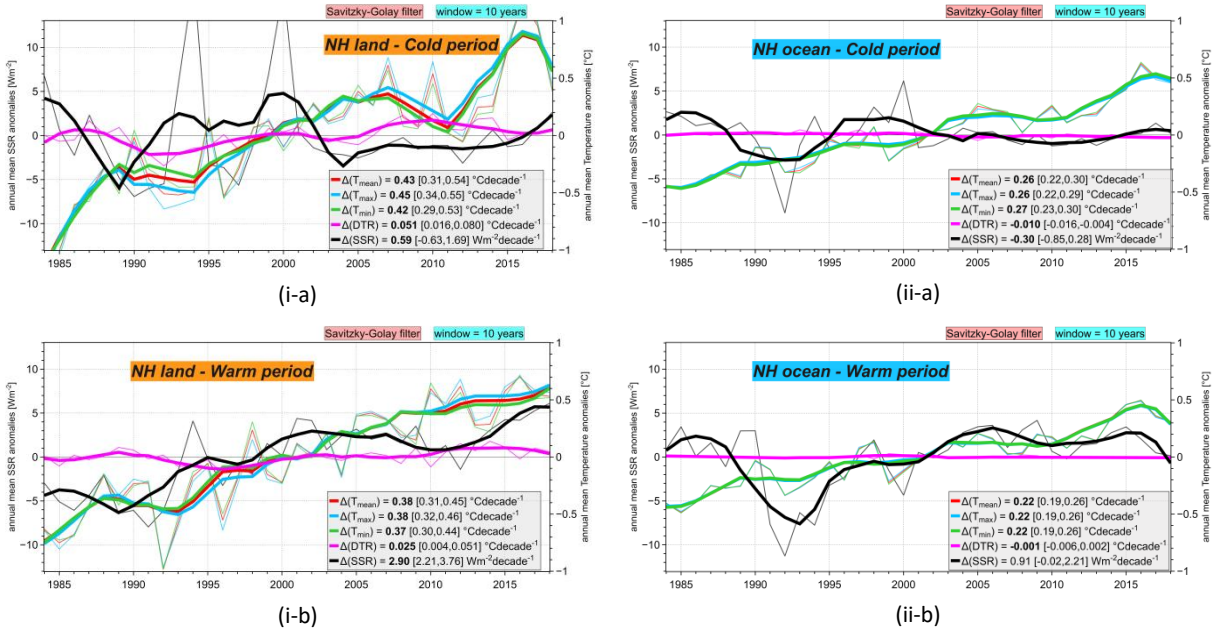


Figure 6.4. Anomalies of spatially averaged timeseries over Northern Hemisphere's land (i) and ocean (ii) for FORTH-RTM SSR (with black) and ERA5 temperatures (T_{mean}-red, T_{max}-blue, T_{min}-green, DTR-purple) during the boreal cold (a, November-April) and warm (b, May-October) period for 1984-2018. The thick lines represent the Savitzky-Golay filtered data with the window size of 10 years. Anomalies are computed with respect to the entire study period 1984-2018, while inside the legend the associated per decade linear trends are shown and specifically with bold the statistically significant trends at the 95% confidence level.

Even though Wild (2016) found an imprint of the 1950s to 1970s dimming on the sea surface temperature changes as provided by the Hadley Centre particularly over the NH oceans, such an imprint is not found in the results of this subsection referring to the period 1984-2018 and obtained using the interdecadal changes of the ERA5 surface temperature over oceans and the FORTH-RTM SSR and its changes (GDB). Probably this is due to the shorter time period and the smaller magnitude of dimming in the 2000s than in 1950s-1970s. Therefore, in the rest of our work, we will examine in detail the trends of surface temperature and SSR only over land areas of the globe, where there is also more confidence of the FORTH-RTM SSR and GDB than over oceans.

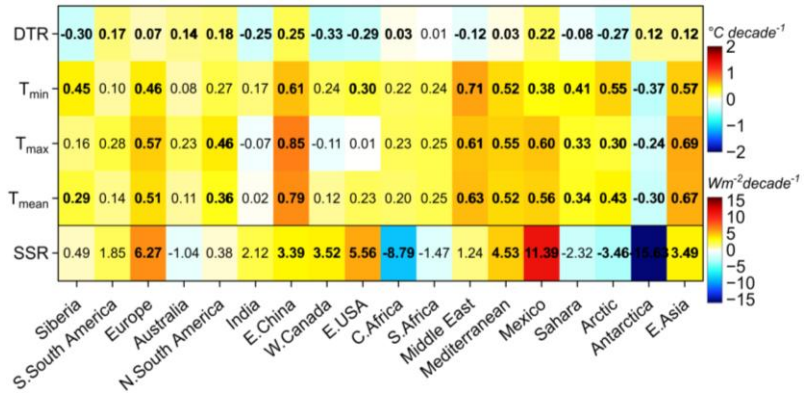
6.4 The relationship between the changes of SSR and surface temperature over various land areas

According to our analysis based on the FORTH-RTM, the SSR experienced a brightening phase over most land regions of the Earth from 1984 to 1999, followed by both dimming and brightening phases in different regions during the 2000s. Also, since 2010, the brightening occurs over all selected areas of this study, while in the 3 time periods the GDB magnitude is different from one region to another. These findings point to the complex nature of the GDB phenomenon. In order to simplify this study, 18 land areas of the planet were selected (shown in Figure AE1) and the study period of GDB was divided into 3

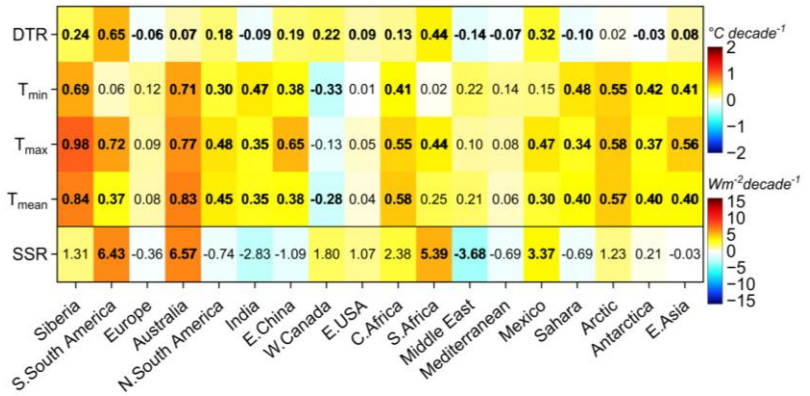
phases/periods. Thus, the long-term changes of SSR and surface temperature (surface-air temperature, T_{mean}), and their interrelationship, were studied for a total of 54 (18x3) cases, for which the trends of SSR and temperatures were investigated and intercompared (cf. Figure 6.5). It should be noted, that for completeness, along with the spatial averages of the long-term changes shown in Figure 6.5, there are also their associated standard deviations in Figure AE2 and the percentage number of grid-cells that have statistically significant trends at the 95% and 70% confidence level in Figure AE3 and AE4, respectively. We initially notice that during 1984-1999 a brightening occurred in most land areas of the Earth, except for Australia, Africa, and in particular the polar regions and especially Antarctica. At the same time, the temperature practically rose all over the globe except for Antarctica, showing that the global warming, wherever it occurred along with solar dimming, was not driven by GDB such as over Africa and the Arctic during 1984-1999. Yet, the absence of surface warming of Antarctica can be partly attributed to the strong dimming in this area. After 2000 and till 2009, in many land areas the brightening is offset, and a dimming is observed in some areas such as the largest part of Europe and the southern and East Asia. During this decade, the warming continues and even strengthens, as expected from the evolving anthropogenic greenhouse effect, but in some areas, there is a stabilization of the warming rate or even a reversal to cooling, such as in Europe, the Middle East, North America and Greenland. It is interesting to note that in most of them, namely Europe, the Middle East and North America, a solar dimming took place in the 2000s, which may have contributed to their surface cooling. Besides, the reversal from dimming to brightening over a significant part of Antarctica may be associated with the remarkable warming over these parts of Antarctica in the 2000s, opposite to the cooling there before 2000, also indicating the existence of a strong relationship between SSR and T_{mean}. During the 2010s, brightening prevails in all the selected areas, which reversed the dimming occurring in the previous decade over many regions, such as Europe, India and Southeast Asia. The rates of warming in 2010s were generally higher than the rates in the previous sub-periods, except for E. USA, where surface cooling occurred, and Sahara and Arctic, where the warming rates were negligible despite the brightening occurring there. Also, during this decade (2010s) it is interesting to note that the strong brightening was associated with strong warming rates in many areas of the planet, such as Europe, India, Southeast Asia and Australia.

As it was shown, it is challenging to analyze the simultaneous change of SSR and surface temperature over all selected world sub-regions and during the three subperiods. Therefore, in order to effectively test the hypothesis that brightening allows surface warming due to anthropogenic greenhouse effect to fully occur, while dimming slows down the rate of warming, it was examined if it is common to observe this notable link between GDB and surface temperature (T_{mean}) over the selected 18 world areas where and when we have brightening and dimming. Thus, for each one of the 18 regions and each of the three time periods, namely for 54 cases, we searched for the cases in which the solar brightening (reddish colors in Figure 6.5) coexists with surface warming (yellow and red colors, Figure 6.5), as well as the dimming (bluish colors, Figure 6.5) coexists with weak warming (light yellow colors in Figure 6.5). Our analysis revealed that in 89% of the cases (48/54) this happens, indicating the existence of a potential relation between SSR and the rates of change of temperature. Moreover, during the selected 3 time-periods, it was found that there are 31/54 cases (or 57%) which satisfy the criterion of the co-existence of strong brightening along with strong warming and dimming or weak brightening along with weak warming. In a further step, in order to examine the validity of the hypothesis on a more rigorous basis, we examined if the hypothesis (that dimming slows down the rate of warming, while brightening accelerates

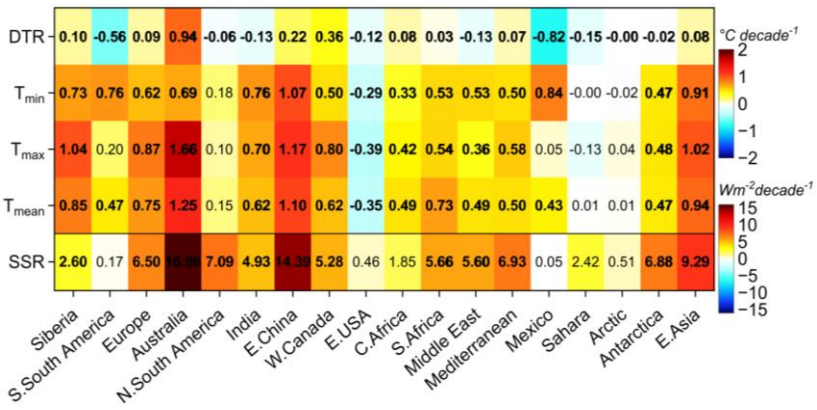
it) is valid continuously, i.e. in all 3 time periods, over a region, in other words we searched for areas where there is a strong connection between the GDB and global warming during the entire 35-year study period. It is found that the areas where this happens are Europe, East Asia, East China, the Middle East, the Mediterranean and Australia. It should be noted that these are either areas with intense anthropogenic activity and pollution (such as Europe and East Asia (Di Antonio et al. 2023; Yoon et al. 2011)) or with frequent export of desert dust (such as the Mediterranean and the Middle East (Gavrouzou et al. 2021; Gkikas et al. 2013). On the other hand, in all other regions the hypothesis does not seem to be valid for all 3 periods (continuously). For example, over South America and Mexico, in one period (2000s) the brightening may have kept pace with the warming, but in the next period (2010s) with a weaker brightening, a stronger warming was observed. It is well known that aerosols, through scattering and absorption in the atmosphere, depending on their type and loading, cool or heat the atmosphere and the surface of the area over which they occur (Korras-Carraca et al. 2021; Krishnan and Ramanathan 2002; Storelvmo et al. 2016). As Wild (2009) pointed out, SSR changes, i.e. GDB, can have a larger and more pronounced impact on land surface temperatures only, when these changes are caused by processes which alter the solar absorption by the entire Earth-atmosphere system (such as through scattering aerosols, cloud reflectance or variations in the solar flux incident at the top of atmosphere). Otherwise, if the SSR changes are caused by a redistribution of solar absorption between atmosphere and surface with little effect on the total amount absorbed by the Earth-atmosphere system (such as through changing absorbing aerosols), the effect of SSR changes on surface temperatures is not expected to be clearly detectable. Indeed, according to our results, in regions with high loads of scattering aerosols, changes in the concentration of scattering aerosols could induce the phases of GDB, simultaneously affecting the solar absorption by the Earth-atmosphere system and consequently the land surface temperatures. This seems to happen above the world sub-regions where GDB is strongly connected to surface warming, namely over Europe, East Asia, East China, the Middle East and the Mediterranean. Note that according to our trend analysis of the input data (not shown here), Europe, East Asia, Mediterranean and the Middle East underwent noticeable changes of scattering AOD and cloud amount during the 3 sub-periods, which are in line, as expected, with the FORTH-RTM GDB phases there. Also, over Australia, changes in cloud amount seem to be more consistent with the FORTH-RTM GDB phases there during the 3 sub-periods, with scattering AOD contributing only to the brightening during the 2010s. Nevertheless, our results show that the strong connection between GDB and warming exists only in specific regions of the planet and for the global mean land, while not being a general phenomenon on regional scales. Indeed, the relationship between solar radiation and temperature is complex and therefore it cannot be assumed to exist across all areas and atmospheric conditions (Barbaro et al.2013; Wild 2009; Zhang et al. 2010). Moreover, apart from the good qualitative agreement found in the specific 6 sub-regions we mentioned, for areas with at least two brightening phases, e.g. Australia, Siberia, the Middle East and South America, the magnitude of the surface temperature changes in these two brightening periods is not exactly proportional to the magnitude of the brightening. The above-mentioned findings of our analysis confirm that the general main factor that regulates the recent, beyond 1980, rapid global warming is not GDB, but the anthropogenic greenhouse effect. However, GDB should always be accounted for, since ignoring it could lead to an underestimation/overestimation of the true magnitude of the observed greenhouse warming in the dimming/brightening phases.



(a)



(b)



(c)

Figure 6.5. Spatially averaged values of the decadal changes in T_{mean}, T_{max}, T_{min}, DTR as well as SSR over 18 world land areas (Figure AE1) for three periods: 1984 – 1999 (a) and 2000 – 2009 (b) and 2010-2018 (c). Green and blue colors indicate decreasing trends, while yellow and red colors indicate increasing trends. Trend values in bold denote that their percentage per decade changes are larger than the global land average of long-term changes.

After the study of the relationship between the changes in T_{mean} (global warming) and SSR (GDB) that was found to exist in certain regions of the planet, our study also focused on a similar analysis, but for T_{max} and T_{min}, in order to distinguish between the effects of surface solar and thermal radiation on global warming, also emphasizing the comparison between them, considering that the daily course of

temperature is affected differently by solar and thermal radiation. Indeed, it is very well known that T_{max}, occurring around midday, is largely determined by the incoming solar flux at the surface (SSR), while T_{min}at nighttime is mainly driven by the surface net longwave radiation and the associated surface radiative cooling, which is significantly affected by the ability of the atmosphere to absorb and reemit thermal radiation downwards to the surface. The anthropogenic greenhouse effect, by inducing global warming, also contributes to the observed increase of the daily T_{min} and T_{max}. Besides, T_{max} is greatly affected by the GDB. In order to explore if the T_{max} changes are more associated with the GDB or the anthropogenic greenhouse effect, we compared the magnitudes of the changes of both T_{min} and T_{max}. The stronger increase of T_{max} (affected by both GDB and anthropogenic greenhouse effect) than T_{min} (affected mainly by the greenhouse effect), such as in Europe and Mexico during 1984-1999 (Figure 6.5a), could be attributed to the solar brightening. On the other hand, the weaker increase of T_{max} compared to that of T_{min}, such as in Europe and India in the 2000s (Figure 6.5b), could be attributed to the global dimming. We found that in 65% of the cases (35/54), the GDB has a decisive impact on the changes of T_{max} along with the impact of greenhouse warming. These findings suggest that, as expected, the solar brightening played an important role in the observed increase of the maximum temperature. It is notable, for example, that over Europe and East Asia T_{max} is increasing with the lowest rate over the time of dominant solar dimming of the 2000s. This low surface warming rate supports the idea that solar dimming had a noticeable impact on the daily maximum surface temperature, i.e. caused its decrease, throughout the 2000s. However, in the other 19/54 cases the previous pattern (larger increase in T_{max} during brightening and smaller increase in T_{max} during dimming compared to T_{min}) is not observed, as in Australia and the Middle East during 1984-1999 and in East China in the 2000s. On the other hand, as expected, T_{min} is weakly related to the solar dimming of the 2000s over Europe, East Asia, India, the Middle East, Sahara and N. South America, exhibiting an increase, which is suggestive of a rising greenhouse forcing (Padma Kumar et al. 2007; Scherrer and Begert 2019; Wild 2009). In general, it is found that over all sub-regions the changes of T_{min} are weakly related to GDB, sometimes exhibiting different signs (Figure 6.5b). Finally, changes in the diurnal temperature range (DTR, difference between T_{max} and T_{min}), were also investigated. According to ERA5, the DTR trends over the period 1984-2018 in most regions are smaller than the changes in T_{mean}, T_{max} and T_{min}, which is in line with Figure 6.2 and the literature (Wild 2009). Negative trends in DTR are often associated with large increasing trends in T_{min}, while positive trends in DTR are typically linked with large increasing trends in T_{max}. However, even if SSR is strongly correlated with DTR over land, as also shown in Figure 6.1d, it does not always mean that brightening leads to an increase in DTR. Changes in SSR and DTR with the same sign can occur if the brightening is strong enough and the T_{max} increases a lot and more than the T_{min}, which increases itself due to the greenhouse effect. This happens in many cases, e.g. in Europe, East Asia and East China in the 1984-1999 and 2010s and suggested also by other studies (Makowski et al. 2009; Wild et al. 2007). However, there are also cases, such as Siberia and the Middle East during 1984-1999 and South America and Mexico in the 2010s, where weak brightening and corresponding increase in T_{max} is accompanied by a stronger increase in T_{min}, resulting in a reduction of DTR. Also, it should be noted that inconsistencies between the increases/decreases of SSR and T_{max} or DTR can exist due to the fact that other parameters affecting the maximum and minimum temperatures, such as atmospheric circulation (warm/cold advection), synoptic conditions, nighttime clouds and surface reflectivity, while inaccuracies in the calculated SSR trends could also induce inconsistencies.

6.5 Limitations of this study

One of the advantages of our study is that it examines the existence of a relationship between GDB and global warming rates at a global scale and on a long-term climatological basis. Although the evaluation of our model against reference surface station networks is satisfactory and the results of our analysis largely agree with other studies, this study is not based on direct observations, but uses (compares) RTM simulated SSR fluxes and reanalysis temperature data. The FORTH-RTM SSR fluxes, and the associated GDB (SSR trends), are derived from input data for which uncertainties have been identified, particularly for clouds (Feng and Wang, 2021) and aerosols (Feng and Wang, 2019). Despite the identified agreement between the sign of FORTH-RTM GDB and the corresponding one from the surface stations, there are still some necessary improvements as noted in section 3.1. Additionally, another factor that could introduce uncertainties in the results of our analysis is that the model uses day-time only clouds, which is appropriate since during night-time there is no solar radiation, to estimate SSR changes and this might induce uncertainties when these SSR changes are compared with T_{mean}, which is affected by both day- and night-time clouds. Moreover, we lack strong confidence on the FORTH-RTM SSR and GDB over oceans, since a validation there is practically impossible, which restricts the confidence of our findings over land areas. Certainly, with future improvements in model input and reanalysis data, the uncertainty in the identified relationship between SSR changes and warming rates is expected to be further reduced.

Chapter 7: Summary and conclusions

7.1. Summary and main findings

The benefits of radiative transfer model calculations using input data from satellite observations and reanalyses are that they enable long-term and global coverage for the key climate parameters that determine SSR and its long-term changes (GDB), and thus for SSR and GDB themselves. However, even more important is that radiative transfer modeling provides the unique ability, by controlling the RTM input parameters, to examine their effects on the calculated solar fluxes and thus disentangle the phenomenon and determine its causes. This is crucial in order to gain a deeper understanding of GDB, to perceive its interplay and interaction with other climatic phenomena and to make plausible future forecasts. The advantages of this approach were exploited in the present PhD work, where the GDB, its causes and the possible links with global warming rates were investigated for the 35-year period 1984-2018. To this aim, radiative transfer calculations were performed by the FORTH-RTM on a monthly basis and 0.5°x0.625° spatial resolution using modern and improved satellite and reanalysis datasets for clouds and aerosols, respectively. This analysis was also performed on decadal time periods of the entire study period, since GDB is a decadal scale phenomenon. It has been also done worldwide, hemispherically, over ocean and land, and over specific land areas, enabling a complete understanding of the spatial and temporal features of GDB on a climatological basis all over the world. In the first part of the study, the FORTH RTM ran to provide the SSR and the corresponding GDB was computed. In the second part of the study, the reliability of the FORTH-RTM SSR and GDB was investigated. The results are reliable, as proven from their evaluation against data from reference global station networks (BSRN & GEBA). In the third step, the causes of GDB investigated based on the trends of the SSR and the input parameters to the FORTH-RTM. Furthermore, the contribution to GDB of each input parameter P was computed. In order to identify and determine more accurately the GDB drivers, namely the contribution of changes in clouds (cloud amount-CA and cloud optical thickness-COT of low, middle, high-level clouds), aerosol optical properties (AOD, SSA and AP), water vapor and ozone to GDB during the 35-year period 1984-2018, another method was applied. According to this, the contribution to GDB (in Wm^{-2}) of each physical input parameter P is estimated through two RTM runs in which, first, the P parameter is kept 'frozen' at its initial conditions, that is those in the first year of the study period, i.e. 1984, and second all the input parameters were activated (main RTM run). Next, the changes of SSR (GDB) have been estimated based on the two RTM runs. Then, from the difference between the GDB of the main RTM run, with all parameters being activated, and the GDB from runs with 'frozen' P parameters, the contribution of the P parameter to the overall GDB was estimated. When the contribution of a parameter is positive (reddish colors on the maps), it means that the changes of the P parameter resulted in an increase of SSR, and the interdecadal changes of this parameter contributed to, or partially caused, the estimated brightening or counteracted the estimated dimming. On the other hand, if the contribution of one parameter is negative (bluish colors on the maps below), it means that the changes of P parameter resulted in a decrease of SSR and the interdecadal changes of this parameter contributed to, or partially caused, the estimated dimming or counteracted the estimated brightening. It should be noted that the study period encompasses and coincides with the rapid anthropogenic warming occurring since the early 1980s. Thus, the role of solar

dimming and brightening (decadal changes in SSR) in relation to the recent global warming was also examined in the present study. The main conclusions are outlined below:

- The FORTH-RTM results are reliable, as proven from their evaluation against data from reference global station networks. Indeed, the model SSR fluxes and their anomalies correlate very well with GEBA and BSRN ground-based stations. The R is equal to 0.97 using SSR fluxes or 0.75 using deseasonalized SSR anomalies against GEBA and 0.94 using SSR fluxes or 0.71 using deseasonalized SSR anomalies, against BSRN. On a station level, the computed R values range from −0.21 to 0.98, but the majority of them (70%) are higher than 0.7, with the lowest values occurring in low latitudes, possibly due to uncertainties in the cloud and aerosol input data.

- In general, there is a relatively small overestimation of FORTH-RTM SSR compared to GEBA and a weak underestimation compared to BSRN measurements. The mean bias being equal to 4.46 Wm^{-2} and −2.49 Wm^{-2} or 2.7% and −1.3%, respectively. The FORTH-RTM stronger overestimates SSR at low latitudes, probably because of an underestimation of changes in cloud cover and aerosol optical depth data in these regions. The general overestimation suggests that the atmosphere of FORTH-RTM is more transparent than it should be. The average RMSE value is equal to 20.93 Wm^{-2} (equivalent to 12.8%) for the comparison of FORTH-RTM with GEBA, while the corresponding value for BSRN is equal to 29.02 Wm^{-2} or 15.4%, pointing to a rather small deviation of the modeled from the measured SSR. The largest RMSE values exist in low and high-latitude regions.

- The comparison of the time series of 12-month moving averages between FORTH-RTM SSR anomalies and GEBA/BSRN sites shows a larger model than station SSR anomalies, negative at the beginning of the study period and positive after 2010, which can affect the computed GDB. Indeed, the FORTH-RTM SSR trends show a stronger brightening than the stations' trends.

- The model estimated GDB nicely agrees in terms of sign with the stations, namely for 80% of GEBA and 65% of BSRN stations, while the agreement is even better for statistically significant trends (for 90% of GEBA and 88% of BSRN). A similar evaluation was also conducted separately for the 4 decades of the study period and the agreement was again very good (ranging from 62% to 73%). For Europe, India, and Japan, there is a strong agreement between the FORTH-RTM and stations in terms of GDB signs, putting confidence in the qualitative GDB patterns in these world areas. On the other hand, the FORTH-RTM presents a weak agreement against stations in terms of the SSR changes' magnitude. More specifically, it overestimates the brightening of most sites. This could be due to inadequate model input data, but also to issues with the stations' measurements of their own.

- Also, the evaluations against ground truth were performed and inter-compared for several SSR and GDB datasets during 1984-2018 and 2001-2018. The results of this inter-comparison approved that FORTH-RTM is a top-performing model in qualitative agreement for GDB (also better than the previous versions of this model) when compared to observational measurements, further reinforcing its reliability. Additionally, FORTH-RTM ranks among the best-performing

datasets for SSR, enhancing confidence in its ability to study long-term GDB trends on a global scale.

- The model indicates a global mean brightening (increasing SSR) from 1984 to 2018, equal to 0.88 $Wm^{-2}decade^{-1}$. This brightening is observed in 63% of the global grid points. Both land and ocean regions of the world underwent brightening; yet the land increase is stronger than the oceans (2.57 $Wm^{-2}decade^{-1}$ vs 0.19 $Wm^{-2}decade^{-1}$). Also, a stronger brightening occurred over the NH, equal to 1.4 $Wm^{-2}decade^{-1}$, versus the weak brightening of 0.39 $Wm^{-2}decade^{-1}$ over the SH. All the above SSR changes are statistically significant at the 95% confidence level. The spatially averaged GDB conceals diversified, in terms of sign and magnitude, patterns. Thus, strong tendencies toward brightening are noteworthy over Europe, the Americas, the Tibetan Tableau, Indonesia, Antarctica, Australia and some oceanic regions, whereas the dimming dominates over parts of China and India, the Arabian Peninsula, the Sahara, the Arctic, the Southern Ocean and the marine stratocumulus areas. These results revise the findings of a previous study which suggested a global dimming over the same period, and this revision is due to more realistic cloud information (CLARISC instead of ISCCP-H cloud dataset).

- Over the four decades, surface solar radiation (SSR) exhibited distinct trends. In the 1980s, a weak global dimming (-0.69 $\%decade^{-1}$) occurred over NH while a weak brightening over SH (0.53 $\%decade^{-1}$), followed by a significant brightening in the 1990s (+2.43 $\%decade^{-1}$) due to large reductions in aerosol optical depth (AOD) and cloud optical thickness (COT). The 2000s saw a weaker global brightening (+0.74 $\%decade^{-1}$) as increases in aerosols and low/high cloud amounts were partially offset by reductions in COT and mid-level cloud amount. Finally, the 2010s experienced another period of brightening (+0.83 $\%decade^{-1}$), driven by reductions in both clouds and aerosols, particularly over land.

- Over the entire time period (e.g. 1984-2018), there have been large declines in high-level COT and mid-level CA across the planet in line with the general (global) increase in SSR. On the contrary, there were large increases in the COT of middle and low clouds as well as of low-level cloud amount over the SH and the oceans. The AOD decreased except overland areas of the SH. According to our analysis, the major drivers of GDB (brightening) have been changes (decreases) in mid-level CA and high-level COT, while the contribution of the AOD changes (decreases) is remarkable over specific land areas with intense anthropogenic pollution, such as Europe, India and East China. The contribution of other aerosol optical properties, i.e. SSA, AP, as well as of water vapor and ozone was insignificant.

- During the 1980s (1984-1989), AOD generally decreased, whereas COT3 increased globally and high-level CA also increased everywhere except over land of the SH. The existence of positive and negative trends of the GDB drivers resulted either in a weak dimming, as in the NH and over land, or in a weak brightening, as in the SH. AOD changes had the largest contribution to GDB during this decade either globally or over 11/18 land areas, being followed by changes in high-level CA.

- Throughout the 1990s, large reductions in AOD, COT, and partially in CA, explain the general increase in SSR during this decade. More specifically, AOD changes are found to have been the strongest contributor to GDB during this decade in general, and over 11/18 land areas, followed by changes in high-level CA. Notably, water vapor, in spite of its generally weak role for GDB, showed some significant contribution over Australia and Mexico.

- Across the 2000s, AOD, and cloud amount of low- and high-level clouds increased, while COT and mid-level CA largely decreased. The coincidence of these trends led to an overall weak brightening. Especially, the changes of high-level COT, followed by those of AOD, had the strongest contribution to GDB in the 2000s either globally or over 7/18 land areas. Besides, SSA changes had significant contribution to GDB over East China.

- In the 2010s, there were large reductions in both clouds and aerosols, being stronger over land areas. On the contrary, there was an increase in COT of low clouds, and cloud amount of mid- and high-level clouds over the oceans. The general reduction in GDB drivers led to a general brightening, except over the oceans of SH, where dimming prevailed. Changes in both AOD and clouds contributed strongly to GDB, with AOD being the most common contributor (over 8/18 land areas) followed by high-level CA. Moreover, water vapor significantly contributed over Mexico.

- Overall, this work confirmed the decadal scale variability of SSR, revealing that SSR experienced notable changes during the last 4 decades since the early 1980s. It also proved the complex nature of the phenomenon, which changes magnitude, and even the sign, between adjacent world areas. The complexity is further strengthened since the causes of GDB (SSR changes) vary from a decade to another or from a region to another over the Earth. It was found that the drivers of the phenomenon are both natural and anthropogenic, which perplexes the situation even more. It is important that the changes of aerosol loads (AOD) were the main driver of GDB over areas with significant anthropogenic activity, namely Europe, East China and India. However, the role of AOD was significant also globally during the 1980s and 1990s.

- These results highlight the climatic role of reduced anthropogenic particulate emissions, which can mitigate their role towards counterbalancing greenhouse warming (GHW). On the other hand, cloud changes, especially changing COT of high-level clouds and CA of mid-level clouds, are the main GDB drivers globally and hemispherically over the entire climatic time period and also during the 2000s. Such changes in cloud properties can be the result of both natural and anthropogenic processes, which remains to be investigated. The present study certainly highlights the important role of GDB for the Earth's climate, since it has the potential to induce a global radiative cooling/warming that has the ability either to weaken or strengthen greenhouse-gas induced warming.

- Yet, although the FORTH-RTM GDB is in fairly good agreement with the stations' GDB, it can be further improved and increase its reliability through substantial improvements in the model input

satellite and reanalysis data. Such an improvement can further reduce the uncertainties about the causes of the estimated GDB.

- The role of solar dimming and brightening (decadal changes in SSR) in relation to the recent global warming was also examined in the present study. According to the findings of this study, the estimated GDB phases are in line with the decadal variations of T_{mean} as well as T_{max}, T_{min}, and DTR over certain land areas of the globe with significant anthropogenic pollution, such as Europe and East Asia, as well as over global land. The interdecadal phases of GDB seem to complementarily modify and differentiate the rates of warming primarily caused by the monotonically increasing concentration of greenhouse gases.

- More specifically, since the mid-1980s, when solar brightening took place, the global land mean temperature response, originally driven by the evolving anthropogenic greenhouse effect, was a rapid warming, which was decelerated or even stopped in the 2000s when solar dimming occurred in areas with intense anthropogenic pollution such as Europe, India and East Asia and partly masked the anthropogenic greenhouse global warming. Then, during the transition from dimming to a renewed brightening in the 2010s, the greenhouse warming was no longer masked and the warming rates increased again. This relationship between GDB, namely the rates of change of SSR, and the Earth's surface temperature during the 35-year period 1984-2018 is in line with the conclusions drawn by (Wild et al. 2007) for the decades from 1950-2000.

- Moreover, it is found that the inter-annual SSR variation also plays a role in the year-to-year changes of the Earth's surface temperature, although of course these are also driven by other factors, e.g. anthropogenic greenhouse gases warming, volcanic eruptions or ENSO (Gou et al. 2022; Santer 2014; Solomon 2011; Watanabe et al. 2014).

- The GDB was found to largely drive and to be more strongly related to T_{max} and secondarily to the mean surface-air temperature and the daily temperature range. The derived conclusions are more valid over the global land than ocean areas and apply to a considerable degree on the global scale. Also, in many regions where strong brightening occurred, T_{max} increased more than T_{min} (which increased primarily due to greenhouse warming), leading to an increase of DTR, confirming that GDB plays an important role in the T_{max} and DTR changes. However, the rates of brightening before and after the 2000s' dimming are not associated with proportional surface warming rates, confirming the complexity of the straight connection between SSR and surface temperature changes as well as the importance of the anthropogenic greenhouse effect as main factor of the ongoing global warming.

7.2. Future plans

Building upon the significant advancements achieved in this PhD research, several directions are envisioned for future work to further deepen our understanding of GDB and its climatic implications:

- Extension of the study period: With new datasets becoming available, future work could extend the analysis beyond 2018, enabling the investigation of the most recent trends in SSR and its drivers. This would also allow exploration of how recent climate policies, emission changes, and aerosol reductions—particularly in Asia—may have influenced SSR.
- Improved temporal and spatial resolution: While this study focused on monthly and decadal scales, future analyses could target finer temporal resolutions such as daily or hourly. This could enable to distinguish the clear sky days from the cloudy sky days and compute the GDB separately to distinguish the aerosol induced GDB from the corresponding cloud induced GDB. The finer temporal resolution could also enable to assess short-term SSR variability and its links to weather and climate extremes. The increased spatial resolution could also enable more detailed and accurate patterns even in sub-country levels, which could help for the solar power estimations.
- Enhancement of input datasets and RTM algorithm**:** Future work could benefit from the use of improved and more detailed input datasets for clouds (ideally improved ISCCP or CLARISC datasets) and aerosols (e.g. improved MERRA-2) as they become available. Additionally, further refinement of the FORTH-RTM algorithm itself could enhance its accuracy and extend its applicability to more complex atmospheric conditions, such as such as overlapping cloud layers, and/or mixed-phase clouds (both ice and water).
- Expanded use of machine learning: Building on the initial machine learning applications in this study, future work could further develop data-driven models in conjunction with the FORTH-RTM to better identify complex, nonlinear relationships among GDB drivers and regional SSR trends. More sophisticated techniques, such as neural networks and ensemble learning methods, could enhance the ability to detect and quantify the key contributors to GDB. These approaches may also be used to predict future SSR changes under various emission scenarios and to uncover interactions among variables that traditional methods may overlook.
- Investigation of GDB feedbacks with surface processes: Further work could explore how SSR trends influence land-surface processes, such as evapotranspiration, soil moisture, and vegetation dynamics, especially in regions undergoing significant SSR changes.

  By pursuing these future directions, the insights gained from this thesis can be extended to address open questions in climate science, support climate adaptation strategies, and contribute to a more comprehensive understanding of Earth's energy balance and climate system dynamics.

7.3. EarthSense: Interactive exploration of this PhD

To manage the large volume of data and results generated during this PhD, and to streamline their visualization and analysis, an interactive web application was developed in the final year of the PhD. This tool was designed to provide fast, user-friendly access to the study’s outcomes. Although the application is currently in internal testing, there are plans to make it publicly available after the thesis defense, aiming to support the wider research, scientific and open-source community. Screenshots of this tool are shown in Figure AF1. The application leverages high-performance and widely adopted libraries. The backend was developed in Python, utilizing FastAPI for efficient API management and Bokeh for fast, interactive visualizations. The frontend is built using Bootstrap and JavaScript, ensuring a responsive and

intuitive user interface. From the main menu (Figure AF1a), users can navigate to three core modules or access an introduction to the PhD (Figure AF1b) or additional information (Figure AF1f) about the application and its creator.

- EarthSense1 or SSR Visualization Module:
  This module (Figure AF1c) presents the SSR data as computed by the FORTH-RTM. It offers multiple visualization options, including global monthly maps, full-period time series, latitudinal averages, and annual SSR cycles. Users can select any month to view the corresponding planetary SSR distribution or click on anomalies to update the map view dynamically. Additionally, interacting with bars on the annual cycle graph will display maps averaged over the selected months.

- EarthSense2 or Model Evaluation Module:
  This section (Figure AF1d) allows users to assess the model's performance against ground-based stations. By selecting a station on the map, the user can view detailed evaluation outputs such as SSR time series comparisons, scatter plots, statistical tables, and seasonal cycles.

- EarthSense3 or Climate Explorer Module:
  Serving as the core of the application, this tool (Figure AF1e) enables users to select any rectangular region or specific pixel on the map and retrieve normalized time series data of key GDB drivers alongside climate parameters like temperature, precipitation, and evaporation. The data are low-pass filtered with SG filter and normalized for comparative analysis. A bar chart identifies the dominant GDB driver for the selected location, and a comprehensive data table summarizes statistical relationships between SSR and climate variables. This includes Pearson's and Spearman's correlations, trends, and their significance at 95% confidence level.

This final module effectively functions as a climate exploration tool, offering valuable insights into the climate dynamics and solar radiation trends of the past decades.

Bibliography

Abakumova, GM et al. (1996). 'Evaluation of long-term changes in radiation, cloudiness, and surface temperature on the territory of the former Soviet Union'. In:Journal of Climate 9.6, pp. 1319–1327.

Alados-Arboledas, L., Olmo, F. J., Ohvril, H. O., Teral, H., and Arak, M. (1997).Evolution of solar radiative effects of Mount Pinatubo at ground level. Tellus B, 49(B):190–198.

Alexandri, G.; Georgoulias, A.K.; Meleti, C.; Balis, D.; Kourtidis, K.A.; Sanchez-Lorenzo, A.; Trentmann, J.; Zanis, P. A High Resolution Satellite View of Surface Solar Radiation over the Climatically Sensitive Region of Eastern Mediterranean. *Atmospheric Res.* 2017, *188*, 107–121, doi:10.1016/j.atmosres.2016.12.015.

Allen, R. J., J. R. Norris, and M. Wild (2013), Evaluation of multidecadal variability in CMIP5 surface solar radiation and inferred underestimation of aerosol direct effects over Europe, China, Japan, and India, J. Geophys. Res. Atmos., 118, 6311–6336, doi:10.1002/jgrd.50426.

Alpert, P., P. Kishcha, Y. J. Kaufman, and R. Schwarzbard (2005), Global dimming or local dimming?: Effect of urbanization on sunlight availability, Geophys. Res. Lett., 32, L17802, doi:10.1029/2005GL023320.

Aparicio, A. J. P., Gallego, M. C., Anton, M., & Vaquero, J. M. (2020). Relationship between solar activity and direct solar irradiance in Madrid (1910–1929).Atmospheric Research, 235, 104766.https://doi.org/10.1016/j.atmosres.2019.1

Arora A, Rao SA, Chattopadhyay R, Tanmoy G, Gibies G, Sabeerali CT (2016) Role of Indian Ocean SST Variability on the Recent Global Warming Hiatus. Global and Planetary Change 143: 21-30. Https://Doi.Org/10.1016/j.Gloplacha.2016.05.009.

Augustine, J. A., & Capotondi, A. (2022).Forcing for multidecadal surface solar radiation trends over Northern Hemisphere continents. Journal of Geophysical Research: Atmospheres, 127, e2021JD036342. https://doi. org/10.1029/2021JD036342

Augustine, J. A., & Dutton, E. G. (2013). Variability of the surface radiation budget over the United States from 1996 through 2011 from high-quality measurements. Journal of Geophysical Research: Atmospheres, 118, 43–53. https://doi.org/10.1029/2012JD018551

Badarinath, K.V.S.; Sharma, A.R.; Kaskaoutis, D.G.; Kharol, S.K.; Kambezidis, H.D. Solar Dimming over the Tropical Urban Region of Hyderabad, India: Effect of Increased Cloudiness and Increased Anthropogenic Aerosols. *J. Geophys. Res. Atmospheres* 2010, *115*, doi:https://doi.org/10.1029/2009JD013694.

Baker, M.B.; Peter, T. Small-Scale Cloud Processes and Climate. *Nature* 2008, *451*, 299–300, doi:10.1038/nature06594.

Barbaro E, Vilà-Guerau de Arellano J, Krol M, Holtslag A (2013) Impacts of Aerosol Shortwave Radiation Absorption on the Dynamics of an Idealized Convective Atmospheric Boundary Layer. Boundary Layer Meteorol. 148: 31–49. Doi:10.1007/S10546-013-9800-7.

Barker, T. (2007). Climate Change 2007 : An Assessment of the Intergovernmental Panel on Climate Change. Change, 446(November):12–17.

Bellouin, N., et al. (2020). "Aerosol forcing in the Climate Model Intercomparison Project (CMIP6)." Geophysical Research Letters, 47(10), e2020GL087647.

Benesty, J., Chen, J., Huang, Y. and Cohen, I. (2009) Pearson Correlation Coefficient. In: Cohen, I., Huang, Y., Chen, J.D. and Benesty, J., Eds., Noise Reduction in Speech Processing, Springer, 1-4. https://doi.org/10.1007/978-3-642-00296-0_5

Bengtsson, L., Hodges, K. I., and Roeckner, E. (2006). Storm tracks and climate change. Journal of Climate, 19:3518–3543.

Bian, L.-G., Z. Lin, X.-D. Zheng, et al., 2012: Trend of Antarctic ozone hole and its influencing factors. Adv. Clim. Change Res., 3(2), doi: 10.3724/SP.J.1248.2012.00068.

Boucher, O et al. (2013). 'Clouds and Aerosols'. In: Climate Change 2013: The Physical Science Basis. Contribution of Working Group I to the Fifth Assessment Report of the Intergovernmental Panel on Climate Change. Ed. by T.F. Stocker et al. Cambridge, United Kingdom and New York, NY, USA: Cambridge University Press. Chap. 7, pp. 571–658. ISBN: ISBN 978-1-107-66182-0.

Boudala, F.S.; Milbrandt, J.A. Evaluations of the Climatologies of Three Latest Cloud Satellite Products Based on Passive Sensors (ISCCP-H, Two CERES) against the CALIPSO-GOCCP. Remote Sens. 2021, 13, 5150. Https://Doi.Org/10.3390/Rs13245150.

Bony, S., Dufresne, JL., Le Treut, H. et al. On dynamic and thermodynamic components of cloud changes. Climate Dynamics 22, 71–86 (2004). https://doi.org/10.1007/s00382-003-0369-6

Bouniol, Dominique & Couvreux, F. & Kamsu Tamo, Pierre Honoré & Leplay, Madeleine & Guichard, Françoise & Favot, Florence & O'Connor, Ewan. (2012). Diurnal and Seasonal Cycles of Cloud Occurrences, Types, and Radiative Impact over West Africa. Journal of Applied Meteorology and Climatology. 51. 534-553. 10.1175/JAMC-D-11-051.1.

Breiman, L. Random Forests. Machine Learning 45, 5–32 (2001). https://doi.org/10.1023/A:1010933404324

Campbell GG, VonderHaar TH (1997) Comparison of Surface Temperature Minimum and Maximum and Satellite Measured Cloudiness and Radiation Budget. J. Geophys. Res. 102: 16639–16645.

Campbell, G. G., 2004: View Angle Dependence of Cloudiness and the Trend in ISCCP Cloudiness. 13th Conf. on Satellite Meteorology and Oceanography, Norfolk, VA, Amer. Meteor. Soc., P6.7. [Available Online at Https://Ams.Confex.Com/Ams/13SATMET/Techprogram/Paper_79041.Htm.].

CERES Data Products. Https://Ceres.Larc.Nasa.Gov/Data/ (accessed on 30 June 2023).

Che, H., Gui, K., Xia, X., Wang, Y., Holben, B. N., Goloub, P., Cuevas-Agulló, E., Wang, H., Zheng, Y., Zhao, H., and Zhang, X.: Large contribution of meteorological factors to inter-decadal changes in regional aerosol optical depth, Atmos. Chem. Phys., 19, 10497–10523, https://doi.org/10.5194/acp-19-10497-2019, 2019

Cherian, R., & J. Quaas (2020). Trends in AOD, clouds, and cloud radiative effects in satellite data and CMIP5 and CMIP6 model simulations over aerosol source regions. Geophysical Research Letters, 47, e2020GL087132. https://doi.org/10.1029/2020GL087132

Cheshmehzangi A (2020) The Analysis of Global Warming Patterns from 1970s to 2010s. Atmospheric and Climate Sciences 10: 392-404.Doi: 10.4236/Acs.2020.103022.

Chin, M., T. Diehl, Q. Tan, J.M. Prospero, R.A. Kahn, L.A. Remer, H. Yu, A.M. Sayer, H. Bian, I.V. Geogdzhayev, B.N. Holben, S.G. Howell, B.J. Huebert, N.C. Hsu, D. Kim, T.L. Kucsera, R.C. Levy, M.I. Mishchenko, X. Pan, P.K. Quinn, G.L. Schuster, D.G. Streets, S.A. Strode, O. Torres, and X.-P. Zhao, 2014: Multi-decadal variations of atmospheric aerosols from 1980 to 2009: Sources and regional trends. Atmos. Chem. Phys., 14, 3657-3690, doi:10.5194/acp-14-3657-2014.

Chou, M.D.; Suarez, M.J. A Solar Radiation Parameterization (CLIRAD-SW) for Atmospheric Studies; NASA Technical Memorandum NASA/TM-1999-104606, 40; NASA Goddard Space Flight Center: Greenbelt, MD, USA, 1999.

Chtirkova, B., Folini, D., Correa, L. F., & Wild, M. (2022). Internal variability of all-sky and clear-sky surface solar radiation on decadal timescales. Journal of Geophysical Research: Atmospheres, 127, e2021JD036332. https://doi.org/10.1029/2021JD036332

Chtirkova, B., Folini, D., Correa, L. F., & Wild, M. (2023). Internal variability of the climate system mirrored in decadal-scale trends of surface solar radiation. Journal of Geophysical Research: Atmospheres, 128, e2023JD038573. https://doi.org/10.1029/2023JD038573

Chtirkova, B., Folini, D., Ferreira Correa, L., and Wild, M., 2024: Shortwave radiative flux variability through the lens of the Pacific Decadal Oscillation. Journal of Geophysical Research: Atmospheres, 129, e2023JD040520. https://doi.org/10.1029/2023JD040520

Correa, L. F., Folini, D., Chtirkova, B., & Wild, M.: Causes for decadal trends in surface solar radiation in the Alpine region in the 1981–2020 period. Journal of Geophysical Research: Atmospheres, 129, e2023JD039998., 2024a. https://doi.org/10.1029/2023JD039998

Correa, L. F., Folini, D., Chtirkova, B., & Wild, M.: Trends in observed surface solar radiation and their causes in Brazil in the first two decades of the 21st century, Atmos. Chem. Phys.,24, 8797–8819, https://doi.org/10.5194/acp-24-8797-2024 ,2024b.

Correa, L.F., Folini, D., Chtirkova, B., and Wild, M., 2024c: From internal variability to aerosol effects: physical mechanisms behind observed decadal trends in Surface Solar Radiation in the Western Pacific Ocean, Journal of Geophysical Research: Atmospheres, 129, e2024JD041014, https://doi.org/10.1029/2024JD041014

Cullather, R.I.; Bosilovich, M.G. The Energy Budget of the Polar Atmosphere in MERRA. *J. Clim.* 2012, *25*, 5–24, doi:10.1175/2011JCLI4138.1.

Cutchis, P. (1974). Stratospheric ozone depletion and solar ultraviolet radiation on Earth. Science (New York, N.Y.), 184(4132):13–9.

Darnell, W. L., Staylor, W. F., Gupta, S. K., Ritchey, N. A., and Wilber, A. C.: Seasonal variation of surface radiation budget derived from International Satellite Cloud Climatology Project C1 data, J. Geophys. Res., 97, 15 741–15 760, 1992

Deneke, H.M.; Feijt, A.J.; Roebeling, R.A. Estimating Surface Solar Irradiance from METEOSAT SEVIRI-Derived Cloud Properties. *Remote Sens. Environ.* 2008, *112*, 3131–3141, doi:10.1016/j.rse.2008.03.012.

Devasthale, A.; Karlsson, K.-G. Decadal Stability and Trends in the Global Cloud Amount and Cloud Top Temperature in the Satellite-Based Climate Data Records.Remote Sens. 2023, 15, 3819.https://doi.org/10.3390/rs15153819

Di Antonio L, Di Biagio C, Foret G, Formenti P, Siour G, Doussin JF, Beekmann M (2023) Aerosol Optical Depth Climatology from the High-Resolution MAIAC Product over Europe: Differences between Major European Cities and Their Surrounding Environments. Atmos. Chem. Phys. 23: 12455–12475. Https://Doi.Org/10.5194/Acp-23-12455-2023.

Doelling, D.R.; Loeb, N.G.; Keyes, D.F.; Nordeen, M.L.; Morstad, D.; Nguyen, C.; Wielicki, B.A.; Young, D.F.; Sun, M. Geostationary Enhanced Temporal Interpolation for CERES Flux Products. *J. Atmospheric Ocean. Technol.* 2013, *30*, 1072–1090, doi:10.1175/JTECH-D-12-00136.1.

Dong, B.; Sutton, R.T.; Wilcox, L.J. Decadal Trends in Surface Solar Radiation and Cloud Cover over the North Atlantic Sector during the Last Four Decades: Drivers and Physical Processes. *Clim. Dyn.* 2023, *60*, 2533–2546, doi:10.1007/s00382-022-06438-3.

Dong S, Xu T, Chen M (2022) Solar Radiation Characteristics in Shanghai. Journal of Physics: Conference Series 2351: 012016. doi:10.1088/1742-6596/2351/1/012016.

Douville H, Voldoire A, Geoffroy O (2015) The Recent Global Warming Hiatus: What Is the Role of Pacific Variability?. Geophysical Research Letters 42.3: 880-888.

Driemel, A.; Augustine, J.; Behrens, K.; Colle, S.; Cox, C.; Cuevas-Agulló, E.; Denn, F.M.; Duprat, T.; Fukuda, M.; Grobe, H.; et al. Baseline Surface Radiation Network (BSRN): Structure and data description (1992–2017). Earth Syst. Sci. Data 2018, 10, 1491–1501.

Durack, P. J., Wijffels, S. E., and Matear, R. J. (2012). Ocean salinities reveal strong global water cycle intensification during 1950 to 2000. Science (New York, N.Y.), 336(6080):455–8

Dwyer, John G, Joel R Norris and Christian Ruckstuhl (2010). 'Do climate models reproduce observed solar dimming and brightening over China and Japan?' In: Journal of Geophysical Research: Atmospheres 115.D7.

Easterling, D.R.; Wehner, M.F. Is the Climate Warming or Cooling? *Geophys. Res. Lett.* 2009, *36*, doi:https://doi.org/10.1029/2009GL037810.
EEA Technical report (2014). European Union emission inventory report 1990-2012 under the UNECE Convention on Long-range Transboundary Air Pollution (LRTAP). Technical Report 12, European Environment Agency, Luxembourg.
England M, Kajtar J, Maher N (2015) Robust Warming Projections despite the Recent Hiatus. Nature Clim Change 5: 394–396. Https://Doi.Org/10.1038/Nclimate2575.
Evan T.; Heidinger A. K.; Vimont D. J., Arguments against a Physical Long-Term Trend in Global ISCCP Cloud Amounts. *Geophys Res Lett* 2007, *34*, L04701.
Feng, F. and K. Wang (2019). "Does the modern-era retrospective analysis for research and applications-2 aerosol reanalysis introduce an improvement in the simulation of surface solar radiation over China?" International Journal of Climatology 39(3): 1305-1318.
Feng, F.; Wang, K. Determining Factors of Monthly to Decadal Variability in Surface Solar Radiation in China: Evidences From Current Reanalyses. *J. Geophys. Res. Atmospheres* 2019, *124*, 9161–9182, doi:https://doi.org/10.1029/2018JD030214.
Feng, F. and K. C. Wang (2021). "Merging High-Resolution Satellite Surface Radiation Data with Meteorological Sunshine Duration Observations over China from 1983 to 2017." Remote Sensing 13(4): 602.
Folini, D., T. N. Dallafior, M. Z. Hakuba, and M. Wild (2017), Trends of surface solar radiation in unforced CMIP5 simulations, J. Geophys. Res., 122, 469–484, doi:10.1002/2016JD025869.
Foster, G.; Rahmstorf, S. Global Temperature Evolution 1979–2010. *Environ. Res. Lett.* 2011, *6*, 044022, doi:10.1088/1748-9326/6/4/044022.
Fröhlich, C., A four-component proxy model for total solar irradiance calibrated during solar cycles 21-23, Contributions of the Astronomical Observatory Skalnate Pleso, vol. 41, no. 2, pp. 113–132, 2011.
Freychet, N., Tett, S. F. B., Bollasina, M., Wang, K. C., &Hegerl, G. (2019). The local aerosol emission effect on surface shortwave radiation and temperatures. Journal of Advances in Modeling Earth Systems, 11, 806–817. https://doi.org/10.1029/2018MS001530
Gavrouzou M, Hatzianastassiou N, Gkikas A, Korras-Carraca MB, Mihalopoulos N (2021) A Global Climatology of Dust Aerosols Based on Satellite Data: Spatial, Seasonal and Inter-Annual Patterns over the Period 2005–2019. Remote Sens. 13: 359. Https://Doi.Org/10.3390/Rs13030359.
Gelaro R, McCarty W, Suárez MJ, Todling R, Molod A, Takacs L, Randles CA, Darmenov A, Bosilovich MG, Reichle R et al. (2017) The Modern-Era Retrospective Analysis for Research and Applications, Version 2 (MERRA-2). Journal of Climate 30: 5419–5454. doi:10.1175/JCLI-D-16-0758.1.
Gilgen, H.; Wild, M.; Ohmura, A. Means and Trends of Shortwave Irradiance at the Surface Estimated from Global Energy Balance Archive Data. *J. Clim.* 1998, *11*, 2042–2061, doi:10.1175/1520-0442(1998)011<2042:MATOSI>2.0.CO;2.
Gkikas A, Hatzianastassiou N, Mihalopoulos N, Katsoulis V, Kazadzis S, Pey J, Querol X, and Torres, O. (2013) The Regime of Intense Desert Dust Episodes in the Mediterranean Based on Contemporary Satellite Observations and Ground Measurements, Atmos. Chem. Phys. 13: 12135–12154. Https://Doi.Org/10.5194/Acp-13-12135-2013.
Glantz P, Fawole OG, Ström J, Wild M, Noone KJ (2022) Unmasking the Effects of Aerosols on Greenhouse Warming over Europe. Journal of Geophysical Research: Atmospheres 127: e2021JD035889. Https://Doi.Org/10.1029/2021JD035889.
Global Energy Balance Archive. Available online: https://geba.ethz.ch/ (accessed on 2nd August 2024).
Gou R, Liu Y, Wang C (2022) The Controlling Mechanisms of the Recent Global Warming Hiatus: A Focus on the Internal Variabilities. Tellus A: Dynamic Meteorology and Oceanography 74(1): 172–186.DOI: Https://Doi.Org/10.16993/Tellusa.38.

Goudie, A. S. (2009). Dust storms: recent developments. Journal of environmental management, 90(1):89–94.

Gueymard, C.A. (2004) The Sun's Total and Spectral Irradiance for Solar Energy Applications and Solar Radiation Models. Solar Energy, 76, 423-453.

Gulev, S.K., P.W. Thorne, J. Ahn, F.J. Dentener, C.M. Domingues, S. Gerland, D. Gong, D.S. Kaufman, H.C. Nnamchi, J. Quaas, J.A. Rivera, S. Sathyendranath, S.L. Smith, B. Trewin, K. von Schuckmann, and R.S. Vose, 2021: Changing State of the Climate System. In Climate Change 2021: The Physical Science Basis. Contribution of Working Group I to the Sixth Assessment Report of the Intergovernmental Panel on Climate Change [Masson-Delmotte, V., P. Zhai, A. Pirani, S.L. Connors, C. Péan, S. Berger, N. Caud, Y. Chen, L. Goldfarb, M.I. Gomis, M. Huang, K. Leitzell, E. Lonnoy, J.B.R. Matthews, T.K. Maycock, T. Waterfield, O. Yelekçi, R. Yu, and B. Zhou (Eds.)]. Cambridge University Press, Cambridge, United Kingdom and New York, NY, USA, Pp. 287–422, Doi:10.1017/9781009157896.004.

Hansen J, Sato M, Ruedy R, Lo K, Lea DW, Medina-Elizade M (2006) Global Temperature Change. Proc. Natl. Acad. Sci. USA 103: 14288–14293.

Hastenrath S (1991) Interannual variability of the atmosphere-ocean system.In S. Hastenrath (Ed.), Climate dynamics of the tropics (Chap. 8, pp. 264–346). Netherlands: Springer. https://doi.org/10.1007/978-94-011-3156-8

Hatzianastassiou, N. and Vardavas, I.: Shortwave radiation budget of the Northern Hemisphere using International Satellite Cloud Climatology Project and NCEP/NCAR climatological data, J. Geophys. Res., 104, 24 401–24 421, 1999.

Hatzianastassiou, N.; Katsoulis, B.; Vardavas, I. Global Distribution of Aerosol Direct Radiative Forcing in the Ultraviolet and Visible Arising under Clear Skies. *Tellus B* 2004, *56*, 51–71, doi:10.1111/j.1600-0889.2004.00085.x.

Hatzianastassiou, N.; Matsoukas, C.; Fotiadi, A.; Pavlakis, K.G.; Drakakis, E.; Hatzidimitriou, D.; Vardavas, I. Global Distribution of Earth's Surface Shortwave Radiation Budget. Atmos. Chem. Phys. 2005, 5, 2847–2867. https://doi.org/10.5194/acp-5-2847-2005

Hatzianastassiou, N., Matsoukas, C., Drakakis, E., Stackhouse Jr., P. W., Koepke, P., Fotiadi, A., Pavlakis, K. G., and Vardavas, I.: The Direct Effect of Aerosols on Solar Radiation Based on Satellite Observations, Reanalysis Datasets, and Spectral Aerosol Optical Properties from Global Aerosol Data Set (GADS), Atmos. Chem. Phys., 7, 2585–2599, Https://Doi.Org/10.5194/Acp-7-2585-2007, 2007.

Hatzianastassiou, N., Papadimas, C.D., Matsoukas, C., Pavlakis, K., Fotiadi, A., Wild, M. and Vardavas, I. (2012), Recent regional surface solar radiation dimming and brightening patterns: inter-hemispherical asymmetry and a dimming in the Southern Hemisphere. Atmosph. Sci. Lett., 13: 43-48. https://doi.org/10.1002/asl.361

Hatzianastassiou N, Ioannidis E, Korras-Carraca M-B, Gavrouzou M, Papadimas CD, Matsoukas C, Benas N, Fotiadi A, Wild M, Vardavas I (2020) Global Dimming and Brightening Features during the First Decade of the 21st Century. Atmosphere 11 doi:10.3390/atmos11030308.

Haywood, J.M.; Bellouin, N.; Jones, A.; Boucher, O.; Wild, M.; Shine, K.P. The Roles of Aerosol, Water Vapor and Cloud in Future Global Dimming/Brightening. *J. Geophys. Res. Atmospheres* 2011, *116*, doi:https://doi.org/10.1029/2011JD016000.

Hersbach H, Bell B, Berrisford P et al. (2020) The ERA5 Global Reanalysis. Quarterly Journal of the Royal Meteorological Society 146: 1999–2049. doi:https://doi.org/10.1002/qj.3803. https://Cds.Climate.Copernicus.Eu/Cdsapp#!/Dataset/Reanalysis-Era5-Single-Levels?Tab=overview. Accessed 31 December 2023

Hinkelman, L.M.; Stackhouse Jr., P.W.; Wielicki, B.A.; Zhang, T.; Wilson, S.R. Surface Insolation Trends from Satellite and Ground Measurements: Comparisons and Challenges. *J. Geophys. Res. Atmospheres* 2009, *114*, doi:https://doi.org/10.1029/2008JD011004.

Hinkelman, L.M. The Global Radiative Energy Budget in MERRA and MERRA-2: Evaluation with Respect to CERES EBAF Data. *J. Clim.* 2019, *32*, 1973–1994, doi:10.1175/JCLI-D-18-0445.1.
Hoerl, A. E., & Kennard, R. W. (1970). Ridge Regression: Biased Estimation for Nonorthogonal Problems. Technometrics, 12(1), 55–67. https://doi.org/10.1080/00401706.1970.10488634
Hoyt, Douglas V and Kenneth H Schatten (1993). 'A discussion of plausible solar irradiance variations, 1700-1992'. In: Journal of Geophysical Research: Space Physics 98.A11, pp. 18895–18906.
Hudson, J. (1993). Cloud condensation nuclei. Journal of Applied Meteorology, 32:596–607.
IPCC, 2013: Climate Change 2013: The Physical Science Basis. Contribution of Working Group I to the Fifth Assessment Report of the Intergovernmental Panel on Climate Change [Stocker, T.F., D. Qin, G.-K. Plattner, M. Tignor, S.K. Allen, J. Boschung, A. Nauels, Y. Xia, V. Bex and P.M. Midgley (Eds.)]. Cambridge University Press, Cambridge, United Kingdom and New York, NY, USA, 1535 Pp.
IPCC, 2013: Summary for Policymakers. In: Climate Change 2013: The Physical Science Basis. Contribution of Working Group I to the Fifth Assessment Report of the Intergovernmental Panel on Climate Change [Stocker, T.F., D. Qin, G.-K. Plattner, M. Tignor, S.K. Allen, J. Boschung, A. Nauels, Y. Xia, V. Bex and P.M. Midgley (Eds.)]. Cambridge University Press, Cambridge, United Kingdom and New York, NY, USA.
IPCC (2021) Climate Change 2021: The Physical Science Basis. In V. Masson-Delmotte, et al. (Eds.), Contribution of Working Group I to the Sixth Assessment Report of the Intergovernmental Panel on Climate Change. Cambridge University Press.
IPCC (2022) Global Warming of 1.5°C: IPCC Special Report on Impacts of Global Warming of 1.5°C above Pre-Industrial Levels in Context of Strengthening Response to Climate Change, Sustainable Development, and Efforts to Eradicate Poverty. Cambridge: Cambridge University Press. Doi:10.1017/9781009157940.
Iqbal, M. (1983). An introduction to solar radiation. Academic press Canada, Ontario, 1 edition.
Japan Meteorological Agency/Japan. 2013, updated monthly. JRA-55: Japanese 55-year Reanalysis, Daily 3-Hourly and 6-Hourly Data. Research Data Archive at the National Center for Atmospheric Research, Computational and Information Systems Laboratory. https://doi.org/10.5065/D6HH6H41. Accessed† dd mmm yyyy.
Jenkins S, Povey A, Gettelman A, Grainger R, Stier P, Allen M (2022) Is Anthropogenic Global Warming Accelerating?.J. Climate, 35: 7873–7890. Https://Doi.Org/10.1175/JCLI-D-22-0081.1.
Jia, B.; Xie, Z.; Dai, A.; Shi, C.; Chen, F. Evaluation of Satellite and Reanalysis Products of Downward Surface Solar Radiation over East Asia: Spatial and Seasonal Variations. *J. Geophys. Res. Atmospheres* 2013, *118*, 3431–3446, doi:https://doi.org/10.1002/jgrd.50353.
Jones, P.W. First-and Second-Order Conservative Remapping Schemes for Grids in Spherical Coordinates. Monthly Weather Review 1999, 127, 2204–2210.
Joseph, J.H.; Wiscombe, W.J.; Weinman, J.A. The Delta-Eddington Approximation for Radiative Flux Transfer. J. Atmos. Sci. 1976, 33, 2452–2459.
Kambezidis, H. "Solar Radiation Modelling: The Latest Version and Capabilities of MRM." J. Fundam. Renew. Energy Appl 7 (2017): E114.
Kambezidis, H.D. The Solar Radiation Climate of Greece. *Climate* 2021, *9*, doi:10.3390/cli9120183.
KANG Ying, WANG Lili, XIN Jinyuan, TAO Minghui, SONG Tao, GONG Chongshui, WANG Yuesi, LI Guang. Analysis of the Change Trend of Aerosol Single-Scattering Albedo in the Areas of Northern China Based on AERONET and OMI Data[J]. Climatic and Environmental Research, 2019, 24(5): 537-551. DOI: 10.3878/j.issn.1006-9585.2018.18006
Kanamitsu, M., W. Ebisuzaki, J. Woollen, S. Yang, J. J. Hnilo, M. Fiorino, and G. L. Potter, 2002: NCEP–DOE AMIP-II Reanalysis (R-2). Bull. Amer. Meteor. Soc., 83, 1631–1644, https://doi.org/10.1175/BAMS-83-11-1631.

Karlsson, K.-G., Riihelä, A., Müller, R., Meirink, J. F., Sedlar, J., Stengel, M., Lockhoff, M., Trentmann, J., Kaspar, F., Hollmann, R., and Wolters, E.: CLARA-A1: a cloud, albedo, and radiation dataset from 28 yr of global AVHRR data, Atmos. Chem. Phys., 13, 5351–5367, https://doi.org/10.5194/acp-13-5351-2013, 2013.

Karlsson, K.-G., Anttila, K., Trentmann, J., Stengel, M., FokkeMeirink, J., Devasthale, A., Hanschmann, T., Kothe, S., Jääskeläinen, E., Sedlar, J., Benas, N., van Zadelhoff, G.-J., Schlundt, C., Stein, D., Finkensieper, S., Håkansson, N., and Hollmann, R.: CLARA-A2: the second edition of the CM SAF cloud and radiation data record from 34 years of global AVHRR data, Atmos. Chem. Phys., 17, 5809–5828, https://doi.org/10.5194/acp-17-5809-2017, 2017.

Karlsson, K.-G.; Devasthale, A. Inter-Comparison and Evaluation of the Four Longest Satellite-Derived Cloud Climate Data Records: CLARA-A2, ESA Cloud CCI V3, ISCCP-HGM, and PATMOS-x. Remote Sens. 2018, 10, 1567. Https://Doi.Org/10.3390/Rs10101567.

Karlsson, K.-G.; Håkansson, N. Characterization of AVHRR global cloud detection sensitivity based on CALIPSO-CALIOP cloud optical thickness information: Demonstration of results based on the CM SAF CLARA-A2 climate data record. Atmos. Meas. Tech. 2018, 11, 633–649.

Karlsson KG, Anttila K, Trentmann J et al. (2020) CLARA-A2.1: CM SAFcLoud, Albedo and surface RAdiation dataset from AVHRR data - Edition 2.1. Satellite Application Facility on Climate Monitoring. DOI:10.5676/EUM_SAF_CM/CLARA_AVHRR/V002_01. https://doi.org/10.5676/EUM_SAF_CM/CLARA_AVHRR/V002_01. Accessed 31 December 2023

Karlsson, K.-G.; Devasthale, A.; Eliasson, S. Global Cloudiness and Cloud Top Information from AVHRR in the 42-Year CLARA-A3 Climate Data Record Covering the Period 1979–2020. Remote Sens. 2023, 15, 3044. https://doi.org/10.3390/rs15123044

Karlsson, K.-G., Stengel, M., Meirink, J. F., Riihelä, A., Trentmann, J., Akkermans, T., Stein, D., Devasthale, A., Eliasson, S., Johansson, E., Håkansson, N., Solodovnik, I., Benas, N., Clerbaux, N., Selbach, N., Schröder, M., and Hollmann, R.: CLARA-A3: The third edition of the AVHRR-based CM SAF climate data record on clouds, radiation and surface albedo covering the period 1979 to 2023, Earth Syst. Sci. Data, 15, 4901–4926, https://doi.org/10.5194/essd-15-4901-2023, 2023.

Kato, S.; Rose, F.G.; Rutan, D.A.; Thorsen, T.J.; Loeb, N.G.; Doelling, D.R.; Huang, X.L.; Smith, W.L.; Su, W.Y.; Ham, S.H. Surface irradiances of edition 4.0 clouds and the earth's radiant energy system (CERES) energy balanced and filled (EBAF) data product. J. Clim. 2018, 31, 4501–4527.

Kato, S.; Loeb, N.G.; Rose, F.G.; Doelling, D.R.; Rutan, D.A.; Caldwell, T.E.; Yu, L.S.; Weller, R.A. Surface irradiances consistent with CERES-derived top-of-atmosphere shortwave and longwave irradiances. J. Clim. 2013, 26, 2719–2740.

Katz, J. L. and Ostermier, B. J. (1967). Diffusion Cloud-Chamber Investigation of Homogeneous Nucleation. The Journal of Chemical Physics, 47(2):478–487.

Kaufmann RK (2011) Reconciling Anthropogenic Climate Change with Observed Temperature 1998–2008. PNAS 108(29): 11790–11793. DOI: Https://Doi.Org/10.1073/Pnas.1102467108.

Kendall, M.G. (1975) Rank Correlation Methods. 4th Edition, Charles Griffin, London.

Kim, D., and V. Ramanathan (2008), Solar radiation budget and radiative forcing due to aerosols and clouds, J. Geophys. Res., 113, D02203, doi:10.1029/2007JD008434.

Kishcha, Pavel, Boris Starobinets, and Pinhas Alpert. "Latitudinal variations of cloud and aerosol optical thickness trends based on MODIS satellite data." Geophysical research letters 34.5 (2007).

Kokhanovsky, A. (2004). Optical properties of terrestrial clouds. Earth-Science Reviews, 64:189–241.

Korras-Carraca, M. B., Hatzianastassiou, N., Matsoukas, C., Gkikas, A., and Papadimas, C. D.: The regime of aerosol asymmetry parameter over Europe, the Mediterranean and the Middle East based on MODIS satellite data: evaluation against surface AERONET measurements, Atmos. Chem. Phys., 15, 13113–13132, https://doi.org/10.5194/acp-15-13113-2015, 2015.

Korras-Carraca MB, Gkikas A, Matsoukas C, Hatzianastassiou N (2021) Global Clear-Sky Aerosol Speciated Direct Radiative Effects over 40 Years (1980–2019). Atmosphere 12.doi:10.3390/atmos12101254.
Koren, I. and Feingold, G. (2011). Aerosol-cloud-precipitation system as a predator-prey problem. Proceedings of the National Academy of Sciences of the United States of America, 108(30):12227–32.
Kotarba, A.Z. Evaluation of ISCCP Cloud Amount with MODIS Observations. *Atmospheric Res.* 2015, *153*, 310–317, doi:10.1016/j.atmosres.2014.09.006.
Krishnan R, Ramanathan V (2002) Evidence of Surface Cooling from Absorbing Aerosols, Geophys. Res. Lett., 29(9). Doi:10.1029/2002GL014687.
Kumari, B. P., &Goswami, B. N. (2010). Seminal role of clouds on solar dimming over the Indian monsoon region.Geophysical Research Letters, 37, L06703.https://doi.org/10.1029/2009GL042133
Kvalevåg, M. M. &Myhre G.: Human Impact on Direct and Diffuse Solar Radiation during the Industrial Era. Journal of Climate. 20. 4874-4883, 2007. DOI: 10.1175/JCLI4277.1
Lange, Stefan (2019): WFDE5 over land merged with ERA5 over the ocean (W5E5). V. 1.0. GFZ Data Services. https://doi.org/10.5880/pik.2019.023
Lean, J.L. (2010), Cycles and trends in solar irradiance and climate†. WIREs Clim Change, 1: 111-122. https://doi.org/10.1002/wcc.18
Lenaerts, J.T.M.; Van Tricht, K.; Lhermitte, S.; L'Ecuyer, T.S. Polar clouds and radiation in satellite observations, reanalyses, and climate models. Geophys. Res. Lett. 2017, 44, 3355–3364.
Liepert, B. G. (1997). Recent changes in solar radiation under cloudy conditions in Germany. International Journal of Climatology, 17(14), 1581–1593.
Liepert, B.; Romanou, A. Global Dimming and Brightening and the Water Cycle. *Bull Amer Meteorol Soc* 2005, *86*, 622–623.
Liepert, B.G. Observed Reductions of Surface Solar Radiation at Sites in the United States and Worldwide from 1961 to 1990. *Geophys. Res. Lett.* 2002, *29*, 61-1-61–64, doi:https://doi.org/10.1029/2002GL014910.
Liley, J. B. (2009). New Zealand dimming and brightening.Journal of Geophysical Research, 114, D00D10.https://doi.org/10.1029/2008JD011401
Liou, K.N. (2002) An Introduction to Atmospheric Radiation. 2nd Edition, Academic Press, San Diego, CA.
Liu W, Xie, SP, Lu J (2016) Tracking Ocean Heat Uptake during the Surface Warming Hiatus. Nat Commun 7: 10926. Https://Doi.Org/10.1038/Ncomms10926.
Liu, X., He, T., Liang, S., Li, R., Xiao, X., Ma, R., and Ma, Y.: A monthly 1° resolution dataset of daytime cloud fraction over the Arctic during 2000–2020 based on multiple satellite products, Earth Syst. Sci. Data, 15, 3641–3671, https://doi.org/10.5194/essd-15-3641-2023, 2023.
Loeb, N.G.; Priestley, K.J.; Kratz, D.P.; Geier, E.B.; Green, R.N.; Wielicki, B.A.; Hinton, P.O.; Nolan, S.K. Determination of Unfiltered Radiances from the Clouds and the Earth's Radiant Energy System Instrument. *J. Appl. Meteorol.* 2001, *40*, 822–835, doi:10.1175/1520-0450(2001)040<0822:DOURFT>2.0.CO;2
Loeb, N.G.; Doelling, D.R.; Wang, H.; Su, W.; Nguyen, C.; Corbett, J.G.; Liang, L.; Mitrescu, C.; Rose, F.G.; Kato, S. Clouds and the Earth's Radiant Energy System (CERES) Energy Balanced and Filled (EBAF) Top-of-Atmosphere (TOA) Edition-4.0 Data Product. *J. Clim.* 2018, *31*, 895–918, doi:10.1175/JCLI-D-17-0208.1.
Loeb, N. G., Thorsen, T., Norris, J., Wang, H., & Su, W. (2018). Changes in Earth's energy budget during and after the "pause" in global warming: An observational perspective. Climate, 6 (3), 62. https://doi.org/10.3390/cli6030062

Lohmann, U., Zhang, J., & Pi, J. (2003). Sensitivity studies of the effect of increased aerosol concentrations and snow crystal shape on the snowfall rate in the arctic. Journal of Geophysical Research: Atmospheres, 108(D11). https://doi.org/10.1029/2003jd003377
Lohmann, U. and Feichter, J.: Global indirect aerosol effects: a review, Atmos. Chem. Phys., 5, 715–737, https://doi.org/10.5194/acp-5-715-2005, 2005.
Long, C. N., E. G. Dutton, J. A. Augustine, W. Wiscombe, M. Wild, S. A. McFarlane, and C. J. Flynn (2009), Significant decadal brightening of downwelling shortwave in the continental United States, J. Geophys. Res., 114, D00D06, doi:10.1029/2008JD011263.
Ma, Q.; Wang, K.; Wild, M. Impact of Geolocations of Validation Data on the Evaluation of Surface Incident Shortwave Radiation from Earth System Models. *J. Geophys. Res. Atmospheres* 2015, *120*, 6825–6844, doi:https://doi.org/10.1002/2014JD022572.
Magnus, Jan R. and Melenberg, Bertrand and Muris, Chris, Global Warming and Local Dimming: The Statistical Evidence (January 21, 2011). CentER Discussion Paper Series No. 2011-004, Available at SSRN: https://ssrn.com/abstract=1744872 or http://dx.doi.org/10.2139/ssrn.1744872
Makowski K, Wild M, Ohmura A, Diurnal Temperature Range over Europe between 1950 and 2005 (2008) AtmosChemPhys 8: 6483–6498.
Makowski K, Jaeger EB, Chiacchio M, Wild M, Ewen T, Ohmura A (2009) On the Relationship between Diurnal Temperature Range and Surface Solar Radiation in Europe. J. Geophys. Res. 114: D00D07. Doi:10.1029/2008JD011104.
Manara, V., Brunetti, M., Celozzi, A., Maugeri, M., Sanchez-Lorenzo, A., and Wild, M.: Detection of dimming/brightening in Italy from homogenized all-sky and clear-sky surface solar radiation records and underlying causes (1959–2013), Atmos. Chem. Phys., 16, 11145–11161, https://doi.org/10.5194/acp-16-11145-2016, 2016.
Mann, H.B. Nonparametric Tests Against Trend. *Econometrica* 1945, *13*, 245–259, doi:10.2307/1907187.
Mateos, D., Sanchez-Lorenzo, A., Anton, M., Cachorro, V. E., Calbo, J., Costa, M. J., et al. (2014). Quantifying the respective roles of aerosols and clouds in the strong brightening since the early 2000s over the Iberian Peninsula. Journal of Geophysical Research: Atmospheres, 119, 10382–10393. https://doi.org/10.1002/2014JD022076
Matuszko, D. (2012), Influence of the extent and genera of cloud cover on solar radiation intensity. Int. J. Climatol., 32: 2403-2414. https://doi.org/10.1002/joc.2432
Meehl, Gerald A et al. (2000). 'The coupled model intercomparison project (CMIP)'. In: Bulletin of the American Meteorological Society 81.2, pp. 313–318.
Mercado, L.M.; Bellouin, N.; Sitch, S.; Boucher, O.; Huntingford, C.; Wild, M.; Cox, P.M. Impact of changes in diffuse radiation on the global land carbon sink. Nature 2009, 458, 1014–1017.
Michalsky, J.; Dutton, E.; Rubes, M.; Nelson, D.; Stoffel, T.; Wesely, M.; Splitt, M.; Deluisi, J.; Environmental Research; State Univ. of New York; et al. Optimal Measurement of Surface Shortwave Irradiance Using Current Instrumentation. *J Atmos Ocean Technol* 1999, *16*, doi:10.1175/1520-0426(1999)016<0055:OMOSSI>2.0.CO;2.
Miller, J. D., Skinner, C. N., Safford, H. D., Knapp, E. E., and Ramirez, C. M. (2012). Trends and causes of severity, size, and number of fires in northwestern California, USA. Ecological applications : a publication of the Ecological Society of America, 22(1):184–203.
Minnis, P.; Sun-Mack, S.; Young, D.F.; Heck, P.W.; Garber, D.P.; Chen, Y.; Spangenberg, D.A.; Arduini, R.F.; Trepte, Q.Z.; Smith, W.L.; et al. CERES Edition-2 cloud property retrievals using TRMM VIRS and Terra and Aqua MODIS data—Part I: Algorithms. IEEE Trans. Geosci. Remote Sens. 2011, 49, 4374–4400.
Mishchenko, M.I., B. Cairns, G. Kopp, C.F. Schueler, B.A. Fafaul, J.E. Hansen, R.J. Hooker, T. Itchkawich, H.B. Maring, and L.D. Travis, 2007: Accurate monitoring of terrestrial aerosols and total solar

irradiance: Introducing the Glory mission. Bull. Amer. Meteorol. Soc., 88, 677-691, doi:10.1175/BAMS-88-5-677.
Morice, C. P., Kennedy, J. J., Rayner, N. A., Winn, J. P., Hogan, E., Killick, R. E., et al. (2021). An Updated Assessment of near-Surface Temperature Change from 1850: The HadCRUT5 Data Set. Journal of Geophysical Research: Atmospheres, 126, E2019JD032361. Https://Doi.Org/10.1029/2019JD032361.
Moseid, Kine Onsum et al. (2020). 'Bias in CMIP6 models compared to observed regional dimming and brightening trends (1961–2014)'. In: Atmospheric Chemistry and Physics Discussions, pp. 1–20
Mueller, R.W.; Matsoukas, C.; Gratzki, A.; Behr, H.D.; Hollmann, R. The CM-SAF operational scheme for the satellite based retrieval of solar surface irradiance—A LUT based eigenvector hybrid approach. Remote Sens. Environ. 2009, 113, 1012–1024.
Muneer, T. and Gueymard, C.H.K. (2004) Radiation and Daylight Models. Second Edition, Elsevier Butterworth Heinemann, 13-17.;
Murphy, D. M., S. Solomon, R. W. Portmann, K. H. Rosenlof, P. M. Forster, and T. Wong (2009), An observationally based energy balance for the Earth since 1950, J. Geophys. Res., 114, D17107, doi:10.1029/2009JD012105.
Myhre, G, CEL Myhre et al. (2013). 'Aerosols and their relation to global climate and climate sensitivity'. In: Nature Education Knowledge 4.5, p. 7.
Nabat, P., S. Somot, M. Mallet, I. Chiapello, J.J. Morcrette, F. Solmon, S. Szopa, F. Dulac, W. Collins, S. Ghan, L.W. Horowitz, J.F. Lamarque, Y.H. Lee, V. Naik, T. Nagashima, D. Shindell, and R. Skeie, 2013: A 4-D climatology (1979-2009) of the monthly tropospheric aerosol optical depth distribution over the Mediterranean region from a comparative evaluation and blending of remote sensing and model products. Atmos. Meas. Tech., 6, 1287-1314, doi:10.5194/amt-6-1287-2013.
Nabat, P., Somot, S., Mallet, M., Sanchez-Lorenzo, A., and Wild, M.: Contribution of anthropogenic sulfate aerosols to the changing Euro-Mediterranean climate since 1980, Geophys. Res. Lett., 41, 5605–5611, https://doi.org/10.1002/2014GL060798, 2014.
NOAA National Centers for Environmental Information, Climate at a Glance: Global Mapping 2022.
Norris, J.R. What Can Cloud Observations Tell Us about Climate Variability. Space Sci. Rev. 2000, 94, 375–380.
Norris, J. R., and M. Wild (2007), Trends in aerosol radiative effects over Europe inferred from observed cloud cover, solar "dimming," and solar "brightening", J. Geophys. Res., 112, D08214, doi:10.1029/2006JD007794.
Norris JR, Wild M (2009) Trends in Aerosol Radiative Effects over China and Japan Inferred from Observed Cloud Cover, Solar "Dimming," and Solar "Brightening." Journal of Geophysical Research: Atmospheres 114. doi:https://doi.org/10.1029/2008JD011378.
Norris, J.R.; Evan, A.T. Empirical Removal of Artifacts from the ISCCP and PATMOS-x Satellite Cloud Records. *J. Atmospheric Ocean. Technol.* 2015, *32*, 691–702, doi:10.1175/JTECH-D-14-00058.1.
Norris, J., Allen, R., Evan, A. et al. Evidence for climate change in the satellite cloud record. Nature 536, 72–75 (2016).https://doi.org/10.1038/nature18273
Ohmura, A., & Lang, H. (1989). Secular variations of global radiation in Europe. In J. Leonoble& J. F. Geleyn (Eds.), IRS '88: Current problems in atmospheric radiation (pp. 98–301). Lille, France: A. Deepak Publ.
Ohmura A (2009) Observed Decadal Variations in Surface Solar Radiation and Their Causes. Journal of Geophysical Research: Atmospheres 114. doi:https://doi.org/10.1029/2008JD011290.
Ohvril, H., et al. (2009), Global dimming and brightening versus atmospheric column transparency, Europe, 1906–2007, J. Geophys. Res., 114, D00D12, doi:10.1029/2008JD010644.
Padma Kumari, B.; Goswami, B.N. Seminal Role of Clouds on Solar Dimming over the Indian Monsoon Region. *Geophys. Res. Lett.* 2010, *37*, doi:https://doi.org/10.1029/2009GL042133.

Parding, Kajsa (2014). 'Decadal solar irradiance variability in northern Europe'. The University of Bergen, https://hdl.handle.net/1956/8974

Parracho, A. C., Bock, O., and Bastin, S.: Global IWV trends and variability in atmospheric reanalyses and GPS observations, Atmos. Chem. Phys., 18, 16213–16237, https://doi.org/10.5194/acp-18-16213-2018, 2018.

Pfeifroth, U.; Sanchez-Lorenzo, A.; Manara, V.; Trentmann, J.; Hollmann, R. Trends and Variability of Surface Solar Radiation in Europe Based on Surface- and Satellite-Based Data Records. J. Geophys. Res. Atmos. 2018, 123, 1735–1754. https://doi.org/10.1002/2017JD027418

Philipona, R.; Behrens, K.; Ruckstuhl, C. How Declining Aerosols and Rising Greenhouse Gases Forced Rapid Warming in Europe since the 1980s. *Geophys. Res. Lett.* 2009, *36*, doi:https://doi.org/10.1029/2008GL036350.

Pierce, D. W., Gleckler, P. J., Barnett, T. P., Santer, B. D., and Durack, P. J. (2012). The fingerprint of human-induced changes in the ocean's salinity and temperature fields. Geophysical Research Letters, 39(21)

Pinker, R.T.; Zhang, B.; Dutton, E.G. Do Satellites Detect Trends in Surface Solar Radiation? Science 2005, 308, 850–854. DOI: 10.1126/science.1103159

Posselt, R., Mueller, R., Trentrnann, J., Stockli, R., &Liniger, M. A. (2014). A surface radiation climatology across two Meteosat satellite generations. Remote Sensing of Environment, 142, 103–110. https://doi.org/10.1016/j.rse.2013.11.007

Power, H. C. (2003), Trends in solar radiation over Germany and an assessment of the role of aerosols and sunshine duration, Theor. Appl. Climatol., 76, 47–63, doi:10.1007/s00704-003-0005-8.

Pyrgou, A.; Santamouris, M.; Livada, I. Spatiotemporal Analysis of Diurnal Temperature Range: Effect of Urbanization, Cloud Cover, Solar Radiation, and Precipitation. Climate 2019, 7, 89. https://doi.org/10.3390/cli7070089

Qian, Y., D. P. Kaiser, L. R. Leung, and M. Xu (2006), More frequent cloud-free sky and less surface solar radiation in China from 1955 to 2000, Geophys. Res. Lett., 33, L01812, doi:10.1029/2005GL024586.

R. W. Schafer, "What Is a Savitzky-Golay Filter? [Lecture Notes]," in IEEE Signal Processing Magazine, vol. 28, no. 4, pp. 111-117, July 2011, doi: 10.1109/MSP.2011.941097

Rahimikhoob, A.; Behbahani, S.M.R.; Banihabib, M.E. Comparative study of statistical and artificial neural network's methodologies for deriving global solar radiation from NOAA satellite images. Int. J. Climatol. 2013, 33, 480–486.

Ramachandran S., Rupakheti Maheswar, Cherian R., Insights into recent aerosol trends over Asia from observations and CMIP6 simulations, Science of The Total Environment, Volume 807, Part 1, 2022, 150756, ISSN 0048-9697, https://doi.org/10.1016/j.scitotenv.2021.150756.

Ramanathan V, Crutzen PJ, Kiehl JT, and Rosenfeld D (2001) Aerosol, Climate and the Hydrological Cycle, Science 294: 2119–2124. Doi:10.1126/Science.1064034.

Ramanathan V (2007) Global Dimming by Air Pollution and Global Warming by Greenhouse Gases: Global and Regional Perspectives. In: O'Dowd, C.D., Wagner, P.E. (Eds) Nucleation and Atmospheric Aerosols. Springer, Dordrecht. Https://Doi.Org/10.1007/978-1-4020-6475-3_94.

Ramanathan, V.; Ramana, M.V.; Roberts, G.; Kim, D.; Corrigan, C.; Chung, C.; Winker, D. Warming Trends in Asia Amplified by Brown Cloud Solar Absorption. *Nature* 2007, *448*, 575–578, doi:10.1038/nature06019.

Randles, C.A.; Da Silva, A.M.; Buchard, V.; Colarco, P.R.; Darmenov, A.; Govindaraju, R.; Smirnov, A.; Holben, B.; Ferrare, R.; Hair, J.; et al. The MERRA-2 Aerosol Reanalysis, 1980 - Onward, Part I: System Description and Data Assimilation Evaluation. *J. Clim.* 2017, *30*, 6823–6850, doi:10.1175/JCLI-D-16-0609.1.

Rao G. S. P., Jaswal A. K., and Kumar M. S., "Effects of urbanization on meteorological parameters", MAUSAM, vol. 55, no. 3, pp. 429–440, Jul. 2004.

Riihelä, A., J. R. Key, J. F. Meirink, P. KuipersMunneke, T. Palo, and K.-G. Karlsson (2017), Anintercomparison and validation of satellite-based surface radiative energy flux estimates over the Arctic, J. Geophys. Res. Atmos., 122, 4829–4848, doi:10.1002/2016JD026443.

Romanou, A., B. Liepert, G. A. Schmidt, W. B. Rossow, R. A. Ruedy, and Y. Zhang (2007), 20th century changes in surface solar irradiance in simulations and observations, Geophys. Res. Lett., 34, L05713, doi:10.1029/2006GL028356.

Ruckstuhl, C.; Philipona, R.; Behrens, K.; Collaud Coen, M.; Dürr, B.; Heimo, A.; Mätzler, C.; Nyeki, S.; Ohmura, A.; Vuilleumier, L.; et al. Aerosol and Cloud Effects on Solar Brightening and the Recent Rapid Warming. *Geophys. Res. Lett.* 2008, *35*, doi:https://doi.org/10.1029/2008GL034228.

Ruckstuhl, C., & Norris, J. R. (2009). How do aerosol histories affect solar "dimming" and "brightening" over Europe?: IPCC-AR4 models versus observations. Journal of Geophysical Research, 114, D00D04.https://doi.org/10.1029/2008JD011066

Russak, V (1990). 'Trends of solar radiation, cloudiness and atmospheric transparency during recent decades in Estonia'. In: Tellus B 42.2, pp. 206–210.

Sanchez-Lorenzo, A., Calbo, J., Brunetti, M., &Deser, C. (2009). Dimming/brightening over the Iberian Peninsula: Trends in sunshine duration and cloud cover and their relations with atmospheric circulation.Journal of Geophysical Research, 114, D00D09.https://doi.org/10.1029/2008JD011394

Sanchez-Lorenzo A, Wild M, Brunetti M, Guijarro JA, HakubaMZ, Calbó J, Mystakidis S, Bartok B (2015) Reassessment and Update of Long-Term Trends in Downward Surface Shortwave Radiation over Europe (1939–2012). Journal of Geophysical Research: Atmospheres 120: 9555–9569. doi:https://doi.org/10.1002/2015JD023321.

Sanchez-Lorenzo, A., Enriquez-Alonso, A., Wild, M., Trentmann, J., Vicente-Serrano, S. M., Sanchez-Romero, A., et al. (2017). Trends in downward surface solar radiation from satellites and ground observations over Europe during 1983–2010. Remote Sensing of Environment, 189, 108–117. https://doi.org/10.1016/j.rse.2016.11.018

Santer BD (2014) Volcanic Contribution to Decadal Changes in Tropospheric Temperature. Nature Geoscience 7(3): 185–189. DOI: Https://Doi.Org/10.1038/Ngeo2098.

Sato, T., F. Kimura, and A. S. Hasegawa (2007), Vegetation and topographic control of cloud activity over arid/semiarid Asia, J. Geophys. Res., 112, D24109, doi:10.1029/2006JD008129.

Scherrer SC, Begert M (2019) Effects of Large-Scale Atmospheric Flow and Sunshine Duration on the Evolution of Minimum and Maximum Temperature in Switzerland.TheorApplClimatol 138: 227–235. Https://Doi.Org/10.1007/S00704-019-02823-x.

Schneider, D. P., C. Deser, J. Fasullo, and K. E. Trenberth, 2013: Climate Data Guide Spurs Discovery and Understanding. Eos Trans. AGU, 94, 121–122, https://doi.org/10.1002/2013eo130001

Semenov VA, Latif M, Dommenget D, Keenlyside NS, Strehz A, Martin T, Park W (2010) The Impact of North Atlantic–Arctic Multidecadal Variability on Northern Hemisphere Surface Air Temperature. J. Climate 23: 5668–5677. Https://Doi.Org/10.1175/2010JCLI3347.1.

Sen, P.K. Estimates of the Regression Coefficient Based on Kendall's Tau. *J. Am. Stat. Assoc.* 1968, *63*, 1379–1389, doi:10.1080/01621459.1968.10480934.

Shettle, E. P., and J. A. Weinman, 1970: The Transfer of Solar Irradiance Through Inhomogeneous Turbid Atmospheres Evaluated by Eddington's Approximation. J. Atmos. Sci., 27, 1048–1055, https://doi.org 10.1175/15200469(1970)027<1048:TTOSIT>2.0.CO;2.

Shi, H.; Xiao, Z.; Zhan, X.; Ma, H.; Tian, X. Evaluation of MODIS and Two Reanalysis Aerosol Optical Depth Products over AERONET Sites. *Atmospheric Res.* 2019, *220*, 75–80, doi:10.1016/j.atmosres.2019.01.009.

Shi, H., Zhang, J., Zhao, B., Xia, X., Hu, B., Chen, H., et al. (2021). Surface brightening in eastern and central China since the implementation of the Clean Air Action in 2013: Causes and implications. Geophysical Research Letters, 48, e2020GL091105. https://doi.org/10.1029/2020GL091105

Sikma M., Ouwersloot H.G., Pedruzo-Bagazgoitia X., van Heerwaarden C.C., J. Vilà-Guerau de Arellano, Interactions between vegetation, atmospheric turbulence and clouds under a wide range of background wind conditions, Agricultural and Forest Meteorology, Volume 255, 2018, Pages 31-43, ISSN 0168-1923, https://doi.org/10.1016/j.agrformet.2017.07.001

Solomon S (2011) The Persistently Variable "Background" Stratospheric Aerosol Layer and Global Climate Change. Science 333(6044): 866–870. DOI: Https://Doi.Org/10.1126/Science.1206027.

Soni, V.K., Pandithurai, G. and Pai, D.S. (2012), Evaluation of long-term changes of solar radiation in India. Int. J. Climatol., 32: 540-551. https://doi.org/10.1002/joc.2294

Soni, V.K., Pandithurai, G. and Pai, D.S., Is there a transition of solar radiation from dimming to brightening over India?, Atmospheric Research, Volume 169, Part A, 2016,Pages 209-224,ISSN 0169-8095,https://doi.org/10.1016/j.atmosres.2015.10.010.

Stamatis M, Hatzianastassiou N, Korras-Carraca MB, Matsoukas C, Wild M, Vardavas I (2022) Interdecadal Changes of the MERRA-2 Incoming Surface Solar Radiation (SSR) and Evaluation against GEBA & BSRN Stations. Applied Sciences 12.doi:10.3390/app121910176.

Stamatis M, Hatzianastassiou N, Korras-Carraca M-B, Matsoukas C, Wild M, Vardavas I (2023) An Assessment of Global Dimming and Brightening during 1984–2018 Using the FORTH Radiative Transfer Model and ISCCP Satellite and MERRA-2 Reanalysis Data. Atmosphere 14: 1258. Https://Doi.Org/10.3390/Atmos14081258.

Stanhill, G., &Moreshet, S. (1992). Global radiation climate changes—The world network. 6. Climatic Change, 21(1), 57–75.

Stanhill, G and S Moreshet (1994). 'Global radiation climate change at seven sites remote from surface sources of pollution'. In: Climatic Change 26.1, pp. 89–103.

Stanhill, G and JD Kalma (1995). 'Solar dimming and urban heating at Hong Kong'. In:International Journal of Climatology 15.8, pp. 933–941.

Stanhill G, Cohen S (2001) Global Dimming: A Review of the Evidence for a Widespread and Significant Reduction in Global Radiation with Discussion of Its Probable Causes and Possible Agricultural Consequences.Agricultural and Forest Meteorology 107: 255–278. Doi:10.1016/S0168-1923(00)00241-0.

Stanhill, Gerald, Ori Achiman et al. (2014). 'The cause of solar dimming and brightening at the Earth's surface during the last half century: Evidence from measurements of sunshine duration'. In: Journal of Geophysical Research: Atmospheres 119.18, pp. 10–902.

Steinbrecht, W., Hegglin, M. I., Harris, N., and Weber, M. (2018). Is global ozone recovering? ComptesRendusGeosci. 350, 368–375. doi:10.1016/j.crte.2018.07.012

Stensrud, D.J. *Parameterization Schemes: Keys to Understanding Numerical Weather Prediction Models*; Cambridge University Press, 2007;

Stern, D. I. (2006). Reversal of the trend in global anthropogenic sulfur emissions. Global Environmental Change-Human and Policy Dimensions, 16(2), 207–220. https://doi.org/10.1016/j.gloenvcha.2006.

Stevens, B., Feingold, G. Untangling aerosol effects on clouds and precipitation in a buffered system. Nature 461, 607–613 (2009). https://doi.org/10.1038/nature08281

Stine, A., Huybers, P. Arctic tree rings as recorders of variations in light availability. Nat Commun 5, 3836 (2014). https://doi.org/10.1038/ncomms4836

Storelvmo T, Leirvik T, Lohmann U et al. (2016) Disentangling Greenhouse Warming and Aerosol Cooling to Reveal Earth's Climate Sensitivity. Nature Geosci 9: 286–289. Https://Doi.Org/10.1038/Ngeo2670.

Storelvmo, Trude et al. (2018). 'Lethargic response to aerosol emissions in current climate models'. In: Geophysical Research Letters 45.18, pp. 9814–9823.

Streets, D. G., Wu, Y., & Chin, M. (2006). Two-decadal aerosol trends as a likely explanation of the global dimming/brightening transition. Geophysical Research Letters, 33, L15806. https://doi.org/10.1029/2006GL026471

Streets, D. G., F. Yan, M. Chin, T. Diehl, N. Mahowald, M. Schultz, M. Wild, Y. Wu, and C. Yu (2009), Discerning human and natural signatures in regional aerosol trends, 1980–2006, J. Geophys. Res., doi:10.1029/2008JD011624

Su, W.; Corbett, J.; Eitzen, Z.; Liang, L. Next-Generation Angular Distribution Models for Top-of-Atmosphere Radiative Flux Calculation from CERES Instruments: Methodology. *Atmospheric Meas. Tech.* 2015, *8*, 611–632, doi:10.5194/amt-8-611-2015.

Su Yang et al 2021 Environ. Res. Lett. 16 034013, DOI 10.1088/1748-9326/abdf89

Sun, B., P. Y. Groisman, R. S. Bradley, and F. T. Keimig, 2000: Temporal Changes in the Observed Relationship between Cloud Cover and Surface Air Temperature. J. Climate, 13, 4341–4357, https://doi.org/10.1175/1520-0442(2000)013<4341:TCITOR>2.0.CO;2.

Schwarz, Matthias et al. (2020). 'Changes in atmospheric shortwave absorption as important driver of dimming and brightening'. In: Nature Geoscience 13.2, pp. 110–115.

Tanaka, K., Ohmura, A., Folini, D., Wild, M., and Ohkawara, N.: Is Global Dimming and Brightening in Japan Limited to Urban Areas?, Atmos. Chem. Phys., 16, 13969–14001, Https://Doi.Org/10.5194/Acp-16-13969-2016, 2016.

Tang, W., J. Qin, K. Yang, S. Liu, N. Lu, and X. Niu, 2016: Retrieving high-resolution surface solar radiation with cloud parameters derived by combining MODIS and MTSAT data. Atmos. Chem. Phys., 16, 2543–2557, https://doi.org/10.5194/ acp-16-2543-2016.

Tang, W., K. Yang, Z. Sun, J. Qin, and X. Niu, 2017: Global performance of a fast parameterization scheme for estimating surface solar radiation from MODIS data. IEEE Trans. Geosci. Remote Sens., 55, 3558–3571, https://doi.org/10.1109/TGRS.2017.2676164

Tang, W., J. Qin, X. Li, and X. Niu, 2019: A 16-year dataset (2000– 2015) of high-resolution (3 h, 10 km) global surface solar radiation. Earth Syst. Sci. Data, 11, 1905–1915, https://doi.org/ 10.5194/essd-11-1905-2019.

Teng, H.-F., C.-S. Lee, and H.-H. Hsu (2014), Influence of ENSO on formation of tropical cloud clusters and their development into tropical cyclones in the western North Pacific, Geophys. Res. Lett., 41, 9120–9126, doi:10.1002/2014GL061823.

Theil, H. A Rank-Invariant Method of Linear and Polynomial Regression Analysis. In Henri Theil's Contributions to Economics and Econometrics: Econometric Theory and Methodology; Raj, B., Koerts, J., Eds.; Springer: Dordrecht, The Netherlands, 1992; pp. 345–381. ISBN 978-94-011-2546-8.

Trenberth KE, Fasullo JT (2009) Global Warming Due to Increasing Absorbed Solar Radiation, Geophys. Res. Lett. 36: L07706. Doi:10.1029/2009GL037527.

Trenberth KE, Fasullo JT (2013) An Apparent Hiatus in Global Warming?. Earth's Future, 1: 19-32. Https://Doi.Org/10.1002/2013EF000165.

Trenberth, K. E., J. T. Fasullo, and J. Kiehl, 2009: Earth's Global Energy Budget. *Bull. Amer. Meteor. Soc.*, **90**, 311–324, https://doi.org/10.1175/2008BAMS2634.1.

Turnock, S. T., Spracklen, D. V., Carslaw, K. S., Mann, G. W., Woodhouse, M. T., Forster, P. M., et al. (2015). Modelled and observed changes in aerosols and surface solar radiation over Europe between 1960 and 2009. Atmospheric Chemistry and Physics, 15(16), 9477–9500. https://doi.org/10.5194/acp-15-9477-2015

Twomey, S. (1977). "The influence of pollution on the shortwave albedo of clouds." Journal of the Atmospheric Sciences, 34(7), 1149–1152.

Tzallas, V.; Hatzianastassiou, N.; Benas, N.; Meirink, J.F.; Matsoukas, C.; Stackhouse, P., Jr.; Vardavas, I. Evaluation of CLARA-A2 and ISCCP-H Cloud Cover Climate Data Records over Europe with ECA&D Ground-Based Measurements. Remote Sens. 2019, 11, 212.

Vardavas, I.M.; Carver, J.H. Solar and Terrestrial Parameterizations for Radiative-Convective Models. *Planet. Space Sci.* 1984, *32*, 1307–1325, doi:10.1016/0032-0633(84)90074-6.

Vardavas, I., & Taylor, F.J. (2011). Radiation and Climate: Atmospheric energy budget from satellite remote sensing: 138 (International Series of Monographs on Physics). ISBN: 9780199697144

Wagner, T., S. Beirle, M. Grzegorski, S. Sanghavi, and U. Platt (2005), El Niño induced anomalies in global data sets of total column precipitable water and cloud cover derived from GOME on ERS-2, J. Geophys. Res., 110, D15104, doi:10.1029/2005JD005972.

Wallace, J. M. and Hobbs, P. V. (2006). Atmospheric Science: An Introductory Survey. Elsevier Academic Press, 2nd edition.

Wang, J., Lee, Y.-N., Daum, P. H., Jayne, J., and Alexander, M. L.: Effects of aerosol organics on cloud condensation nucleus (CCN) concentration and first indirect aerosol effect, Atmos. Chem. Phys., 8, 6325–6339, https://doi.org/10.5194/acp-8-6325-2008, 2008.

Wang, K. C., Dickinson, R. E., Wild, M., & Liang, S. (2012). Atmospheric impacts on climatic variability of surface incident solar radiation. Atmospheric Chemistry and Physics, 12, 9581–9592. https://doi.org/10.5194/acp-12-9581-2012

Wang K, Dickinson RE (2013) Contribution of Solar Radiation to Decadal Temperature Variability over Land. Proc. Natl. Acad. Sci. U. S. A. 110 (37): 14877-14882. 10.1073/Pnas.1311433110.

Wang, Y.; Wild, M. A New Look at Solar Dimming and Brightening in China. *Geophys. Res. Lett.* 2016, *43*, 11,777-11,785, doi:https://doi.org/10.1002/2016GL071009.

Wang, Y.; Trentmann, J.; Yuan, W.; Wild, M. Validation of CM SAF CLARA-A2 and SARAH-E Surface Solar Radiation Datasets over China. *Remote Sens.* 2018, *10*, doi:10.3390/rs10121977.

Wang, Z.; Zhang, M.; Wang, L.; Qin, W. A Comprehensive Research on the Global All-Sky Surface Solar Radiation and Its Driving Factors during 1980–2019. *Atmospheric Res.* 2022, *265*, 105870, doi:10.1016/j.atmosres.2021.105870.

Watanabe M, Shiogama H, Tatebe H et al. (2014) Contribution of Natural Decadal Variability to Global Warming Acceleration and Hiatus. Nature Clim Change 4: 893–897. Https://Doi.Org/10.1038/Nclimate2355.

Wild, M. F. (1997). The heat balance of the Earth in General Circulation Model simulations of present and future climates presented by. PhD thesis, Swiss Federal Institute of Technology Zurich.

Wild M, Gilgen H, Roesch A, Ohmura A, Long CN, Dutton EG, Forgan B, Kallis A, Russak V, Tsvetkov A (2005) From Dimming to Brightening: Decadal Changes in Solar Radiation at Earth's Surface. Science 308: 847–850, doi:10.1126/science.1103215.

Wild M, Ohmura A, Makowski K (2007) Impact of Global Dimming and Brightening on Global Warming. Geophysical Research Letters 34.Doi:Https://Doi.Org/10.1029/2006GL028031.

Wild M (2009) Global Dimming and Brightening: A Review. Journal of Geophysical Research: Atmospheres 114. doi:https://doi.org/10.1029/2008JD011470.

Wild, M.; Trüssel, B.; Ohmura, A.; Long, C.N.; König-Langlo, G.; Dutton, E.G.; Tsvetkov, A. Global Dimming and Brightening: An Update beyond 2000. *J. Geophys. Res. Atmospheres* 2009, *114*, doi:https://doi.org/10.1029/2008JD011382.

Wild, M., Schmucki, E. Assessment of global dimming and brightening in IPCC-AR4/CMIP3 models and ERA40. *Clim Dyn* **37**, 1671–1688 (2011). https://doi.org/10.1007/s00382-010-0939-3

Wild M (2012) Enlightening Global Dimming and Brightening. Bulletin of the American Meteorological Society 93: 27–37. doi:10.1175/BAMS-D-11-00074.1.

Wild, M.; Roesch, A.; Ammann, C. Global Dimming and Brightening - Evidence and Agricultural Implications. *CABI Rev.* 2012, *2012*, 1–7.

Wild, M.; Folini, D.; Schär, C.; Loeb, N.; Dutton, E.G.; König-Langlo, G. The Global Energy Balance from a Surface Perspective. *Clim. Dyn.* 2013, *40*, 3107–3134, doi:10.1007/s00382-012-1569-8.

Wild, M.; Folini, D.; Schär, C.; Loeb, N.; Dutton, E.G.; König-Langlo, G. Basic Measurements of Radiation from the Baseline Surface Radiation Network (BSRN) in the Years 1992 to 2012, Reference List of 6378 Datasets 2013.

Wild, M. (2016). Decadal changes in radiative fluxes at land and ocean surfaces and their relevance for global warming. WIREs Climate Change, 7(1), 91–107. https://doi.org/10.1002/wcc.372
Wild M, Ohmura A, Schar C, Muller G, Folini D, Schwarz M, Hakuba MZ, Sanchez-Lorenzo A (2017) The Global Energy Balance Archive (GEBA) version 2017: A database for worldwide measured surface energy fluxes. Earth Syst Sci Data 9 (2):601-613. doi:10.5194/essd-9-601-2017
Wild M, Wacker S, Yang S, Sanchez-Lorenzo A (2021) Evidence for Clear-Sky Dimming and Brightening in Central Europe. Geophysical Research Letters 48: e2020GL092216. Https://Doi.Org/10.1029/2020GL092216.
Willson, R. C., & Mordvinov, A. V. (2003). Secular total solar irradiance trend during solar cycles 21–23.Geophysical Research Letters, 30(5), 1199.https://doi.org/10.1029/2002GL016038
Wohland J, Brayshaw D, Bloomfield H, Wild M (2020) European Multidecadal Solar Variability Badly Captured in All Centennial Reanalyses except CERA20C. Environmental Research Letters 15: 104021. doi:10.1088/1748-9326/aba7e6.
World Radiation Monitoring Center (WRMC) Baseline Surface Radiation Network (BSRN) 2022.
Wu, Y., Ting, M., Seager, R., Huang, H. P., and Cane, M. A. (2010). Changes in storm tracks and energy transports in a warmer climate simulated by the GFDL CM2 .1 model. Climate dynamics, 37(1-2):53–72.
Xia, X.A.; Wang, P.C.; Chen, H.B.; Liang, F. Analysis of Downwelling Surface Solar Radiation in China from National Centers for Environmental Prediction Reanalysis, Satellite Estimates, and Surface Observations. *J. Geophys. Res. Atmospheres* 2006, *111*, doi:https://doi.org/10.1029/2005JD006405.
Xiang, B., Xie, SP., Kang, S.M. et al. An emerging Asian aerosol dipole pattern reshapes the Asian summer monsoon and exacerbates northern hemisphere warming. npj Clim Atmos Sci 6, 77 (2023). https://doi.org/10.1038/s41612-023-00400-8
Xue, H., Feingold, G., & Stevens, B. (2008). Aerosol effects on clouds, precipitation, and the organization of shallow cumulus convection. Journal of the Atmospheric Sciences, 65(2), 392-406. https://doi.org/10.1175/2007jas2428.1
Yan, Xiao-Hai, et al. (2016) The Global Warming Hiatus: Slowdown or Redistribution?. Earth's Future 4.11: 472-482.
Yang H, Zhou X, Yang Q et al. (2023) Roles of Climate Feedback and Ocean Vertical Mixing in Modulating Global Warming Rate. ClimDyn 60: 1187–1201. Https://Doi.Org/10.1007/S00382-022-06374-2.
Yang, K., Ding, B., Qin, J., Tang, W., Lu, N., and Lin, C. (2012). Can aerosol loading explain the solar dimming over the Tibetan Plateau? Geophysical Research Letters, 39:L20710.
Yang, S., X. L. Wang, and M. Wild, 2019: Causes of Dimming and Brightening in China Inferred from Homogenized Daily Clear-Sky and All-Sky in situ Surface Solar Radiation Records (1958–2016). J. Climate, 32, 5901–5913, https://doi.org/10.1175/JCLI-D-18-0666.1.
Yoon J, von Hoyningen-Huene W, Vountas M, Burrows JP (2011) Analysis of Linear Long-Term Trend of Aerosol Optical Thickness Derived from SeaWiFS Using BAER over Europe and South China. Atmos. Chem. Phys. 11: 12149–12167. Https://Doi.Org/10.5194/Acp-11-12149-2011.
Young, A. H., Knapp, K. R., Inamdar, A., Hankins, W., and Rossow, W. B.: The International Satellite Cloud Climatology Project H-Series Climate Data Record Product, Earth Syst. Sci. Data, 10, 583–593, Https://Doi.Org/10.5194/Essd-10-583-2018, 2018.
Yuan, T., Remer, L. A., & Yu, H. (2011). Microphysical, macrophysical and radiative signatures of volcanic aerosols in trade wind cumulus observed by the a-train. Atmospheric Chemistry and Physics, 11(14), 7119-7132. https://doi.org/10.5194/acp-11-7119-2011
Zerefos, C.S., K. Eleftheratos, C. Meleti, S. Kazadzis, A. Romanou, C. Ichoku, G. Tselioudis, A. Bais, "Solar dimming and brightening over Thessaloniki, Greece, and Beijing, China", Tellus B, DOI: 10.1111/j.1600-0889.2009.00425.x, 2009.

Zhang Hua, Zhao Min, Chen Qi, Wang Qiuyan, Zhao Shuyun, Xixun Zhou, Jie Peng, Water and ice cloud optical thickness changes and radiative effects in East Asia, Journal of Quantitative Spectroscopy and Radiative Transfer, Volume 254, 2020,107213, ISSN 0022-4073,https://doi.org/10.1016/j.jqsrt.2020.107213.

Zhang, Q.; Cui, N.; Feng, Y.; Jia, Y.; Li, Z.; Gong, D. Comparative Analysis of Global Solar Radiation Models in Different Regions of China. *Adv. Meteorol.* 2018, *2018*, 3894831, doi:10.1155/2018/3894831.

Zhang, X.; Liang, S.; Wild, M.; Jiang, B. Analysis of Surface Incident Shortwave Radiation from Four Satellite Products. *Remote Sens. Environ.* 2015, *165*, 186–202, doi:10.1016/j.rse.2015.05.015.

Zhang, X.; Liang, S.; Wang, G.; Yao, Y.; Jiang, B.; Cheng, J. Evaluation of the Reanalysis Surface Incident Shortwave Radiation Products from NCEP, ECMWF, GSFC, and JMA Using Satellite and Surface Observations. *Remote Sens.* 2016, *8*, doi:10.3390/rs8030225.

Zhang, X.; Lu, N.; Jiang, H.; Yao, L. Evaluation of Reanalysis Surface Incident Solar Radiation Data in China. *Sci. Rep.* 2020, *10*, 3494, doi:10.1038/s41598-020-60460-1.

Zhang Y, Wen XY, Jang C (2010) Simulating Chemistry-Aerosol-Clouds-Radiations-Climate Feedbacks over the Continental US Using the Online-Coupled Weather Research Forecasting Model with Chemistry (WRF/Chem). Atmos. Environ. 44: 3568–3582. Doi:10.1016/j.Atmosenv.2010.05.056.

Zhao, Y., Zhang, C., Wang, S., Xu, Y., and Yu, H.: Trends in Water Vapor in North America Based on GNSS observation and ERA5 reanalysis, EGUsphere [preprint], https://doi.org/10.5194/egusphere-2023-2508, 2023.

Zixuan Tang, Jing Tian, Yongqiang Zhang, Xuanze Zhang, Junlong Zhang, Ning Ma, Xiaojie Li, PeilinSong,Anthropogenic aerosols dominated the decreased solar radiation in eastern China over the last five decades,Journal of Cleaner Production,Volume 380, Part 2,2022,135150,ISSN 0959-6526,https://doi.org/10.1016/j.jclepro.2022.135150.

Κόρας-Καράσα, Μ.-Μ., 2022. Προσδιορισμός της επίδρασης των αερολυμάτων στο κλιματικό ισοζύγιο ακτινοβολίας με χρήση δορυφορικών δεδομένων και δεδομένων επανανάλυσης.

Appendices

Appendix A: GEBA & BSRN tables and CLARISC assessment
Appendix B: FORTH-RTM's input data, SSR and GDB
Appendix C: FORTH-RTM's SSR and GDB evaluation
Appendix D: The causes of GDB
Appendix E: The links between GDB and global warming
Appendix F: EarthSense: Interactive exploration of this PhD

Appendix A

Table AA1. The id, coordinates, altitude, available years, and the start and end year of the GEBA stations which were used for the evaluation of FORTH-RTM and other datasets.

id	Lat (°)	Lon (°)	Alt (m)	years	start	end	id	Lat (°)	Lon (°)	Alt (m)	years	start	end
8	28.22	85.57	3920	1	1986	1986	**2041**	41.73	123.45	43	36	1980	2015
17	47.93	7.62	201	1	1980	1980	**2042**	39.93	116.28	55	36	1980	2015
19	-69.00	39.58	3	4	1980	1987	**2043**	36.05	103.88	1517	24	1980	2003
29	-54.28	-36.50	3	1	1980	1980	**2044**	31.40	121.48	7	25	1991	2015
46	12.73	34.13	445	7	1980	1990	**2045**	30.67	104.02	506	24	1980	2003
50	9.03	38.75	2408	3	1980	1988	**2046**	30.62	114.13	23	36	1980	2015
54	15.83	36.15	430	5	1981	1990	**2047**	25.02	102.68	1891	36	1980	2015
57	23.97	32.78	192	28	1980	2016	**2048**	23.13	113.32	7	36	1980	2015
58	27.20	31.17	52	28	1980	2010	**2049**	33.62	73.10	507	5	1991	1995
59	11.33	27.82	453	3	1981	1985	**2054**	-27.17	-109.43	47	10	1988	2000
61	30.15	31.25	17	22	1980	2010	**2055**	24.23	55.78	299	3	1988	1990
63	14.70	-16.47	20	3	1984	1987	**2056**	23.58	58.28	15	3	1988	1990
68	-19.83	34.85	17	10	1980	1996	**2057**	22.53	59.48	14	3	1988	1990
69	6.55	5.62	156	12	1980	1991	**2058**	22.35	56.48	170	3	1988	1990
76	-0.22	20.85	375	3	1980	1982	**2059**	20.67	58.90	19	3	1988	1990
81	-2.52	28.85	1635	1	1980	1980	**2060**	18.13	55.18	269	3	1988	1990
83	-20.15	28.62	1344	25	1980	2005	**2061**	17.03	54.08	20	2	1988	1989
85	2.78	24.78	450	9	1980	1988	**2062**	21.03	105.85	5	2	1990	1992
87	33.57	-7.67	55	29	1980	2016	**2067**	-45.58	-72.12	310	25	1990	2018
89	-19.12	33.47	731	13	1980	1993	**2068**	-33.38	-70.78	474	14	1988	2005
90	-24.53	33.00	33	15	1980	1998	**2069**	4.70	-74.13	2547	7	1989	1995
91	14.73	-17.50	27	7	1980	1990	**2070**	4.55	-70.92	165	8	1989	1996
97	19.17	30.48	225	7	1980	1991	**2072**	-22.23	114.08	6	19	1987	2015
101	13.62	25.33	733	5	1980	1987	**2073**	5.93	116.05	3	18	1989	2006

102	25.45	30.53	78	31	1980	2017	**2074**	1.48	110.33	27	19	1987	2009
103	14.22	35.85	510	8	1980	1987	**2075**	-33.82	121.88	25	8	1988	1995
104	0.53	35.28	2120	14	1980	1998	**2077**	42.55	9.48	8	27	1991	2019
107	32.63	-16.90	58	15	2000	2018	**2078**	47.92	7.40	211	13	1991	2019
109	-0.47	39.63	138	13	1980	1992	**2079**	46.70	-2.33	32	2	1989	1990
111	11.47	26.45	481	3	1982	1986	**2080**	49.03	2.53	108	16	1990	2019
112	-20.88	55.52	21	14	1981	2018	**2081**	43.63	1.37	152	9	2011	2019
114	-1.66	29.23	1555	1	1982	1982	**2082**	48.02	21.73	105	2	1988	1989
117	-15.47	36.98	734	1	1981	1981	**2083**	46.73	12.22	1222	14	1990	2009
118	-17.83	31.02	1472	19	1980	2003	**2084**	45.65	12.18	18	4	1992	1999
120	17.57	33.93	350	9	1980	1990	**2085**	45.38	10.87	67	11	1992	2011
121	-23.87	35.38	14	8	1981	1998	**2086**	44.92	9.73	134	16	1990	2013
122	-1.97	18.27	300	8	1980	1988	**2087**	44.22	12.30	6	13	1990	2014
125	4.87	31.60	460	3	1980	1985	**2088**	43.08	12.50	208	10	1990	2001
126	11.00	29.72	501	9	1980	1991	**2089**	42.73	10.40	396	5	1992	1998
127	30.08	31.28	36	26	1980	2016	**2090**	42.43	12.08	300	15	1993	2013
130	-5.88	22.42	654	6	1982	1989	**2091**	42.00	15.00	16	14	1990	2011
133	12.57	-12.22	178	1	1990	1990	**2092**	41.05	14.07	9	15	1992	2014
137	-2.95	25.92	515	3	1980	1982	**2093**	40.92	12.95	184	10	1991	2002
138	-4.37	15.25	445	8	1981	1989	**2094**	40.52	8.17	204	8	1990	2012
140	-0.10	34.75	1157	14	1980	1993	**2095**	39.93	9.72	138	14	1990	2008
141	1.02	35.00	1890	13	1980	1992	**2096**	39.82	18.35	104	6	1990	2014
144	-13.28	35.25	1365	3	1980	1984	**2097**	36.68	15.13	46	13	1990	2014
145	15.38	-15.12	20	4	1988	1991	**2098**	39.33	16.40	1710	9	2002	2014
146	3.12	35.62	506	26	1980	2007	**2099**	60.43	15.50	153	31	1989	2019
147	15.62	-16.22	38	4	1980	1990	**2100**	57.70	12.00	5	27	1989	2019
148	-8.82	13.22	44	1	1986	1986	**2101**	59.37	13.47	46	36	1983	2019
150	-15.03	40.67	15	3	1981	1985	**2102**	55.72	13.22	73	29	1989	2019

152	9.55	31.65	390	3	1980	1982	**2103**	58.58	16.25	5	31	1989	2019
154	-3.23	40.10	20	9	1980	1988	**2104**	63.18	14.50	876	37	1983	2019
155	3.95	41.87	230	12	1980	1992	**2105**	63.82	20.25	10	31	1989	2019
156	-24.73	33.53	13	8	1980	1996	**2106**	56.93	14.73	182	37	1983	2019
157	-25.97	32.60	70	30	1980	2009	**2107**	57.67	18.35	51	37	1983	2019
158	-25.92	32.57	37	7	1980	1988	**2108**	47.25	9.35	2500	30	1987	2019
160	15.65	-13.25	15	6	1984	1991	**2109**	46.82	6.95	490	12	1994	2007
161	0.05	18.27	345	9	1980	1989	**2110**	46.82	6.95	490	30	1981	2010
164	31.33	27.22	38	21	1982	2006	**2111**	46.80	9.82	1592	31	1989	2019
167	-16.83	36.98	134	4	1980	1984	**2112**	46.43	6.10	1670	39	1981	2019
168	-4.03	39.62	57	5	1980	1992	**2113**	46.25	6.13	416	15	1989	2007
174	-1.30	36.75	1798	13	1980	1992	**2114**	47.55	7.58	316	31	1989	2019
175	-1.32	36.92	1624	18	1981	2007	**2118**	46.42	9.82	3315	39	1981	2019
176	-0.27	36.07	1871	9	1981	1990	**2122**	11.15	-60.83	3	2	1991	1993
177	-15.10	39.28	441	13	1982	2002	**2123**	10.62	-61.35	12	23	1987	2018
180	-1.13	35.83	1890	13	1980	1992	**2132**	4.93	114.93	22	7	1988	1994
189	-12.97	40.50	50	17	1980	1999	**2133**	48.45	-4.42	99	31	1987	2019
191	16.65	-14.97	6	5	1987	1991	**2134**	47.07	2.37	161	32	1987	2019
193	4.77	7.02	15	10	1980	1989	**2200**	40.03	-105.27	1600	3	1986	1988
194	19.58	37.22	3	5	1980	1984	**2213**	78.92	11.93	12	5	1982	1987
195	33.07	-16.35	78	16	1980	2018	**2214**	-40.68	144.69	94	21	1991	2018
208	15.67	32.53	376	12	1980	1991	**2220**	54.68	13.43	42	6	1991	1996
209	31.63	25.40	27	10	1985	2005	**2221**	50.80	12.87	418	7	1991	1998
210	36.87	10.35	127	19	1980	1999	**2222**	53.32	13.93	55	1	1991	1991
216	30.65	30.70	16	15	1980	1998	**2223**	51.52	11.95	96	8	1991	1998
219	22.78	5.52	1377	24	1995	2018	**2224**	51.65	11.13	404	8	1991	1998
220	13.77	-13.68	49	2	1982	1984	**2225**	52.22	14.12	98	24	1991	2019
221	-18.90	47.53	1300	4	1989	1992	**2228**	53.55	13.20	83	7	1992	1998

222	-16.18	33.58	154	10	1981	1997	**2229**	52.90	11.73	21	7	1992	1998
228	-26.05	32.38	12	13	1980	1993	**2230**	50.98	11.32	257	8	1991	1998
230	-3.40	38.57	560	26	1980	2007	**2231**	50.73	13.75	877	8	1991	1998
231	14.40	33.48	408	10	1980	1990	**2232**	51.45	7.27	187	7	1992	1998
236	12.90	23.48	900	1	1980	1980	**2301**	-75.50	-26.90	20	2	1989	1990
238	12.55	-16.27	26	4	1980	1990	**2344**	22.78	5.52	1377	21	2000	2020
256	-15.42	28.32	1283	8	1981	1997	**2345**	8.53	4.57	350	4	1993	1999
260	31.12	33.75	17	18	1986	2007	**2346**	24.65	48.77	650	15	2000	2014
308	6.10	0.12	18	6	1980	1991	**2347**	-27.47	-48.48	11	10	1995	2020
311	9.02	-2.42	299	5	1989	1993	**2350**	50.20	-104.28	587	16	1995	2011
316	6.72	-1.60	283	7	1980	1988	**2351**	71.32	-156.40	8	9	1992	2016
324	4.88	-1.77	4	3	1980	1982	**2352**	36.60	-97.33	318	24	1994	2018
325	9.42	-0.88	180	1	1980	1980	**2353**	40.05	-105.98	1577	23	1992	2014
327	9.45	-0.02	195	3	1981	1983	**2354**	40.22	-105.40	1689	23	1996	2019
362	-70.65	-8.25	40	9	1983	1992	**2374**	48.52	-105.20	634	19	1995	2013
386	82.50	-62.33	62	12	1981	2000	**2375**	36.62	-116.02	1007	10	1999	2008
387	51.32	-108.40	637	6	1980	1985	**2376**	32.27	-64.33	8	20	1992	2012
388	64.30	-96.00	49	10	1982	2000	**2377**	34.25	-89.87	98	25	1995	2019
389	55.18	-119.37	762	10	1983	1994	**2378**	40.72	-102.07	376	4	1999	2002
390	53.83	-89.87	219	7	1980	1991	**2379**	36.60	-82.52	318	20	1998	2018
391	69.10	-105.12	27	9	1980	1994	**2380**	-45.05	169.68	350	18	2000	2018
392	46.28	-63.13	48	13	1980	1994	**2381**	-2.10	147.72	6	7	1997	2003
393	58.75	-94.07	35	4	1982	1986	**2383**	-70.65	-8.25	42	11	1993	2003
394	64.20	-83.37	59	11	1983	1995	**2385**	44.08	5.05	99	21	1997	2018
396	53.55	-114.10	767	12	1980	2000	**2386**	52.22	14.12	125	23	1995	2018
397	43.65	-80.42	376	14	1980	1996	**2387**	78.93	11.95	11	28	1993	2020
398	79.98	-85.93	10	1	1990	1990	**2392**	8.72	167.73	10	18	1993	2015
399	58.83	-122.60	378	15	1980	1995	**2393**	-0.52	166.92	7	14	1999	2012

401	60.03	-111.93	203	7	1981	1987	**2394**	40.10	-88.62	213	25	1995	2019
402	45.92	-66.62	40	16	1980	1998	**2401**	24.47	54.42	16	22	1982	2006
403	63.75	-68.55	21	6	1980	1986	**2411**	47.50	9.75	424	27	1993	2019
404	53.32	-60.42	46	15	1980	1995	**2412**	47.25	11.35	579	35	1980	2019
406	44.65	-63.58	70	16	1980	1996	**2413**	47.78	13.05	420	38	1980	2019
407	68.78	-81.25	7	13	1980	1994	**2414**	48.20	16.57	153	15	1988	2005
408	58.45	-78.12	5	14	1981	1994	**2415**	51.20	2.87	5	23	1980	2007
409	68.32	-133.53	103	10	1980	1996	**2421**	49.58	15.08	534	24	1996	2019
412	45.07	-64.48	49	15	1980	1994	**2431**	62.40	25.68	141	25	1991	2016
415	58.10	-68.42	36	15	1980	1994	**2441**	39.00	-1.87	674	16	1999	2019
418	45.50	-73.62	133	5	1980	1984	**2442**	36.53	-6.28	16	17	1994	2019
419	51.27	-80.65	10	9	1981	1992	**2444**	38.88	-7.02	185	17	2003	2019
420	76.23	-119.33	15	3	1981	1986	**2445**	43.30	-2.93	40	20	1996	2019
421	49.22	-123.95	8	7	1980	1986	**2446**	38.98	-3.92	628	24	1996	2019
422	53.20	-70.90	536	5	1980	1984	**2447**	37.13	-3.63	687	17	2001	2019
423	48.85	-72.53	137	15	1980	1994	**2448**	37.28	-6.92	19	16	1997	2019
424	65.28	-126.80	67	11	1980	1992	**2449**	38.87	1.37	10	19	1997	2019
425	45.38	-75.72	79	15	1980	1997	**2450**	43.37	-8.42	58	23	1996	2019
426	50.68	-127.37	23	13	1980	1994	**2451**	42.58	-5.65	914	19	1998	2019
427	53.88	-122.68	676	12	1980	1994	**2452**	41.62	0.58	201	19	1997	2019
429	43.93	-60.02	4	7	1980	1987	**2453**	42.45	-2.33	353	23	1996	2019
430	72.00	-125.27	88	3	1981	1983	**2454**	36.72	-4.48	61	19	1999	2019
431	51.93	-131.02	92	11	1980	1990	**2455**	40.82	0.50	44	14	1998	2019
432	47.52	-52.78	114	14	1980	1996	**2456**	40.95	-5.92	803	18	2002	2019
433	53.25	-131.82	8	12	1980	1993	**2457**	43.30	-2.05	258	22	1996	2019
435	50.22	-66.25	53	14	1980	1994	**2458**	41.60	-2.50	1090	16	2000	2019
436	50.27	-111.18	775	7	1981	1989	**2459**	39.88	-4.05	515	10	1996	2010
437	49.57	-119.65	454	10	1980	1994	**2460**	39.48	-0.38	23	6	1997	2003

438	50.27	-107.73	825	17	1980	2000	**2461**	41.65	-4.77	734	24	1996	2019
439	53.97	-101.10	272	18	1980	1997	**2462**	42.60	-8.75	15	14	2003	2017
440	43.67	-79.40	116	18	1980	2000	**2463**	42.87	-1.67	550	18	2001	2019
441	49.25	-123.25	87	7	1980	1986	**2464**	41.63	-1.00	263	19	2001	2019
442	60.72	-135.07	703	13	1980	1994	**2465**	47.25	5.98	307	14	1993	2019
443	49.90	-97.23	240	12	1980	1994	**2471**	43.45	5.23	6	30	1980	2010
444	35.05	-106.62	1631	11	1980	2006	**2472**	44.58	4.73	73	25	1995	2019
451	46.77	-100.75	506	13	1980	2006	**2473**	48.72	2.38	89	19	2001	2019
456	25.90	-97.43	15	1	1980	1980	**2474**	43.03	6.47	110	11	1988	2019
458	46.87	-68.02	195	1	1980	1980	**2488**	56.45	-3.07	30	19	1988	2010
461	38.82	-92.22	277	1	1980	1980	**2489**	47.68	16.60	233	11	1996	2006
463	31.80	-106.40	1205	1	1993	1993	**2490**	50.92	5.78	114	34	1980	2014
465	64.82	-147.87	138	3	1980	1982	**2492**	56.80	60.63	237	35	1980	2018
470	47.48	-111.37	1118	1	1980	1980	**2493**	53.25	50.45	44	26	1980	2018
475	28.03	-81.95	82	1	2000	2000	**2501**	41.57	14.65	793	7	1998	2014
476	42.82	-108.73	1703	1	1992	1992	**2511**	45.03	7.73	709	7	1980	1990
480	43.13	-89.33	263	10	1993	2006	**2513**	45.98	13.03	51	13	1992	2009
481	42.37	-122.87	405	1	1980	1980	**2514**	45.83	16.00	182	11	1994	2007
483	31.95	-102.18	875	2	1980	2000	**2515**	45.78	21.28	90	37	1980	2017
485	36.12	-86.68	180	3	1991	1993	**2521**	-37.67	144.83	132	19	2000	2018
487	36.02	-84.23	287	12	1995	2006	**2531**	-45.03	169.68	350	5	2000	2004
489	41.37	-96.02	399	1	1980	1980	**2533**	26.20	32.75	96	5	2003	2010
495	40.78	-111.97	1288	7	1980	2003	**2534**	30.40	30.37	49	5	2003	2010
499	47.45	-122.30	137	2	1990	1993	**2535**	4.87	-2.23	38	4	1995	1999
501	38.98	-77.47	87	10	1980	2006	**2540**	28.95	-13.60	20	17	1997	2018
502	30.38	-84.37	25	5	1995	2000	**2541**	35.28	-2.95	55	6	1997	2003
503	27.97	-82.53	3	1	2000	2000	**2556**	46.15	11.03	2125	6	1992	2014
526	36.12	140.10	27	10	1982	1991	**2571**	44.63	-63.50	51	2	1987	1996

531	31.67	35.45	-395	6	1983	1990	**2572**	63.75	-68.55	20	14	1980	1997
545	44.57	-123.23	65	1	1981	1981	**2581**	50.35	80.25	206	12	1980	1991
559	15.35	-61.25	2	1	1986	1986	**2582**	10.57	-71.73	66	7	1987	1997
561	-71.53	24.13	965	2	1988	1990	**2591**	44.23	-79.78	0	2	1996	1998
850	47.38	8.57	556	27	1981	2007	**2592**	60.02	-111.97	205	1	1993	1993
853	71.25	-177.50	0	12	1980	1994	**2593**	53.75	-73.67	306	9	1988	1999
863	22.32	114.17	66	32	1984	2018	**2594**	45.47	-73.75	31	10	1980	1996
864	28.58	77.20	212	7	1981	2012	**2595**	45.32	-75.67	116	1	1997	1997
865	26.30	73.02	217	8	2006	2017	**2596**	51.48	-107.05	0	6	1989	1994
866	25.57	91.88	1600	15	1989	2018	**2597**	55.80	-97.87	206	1	1995	1995
867	23.07	72.63	55	29	1980	2018	**2601**	50.13	1.83	74	8	2012	2019
868	22.65	88.45	4	30	1980	2018	**2611**	-35.97	-72.33	142	4	1997	2000
869	22.53	88.33	4	7	1980	2002	**2612**	-42.92	-72.72	7	3	1997	2000
870	21.75	72.20	5	12	1980	1991	**2613**	-34.97	-71.23	228	11	1997	2007
871	21.10	79.05	308	22	1980	2014	**2614**	-34.10	-71.75	296	6	1998	2003
872	19.12	72.85	15	19	1980	2016	**2615**	-37.40	-72.43	109	2	1997	1999
873	18.53	73.85	555	23	1981	2018	**2616**	-41.42	-73.08	85	14	1997	2018
874	17.72	83.23	41	26	1981	2018	**2617**	51.13	13.75	226	20	1999	2019
875	15.48	73.82	55	25	1981	2018	**2618**	8.93	-67.42	100	2	1996	1997
876	13.00	80.18	10	20	1981	2017	**2619**	9.42	-66.92	160	1	1997	1997
877	10.23	77.47	2339	3	2007	2014	**2620**	8.63	-71.65	103	2	1996	1997
878	8.48	76.95	60	28	1980	2016	**2621**	9.02	-69.73	163	2	1996	1997
879	43.33	145.58	26	30	1980	2009	**2622**	7.23	-70.80	130	2	1996	1997
880	43.05	141.33	17	39	1980	2018	**2623**	10.57	-71.73	66	3	1994	1997
881	39.72	140.10	9	39	1980	2018	**2624**	9.82	-70.93	27	2	1996	1997
882	39.65	141.97	43	28	1980	2007	**2625**	10.30	-68.23	1000	2	1996	1997
883	38.27	140.90	38	28	1980	2007	**2626**	10.92	-63.97	24	2	1996	1997
884	37.38	136.90	5	30	1980	2009	**2627**	9.92	-67.33	429	2	1996	1997

885	36.25	137.97	610	27	1980	2006	**2628**	10.17	-67.93	430	2	1996	1997
886	36.05	140.13	25	37	1980	2018	**2629**	9.35	-70.57	628	2	1996	1997
887	35.43	133.35	7	28	1980	2007	**2630**	9.22	-66.02	125	2	1996	1997
888	34.82	135.53	6	28	1980	2007	**2631**	27.83	-15.95	25	13	2004	2018
889	33.58	130.38	3	39	1980	2018	**2643**	45.42	141.68	3	28	1980	2007
890	33.45	135.77	73	29	1980	2008	**2646**	43.75	142.37	120	28	1980	2007
891	32.72	133.02	30	29	1980	2008	**2647**	44.93	142.58	7	23	1980	2002
892	31.57	130.55	4	39	1980	2018	**2648**	43.95	141.63	24	23	1980	2002
893	27.08	142.18	4	39	1980	2018	**2649**	42.92	143.22	38	28	1980	2007
894	26.23	127.68	35	39	1980	2018	**2650**	42.80	140.22	33	23	1980	2002
895	24.33	124.17	6	39	1980	2018	**2651**	42.32	140.98	40	23	1980	2002
896	24.30	153.97	8	39	1980	2018	**2652**	42.02	142.78	33	23	1980	2002
897	41.68	129.68	8	13	1980	1992	**2653**	41.82	140.75	35	28	1980	2007
898	39.03	125.78	35	13	1980	1992	**2654**	40.82	140.77	3	28	1980	2007
899	38.03	125.70	79	13	1980	1992	**2655**	40.53	141.52	27	23	1980	2002
901	37.75	128.90	26	32	1986	2018	**2656**	39.70	141.17	155	28	1980	2007
902	37.57	126.97	86	33	1986	2018	**2657**	38.92	139.85	3	23	1980	2002
903	35.10	129.03	69	32	1986	2017	**2658**	38.25	140.35	152	28	1980	2007
904	34.78	126.38	53	33	1986	2018	**2660**	37.77	140.47	67	28	1980	2007
905	6.90	79.87	7	2	2000	2002	**2661**	36.95	140.90	3	28	1980	2007
906	49.85	92.07	934	36	1980	2018	**2662**	37.92	139.05	2	23	1980	2002
907	49.63	100.17	1288	28	1980	2018	**2663**	36.72	137.20	9	23	1980	2002
908	47.85	106.75	1264	38	1980	2018	**2664**	37.10	138.25	13	27	1980	2006
909	47.75	96.85	1751	33	1980	2018	**2665**	36.55	139.87	119	23	1980	2002
910	43.58	104.42	1469	31	1980	2018	**2666**	36.05	136.22	9	23	1980	2002
912	22.20	113.55	57	24	1980	2018	**2667**	36.40	139.07	112	23	1980	2002
913	34.00	71.52	360	1	1980	1980	**2668**	35.02	136.97	51	28	1980	2007
914	31.55	74.33	214	7	1981	2002	**2669**	35.67	138.55	273	23	1980	2002

915	30.20	71.43	123	5	1984	1990	**2670**	35.73	140.85	20	23	1980	2002
916	30.18	66.95	1799	12	1980	2003	**2671**	34.60	138.22	45	23	1980	2002
917	24.90	67.13	22	8	1980	1988	**2673**	35.68	139.77	6	28	1980	2007
925	73.50	80.40	47	7	1982	1988	**2675**	35.45	135.32	2	28	1980	2007
926	70.97	-178.53	2	15	1980	1994	**2676**	34.90	132.07	19	23	1980	2002
927	70.63	162.40	6	14	1980	1993	**2677**	35.28	136.25	87	28	1980	2007
928	68.50	112.43	127	12	1980	1992	**2678**	33.95	130.93	3	28	1980	2007
929	67.55	133.38	137	14	1980	2003	**2679**	34.40	132.47	4	28	1980	2007
930	65.78	87.95	32	15	1980	1995	**2680**	34.70	135.83	104	28	1980	2007
931	63.27	143.15	726	27	1980	2017	**2681**	34.20	129.30	4	28	1980	2007
932	62.08	129.75	103	30	1980	2018	**2682**	33.27	130.30	6	28	1980	2007
933	60.43	77.87	47	14	1980	1993	**2683**	33.23	131.62	5	28	1980	2007
934	60.33	102.27	259	18	1980	2004	**2684**	32.73	129.87	27	28	1980	2007
935	59.37	143.20	8	9	1980	1991	**2685**	32.82	130.70	38	28	1980	2007
936	56.80	60.63	290	11	1980	1990	**2686**	31.93	131.42	9	28	1980	2007
937	54.93	73.40	119	32	1980	2018	**2687**	33.85	132.78	32	23	1980	2002
938	53.25	50.45	137	10	1980	1990	**2688**	34.32	134.05	9	28	1980	2007
939	52.97	158.75	32	32	1980	2018	**2689**	33.57	133.55	1	28	1980	2007
940	52.27	104.35	467	29	1980	2018	**2690**	28.38	129.50	3	28	1980	2007
941	52.02	113.33	671	23	1981	2011	**2691**	24.80	125.28	40	26	1982	2007
942	50.35	80.25	195	11	1980	1990	**2692**	25.83	131.23	15	28	1980	2007
943	48.52	135.17	87	12	1980	1995	**2693**	44.02	144.28	38	28	1980	2007
944	46.92	142.73	22	31	1980	2018	**2703**	34.98	138.40	14	23	1980	2002
946	46.78	61.67	62	4	1984	1988	**2705**	34.75	139.37	74	23	1980	2002
947	43.12	131.90	138	26	1980	2014	**2706**	33.12	139.78	151	23	1980	2002
948	41.27	69.27	428	13	1980	1992	**2732**	53.47	122.37	0	4	1997	2000
951	13.73	100.57	16	26	1980	2014	**2733**	39.47	75.98	1289	21	1980	2000
958	-34.58	-58.48	25	8	1985	2018	**2734**	36.42	94.90	2808	21	1980	2000

962	-18.33	-70.33	58	13	1980	2018	**2735**	41.95	101.07	940	9	1992	2000
969	-22.47	-68.92	2270	13	1997	2016	**2736**	29.67	91.13	3649	21	1980	2000
970	-23.43	-70.43	120	20	1980	2018	**2737**	34.72	113.65	110	21	1980	2000
974	-27.08	-70.85	14	5	2007	2011	**2738**	18.23	109.52	6	9	1992	2000
975	-27.28	-70.40	290	8	1988	1997	**2739**	23.40	116.68	1	21	1980	2000
977	-29.90	-71.25	32	1	1980	1980	**2740**	22.82	108.35	73	21	1980	2000
985	-33.45	-70.70	520	11	1980	2018	**2741**	20.03	110.35	14	20	1981	2000
996	-36.77	-73.07	13	7	1980	2008	**2742**	26.08	119.28	0	21	1980	2000
1001	-38.82	-72.97	98	5	1980	2000	**2743**	30.23	120.17	42	21	1980	2000
1008	-53.13	-70.97	37	23	1988	2012	**2744**	32.00	118.80	9	21	1980	2000
1016	4.83	-52.37	5	20	1980	2018	**2745**	31.87	117.23	28	21	1980	2000
1017	-5.18	-80.60	49	3	1985	1987	**2746**	29.58	106.47	260	13	1988	2000
1018	-7.17	-78.50	2536	1	1983	1983	**2747**	28.22	112.92	68	14	1987	2000
1019	-12.03	-75.32	3313	1	1986	1986	**2748**	26.58	106.72	1074	21	1980	2000
1020	-12.12	-75.33	3380	1	1983	1983	**2749**	25.32	110.30	194	21	1980	2000
1021	-12.15	-75.58	4600	1	1983	1983	**2750**	22.00	100.80	0	21	1980	2000
1022	-13.55	-71.98	3248	1	1983	1983	**2751**	34.30	108.93	0	21	1980	2000
1024	-16.47	-72.48	2451	4	1983	1986	**2752**	36.68	116.98	52	21	1980	2000
1026	11.42	-69.68	16	16	1980	1997	**2753**	43.65	111.97	965	21	1980	2000
1027	10.65	-71.60	40	11	1980	1992	**2754**	38.48	106.22	1111	21	1980	2000
1028	10.60	-66.98	43	17	1980	1997	**2755**	37.78	112.55	778	21	1980	2000
1029	10.58	-62.32	13	10	1980	1995	**2756**	43.90	125.22	237	20	1980	2000
1030	10.50	-66.88	835	17	1980	1997	**2757**	39.08	117.07	3	21	1980	2000
1031	10.25	-67.65	436	17	1980	1997	**2758**	37.13	79.93	1375	21	1980	2000
1032	10.12	-64.68	7	13	1980	1997	**2759**	42.82	93.52	737	21	1980	2000
1033	10.07	-69.32	613	16	1980	1997	**2760**	36.62	101.77	2261	21	1980	2000
1034	9.75	-63.18	65	14	1980	1997	**2761**	50.25	127.45	166	21	1980	2000
1035	8.60	-71.17	1479	16	1980	1996	**2769**	47.73	88.08	735	21	1980	2000

1036	8.15	-63.55	43	15	1980	1997	**2770**	43.95	81.33	663	21	1980	2000
1037	7.90	-67.42	47	14	1980	1997	**2771**	40.15	94.68	1139	21	1980	2000
1038	7.84	-72.44	377	14	1980	1995	**2772**	32.50	80.08	0	20	1980	2000
1039	7.30	-61.45	180	16	1980	1997	**2773**	31.15	97.17	3306	21	1980	2000
1040	5.60	-67.50	73	17	1980	1997	**2774**	28.60	115.92	47	20	1980	2000
1041	4.60	-61.12	907	10	1980	1991	**2775**	37.50	121.25	0	9	1992	2000
1044	43.80	-79.55	149	8	1980	1987	**2776**	49.22	119.75	610	19	1982	2000
1046	23.17	-82.35	50	10	1986	1995	**2777**	46.73	83.00	535	8	1993	2000
1047	23.15	-82.35	50	5	1991	1995	**2778**	46.77	130.28	81	19	1982	2000
1049	16.27	-61.52	7	32	1987	2018	**2779**	30.70	111.30	133	21	1980	2000
1051	14.60	-61.00	3	31	1987	2018	**2780**	28.83	105.43	335	17	1984	2000
1053	20.58	-99.20	1745	10	1980	1994	**2781**	25.02	98.50	1655	21	1980	2000
1054	19.33	-99.18	2268	34	1980	2017	**2782**	31.47	104.68	471	21	1980	2000
1055	46.77	-56.17	3	39	1980	2018	**2783**	29.52	103.33	3047	21	1980	2000
1064	36.62	-116.02	1007	18	1996	2018	**2784**	31.48	92.07	4507	20	1980	2000
1068	-12.40	130.87	31	19	1980	2000	**2785**	33.02	97.02	3681	21	1980	2000
1070	-16.30	149.98	6	13	1980	1992	**2786**	35.65	111.37	434	21	1980	2000
1071	-16.88	145.75	3	6	1998	2003	**2787**	40.10	113.33	1067	21	1980	2000
1072	-17.95	122.23	17	22	1988	2016	**2788**	36.00	106.27	1753	16	1985	2000
1073	-18.22	127.65	410	9	1980	1990	**2789**	39.03	88.17	888	21	1980	2000
1074	-19.25	146.75	5	3	2013	2018	**2790**	38.63	103.08	1367	21	1980	2000
1075	-19.63	134.17	375	10	1996	2005	**2791**	25.85	114.95	123	20	1980	2000
1077	-20.37	118.62	9	11	1980	1990	**2792**	42.93	89.20	35	21	1980	2000
1080	-23.38	150.48	10	29	1980	2017	**2793**	47.80	124.48	162	8	1993	2000
1081	-23.43	144.27	191	7	1980	2013	**2794**	46.60	121.22	500	9	1992	2000
1082	-23.80	133.90	545	34	1980	2015	**2795**	42.08	86.57	0	8	1993	2000
1084	-24.88	113.67	4	7	1987	1994	**2796**	41.17	80.23	1103	8	1993	2000
1086	-26.60	118.52	522	7	1987	1993	**2797**	39.77	98.48	1477	8	1993	2000

1087	-27.43	153.08	5	11	1984	1995	**2798**	37.33	100.13	3302	8	1993	2000
1088	-28.78	114.70	37	21	1980	2018	**2799**	41.57	108.52	1288	9	1992	2000
1092	-30.77	121.45	360	17	1980	2005	**2800**	39.83	109.98	1460	9	1992	2000
1093	-30.83	128.10	156	5	1981	1987	**2801**	36.60	109.50	959	11	1990	2000
1095	-31.13	136.82	165	3	1980	2012	**2802**	36.12	114.37	0	11	1980	1990
1096	-31.48	145.82	221	1	2013	2013	**2803**	43.95	116.07	0	11	1990	2000
1099	-31.93	115.87	19	5	1989	1993	**2804**	43.60	122.27	0	21	1980	2000
1102	-32.78	151.82	9	4	1980	1984	**2805**	42.83	129.47	177	21	1980	2000
1104	-33.87	151.20	42	3	1982	1990	**2806**	41.55	120.45	169	21	1980	2000
1105	-33.95	151.18	6	10	1984	1993	**2807**	38.90	121.63	92	20	1981	2000
1106	-34.23	142.08	51	24	1980	2012	**2808**	35.58	118.83	107	11	1990	2000
1107	-34.28	146.05	131	1	1980	1980	**2809**	34.47	100.25	3719	8	1993	2000
1110	-34.93	138.52	6	27	1983	2018	**2810**	31.62	100.00	3394	7	1994	2000
1111	-34.95	117.80	71	6	1980	1985	**2811**	32.80	102.38	5	7	1994	2000
1112	-35.15	147.45	221	21	1980	2008	**2812**	26.87	100.22	2393	21	1980	2000
1113	-35.30	149.18	575	8	1985	1993	**2813**	23.38	103.38	1300	21	1980	2000
1118	-37.73	140.78	65	22	1980	2005	**2814**	33.03	112.58	129	11	1990	2000
1119	-37.82	144.97	38	6	1980	1985	**2816**	28.32	109.73	207	9	1992	2000
1120	-37.85	144.73	16	14	1980	1993	**2817**	26.42	112.40	117	8	1993	2000
1121	-38.03	145.10	6	2	1980	1981	**2818**	33.60	119.03	18	8	1993	2000
1127	-42.83	147.50	4	10	1980	1991	**2823**	32.17	115.67	57	21	1980	2000
1129	-54.48	158.97	6	8	1980	1992	**2824**	32.07	121.60	6	9	1992	2000
1131	-17.75	177.45	16	26	1980	2007	**2825**	29.72	118.28	143	9	1992	2000
1132	-18.15	178.45	6	18	1985	2008	**2826**	28.45	121.42	1	9	1992	2000
1133	13.55	144.83	112	1	1993	1993	**2827**	27.05	118.32	0	9	1992	2000
1139	6.17	102.28	5	22	1980	2008	**2828**	21.48	109.12	0	7	1994	2000
1140	5.30	100.27	3	26	1980	2009	**2830**	16.83	112.33	0	9	1992	2000
1141	3.12	101.55	17	30	1980	2009	**2831**	44.02	89.57	0	4	1987	1990

1142	-20.57	164.28	18	34	1982	2019	**2832**	41.80	82.90	0	11	1980	1990
1144	-37.02	174.80	6	10	1980	1989	**2834**	40.68	111.15	0	12	1980	1991
1145	-40.20	175.38	55	11	1980	1990	**2835**	39.37	109.80	0	12	1980	1991
1147	-41.28	174.77	126	10	1981	1990	**2836**	37.53	121.40	0	20	1981	2000
1148	-43.48	172.53	34	11	1980	1990	**2837**	29.50	103.75	0	11	1980	1990
1149	-43.98	170.47	1026	5	1983	1987	**2838**	26.85	104.25	0	11	1980	1990
1150	-46.42	168.32	2	10	1980	1990	**2840**	30.27	121.17	0	11	1980	1990
1153	14.63	121.02	45	25	1980	2019	**2841**	28.22	113.10	0	8	1980	1987
1154	1.37	103.92	32	21	1980	2003	**2842**	29.85	106.43	0	8	1980	1987
1157	21.33	-157.92	5	1	1980	1980	**2843**	31.17	121.43	4	11	1980	1990
1159	48.27	16.72	150	3	1980	1982	**2844**	22.58	113.35	0	11	1980	1990
1161	48.20	16.57	153	34	1984	2019	**2845**	24.80	113.60	0	11	1980	1990
1162	48.07	14.60	309	5	1980	1984	**2846**	27.68	106.92	0	11	1980	1990
1164	47.82	13.73	1598	4	1980	1987	**2847**	30.80	106.08	0	11	1980	1990
1165	47.80	13.00	435	16	1980	2002	**2848**	30.80	108.35	0	11	1980	1990
1169	47.27	11.40	582	14	1980	1993	**2849**	29.58	115.98	0	11	1980	1990
1171	47.05	12.95	3106	34	1980	2019	**2851**	32.72	109.05	0	11	1980	1990
1172	46.98	15.45	342	35	1980	2019	**2852**	27.33	103.75	0	11	1980	1990
1173	46.65	14.33	452	38	1980	2019	**2853**	26.58	101.72	1190	9	1992	2000
1174	51.23	2.92	12	11	1980	1993	**2854**	35.45	116.58	0	11	1980	1990
1175	50.98	3.83	15	24	1980	2007	**2855**	40.47	124.13	0	11	1980	1990
1176	50.80	4.35	105	31	1980	2011	**2861**	-34.97	138.52	49	1	2003	2003
1179	50.03	5.40	563	25	1980	2007	**2863**	-12.42	130.88	31	17	1994	2018
1180	43.45	24.57	131	4	1985	1988	**2866**	-37.70	144.95	108	5	1998	2003
1181	43.20	27.92	14	11	1980	1992	**2867**	51.97	5.65	7	26	1980	2005
1182	42.68	23.33	588	24	1980	2009	**2868**	-5.17	-48.75	170	1	1992	1992
1183	42.58	23.25	2286	9	1980	1989	**2869**	-3.10	-60.17	60	2	1991	1992
1184	42.20	25.33	175	10	1985	1995	**2870**	-5.75	-49.17	150	1	1993	1993

1186	41.52	23.27	206	5	1988	2004	**2871**	-10.08	-61.92	120	2	1992	1993
1187	46.82	9.85	1590	28	1980	2007	**2872**	-10.75	-62.37	220	2	1992	1993
1188	46.17	8.78	380	40	1980	2019	**2873**	-2.32	-59.95	80	3	1991	1993
1189	50.25	15.85	241	40	1980	2019	**2874**	-65.30	-64.30	5	3	1986	1989
1190	49.82	18.15	242	33	1986	2019	**2876**	46.78	8.42	2450	1	1991	1991
1191	49.12	20.08	1353	24	1980	2007	**2877**	46.78	8.42	3020	1	1991	1991
1192	49.07	13.62	1122	33	1986	2019	**2894**	-33.03	-71.48	70	25	1980	2004
1193	48.88	16.08	334	34	1986	2019	**2895**	-23.80	133.90	545	24	1995	2019
1194	48.67	21.73	107	29	1986	2019	**2896**	36.90	-75.72	12	4	2001	2004
1195	48.17	17.10	289	35	1980	2019	**2897**	-30.67	24.00	0	7	2002	2019
1196	54.15	11.85	21	16	1980	1996	**2899**	30.87	34.77	0	9	2003	2011
1197	52.38	13.10	33	26	1980	2005	**2900**	36.05	140.13	25	22	1998	2020
1198	51.12	13.68	271	16	1980	1995	**2901**	58.27	26.47	70	11	2000	2010
1199	50.43	12.95	1214	17	1980	1998	**3651**	29.30	-81.03	20	9	1989	2000
1200	55.02	8.42	33	19	1980	1998	**3652**	37.28	-81.23	803	17	1986	2004
1201	54.53	9.55	59	18	1981	1998	**3653**	38.30	-76.25	4	19	1987	2012
1202	53.72	7.15	29	19	1980	1998	**3654**	35.83	-90.55	52	13	1986	1999
1203	53.65	10.12	49	29	1980	2010	**3660**	36.30	-119.63	73	6	1996	2001
1204	53.05	8.80	24	19	1980	1998	**3661**	47.68	-122.25	20	7	1996	2006
1205	52.30	10.45	81	39	1980	2019	**3662**	32.05	-81.12	11	14	1986	2000
1206	52.25	8.05	104	19	1980	1998	**3663**	39.73	-105.18	1829	31	1986	2018
1207	51.83	6.53	24	19	1980	1998	**3666**	33.75	-80.92	96	9	1986	1995
1208	51.78	8.83	162	17	1982	1998	**3700**	-54.85	-68.31	10	11	1995	2018
1209	51.72	10.62	615	19	1980	1998	**3701**	-35.16	147.46	221	29	1980	2017
1210	51.50	7.08	63	12	1980	1991	**3702**	-0.20	100.32	864	20	1996	2019
1211	51.30	9.45	237	19	1980	1998	**3703**	40.63	22.96	60	22	1994	2019
1212	50.70	7.15	65	18	1980	1997	**3704**	40.72	-77.73	376	17	2002	2018
1213	50.58	8.70	201	18	1981	1998	**3705**	43.73	-96.62	473	15	2004	2018

1214	50.27	10.95	357	17	1982	1998	**3706**	56.48	21.02	4	1	2019	2019
1215	49.98	7.95	131	19	1980	1998	**3707**	57.14	25.90	188	23	1994	2019
1216	49.77	9.97	275	39	1980	2019	**3750**	46.87	8.63	449	27	1981	2007
1217	49.75	6.67	278	38	1980	2019	**3751**	46.99	7.46	553	27	1981	2007
1218	49.52	8.55	106	19	1980	1998	**3752**	45.87	7.17	2472	26	1982	2007
1219	49.50	11.08	312	19	1980	1998	**3753**	46.24	6.12	420	39	1981	2019
1220	49.22	7.12	325	16	1982	1998	**3754**	46.57	8.33	1980	18	1990	2007
1221	49.02	10.97	428	17	1982	1998	**3755**	46.65	8.62	2287	27	1981	2007
1222	48.83	9.20	318	19	1980	1998	**3756**	47.09	6.80	1018	27	1981	2007
1223	48.58	13.47	412	17	1980	1996	**3757**	46.00	8.96	273	27	1981	2007
1224	48.40	11.70	469	38	1980	2019	**3758**	47.04	8.30	454	27	1981	2007
1225	48.00	7.85	269	19	1980	1998	**3759**	47.43	8.52	443	27	1981	2007
1226	47.80	11.02	990	40	1980	2019	**3760**	46.46	9.18	1639	26	1982	2007
1227	55.67	12.30	28	22	1980	2001	**3761**	46.22	7.34	482	27	1981	2007
1228	43.47	-3.82	78	34	1986	2019	**3762**	47.43	9.40	1030	26	1982	2007
1229	43.35	-5.87	335	36	1981	2019	**3770**	38.52	-28.63	60	8	2006	2015
1230	42.47	-2.40	364	12	1981	2007	**3771**	36.97	-25.17	100	4	2010	2014
1231	40.45	-3.72	664	35	1981	2019	**3772**	41.55	24.73	1750	1	1996	1996
1232	39.55	-4.33	910	26	1986	2019	**3774**	56.17	21.17	18	10	2008	2017
1233	39.55	2.62	6	32	1981	2019	**3780**	40.72	-7.88	644	1	2007	2007
1234	39.47	-6.33	405	31	1983	2019	**3781**	49.03	20.32	706	12	2008	2019
1235	38.00	-1.17	61	37	1981	2019	**3783**	56.45	-3.07	30	29	1982	2016
1236	37.42	-5.90	34	5	1981	1987	**3784**	51.23	-0.95	124	11	2006	2016
1237	67.37	26.65	178	29	1980	2008	**3785**	53.17	-0.52	73	11	2006	2016
1238	60.82	23.50	104	37	1980	2016	**3786**	52.12	0.96	91	11	2006	2016
1239	60.20	24.92	45	12	1980	1991	**3787**	38.28	-0.55	31	16	2004	2019
1240	49.82	3.20	98	26	1980	2019	**3788**	41.30	2.05	10	16	2004	2019
1241	49.30	4.03	95	30	1981	2011	**3789**	37.83	-4.85	91	9	2009	2019

1242	49.18	-0.47	78	39	1980	2019	**3790**	41.90	2.75	127	15	2004	2019
1243	48.82	2.33	75	25	1980	2019	**3791**	37.18	-3.78	573	15	2004	2019
1245	48.77	2.02	168	26	1980	2019	**3792**	43.30	-8.37	97	11	2008	2019
1246	48.68	6.22	225	32	1980	2019	**3793**	41.62	0.60	201	7	1997	2007
1247	48.55	7.63	153	38	1980	2019	**3794**	40.45	-3.55	582	15	2005	2019
1248	48.07	-1.73	37	36	1980	2019	**3795**	42.77	-1.63	452	13	2007	2019
1249	47.80	3.55	207	33	1980	2019	**3796**	42.57	-6.60	550	12	2008	2019
1250	47.45	0.72	108	40	1980	2019	**3797**	40.92	-5.58	550	3	2011	2013
1251	47.27	5.08	222	39	1980	2019	**3798**	37.78	-0.80	2	14	2004	2019
1252	47.17	-1.60	27	32	1986	2019	**3799**	40.35	-1.12	900	12	2008	2019
1253	47.00	-2.33	2	5	1986	1990	**3800**	39.50	-0.47	62	15	2005	2019
1254	46.70	-1.38	91	21	1986	2019	**3801**	42.22	-8.63	255	16	2004	2019
1255	46.30	4.80	218	27	1980	2019	**3803**	28.45	-13.85	29	14	2004	2018
1256	46.15	-1.15	4	40	1980	2019	**3804**	28.30	-16.50	2400	13	2006	2018
1257	45.82	1.28	282	39	1980	2019	**3805**	27.93	-15.20	24	11	2008	2018
1258	45.78	3.17	332	37	1980	2019	**3806**	28.47	-16.32	670	11	2008	2018
1259	44.83	-0.70	49	40	1980	2019	**3807**	28.27	-16.20	25	12	2007	2018
1260	44.57	6.50	871	39	1980	2019	**3808**	28.03	-16.57	25	12	2006	2018
1261	44.43	-1.25	33	24	1980	2019	**3809**	-12.20	96.83	6	5	2008	2018
1262	44.18	-0.28	38	2	1981	1982	**3811**	-31.93	115.95	20	13	1980	1993
1263	44.18	0.60	61	26	1980	2019	**3812**	30.70	103.83	539	12	2004	2015
1264	44.12	3.02	715	34	1980	2019	**3813**	35.87	104.15	1875	12	2004	2015
1265	44.08	5.05	99	30	1980	2019	**3814**	25.50	49.57	616	9	1980	1990
1266	43.65	7.20	4	39	1980	2019	**3815**	24.72	46.72	636	3	1985	1988
1267	43.58	3.97	5	40	1980	2019	**3816**	21.48	40.55	1478	10	1980	1990
1268	43.43	5.22	4	39	1980	2019	**3817**	19.53	41.05	53	1	1980	1980
1269	43.38	-0.42	188	26	1980	2019	**3818**	20.47	45.62	16	9	1981	1990
1270	43.22	2.32	130	26	1980	2019	**3819**	28.37	36.63	778	2	1981	1985

1271	43.03	6.47	133	10	1980	1990	**3820**	18.23	42.65	2090	9	1982	1990
1272	42.73	2.87	43	39	1981	2019	**3821**	26.07	43.98	724	10	1980	1989
1273	42.48	2.12	1580	7	1983	1990	**3822**	25.33	55.52	33	1	1991	1991
1274	41.92	8.80	4	40	1980	2019	**3825**	9.55	-69.23	226	1	1996	1996
1276	60.13	-1.18	82	36	1980	2015	**3826**	8.62	-70.22	203	2	1996	1997
1278	57.20	-3.83	220	32	1984	2016	**3827**	10.52	-71.65	26	2	1996	1997
1279	57.17	-2.08	35	35	1981	2016	**3828**	7.58	-72.07	327	2	1996	1997
1280	56.47	-5.43	3	29	1981	2016	**3829**	9.02	-62.62	327	1	1996	1996
1281	56.45	-3.07	30	5	1982	1990	**3850**	82.49	-62.42	127	9	2005	2013
1282	56.43	-2.87	4	8	1984	1991	**3851**	-15.60	-47.71	1023	6	2009	2014
1283	55.32	-3.20	242	35	1980	2016	**3852**	51.97	4.93	0	15	2005	2020
1284	54.65	-6.22	81	25	1980	2007	**3853**	50.22	-5.32	88	9	2001	2016
1287	53.55	-2.92	55	12	1984	1995	**3854**	36.91	-75.71	37	15	2001	2016
1288	53.48	-1.00	17	10	1984	1994	**3855**	42.82	-1.60	471	10	2010	2020
1290	52.68	1.68	13	15	1984	2000	**3856**	-12.19	96.84	2	9	2007	2019
1293	52.13	-4.57	134	34	1980	2016	**3857**	-12.43	130.89	30	12	2003	2014
1299	51.52	-0.12	77	25	1980	2006	**3858**	-12.42	130.89	32	11	2008	2019
1301	51.38	-0.78	74	23	1980	2002	**3859**	36.63	-116.02	1007	20	1998	2019
1302	51.08	-0.22	144	11	1981	1991	**3860**	-75.10	123.37	3233	13	2006	2020
1303	50.22	-5.32	88	33	1984	2016	**3861**	79.99	-85.94	85	1	2011	2011
1304	49.22	-2.20	84	20	1980	1999	**3862**	48.32	-105.10	634	23	1995	2019
1306	40.58	22.55	1	10	1982	1993	**3863**	33.58	130.38	3	9	2011	2020
1307	39.17	21.00	11	13	1980	1993	**3864**	-23.56	15.04	0	7	2013	2020
1308	38.38	23.10	110	12	1980	1993	**3865**	-70.65	-8.25	42	22	1993	2014
1309	38.05	23.67	138	6	1981	1987	**3866**	24.34	124.16	0	9	2011	2020
1310	37.98	22.73	150	8	1984	1993	**3867**	28.31	-16.50	2373	11	2009	2020
1311	37.97	23.72	107	6	1980	1985	**3868**	-45.05	169.69	350	15	2000	2014
1312	37.92	21.28	12	6	1981	1988	**3869**	60.14	-1.18	80	9	2001	2016

1313	37.60	22.78	13	9	1983	1992	**3870**	37.10	-76.39	3	5	2016	2020
1314	35.00	24.77	7	6	1980	1992	**3871**	-2.06	147.43	6	15	1997	2012
1317	47.72	16.58	427	21	1980	2006	**3872**	24.29	153.98	7	9	2011	2020
1319	47.50	21.63	123	6	1980	1985	**3873**	48.71	2.21	156	13	2006	2019
1320	47.43	19.18	138	25	1980	2006	**3874**	40.72	-77.93	376	21	1999	2019
1324	46.87	20.53	85	25	1980	2006	**3875**	-9.07	-40.32	387	8	2009	2017
1329	55.37	-7.33	25	37	1982	2019	**3877**	43.06	141.33	17	9	2011	2020
1330	54.23	-10.00	10	38	1982	2019	**3878**	-29.44	-53.82	489	8	2007	2016
1331	54.18	-7.23	86	35	1982	2016	**3879**	47.05	12.96	3109	7	2013	2020
1332	53.43	-6.25	85	39	1980	2019	**3880**	-89.98	24.80	2800	19	1992	2016
1333	53.08	-7.88	72	32	1980	2011	**3881**	43.73	-96.62	473	15	2004	2019
1334	52.67	-7.27	64	29	1980	2008	**3883**	58.25	26.46	70	19	2000	2019
1335	51.93	-10.25	30	40	1980	2019	**3884**	39.75	116.96	32	9	2005	2015
1336	32.00	34.82	30	8	1980	1988	**3885**	46.82	6.94	491	27	1993	2020
1338	64.13	-21.90	52	38	1980	2019	**3886**	24.91	46.41	650	4	1999	2002
1339	46.47	11.33	241	8	1980	1987	**3887**	-69.01	39.59	18	13	2008	2020
1340	46.03	13.18	92	19	1980	2009	**4495**	-27.55	135.45	117	1	1980	1980
1341	45.93	7.70	3488	4	1980	1990	**4497**	39.45	-31.13	29	5	2009	2015
1342	45.65	13.75	20	18	1980	2014	**4498**	39.10	-28.03	25	6	2013	2019
1343	45.43	9.28	103	16	1980	2010	**4499**	37.83	-25.15	251	3	2013	2015
1344	45.50	12.33	6	8	1981	1988	**4500**	38.55	-28.45	33	3	2016	2019
1345	45.18	7.65	282	6	1980	1985	**4501**	37.73	-25.70	71	8	2006	2019
1347	44.53	11.30	49	9	1980	1988	**4502**	70.48	-68.52	26	6	1988	1994
1348	44.42	8.85	3	9	1980	1988	**4505**	-30.17	-70.70	2154	13	2004	2017
1351	44.20	10.70	2173	3	1981	1988	**4509**	27.05	27.97	82	1	2010	2010
1352	43.95	8.17	221	18	1980	2002	**4511**	29.90	33.73	401	6	2009	2017
1353	43.68	10.38	1	22	1980	2014	**4512**	43.52	5.42	173	3	2013	2015
1355	43.62	13.37	10	2	1986	1987	**4513**	43.90	2.10	172	9	2011	2019

1357	42.47	12.98	1875	11	1984	2004	**4514**	48.43	0.10	143	9	2011	2019
1358	42.43	14.20	16	7	1980	1986	**4515**	45.97	5.32	250	2	2018	2019
1359	42.08	12.22	262	25	1980	2013	**4516**	44.53	4.37	280	3	2013	2015
1360	41.80	12.58	131	20	1980	2009	**4517**	43.68	0.60	121	9	2011	2019
1361	41.53	15.72	56	25	1980	2009	**4518**	44.88	2.42	639	10	2010	2019
1364	40.87	9.50	13	6	1980	1987	**4519**	47.47	-0.60	50	11	2009	2019
1365	40.85	14.30	72	8	1981	1988	**4520**	49.43	2.12	89	10	2010	2019
1367	40.65	17.95	15	28	1980	2013	**4521**	44.82	0.50	49	9	2011	2019
1368	40.63	8.28	40	8	1980	1988	**4522**	43.47	-1.53	71	8	2012	2019
1369	40.02	15.28	185	16	1980	2013	**4523**	47.67	1.22	121	7	2013	2019
1370	39.25	9.05	18	21	1980	2012	**4524**	45.60	6.75	865	1	2019	2019
1371	39.00	17.07	158	9	1980	1988	**4525**	45.13	1.47	112	9	2011	2019
1372	38.70	13.18	250	14	1980	1996	**4526**	50.95	1.95	2	7	2013	2019
1373	38.20	15.55	59	22	1980	2004	**4527**	45.63	5.87	235	10	2010	2019
1374	37.92	12.52	14	17	1980	2014	**4528**	49.77	4.63	149	10	2010	2019
1375	37.08	14.22	33	14	1980	1996	**4529**	48.45	1.50	155	10	2010	2019
1376	36.82	11.97	170	15	1980	2008	**4530**	48.05	1.37	126	9	2011	2019
1377	33.82	35.48	18	1	1980	1980	**4531**	46.87	1.73	158	10	2010	2019
1379	53.13	6.58	4	35	1980	2014	**4532**	47.83	4.57	262	7	2013	2019
1380	52.92	4.78	0	35	1980	2014	**4533**	47.07	-0.87	134	3	2013	2015
1381	52.10	5.18	40	35	1980	2014	**4534**	49.25	2.52	88	11	2009	2019
1382	51.45	3.60	8	35	1980	2014	**4535**	43.68	-1.07	31	8	2012	2019
1383	50.92	5.77	114	10	1980	1989	**4536**	48.58	-2.07	65	8	2012	2019
1384	60.40	5.32	45	34	1980	2013	**4538**	49.02	1.22	138	5	2012	2016
1386	54.18	15.58	16	38	1980	2017	**4539**	49.65	-1.45	134	8	2012	2019
1389	52.27	20.98	130	39	1980	2019	**4540**	44.73	1.38	260	3	2017	2019
1391	51.83	20.78	180	40	1980	2019	**4541**	45.35	5.30	384	10	2010	2019
1393	49.28	19.97	857	40	1980	2019	**4542**	46.17	1.95	365	8	2012	2019

1395	41.80	-6.73	691	23	1980	2019	**4543**	46.30	5.83	1133	7	2013	2019
1396	41.13	-8.60	93	19	1980	2012	**4544**	47.83	5.33	467	2	2018	2019
1397	40.42	-7.55	1380	5	1981	1991	**4545**	48.03	-0.73	96	8	2012	2019
1398	40.20	-8.42	141	12	1983	2011	**4546**	43.37	6.38	80	9	2011	2019
1399	39.83	-7.48	390	7	1986	2007	**4547**	47.93	0.18	48	10	2010	2019
1400	38.72	-9.15	77	19	1980	2012	**4548**	45.07	3.75	833	8	2012	2019
1402	38.57	-7.90	309	15	1980	2012	**4549**	50.52	1.62	5	3	2017	2019
1403	37.02	-7.97	8	20	1980	2019	**4550**	50.57	3.08	47	6	2012	2017
1404	47.17	27.63	90	34	1980	2017	**4551**	47.75	-3.43	45	10	2010	2019
1405	46.78	23.57	410	35	1980	2017	**4552**	44.67	5.70	1059	3	2013	2015
1406	45.77	21.25	86	7	1980	1993	**4553**	47.78	6.35	271	3	2017	2019
1407	45.50	28.02	71	36	1980	2017	**4554**	45.72	4.93	197	11	2009	2019
1408	44.50	26.13	91	37	1980	2017	**4555**	48.60	2.67	91	10	2010	2019
1409	44.23	23.87	192	28	1988	2017	**4556**	44.53	3.45	932	9	2011	2019
1410	44.22	28.63	13	26	1980	2006	**4557**	48.98	6.25	260	2	2018	2019
1412	67.85	20.23	505	28	1980	2010	**4558**	45.92	6.10	458	4	2013	2016
1413	65.55	22.13	16	39	1980	2019	**4559**	43.92	-0.50	62	10	2010	2019
1414	59.35	17.95	24	39	1980	2019	**4560**	44.02	1.37	107	10	2010	2019
1415	64.58	40.50	13	20	1980	2016	**4561**	46.62	4.47	602	7	2013	2019
1416	59.97	30.30	4	17	1980	1999	**4562**	46.98	3.10	175	2	2018	2019
1417	55.75	37.57	187	30	1980	2019	**4563**	43.85	4.40	59	7	2013	2019
1418	55.70	37.50	192	40	1980	2019	**4564**	46.30	-0.40	57	10	2010	2019
1419	54.88	23.88	73	12	1980	1993	**4565**	47.98	1.77	125	9	2011	2019
1420	50.40	30.45	121	37	1980	2019	**4566**	46.58	0.30	123	9	2011	2019
1421	46.48	30.63	64	38	1980	2019	**4567**	47.97	-4.17	90	10	2010	2019
1422	41.68	44.95	427	3	1987	1989	**4568**	49.20	4.15	95	7	2013	2019
1427	41.33	36.25	4	1	1983	1983	**4569**	44.40	2.47	578	7	2013	2019
1428	40.80	29.43	130	2	1983	1984	**4570**	44.05	5.98	461	7	2013	2019

1429	39.95	32.88	894	1	1983	1983	**4571**	48.53	-2.85	135	10	2010	2019
1432	36.87	30.73	50	2	1983	1984	**4572**	48.62	4.90	139	8	2012	2019
1433	39.67	-31.12	28	3	1981	2015	**4573**	45.52	4.28	400	3	2017	2019
1434	38.65	-27.23	90	16	1980	2019	**4574**	43.00	1.10	414	8	2012	2019
1435	37.75	-25.67	35	7	1980	2013	**4575**	43.18	0.00	360	9	2011	2019
1436	46.07	14.52	299	11	1980	1991	**4576**	47.03	5.42	195	8	2012	2019
1438	45.92	15.97	988	29	1980	2011	**4577**	48.32	4.02	112	9	2010	2018
1439	45.82	15.98	157	7	1980	1986	**4578**	44.90	4.97	163	2	2015	2016
1442	45.52	13.57	92	7	1980	1991	**4579**	47.63	-2.75	11	7	2013	2019
1444	44.78	20.53	243	11	1980	1990	**4580**	46.17	3.38	249	10	2010	2019
1445	44.78	17.22	153	10	1980	1991	**4581**	5.20	-52.73	12	2	2011	2012
1446	44.23	22.55	42	6	1980	1988	**4582**	3.63	-54.02	106	5	2013	2018
1450	43.28	20.80	1711	6	1985	1991	**4583**	3.89	-51.80	11	6	2013	2018
1452	42.65	21.15	573	7	1981	1990	**4584**	5.48	-54.02	5	6	2013	2018
1453	42.10	19.10	6	9	1980	1990	**4585**	54.67	-6.22	81	34	1980	2016
1456	41.05	21.37	586	8	1980	1988	**4586**	55.42	-1.60	22	11	2006	2016
1457	-70.77	11.83	87	6	1980	1985	**4587**	16.33	-61.00	27	3	2013	2015
1458	-49.33	70.22	18	7	1980	1986	**4588**	53.03	-8.08	76	6	2014	2019
1462	-66.58	93.00	40	6	1980	1985	**4589**	52.30	-6.50	62	6	2014	2019
1463	-66.67	140.02	43	5	1980	1986	**4590**	37.40	14.92	24	3	2012	2014
1468	-78.45	106.87	3488	4	1986	1993	**4591**	39.35	8.97	29	1	2012	2012
1472	-28.60	-70.77	526	12	1988	2002	**4592**	42.75	11.07	7	1	2012	2012
1477	-70.70	44.33	2230	1	1980	1980	**4593**	41.70	15.95	838	1	2012	2012
1478	47.58	7.58	317	27	1981	2007	**4594**	41.65	12.45	12	3	2012	2014
1479	48.25	16.37	202	39	1980	2019	**4595**	46.75	10.53	1461	1	2012	2012
1481	50.07	14.43	262	34	1986	2019	**4596**	36.53	126.32	47	2	2017	2018
1486	10.45	-64.18	2	2	1996	1997	**4597**	56.52	25.92	107	18	1991	2009
1520	41.38	2.20	25	16	1991	2019	**4598**	14.62	-61.05	143	4	2013	2016

1521	22.32	114.17	65	12	1994	2005	**4599**	14.77	-60.87	26	4	2015	2018
1525	42.35	-3.68	870	2	1980	1981	**4600**	47.00	28.82	205	15	2004	2019
1526	-33.92	151.22	500	2	1981	1982	**4601**	54.20	16.15	33	1	2019	2019
1529	-33.85	151.52	42	1	1982	1982	**4603**	40.15	-8.47	170	10	2005	2019
1537	15.52	44.18	2210	1	1981	1981	**4604**	38.72	-9.15	77	22	1980	2012
1558	46.82	6.95	491	3	1988	1990	**4605**	41.23	-8.68	70	9	2000	2012
1559	47.43	8.52	443	2	1989	1990	**4606**	-20.95	55.28	9	2	2017	2018
1560	47.38	9.00	760	2	1989	1990	**4607**	44.68	29.00	2	8	2007	2017
1570	46.82	9.83	2670	27	1981	2007	**4609**	48.73	19.12	427	5	2015	2019
1572	47.48	8.53	436	36	1981	2019	**4610**	47.87	18.18	115	32	1981	2019
1573	47.37	8.45	560	12	1980	1995	**4611**	37.10	-6.73	45	11	2009	2019
1583	13.10	-59.60	42	17	1980	2010	**4612**	43.36	-1.79	4	14	2004	2019
1593	47.68	9.18	450	14	1980	1993	**4613**	36.73	-6.07	27	15	2004	2019
1594	51.22	7.63	465	12	1987	1998	**4614**	40.80	-4.00	1894	7	2013	2019
1605	53.63	10.00	14	39	1980	2019	**4615**	39.57	2.75	10	6	2012	2019
1658	60.17	24.95	9	1	1980	1980	**4616**	41.15	-1.17	73	12	2004	2019
1659	60.32	24.97	53	29	1980	2016	**4617**	42.90	-8.42	370	15	2005	2019
1661	62.40	25.65	140	1	1980	1980	**4618**	56.92	18.15	34	7	2013	2019
1662	69.75	27.03	107	19	1980	2010	**4619**	63.30	12.12	646	7	2013	2019
1668	-27.60	-48.83	7	1	1990	1990	**4620**	59.45	19.50	10	10	2010	2019
1684	46.55	7.97	3576	39	1981	2019	**4623**	11.15	-60.83	15	4	1991	1994
1685	-2.95	-59.95	80	3	1984	1993	**4624**	37.25	9.80	3	1	2008	2008
1690	58.45	26.78	70	15	1980	1994	**4625**	36.85	11.08	30	1	2008	2008
2002	31.20	34.20	73	7	1991	1998	**4626**	33.35	10.48	117	1	2008	2008
2003	7.75	-2.10	339	8	1990	1997	**4627**	34.72	10.68	23	1	2008	2008
2004	-12.35	49.30	105	6	1988	1993	**4628**	36.95	8.75	21	1	2008	2008
2005	-23.40	43.73	8	3	1990	1992	**4629**	36.43	10.77	156	1	2008	2008
2011	13.73	-15.78	18	3	1989	1991	**4630**	24.27	55.60	262	12	1995	2006

2033	-10.22	31.13	1384	3	1988	1990	**4631**	25.25	55.33	8	7	1985	2006
2034	-11.10	28.85	1259	5	1988	1996	**4632**	40.07	-88.37	213	17	2002	2018
2035	-13.00	28.65	1270	2	1989	1990	**4633**	34.25	-89.87	98	14	2003	2018
2036	-13.27	31.93	568	3	1988	1990	**4637**	45.67	-0.32	31	9	2011	2019
2038	-17.82	25.82	986	3	1988	1990	**4638**	36.83	10.23	4	5	2001	2008
2039	45.75	126.77	142	36	1980	2015	**4639**	39.09	-28.03	15	1	2015	2015
2040	43.78	87.62	918	34	1980	2013	**4640**	-21.05	164.84	7	1	2019	2019
							4641	46.81	6.94	490	39	1981	2019
							4642	-45.04	169.68	370	5	2000	2004
							4643	48.31	-105.10	634	17	2002	2018

Table AA2. The id, coordinates, altitude, available years, and the start and end year of the BSRN stations which were used for the evaluation of FORTH-RTM and other datasets.

id	Lat (°)	Lon (°)	Alt (m)	years	start	end
ale	82.49	-62.42	127	11	2004	2014
asp	-23.80	133.89	547	26	1995	2020
bar	71.32	-156.61	8	26	1992	2017
ber	32.27	-64.67	8	24	1992	2017
bil	36.61	-97.52	317	26	1993	2018
bon	40.07	-88.37	213	26	1995	2020
bos	40.13	-105.24	1689	26	1995	2020
bou	40.05	-105.01	1577	25	1992	2016
brb	-15.60	-47.71	1023	12	2006	2019
bud	47.43	19.18	139.1	2	2019	2020
cab	51.97	4.93	0	16	2005	2020
cam	50.22	-5.32	88	17	2001	2017
cap	79.27	101.75		1	2016	2016
car	44.08	5.06	100	23	1996	2018
clh	36.91	-75.71	37	17	2000	2016
cnr	42.82	-1.60	471	12	2009	2020
coc	-12.19	96.84	6	17	2004	2020
daa	-30.67	23.99	1287	12	2000	2020
dar	-12.43	130.89	30	14	2002	2015
dom	-75.10	123.38	3233	15	2006	2020
dra	36.63	-116.02	1007	23	1998	2020
dwn	-12.42	130.89	32	13	2008	2020
e13	36.61	-97.49	318	26	1994	2019
ena	39.09	-28.03	15.2	1	2015	2015
eur	79.99	-85.94	85	5	2007	2011
flo	-27.60	-48.52	11	14	1994	2020
fpe	48.32	-105.10	634	26	1995	2020
fua	33.58	130.38	3	11	2010	2020
gan	23.11	72.63	65	4	2014	2019
gcr	34.25	-89.87	98	26	1995	2020
gim	46.72	-87.41	208	3	2018	2020
gob	-23.56	15.04	407	9	2012	2020
gur	28.42	77.16	259	4	2014	2019
gvn	-70.65	-8.25	42	29	1992	2020
how	22.55	88.31	51	5	2014	2019
ilo	8.53	4.57	350	14	1992	2005
ish	24.34	124.16	5.7	11	2010	2020
iza	28.31	-16.50	2372.9	12	2009	2020
kwa	8.72	167.73	10	26	1992	2017
lau	-45.05	169.69	350	22	1999	2020
ler	60.14	-1.18	80	17	2001	2017
lin	52.21	14.12	125	25	1994	2018
lrc	37.10	-76.39	3	7	2014	2020
lyu	22.04	121.56	324	3	2018	2020
man	-2.06	147.43	6	18	1996	2013
mnm	24.29	153.98	7.1	11	2010	2020

nau	-0.52	166.92	7	16	1998	2013
new	-32.88	151.73	18.5	2	2017	2018
nya	78.93	11.93	11	29	1992	2020
ohy	-12.05	-75.32	3314	3	2017	2019
pal	48.71	2.21	156	17	2003	2019
par	5.81	-55.21	4	1	2019	2019
pay	46.82	6.94	491	29	1992	2020
psu	40.72	-77.93	376	22	1998	2019
ptr	-9.07	-40.32	387	13	2007	2019
reg	50.21	-104.71	578	17	1995	2011
rlm	-11.58	-61.77	252	1	2007	2007
sap	43.06	141.33	17.2	11	2010	2020
sbo	30.86	34.78	500	10	2003	2012
sel	15.78	-91.99	602	1	2020	2020
sms	-29.44	-53.82	489	14	2006	2019
son	47.05	12.96	3108.9	8	2013	2020
sov	24.91	46.41	650	5	1998	2002
spo	-89.98	-24.80	2800	26	1992	2017
sxf	43.73	-96.62	473	17	2003	2019
syo	-69.01	39.59	18	27	1994	2020
tam	22.79	5.53	1385	21	2000	2020
tat	36.06	140.13	25	24	1997	2020
tik	71.59	128.92	48	9	2010	2018
tir	13.09	79.97	36	5	2014	2019
tor	58.25	26.46	70	22	1999	2020
xia	39.75	116.96	32	11	2005	2015
yus	23.49	120.96	3858	3	2018	2020

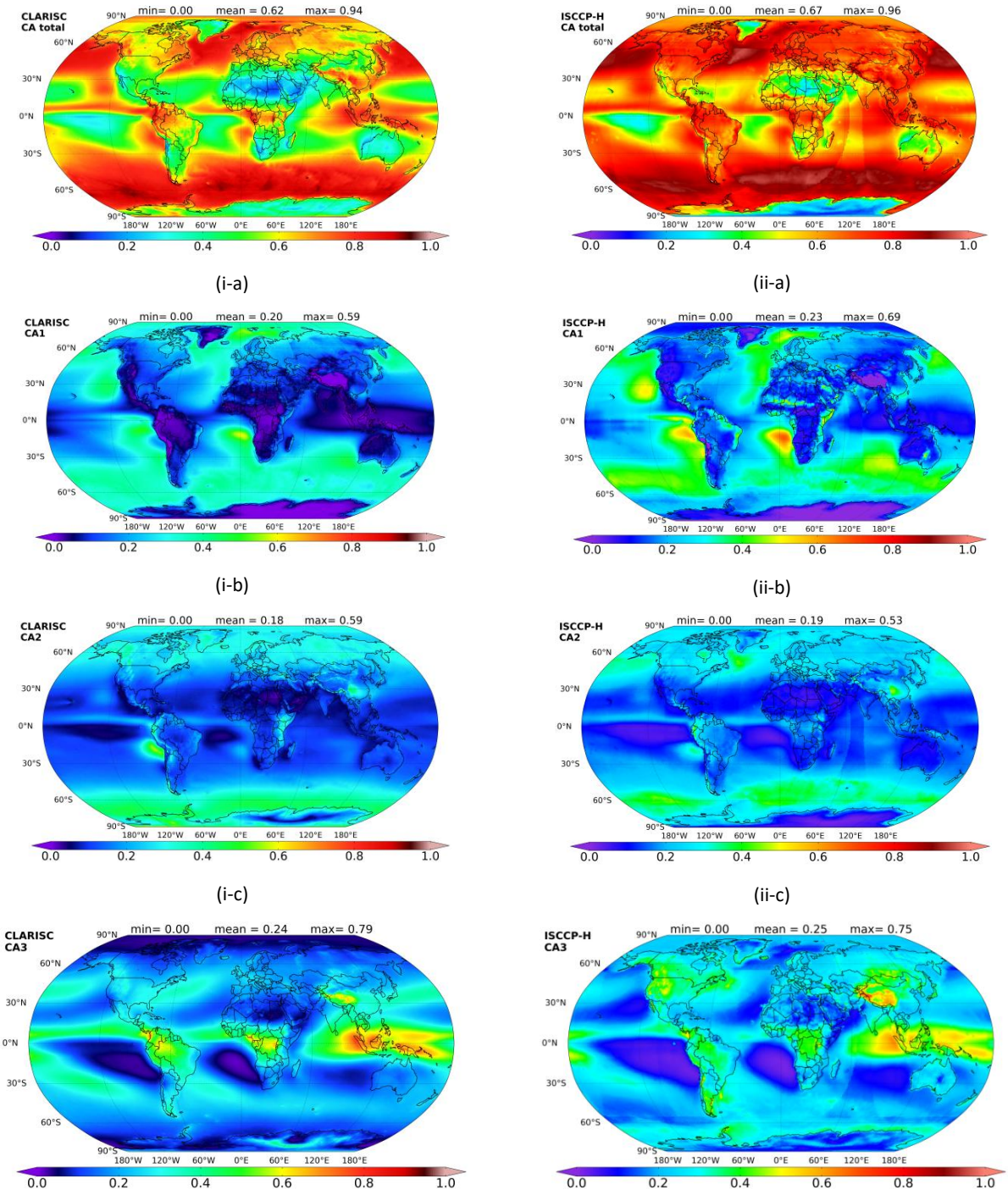


Figure AA1. Global distribution of annual average values of CLARISC (i) and ISCCP-H (ii) total CA (a), CA1 (b), CA2 (c), and CA3 (d), for the time-period 1984-2018.

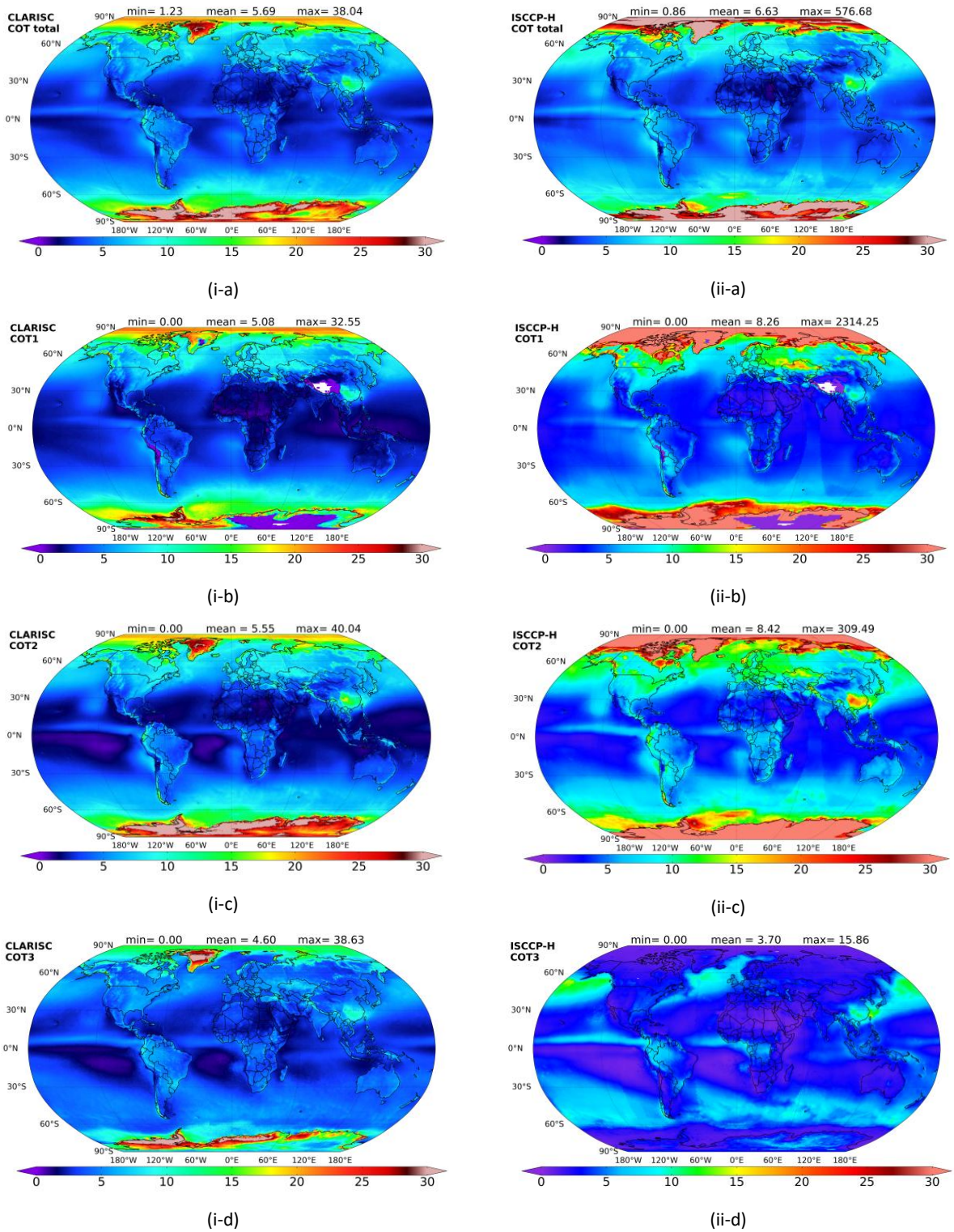


Figure AA2. Global distribution of annual average values of CLARISC (i) and ISCCP-H (ii) total COT (a), COT1 (b), COT2 (c), and COT3 (d), for the time-period 1984-2018.

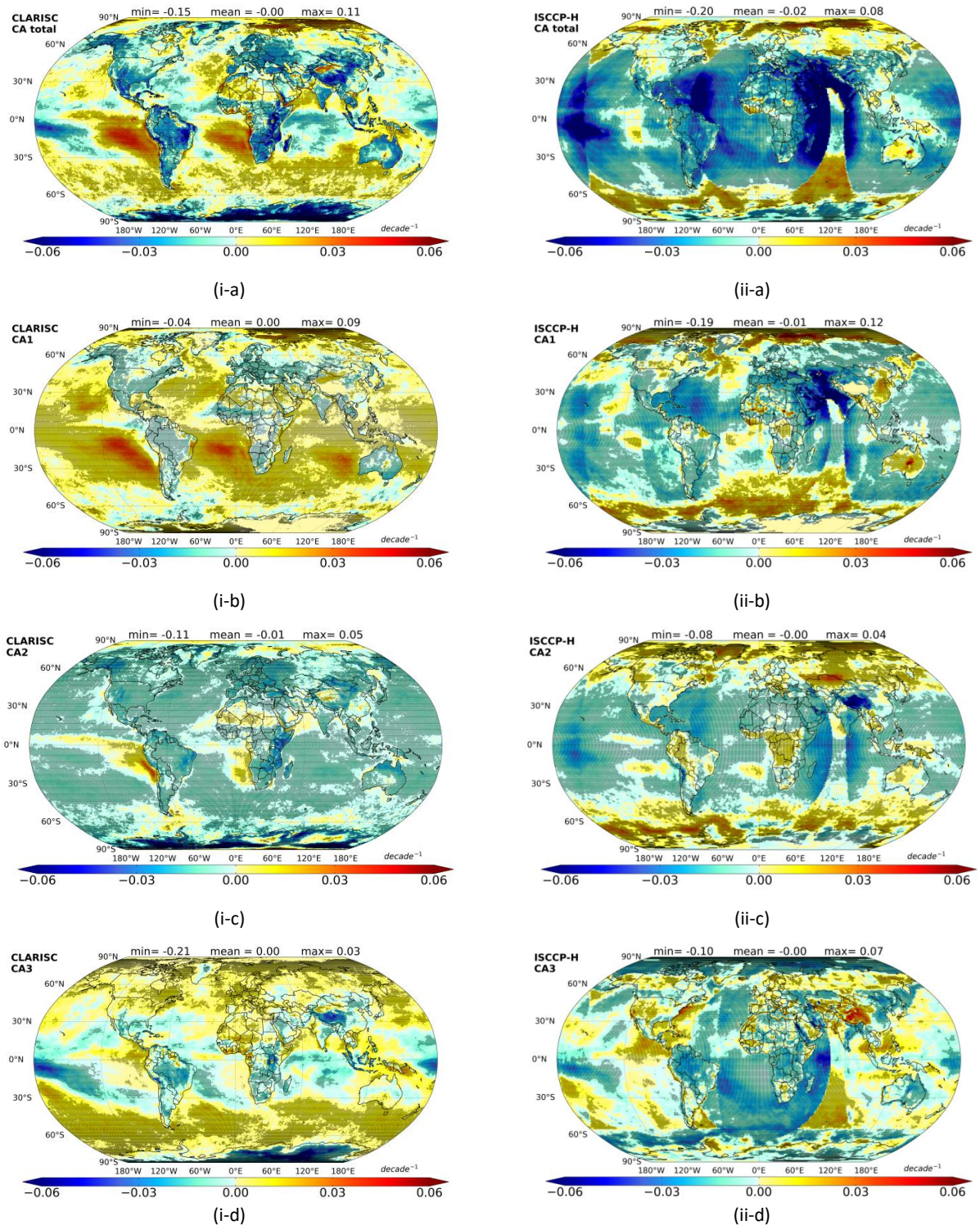


Figure AA3. Global distribution of per decade changes of CLARISC (i) and ISCCP-H (ii) for total CA (a), CA1 (b), CA2 (c), and CA3 (d), for the time-period 1984-2018. Areas shaded with reddish/bluish colors are those with positive/negative trends. Areas (pixels) with statistically significant trends are indicated by black dots.

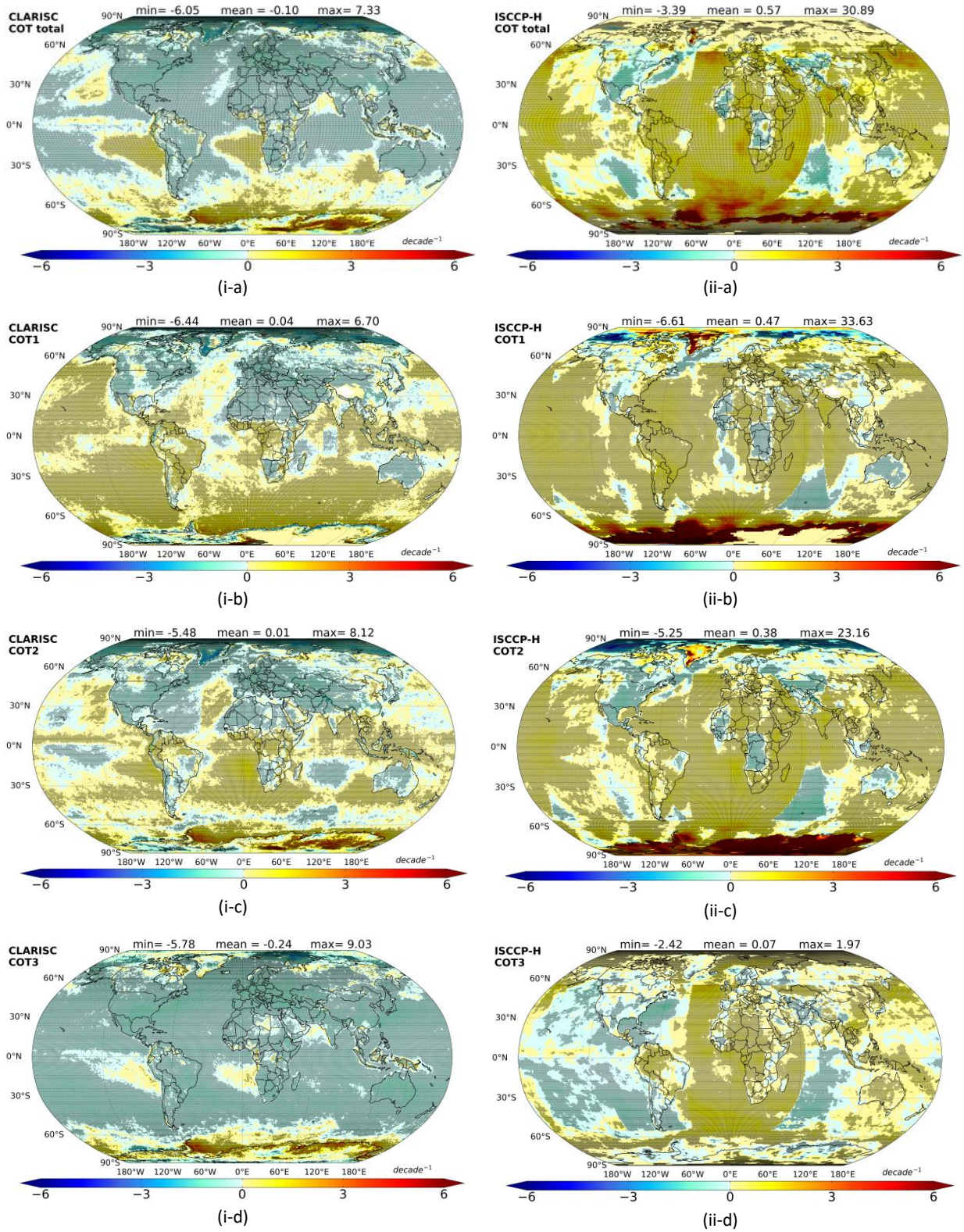
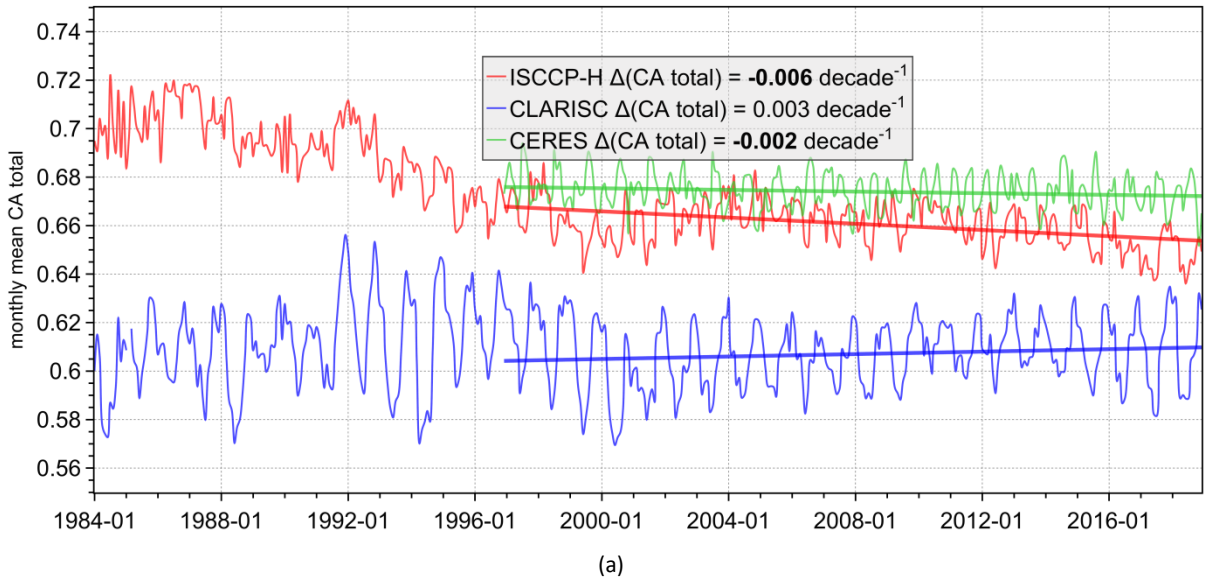
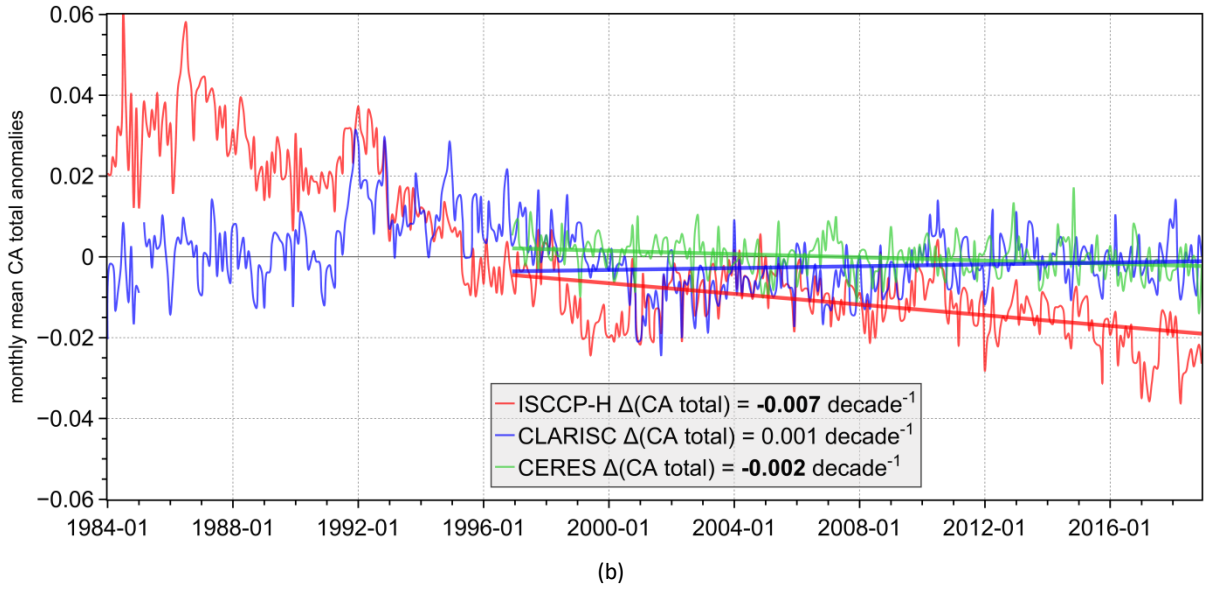


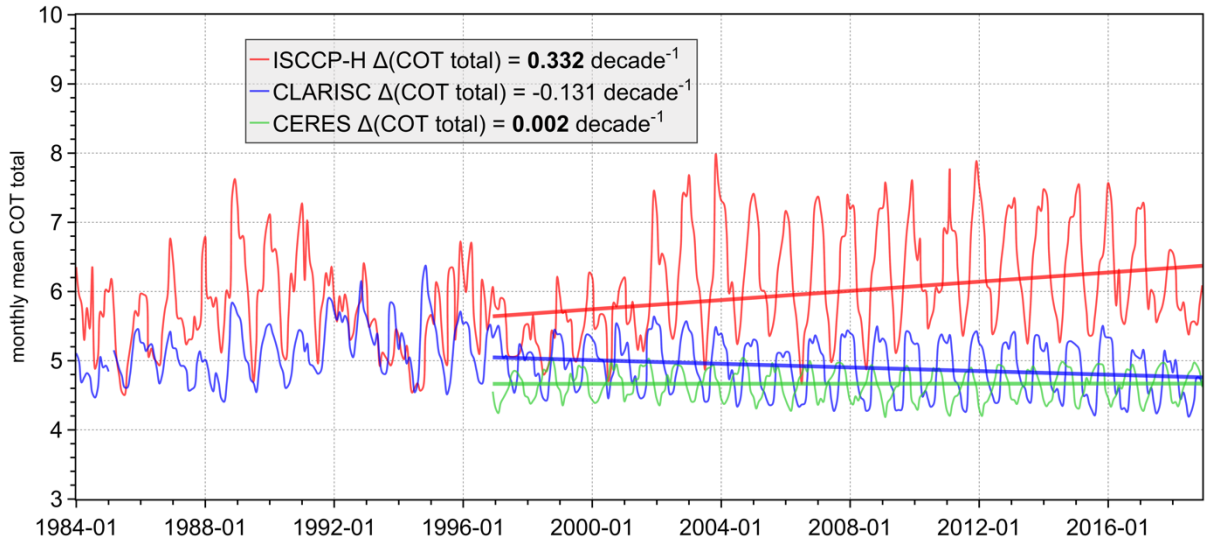
Figure AA4. Global distribution of per decade changes of CLARISC (i) and ISCCP-H (ii) for total COT (a), COT1 (b), COT2 (c), and COT3 (d), for the time-period 1984-2018. Areas shaded with reddish/bluish colors are those with positive/negative trends. Areas (pixels) with statistically significant trends are indicated by black dots.


monthly mean CA total
0.74
0.72
0.7
0.68
0.66
0.64
0.62
0.6
0.58
0.56
1984-01
1988-01
1992-01
1996-01
2000-01
2004-01
2008-01
2012-01
2016-01
ISCCP-H Δ(CA total) = -0.006 decade-1
CLARISC Δ(CA total) = 0.003 decade-1
CERES Δ(CA total) = -0.002 decade-1

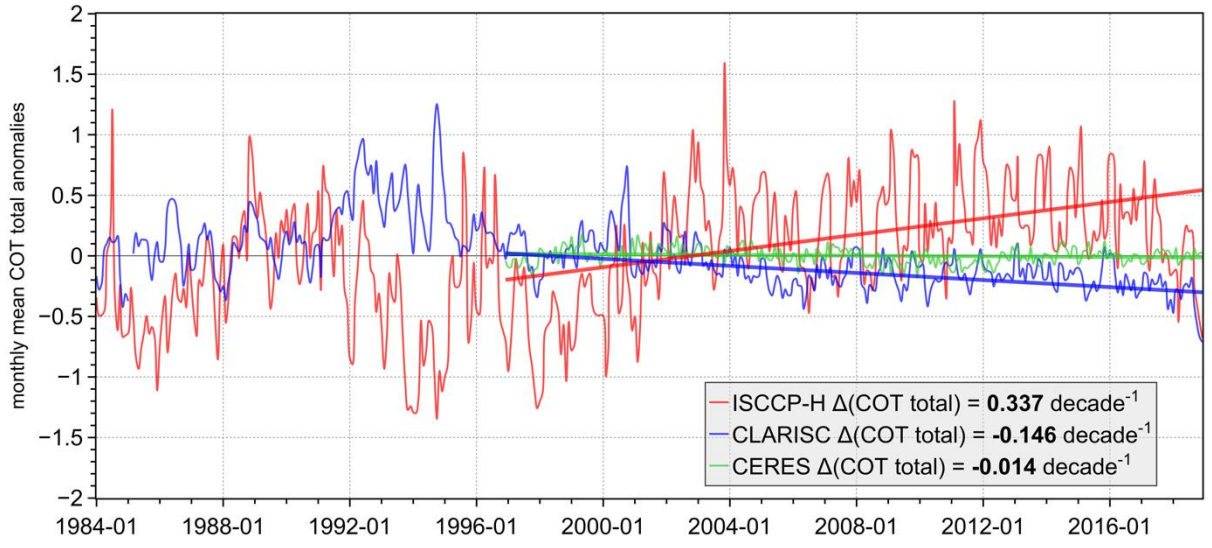
(a)


monthly mean CA total anomalies
0.06
0.04
0.02
0
−0.02
−0.04
−0.06
1984-01
1988-01
1992-01
1996-01
2000-01
2004-01
2008-01
2012-01
2016-01
ISCCP-H Δ(CA total) = -0.007 decade-1
CLARISC Δ(CA total) = 0.001 decade-1
CERES Δ(CA total) = -0.002 decade-1

(b)



(c)



(d)

Figure AA5. Timeseries of absolute values for total CA and COT (a,c) and their deseasonalized monthly anomalies (b,d) of CLARISC (blue) and ISSCP-H (red) for the time-period 1984-2018 along with CERES (green) since 2001. The linear trend lines are also shown along with the per decade changes. Numbers in bold indicate statistically significant trends in 95 CL.

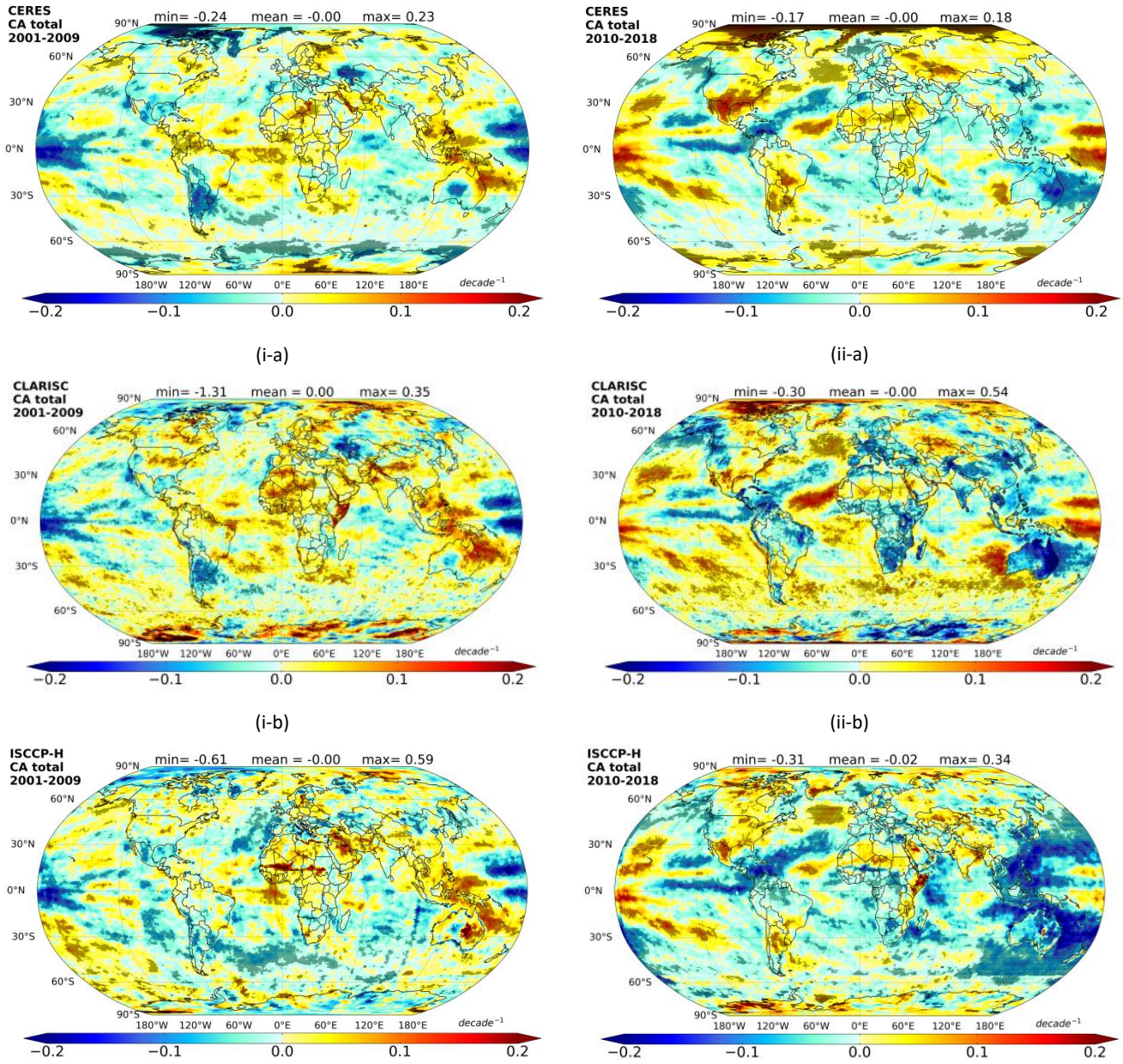


Figure AA6. Global distribution of per decade changes of CERES (a), CLARISC (b) and ISCCP-H (c) for total CA during the time-periods 2001-2009 (i) and 2010-2018 (ii). Areas shaded with reddish/bluish colors are those with positive/negative trends. Areas (pixels) with statistically significant trends are indicated by black dots.

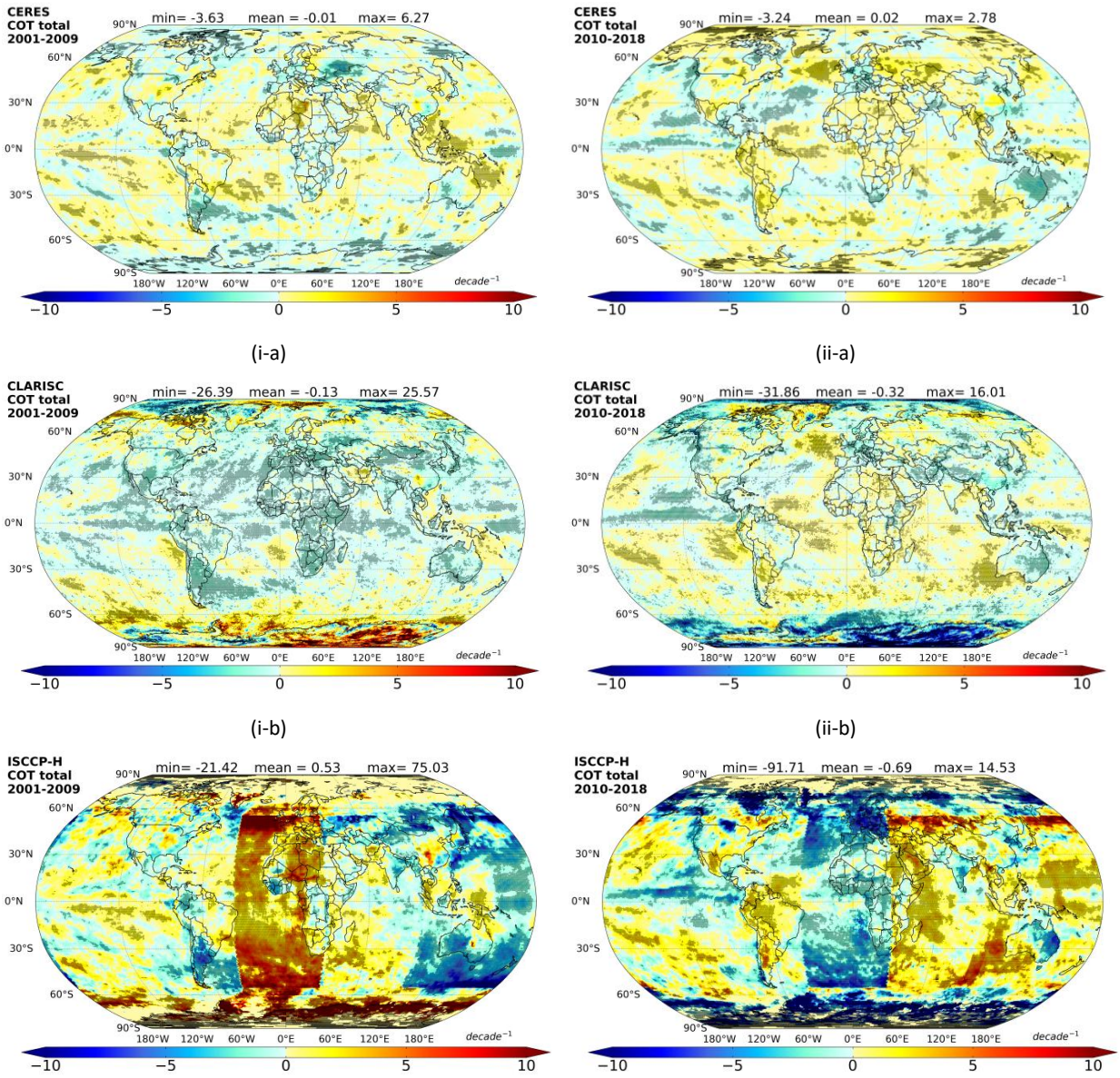
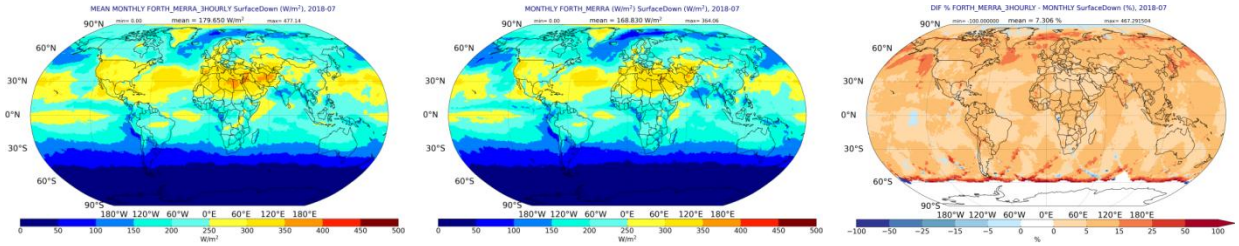


Figure AA7. Global distribution of per decade changes of CERES (a), CLARISC (b) and ISCCP-H (c) for total COT during the time-periods 2001-2009 (i) and 2010-2018 (ii). Areas shaded with reddish/bluish colors are those with positive/negative trends. Areas (pixels) with statistically significant trends are indicated by black dots.

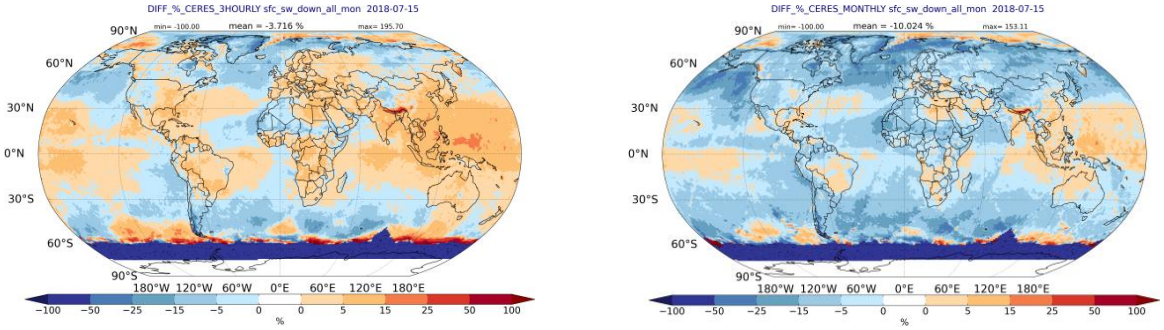
Table AA3. The percentage agreement between CLARISC, ISCCP-H and CERES in terms of sign of the trends of CA total and COT total for 2001-2009 and 2010-2018. The numbers in parenthesis represents the agreement only for statistically significant trends.

Datasets	CA total		COT total	
	2001-2009	2010-2018	2001-2009	2010-2018
CLARISC vs CERES	68% (98%)	67% (99%)	56% (80%)	63% (84%)
ISCCP-H vs CERES	67% (95%)	70% (98%)	47% (59%)	51% (64%)
CLARISC vs ISCCP-H	67% (98%)	61% (86%)	48% (62%)	55% (72%)



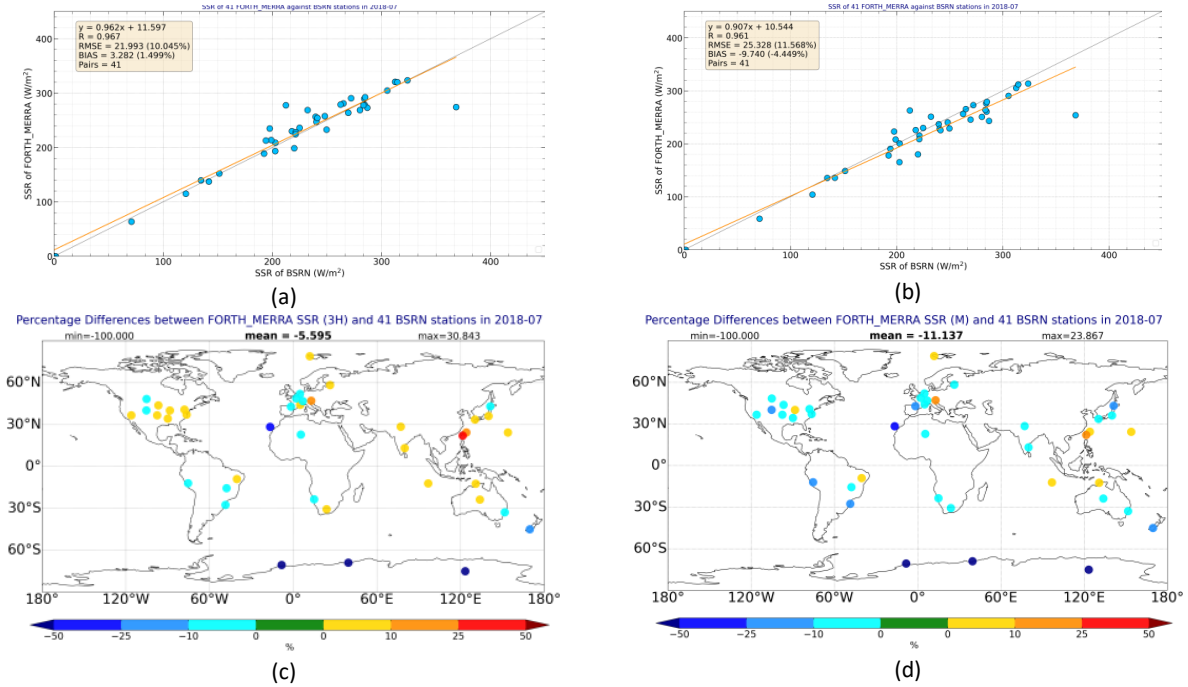
(a) (b) (c)

Figure AA8. Global distribution of average FORTH-RTM SSR (Wm^{-2}) for 2018-07 from monthly means calculated by 3-hourly means (a), direct monthly means (b) and their percentage differences (c). Red/blue colors indicate larger/smaller SSR for the monthly-from-3-hourly than the direct-monthly SSR.



(a) (b)

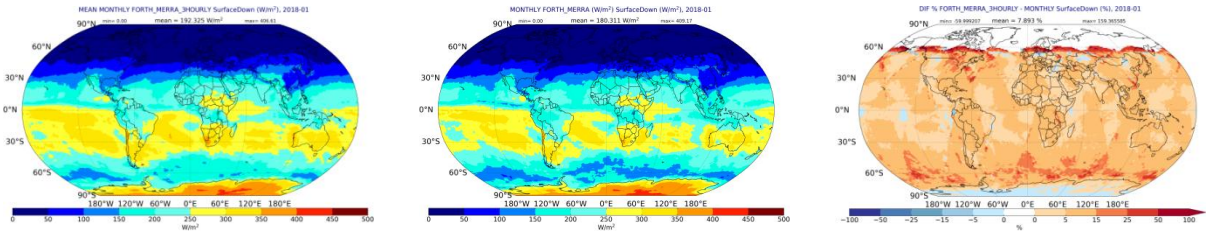
Figure AA9. Global distribution of percentage differences between FORTH-RTM SSR (Wm^{-2}) for 2018-07 from monthly means calculated by 3-hourly means and CERES SSR (a), and between FORTH-RTM direct monthly means and CERES SSR (b). Red/blue colors indicate larger/smaller SSR for CERES than the FORTH-RTM.



(a) (b)

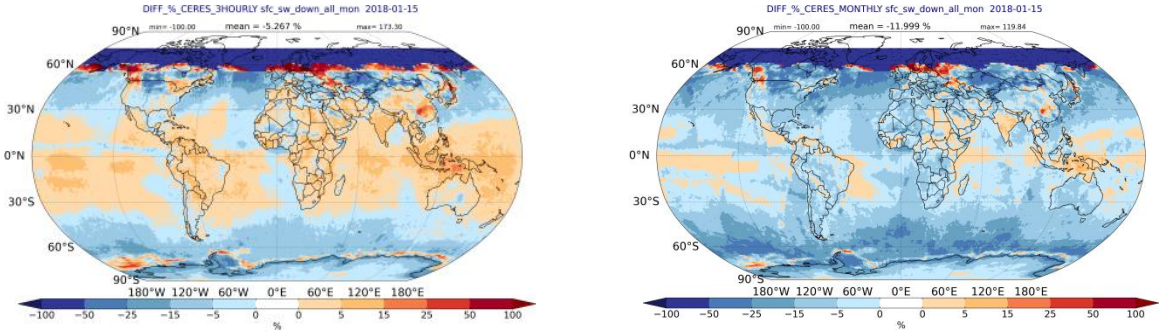
(c) (d)

Figure AA10. Scatterplot comparisons between monthly-from-3-hourly (a) and direct-monthly (b) FORTH-RTM SSR (Wm^{-2}) against BSRN for 2018-07. The corresponding global distribution of the stations is shown in c and d, respectively along with the percentage BIAS FORTH-RTM – BSRN. Red/blue colors indicate overestimation/underestimation of the FORTH-RTM SSR against BSRN stations.



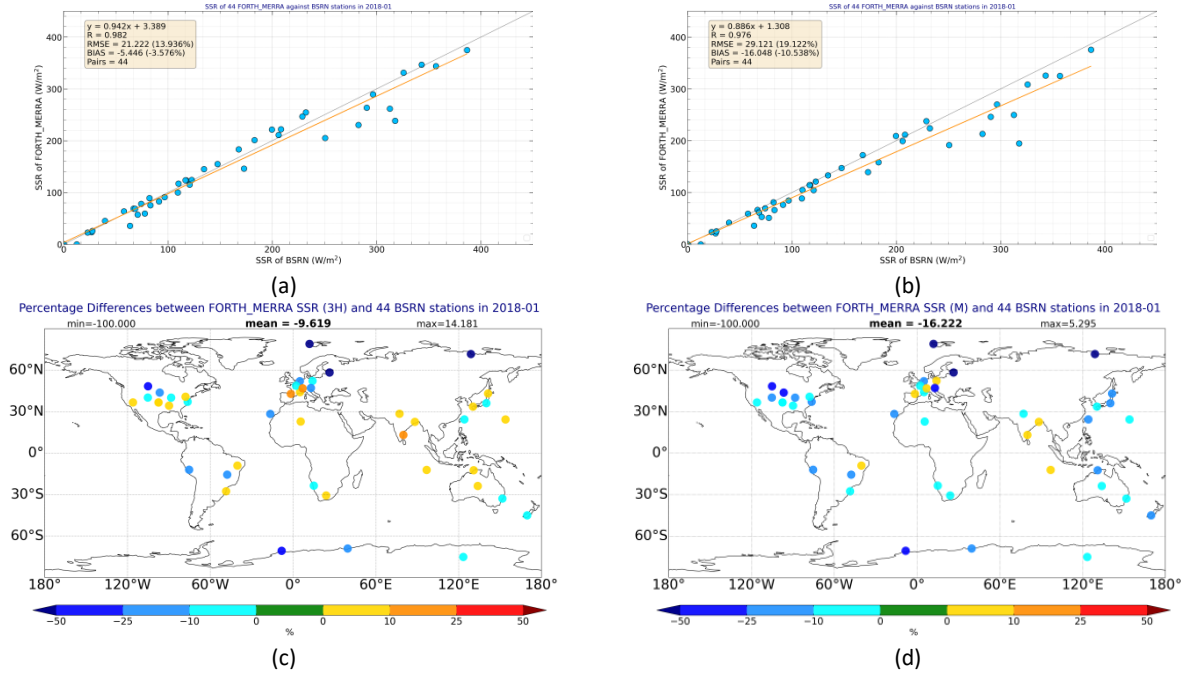
(a) (b) (c)

Figure AA11. Global distribution of average FORTH-RTM SSR (Wm^{-2}) for 2018-01 from monthly means calculated by 3-hourly means (a), direct monthly means (b) and their percentage differences (c). Red/blue colors indicate larger/smaller SSR for the monthly-from-3-hourly than the direct-monthly SSR.



(a) (b)

Figure AA12. Global distribution of percentage differences between FORTH-RTM SSR (Wm^{-2}) for 2018-01 from monthly means calculated by 3-hourly means and CERES SSR (a), and between FORTH-RTM direct monthly means and CERES SSR (b). Red/blue colors indicate larger/smaller SSR for CERES than the FORTH-RTM.



(a) (b)

(c) (d)

Figure AA13. Scatterplot comparisons between monthly-from-3-hourly (a) and direct-monthly (b) FORTH-RTM SSR (Wm^{-2}) against BSRN for 2018-01. The corresponding global distribution of the stations is shown in c and d, respectively along with the percentage BIAS FORTH-RTM – BSRN. Red/blue colors indicate overestimation/underestimation of the FORTH-RTM SSR against BSRN stations.

Appendix B

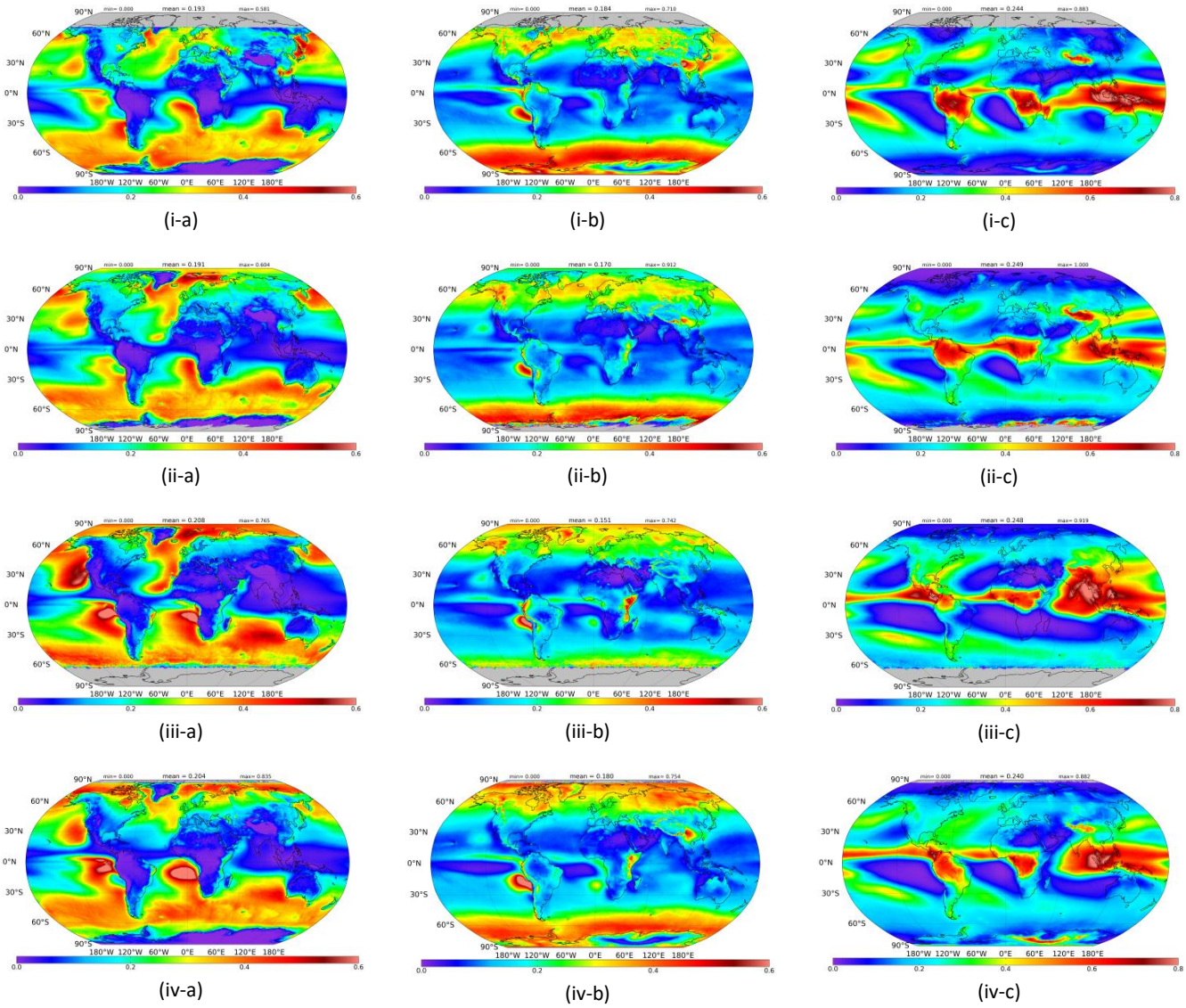


Figure AB1. Global distribution of seasonal average of CA1 (a), CA2 (b), and CA3 (c) for DJF (i), MAM (ii), JJA (iii) and SON (iv) for the 1984-2018 time period.

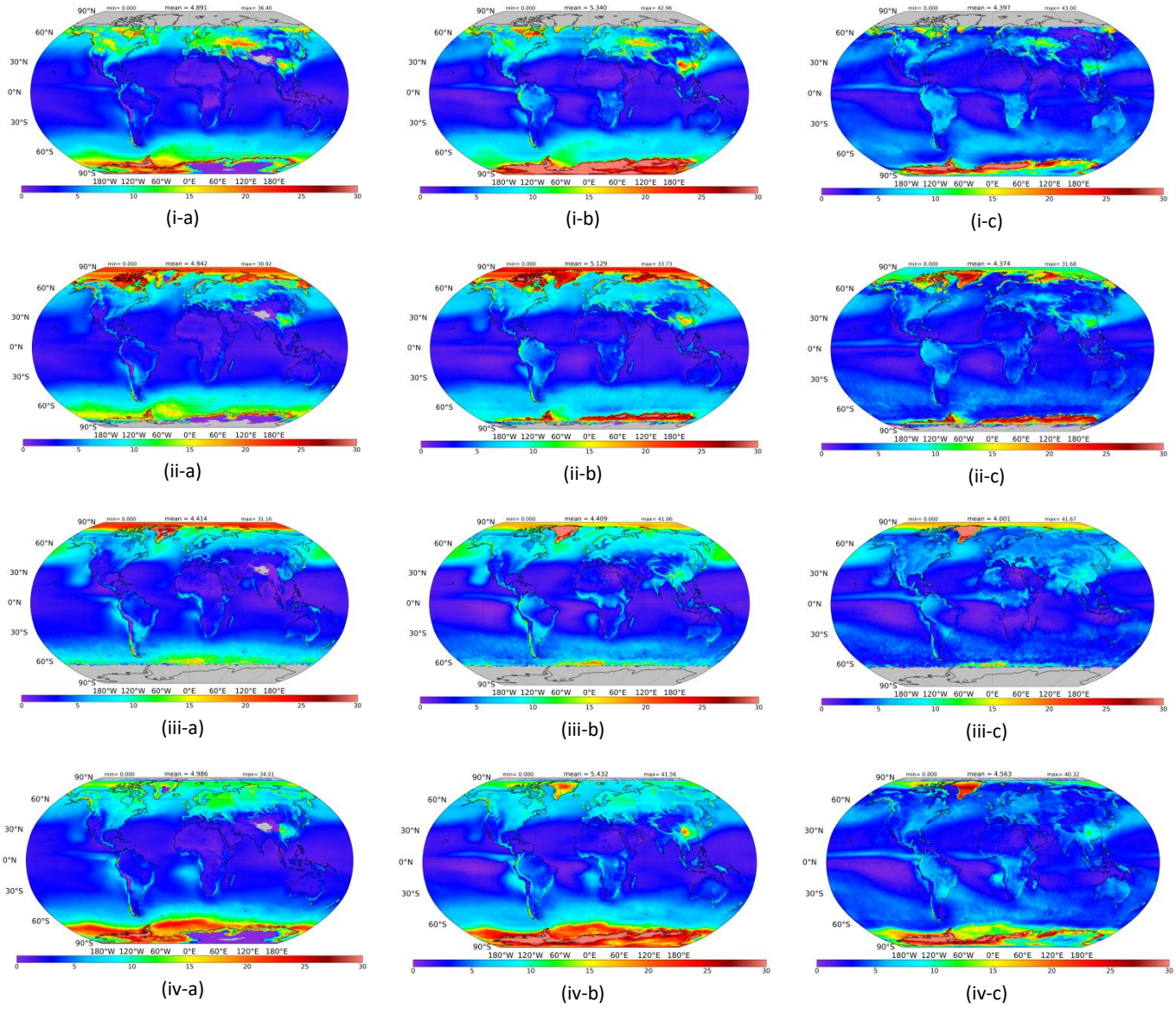


Figure AB2. Global distribution of seasonal average of COT1 (a), COT2 (b), and COT3 (c) for DJF (i), MAM (ii), JJA (iii) and SON (iv) for the 1984-2018 time period.

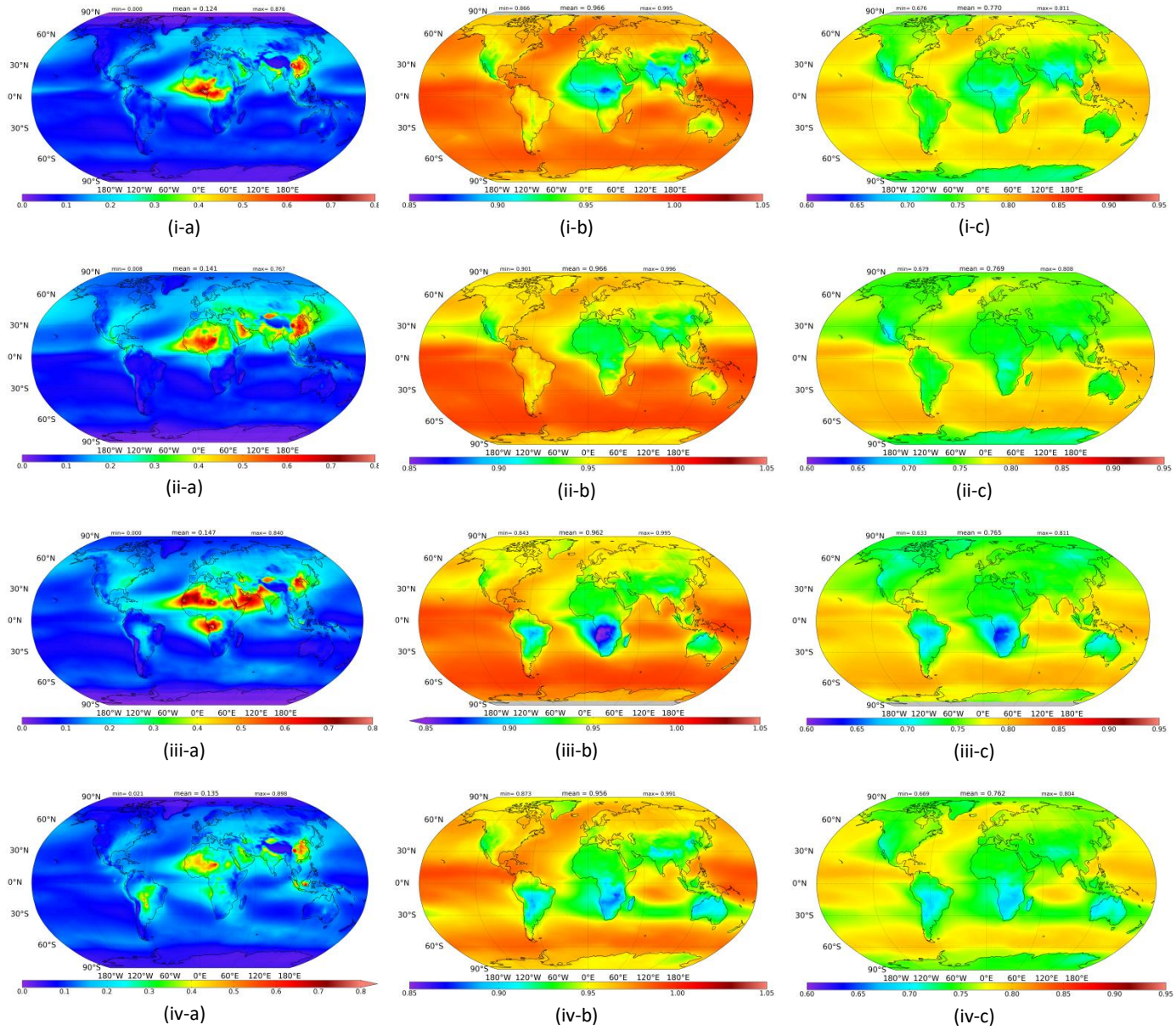


Figure AB3. Global distribution of seasonal average of AOD (a), SSA (b), and AP (c) for DJF (i), MAM (ii), JJA (iii) and SON (iv) for the 1984-2018 time period.

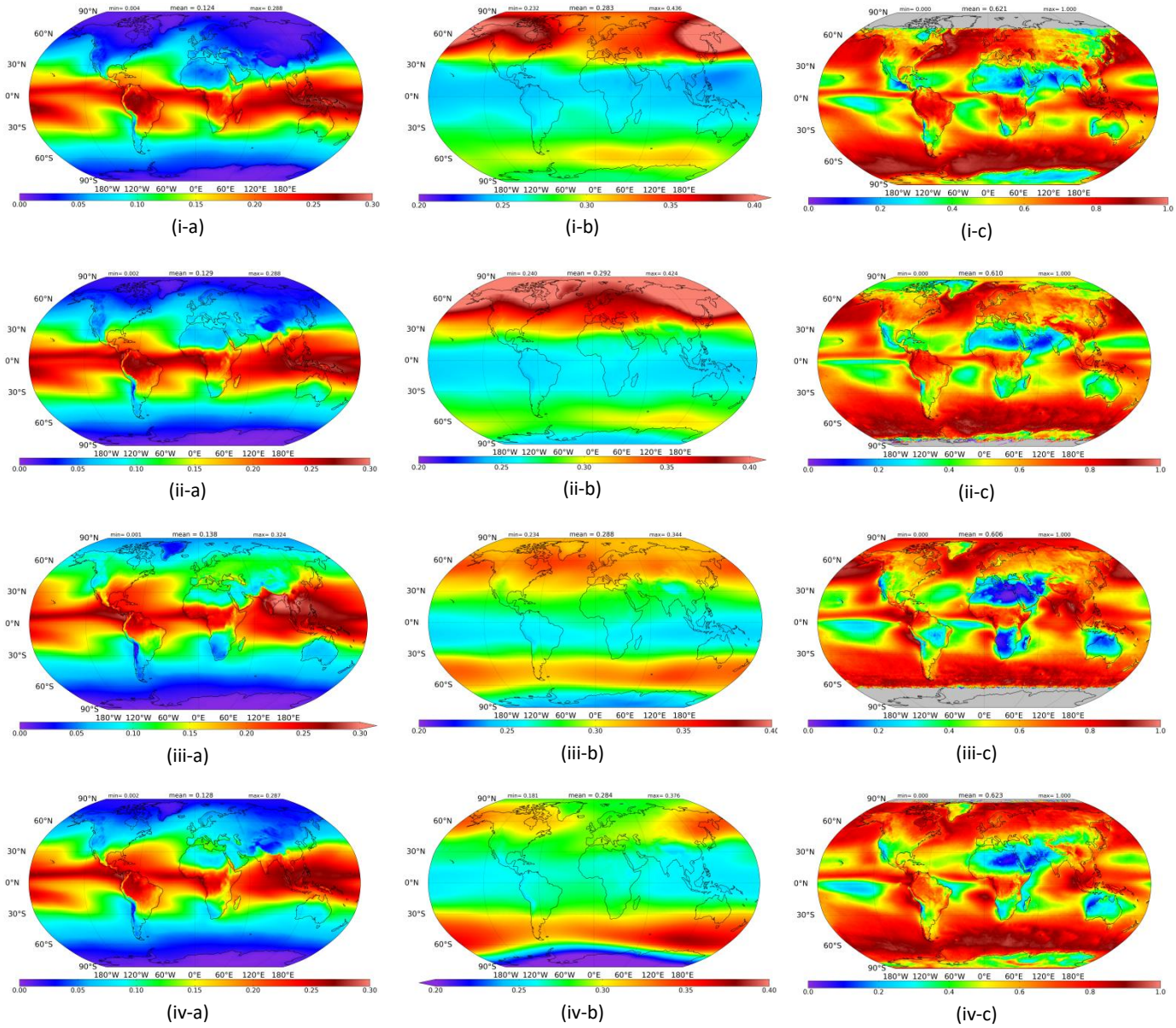


Figure AB4. Global distribution of seasonal average of water vapor (a), ozone (b), and total cloud amount (c) for DJF (i), MAM (ii), JJA (iii) and SON (iv) for the 1984-2018 time period.

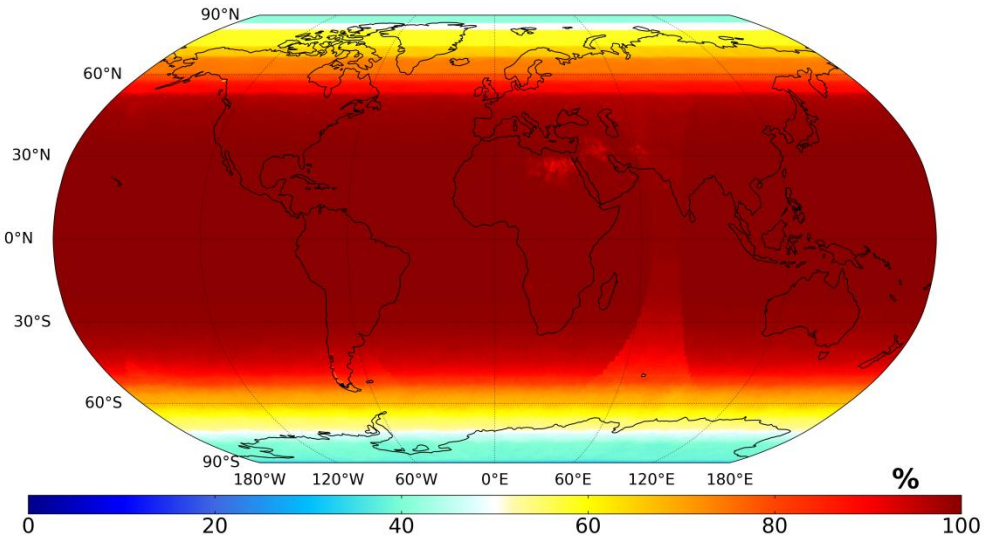


Figure AB5. Global distribution of the percentage number of the available months of FORTH-RTM over the 35-year period 01/1984 – 12/2018.

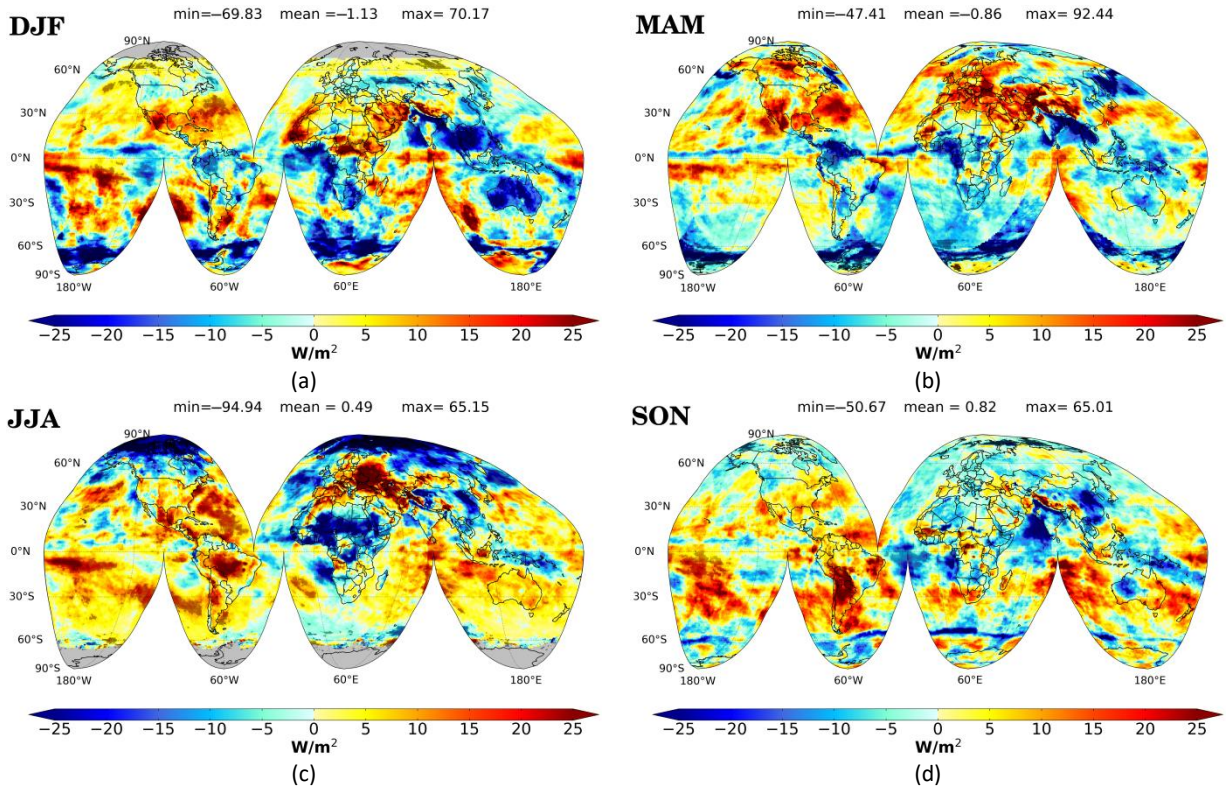


Figure AB6. Global distribution of FORTH-RTM GDB [Δ(SSR)] over the 35-year period 01/1984 – 12/2018, for (a) DJF, (b) MAM, (c) JJA, (d) SON. Reddish colors are those with positive trends (brightening), and those with bluish colors have negative trends (dimming). Statistically significant trends are indicated by black dots.

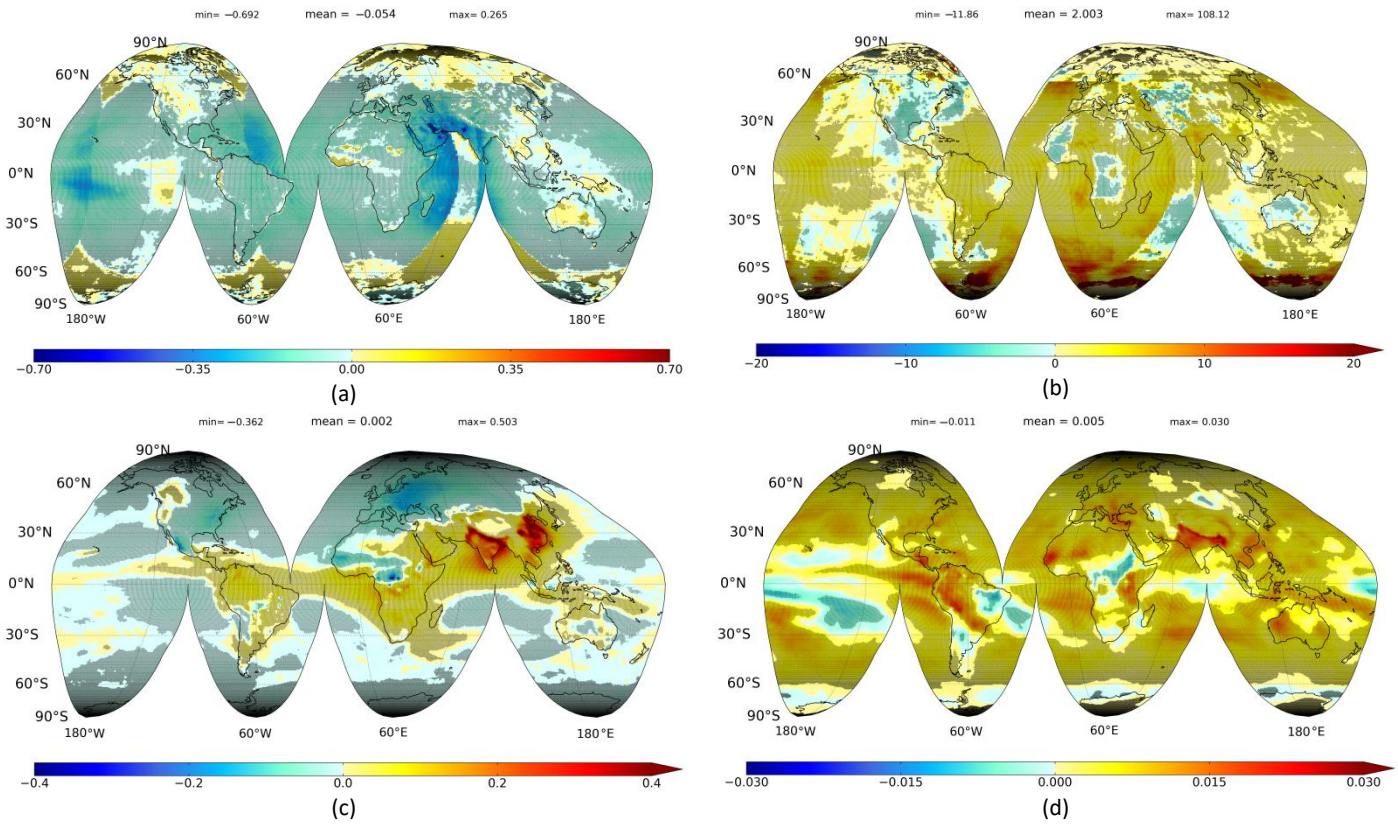


Figure AB7. Global distribution of the changes of model input data that are relevant with SSR and GDB, namely of: total cloud cover (a), total cloud optical thickness (b), aerosol optical depth (c) and water vapor (d) over the period 1984-2018. Bluish colors indicate decreasing trends, while yellow-reddish colors correspond to increasing trends. The statistically significant trends are denoted with black dots.

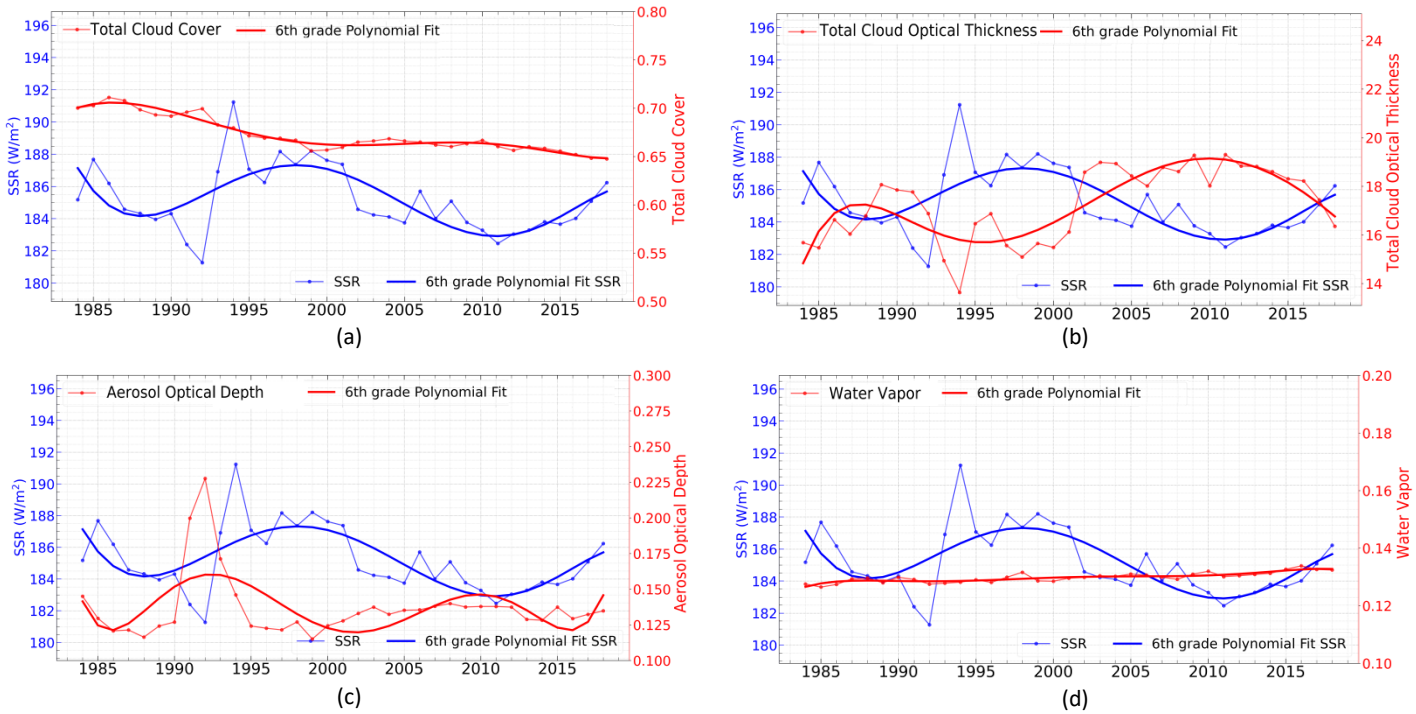


Figure AB8. Time series of annual global mean SSR (in blue) and model input data (in red) which are relevant with GDB: total cloud cover (a), total cloud optical thickness (b), aerosol optical depth (c) and water vapor (d) over the period 1984–2018.The associated 6th grade polynomial fit linesare also shown.

Appendix C

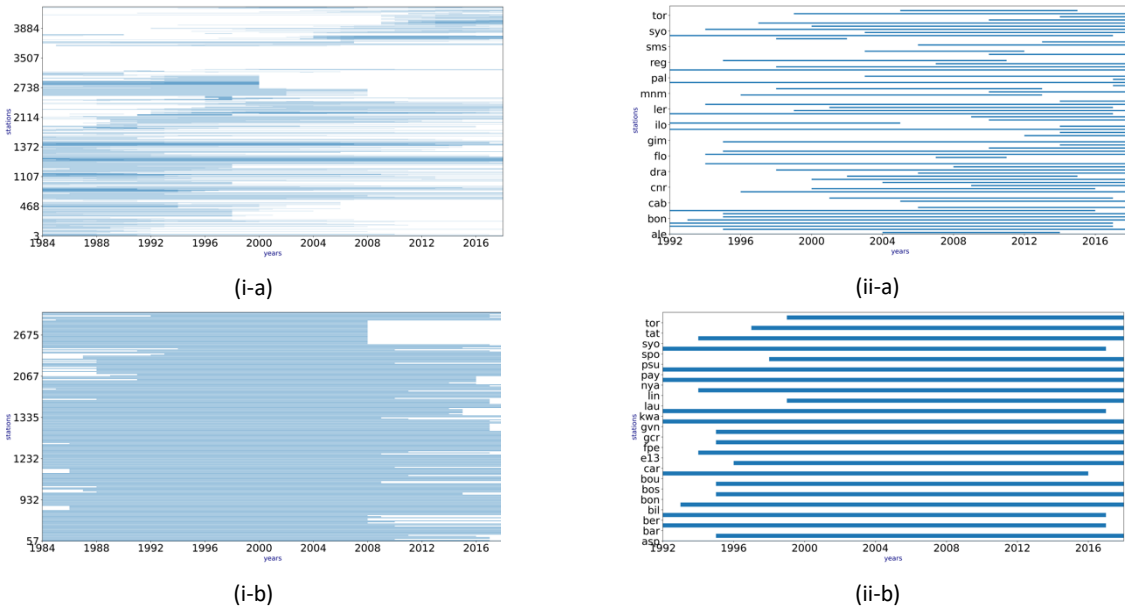


Figure AC1. Time periods covered by measurements of each station of (i) GEBA (1545 stations) and (ii) BSRN (73 stations) networks. Results are given for (a) the total number of stations since 1984 and (b) the number of available stations after applying criteria for computing linear slopes (see Section 2.2 of main paper), i.e., 222 GEBA and 22 BSRN stations.

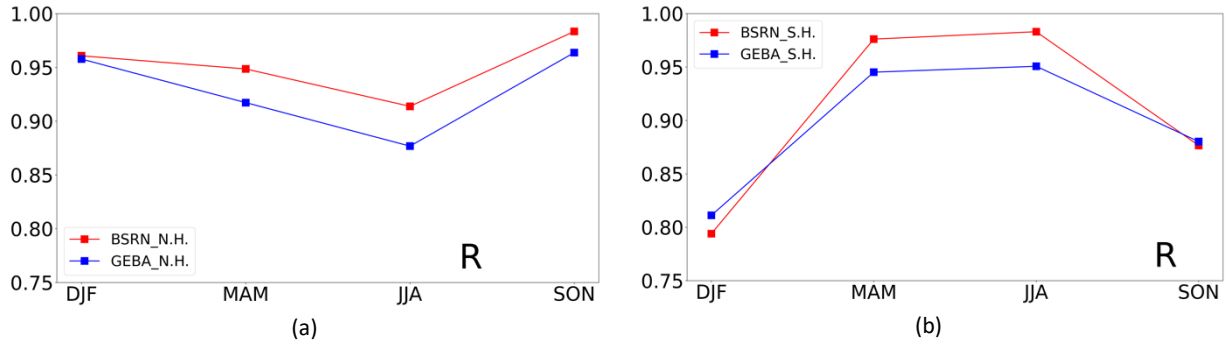


Figure AC2. Seasonal variation of hemispherical mean correlation coefficient R between FORTH-RTM and GEBA (blue color) and between FORTH-RTM and BSRN (red color) stations, computed using SSR fluxes for the North Hemisphere (a) and the South Hemisphere (b).

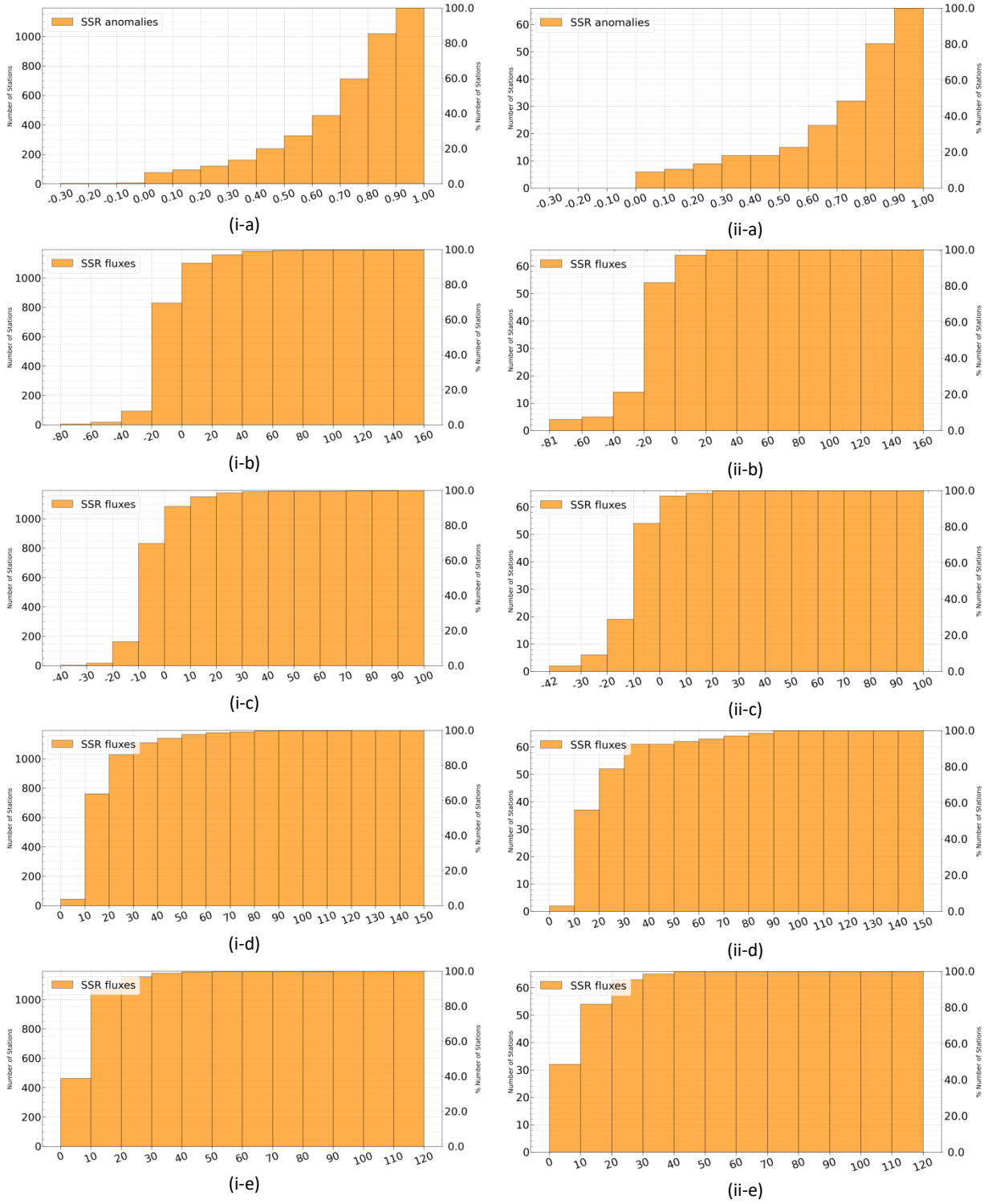
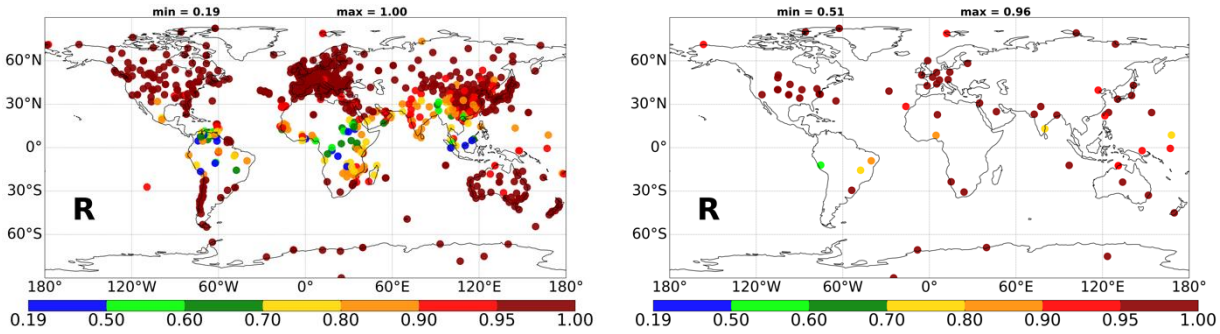


Figure AC3. Cumulative histogram distribution of correlation coefficient R (a), bias (b), relative bias (c), root mean squared error (RMSE) (d), relative RMSE (e), between FORTH and GEBA (i, left column) and BSRN (ii, right column) stations. Results are computed using FORTH-RTM, and GEBA and BSRN station SSR fluxes, except for R, which is computed using deseasonalized SSR anomalies. In the left y axis shown is the number of stations, while in the right y axis the % number of stations.



(a) (b)

Figure AC4. Global distribution of correlation coefficient between FORTH-RTM and each GEBA (a, left column) and BSRN (b, right column) station SSR fluxes.

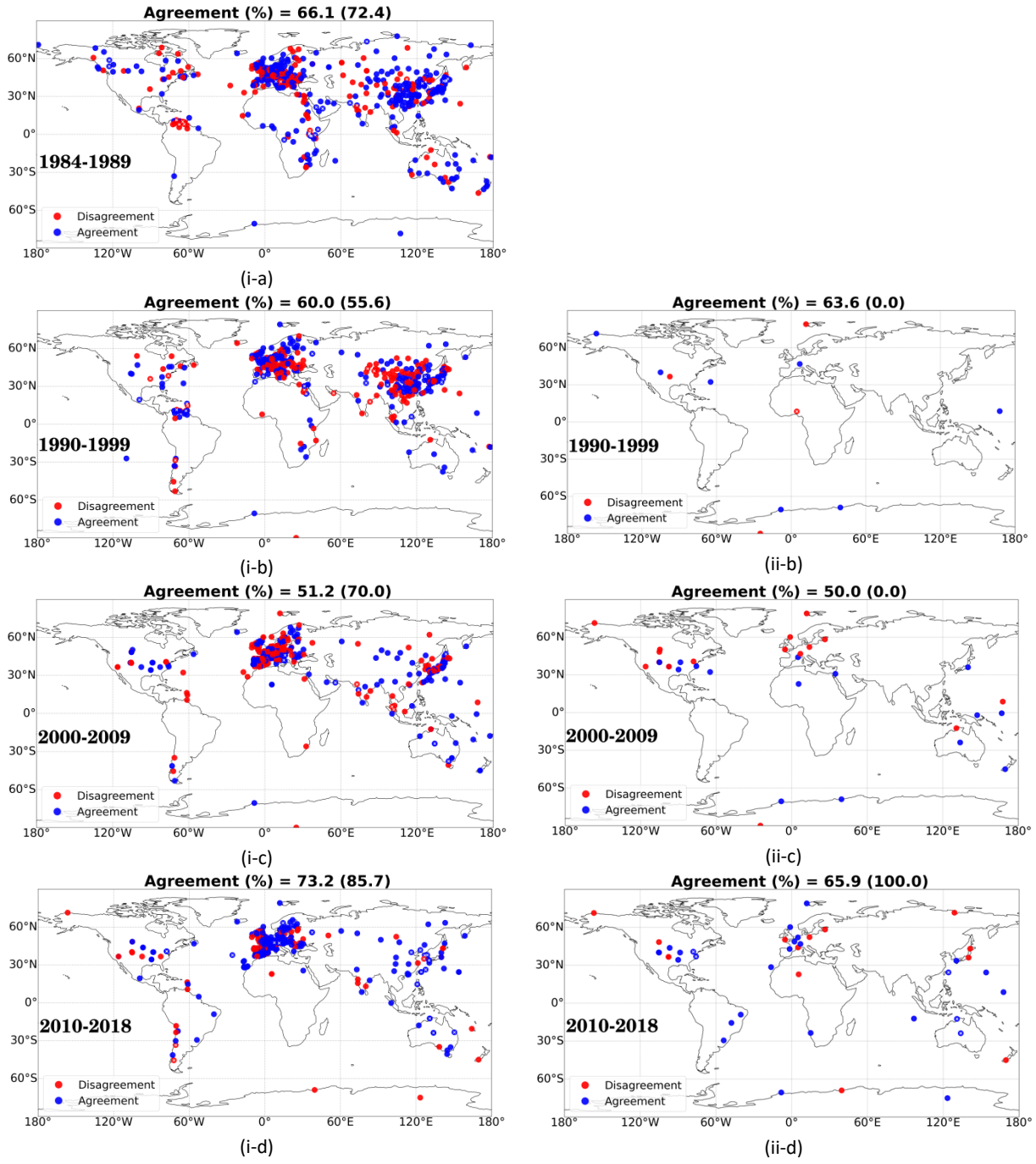


Figure AC5. Agreement (blue dots) and disagreement (red dots) between FORTH-RTM and station GDB (Δ(SSR)). The comparison is done using deseasonalized anomalies for model and GEBA (left column, i) and BSRN (right column, ii) station fluxes per selected time periods that are characterized as Global Dimming & Brightening periods (GDB phases). The embedded white x symbols indicate the statistically significant trends. At the top of each figure is indicated the percent number of stations for which there is agreement in GDB, with respect to the overall number of stations. The numbers in parentheses provide the agreement of statistically significant trends. The GDB phases (according to Wild et al., WIREs Clim. Change 2016, 7:91-107) are: (a) 1984–1989, (b) 1990–1999, (c) 2000–2009, (d) 2010–2018 for GEBA and (a) 1992–1999, (b) 2000–2009, (c) 2010–2018 for BSRN.

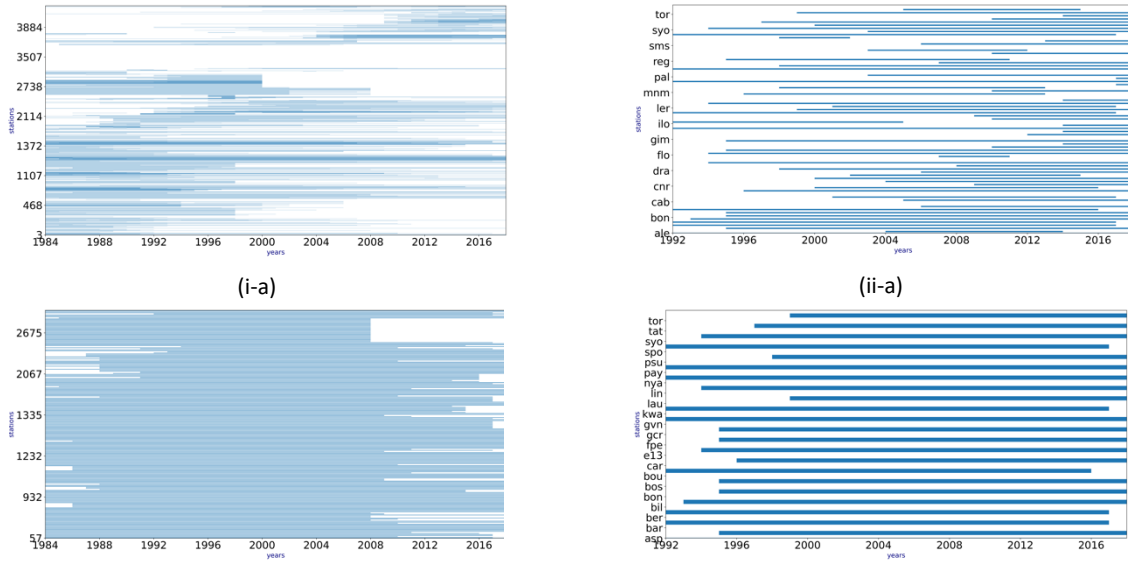


Figure AC6. Time periods covered by measurements of each station of (i) GEBA (1091 stations) and (ii) BSRN (59 stations) networks. Results are given for (a) the total number of stations since 1984 and (b) the number of available stations after applying criteria for computing linear slopes (see Section 2.2 of main paper), i.e., 211 GEBA and 23 BSRN stations.

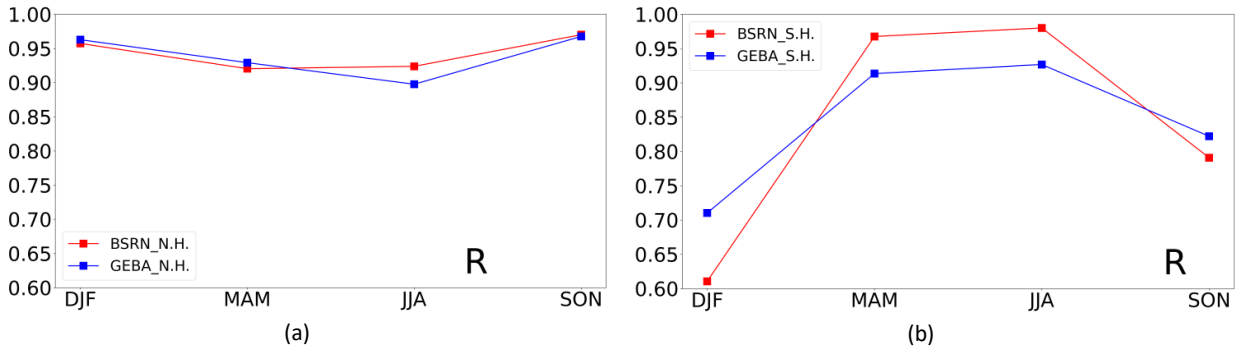


Figure AC7. Seasonal variation of hemispherical mean correlation coefficient R between FORTH-RTM and GEBA (blue color) and between FORTH-RTM and BSRN (red color) stations, computed using SSR fluxes for the North Hemisphere (a) and the South Hemisphere (b).

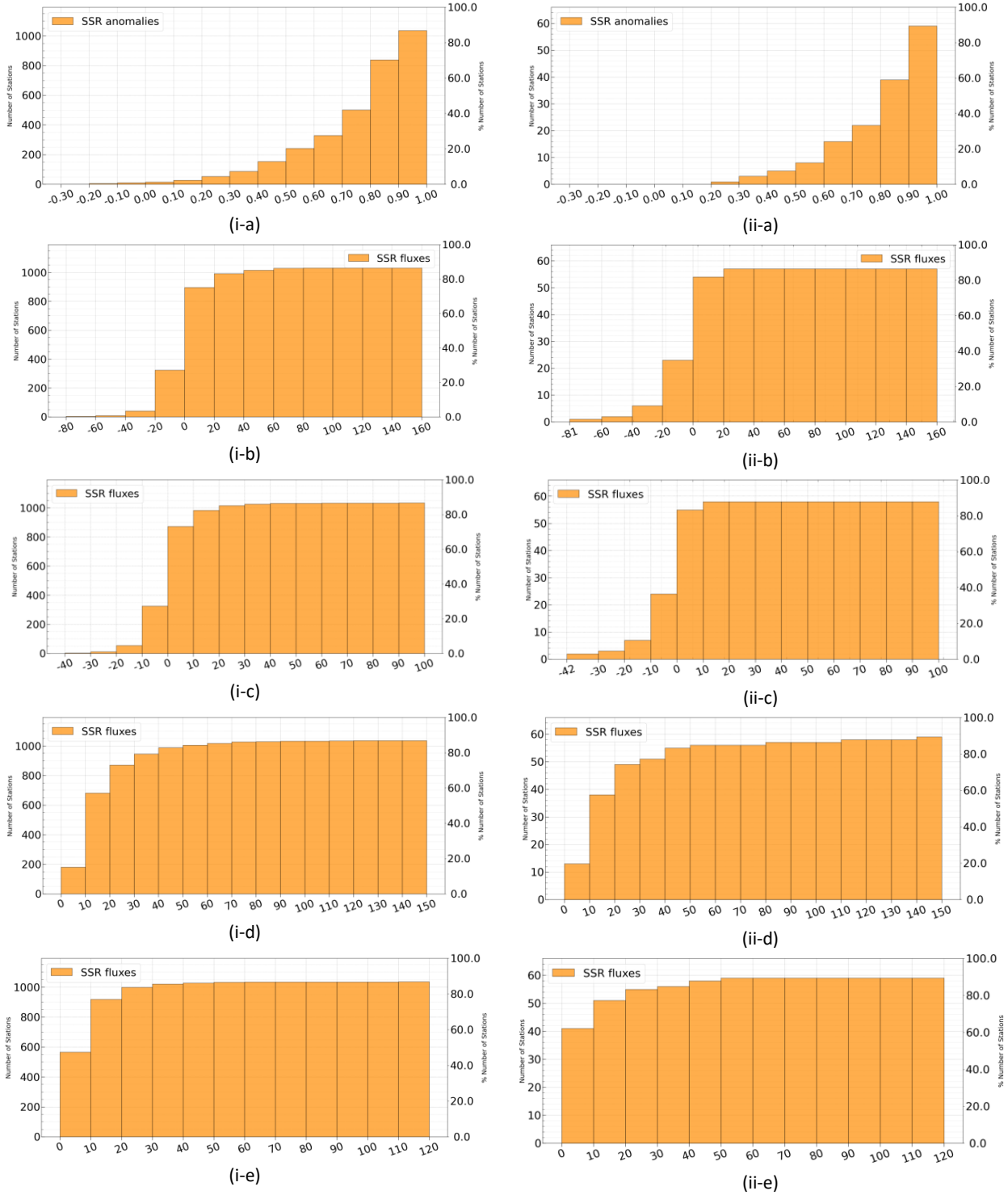
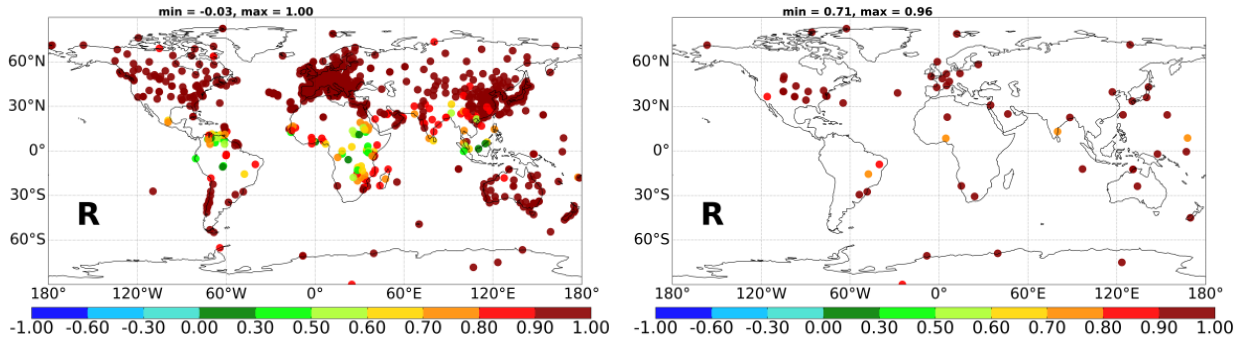


Figure AC8. Cumulative histogram distribution of correlation coefficient R (a), bias (b), relative bias (c), root mean squared error (RMSE) (d), relative RMSE (e), between FORTH and GEBA (i, left column) and BSRN (ii, right column) stations. Results are computed using FORTH-RTM, and GEBA and BSRN station SSR fluxes, except for R, which is computed using deseasonalized SSR anomalies. In the left y axis shown is the number of stations, while in the right y axis the % number of stations.



(a) (b)

Figure AC9. Global distribution of correlation coefficient between FORTH-RTM and each GEBA (a, left column) and BSRN (b, right column) station SSR fluxes.

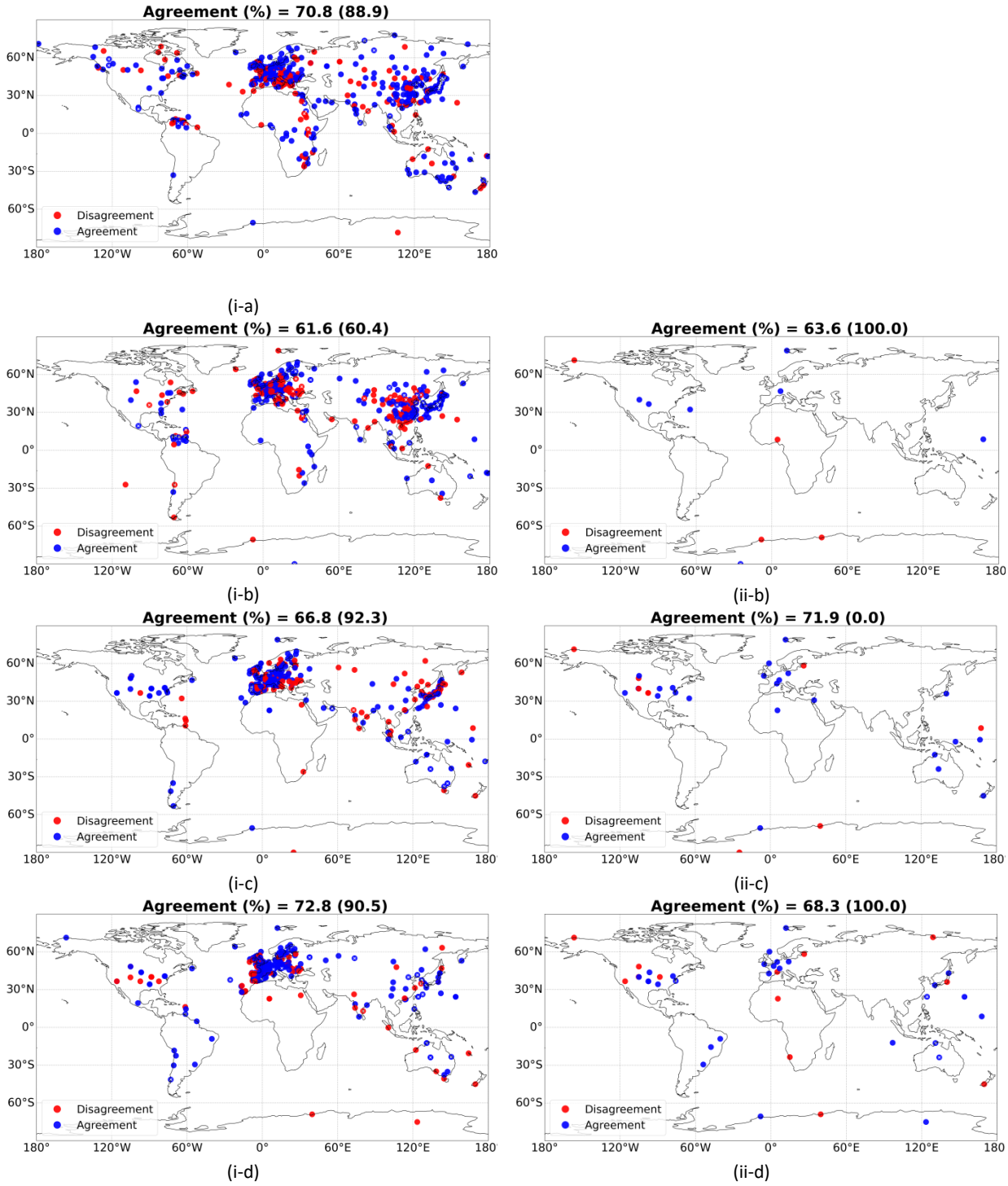


Figure AC10. Agreement (blue dots) and disagreement (red dots) between FORTH-RTM and station GDB (Δ(SSR)). The comparison is done using deseasonalized anomalies for model and GEBA (left column, i) and BSRN (right column, ii) station fluxes per selected time periods that are characterized as Global Dimming & Brightening periods (GDB phases). The embedded white x symbols indicate the statistically significant trends. At the top of each figure is indicated the percent number of stations for which there is agreement in GDB, with respect to the overall number of stations. The numbers in parentheses provide the agreement of statistically significant trends. The GDB phases (according to Wild et al., WIREs Clim. Change 2016, 7:91-107) are: (a) 1984–1989, (b) 1990–1999, (c) 2000–2009, (d) 2010–2018 for GEBA and (a) 1992–1999, (b) 2000–2009, (c) 2010–2018 for BSRN.

Appendix D

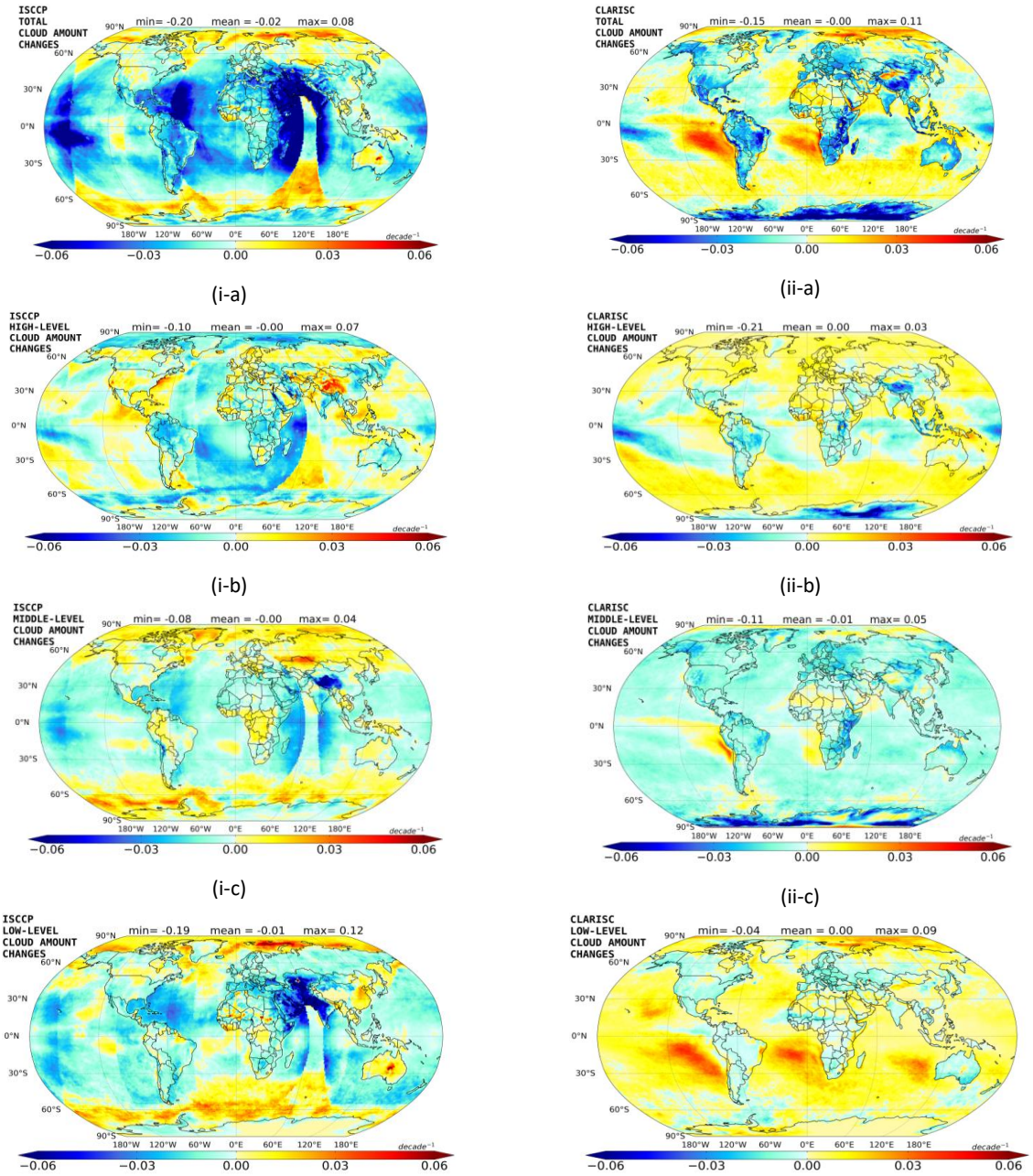


Figure AD1. Global distribution of the per decade changes in total (a), high- (b), middle- (c), and low-level (d) cloud amount for ISSCP-H (i) and CLARISC (ii) datasets during 1984-2018. Blue/reds colors indicate decreasing/increasing trends.

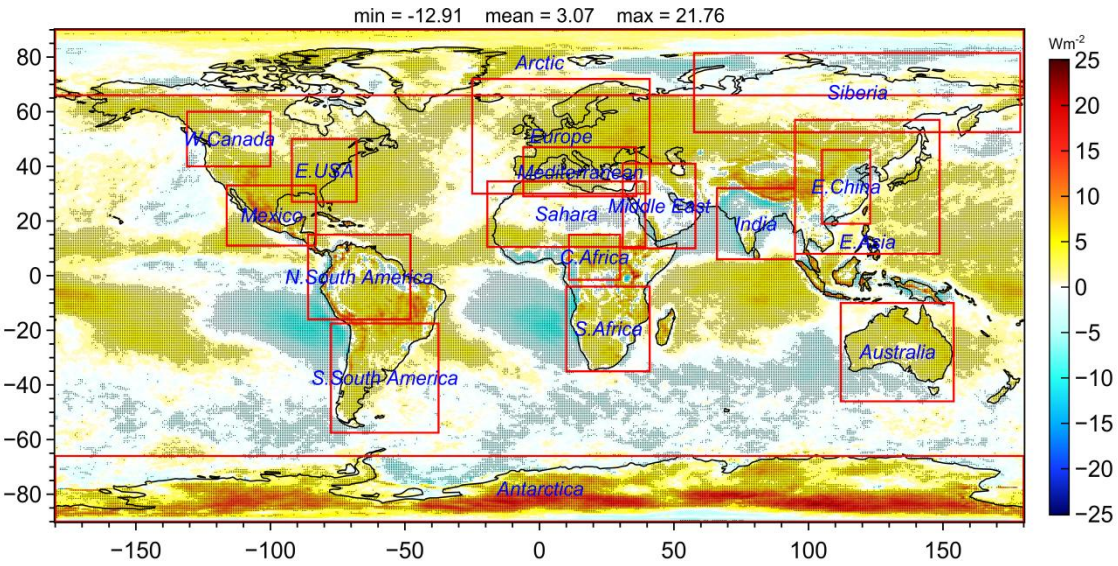
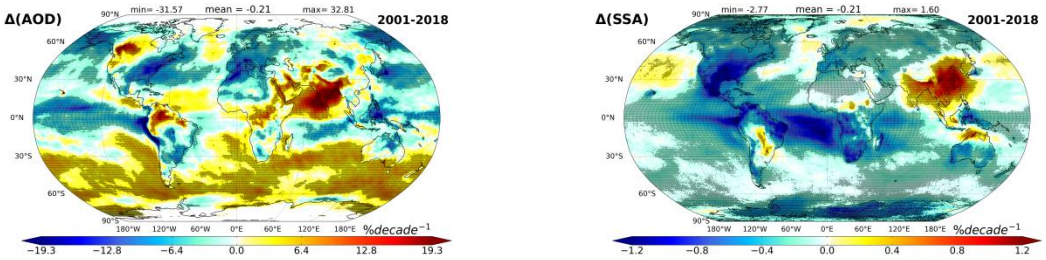


Figure AD2. Global distribution of per decade changes in SSR deseasonalized anomalies for the period 1984-2018 (the reference period for the computation of the anomalies). The red rectangles include the 18 selected land areas over which the trends and contributions to GDB are spatially averaged (Section 5.3). Red and blue colors represent increasing and decreasing trends of SSR, respectively, whilst black dots indicate pixels with statistically significant trends at the 95% confidence level. The values at the top of the map represent the minimum, mean, and maximum per decade trend across the globe.



(a) (b)

Figure AD3. Global distribution of % per decade changes in the aerosol optical depth (AOD, a) and the aerosol single scattering albedo (SSA, b) during 2001-2018. Reddish/bluish colors indicate increasing/decreasing trends while black dots indicate pixels with statistically significant trends.

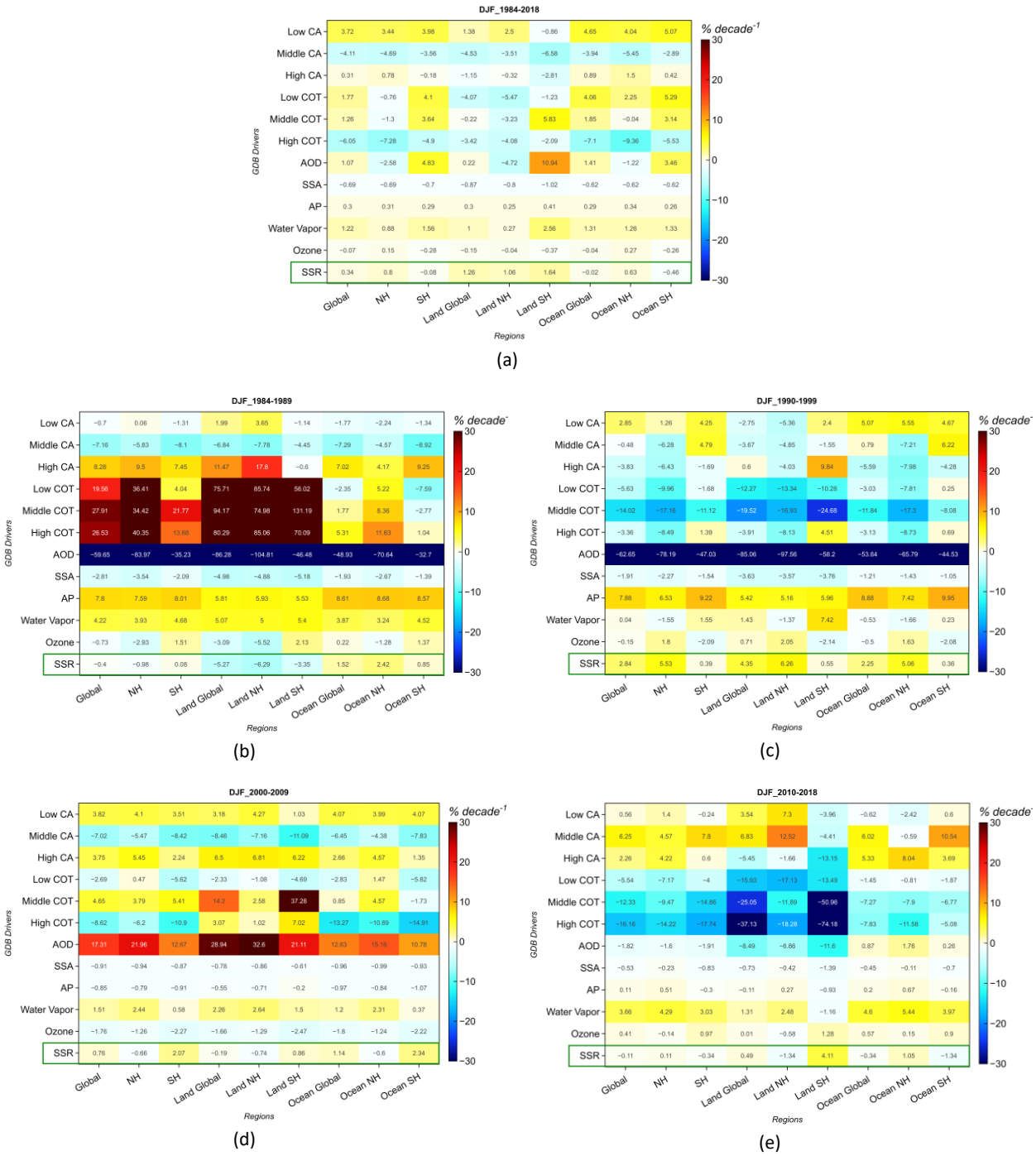


Figure AD4. The spatially averaged percentage per decade changes of the GDB drivers over the globe, the two hemispheres and the globe's and the two hemispheres' land and ocean areas during the entire study period 1984-2018 (a), as well as during 1984-1989 (b), 1990-1999 (c), 2000-2009 (d) and 2010-2018 (e) for the DJF season. Reddish/bluish colors indicate increasing/decreasing trends of the drivers and RTM input parameters along with the SSR in the last row.

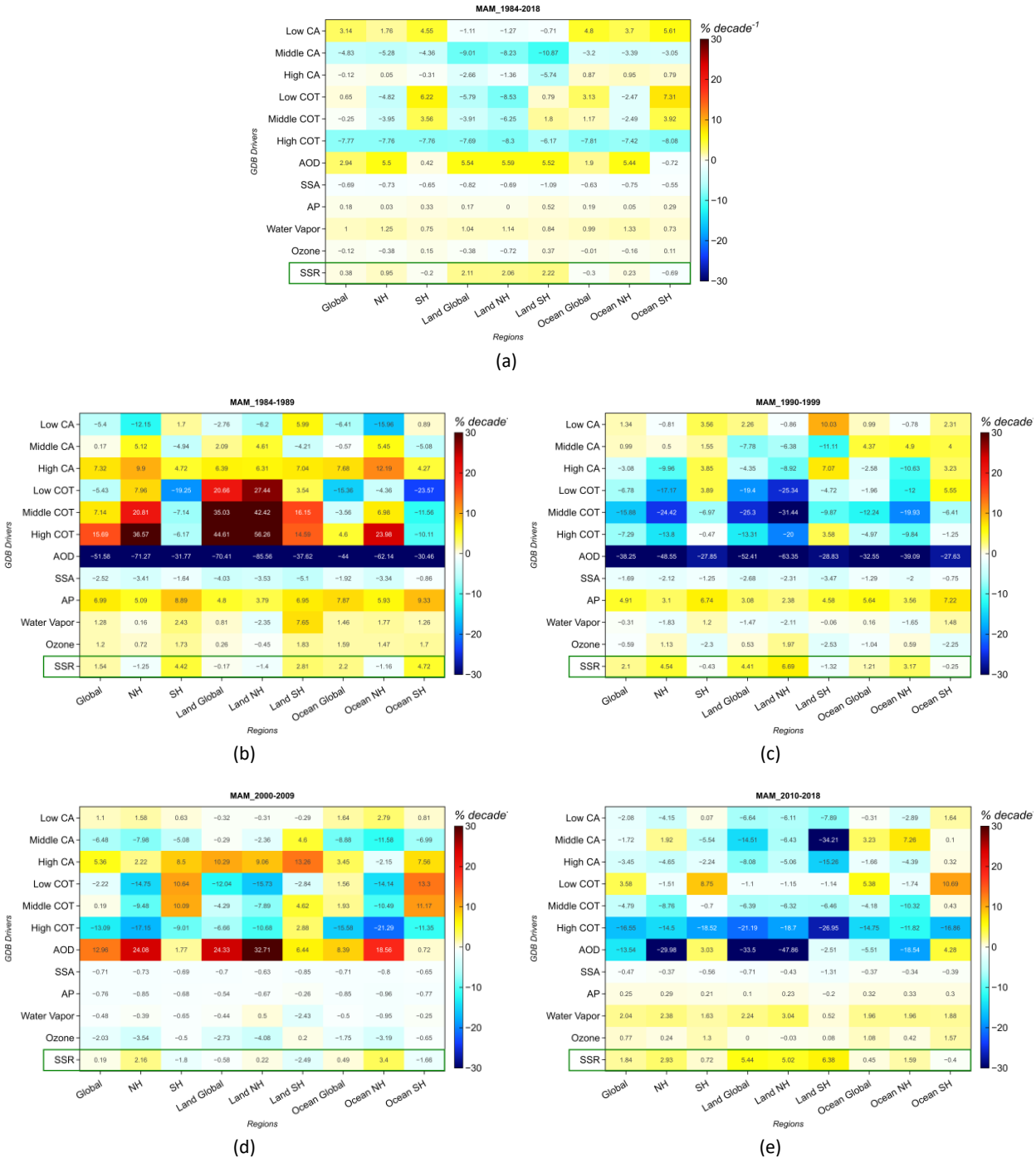


Figure AD5. The spatially averaged percentage per decade changes of the GDB drivers over the globe, the two hemispheres and the globe's and the two hemispheres' land and ocean areas during the entire study period 1984-2018 (a), as well as during 1984-1989 (b), 1990-1999 (c), 2000-2009 (d) and 2010-2018 (e) for the MAM season. Reddish/bluish colors indicate increasing/decreasing trends of the drivers and RTM input parameters along with the SSR in the last row.

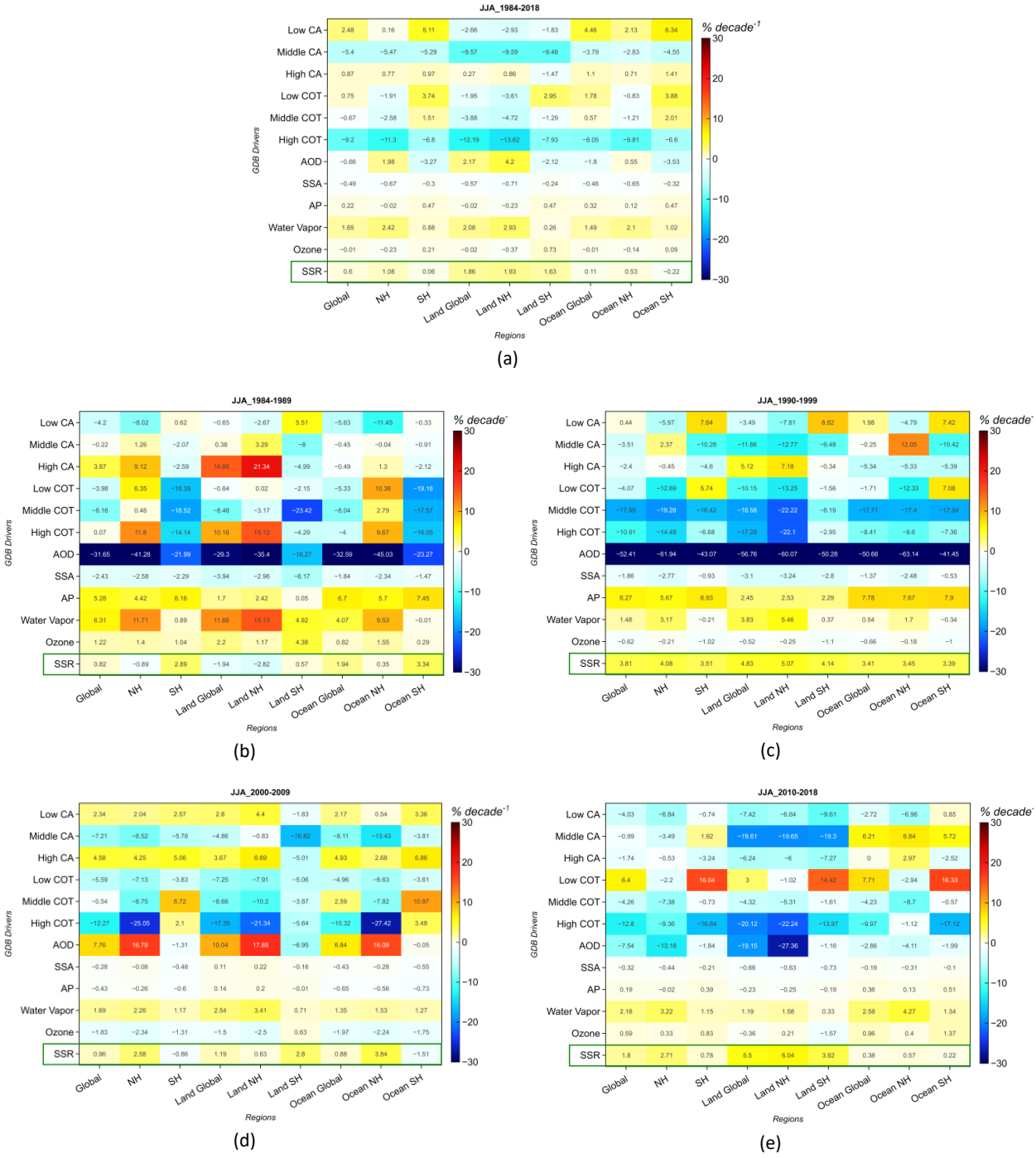


Figure AD6. The spatially averaged percentage per decade changes of the GDB drivers over the globe, the two hemispheres and the globe's and the two hemispheres' land and ocean areas during the entire study period 1984-2018 (a), as well as during 1984-1989 (b), 1990-1999 (c), 2000-2009 (d) and 2010-2018 (e) for the JJA season. Reddish/bluish colors indicate increasing/decreasing trends of the drivers and RTM input parameters along with the SSR in the last row.

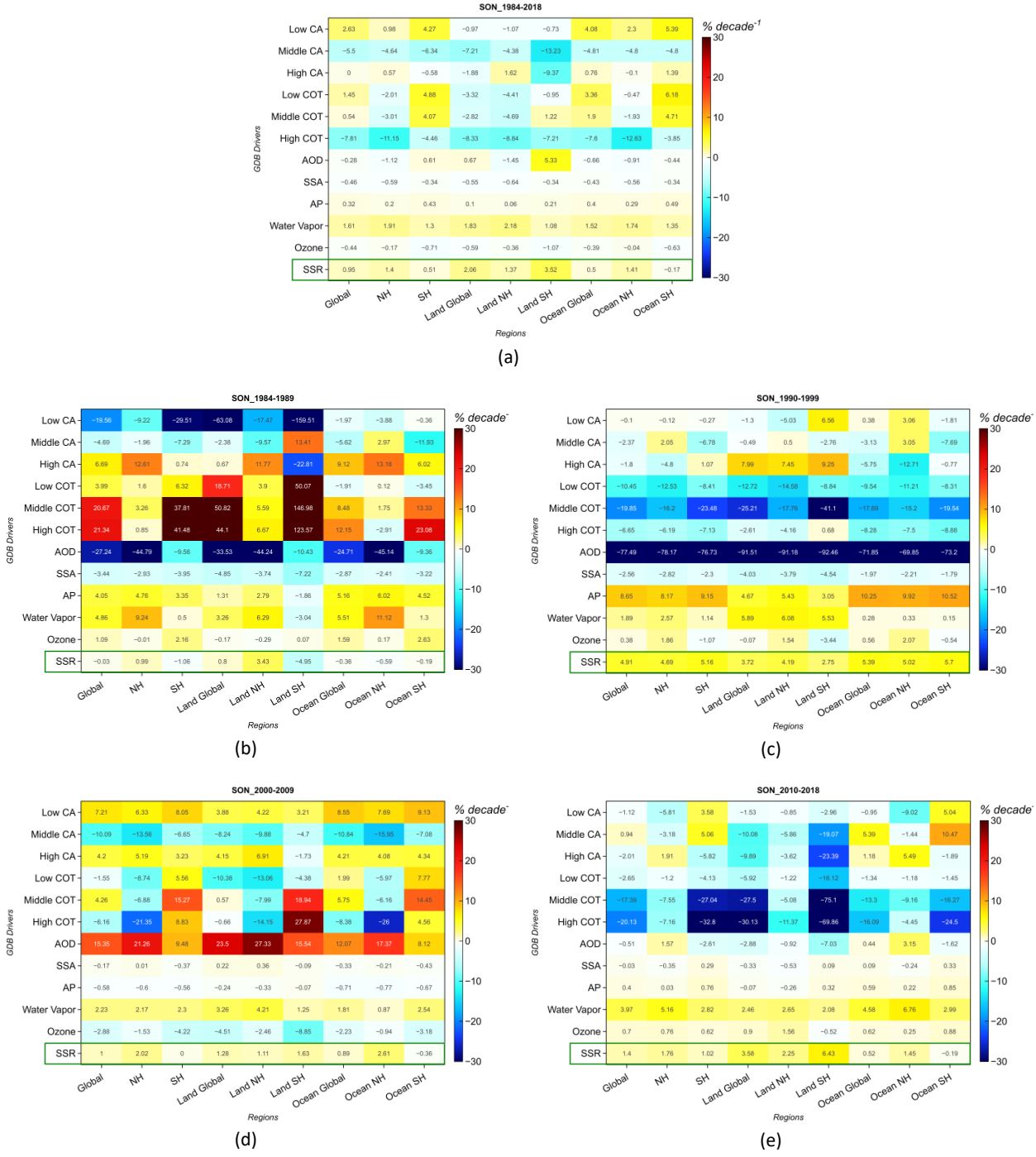


Figure AD7. The spatially averaged percentage per decade changes of the GDB drivers over the globe, the two hemispheres and the globe's and the two hemispheres' land and ocean areas during the entire study period 1984-2018 (a), as well as during 1984-1989 (b), 1990-1999 (c), 2000-2009 (d) and 2010-2018 (e) for the SON season. Reddish/bluish colors indicate increasing/decreasing trends of the drivers and RTM input parameters along with the SSR in the last row.

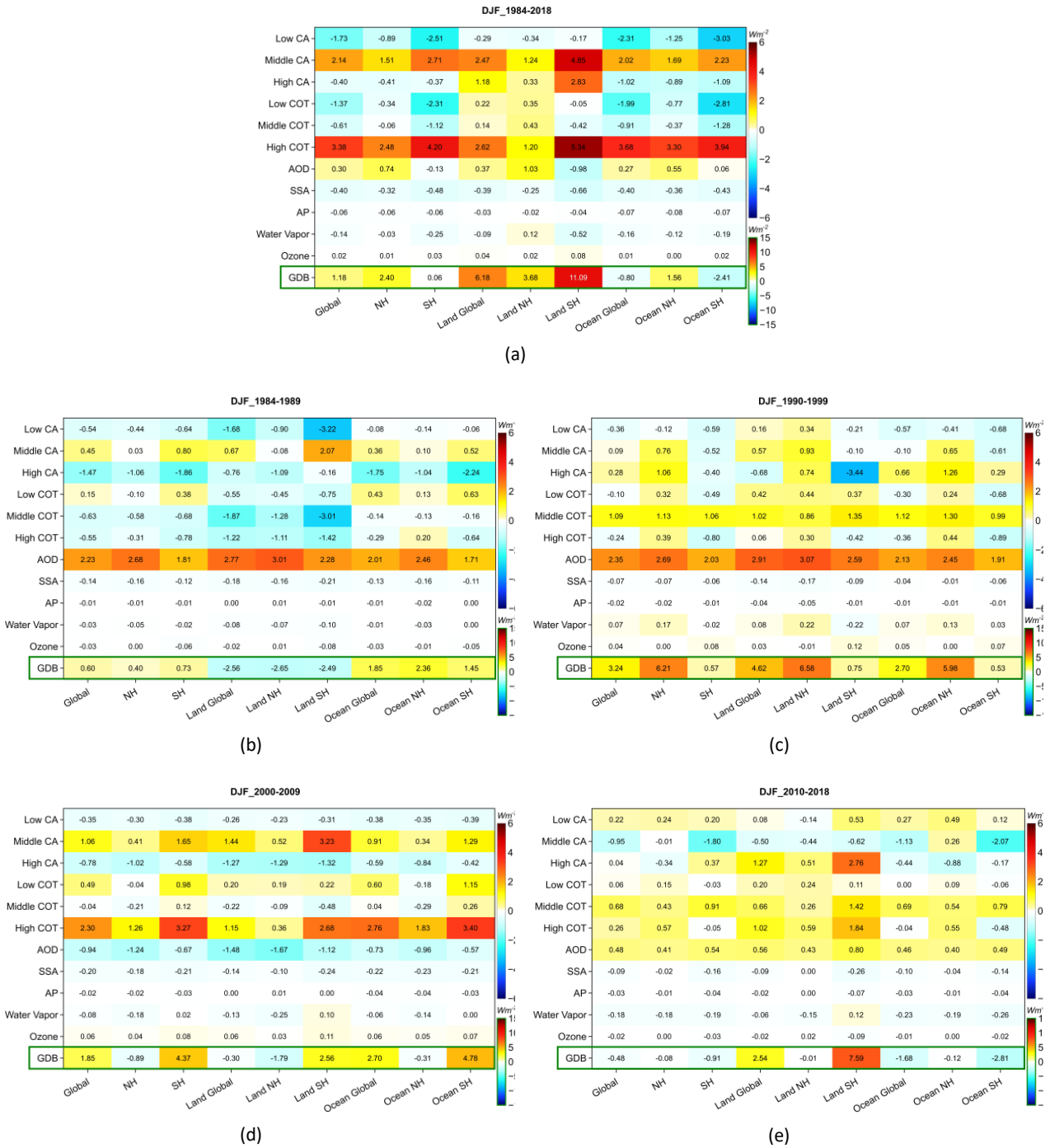
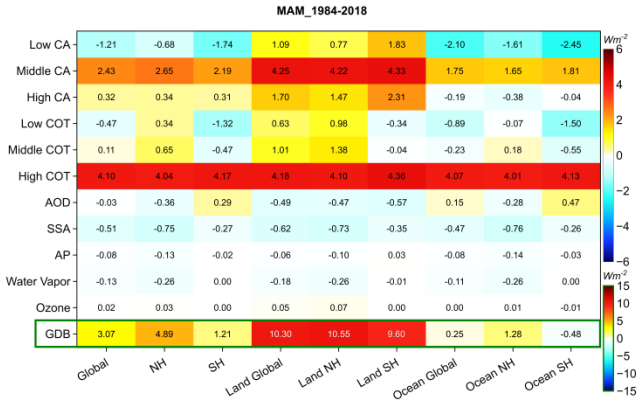
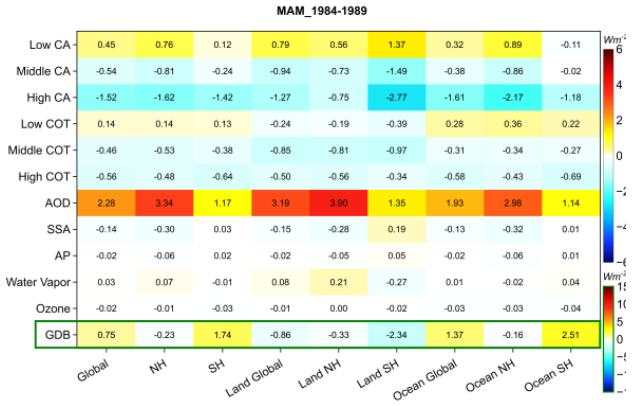


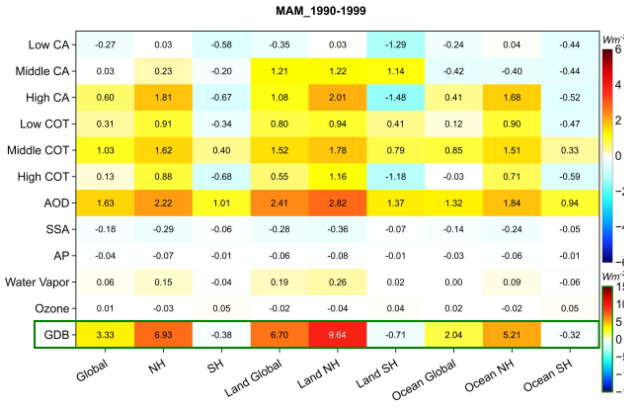
Figure AD8. The spatially averaged contribution to GDB (in Wm^{-2}) of each GDB driver over the globe, the two hemispheres and the globe's and the two hemispheres' land and ocean areas during the entire study period 1984-2018 (a), as well as during 1984-1989 (b), 1990-1999 (c), 2000-2009 (d) and 2010-2018 (e) for the DJF season. Reddish/bluish colors indicate contribution/counteraction to the overall estimated brightening or counteraction/contribution to the overall estimated dimming. The last row includes the corresponding overall GDB in Wm^{-2} with reddish colors indicating brightening and bluish dimming.



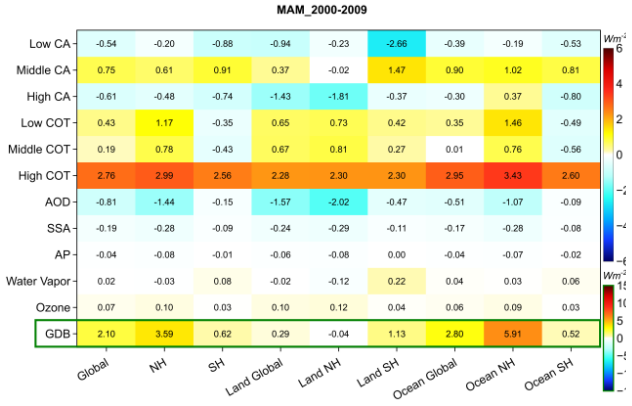
(a)



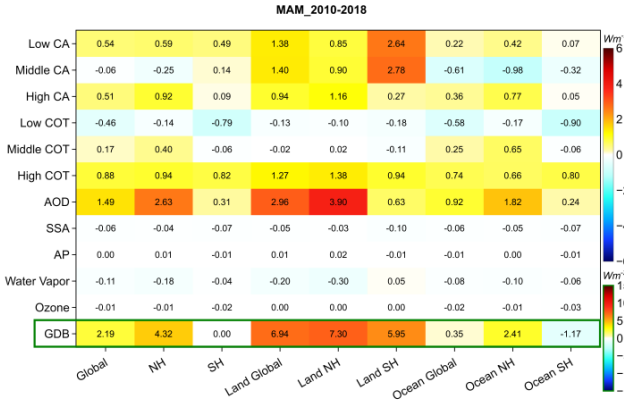
(b)



(c)

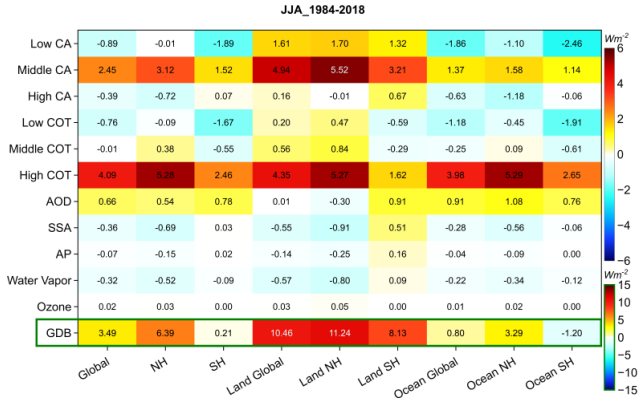


(d)

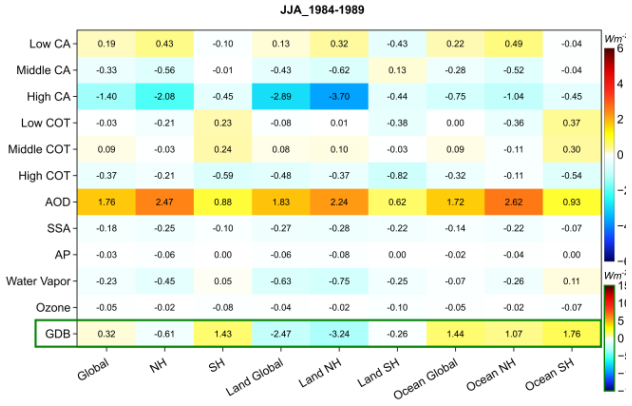


(e)

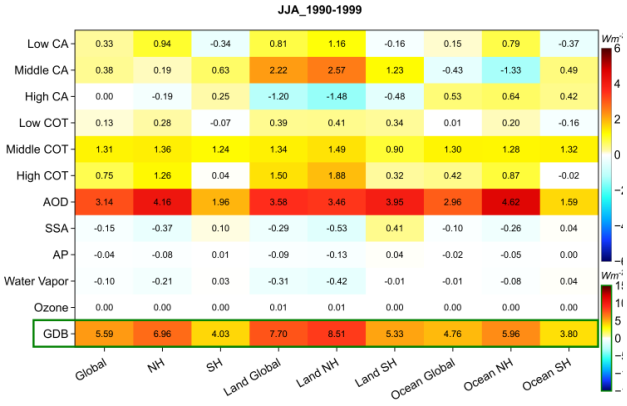
Figure AD9. The spatially averaged contribution to GDB (in Wm^{-2}) of each GDB driver over the globe, the two hemispheres and the globe's and the two hemispheres' land and ocean areas during the entire study period 1984-2018 (a), as well as during 1984-1989 (b), 1990-1999 (c), 2000-2009 (d) and 2010-2018 (e) for the MAM season. Reddish/bluish colors indicate contribution/counteraction to the overall estimated brightening or counteraction/contribution to the overall estimated dimming. The last row includes the corresponding overall GDB in Wm^{-2} with reddish colors indicating brightening and bluish dimming.



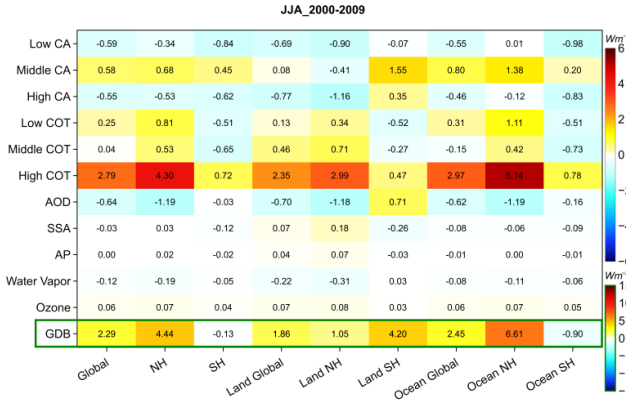
(a)



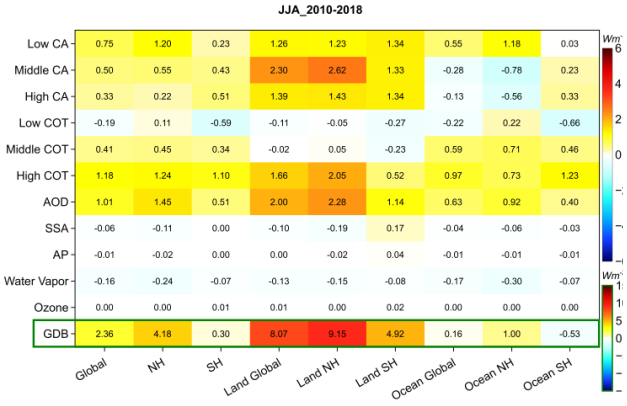
(b)



(c)



(d)



(e)

Figure AD10. The spatially averaged contribution to GDB (in Wm^{-2}) of each GDB driver over the globe, the two hemispheres and the globe's and the two hemispheres' land and ocean areas during the entire study period 1984-2018 (a), as well as during 1984-1989 (b), 1990-1999 (c), 2000-2009 (d) and 2010-2018 (e) for the JJA season. Reddish/bluish colors indicate contribution/counteraction to the overall estimated brightening or counteraction/contribution to the overall estimated dimming. The last row includes the corresponding overall GDB in Wm^{-2} with reddish colors indicating brightening and bluish dimming.

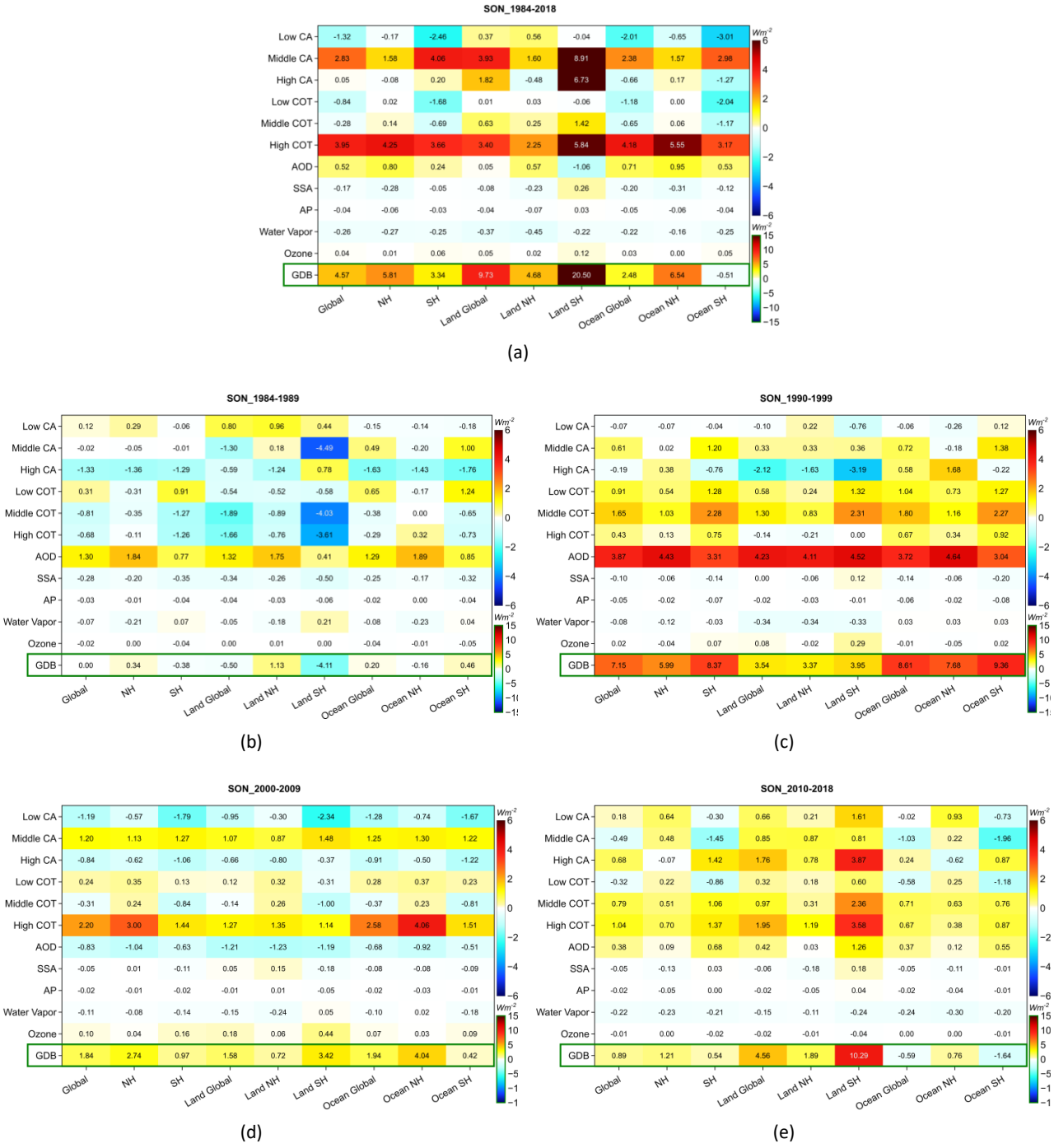


Figure AD11. The spatially averaged contribution to GDB (in Wm^{-2}) of each GDB driver over the globe, the two hemispheres and the globe's and the two hemispheres' land and ocean areas during the entire study period 1984-2018 (a),as well as during 1984-1989 (b), 1990-1999 (c), 2000-2009 (d) and 2010-2018 (e) for the SON season. Reddish/bluish colors indicate contribution/counteraction to the overall estimated brightening or counteraction/contribution to the overall estimated dimming. The last row includes the corresponding overall GDB in Wm^{-2} with reddish colors indicating brightening and bluish dimming.

Appendix E

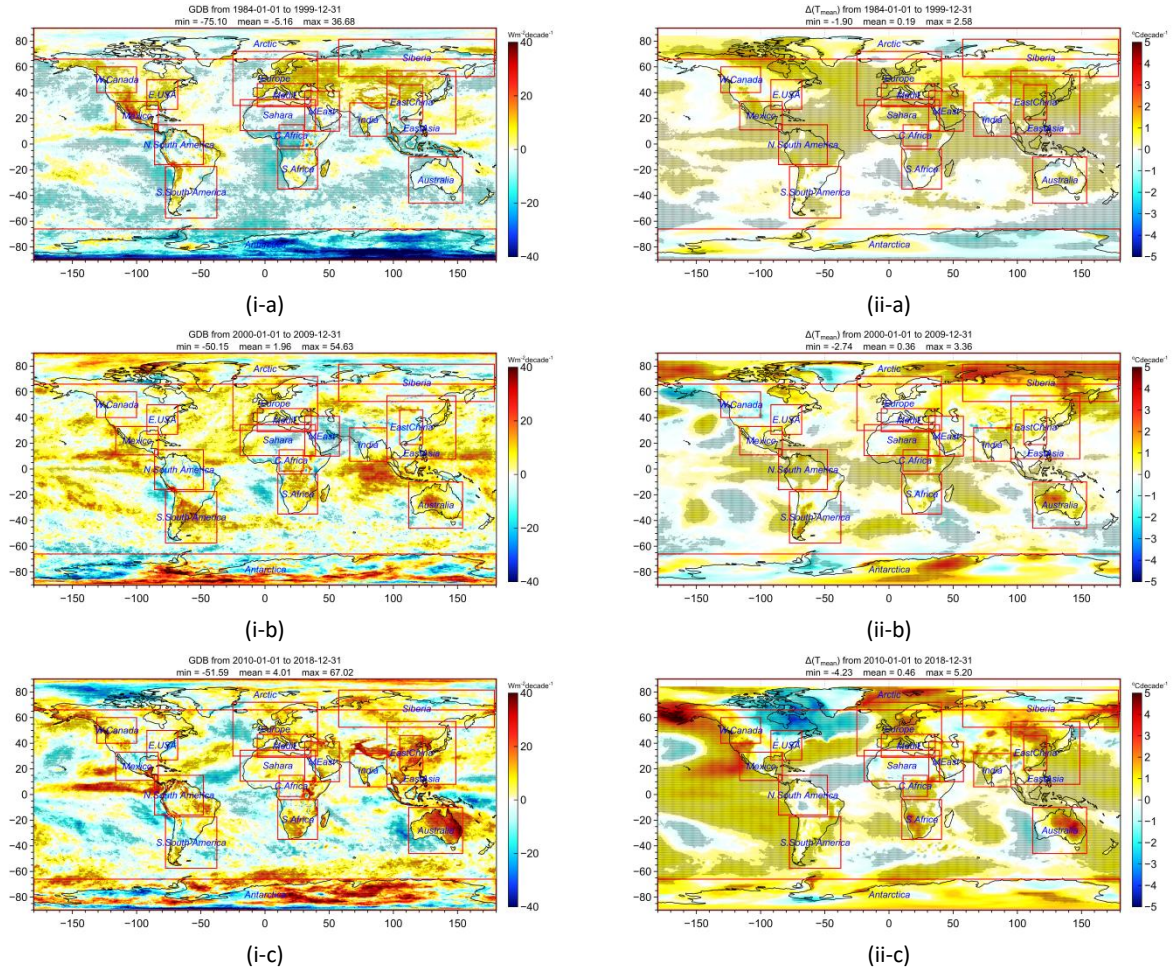
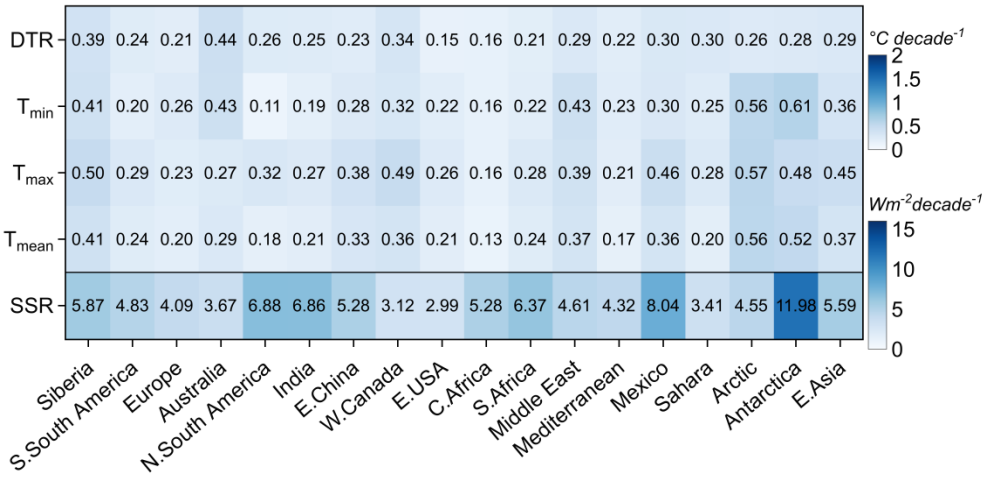


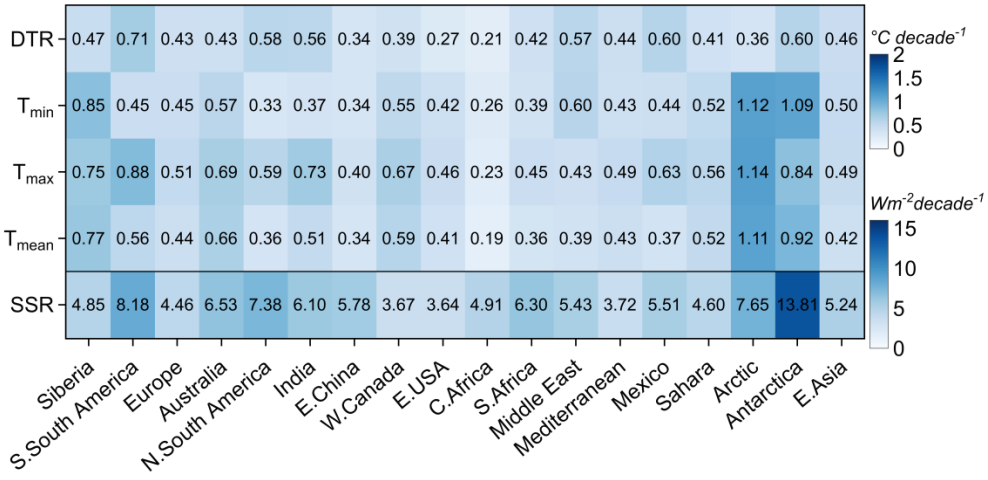
Figure AE1. Global distribution of the per decade changes of SSR (i) and T_{mean} (ii) deseasonalized anomalies for the periods 1984-1999 (a), 2000-2009 (b) and 2010-2018 (c), which are also the reference periods of the anomalies. The 18 selected land areas, over which the trends were spatially averaged, are denoted by the red rectangles. Red/blue colors indicate increasing/decreasing trends, while black dots indicate pixels with statistically significant trends at the 95% confidence level. The values at the top of each figure are the minimum, the mean and the maximum per decade trend over all the continental areas of the globe.

Table AE1. The annual changes of SSR (in $Wm^{-2}decade^{-1}$), T_{mean}, T_{max}, T_{min} and DTR (in $^{o}Cdecade^{-1}$) over the global, northern hemispheric (NH), and southern hemispheric (SH) land and oceans during the time periods of 1984-1999, 2000-2009, 2010-2018 and during the entire study period 1984-2018. The numbers in brackets represents the lower and upper bounds of changes, while in bold are the trends that are statistically significant at the 95% confidence level.

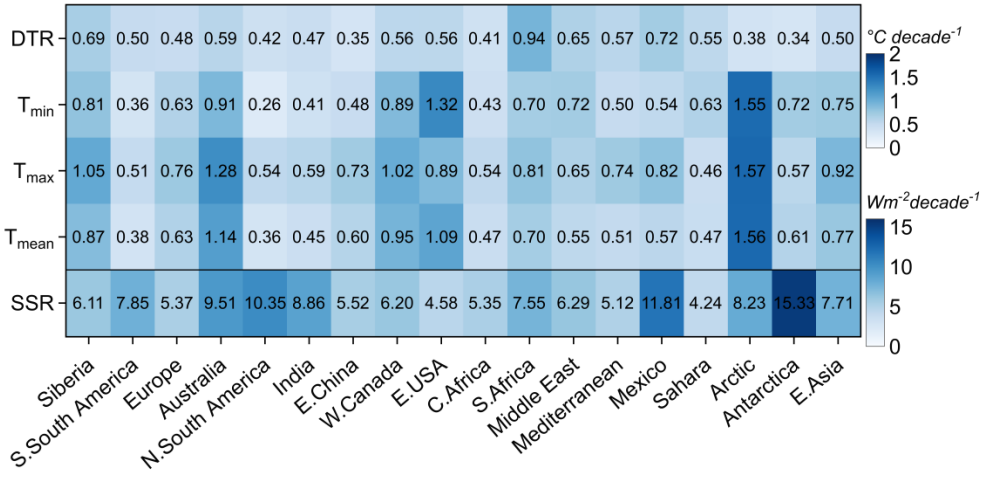
	1984-1999	2000-2009	2010-2018	1984-2018
Globe - Land Δ(SSR)	0.58 [-5.74, 5.71]	-0.02 [-3.56, 2.35]	**7.47 [4.93, 11.18]**	**1.79 [0.58, 3.21]**
Globe - Land Δ(T_{mean})	**0.37 [0.12, 0.63]**	0.19 [-0.45, 0.65]	**0.45 [-0.29, 1.22]**	**0.34 [0.28, 0.4]**
Globe - Land Δ(T_{max})	**0.37 [0.11, 0.68]**	0.26 [-0.38, 0.74]	**0.45 [-0.16, 1.09]**	**0.38 [0.31, 0.44]**
Globe - Land Δ(T_{min})	**0.35 [0.11, 0.63]**	0.11 [-0.32, 0.65]	**0.4 [-0.38, 1.22]**	**0.31 [0.25, 0.37]**
Globe - Land Δ(DTR)	0.004 [-0.05, 0.05]	0.09 [-0.01, 0.22]	- 0.03 [-0.15, 0.13]	**0.06 [0.05, 0.08]**
NH-Land Δ(SSR)	0.62 [-5.27, 6.36]	-1.3 [-8.25, 2.09]	**5.95 [3.43, 10.61]**	**1.55 [0.44, 2.44]**
NH-Land Δ(T_{mean})	**0.48 [0.19, 0.8]**	0.41 [-0.08, 0.77]	**0.37 [-0.22, 1.25]**	**0.4 [0.32, 0.48]**
NH-Land Δ(T_{max})	**0.41 [0.09, 0.77]**	**0.37 [0.01, 0.83]**	**0.36 [-0.13, 1.17]**	**0.42 [0.35, 0.5]**
NH-Land Δ(T_{min})	**0.49 [0.23, 0.81]**	0.42 [-0.14, 0.83]	**0.33 [-0.3, 1.35]**	**0.39 [0.31, 0.47]**
NH-Land Δ(DTR)	-0.06 [-0.14, 0.01]	0.07 [-0.09, 0.2]	-0.02 [-0.19, 0.17]	**0.04 [0.02, 0.07]**
SH-Land Δ(SSR)	-1.02 [-7.86, 8.74]	-0.35 [-8.19, 4.9]	**10.26 [6.87, 14.39]**	**3.1 [1.05, 4.64]**
SH-Land Δ(T_{mean})	0.14 [-0.1, 0.35]	0.42 [-0.34, 1.16]	**0.61 [0.15, 1.14]**	**0.2 [0.14, 0.27]**
SH-Land Δ(T_{max})	**0.21 [-0.03, 0.49]**	0.42 [-0.34, 1.16]	**0.56 [0.37, 0.8]**	**0.27 [0.21, 0.34]**
SH-Land Δ(T_{min})	0.05 [-0.18, 0.33]	0.31 [-0.32, 0.95]	**0.43 [0.21, 0.89]**	**0.15 [0.09, 0.21]**
SH-Land Δ(DTR)	**0.13 [0.07, 0.2]**	0.25 [-0.07, 0.46]	0.13 [-0.25, 0.38]	**0.12 [0.09, 0.15]**
Globe -Ocean Δ(SSR)	-3.37 [-10.19, 3.39]	-0.35 [-7.19, 3.04]	**3.51 [2.09, 5.12]**	**-1.35 [-2.28, -0.26]**
Globe - Ocean Δ(T_{mean})	**0.12 [0.04, 0.27]**	0.12 [-0.07, 0.31]	**0.42 [0.14, 0.64]**	**0.15 [0.12, 0.19]**
Globe - Ocean Δ(T_{max})	**0.13 [0.05, 0.27]**	0.12 [-0.07, 0.27]	**0.39 [0.08, 0.76]**	**0.16 [0.13, 0.19]**
Globe - Ocean Δ(T_{min})	**0.13 [0.03, 0.25]**	0.11 [-0.09, 0.35]	**0.4 [0.2, 0.66]**	**0.15 [0.12, 0.19]**
Globe - Ocean Δ(DTR)	0.01 [-0.01, 0.03]	-0.03 [-0.05, 0.04]	-0.03 [-0.07, 0.03]	**0.005 [0.0, 0.01]**
NH- Ocean Δ(SSR)	-1.54 [-5.95, 4.15]	**1.8 [0.1, 5.79]**	**1.68 [-2.04, 4.04]**	**0.19 [-0.39, 1.06]**
NH- Ocean Δ(T_{mean})	**0.29 [0.14, 0.44]**	**0.31 [0.0, 0.66]**	**0.44 [-0.01, 0.84]**	**0.25 [0.21, 0.28]**
NH- Ocean Δ(T_{max})	**0.29 [0.14, 0.43]**	**0.28 [0.01, 0.58]**	**0.45 [-0.06, 0.84]**	**0.24 [0.2, 0.28]**
NH- Ocean Δ(T_{min})	**0.29 [0.14, 0.43]**	**0.29 [0.05, 0.65]**	**0.43 [0.04, 0.85]**	**0.25 [0.21, 0.28]**
NH- Ocean Δ(DTR)	-0.0001 [-0.01, 0.02]	-0.02 [-0.06, 0.03]	-0.02 [-0.04, 0.02]	**-0.006 [-0.01, -0.0]**
SH- Ocean Δ(SSR)	-4.32 [-15.19, 4.72]	-1.66 [-14.26, 2.16]	**3.76 [1.46, 6.98]**	**-1.77 [-3.14, -0.35]**
SH- Ocean Δ(T_{mean})	**0.04 [-0.08, 0.15]**	-0.01 [-0.23, 0.19]	**0.34 [0.04, 0.63]**	**0.08 [0.05, 0.12]**
SH- Ocean Δ(T_{max})	**0.04 [-0.05, 0.17]**	-0.02 [-0.22, 0.13]	**0.33 [0.04, 0.64]**	**0.09 [0.05, 0.13]**
SH- Ocean Δ(T_{min})	0.04 [-0.07, 0.12]	0.01 [-0.25, 0.2]	0.32 [0.04, 0.62]	**0.08 [0.04, 0.12]**
SH- Ocean Δ(DTR)	0.02 [-0.0, 0.05]	-0.003 [-0.04, 0.05]	-0.05 [-0.12, 0.04]	**0.01 [0.01, 0.02]**



(a)



(b)



(c)

Figure AE2. Standard deviation of the spatially averaged decadal changes in T_{mean}, T_{max}, T_{min}, DTR as well as in SSR over 18 world land areas (see Fig. S1) during the periods: 1984 – 1999 (a), 2000 – 2009 (b) and 2010-2018 (c).

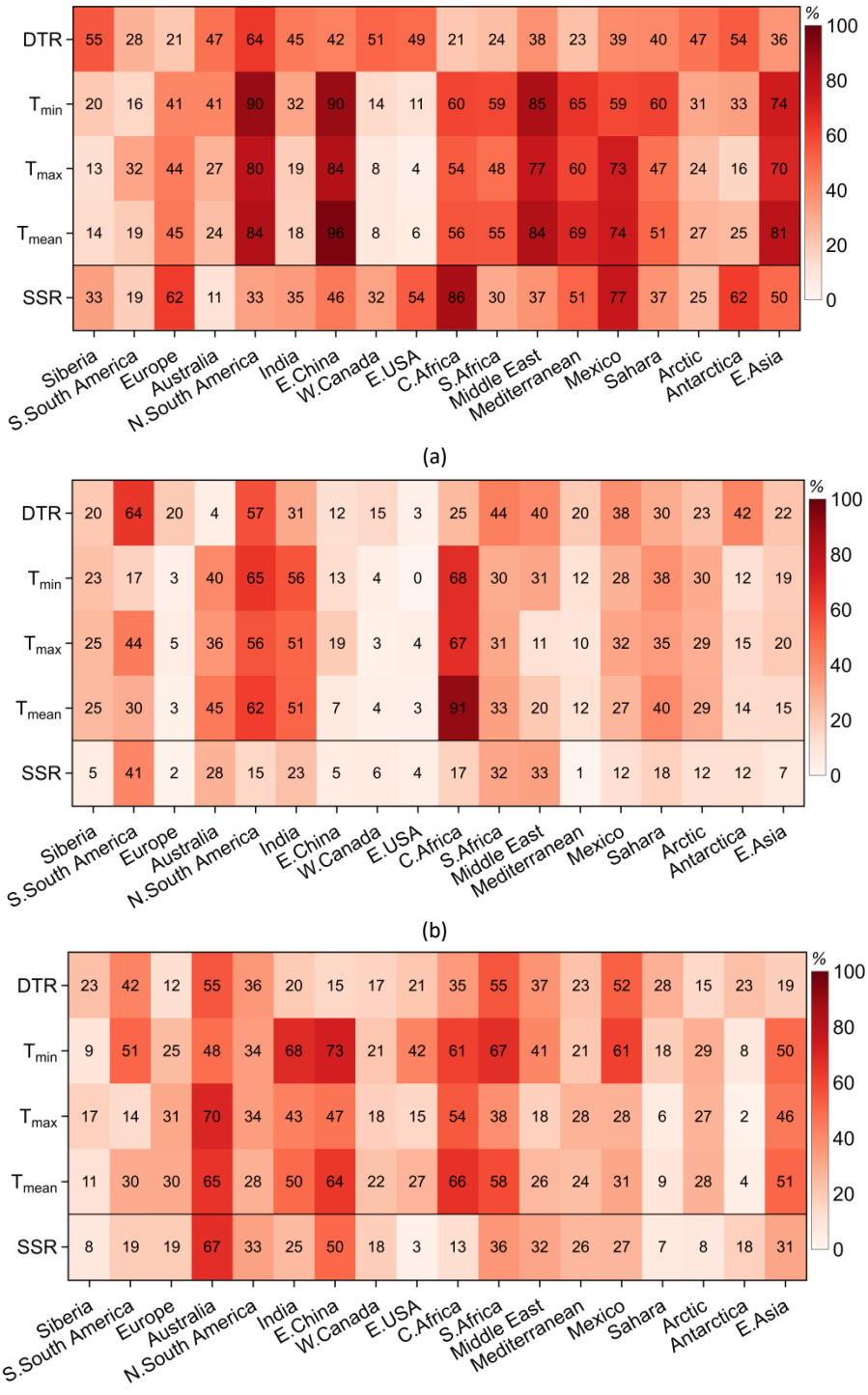
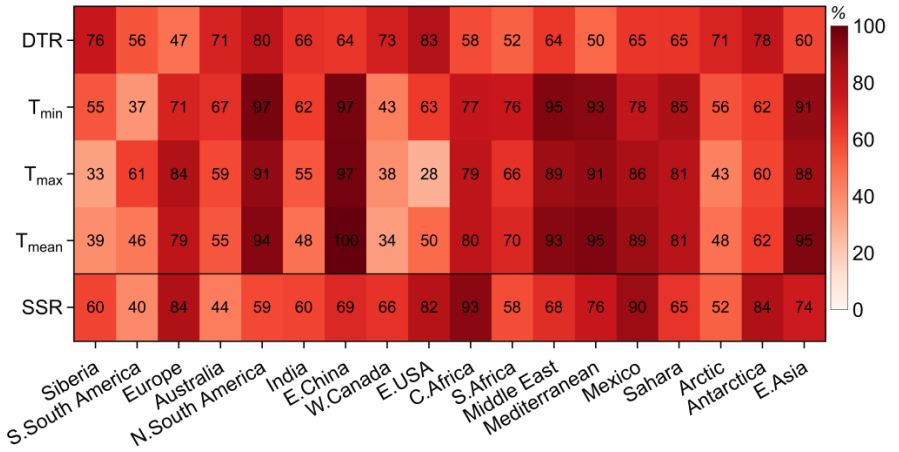
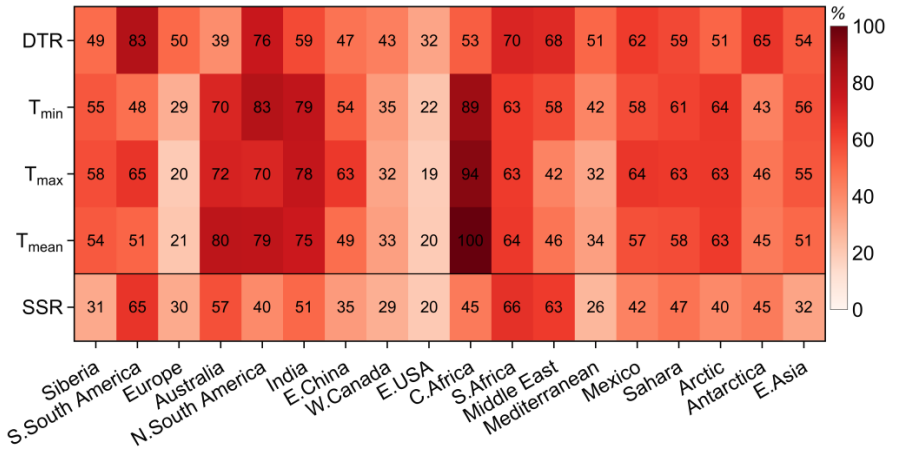


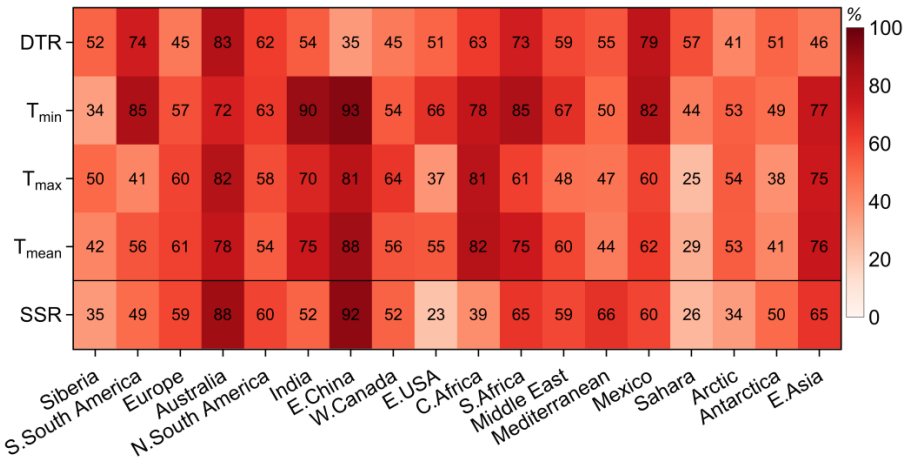
Figure AE3.The percentage of cells that have statistically significant changes atthe 95% confidence level of the decadal changes in T_{mean}, T_{max}, T_{min}, DTR as well as SSR over the 18 world land areas (Fig. S1) during the periods: 1984 – 1999 (a) and 2000 – 2009 (b) and 2010-2018 (c).



(a)



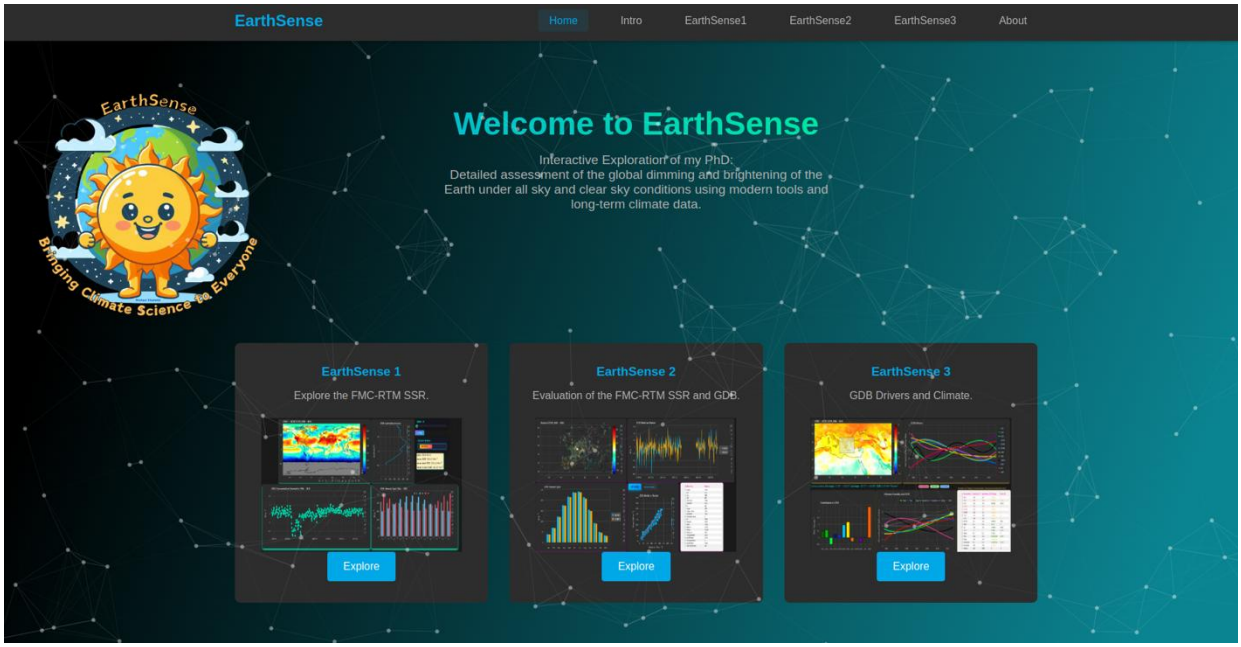
(b)



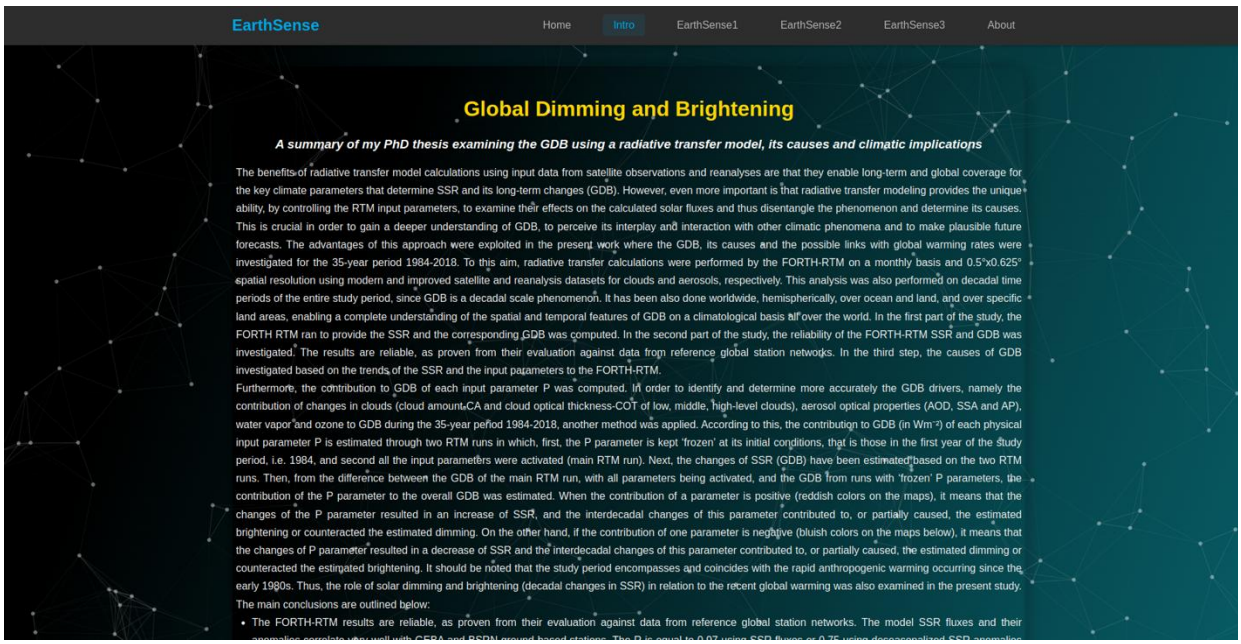
(c)

Figure AE4. The percentage of cells that have statistically significant changes at the70% confidence level of the decadal changes in T_{mean}, T_{max}, T_{min}, DTR as well as SSR over 18 world land areas (Fig. S1) during the periods: 1984 – 1999 (a) and 2000 – 2009 (b) and 2010-2018 (c).

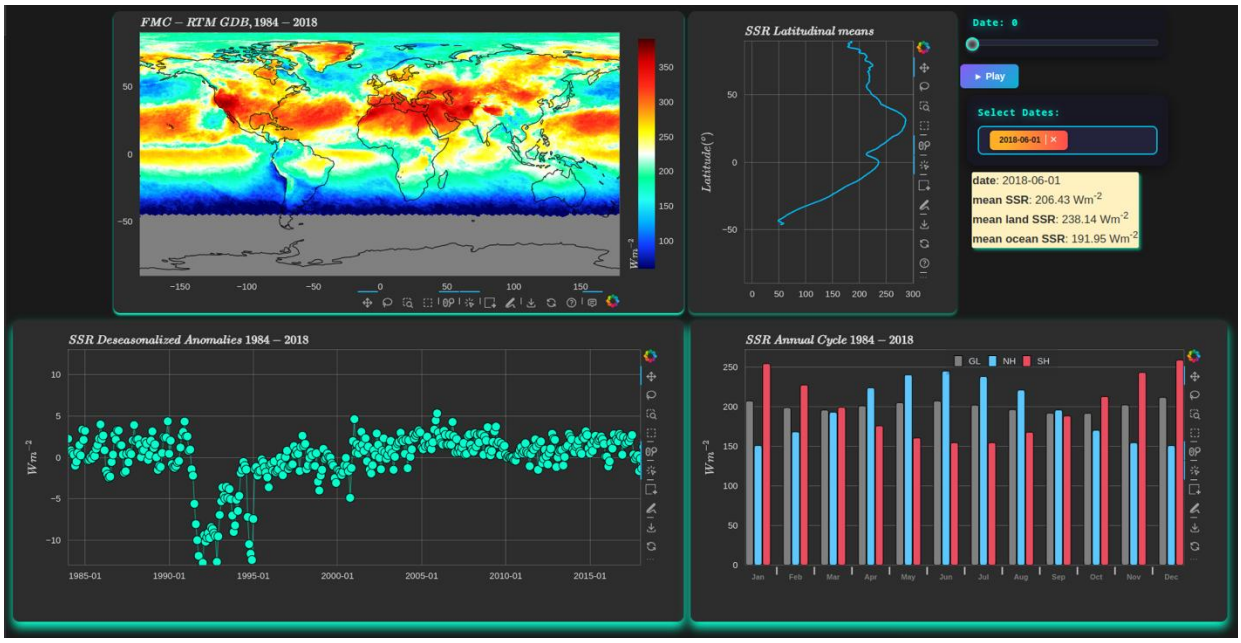
Appendix F



(a)



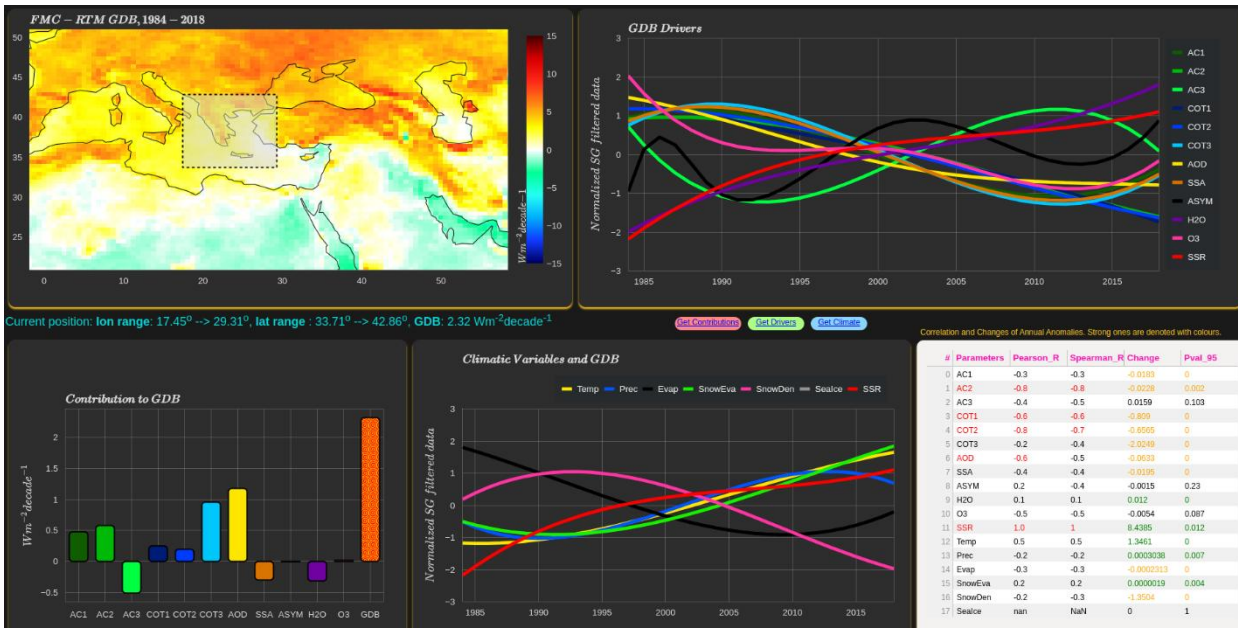
(b)


FMC – RTM GDB, 1984 – 2018
SSR Latitudinal means
Latitude(°)
Date: 0
▸ Play
Select Dates:
2018-06-01
date: 2018-06-01
mean SSR: 206.43 Wm-2
mean land SSR: 238.14 Wm-2
mean ocean SSR: 191.95 Wm-2
SSR Deseasonalized Anomalies 1984 – 2018
SSR Annual Cycle 1984 – 2018
GL
NH
SH

(c)


Stations' GDB, 1984 – 2018
SSR Model vs Station
model
station
SSR Annual Cycle
Model
Station
SSR FLUXES
SSR ANOMALIES
SSR Model vs Station
Model (Wm⁻²)
Station (Wm⁻²)
Metrics Values
0 Name 1249
1 Lat 47.8
2 Lon 3.55
3 Alt 207
4 StartYear 1984
5 EndYear 2018
6 N 324
7 slope 1.01
8 slope_anom 1.09
9 intercept 1.617
10 intercept_anom 0
11 R 0.991
12 Ranom 0.873
13 Bias 2.995
14 Bias % 2.175
15 Rmse 11.112
16 Rmse % 8.07
17 ChangeModel 4.937
18 pv95Model 0.273
19 ChangeStation 0
20 pv95Station 0.928
21 Sign Agreement Yes

(d)



(e)



(f)

Figure AF1. Screenshots of the EarthSense web application. This applications is currently for internal usage and enables the user to interact and explore the main results of this PhD.